

Universität Potsdam
Mathematisch-Naturwissenschaftliche Fakultät



**Kumulative Habilitationsschrift
für die Lehrbefähigung in Geologie**

**Neotectonic deformation
over space and time
as observed by space-based geodesy**

Dr. Sabrina Metzger
GFZ Potsdam

Datum der Disputation:
12 Mai 2023

This work is protected by copyright and/or related rights. You are free to use this work in any way that is permitted by the copyright and related rights legislation that applies to your use. For other uses you need to obtain permission from the rights-holder(s).

<https://rightsstatements.org/page/InC/1.0/?language=en>

Vorsitzender der Prüfungskommission:

- Prof. Dr. Bodo Bookhagen, Universität Potsdam, DE

Gutachter:

- Prof. Dr. Freysteinn Sigmundsson, University of Iceland, Reykjavík, IS
- Prof. Dr. Roland Bürgmann, University of California, Berkeley, US
- Prof. Dr. Peter van der Beek, Universität Potsdam, DE

Published online on the

Publication Server of the University of Potsdam:

<https://doi.org/10.25932/publishup-59922>

<https://nbn-resolving.org/urn:nbn:de:kobv:517-opus4-599225>

Für meine wunderbaren Kinder und ihr Interesse an meinen “Erdbeeren”

Contents

1	Introduction	5
1.1	Towards a better understanding of the seismic cycle	5
1.2	Tackle crustal deformation sources from space	7
1.3	Tectonic settings and personal scientific achievements	8
1.4	Thesis outline	9
2	Tectonic geodesy	11
2.1	Data collection, archives and processing software	11
2.2	Geodetic time-series analysis	13
2.3	From fault slip observations to source models	15
3	Applications	19
3.1	Continental collision: Coseismic, long-term, and triggered slip	19
3.1.1	The 2015 M_w 7.2 Sarez, Pamir, earthquake <i>Metzger et al., 2017, Tectonics</i>	19
3.1.2	Northward shortening of the Pamir <i>Zubovich et al., 2016, Tectonics</i>	37
3.1.3	Coseismically-triggered slip <i>Zubovich et al., 2022, Tectonics</i>	49
3.1.4	Westward flow of the Pamir <i>Metzger et al., 2020, Tectonics</i>	69
3.1.5	Greater Pamir neotectonics from InSAR <i>Metzger et al., 2021, JGR</i>	91
3.1.6	Ongoing slab break-off in the Hindu Kush <i>Kufner et al., 2021, Nat. Comm.</i>	117
3.2	Oceanic subduction: Afterslip, visco-poro-elastic relaxation, earthquake coupling	131
3.2.1	Afterslip following the 2014 Iquique-Pisagua earthquake <i>Hoffmann et al., 2022, JGR</i>	131
3.2.2	The role of poroelasticity in the postseismic stage <i>Peña et al., 2022, GRL</i>	155
3.2.3	Coupling of deep and shallow subduction earthquakes <i>Moreno et al., 2018, Nat. Geosc.</i>	169
3.3	Transform zones: Seismic swarms and fault creep	181
3.3.1	On the nature of tectonic earthquake swarms <i>Passarelli et al., 2018, EPSL</i>	181
3.3.2	Relation between fault creep and seismic scaling laws <i>Tormann et al., 2013, GJI</i>	193
4	Synthesis	201
5	Outlook	205
5.1	Tackling societal problems	205
5.2	Systemic research questions	206
	Bibliography	209
	Acknowledgements	217

Zusammenfassung

Alfred Wegeners Thesen des Kontinentaldrifts fanden erst in den 1960er und 1970er Jahren Akzeptanz, als die krustalen Polarisationswechsel auf dem atlantischen Meeresboden entdeckt wurden und Erdbebenkataloge das Abtauchen von ozeanischer Kruste unter kontinentale Kruste abbildeten (*Wadati-Benioff-Zone*). Es dauerte jedoch weitere 20 Jahre, bis die Geodäsie erstmals Platten*bewegung* sicht- und quantifizierbar machte. Seit dann sind satellitengestützte Messmethoden aus der neotektonischen Forschung nicht mehr wegzudenken.

Dank einer stetig (zeitlich und räumlich) wachsenden Anzahl instrumenteller Beobachtungsdaten wird unser Verständnis des Erdbebenzyklus—das Wechselspiel zwischen tektonischem Spannungsauf- und -abbau—immer komplexer. Das klassische Konzept, nur Erdbeben setzten die zuvor linear aufgebaute Spannungsenergie instantan frei, wird heutzutage durch eine Vielzahl von zusätzlichen schnelleren und langsameren Prozessen ergänzt. Beispiele dafür sind getriggerte Versätze (*triggered slip*), Nachbeben (*afterslip*), postseismische und viskoelastische Relaxation der tieferen Kruste, dynamische, elastische Veränderungen des Gesteins-Porendrucks, aseismisches Kriechen sowie Spannungsabbau durch kleine Erdbebenschwärme.

Anhand von elf begutachteten und bereits veröffentlichten Arbeiten präsentiere ich in meiner Habilitationsschrift die Diversität krustaler Deformationsprozesse. Ich analysiere Zeitreihen von Radar-Satellitenaufnahmen und satellitengestützten Positionierungssystemen um die tektonische Oberflächenbewegung zu quantifizieren. Der Vergleich von kinematischen Beobachtungen mit geologischen und seismischen Indizien sowie die Simulation ebenjener durch rechnergestützte Modelle ermöglichen mir, die verursachenden krustalen Prozesse besser verstehen.

Der Hauptteil meiner Arbeiten beschreibt rezente, krustale Bewegungen im Pamir, Hindu Kush und Tien Shan, welche zusammen das westliche Ende der kontinentalen Kollisionszone zwischen dem indischen und eurasischen Kontinent bilden. Rund um ein starkes Erdbeben, welches 2015 das Zentralpamir erschüttert hat, zeige ich vielseitige Beispiele von hochaktiver krustaler Deformation. Verursacht werden diese Bewegungen durch den nordwestindischen Kontinentalsporn, welcher (fast) ungebremst in den Pamir hineinrammt, ihn auftürmt, zusammenquetscht, und ihn gravitationsbedingt gegen Westen ins tadschikische Becken kollabieren lässt.

Der zweite thematische Schwerpunkt liegt auf Prozessen, welche durch Megathrust-Erdbeben, also Beben mit einer Magnitude >8 , hervorgerufen werden. Diese Anwendungen fokussieren sich auf die ozeanischen Subduktionszone von Chile und zeigen die Wichtigkeit vertikaler Hebungsdaten um, beispielsweise, den Einfluss tektonischer Prozesse auf den Gesteins-Porendruck zu verstehen.

Zusammenfassend veranschaulichen und bestätigen meine Arbeiten, wie stark und komplex die oben beschriebenen Prozesse räumlich und zeitlich korrelieren, und dass das klassische Konzept des Erdbebenzyklus überholt ist. Letztere Einsicht hat grossen Einfluss auf probabilistische seismische Gefährdungsanalysen, welche grundsätzlich statistische Vorhersagbarkeit annehmen.

Abstract

Alfred Wegeners ideas on continental drift were doubted for several decades until the discovery of polarization changes at the Atlantic seafloor and the seismic catalogs imaging oceanic subduction underneath the continental crust (*Wadati-Benioff Zone*). It took another 20 years until plate *motion* could be directly observed and quantified by using space geodesy. Since then, it is unthinkable to do neotectonic research without the use of satellite-based methods.

Thanks to a tremendous increase of instrumental observations in space and time over the last decades we significantly increased our knowledge on the complexity of the seismic cycle, that is, the interplay of tectonic stress build up and release. Our classical assumption, earthquakes were the only significant phenomena of strain release previously accumulated in a linear fashion, is outdated. We now know that this concept is actually decorated with a wide range of slow and fast processes such as triggered slip, afterslip, post-seismic and visco-elastic relaxation of the lower crust, dynamic pore-pressure changes in the elastic crust, aseismic creep, slow slip events and seismic swarms. On the basis of eleven peer-reviewed papers studies I here present the diversity of crustal deformation processes. Based on time-series analyses of radar imagery and satellited-based positioning data I quantify tectonic surface deformation and use numerical and analytical models and independent geologic and seismologic data to better understand the underlying crustal processes.

The main part of my work focuses on the deformation observed in the Pamir, the Hindu Kush and the Tian Shan that together build the highly active continental collision zone between NW-India and Eurasia. Centered around the Sarez earthquake that ruptured the center of the Pamir in 2015 I present diverse examples of crustal deformation phenomena. Driver of the deformation is the Indian indenter, bulldozing into the Pamir, compressing the orogen that then collapses westward into the Tajik depression. A second natural observatory of mine to study tectonic deformation is the oceanic subduction zone in Chile that repeatedly hosts large subduction earthquakes of magnitude 8 and more. These are best to study post-seismic relaxation processes and coupling of large earthquake.

My findings nicely illustrate in a how complex fashion and how much the different deformation phenomena are coupled in space and time. My publications contribute to the awareness that the classical concept of the seismic cycle needs to be revised, which, in turn, has a large influence in the classical, probabilistic seismic hazard assessment that primarily relies on statistically solid recurrence times.

1 Introduction

1.1 Towards a better understanding of the seismic cycle

Driven by mantle convection, tectonic plate drift causes crustal deformation and strain accumulation at the margins and – to a minor extent – also within tectonic plates (Figure 1.1b). Once the accumulated strain energy exceeds the frictional strength of the crust it is usually released instantaneously in an earthquake. Both sides of the ruptured fault exhibit permanent translation and the whole region is moved by elastic waves traveling through the crust and along the surface. By nature, plate-boundaries provide access to fresh water and other georesources and thus are popular regions for large cities (Figure 1.1a). Therefore earthquakes with moment magnitudes of M6 and above often cause high fatalities and infrastructure damage. As consequence, a better understanding of the kinematic and dynamic processes controlling the build up of strain and of the physics of the brittle, upper crust are needed to mitigate the effect of such natural disasters and to build the base for a safe and thriving society. Thus, a better understanding when and how earthquakes occur is a basic prerequisite to achieve the UN’s 2030 Agenda for Sustainable Development (*United Nation Resolution, 2015*).

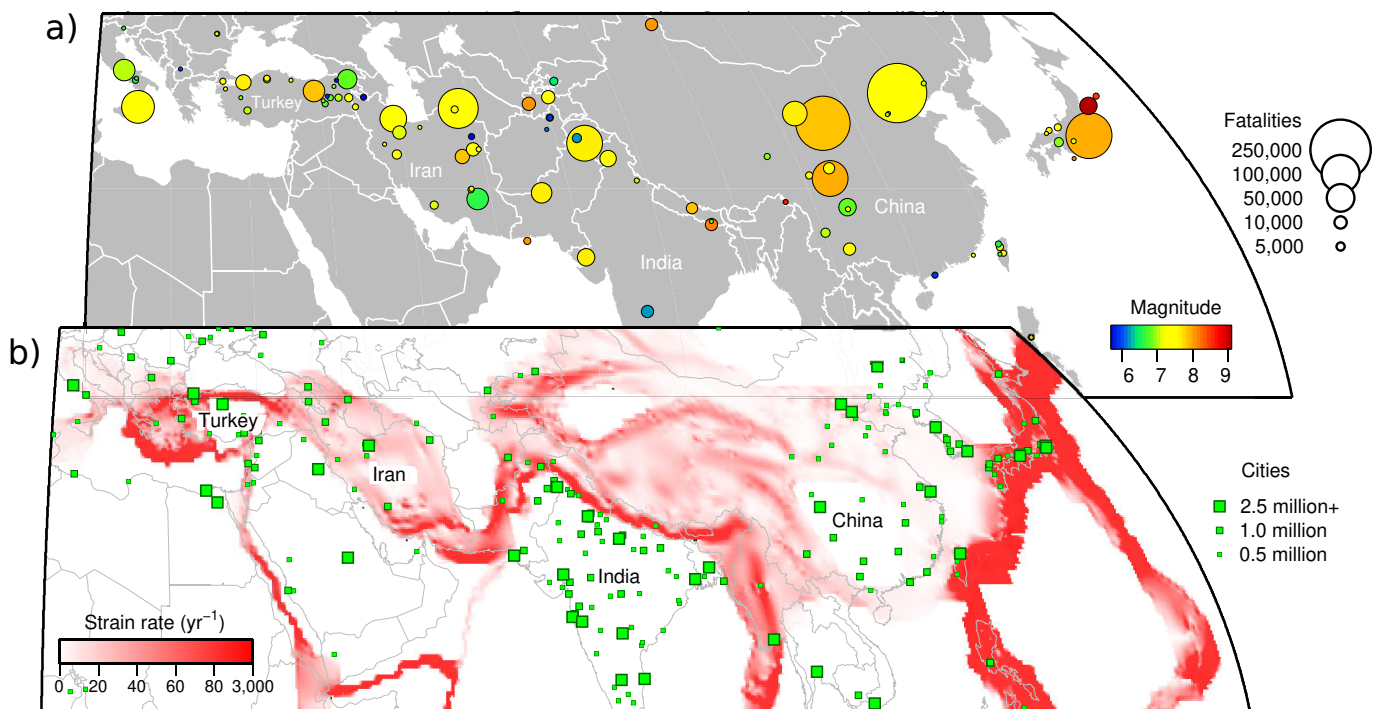


Figure 1.1: Spatial correlation between a) the most destructive earthquakes since 1900 (US Geological Service) and b) densely populated regions and high tectonic strain (*Kreemer et al., 2014*). Figure modified from *Elliott et al. (2016)*.

Plates drift with a quasi-constant rate over the course of millions of years (*Bunge et al., 1998*), but the spatio-temporal behavior of evolving and inherited faults in the brittle upper crust are highly complex. They comprise a repeating series of fast, intermediate and slow-moving epochs, known as the seismic cycle (*Benioff, 1951*). In its most simple form, the cycle begins with a long, *inter*-seismic period of slow strain accumulation across a locked fault system that is then instantaneously released by an abrupt *co*-seismic rupture. Given the geologically short instrumental time-series it is still unclear if these cycles are periodic, random, or clustered in time. For large (M7+) earthquakes the cycle is extended by a significant, stress-driven readjustment of the rupture surface (*afterslip*,

often caused by seismic *aftershocks*) within the days/weeks following the earthquake, and by *post*-seismic, visco-elastic relaxation processes of the more plastic, lower crust within months and decades following the event (*Amos and Gerald, 1974; Wang et al., 2012*).

The occurrence of large earthquakes is so irregular in space, size and time, and depends on so many unknown parameters that the predictive power to forecast the location and size of the next big event is depressingly low as the following examples of larger earthquakes show: The 2010 Haiti (M7) and the 2011 Tohoku-Oki, Japan, (M9) earthquake, for example, occurred in regions that were unexpected to host such devastating earthquakes (e.g. *Huang and Zhao, 2013; Kagan and Jackson, 2013; Stein et al., 2012*). The 2015 Gorkha, Nepal, earthquake (M7.8) produced much lower ground acceleration than anticipated (*Takai et al., 2016*) and than compared to the (much smaller) Haiti earthquake. The 2016 Kaikoura, New Zealand, earthquake (M7.8) caused by an more complex, multi-fault rupture than ever imagined, including several fault systems with sub-faults oriented unfavourably to the preferred slip direction (Figure 1.2a). High-resolution radar satellite imagery of the recent 2019 Ridgecrest earthquake sequence (M6-7) showed that fault damage zones are much wider than anticipated (Figure 1.2b). And finally, the recent improvement on dense temporal data sampling provide evidence of highly variable, aseismic fault slip, usually referred to as fault creep or silent slip events. These data vaporize the concept of a inter-seismic, steady-state phase in the seismic cycle, but also raise hope for the detection of precursory earthquake signals (e.g. *Bedford et al., 2015, 2020; Socquet et al., 2017*). On a larger time scale, the analysis of sea shore data (*Sieh et al., 2008*) and multi-cycle models using analog material (*Kosari et al., 2022*) suggest that, if observed long enough, multiple seismic cycles group together in supercycles.

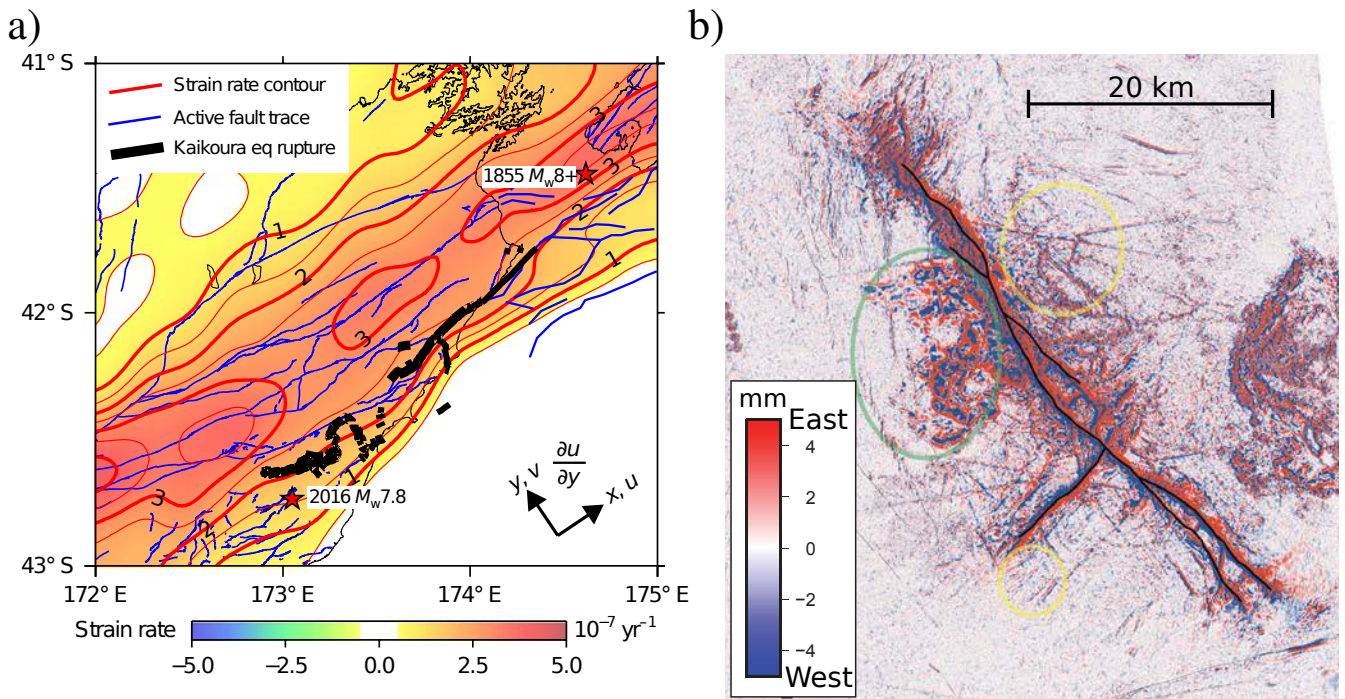


Figure 1.2: Examples of complex earthquake fault ruptures. a) The 2016 M7.8 Kaikoura, New Zealand, earthquake activated a multi-fault system that offsets from the high-strain region and includes unfavourable fault orientations. b) Radar phase gradient map highlighting the broad damage zone of the 2019 Ridgecrest, California, earthquake sequence. Figures modified from a) *Lamb et al. (2018)* and b) *Xu et al. (2020)*.

Naturally, more geodetic observations provide insight into more complex fault loading processes than previously thought of, and it becomes clear that the seismic cycle is a highly non-linear process. As consequence, the concept of probabilistic seismic hazard models must be revisited. It is not sufficient to incorporate seismic catalogs and the current state of crustal strain only, but also more knowledge on the dynamic behaviour of faults and their interaction with their environment, e.g. adjacent fault systems, rheological properties and pore pressure.

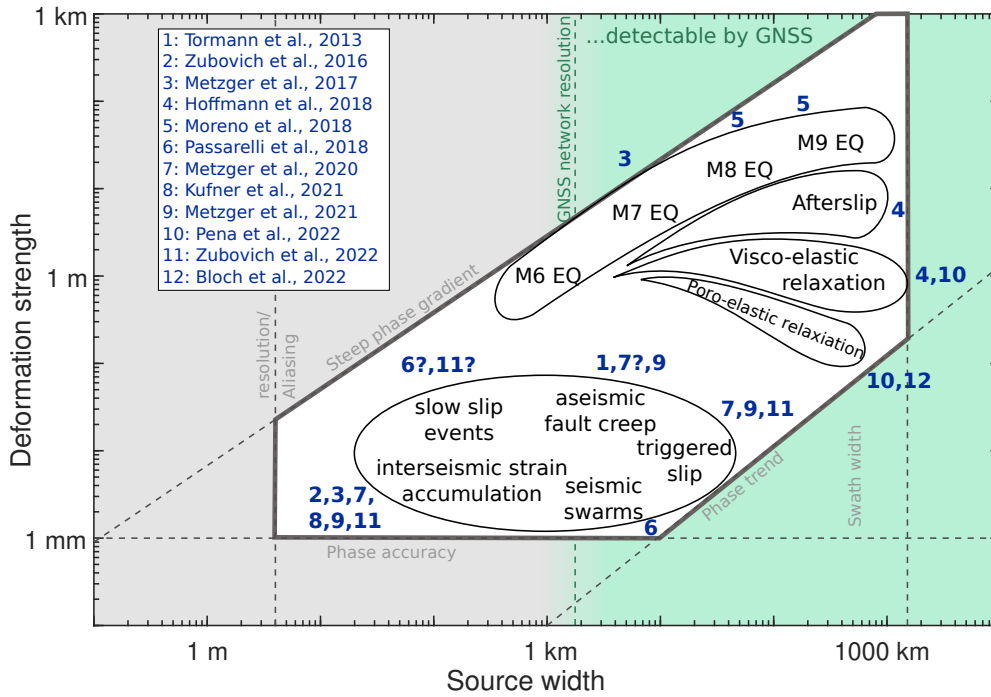


Figure 1.3: Detection range of InSAR and GNSS applications, inspired by a figure of *Massonnet and Feigl* (1998), in relation to the strength of the deforming source. Limiting factors are GNSS network sparsity (fading green background), InSAR signal resolution, and geometry limitations. The numbers refer to my own publications where these phenomena are discussed (Chapter 3).

1.2 Tackle crustal deformation sources from space

Aseismic fault loading significantly contributes to the current state of stress and is best studied using modern geodesy. The interdisciplinary research field of *tectonic geodesy* (Section 2) combines geodetic measurement techniques, geophysical signal analysis, and knowledge of the geologic structures and rheology to observe and interpret recent tectonic deformation using kinematic and dynamic modeling. The most popular observation techniques are Global Navigation Satellite System (GNSS) positioning and synthetic-aperture radar (SAR) data, where the latter is often analyzed as differential interferograms (InSAR, Chapter 2). To study deformation over time these can be analyzed by simply measuring the offset signal between before- and after-event data, or by applying time-series analysis to a whole series of observations to extract also second-order signals that vary in time (transients). Installed on solid ground, GNSS receivers record pointwise positioning offsets or deformation rates in three dimensions (East, North, Up) relative to a geo-centered tectonic plate reference model. Space-borne radar data is confined to two line-of-sights of the ascending and descending orbit passes and are provided in a local reference frame restricted to the satellite's footprint. If combined, these two observation techniques provide surface deformation data with mm-accuracy, sampled at ~ 10 -100 m in space and seconds to days in time covering areas of 100+ km. I will show in several case studies (Chapter 3) that they are capable to detect nearly all phenomena of the seismic cycle, if their deformation signal is propagated to the surface (Figure 1.3).

The observations are validated by numerical and analytical models to constrain key parameters of the responsible deformation source. Of key interest are rupture dimension and geometry, amount and timing of co-seismic slip and afterslip, and accumulation of slip deficit during the interseismic period. Rupture size and slip are valuable information to better constrain the seismic energy release. In the interseismic phase, the amount of locking and the slip deficit provide key aseismic information on seismic hazard estimates. Space-borne observations are preferably ground-truthed by e.g. structural, geomorphologic and seismic observations, which add further constraints to the model assumptions and data/model interpretation. A comparison to the geologic archive (e.g. for slip rates) improves our understanding of long-term (plastic) and short-term (elastic) deformation processes. So far, this so-called *deformation partitioning* was not-well resolved and conventional, but spatio-temporally sparse strain analyses probably overlooked fundamental patterns contributing to permanent deformation. This is also relevant from the perspective of a seismic hazard assessment that is mostly influenced by the short-term, elastic energy release on faults.

1.3 Tectonic settings and personal scientific achievements

The studies presented in my habilitation thesis mostly focus on convergent plate-boundaries in the greater Pamir region (Central Asia) and the Chile Subduction Zone, which are two key natural laboratories of my current employer to study earthquake, plate-boundaries and mountain building. A smaller part of the work presented here deals with the tectonic phenomena observed at volcanic systems at divergent plate-boundaries (North Iceland) and transform plate-boundaries (California Shear Zone).

The **Pamir continental collision zone** (Figure 2.1) is a N–S converging system located at the western tip of the India-Asia collision zone and the Himalayan orogenic belt (*Burtman and Molnar, 1993*). It is a rugged and highly active orogen in a remote, politically instable region of Central Asia. Currently, the Pamir accommodates a third of the Eurasia-India convergence and hosts decadal M7 earthquakes that occur mostly along its northern margin, less in the center, where the most recent, 2015 M7.2 Sarez earthquake ruptured the main NE-trending sinistral, strike-slip fault. To the north the Pamir is confined by the Tian Shan mountains, to the west by the Tajik Basin. The latter forms, together with the Alai valley (embedded between the Pamir and the Tian Shan and nearly consumed by them) two remnants of the Paleo-Tethys ocean (e. g. *van Hinsbergen et al., 2012*). Towards southwest, the Pamir links to the Afghan Hindu Kush. I have quantified the kinematics of the most active faults bounding the Pamir (*Bloch et al., 2022; Kufner et al., 2018, 2021; Metzger et al., 2017, 2020, 2021a; Perry et al., 2018; Zubovich et al., 2016, 2022*). I made use of a new GNSS network crossing the northern and western Pamir and the transition to the Hindu Kush along five dense observation profiles, filling a prominent data gap in the West Pamir. The 2015 Pamir earthquake occurred during the observation period, which is why I could use those data to not only learn about the interseismic, but also the co-seismic behaviour of the most important faults in the Pamir region. I show that several of those faults exhibit 10-20 mm/yr of interseismic slip (which is surprisingly high for a continental setting), that the 2015 earthquake had an impact on many of those, and that oceanic evaporites play an important role in the regional strain accumulation. Thanks to the combination of GNSS with supra-regional InSAR time-series, the surface deformation of the Pamir and the fold-thrust-belt in the Tajik basin is resolved at great detail, and we can observe not only tectonic signals but also halokinesis and seasonal, hydrological effects.

The **Chile oceanic subduction zone** is the central part of the oceanic subduction system stretching along almost the full western margin of the South American continent. Here, the oceanic Nazca plate subducts under the South American plate in a ENE-direction of 65-70 mm/yr (*Angermann et al., 1999; Norabuena et al., 1999*). My contributions to the recent studies on this region deal with phenomena related to the postseismic phase following the 2014 M8.1 Iquique-Pisagua earthquake (*Hoffmann et al., 2018*), the 2010 M8.8 Maule megathrust earthquake (*Peña et al., 2022*) and the 2016 M7.6 southern Chile earthquake that ruptured a plate-boundary segment that was seismically quiet since the great 1960 M9.5 Chile earthquake (*Moreno et al., 2018*). These works highlight the importance of satellite-geodetic observations to better understand aseismic processes like plate-relocking, or large-scale fluid processes that are best seen in vertical deformation data.

Two additional studies deal with strain accumulation in the **California continental shear zone** and an analysis of frequent seismic swarms in the **Icelandic rift zone**. The Californian study was conducted at the Parkfield fault segment, a creeping section of the dextral San Andreas fault in the Western US, separating the Pacific and the North American plate. This segment is famous for M6 earthquakes repeatedly occurring over the last 150 years (*Bakun and Lindh, 1985*). By correlating temporal changes in the b-values and in the observed surface creep we showed that microearthquakes might reflect the loading stage of a fault (*Tormann et al., 2013*). The multi-disciplinary study of repeated seismic swarms at the Húsavík Flatey fault, a transform fault in the Tjörnes Fracture Zone just offshore North Iceland tried to tackle the question how significant the contribution of those swarms is to release tectonic loading (*Passarelli et al., 2018*).

1.4 Thesis outline

Chapter 2 provides a brief account on the data provenience, the more technical aspects of geodetic data processing and tectonic source modeling strategies. I first introduce three projects, in which I could install and monitor my own, respectively, get access to existing GNSS networks in the regions of interest. Then I briefly outline how GNSS and InSAR data are processed into (relative) positioning time-series and how those can be used to extract various types of deformation signals. The last part documents source modeling strategies to constrain best-fitting model parameters using linear inversion and non-linear optimization techniques.

The core of my habilitation builds Chapter 3, which reprints eleven independent publications in peer-reviewed journals, of which six are first-authored by me or count as equal-first-authorships. Together they form a comprehensive documentation of all seismic and aseismic deformation sources currently known (Figure 1.3). Each publication is preceded with a short synthesis of the scientific application, the methodological advances and the individual contributions of all authors.

The habilitation ends with a synthesis of all my works presented here (Chapter 4) and an outlook discussing the potential of space-based geodesy and its relevance to tackle societal problems, to the geoscientific curriculum at Potsdam university in general, and to study mountainbuilding in a systemic fashion (Chapter 5.1).

2 Tectonic geodesy

2.1 Data collection, archives and processing software

The ESA Copernicus radar archive

The European Space Agency (ESA) Earth observation program Copernicus launched two radar satellites – Sentinel-1A in 2014, Sentinel-1B in 2016 – to build the first comprehensive data archive of tectonically active regions worldwide (Torres *et al.*, 2012). Since then, the two satellites provide new acquisitions every 6-12 days of the said regions in two view angles (ascending and descending mode)¹. The satellites operate in the micro-wave domain (C-Band) with a radar wave length of 5.6 cm that can penetrate clouds and work also at night, but is significantly affected by air pressure and water vapor changes in the atmosphere (causing signal delay) and surface changes due to snow and vegetational growth (causing signal destruction and image decorrelation). The data are distributed via the open-access Copernicus Open Access Hub² as unit tiles stretching over 240 km × 200 km (blue/red polygons in Figure 2.1). The original ground resolution is $\sim 2.3 \times 12$ m, but for large-scale, tectonic applications the SAR images are often downsampled (multi-looked) to ~ 100 m. If used in combination with GNSS data providing ground-truth in a continental reference frame, the resulting time-series of now up to 8 years can be used to derive continent-scale tectonic deformation maps (Ou *et al.*, 2022; Weiss *et al.*, 2020).

To compute single interferograms and estimate amplitude offsets (via cross-correlation techniques) as in Metzger *et al.* (2017); Peña *et al.* (2022) I used the GAMMA SAR processing software (Werner *et al.*, 2000). When working with large interferometric time-series covering the whole greater Pamir region (Metzger *et al.*, 2021a) I used automatically-generated interferograms provided by the LiCSAR initiative (Lazeký *et al.*, 2020) and the LiCSBAS time-series analysis code written in python (Morishita *et al.*, 2020). The deformation maps of the large-scale time-series analysis in the greater Pamir region are available in 400 m resolution as data publication (Metzger *et al.*, 2021b).

Overview of GNSS surveys and instrumentation in the Pamir

The rugged topography in the Pamir impedes instrument maintenance, thus, data transfer is difficult and continuously-operating instruments are sparse. The first handful of GNSS stations across the greater Pamir region were installed in 2006 (Mohadjer *et al.*, 2010). A second network in 2009 initiated by the international “Central Asian Water” project (CAWA, Schöne *et al.*, 2013) added a few more stations in the whole region, plus two dense continuous GNSS (cGNSS) profile across the northern margin of the Pamir. The latter build the base of the work presented in Zubovich *et al.* (2016) and Zubovich *et al.* (2022).

The survey GNSS (sGNSS) data presented in Zubovich *et al.* (2010) and Ischuk *et al.* (2013) provided the most detailed insight into the regional kinematics of the greater Pamir before my research activities and field surveys (Figure 2.1). But the existing sGNSS networks did not resolve detailed kinematics in the highly active NW-Pamir and its transition to the Tajik Depression, and the kinematics in the remote Hindu Kush were unclear. In 2013, I built a constantly-growing sGNSS network and supervised the data surveys to close this spatial data gap. Today, ~ 40 markers on five new sGNSS profiles cross the most prominent active faults in the Hindu Kush, and the western, northwestern and northern margin of the Pamir. Their positions were repeatedly measured between 2013

¹Sentinel-1B stopped transmitting data at the end of 2021 and will be replaced by Sentinel-1C (launch planned for April 2023).

²scihub.copernicus.eu

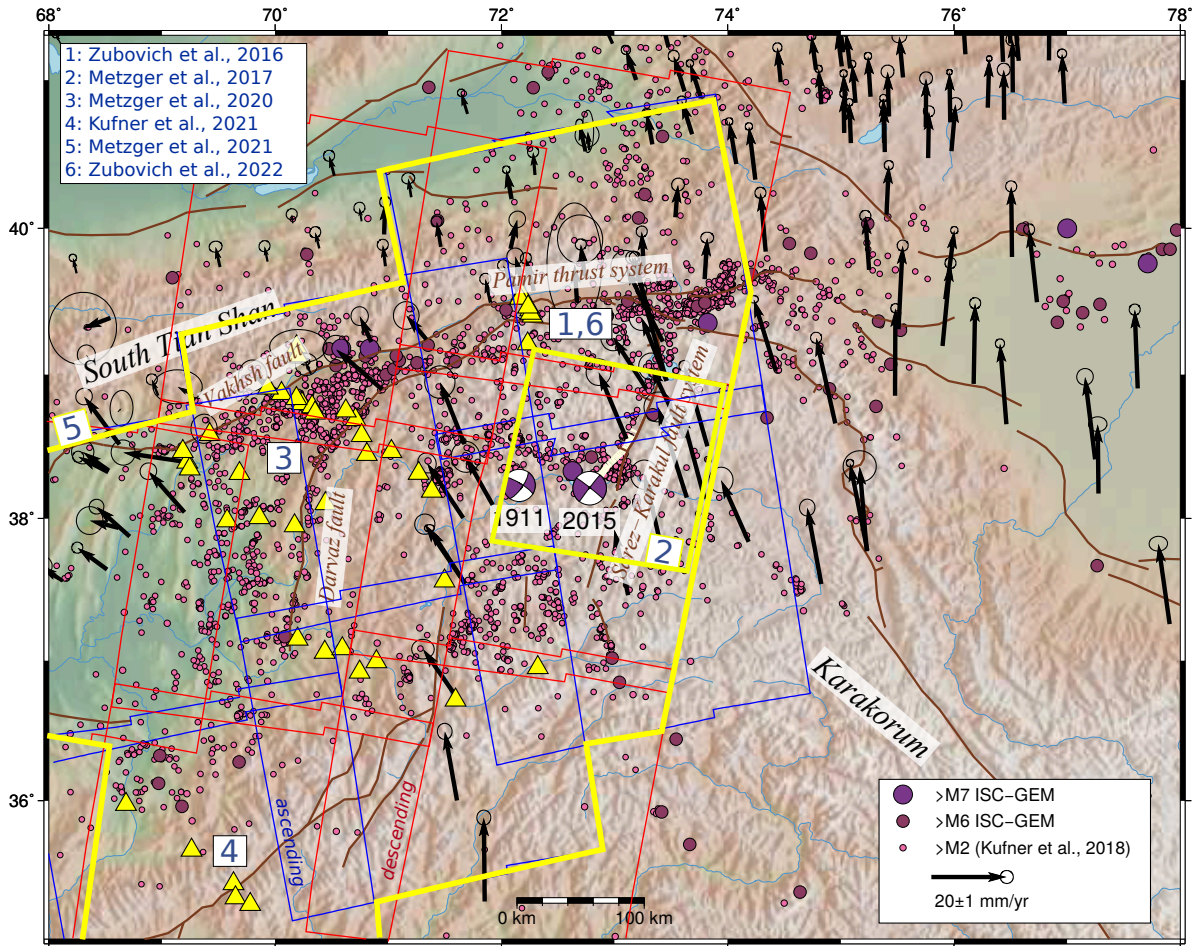


Figure 2.1: Surface deformation rates, crustal seismicity and main active faults (brown lines) in the Greater Pamir area. The yellow triangles mark sites with new positioning data that were collected between 2013 and 2019, the colored polygons outline the radar data used for the individual publications (labeled by numbers).

and 2019 (Figure 2.1) with support of Anatoly Ischuk (Tajik network), Alexander Zubovich (Kyrgyz network) and Najibullah Kakar (Afghan network). The positioning markers were surveyed each year for two consecutive days with a sampling rate of 30 s, using short-braced, two-legged spike mounts, Trimble R7 receivers and Trimble Geodetic Zephyr Model 1 antennas in Tajikistan, respectively, Trimble NetR9 receivers in Afghanistan (*Metzger et al., 2020*, and supporting information therein). In Kyrgyzstan we used a different set up that included a Topcon GB-1000 receiver and Topcon PG-A1 antenna stabilized by a triangular instrument table that was horizontally adjustable by three extendable screws (*Zubovich et al., 2022*, and supporting information therein). Including inherited data from the above-mentioned networks and international, open-access GNSS data, the acquired data were processed to positioning time-series by Zhiguo Deng (GFZ) and – to compare independent solutions – by Olga Mosienko (*Zubovich et al., 2022*) and Mason Perry (*Perry et al., 2018*). Survey reports and raw data in receiver-independent exchange format (RNX) are archived and accessible (*Metzger et al., 2019, 2021c*).

Overview of GNSS surveys and instrumentation in Northern Chile

The Integrated Plate-boundary Observatory in Chile (IPOC, *Klotz et al., 2017; Moreno et al., 2017*) offers multi-parameter observation data of the northern part of the Chile subduction zone. It has been installed as a continuously-operating network in 2007 by an international effort to study upper-plate deformation phenomena related to subduction. IPOC also extends existing sGNSS time-series that were initiated in 1993 by the South American Geodynamic Activities (SAGA, *Klotz et al., 1999*). The data are distributed freely among all collaboration partners³.

³ipoc-network.org

2.2 Geodetic time-series analysis

GNSS positioning data are derived from trilateration, that is, by minimizing distance errors between a GNSS receiver with an unknown position on the ground and at least four GNSS satellites that constantly emit timing information, while orbiting the earth at 25'000 km distance. By including apriori positioning information from reference stations the problem is solved network-wise. The results provide geo-centric positioning information in three dimensions with a precision of a few millimeter. Data are usually sampled at 1-30 s, depending on the scientific focus (static/slow/interseismic vs. dynamic/coseismic/fast phenomena). In static observations, all signals collected within 24 hrs are combined in one single daily positioning measurement.

Radar data, on the other hand, provides information on surface displacement that occurred between two acquisitions, relative to an arbitrarily chosen reference point within the radar images. The measurements provide phase and amplitude information along the satellite's look direction (line-of-sight). Deformation data can be extracted two-fold, either by *amplitude* offset tracking (Figure 2.2a, *Kääb and Vollmer, 2000*), applying cross correlation along azimuth (flight direction) and range (look direction) between the primary and secondary radar image, or by calculating the interferometric *phase* difference (Figure 2.2b, *Massonnet et al., 1993*). Due to its cyclic nature, the interferometric phase is ambiguous and represents deformation as colored fringes, similar to contour lines (Figure 2.2c). To measure the full extent of deformation observed within one interferogram one must unwrap the data, that is integrate over all fringes. This process can be challenging if large parts of the interferogram are decorrelated (showing white noise) due to snow cover, vegetational growth or a complete destruction of the surface. Offset tracking provides significant results only, if the observed deformation that is larger than $\sim 10\%$ of the radar's ground resolution. The most prominent application for offset tracking is glacial flow and large earthquakes, where interferometry fails either due to a complete destruction of the surface or a fringe density larger than the Nyquist frequency. In addition, offsets measured along the flight direction (azimuth) nicely complement interferometric phase measurements along range (line-of-sight).

GNSS and InSAR record also other types of signal such as transient ground motion caused by (ocean tides) or seasonal effects (freeze-thaw-cycle), and are sensitive to atmospheric signal delay due to pressure, water-, and electron-content. InSAR data primarily images topography - for which it was originally developed (*Farr and Kobrick, 2000; Graham, 1974*). Many of the above contributions can be corrected for or suppressed using appropriate filtering, modeling or differential techniques, such as weather conditions, tide models and digital elevation models. The most problematic signal contribution in GNSS data are transient artefacts, caused often by one single, temporarily unreliable reference station, but transported through a whole network solution. For InSAR, the largest problem poses the highly dynamic turbulent atmosphere (also known as weather) particularly, if gentle, inter- and post-seismic deformation signals are to be observed. To get rid of these unwanted signals it is most helpful to analyze whole geodetic time-series rather than single measurements.

GNSS time-series analysis monitors temporal changes in the positioning. Its most simple realization is to apply a linear regression to the time-series and interpret the slope as a secular (in tectonics: interseismic) trend representing plate motion or constant deformation. A more complex approach is trajectory modeling where the signal is decomposed into different trajectories, such as abrupt offsets or cyclic and transient deformation, caused by processes like earthquake offsets or antenna replacements, seasonal signals or (post-seismic) relaxation signals (*Bevis and Brown, 2014; Metzger et al., 2013a*). These processes can be analytically described by

$$x(t) = AH(t) + Bt + C(\sin \omega t + \cos \omega t) + D \arctan \left(\frac{t - t_c}{t_d} \right) + E \log \left(1 + \frac{t - t_0}{T} \right), \quad (2.1)$$

where x is the object position sampled at time t and A , B , C , D , and E the individual signal strengths of each contributing process, such as an offset represented by a Heaviside step-function H , a secular trend, seasonal oscillation signals represented by a combination of a sine and cosine functions (and multiples thereof), transient acceleration processes represented by an arctan-function centered around t_c for the duration of t_d , and, finally, logarithmic relaxation processes starting at t_0 with a non-linear decay defined by T (Figure 2.3). Depending on the number of processes expected to be present in the time-series, this equation can be extended or simplified,

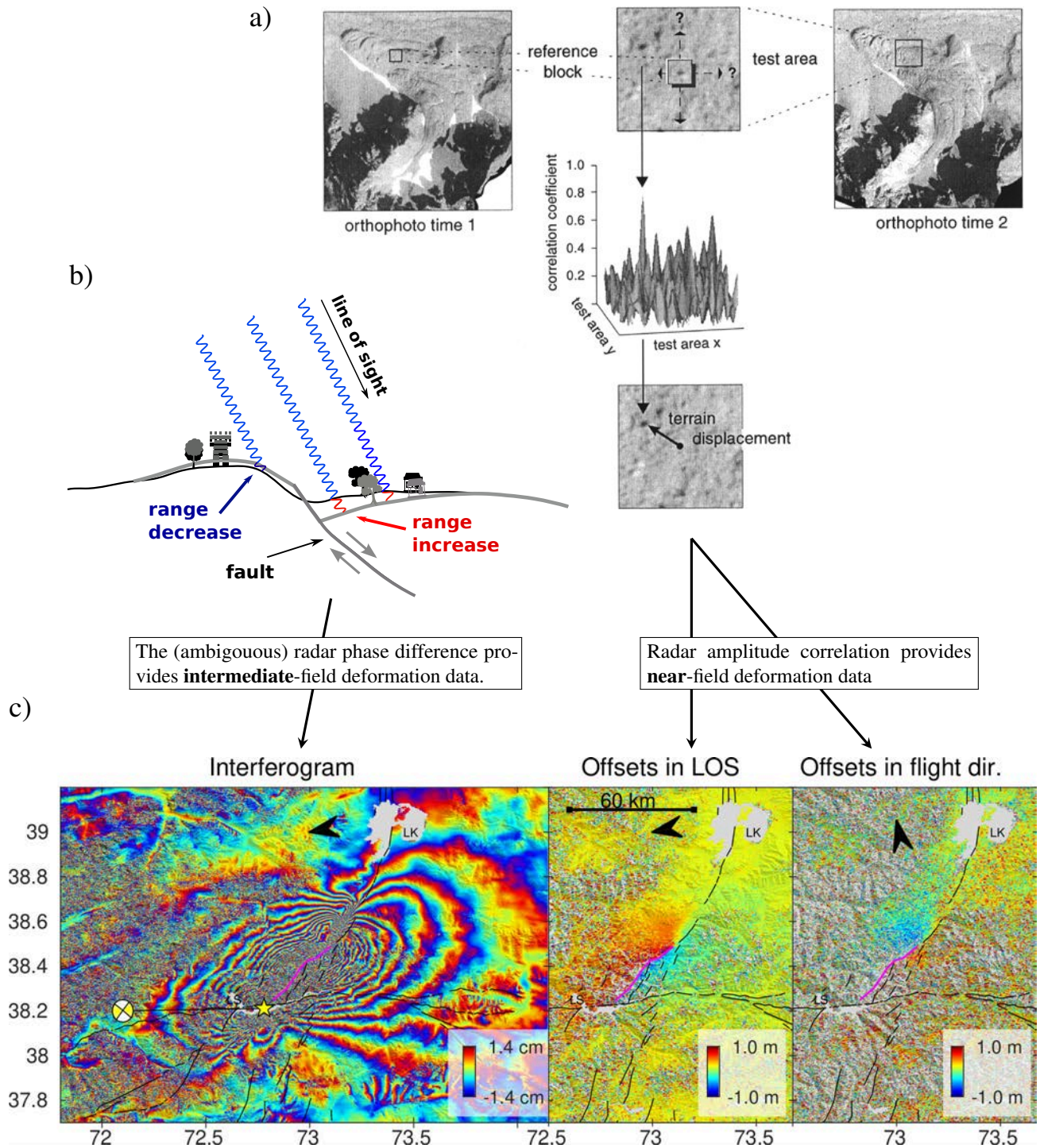


Figure 2.2: Concept of a) amplitude tracking and b) radar interferometry. c) wrapped interferogram and amplitude offsets highlighting displacement caused by the 2015 $M_w 7.2$ Sarez, Central Pamir, earthquake that caused a ~ 80 -km surface rupture (pink line) between Lake Sarez (LS) and Lake Karakul (LK). Black arrows mark the measurement unit direction, black lines additional mapped faults. LOS: line-of-sight. Note the different color scales. Figure compiled from a) *Käüb and Vollmer (2000)*, b) lecture material of S. Metzger & H. Sudhaus and c), *Metzger et al. (2017)*.

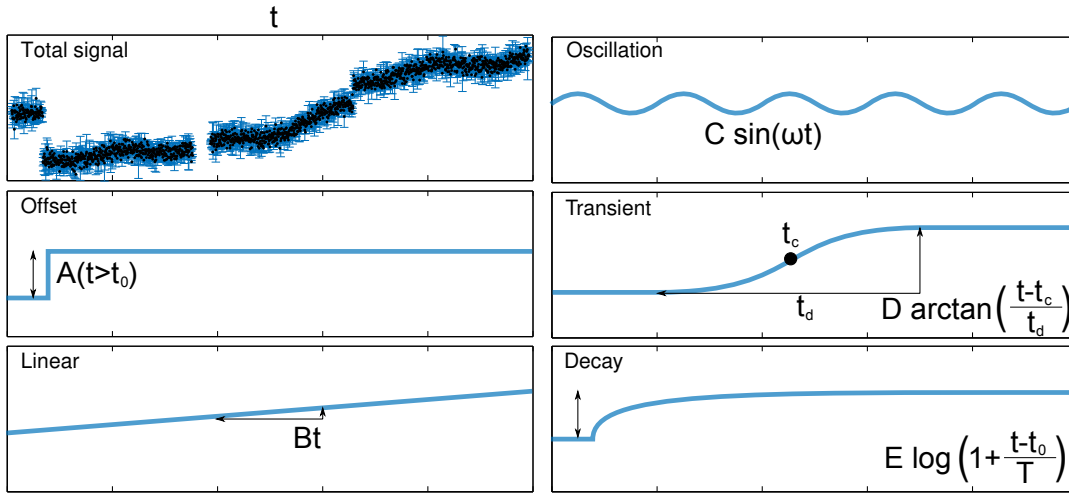


Figure 2.3: Multi-parameter GNSS time-series analysis. GNSS time-series can be decomposed into a subset of trajectory models, each representing one type of deformation process, e.g. (from top to bottom) earthquake offsets, interseismic deformation, seasonals, transients and postseismic relaxation.

and be solved by linear inversion (Menke, 1989) respectively, non-linear optimization (Metzger et al., 2013b; Moreno et al., 2018, supporting information). It goes without saying that cGNSS time-series can be decomposed into more complex trajectory models than temporally sparse sGNSS time-series, which are normally described using a linear rate only.

Radar interferograms provide no direct positioning information, but relative displacement occurring between two radar acquisitions. If M radar images span a network of N unwrapped interferograms (Figure 2.4a), the observed phase information d results from a system of linear equations represented by $d = G \cdot m$, where m corresponds to the $M - 1$ incremental displacements between the M individual acquisition times and the Green's functions G are an $N \times (M - 1)$ matrix containing mostly zeros, but $+1$ and -1 at the positions of the primary and secondary radar image spanning the interferogram (Figure 2.4, Bernardino et al., 2002; Schmidt and Bürgmann, 2003). This is an overdetermined problem ($M < N$) and can be solved for the incremental displacements m using linear inversion (or least-square fit). The individual solutions of m provide the base for the subsequent time-series analysis (e.g. Metzger et al., 2021a). To add spatial constraints for neighboring pixels and smooth the deformation time-series over time, one can apply a spatio-temporal (Gaussian) filter (Bernardino et al., 2002).

A Sentinel-1 radar image has a size of 4 GB, asking for powerful machines to process multiple images efficiently and in an automatized fashion. If the respective infrastructure is not at hand, it is most convenient to use external services, such as the mentioned LiCSAR service that provides automatically processed, downsampled, filtered, atmosphere-corrected (Yu et al., 2018) and unwrapped interferograms (Lazeký et al., 2020). Those can then directly and easily be digested by LiCSBAS, a python-based time-series analysis software (Morishita et al., 2020). Given the dense sampling in time of less than two weeks, Sentinel-1 time-series for the first time also map seasonal processes.

In summary, the combination of GNSS and InSAR data enables us to collect deformation data even in remote places at unprecedented resolution. GNSS data provide reliable, point-wise, three-dimensional data in a geocentered reference frame and high temporal resolution (cGNSS), offering a detailed account on the static and transient deformation processes. Complementary, InSAR time-series provide high spatial resolution (100 m) even at remote places. Thus, modern geodetic data is capable to capture first and second-order signals related to the full seismic cycle at mm-scale and high spatio-temporal resolution.

2.3 From fault slip observations to source models

Tectonic faults are the weakest objects at plate boundaries (and interiors) and release strain that is constantly being build up by ongoing plate motion. Faults host a variety of slip and deformation processes, each of them taking place at a different rupture speed, time period and slip amplitude. The slip (or deformation) type depends on multiple parameters: If it occurs in the more rigid, upper or the more viscous, lower part of the crust; at an early

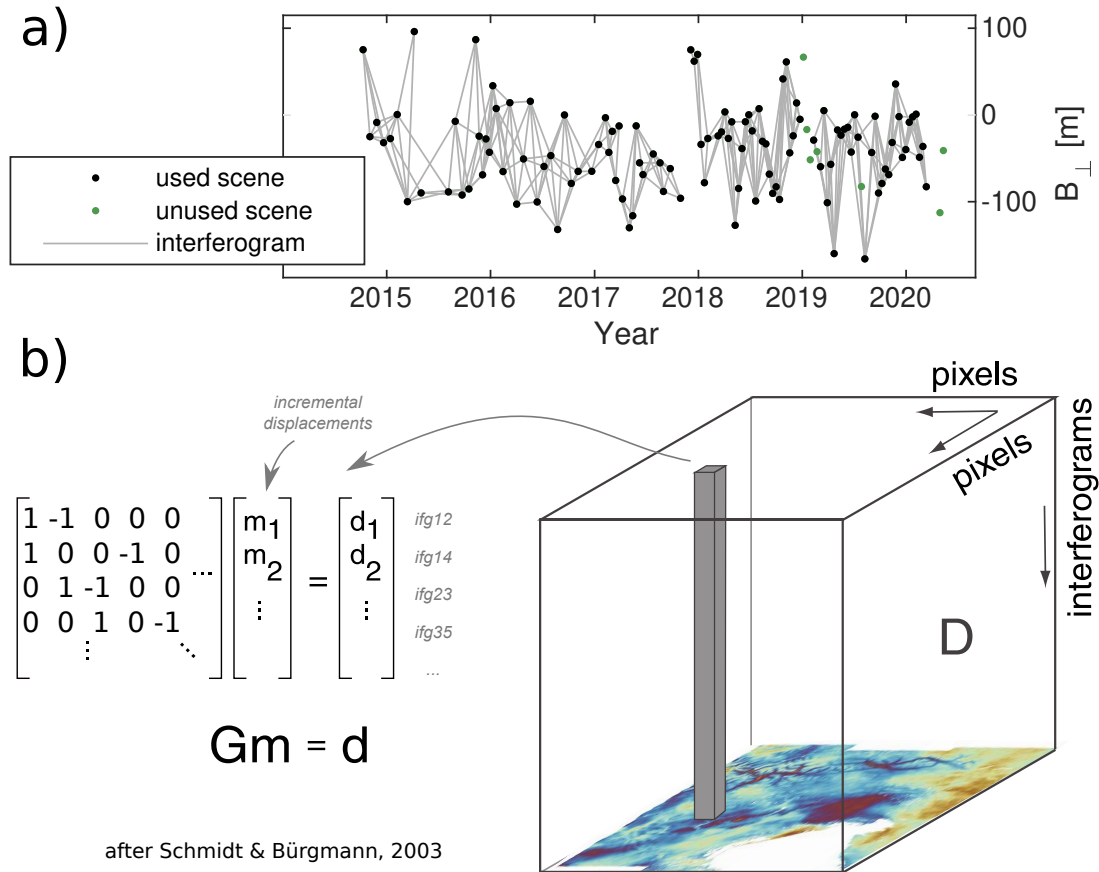


Figure 2.4: a) Geometrical representation of a (disconnected) interferometric small-baseline network (Metzger et al., 2021a). Each radar acquisition is displayed as a function of acquisition date and relative satellite position within the orbital tube (B_{\perp}). b) The observed phase \mathbf{d} of each interferogram (*ifg*) is inverted pixelwise for incremental displacements \mathbf{m} at the given acquisition dates (lecture material S. Metzger & H. Sudhaus).

or late stage of the earthquake cycle; if water is involved or not; the fault rheology in general. Fault slip can also be aseismic and therefore undetectable by seismic instruments. In the following, I summarize the most important fault processes, all being observable by space-based geodesy. The brief presentation of each phenomena includes original references plus references to my own papers presented in Chapter 3. Note that many of the original papers refer to observations related to the 1992 Landers, California (M7.3), and the 1999 İzmit, Turkey, (M7.6) earthquakes, showing the importance of those two events for the research discipline of tectonic geodesy.

- **Interseismic loading:** secular slip along the unlocked (viscous) lower part of the fault and synchronous strain accumulation along the locked (brittle), central (and sometimes upper part) of the fault, causing elastic deformation and strain accumulation (e.g. Liu et al., 1992; Metzger et al., 2011; Wright et al., 2004). The amount of slip (or slip deficit) is equal to or less than the full plate-motion and locking occurs on single faults or whole plate segments.
- **Co-seismic slip:** instantaneous strain release at the (interseismically) locked fault portion, leading to an earthquake rupture (e.g. Bock et al., 1993; Massonnet et al., 1993; Metzger et al., 2017). The rupture lasts seconds to minutes, with a fault slip of up to 30-50 m. The rupture dimension can reach up to 1000 km along strike (M9 earthquakes) and \sim 30-100 km along-dip down the lower end of the seismogenic depth, conserving scaling laws (Mai and Beroza, 2000).
- **Post-seismic, visco-elastic relaxation:** static equilibrium processes in the lower, viscous part of the fault, the upper mantle, and/or the surrounding crust (e.g. Hoffmann et al., 2018; Massonnet et al., 1994; Peña et al., 2022; Pollitz et al., 2000). These processes become instrumentally significant at $M > 7$ earthquakes and decay logarithmically within weeks to decades (depending on the preceding earthquake magnitude). Observed deformation reaches approximately a tenth of the co-seismic offsets.

- **Afterslip:** seismic (aftershocks) or aseismic stress reduction (often) at the fringes of the main fault rupture (e.g. *Bloch et al., 2022; Bürgmann et al., 2002; Ergintav et al., 2002; Hoffmann et al., 2018; Peña et al., 2022*). Afterslip cedes much faster than visco-elastic relaxation.
- **Creep:** aseismic, relatively slow slip on individual (smaller) fault segments occurring during longer periods, sometimes permanently (e.g. *Hearn et al., 2002; Tormann et al., 2013*). The slip rates are comparable to interseismic slip-rates.
- **Poro-elastic flow:** fluid transport to reinstall an equilibrium pressure state after an earthquake (e.g. *Peltzer et al., 1998; Peña et al., 2022*). The signal is comparable to the afterslip signal (maybe with a somewhat smaller amplitude).
- **Slow slip events:** periodical slow slip, often observed at oceanic subduction systems (e.g. *Cavalié et al., 2013; Dragert et al., 2001*) and sometimes linked to seismic tremor. Has also been observed in a continental setting (*Jara et al., 2022*).
- **Tectonic earthquake swarms:** Earthquake sequences without a clear (triggering) mainshock, often migrating along a fault, could be related to fluid or magma migration, also to slow slip events (*Passarelli et al., 2018; Peng and Gomberg, 2010*).

Some of these processes occur simultaneously in space or time, and/or produce similar deformation patterns at the surface (*Hearn, 2003; Savage, 1990*). It is thus necessary to resolve the dynamic deformation in space *and* time to correctly identify the processes ongoing at depth.

In its most simplest form, the above fault processes are described as a dislocation source in a media with layered material properties. The finite dislocation is often a rectangular fault plane (Figure 2.5a, *Okada, 1985*), defined by ten parameters. The slip applied to the dislocation is either in meters (millimeters) or, as a rate, meter/year depending on the process to be studied. Interseismic locking is often mimicked by two freely moving plates (step function), while plate locking is mimicked by backslip on the locked fault segment (*Savage, 1983*). In a co-seismic slip model the fault rupture area scales linearly with the seismic energy release (*Mai and Beroza, 2000*) and can be discretized into any number of sub-fault patches to increase the resolution. Preferably, the patch size scales inversely by the distance to and density of surface observations (Figure 2.5b).

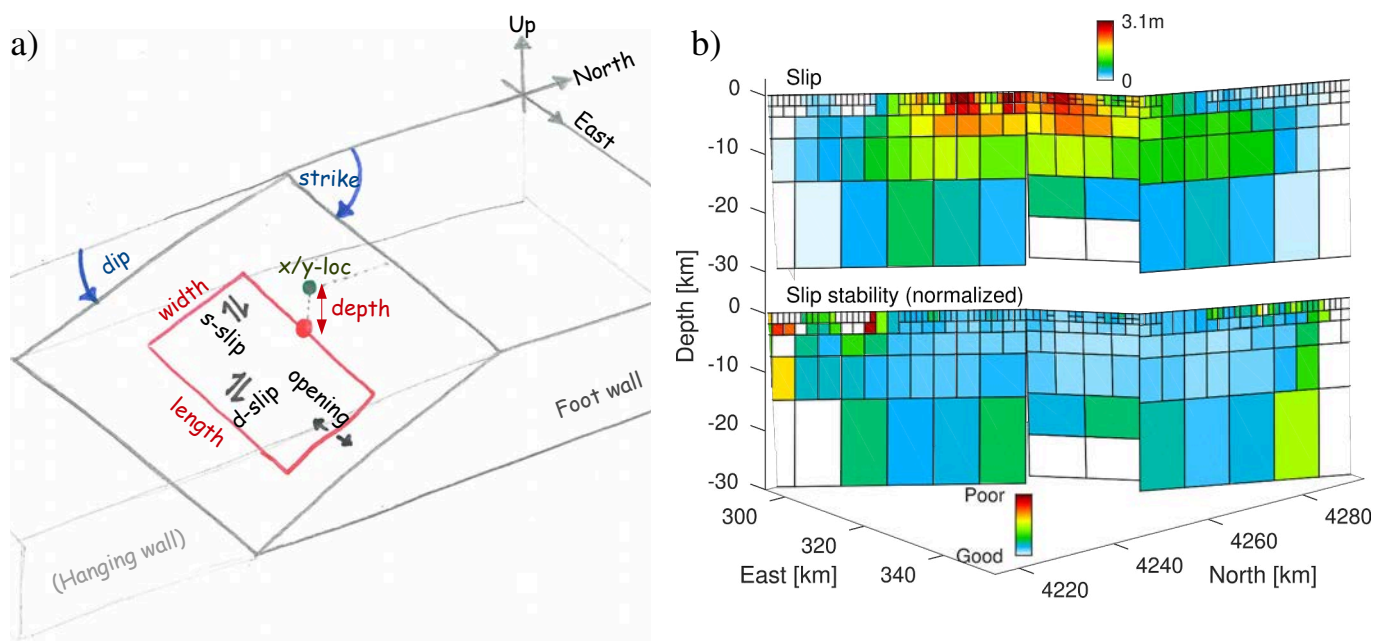


Figure 2.5: a) Rectangular dislocation model after *Okada (1985)*. The rupture is described by ten parameters, of which three define the location (x, y, depth), two the dimension (length, width), two the orientation (dip, strike) and three direction of slip (along-strike, along-dip, out-of-plane). b) Example of an upscaled slip model with data-driven patch resolution that seeks a depth-independent slip stability, respectively, slip uncertainty (modified from *Metzger et al., 2017*).

If the process of interest occurs in the upper, brittle crust, the model space is usually defined as an elastic half-space with one parameter describing the elasticity of the medium (*Christensen, 1996; Zandt and Ammon, 1995*). For deeper sources the model space is upscaled to a multi-layered media with an additional viscous layer at depth. If the model is used to study pore pressure changes, respectively, pore-fluid migration, it must be upscaled to account for those as well.

A set of Green's functions (introduced by George Green in 1828, see *Cannell and Lord, 1993*) describes a finite spatio-temporal source that excites force inside the Earth model, here for example, describing unit slip at each fault patch in each unit direction. To constrain the source parameters this physics-based, analytical set of equations has to be solved such, that it best-represents the observations. If the problem remains linear, it can be inverted using least-squares techniques, where often a quadratic criterion is used to measure the misfit. This holds true for problems with a known fault geometry, example given, by the SLAB 2.0 model (*Hayes et al., 2018*) for the case of great megathrust earthquakes along plate-boundaries, and an elastic model space. The problem links the observations d to a set of model parameters m with the above mentioned Green's functions in a linear fashion, $d = G \cdot m$, or $W \cdot d = W \cdot G \cdot m$, if data weights W are included. This is solved using a least-squares-approach,

$$m = (G^T \Sigma^{-1} G)^{-1} G^T \Sigma^{-1} d, \quad (2.2)$$

where Σ^{-1} represents the data variance-covariance matrix based on the data weights or uncertainties σ ,

$$\Sigma^{-1} = W^T W = 1/\sigma^2. \quad (2.3)$$

Non-linear problems must be solved using optimization algorithms. This applies to problems with unknown fault geometry, for example a blind fault, or an unknown structure of a continental earthquake, or also, if the model is multi-layered. Most popular optimization algorithms are Monte-Carlo techniques, e.g. direct search using simulated annealing (from random sampling to more directed search *Cervelli et al., 2001*), Markov chain (random walk and survival of the fittest *Mosegaard and Tarantola, 1995*) or Bayesian inference (producing probabilistic ensembles of the best-fitting model parameter choices, e.g. *Tarantola, 2005*). If combined with statistical data uncertainty analysis, the Monte Carlo techniques provide the same results as Bayesian probability density functions of the best-fitting parameter choices (cf. Figure 7 in *Metzger et al., 2013a*) and provide an estimate on the model robustness. The incorporation of observation weights in the search of the best-fit model parameters (Equations 2.2 and 2.3) also provides more realistic fault models as the data fit is predominantly steered by high-quality observations. This is particularly important when using a squared misfit criterion (L_2 -norm), otherwise the models are biased by particularly poor observations.

3 Applications

3.1 Continental collision: Coseismic, long-term, and triggered slip

3.1.1 The 2015 M_w 7.2 Sarez strike-slip earthquake in the Pamir interior: Response to the underthrusting of India's western promontory

Published as: [S. Metzger](#), B. Schurr, L. Ratschbacher, H. Sudhaus, S.-K. Kufner, T. Schöne, Y. Zhang, M. Perry, R. Bendick (2017), The 2015 M_w 7.2 Sarez strike-slip earthquake in the Pamir interior: Response to the underthrusting of India's western promontory, *Tectonics*, **36**, 2407–2421. doi:[10.1002/2017TC004581](https://doi.org/10.1002/2017TC004581)

Supporting information: available online

Scientific application: In this project I constrained the source kinematics and mechanism of the 2015 earthquake that ruptured the center of the Pamir. We found that the event occurred at a fault separating the gravitationally-collapsing West Pamir and the internally-stable East Pamir, and that this structure acts as a surface expression of the Indian indenter at depth.

Methodological advances: Based on co-seismic offset data derived from radar phase interferometry, radar amplitude tracking, and GNSS time-series, I carefully designed a distributed slip model of the rupture kinematics including model parameter uncertainties. I have adapted fault patch sizes such that the model resolution varies with depth and distance to the non-homogeneously distributed surface observations.

Individual Contributions: The study was designed, conducted and written by me. I have processed the radar data and designed the model (under the supervision of HS), whose results were confirmed by an independent, but unpublished a-priori seismogeodetic model of YZ. MP, RB and TS provided supporting observation data; LR and SK contributed field evidence. BS and LR helped with the tectonic interpretation. All authors commented on the writing.



Tectonics

RESEARCH ARTICLE

10.1002/2017TC004581

Key Points:

- SAR data and modeling reveal a right-stepping, near-vertical, ~80 km long rupture along the Sarez-Karakul fault with sinistral slip of up to 3.1 m
- Surface breaks in frozen ground record fault segmentation, en échelon secondary structures, mass movements, and up to 2 m sinistral offset
- Faulting is probably driven by northward advance of the northwestern tip of underthrusting Indian mantle lithosphere

Supporting Information:

- Supporting Information S1

Correspondence to:

S. Metzger,
metzger@gfz-potsdam.de

Citation:

Metzger, S., Schurr, B., Ratschbacher, L., Sudhaus, H., Kufner, S.-K., Schöne, T., ... Bendick, R. (2017). The 2015 M_w 7.2 Sarez strike-slip earthquake in the Pamir interior: Response to the underthrusting of India's western promontory. *Tectonics*, 36, 2407–2421. <https://doi.org/10.1002/2017TC004581>

Received 23 MAR 2017

Accepted 29 AUG 2017

Accepted article online 2 OCT 2017

Published online 6 NOV 2017

©2017. American Geophysical Union.
All Rights Reserved.

The 2015 M_w 7.2 Sarez Strike-Slip Earthquake in the Pamir Interior: Response to the Underthrusting of India's Western Promontory

Sabrina Metzger¹ , Bernd Schurr¹ , Lothar Ratschbacher² , Henriette Sudhaus³, Sofia-Katerina Kufner¹ , Tilo Schöne⁴, Yong Zhang⁵ , Mason Perry⁶ , and Rebecca Bendick⁶ 

¹Lithosphere Dynamics, GFZ German Research Centre for Geosciences, Potsdam, Germany, ²Geologie, TU Bergakademie Freiberg, Freiberg, Germany, ³Institute of Geosciences, Christian-Albrechts-University, Kiel, Germany, ⁴Geodetic Hazard Monitoring, GFZ German Research Centre for Geosciences, Potsdam, Germany, ⁵School of Earth and Space Sciences, Peking University, Beijing, China, ⁶Department of Geosciences, University of Montana, Missoula, MT, USA

Abstract The Pamir orogen, Central Asia, is the result of the ongoing northward advance of the Indian continent causing shortening inside Asia. Geodetic and seismic data place the most intense deformation along the northern rim of the Pamir, but the recent 7 December 2015, M_w 7.2 Sarez earthquake occurred in the Pamir's interior. We present a distributed slip model of this earthquake using coseismic geodetic data and postseismic field observations. The earthquake ruptured an ~80 km long, subvertical, sinistral fault consisting of three right-stepping segments from the surface to ~30 km depth with a maximum slip of three meters in the upper 10 km of the crust. The coseismic slip model agrees well with en échelon secondary surface breaks that are partly influenced by liquefaction-induced mass movements. These structures reveal up to 2 m of sinistral offset along the northern, low-offset segment of modeled rupture. The 2015 event initiated close to the presumed epicenter of the 1911 M_w ~7.3 Lake Sarez earthquake, which had a similar strike-slip mechanism. These earthquakes highlight the importance of NE trending sinistral faults in the active tectonics of the Pamir. Strike-slip deformation accommodates shear between the rapidly northward moving eastern Pamir and the Tajik basin in the west and is part of the westward (lateral) extrusion of thickened Pamir plateau crust into the Tajik basin. The Sarez-Karakul fault system and the two large Sarez earthquakes likely are crustal expressions of the underthrusting of the northwestern leading edge of the Indian mantle lithosphere beneath the Pamir.

Plain Language Summary The Pamir mountains in Central Asia are being piled up by the northward advancing Indian continent. Nowadays most of the deformation occurs at the Pamir's rim, but on 7 December 2015, a large earthquake struck the interior of this mountain range (magnitude 7). We use radar satellite data with centimeter accuracy to measure the coseismic displacement of this earthquake and find that an 80 km long segment of the Sarez-Karakul fault was ruptured. This fault splits the Pamir in a western and eastern part. Our geologists, who visited the area 9 months after the earthquake, confirmed our observations and further reported that the rupture was heavily damped at the surface by permafrost. The area was already once struck by a large earthquake in 1911. The question arises if also this event activated the Sarez-Karakul fault, as this fault is the only known large structure in the Pamir's interior. But the center of the Pamir deforms only little, and it is unlikely that this fault ruptures twice in 100 years. Finally, we show that both earthquakes occurred directly on top of the Indian promontory bulldozing into the Asian crust underneath the Pamir.

1. Introduction

The Pamir, situated northwest of the Tibetan Plateau, is part of the India-Asia collision zone (Figure 1). The region is seismically active producing magnitude >6 earthquakes approximately every 10 years. Over the last 50 years, those occurred mainly along the Pamir's northern perimeter, the Pamir thrust system, which accommodates 13–19 mm/yr of the India-Asia convergence (Ischuk et al., 2013; Zubovich et al., 2010, 2016). The Pamir interior is seismically less active, both in long-term global earthquake catalogs (Storchak et al., 2013) and observed by a dense local seismic network (Schurr et al., 2014). On 7 December 2015, a M_w 7.2 strike-slip

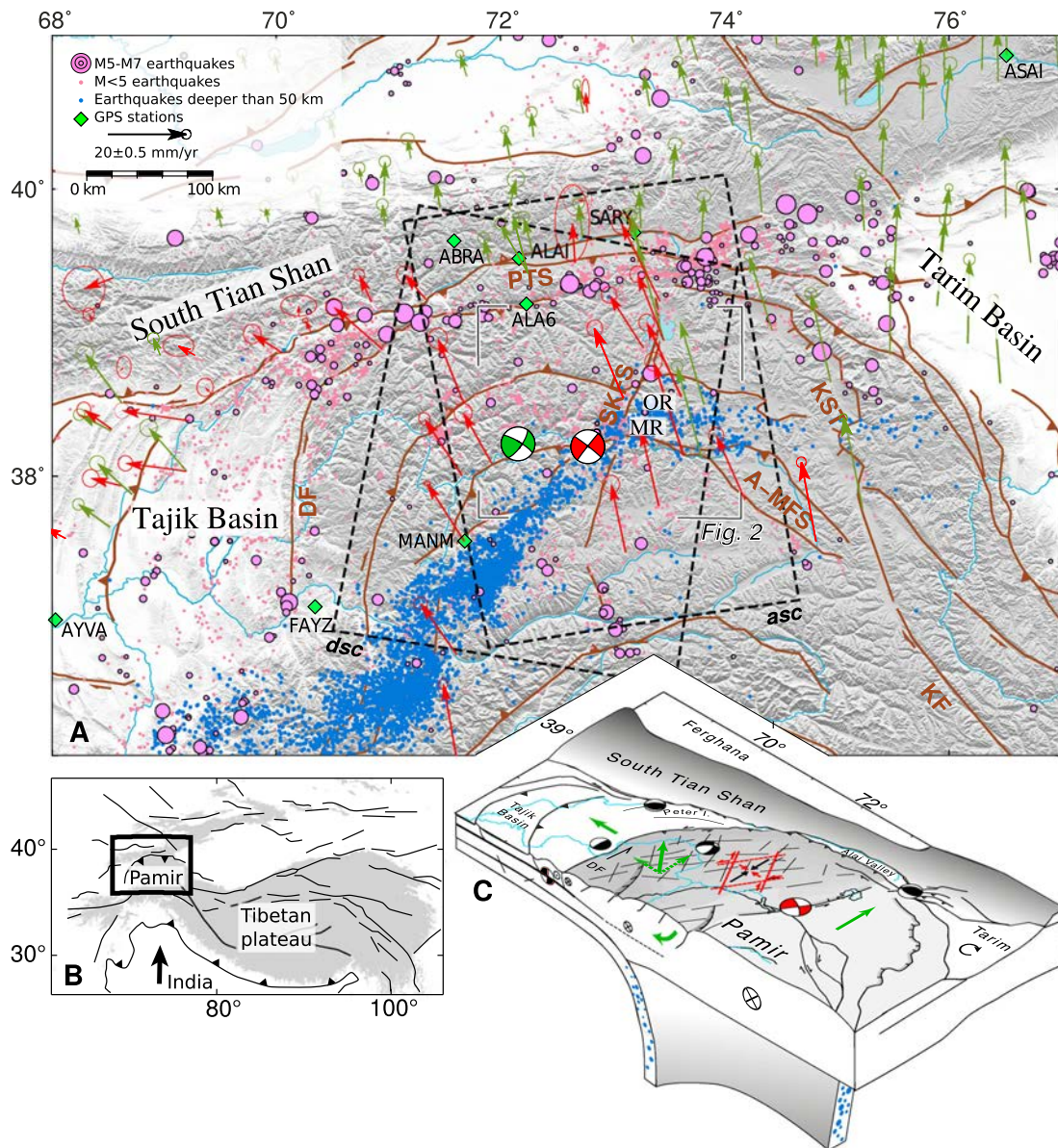


Figure 1. (a) Tectonic setting of the Pamir with main active faults (brown) (Schurr et al., 2014), microseismicity (2008–2010 and 2012–2014) (Kufner et al., 2017; Sippl, Schurr, Yuan, et al., 2013), instrumentally recorded seismicity (1900–2012) above magnitude 5 (Storchak et al., 2013), and GPS rates of Ischuk et al. (2013) (red) and Zubovich et al. (2010) (green) in a stable Eurasia reference frame. The focal mechanisms indicate the locations and mechanisms for the 1911 (green) (Kulikova et al., 2015) and the 2015 (red) earthquake (USGS, 2015). A-MFS: Aksu-Murgab fault system, DF: Darvaz fault, KF: Karakorum fault system, KST: Kongur Shan-Tashkorgan normal fault system, MR: Muzkol range, OR: Officers range, PTS: Pamir thrust system, SKFS: Sarez-Karakul fault system. (b) The Pamir and the Tibetan plateau are a result of northward advancing India (arrow). Regions above 2500 m sea level are shaded. (c) Block diagram, modified from Schurr et al. (2014), illustrating kinematics (green arrows), resulting stresses and type of faulting. The eastern Pamir is pushed north en bloc; the western Pamir deforms internally by conjugate strike-slip faulting under north-south compression, causing—together with normal faulting—westward extrusion.

earthquake occurred in the interior of the Pamir along the Sarez-Karakul fault system (SKFS) with the epicenter near Lake Sarez (Figure 1a) (Sangha et al., 2017; USGS, 2015). The earthquake killed two persons and left more than a thousand homeless. In 1911, an earthquake of similar size ($M_w \sim 7.3$) and mechanism occurred in the same region as the 2015 event (Ambraseys & Bilham, 2012; Bindi et al., 2014; Kulikova et al., 2015). This earthquake triggered a massive rockfall forming the Earth's highest dam, the Usoi dam, which confines

today's 17 km³ Lake Sarez (Ischuk, 2006; Schuster & Alford, 2004). The proximity and similarities in mechanism and size of the two earthquakes (Kulikova et al., 2015) are striking and the question arises if the 2015 event repeated the 1911 earthquake. Herein, we present an analysis of fault location, geometry, slip distribution, and amplitude of the 2015 earthquake based on space-geodetic and field data. We discuss model parameter uncertainties and fault model resolution and compare our findings to geomorphologic near-field observations acquired 9 months after the earthquake. Finally, we interpret both earthquakes in the framework of the late Cenozoic tectonics of the Pamir.

2. Tectonic Setting

The crust of both Tibet and Pamir formed by the accretion of microcontinents, arcs, and subduction-accretion complexes to Asia's southern margin during the Paleozoic and Mesozoic (Schwab et al., 2004). During the late Miocene (~12–11 Ma), the Pamir began indenting the lithosphere of the formerly connected Tajik-Tarim basin (Kufner et al., 2016) (Figure 1). Northward displacement and crustal shortening is accommodated along the Pamir thrust system in the north, the sinistral-transpressive Darvaz fault system in the (north)west, the dextral Aksu-Murgab and Karakorum fault systems in the southeast, and the Kongur Shan-Tashkorgan normal fault system in the Chinese Pamir, which has a weak dextral component (Chevalier et al., 2015) (Figure 1a). Plate-scale processes at depth likely drive Pamir crustal tectonics (Figure 1c). Beneath the Pamir, Asian lithosphere forms a 90° arc that is retreating northward and westward as traced by intermediate-depth seismicity (60–300 km, Figure 1c) (Schneider et al., 2013; Sippl, Schurr, Typel, et al., 2013; Sippl, Schurr, Yuan, et al., 2013). Kufner et al. (2016) suggested that Asian slab retreat is forced by indentation of the Indian lithosphere, bulldozing into the cratonic lithosphere of the Tajik-Tarim basin at mantle depth.

The high recent shortening rates across the Pamir thrust system cause frequent thrust earthquakes with the 2008 M_w 6.7 Nura (Sippl et al., 2014; Teshebaeva et al., 2014) and 2016 M_w 6.4 Sary Tash (USGS, 2016) earthquakes being the most recent. In the Pamir interior, thrusting has ceased and the displacement field is composed of bulk northward movement combined with E-W extension (Ischuk et al., 2013; Zhou et al., 2016). The latter is driven by westward gravitational collapse of thickened Pamir plateau crust into the Tajik basin, where it causes approximately E-W shortening of the sedimentary strata of the Tajik basin above an evaporitic décollement (Nikolaev, 2002; Schurr et al., 2014; Stübner et al., 2013) (Figure 1c). Within the Pamir, the brittle crust responds to this deformation by sinistral strike-slip faulting on NE trending or conjugate planes and to a lesser degree by normal faulting on N-S striking planes contributing to N-S shortening and westward escape (Schurr et al., 2014) (Figure 1c). Distributed strike-slip faulting, particularly in the western Pamir, also takes up shear between the northward moving Pamir and the Tajik basin lithosphere. The current deformation field has not yet left a strong imprint on the structural grain of the Pamir interior. Here the only NE striking sinistral fault system, which has a clear morphological expression and is seismically active, is the transtensional SKFS that stretches from Lake Sarez to north of Lake Karakul (Figure 1) (Rutte et al., 2017; Schurr et al., 2014; Strecker et al., 1995).

The SKFS (Figure 1) is little studied in detail by field surveys. Nöth (1932) mapped the Lake Karakul depression as a horst-graben structure. Strecker et al. (1995) traced these structures southward, outlining three stages of late Cenozoic deformation. The youngest—likely active one—has right-stepping normal faults with a minimum offset of 1–2 m, cutting alluvium in the river plain south of Lake Karakul. Here unconsolidated fluvial and aeolian sands fill the hanging wall depressions. Sippl et al. (2014) suggested that the faults at the northern end of the Karakul graben interact with active deformation along the Pamir thrust system. Overall, the northern SKFS was interpreted as a horst-graben structure with dominant normal and subordinate sinistral strike-slip displacements.

Schurr et al. (2014) and Rutte et al. (2017) traced sinistral-oblique normal faulting to the eastern escarpment of the Officers range (Figure 1a), where a series of WNW dipping, en échelon range front normal faults separate a hanging wall basin at ~3700 m from a footwall range peaking at >6000 m. At the range front, sinistral-normal slip scarps mark events along the central section of the SKFS prior to the 2015 earthquake (Figures 6b and 6c in Schurr et al. (2014) and Figures 4e–4h in Rutte et al. (2017)). The southern segments, crossing the remote Muzkol range (Figure 1a), are interpreted based on geological maps and satellite images. Structural data of late Cenozoic deformation from these studies is compiled in Figure S1 in the supporting information; these constrain the overall sinistral-oblique normal slip along the SKFS.

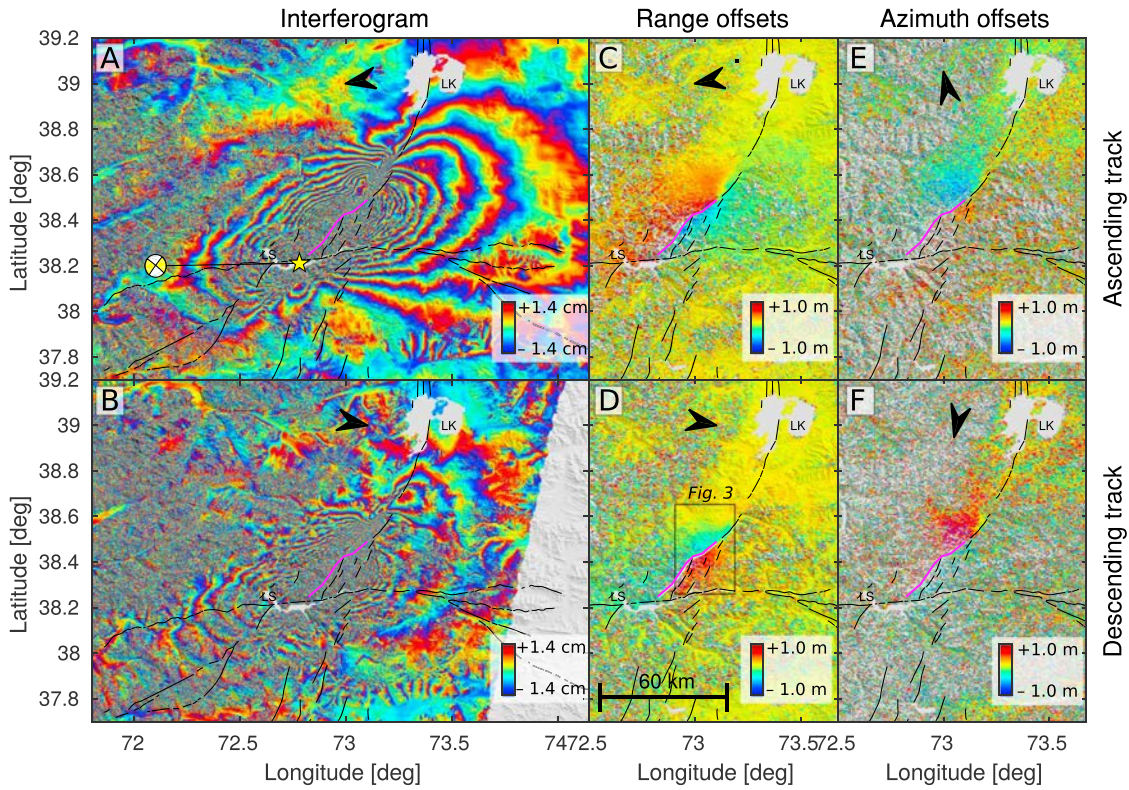


Figure 2. (a, b) Wrapped Sentinel-1A interferograms and (c, d) pixel offsets in range (i. e., line of sight) and (e, f) azimuth direction (i. e., flight direction) showing the color-coded, coseismic deformation of the 2015 Sarez earthquake. The direction of deformation is indicated in all panels by arrows, with Figures 2a–2d being also sensitive to vertical displacements. Additional features are mapped faults (black) (Schurr et al., 2014), the trace of highest deformation gradient (pink), the earthquake epicenter (yellow star), and the focal mechanism (USGS, 2015). To highlight the details near the epicenter, we only show an excerpt of the full data set that was used as model input (see Figure 1 for orientation). LK: Lake Karakul; LS: Lake Sarez.

3. Geodetic Analysis

3.1. Input Data

In this study, we use synthetic aperture radar (SAR) data from the Sentinel-1A satellite mission to extract earthquake-induced ground displacements. Displacements from SAR data are measured along the radar line-of-sight (LOS) direction as interferometric phase changes, or by cross correlation of the radar intensity signal (amplitude pixel offset tracking) along LOS and horizontally along the satellite flight direction (azimuth) (Michel & Rignot, 1999; Strozzi et al., 2002). By combining two pre-event and two post-event scenes in the ascending and descending acquisition modes, we retrieved independent coseismic observations in three dimensions and complemented these observations with GPS data.

Each interferogram and pixel offset map covers a time span of 24 days (Table S1). The post-event SAR images were acquired 5 and 23 days after the earthquake, hence comprising a fraction of postseismic deformation. We concatenated two contiguous SAR scenes for each acquisition mode to cover the full surface deformation pattern and processed the data with the GAMMA software (Wegmüller & Werner, 1997). We used the 90 m digital elevation model of the shuttle radar topography mission (Farr et al., 2007; Jarvis et al., 2008) to build differential interferograms and corrected for the height-dependent, atmospheric phase contribution empirically. More details on the interferometric data processing are given in the supporting information.

The quality of the wrapped interferograms is good for the ascending and satisfactory for the descending acquisition mode (Figures 2a and 2b). Particularly, the mountainous western Pamir exhibits interferometric phase-coherence loss, probably due to snow. East of the earthquake epicenter, on the more arid eastern Pamir plateau, the interferometric phase is highly coherent but topography-related signal contributions are apparent, e.g., in the east trending valleys southeast of the epicenter. However, their short spatial wavelength

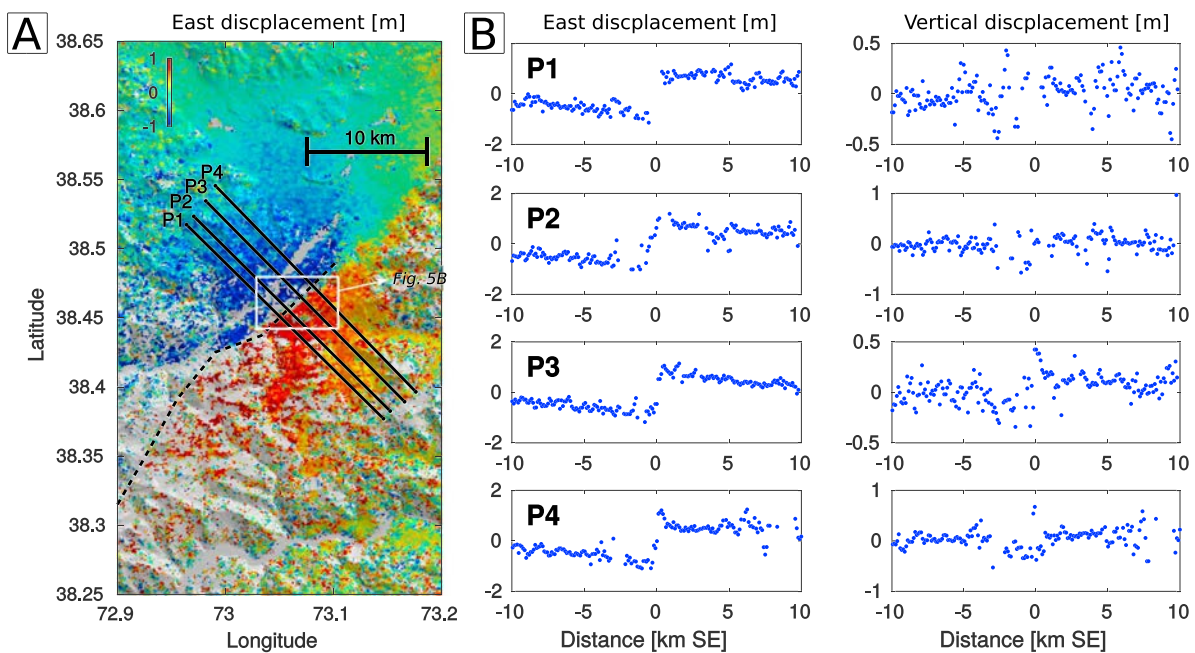


Figure 3. (a) Eastward displacement near the surface ruptures (obtained from a linear combination of Figures 2c and 2d). The dashed line marks the sign change in the data and thus the rupture surface trace. (b) Eastward and (near-)vertical displacements at the cross-fault profiles P1 to P4 (marked with black lines in Figure 3a). Each profile contains the measurements of a ~ 500 m wide corridor.

signals differ from the coseismic deformation pattern and do not influence the modeling results. Approaching the rupture from the undeformed area, we count more than 20 fringes on both sides of the fault. This translates to more than 56 cm of LOS displacement or over 100 cm of ground displacement (Figures 2a and 2b) on both sides, if we assume pure horizontal motion.

Displacements are highest in the near field of the rupture, where the fringe density exceeds the spatial sampling and causes interferometric phase decorrelation (Figures 2a and 2b). We unwrapped the data in a conservative fashion by masking out the near-fault area (10–20 km around the surface rupture) to prevent unwrapping errors (Figure S2). Here in the presence of large ground displacement, the pixel offset estimations deliver valuable near-fault information in range direction (i. e., LOS) and azimuth (i. e., flight direction). Given the higher spatial SAR resolution in range we average more offset estimates, which results in a better signal-to-noise ratio compared to the azimuth offsets (Figures 2c–2f). All offset data trace a sharp sign change of ~ 40 km length that stretches from just north of Lake Sarez northeastward toward Lake Karakul, possibly induced by a surface rupture. Eastward and near-vertical displacement profiles obtained by a linear combination of the range offsets show a relatively sharp offset of ~ 2 m in LOS across 1 kilometer (Figure 3). More details on the amplitude pixel offset estimation are provided in the supporting information.

Only 13 GPS markers in the Pamir region are equipped with continuously operating instruments, and they are mostly located along the active northern rim (Mohadjer et al., 2010; Schöne et al., 2013; Zubovich et al., 2016). In this study, we used the data of eight GPS stations at distances from 100 to 500 km of the epicenter (Figure 1a). The daily solutions of FAYZ and MANM were processed with GaMIT/GLOBK (Herring et al., 2010a, 2010b, 2010c); the (1 Hz) data of the other stations were analyzed with the Precise Point Positioning (PPP) software from the Canadian Spatial Reference System (CSRS) (Kouba & Héroux, 2001). Only the stations ALA6 and MANM observed a measurable coseismic displacement (Table S2 and Figure S3); all other stations are located outside the deformed area. In the modeling, we used these results as maximum constraints on the coseismically affected area. Further details on the GPS data processing are given in the supporting information.

3.2. Modeling

All SAR data were subsampled based on the phase gradient, following Jónsson et al. (2002) (Figure S2). The position of each subsampled cell was defined by the center of mass (of all coherent data samples within the cell) rather than the geometrical center. Each cell was given a weight based on the data error calculated with a full variance-covariance matrix (Figure S4) (Sudhaus & Jónsson, 2009) (we refer to the supporting information for more information). For the GPS offset data, we estimated the uncertainties based on the standard deviations of the time series and used their inverse as weights (Table S2). The distributed slip model was obtained in a two-step procedure. First, we constrained the fault location and geometry, using a nonlinear optimization routine. The amplitude pixel offsets show a clear double bend of the fault surface trace (Figures 2c–2f), so we solved for a geometry of three fault segments. Then, we linearly inverted for a variable slip on discretized fault patches, using rectangular dislocations in an elastic half-space (Okada, 1985) with a Poisson's ratio of 0.25 and an empirically derived smoothing factor resulting from a trade-off curve between data fit and maximum slip (see Figure S5 and the supporting information for further explanations). We tested two different fault-patch resolutions, namely, a uniform and a data distribution driven one. Finally, we estimated the model parameter uncertainties by propagating the data uncertainties through both the nonlinear geometry optimization and the linear slip inversion.

To constrain the fault geometry, we used a Monte Carlo type, simulated annealing approach (Cervelli et al., 2001) that first samples the model space in a random fashion and then gradually favors model parameter sets producing low misfits (Creutz, 1980; Metropolis et al., 1953). We solved for the parameters that define size, position, orientation, and lateral slip of the three fault segments and included six parameters controlling the phase ambiguity and potential tilt signal of the interferograms due to imprecise satellite-orbit information. We constrained the segments to connect at the up-dip end but all other parameters could converge freely within the given boundaries. Finally, we estimated the model geometry uncertainties by propagating the data—including a random manifestation of the data uncertainties—500 times through the optimization and performed statistics on the outcome (Figures S6 and S7) (Metzger et al., 2011; Metzger & Jónsson, 2014). The resulting best fit fault geometry contains a central fault segment of $18.5^{+0.2}_{-2.8}$ km length with a strike of $047.6^{+2.0}_{-0.0}$ °. It is bounded by a northeastern segment with a length of $23.8^{+0.9}_{-0.8}$ km and a strike of $025.6^{+0.7}_{-0.6}$ °, and a southwestern segment with a length of $23.5^{+2.4}_{-0.2}$ km and strike of $037.4^{+0.1}_{-0.3}$ ° (Table S3). Our solution agrees well with the fault model of Sangha et al. (2017) (Figure S6), except that all our model segments dip more steeply. In addition to the Sentinel-1 interferograms presented here, Sangha et al. (2017) included three interferometric pairs from the ALOS-2 mission. The longer wavelength (L band) of ALOS-2 provides valuable near-field information, similar to the pixel offset data used in this study. From SW to NE, our segments dip $87.7^{+1.3}_{-0.8}$ ° northwest, $81.8^{+0.9}_{-3.0}$ ° northwest, and $89.3^{+0.9}_{-1.1}$ ° southeast; those of Sangha et al. (2017) $89.0^{+2.3}_{-6.8}$ ° southeast, $80^{+9.3}_{-7.2}$ ° northwest, and $83^{+8.2}_{-3.5}$ ° northwest.

To constrain the fault slip distribution, we first extended the modeled fault planes vertically from 0 to 60 km and elongated the outer two segments north and south for 60 km in order to capture the full slip pattern. Then, we partitioned the three fault segments using two different approaches: (1) 336 uniform subpatches of 5×5 km width and length (4.6×5 km for the central fault segment) and (2) 284 subpatches subdivided optimally with respect to their data sensitivity (Atzori & Antonioli, 2009). This subdivision process relies on three criteria, that is, patch depth, data coverage, and presence of adjacent patches that already have passed the optimum resolution threshold. In addition, we constrained the patch size to be in the limits of 1–25 km. This data-driven, “optimal-patch” resolution allows only as much detail as can be resolved by the data and thus aims at suppressing artifacts (Page et al., 2009). We inverted for the slip on each of these patches, allowing for slip with a rake of ± 45 ° only. We again solved for the best parameters representing SAR phase ambiguities and orbital signal components. The slip parameter uncertainties were estimated statistically by inverting slip on the 500 perturbed geometry realizations of the prior optimization approach (Figure S7 and text in the supporting information). Atmospheric signal contributions in the southwestern corner of the ascending interferogram would cause a significant amount of slip on the lower southwestern corner of the rupture plane. Therefore, we set the slip on the deepest patches to zero. For the optimal-patch resolution, this means that only slip above 30 km was allowed, which is in agreement with the thickness of the seismogenic layer in the Pamir (Schurr et al., 2014).

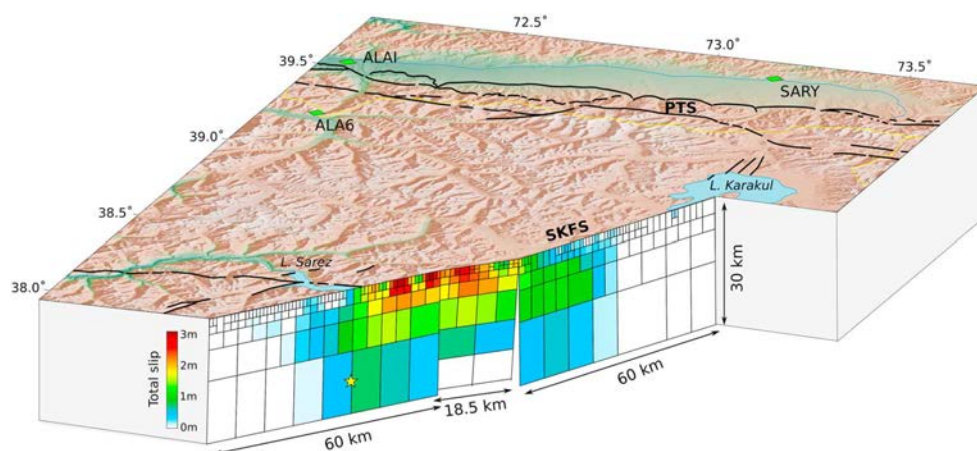


Figure 4. Perspective view on the fault-rupture plane with color-coded slip magnitudes. Mapped faults are shown in black (Schurr et al., 2014), the star marks the 2015 hypocenter (USGS, 2015), and green diamonds the closest GPS stations. We refer to Figure S8 for the rakes of the slip patches. PTS: Pamir thrust system; SKFS: Sarez-Karakul fault system.

Both slip model parameterizations reveal significant fault slip (>50 cm) on an 80 km long fault from ~ 25 to 30 km depth to the surface (Figures 4 and S8). Slip >2 m is confined to the upper 7.5 km of the crust (10 km for the uniform-patch slip model) along a 30 km stretch; the maximum slip is 3.1 m (2.5 m). This is less than the 4.3 m maximum along-strike slip from Landsat-8 offset estimations and less than the maximum modeled slip (3.5 m) observed by Sangha et al. (2017). The slip sense is sinistral with a minor dip-slip component at the southwestern and northeastern end of the rupture (Figure S8).

The model of Sangha et al. (2017) and our uniform and our data-driven patch slip model all show a similar slip pattern (Figure S8), but the derived slip parameter uncertainties highlight the strength of the data-driven patch resolution. The slip parameter uncertainties are generally lower and depth independent. For the uniform-patch model, the slip uncertainties are highest at deep patches, where the fault-patch resolution is suboptimal. These patches are most distant to the data samples; their patch size should be increased. Accordingly, shallow patches could be subdivided further (Figure S8). Hence, we favor the data-driven patch partitioning to the common-practice uniform fault patches. The misfit between data and modeled predictions (Figure S9) average into root-mean-square (RMS) values of 4.7 ± 0.1 cm (data-driven patches) and 4.9 ± 0.1 cm (uniform patches), respectively.

Some signal characteristics could not be reproduced, for example, the long-wavelength signal in the north-eastern corner of the ascending interferogram and various areas in the descending interferogram, which were probably caused by turbulent atmospheric conditions (Figure S9). Given the poor quality of the descending amplitude pixel offsets (Figure S4), it was anticipated that the model struggles to reproduce these data well.

The total slip is equal to a seismic moment M_0 of $6.2 \pm 0.2 \cdot 10^{19}$ Nm (data-driven patches) and $5.7 \pm 0.1 \cdot 10^{19}$ Nm (uniform patches), which are equal to moment magnitudes $M_w 7.12 \pm 0.01$ and $M_w 7.10 \pm 0.01$, respectively. Both of our modeled seismic moments are slightly smaller than the results from the global seismic moment tensor inversion ($7.8 \cdot 10^{19}$ Nm of the Global Centroid Moment Tensor catalog, $10.1 \cdot 10^{19}$ Nm, USGS, 2015) and from the study of Sangha et al. (2017) ($13.7 \cdot 10^{19}$ Nm).

4. Surface Expression From Field Data: Structural Features and Their Interpretation

Field studies of surface expressions of the 2015 earthquake north of Lake Sarez are difficult to execute due to the remoteness of the glaciated Muzkol range (Figure 1a). We accessed the northern segment of the rupture, which exhibited lower slip in our model compared to the two southern segments (Figure 4). Our field studies at the southwestern tip of the Officers range (Figure 1a) aimed on mapping earthquake-related surface breaks and possible precursors, addressing fault reactivation versus neoformed breaks, fault geometry, kinematics, and coseismic offsets. Because the previous work (Rutte et al., 2017; Schurr et al., 2014; Strecker et al., 1995) indicated regional en échelon fault segmentation, we further aimed to determine the tips of one

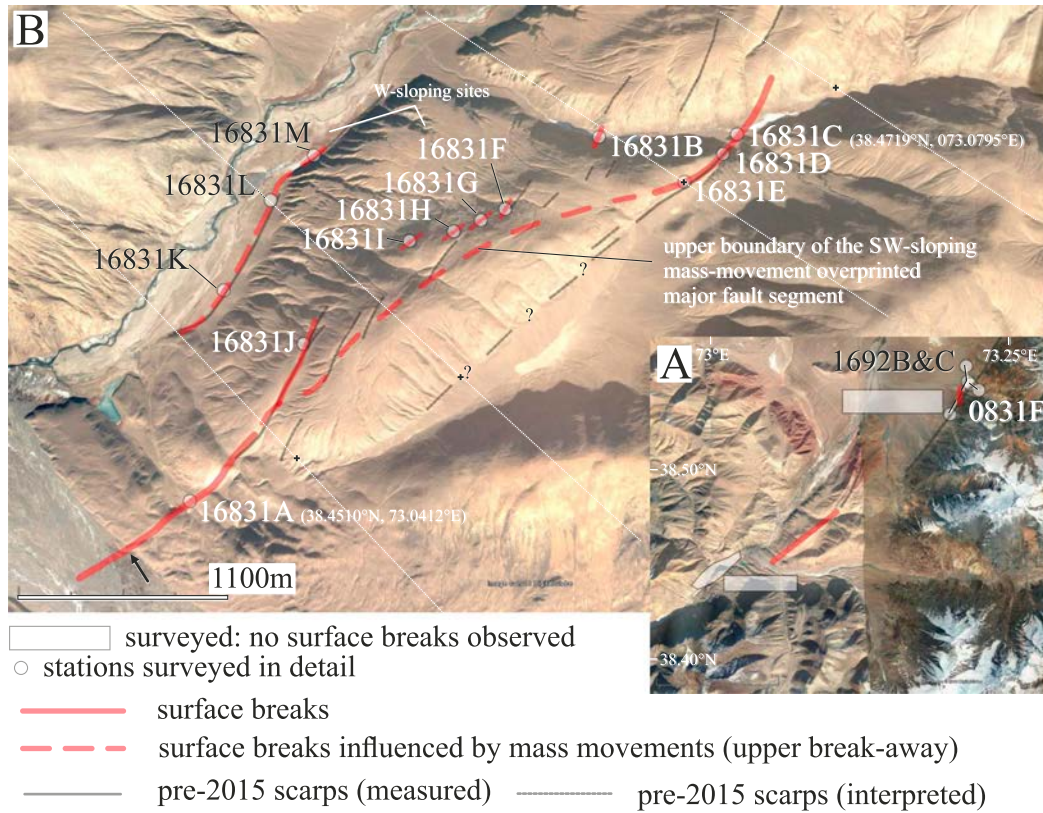


Figure 5. Overview map of (a) field observations including (b) site locations. Images from Google Earth. In Figure 5b we provide coordinates for the two key sites 16831A and 16831C (see Figure 6). The black arrow in the lower left corner marks an apparent riverbank offset. The approximately NW trending white lines are the across-fault amplitude pixel offset tracking profiles shown in Figure 3, and the black crosses on these lines mark the best estimates for the 2015 rupture trace.

segment of the 2015 event to verify its segmentation. As this event affected frozen ground, another goal was the understanding of secondary effects, that is how far liquefaction-inducing mass movements affected earthquake-induced features.

The studied area (Figure 5a) colocalizes with the southern 15 km of the northeastern fault model segment with near-surface slip of to 1–2 m (Figure 4) and a steep, 2 m gradient in the E-W direction across the SAR amplitude pixel offset data (Figure 3). We mapped surface breaks characterized by a right-stepping geometry indicating sinistral strike-slip displacement on the bulk structure. At sites 16831A and 16831C (Figures 5 and 6), the surface breaks cross alluvial fan deposits on subhorizontal ground, making gravitationally induced ground motion overprint unlikely. The structures at these sites (Figure 6) are en échelon secondary fractures that show sinistral offset of small-scale alluvial channels and levees and are characteristically connecting open tension fractures. The latter are mostly longer than the strike-slip fractures. The mean orientations of these secondary structures are similar between these sites (separated by ~3.7 km). The in-site orientation variability is ~45°, with pure-tension fractures and others with a measured or assumed strike-slip component. The fracture walls are uneven and reach up to 1.5 m deep (e.g., image top right in Figure 6a). When crossing vegetated creek beds (e.g., Figure 6c), identical small-scale segmentation is observed. Subordinate features are pressure ridges (<0.5 m high, Figures 6a and 6c), again arranged en échelon, and rare antithetic fractures. We measured the trend of the enveloping surfaces of the largest en échelon secondary features, which likely approximates the orientation of the underlying primary fault. The ~045° trend is similar at both sites, ~019° off the model-determined trend of ~026°, which is better reflected by the mean trend of the secondary features (Figures 6a to 6c). At the southern end of site 16831C, the fault zone narrows and offsets a levee ridge by ~2 m, providing the best field-based offset estimate.

At the northern end of site 16831A, the surface breaks run into a hillside where earthquake-induced mass movements expose grayish-black fault gouge of a preexisting fault zone. Southwest of this site, the riverbank appears sinistrally offset by ~ 30 m on both sides. On the orographic right riverbank (black arrow in Figure 5b), the terrane promontory caused damming and a vegetated floodplain. The only traces of the 2015 event are several meters long fissures with a few centimeters of E-W opening; there are no surface breaks on the orographic left side and on the hilly terrane farther southwest. This “offset” either marks an erosional feature or pre-2015 events; we favor the latter, as this riverbank offset is along strike of the gouge zone observed in 16831A. At site 16831C, we mapped the ~ 10 m wide zone of surface breaks southwestward up a hillslope (Figure S10a, subsite 1), where it narrows to less than one meter and reactivates a preexisting fault zone that cuts consolidated moraine and alluvial fan material and forming a scarp. Slickenlines on different faces of the polished master fault allow the calculation of the reduced stress tensor (e.g., Angelier, 1984), revealing a strike-slip solution with a $\sim 35^\circ$ trending fault plane, similar to the modeled 2015 fault plane. Sites 1692B and 1692C characterize the northernmost surface breaks of the 2015 earthquake. These comprise a few meters long, $\sim N$ trending tension fractures with sinistral strike-slip offset of a few centimeters in horizontal gravelly riverbank deposits (Figure S10b). An ~ 2 m high, pre-2015, $\sim NE$ trending scarp was not reactivated. The piedmont-hillslope transition, partly comprising moraine material, shows several en échelon fractures, some > 10 m long and with up to 0.5 m wide dilatant offset that are likely gravitational mass flow controlled. Farther north, where Schurr et al. (2014) and Rutte et al. (2017) mapped pre-2015 range front faults, we did not find surface breaks.

Sites 16831E to 16831J (Figures 5b and S10c) characterize mass movement overprinted fault segments west of the main, continuous zone of surface breaks. Although these sites show the typical en échelon arrangement of tensional fractures, they are shorter and wider than those on the horizontal sites and are characteristically downhill concave. At least sites 16831F and 16831J follow older gouge zones. Sites 16831K to 16831M (Figures 5b and S10c) are on an abandoned riverbank above the recent one and mark the westernmost observed surface breaks. The structures at these sites reactivate down-to-the-west, pre-recent scarps that can be traced across alluvial fans on pre-2015 Google Earth imagery. The strike of the 2015 features, dominantly pure-tension fractures with up to 0.75 m displacement, but also including en échelon strike-slip and transtensional segments, is approximately NNE and parallel to the riverbank edge; we suspect a mass movement overprint.

Figure 5b summarizes the structures that are expected to be initiated in cohesive material by a small increment of regional shear strain along an approximately NW trending sinistral strike-slip zone. The mapped surface breaks resemble this idealized structural inventory. In our natural case, antithetic strike-slip faults are nearly absent and the secondary structures show a large orientation variation. We attribute the latter mostly to the difficulty to discriminate tensional from strike-slip faults and possibly to rotation during progressive deformation. The mapping shows that the 2015 earthquake created an array of surface breaks compatible with the focal mechanism (Figure 1a) (USGS, 2015) and the geodetically derived fault slip model (Figure 4); they outline a sinistral strike-slip fault zone characterized by segmentation. No primary surface breaks—parallel to the inferred major fault trend—are developed, but the envelope of the secondary features (marked as primary in Figure 6) likely approximates the trend of underlying fault zone. Clearly, the 2015 surface rupture reactivated preexisting faults. The field-derived offset of ≤ 2 m agrees with the observed SAR amplitude pixel offsets (Figure 3). Short-time liquefaction of the frozen ground facilitated the overprint of earthquake-induced structures by gravitationally induced mass movements across a zone much wider than the actual rupture.

Figure 6. Details of the field observations. (a) Site 16831A (see Figure 5b for location and coordinates). The dominant structures are en échelon secondary fractures that show sinistral offset of small-scale alluvial surface morphology. They are characteristically connecting open fractures (top right). These tension fractures are mostly longer than the strike-slip fractures (bottom right), and the fracture walls are uneven and reach up to 1.5 m deep (top right). Pressure ridges are uncommon (top left). Structures are plotted as great circles in lower hemisphere, equal area stereoplots. (b) Idealized summary of structures expected to be initiated in cohesive material by a small increment of regional shear strain along an approximately NW trending sinistral strike-slip zone. The mapped surface breaks resemble this idealized structural inventory. (c) Sites 16831B and 16831C (see Figure 5b for location and coordinates). Vegetated creek beds show identical small-scale segmentation of structures as alluvial fan deposits. The fractures cut grass and small bushes and their root network razor sharp, emphasizing displacement under frozen-ground conditions. Pressure ridges (top right) are arranged en échelon.

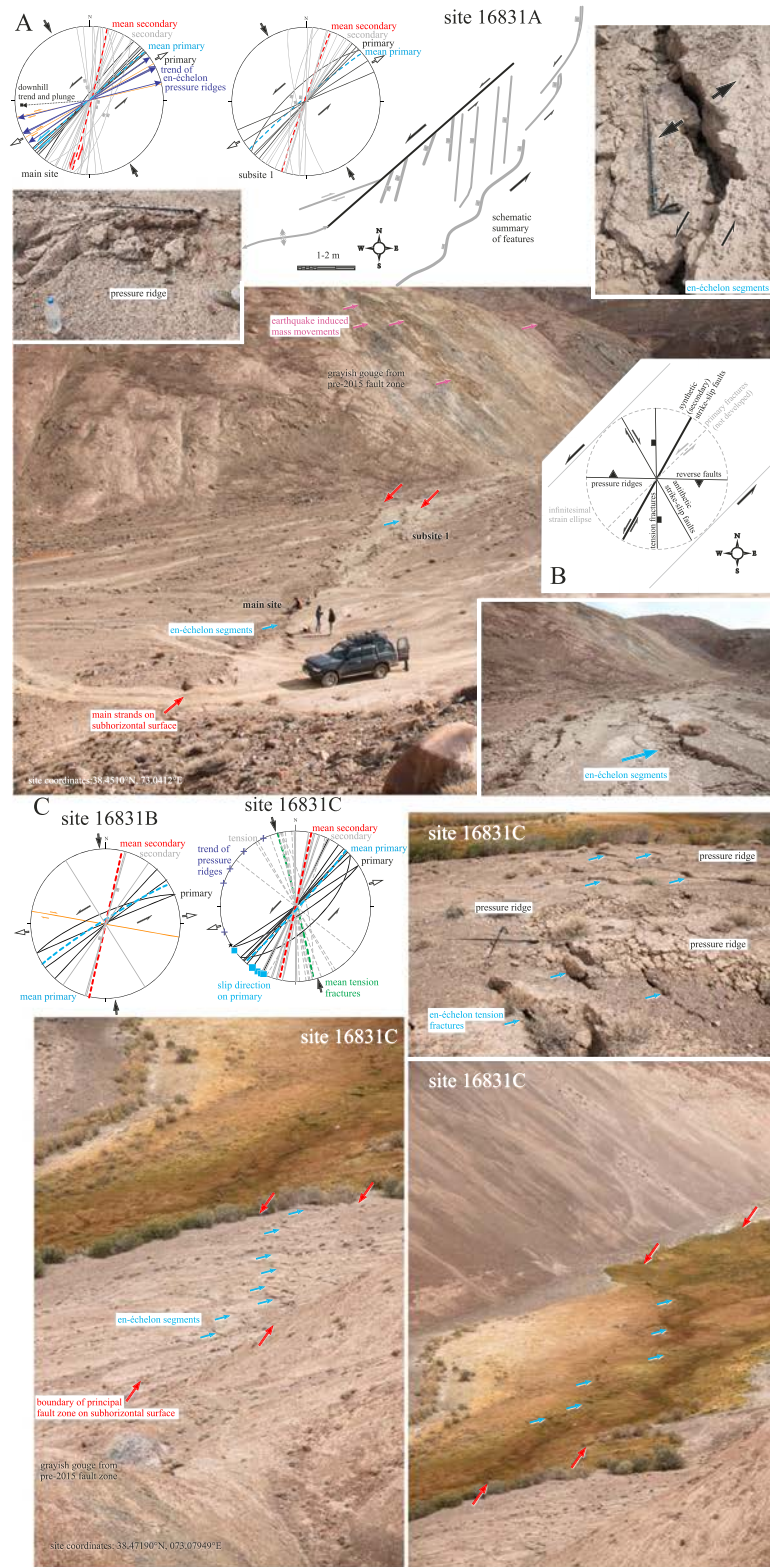


Figure 6. (continued)

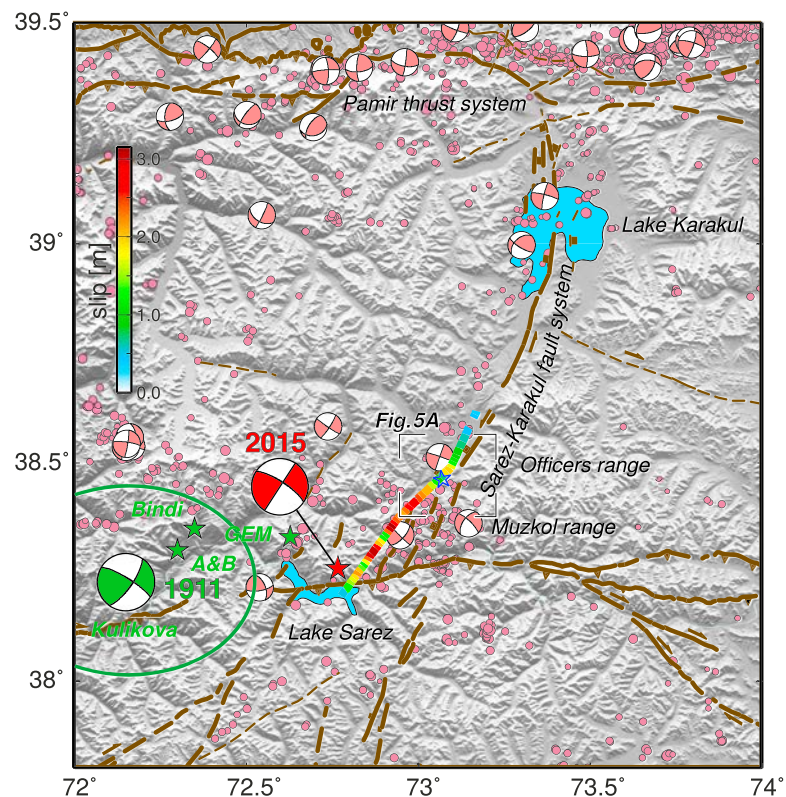


Figure 7. Close-up of the Sarez-Karakul fault system including shallow seismicity (2008–2010 and 2012–2014, purple) (Kufner et al., 2017; Sippl, Schurr, Yuan, et al., 2013), main active faults in brown, focal mechanisms of selected earthquakes in pink (Schurr et al., 2014), the 1911 event in green (Ambraseys & Bilham, 2012; Bindi et al., 2014; Kulikova et al., 2015; Storchak et al., 2013), and the 2015 earthquake in red (USGS, 2015). The color-coded line represents the modeled slip of the 2015 earthquake in the upper 2.5 km of the crust (only slip >0.5 m is shown). The inner frame marks the area of the field observations (Figure 5a), and the blue star (near 73.1°E/38.4°N) highlights the fault offset measurements discussed in section 4 and Figure 5b.

5. Discussion

The 2015 Sarez earthquake rupture appears to have initiated near Lake Sarez based on estimates of its epicenter. It then spreads northeastward crossing the Muzkol range and tapered out between Lake Sarez and Karakul (Figure 7). Seismic back projection of high-frequency emitters confirms the rupture direction (Sangha et al., 2017). Our preferred slip model exhibits highest displacements in the uppermost ~5 km. This is in contrast to other large strike-slip earthquakes (e.g., 1992 Landers and 1999 Hector Mine, California, USA, and 2003 Bam, Iran), which exhibited a slip deficit in the upper few kilometers of the fault (Fialko et al., 2005), possibly due to off-fault inelastic deformation. The amount of slip deficit scales with low values of rock cohesion in dynamic models (Kaneko & Fialko, 2011). Low cohesion occurs, for example, in the damage zone surrounding a fault core. The fact that the southern and central segments of the 2015 rupture—where we modeled the largest offsets—broke midcrustal crystalline rocks, which make up the currently exposed crust of the Muzkol range (Rutte et al., 2017), may have promoted slip reaching the surface. However, whether the earthquake broke the surface and occurred in pristine rocks along these two segments is still unclear, because this part of the rupture was not accessible in our field reconnaissance. The northeastern segment, where we made our field observation, likely is different. There, weakly to nonmetamorphic upper crustal rocks crop out, and we observed preexisting fault zones (gouge, pre-2015 scarps) nearly along the entire rupture. Characteristically, the modeled total slip increases downward along this segment (Figure 4). In addition, the more northerly trend of this rupture segment is akin to the bulk SKFS trend. Thus, we speculate that the preexisting SKFS structure controlled the northeastern segment of the 2015 earthquake (Figure 7).

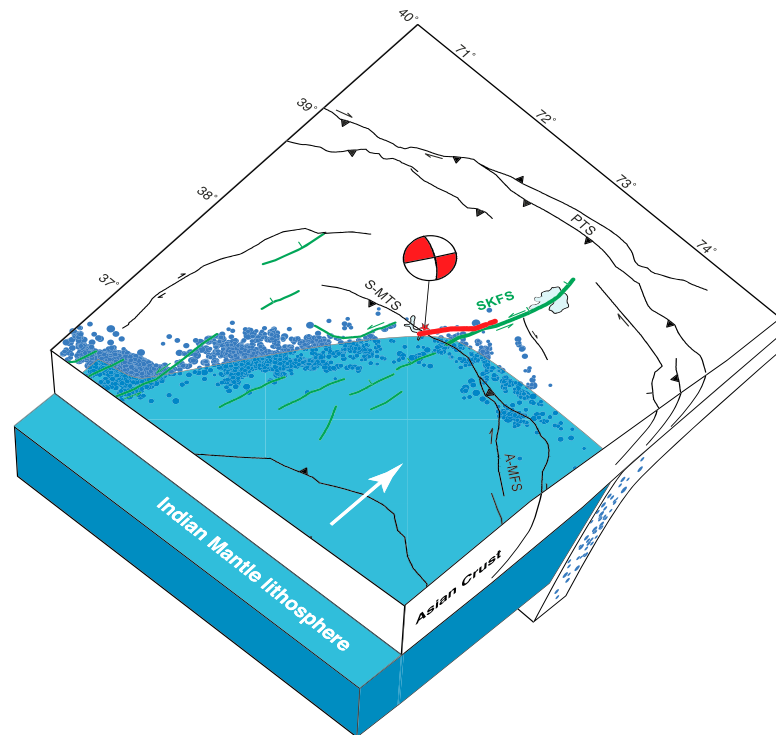


Figure 8. Perspective view of the Indian lithosphere promontory (blue) underthrusting Asian crust (white) beneath the southern and central Pamir. Intermediate-depth seismicity is marked in blue (both 2008–2010 and 2012–2014) (Kufner et al., 2017; Sippl, Schurr, Yuan, et al., 2013) and the surface projection of the rupture plane and focal mechanism of the 2015 event in red. The SKFS and faults that likely formed in the same strain field are in green. A-MFS: Ak-su-Murgab fault system, PTS: Pamir thrust system, SKFS: Sarez-Karakul fault system, and S-MTS: Sarez-Murgab thrust system.

The morphologically expressed trace of the SKFS ends at the southeastern termination of the Officers range (Figure 7). Farther south, Stübner et al. (2013) and Schurr et al. (2014) mapped an array of distributed, morphologically weakly expressed, en échelon, right-stepping faults across the southwestern Pamir (Figures 1, 7, and 8). The modeled southern segment of the 2015 rupture lines up with this system of NNE to NE trending faults (Figures 7 and 8). We infer that the southern segment of the 2015 rupture is transitional to this array and connects deformation along the SKFS to the active, sinistral NNE trending faults of the Hindu Kush farther southwest (Schurr et al., 2014).

The southern end of both the 2015 rupture and the SKFS roughly coincide with a kink in the deep Pamir seismic zone where its strike changes from NE to east (Figures 1 and 8). This kink is overlain by a cluster of shallow seismicity detected during the 2008–2010 campaign (Figure 7) (Schurr et al., 2014), indicating that deformation was active there before the 2015 event.

The deep seismic zone traces the top of the delaminating and retreating Asian lithosphere between about 80 and 150 km depth (Schneider et al., 2013). According to Kufner et al. (2016), an indenter, likely the northwestern edge of the Indian lithosphere (Figure 8), molds the arc shape of this slab. The southern tip of both the 2015 Sarez rupture and the SKFS would hence coincide with the leading northwestern edge of India that has been thrust several hundred kilometers underneath Asian crust. The NE striking fault zones traversing the Pamir may therefore be the crustal manifestation of a plate boundary at mantle depth (Schurr et al., 2014). The fault zones are thus likely accommodating displacement between Asian crust carried on top of Indian lithosphere northward and more stationary Asian crust and mantle farther west. Left-lateral shear measured with the global positioning system between the eastern Pamir and Tajik basin amounts to ~ 15 mm/yr (Ischuk et al., 2013). Most of this shear has been attributed to the Darvaz fault zone separating the western

Pamir and Tajik basin (Figure 1) (Ischuk et al., 2013; Trifonov, 1978). In view of the two most recent large earthquakes, 1911 and 2015, the NE striking shear zones in the western and central Pamir may play a more important role in accommodating this shear. In this context, the 2015 Sarez rupture may be the most recent manifestation of the activation of this shear zone at the northwestern tip of indenting India.

The sign change on the pixel amplitude offset maps show that the rupture stepped right north of the Muzkol range to merge with the range front sinistral-oblique normal faults of the southern SKFS (Figures 3, 4, and 7). The approximately NE trend of the southern SKFS, as emphasized by the 2015 Sarez earthquake and the geodetic and field-based analysis, changes to an approximately north trend at Lake Karakul with increasing importance of normal faulting. We attribute this to a northward increase in the active westward motion of the Pamir plateau into the Tajik basin. This northward increasing rotational component in the westward gravitational collapse of the Pamir crust is traced by (1) (north)westward increasing seismicity (Schurr et al., 2014), (2) (north)westward increasing anticlockwise rotation derived from the GPS velocity field (e.g., Ischuk et al., 2013; Zubovich et al., 2010, 2016), (3) larger paleomagnetically derived anticlockwise rotations in the northeastern than southeastern part of the eastern Tajik basin (Thomas et al., 1994), and (4) a higher abundance of the dextral strike-slip faults along the Pamir thrust system (e.g., range front segmentation) (Sippl et al., 2014; Strecker et al., 2003) than in the Pamir interior.

In 1911, an earthquake of similar size struck the Sarez region. This raises the question of the spatiotemporal and mechanical relationship between this and the 2015 event. Analyzing digitized paper seismograms of the 1911 event, Kulikova et al. (2015) reestimated the magnitude and determined a source mechanism. With a surface wave magnitude M_s 7.7 and a moment magnitude M_w 7.3, this event was slightly larger than the 2015 one (M_s 7.6, M_w 7.2, USGS, 2015). Its mechanism was also similar to the one of the 2015 event and, considering uncertainties, could have been the same. Based on intensity reports, the 1911 event was placed slightly west of Lake Sarez (Figure 7) (Ambraseys & Bilham, 2012; Bindi et al., 2014); the instrumental Global Earthquake Model catalog (Storchak et al., 2013) placed it close to Lake Sarez. Kulikova et al. (2015) relocated the event relative to the 2015 event using absolute arrival times and arrival time differences between *P* and *S* phases. The 2015 event served as a master event that provided traveltimes corrections for the historical stations. This procedure located the event ~40 km west of Lake Sarez and about 50 km west of the 2015 epicenter (Figure 7). Earthquakes of this size with rupture dimensions of ~100 km do not break intact rock but need faults of some maturity. As faults grow, they cast a stress shadow, in which parallel faulting is impeded, setting a lower limit to the separation of the events, if they occurred on separate structures. Stress drop fades at distances away from the fault somewhat smaller than fault length. This would make a rupture at the epicenter of Kulikova et al. (2015) possible, considering its separation from the 2015 event. However, the locations of the 1911 event, based on both intensities and travel times suffer from significant uncertainty due to the sparse, unevenly distributed, and low-quality data available from that time. Considering just the scatter of published epicenters, a location close to or at the 2015 epicenter seems possible.

Could the 2015 event have been a repeater of the 1911 event? The relatively low strain rates in the central Pamir are hardly enough to reload the same fault in slightly more than 100 years: Compared to average GPS rates in the West Pamir, the East Pamir block exhibits 5 ± 2 mm/yr of increased NNE motion (Figure S11). *S-P* phase arrival times measured at European stations are about 6 s less for the 1911 event compared to the 2015 event (Kulikova et al., 2015), indicating that they did not occur at the same location but that the 1911 event was closer to Europe. From a stress perspective, a location of the 1911 event contiguous north or south of the 2015 rupture would be most plausible, albeit less consistent with intensities of shaking and travel times. This question may ultimately be resolved, if a surface rupture of the 1911 event could be found. Given that nearly 10 field expeditions to the Pamir have—albeit the difficulties in accessing remote terranes—not encountered well-expressed, subrecent, NE trending fault scarps in the central Pamir except along the SKFS, we prefer to locate the 1911 event along and NW of the range front faults of the Officers range (Figure 7). This speculation would hint to a reactivation of a pre-2015 fault zone (the SKFS) and locate it along the most prominent mapped, pre-recent scarps. It would place the 2015 event in an area strongly loaded by the 1911 event, and interpreting it as the most recent manifestation of the building of a continuous fault zone along the western edge of the deep Indian intender (connecting the Hindu Kush with the SKFS) (Schurr et al., 2014).

6. Conclusion

We have presented a finite-fault slip model of the 7 December 2015, M_w 7.2 Sarez, Pamir, earthquake, using SAR interferometry, SAR amplitude pixel offsets, and GPS data. The earthquake ruptured on a right-stepping, ~80 km long NE trending fault, accommodating sinistral slip of up to 3.1 m in the uppermost part of the fault. Our data-distribution-driven slip-patch model showed less variance in the slip parameter uncertainties compared to a model with uniform slip patches.

The results of the geodetic modeling were compared to field observations acquired 9 months after the earthquake. Where the rupture was accessible, the field observations such as fault strike and sense and amplitude of slip agree well with what we observed in the seismic and geodetic data.

The 2015 Sarez earthquake rupture shows a compelling geometric relation to the deep Pamir earthquake zone. In a geodynamic context, we suggest that the 2015 Sarez rupture may be the most recent manifestation of a shear zone at the northwestern tip of the Indian indenter at mantle depth.

Acknowledgments

Anatoly Ischuk (Tajik Academy of Sciences), Najibullah Kakar (Norwegian Afghanistan Committee), and Alexander Zubovich (Central Asian Institute of Applied Geosciences) maintain the CGPS stations and provided the raw data. Shokhrukh Murodkulov and Sharifov Umedzhon (both Tajik Academy of Sciences) assisted during fieldwork, which was funded by GFZ. ESA Sentinel-1A SAR data are provided by the Copernicus Sentinels Scientific Data Hub (<https://scihub.copernicus.eu/dhus>). Simone Atzori supported us in implementing the optimal-patch resolution code. Some figures were produced using the Generic Mapping Tools (GMT) public domain software (Wessel et al., 2013).

References

- Ambraseys, N., & Bilham, R. (2012). The Sarez-Pamir earthquake and landslide of 18 February 1911. *Seismological Research Letters*, 83(2), 294–314. <https://doi.org/10.1785/gssrl.83.2.294>
- Angelier, J. (1984). Tectonic analysis of fault-slip data sets. *Journal of Geophysical Research*, 89(B7), 5853–5848. <https://doi.org/10.1029/JB089iB07p05835>
- Atzori, S., & Antonioli, A. (2009). Optimal fault resolution in geodetic inversion of coseismic data. *Geophysical Journal International*, 185, 529–530. <https://doi.org/10.1111/j.1365-246X.2011.04955.x>
- Bindi, D., Parolai, S., Gómez-Capera, A., Locatid, M., Kalmetyeva, Z., & Mikhailova, N. (2014). Locations and magnitudes of earthquakes in Central Asia from seismic intensity data. *Journal of Seismology*, 18, 1–21. <https://doi.org/10.1007/s10950-031-9392-1>
- Cervelli, P., Murray, M. H., Segall, P., Aoki, Y., & Kato, T. (2001). Estimating source parameters from deformation data, with an application to the March 1997 earthquake swarm off the Izu Peninsula. *Journal of Geophysical Research*, 106(B6), 11,217–11,237. <https://doi.org/10.1029/2000JB900399>
- Chevalier, M. L., Pan, J., Li, H., & Wang, M. (2015). Quantification of both normal and right-lateral late Quaternary activity along the Kongur Shan extensional system, Chinese Pamir. *Terra Nova*, 27, 379–391. <https://doi.org/10.1111/ter.12170>
- Creutz, M. (1980). Monte-Carlo study of quantized SU(2) gauge-theory. *Physical Review D: Particles and Fields*, 21(8), 2308–2315. <https://doi.org/10.1103/PhysRevD.21.2308>
- Farr, T. G., Rosen, P. A., Caro, E., Crippen, R., Duren, R., Hensley, S., ... Alsdorf, D. (2007). The shuttle radar topography mission. *Reviews of Geophysics*, 45, RG2004. <https://doi.org/10.1029/2005RG000183>
- Fialko, Y., Sandwell, D., Simons, M., & Rosen, P. (2005). Three-dimensional deformation caused by the Bam, Iran, earthquake and the origin of shallow slip deficit. *Nature*, 435(7040), 295–299. <https://doi.org/10.1038/nature03425>
- Herring, T. A., King, R. W., & McClusky, S. C. (2010a). *GAMIT reference manual—GPS analysis at MIT, release 10.4*. Cambridge, MA: Department of Earth, Atmospheric, and Planetary Sciences, Massachusetts Institute of Technology.
- Herring, T. A., King, R. W., & McClusky, S. C. (2010b). *GLOBK reference manual—Global Kalman filter VLBI and GPS analysis program, release 10.4*. Cambridge, MA: Department of Earth, Atmospheric, and Planetary Sciences, Massachusetts Institute of Technology.
- Herring, T. A., King, R. W., & McClusky, S. C. (2010c). *Introduction to GAMIT/GLOBK, release 10.4*. Cambridge, MA: Department of Earth, Atmospheric, and Planetary Sciences, Massachusetts Institute of Technology.
- Ischuk, A. (2006). Usay natural dam: Problem of security; Lake Sarez, Pamir Mountains, Tadjikistan. *Italian Journal of Engineering Geology and the Environment Special Issue*, 1, 189–192. <https://doi.org/10.4408/IJEGE2006-01.S-26>
- Ischuk, A., Bendick, R., Rybin, A., Molnar, P., Khan, F. S., Kuzikov, S., ... Zubovich, A. V. (2013). Kinematics of the Pamir and Hindu Kush regions from GPS geodesy. *Journal of Geophysical Research: Solid Earth*, 118, 2408–2416. <https://doi.org/10.1002/jgrb.50185>
- Jarvis, A., Reuter, H. I., Nelson, A., & Guevara, E. (2008). Hole-filled SRTM for the globe version 4. Available from the CGIAR-CSI SRTM 90 m Database <http://srtm.csi.cgiar.org>.
- Jónsson, S., Zebker, H., Segall, P., & Amelung, F. (2002). Fault slip distribution of the 1999 M_w 7.1 Hector Mine, California, earthquake, estimated from satellite radar and GPS measurements. *Bulletin of the Seismological Society of America*, 92(4), 1377–1389. <https://doi.org/10.1785/0120000922>
- Kaneko, Y., & Fialko, Y. (2011). Shallow slip deficit due to large strike-slip earthquakes in dynamic rupture simulations with elasto-plastic off-fault response. *Geophysical Journal International*, 186, 1389–1403. <https://doi.org/10.1111/j.1365-246X.2011.05117.x>
- Kouba, J., & Héroux, P. (2001). Precise point positioning using IGS orbit and clock products. *GPS solutions*, 5(2), 12–28. <https://doi.org/10.1007/PL00012883>
- Kufner, S.-K., Schurr, B., Haberland, C., Zhang, Y., Saul, J., Ischuk, A., & Oimahmadov, I. (2017). Zooming into the Hindu Kush slab break-off: A rare glimpse on the terminal stage of subduction. *Earth and Planetary Science Letters*, 461, 127–140. <https://doi.org/10.1016/j.epsl.2016.12.043>
- Kufner, S.-K., Schurr, B., Sippl, C., Yuan, X., Ratschbacher, L., Akbar, A. s/of Mohammad, ... Tilmann, F. (2016). Deep India meets deep Asia: Lithospheric indentation, delamination and break-off under Pamir and Hindu Kush, Central Asia. *Earth and Planetary Science Letters*, 435, 171–184. <https://doi.org/10.1016/j.epsl.2015.11.046>
- Kulikova, G., Schurr, B., Krüger, F., Brzoska, E., & Heimann, S. (2015). Source parameters of the Sarez-Pamir earthquake of 1911 February 18. *Geophysical Journal International*, 205(2), 1086–1098. <https://doi.org/10.1093/gji/ggw069>
- Metropolis, N., Rosenbluth, A. W., Rosenbluth, M. N., Teller, A. H., & Teller, E. (1953). Equation of state calculations by fast computing machines. *Journal of Chemical Physics*, 21(6), 1087–1092. <https://doi.org/10.1063/1.1699114>
- Metzger, S., & Jónsson, S. (2014). Plate boundary deformation in North Iceland during 1992–2009 revealed by InSAR time-series analysis and GPS. *Tectonophysics*, 634, 127–138. <https://doi.org/10.1016/j.tecto.2014.07.027>
- Metzger, S., Jónsson, S., & Geirsson, H. (2011). Locking depth and slip-rate of the Husavik Flatey fault, North Iceland, derived from continuous GPS data 2006–2010. *Geophysical Journal International*, 187(2), 564–576. <https://doi.org/10.1111/j.1365-246X.2011.05176.x>

- Michel, R., & Rignot, E. (1999). Flow of Glaciar Moreno, Argentina, from repeat-pass Shuttle Imaging Radar images: Comparison of the phase correlation method with radar interferometry. *Journal of Glaciology*, 45(149), 93–100. <https://doi.org/10.1017/S002214300003075>
- Mohadjer, S., Bendick, S. R., Ischuk, A., Kuzikov, S., Kostuk, A., Saydullaev, U., ... Zubovich, A. V. (2010). Partitioning of India/Eurasia convergence in the Pamir-Hindu Kush from GPS measurements. *Geophysical Research Letters*, 37, L04305. <https://doi.org/10.1029/2009GL041737>
- Nikolaev, V. (2002). Afghan-Tajik depression: Architecture of sedimentary cover and evolution. *Russian Journal of Earth Sciences*, 4(6), 399–421. <https://doi.org/10.2205/2002ES000106>
- Nöth, L. (1932). Geologische Untersuchungen im nordwestlichen Pamirgebiet und mittleren Transalai. In H. V. Ficker & W. Rickmers (Eds.), *Wissenschaftliche ergebnisse der Alai-Pamir expedition 1928, Teil II*. Berlin: Reimer-Vohsen.
- Okada, Y. (1985). Surface deformation due to shear and tensile faults in a half-space. *Bulletin of the Seismological Society of America*, 75(4), 1135–1154.
- Page, M. T., Custódio, S., Archuleta, R., & Carlson, J. M. (2009). Constraining earthquake source inversions with GPS data: 1. Resolution-based removal of artifacts. *Journal of Geophysical Research*, 114, B01314. <https://doi.org/10.1029/2007JB005449>
- Rutte, D., Ratschbacher, L., Schneider, S., Stübner, K., Stearns, M. A., Gulzar, M. A., & Hacker, B. R. (2017). Building the Pamir-Tibet Plateau—Crustal stacking, extensional collapse, and lateral extrusion in the Central Pamir: 1. Geometry and kinematics. *Tectonics*, 36, 342–384. <https://doi.org/10.1002/2016TC004293>
- Sangha, S., Peltzer, G., Zhang, A., Meng, L., Lian, C., Lundgren, P., & Fielding, E. (2017). Fault geometry of 2015, M_w 7.2 Murghab, Tajikistan earthquake controls rupture propagation: Insights from InSAR and seismological data. *Earth and Planetary Science Letters*, 462, 132–141. <https://doi.org/10.1016/j.epsl.2017.01.018>
- Schneider, F. M., Yuan, X., Schurr, B., Mechie, J., Sippl, C., Haberland, C., ... Negmatullaev, S. (2013). Seismic imaging of subducting continental lower crust beneath the Pamir. *Earth and Planetary Science Letters*, 375, 101–112. <https://doi.org/10.1016/j.epsl.2013.05.015>
- Schöne, T., Zech, C., Unger-Shayesteh, K., Rudenko, V., Thoss, H., Wetzel, H.-U., ... Zubovich, A. (2013). A new permanent multi-parameter monitoring network in Central Asian high mountains—From measurements to data bases. *Geoscience Instrumentation Methods Data Systems*, 2, 97–111. <https://doi.org/10.5194/gid-2-301-2012>
- Schurr, B., Ratschbacher, L., Sippl, C., Gloaguen, R., Yuan, X., & Mechie, J. (2014). Seismotectonics of the Pamir. *Tectonics*, 33(8), 1501–1518. <https://doi.org/10.1002/2014TC003576>
- Schuster, R. L., & Alford, D. (2004). Usoi landslide dam and Lake Sarez, Pamir Mountains, Tajikistan. *Environmental and Engineering Geoscience*, 2, 151–168. <https://doi.org/10.2113/10.2.151>
- Schwab, M., Ratschbacher, L., Siebel, W., McWilliams, M., Lutkov, V., Minaev, V., ... Wooden, J. (2004). Assemblage of the Pamirs: Age and origin of magmatic belts from the southern Tien Shan to the southern Pamirs and their relation to Tibet. *Tectonics*, 23, TC4002. <https://doi.org/10.1029/2003TC001583>
- Sippl, C., Schurr, B., Tympel, J., Angiboust, S., Mechie, J., Yuan, X., ... TIPAGE-Team (2013). Deep burial of Asian continental crust beneath the Pamir imaged with local earthquake tomography. *Earth and Planetary Science Letters*, 384, 165–177. <https://doi.org/10.1016/j.epsl.2013.10.013>
- Sippl, C., Schurr, B., Yuan, X., Mechie, J., Schneider, F. M., Gadoev, M., ... Radjabov, N. (2013). Geometry of the Pamir-Hindu Kush intermediate-depth earthquake zone from local seismic data. *Journal of Geophysical Research: Solid Earth*, 118, 1438–1457. <https://doi.org/10.1002/jgrb.50128>
- Sippl, C., Ratschbacher, L., Schurr, B., Krumbiegel, C., Rui, H., Pingren, L., & Abydybaeva, U. (2014). The 2008 Nura earthquake sequence at the Pamir-Tian Shan collision zone, southern Kyrgyzstan. *Tectonics*, 33(12), 2382–2399. <https://doi.org/10.1002/2014TC003705>
- Storchak, D. A., Di Giacomo, D., Bondár, I., Engdahl, E., Harris, J., Lee, W. H. K., ... Bormann, P. (2013). Public release of the ISC-GEM global instrumental earthquake catalogue (1900–2009). *Seismological Research Letters*, 84, 810–815. <https://doi.org/10.1785/0220130034>
- Strecker, M. R., Arrowsmith, J. R., & Coutand, I. (2003). Differential structural and geomorphic mountain-front evolution in an active continental collision zone: The northwest Pamir, southern Kyrgyzstan. *Geological Society of America Bulletin*, 115(2), 166–181. [https://doi.org/10.1130/0016-7606\(2003\)115<0166:DSAGMF>2.0.CO;2](https://doi.org/10.1130/0016-7606(2003)115<0166:DSAGMF>2.0.CO;2)
- Strecker, M. R., Frisch, W., Hamburger, M. W., Ratschbacher, L., Semiletkin, S., Zamoruyev, A., & Sturchio, N. (1995). Quaternary deformation in the Eastern Pamirs, Tadjikistan and Kyrgyzstan. *Tectonics*, 14(5), 1061–1079. <https://doi.org/10.1029/95TC00927>
- Strozzi, T., Luckman, A., Murray, T., Wegmüller, U., & Werner, C. L. (2002). Glacier motion estimation using SAR offset-tracking procedures. *IEEE Transactions on Geoscience and Remote Sensing*, 40(11), 2384–2391. <https://doi.org/10.1109/TGRS.2002.805079>
- Stübner, K., Ratschbacher, L., Rutte, D., Stanek, K., Minaev, V., Wiesinger, R., ... Project TIPAGE members (2013). The giant Shakh-dara migmatitic gneiss dome, Pamir, India-Asia collision zone. 1: Geometry and kinematics. *Tectonics*, 32, 948–979. <https://doi.org/10.1002/tect.20057>
- Sudhaus, H., & Jónsson, S. (2009). Improved source modeling through combined use of InSAR and GPS under consideration of correlated data errors: Application to the June 2000 Kleifarvatn earthquake Iceland. *Geophysical Journal International*, 176(2), 389–404. <https://doi.org/10.1111/j.1365-246X.2008.03989.x>
- Teshebaeva, K., Sudhaus, H., Echlter, H., Schurr, B., & Roessner, S. (2014). Strain partitioning at the eastern Pamir-Alai revealed through SAR data analysis of the 2008 Nura earthquake. *Geophysical Journal International*, 198(2), 760–774. <https://doi.org/10.1093/gji/ggu158>
- Thomas, J., Chauvin, A., Gapais, D., Bazhenov, M., Perroud, H., Cobbold, P., & Burtman, V. (1994). Paleomagnetic evidence for Cenozoic block rotations in the Tadjik depression (Central Asia). *Journal of Geophysical Research*, 99(B8), 15,141–15,160. <https://doi.org/10.1029/94JB00901>
- Trifonov, V. (1978). Late Quaternary tectonic movements of western and central Asia. *Bulletin of the Geological Society America*, 89(7), 1059–1072.
- U.S. Geological Survey (USGS) (2015). *M* 7.2—104 km W of Murghob, Tajikistan (Tech. Rep.). Menlo Park, CA: US Geological Survey.
- U.S. Geological Survey (USGS) (2016). *M* 6.4—28 km SSE of Sary-Tash, Kyrgyzstan (Tech. Rep.). Menlo Park, CA: US Geological Survey.
- Wegmüller, U., & Werner, C. (1997). Gamma SAR processor and interferometry software. In *ERS symposium on space at the service of our environment* (pp. 1687–1692). Florence, Italy: European Space Agency.
- Wessel, P., Smith, W. H. F., Scharroo, R., Luis, J. F., & Wobbe, F. (2013). Generic Mapping Tools: Improved version released. *Eos, Transactions American Geophysical Union*, 94, 409–410. <https://doi.org/10.1002/2013EO450001>
- Zhou, Y., He, J., Oimahmadov, I., Gadoev, M., Pan, Z., Wang, W., ... Rajabov, N. (2016). Present-day crustal motion around the Pamir Plateau from GPS measurements. *Gondwana Research*, 35, 144–154. <https://doi.org/10.1016/j.gr.2016.03.011>
- Zubovich, A., Schöne, T., Metzger, S., Mosenko, O., Mukhamediev, S., Sharshebaeva, A., & Zech, C. (2016). Tectonic interaction between the Pamir and Tien Shan observed by GPS. *Tectonics*, 35(2), 283–292. <https://doi.org/10.1002/2015TC004055>
- Zubovich, A. V., Wang, X.-Q., Scherba, Y. G., Schelochkov, G. G., Reilinger, R., Reigber, C., ... Beisenbaev, R. T. (2010). GPS velocity field of the Tien Shan and surrounding regions. *Tectonics*, 29, TC6014. <https://doi.org/10.1029/2010TC002772>

3.1.2 Tectonic interaction between the Pamir and Tien Shan observed by GPS

Published as: A. Zubovich, T. Schöne, S. Metzger, O. Mosienko, Sh. Mukhamediev, A. Sharshebaev, C. Zech (2016), Tectonic interaction between the Pamir and Tien Shan observed by GPS, *Tectonics*, **35**. doi:10.1002/2015TC004055

Supporting information: –

Scientific application: Previously-published GNSS survey data across the northern Pamir's rim showed mostly N-S shortening (*Zubovich et al., 2010*). Here, we present dense GNSS data acquired further west and document an increase in dextral shear, providing more evidence for a westward-collapse of the West Pamir. We used high-quality continuous measurements along a short, but densely-spaced GNSS profile across the north-advancing front to constrain the (minimum) slip rate of the Main Pamir thrust.

Methodological advances: A unique high-rate GNSS profile across two continents with a instrument-spacing of a few kilometers only.

Individual Contributions: The network was designed by AZ and TS and me, and installed and maintained by AZ, ShM and AS. The raw GNSS data was processed by OM and CZ, and the kinematics modeled by AZ and me. My main responsibility was the data interpretation. The manuscript was written and edited by AZ, me and TS, all others provided comments.



Tectonics

RESEARCH ARTICLE

10.1002/2015TC004055

Key Points:

- Basic displacement between the Pamir and Tien Shan occurs within 5 km distance around a PFT fault
- There is a zone of increased deformation up to 50-70 km width along the PFT

Correspondence to:

A. Zubovich,
a.zubovich@ciaiag.kg

Citation:

Zubovich, A., T. Schöne, S. Metzger, O. Mosienko, Sh. Mukhamediev, A. Sharshebaev, and C. Zech (2016), Tectonic interaction between the Pamir and Tien Shan observed by GPS, *Tectonics*, 35, doi:10.1002/2015TC004055.

Received 18 OCT 2015

Accepted 14 JAN 2016

Accepted article online 17 JAN 2016

Tectonic interaction between the Pamir and Tien Shan observed by GPS

A. Zubovich¹, T. Schöne², S. Metzger², O. Mosienko¹, Sh. Mukhamediev³, A. Sharshebaev¹, and C. Zech²

¹Central-Asian Institute for Applied Geosciences, Bishkek, Kyrgyzstan, ²GFZ German Research Center for Geosciences, Potsdam, Germany, ³Institute of Physics of the Earth of RAS, Moscow, Russia

Abstract The complex tectonic interplay between the Central Asian Southwest Tien Shan and the north advancing Pamir as well as the role of the Pamir Frontal Thrust (PFT) separating these two orogens along the intervening Alai Valley is yet unclear. In this paper we present data of the newly installed Western Alai GPS profile (WAGP), capturing the deformation signal of both mountain ranges. The 20 km long WAGP records a maximum displacement rate of 9.3 ± 0.8 mm yr⁻¹. The lion's share of displacement (6.0 ± 0.8 mm yr⁻¹) is accommodated between the two stations located directly north and south of the PFT in 5 km distance. The WAGP data nicely complement the existing South Tien Shan and the Pamir GPS network data, which we present here in a combined reference frame and use it as input for horizontal block rotation/strain models. The model results show that both the Southwest Tien Shan and the Pamir behave as uniformly strained blocks and rotate counterclockwise (with respect to Eurasia) by $0.93 \pm 0.11^\circ$ Myr⁻¹ and $0.62 \pm 0.05^\circ$ Myr⁻¹, respectively. The Southwest Tien Shan undergoes NNE-SSW shortening of $-22.1 \pm 1.5 \times 10^{-9}$ year⁻¹ with an insignificant perpendicular extension. The Pamir is shortening with a rate of $-10.2 \pm 3.8 \times 10^{-9}$ year⁻¹ in a NNE-SSW direction, which is nearly 2.5 times less than its lateral extension rate. A band of increased deformation along the PFT is bounded to the north by the northern rim of the Alai Valley and extends up to 30–50 km south into the Pamir.

1. Introduction

Located in the northwestern part of the India-Asia collisional belt, the Pamir and Tien Shan are mountain belts formed by the same tectonic processes as the ongoing Indian-Eurasian collision (Figure 1). The Tien Shan is a mountain belt of ~2000 km length consisting of alternating ranges and valleys striking W-E to WSW-ENE. The belt width varies between ~100 km in the east and ~350 km in the west, where it is parted by the NW-SE oriented, right-lateral Talas-Ferghana fault (TFR). West of the TFR the Ferghana Valley splits the Southwest Tien Shan into the northern Chatkal-Kurama range system and the South Tien Shan with the series of E-W oriented, narrow ranges, and valleys (Figure 1). The Pamir is a high-mountain plateau elevated to 4000 m and more with a complex interior structure of an arcuate northward convex shape. Today, it acts as a relatively rigid indenter penetrating northward into the Eurasian plate and thus overriding the former Tajik-Tarim basin [Burtman and Molnar, 1993; Sobel *et al.*, 2013].

The Pamir links to the western flank of the massive Tibetan Plateau with a mean altitude of 5000 m [Fielding *et al.*, 1994]. The Pamir-Tien Shan region accommodates a higher deformation over a shorter distance compared to the Tibetan Plateau [Schmidt *et al.*, 2011; van Hinsbergen *et al.*, 2011] and is capable to produce magnitude 7 earthquakes in nearly decadal repeat times (ISC-GEM catalog) [Storchak *et al.*, 2013]. The last large seismic event in the vicinity was the 2008 magnitude 6.6 Nura earthquake with an epicenter just east of the Alai Valley [Sippl *et al.*, 2014; Teshebaeva *et al.*, 2014]. The seismic data indicating an inclined zone at the northern Pamir front and matching high strain rate at the surface suggest a subduction of the Tien Shan lithosphere beneath the Pamir [Burtman and Molnar, 1993; Strecker *et al.*, 2003; Zubovich *et al.*, 2010; Sobel *et al.*, 2013] excluding the upper crust [Mechie *et al.*, 2012; Sippl *et al.*, 2013a, 2013b]. The Alai Valley, the last remnant of the formerly connected Tajik-Tarim basin, is squeezed between the South Tien Shan and the Pamir. It has an extent of ~120 km in lateral and ~20 km in longitudinal directions, an average elevation of 3000 m, and the Neogene sediment thickness reaches at least 3 km adjacent to the Trans Alai range (Figure 2a) [Arrowsmith and Strecker, 1999]. Its main tectonic features are the recently active Pamir Frontal Thrust (PFT) system (Figure 1), which runs parallel to the Pamir's front and, a 10–15 km farther south but rooting in the same decollement, the Main Pamir Thrust (MPT) that was activated ~25 Ma ago [Sobel and Dumitru, 1997; Coutand *et al.*, 2002; Sobel *et al.*, 2013; Thompson *et al.*, 2015]. Published displacement rates

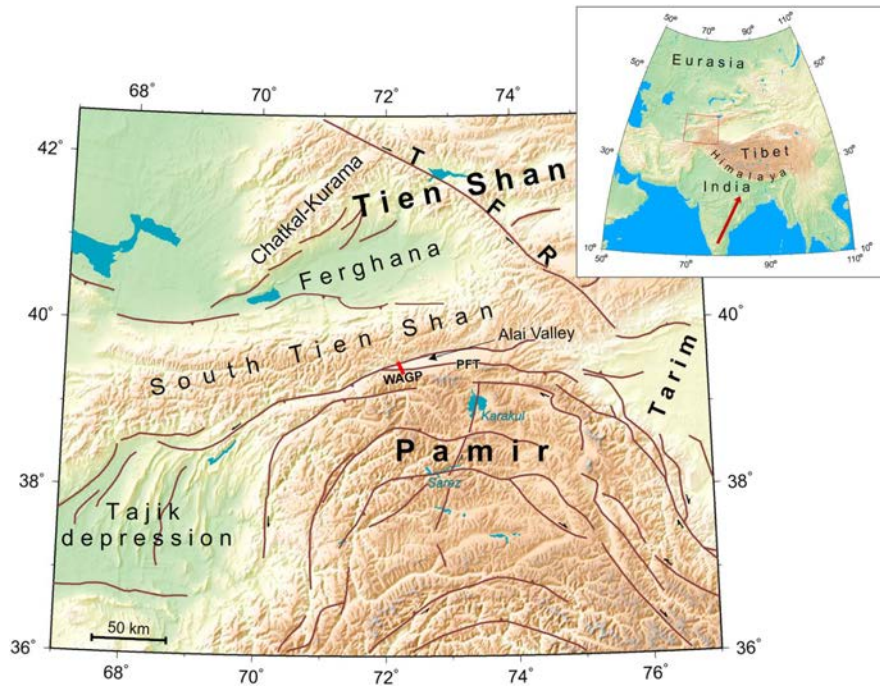


Figure 1. Topographic map of the Pamir and Southwest Tien Shan located at the northwestern end of the India-Asia collisional belt (inset). Brown lines here and on other figures are faults from Schurr *et al.* [2014]. The red line indicates the location of the Western Alai GPS profile (WAGP). The red arrow on the insert represents the northeastern advance of India (IGS station IISC) relative to the Eurasian plate.

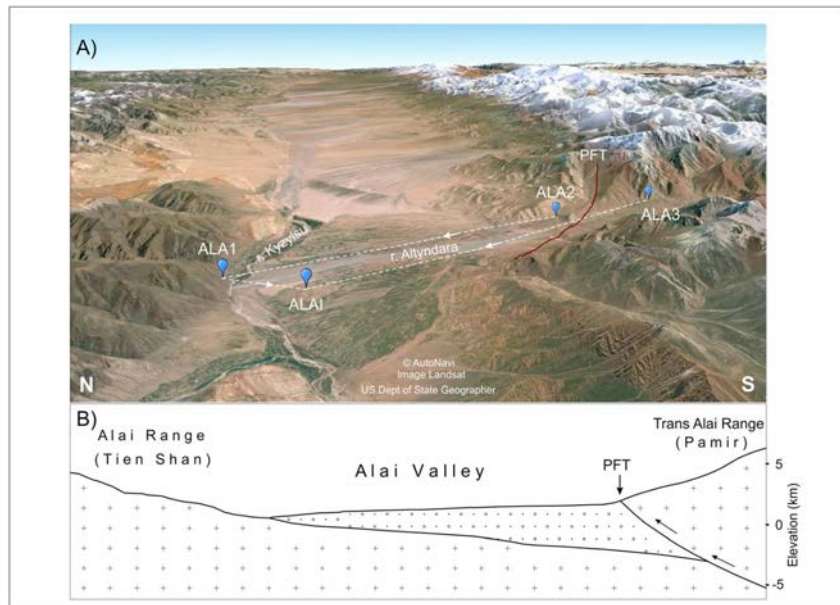


Figure 2. (a) View of the Alai Valley from its western toward its eastern end (3-D Google™ image). The blue pins mark the WAGP stations along the Altyndara River. The stations are named from north to south as ALA1, ALA2, and ALA3. The white dashed lines illustrate the data transfer directions and the brown line marks the PFT surface fault trace. (b) Simplified sketch of the N-S cross section of Alai Valley illustrating the Pamir overthrusting the Tien Shan. Topography after Figure 12d of Coutand *et al.* [2002].

Table 1. Locations, Horizontal Rates and Uncertainties of WAGP Stations

Station	Coordinates		Velocities in a Eurasian-Fixed Reference Frame (mm yr^{-1})		Velocities Relative to ALA1 (mm yr^{-1})	
	Longitude	Latitude	East	North	East	North
ALA1	72°10.748'	39°33.179'	-0.7 ± 1.6	8.4 ± 1.6		
ALAI	72°09.953'	39°31.592'	-1.4 ± 1.5	9.5 ± 1.5	-0.5 ± 0.6	1.1 ± 0.7
ALA2	72°15.104'	39°26.596'	-2.8 ± 1.6	11.0 ± 1.6	-2.1 ± 0.7	2.6 ± 0.8
ALA3	72°16.472'	39°24.134'	-7.5 ± 1.6	14.8 ± 1.6	-6.8 ± 0.8	6.4 ± 0.8

across these marginal features span a wide range. *Coutand et al.* [2002] reconstructed rates of 0.6–0.8 mm/yr from balanced cross sections. *Burtman and Molnar* [1993] estimated rates of ~ 3.5 mm/yr based on the seismic moment release calculation of earthquakes between 1963 and 1988, and *Arrowsmith and Strecker* [1999] found ~ 6 mm/yr rates during the Holocene by measuring the displaced river terraces. The highest observed rate of the N-S convergence is between 10 and 15 mm/yr as derived from Global Positioning System (GPS) measurements [*Zubovich et al.*, 2010].

The tectonically highly interesting area of the Pamir and Tien Shan was subject of various GPS research projects [*Abdrakhmatov et al.*, 1996; *Reigber et al.*, 2001; *Mohadjer et al.*, 2010; *Zubovich et al.*, 2010; *Ischuk et al.*, 2013]. First GPS observations in the Tien Shan were carried out in 1992, and since then more than 300 GPS points were installed and measured. Tajik GPS observations started in 2007 and covered the Pamir and Tajik depression, although the Northeast Pamir was measured earlier within the campaigns mentioned above. The obtained data showed that the internal deformation of the Pamir is minor and that E-W elongation exceeds the N-S shortening [*Ischuk et al.*, 2013]. The highest deformation rates in the Pamir-Tien Shan region are observed across the Alai Valley with at least 10 mm yr^{-1} to possibly 15 mm yr^{-1} [*Zubovich et al.*, 2010]. The authors suggested that this high velocity gradient is accommodated by the PFT. However, due to the sparse spatial data sampling it has so far been impossible to define the exact distribution of the deformation. This motivated us to study the high deformation zone in the Alai Valley in more detail in order to better understand the Pamir-Tien Shan interaction and also the relation between tectonic faults like the PFT and seismicity.

2. West Alai GPS Profile

The Alai Valley with the PFT fault system located at its southern rim is a suitable area to study active fault strands and their behavior using GPS data. Some of the highest shortening rates in central Asia are observed here. Displacement rates of more than 10 mm yr^{-1} over 20 km and data uncertainties of less than $1\text{--}2 \text{ mm yr}^{-1}$ allow relatively quick and reliable rate estimates.

In fall 2013 we installed a profile of four continuously operating GPS stations in the western part of the Alai Valley (Figure 2a and Table 1) to better identify the recent deformation pattern between the Pamir and the Tien Shan. The profile layout was partly chosen by the location of a clearly identified surface trace of the PFT system [*Arrowsmith and Strecker*, 1999; *Strecker et al.*, 2003] (Figure 3). The area is relatively easy accessible and inhabited, which allows regular station maintenance. Limiting factors for the installation were the spatial extent of the profile (~ 20 km), the topography (high-frequency data transfer), and restricted site access due to the nearby state border.

The stations ALA3 and ALA1 mark the southern and northern ends of the profile. They were installed on bedrock outcrops of the Pamir Trans Alai and Tien Shan Alai ranges, respectively, on a metallic tube of 8 cm diameter and ~ 100 cm length. The inner stations ALAI and ALA2 were installed on sediment on a 350 cm long metallic tube driven and concreted 160–180 cm into the ground. All stations are equipped with Septentrio (Global Navigation Satellite Systems) GNSS receivers and NavXperience antennas. Power supply of each of the stations ALA1, ALA2, and ALA3 is ensured by a 120 Wp solar panel and a 30 Ah battery for backup. The power management is controlled by a solar regulator, which also provides fail-over prevention and reboots the system every other day. The sampling rate is 10 s. All three stations are connected to the main station, ALAI, by 2.4 GHz radio communication links. While ALA1 and ALA3 send the data directly to the main station, ALA2 is routing the data through ALA1, using it as a bridge (Figure 2b). Being the master station, ALAI is built as consistent as possible with the Remotely Operated Monitoring Station concept [*Schöne et al.*, 2013].

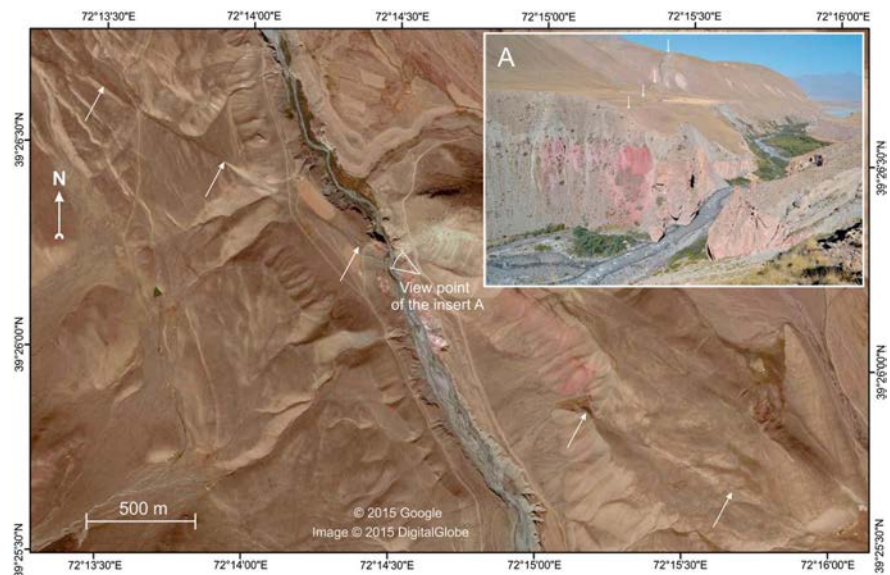


Figure 3. PFT surface fault trace, highlighted by white arrows in Google™ aerial imagery and on personal field observations (a) with a view to the northwest.

It transfers the data of all four stations to our processing center via the satellite system VSAT. ALAI is also equipped with a low-bandwidth satellite system link (Iridium) that is used for information reception and station management during VSAT outages. The ALAI GPS data are sampled at 1 Hz in accordance to Schöne *et al.* [2013].

3. Data Processing and WAGP Velocity Results

Standard GPS processing with GAMIT/GLOBK is generally performed in three steps [Herring, 2004; Herring *et al.*, 2009]: (1) Calculation of daily solutions including station coordinates and covariance matrices (H files), (2) combination of the daily solutions to one campaign solution for the time period of each field campaign, and (3) the computation of velocity vectors on the basis of the campaign solutions. For the continuous Western Alai GPS profile (WAGP) data we skipped step (2) and combined the WAGP daily solutions with the GPS campaign data of the Tien Shan-Pamir region acquired since 1995 [Zubovich *et al.*, 2010; Ischuk *et al.*, 2013] into a common Eurasian-fixed reference frame tied by the 15 IGS (International GNSS Service) stations VILL, MADR, IRKT, NRIL, NVSK, POL2, ARTU, GLSV, POTS, WTZR, ONSA, NYAL, CAGL, WSRT, and KOSG (<http://igs.org/network>). By doing so, we can compare the current WAGP displacement rates with the existing campaign GPS rates. The resulting data set covers the vast territory from the Tarim basin and the Tajik depression to the Kazakh platform including the Tien Shan and the Pamir. The resulting relative rates of the WAGP stations sufficiently exceed the signal-to-noise ratio and can be used for further analysis. In Table 1 they present by the east and north velocity components parallel and perpendicular to the Pamir front—one of the main structures here.

The endpoints of the GPS profile ALA3 and ALA1 are located in the Pamir and the Tien Shan, respectively, and measure the relative motion of the margins of these mountain belts. They show a total relative displacement of $9.3 \pm 0.8 \text{ mm yr}^{-1}$ with an azimuth of -43° (measured clockwise from north). This is slightly less but within the error of the $10\text{--}15 \text{ mm yr}^{-1}$ of shortening observed at the eastern end of the Alai Valley [Zubovich *et al.*, 2010]. Reasons for this lower shortening rate might be the fact that the motion of ALA3 is affected by the partially or fully locked MPT, or that there exist other active fault strands farther south in the Altyndara Valley, outside the WAGP. The highest rate change is observed between stations ALA3 and ALA2 with $6.0 \pm 0.8 \text{ mm yr}^{-1}$ over a distance of only 5 km along an azimuth of -39° . We assume that the observed difference is associated with an active fault branch of the PFT system located between both stations (Figures 3 and 4).

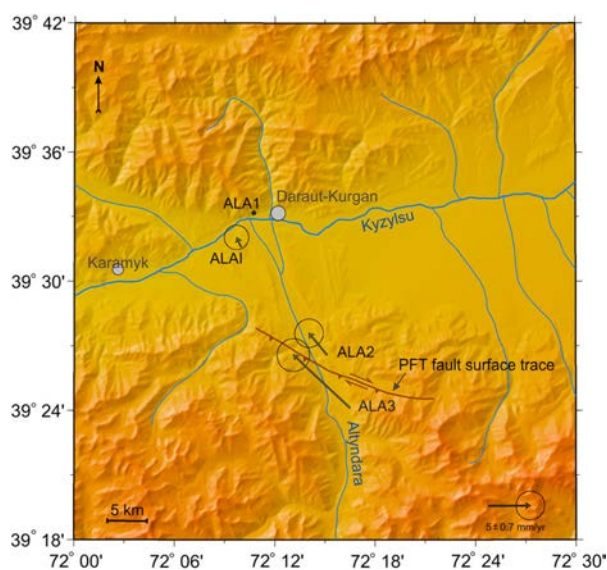


Figure 4. GPS velocities and 95% confidence ellipses of the WAGP stations relative to the station ALA1. The fault surface trace of the PFT system is identified by field observations and aerial photographs (see Figure 3).

Google™ aerial imagery nicely delineates the surface trace of this active fault with an azimuth of -61° inside the ALA3-ALA2 sector (Figure 3). From this, we calculate a right-lateral fault-parallel rate component of $5.6 \pm 0.8 \text{ mm yr}^{-1}$ and a fault-perpendicular shortening of $2.2 \pm 0.8 \text{ mm yr}^{-1}$ between ALA3 and ALA2. Despite the relatively low shortening rate across the fault there is field evidence of at least 3 m of vertical offset on its southern side (insert on Figure 3). Undoubtedly, this fault was described by *Arrowsmith and Strecker* [1999] as clearly shown by a 4 m vertical offset (115° – 120° strike, south side up). The fault was reactivated several times during Quaternary time, and Quaternary slip rate for this zone was defined at least 2.5 mm/yr and could be as high as 6 mm/yr .

The relative displacement rate between the stations ALA2 and ALA1 is $2.2 \pm 0.6 \text{ mm yr}^{-1}$ with an azimuth of -42°

over a distance of $\sim 12 \text{ km}$. The data do not give evidence whether this deformation is due to another active fault strand north of ALA2 as published on several maps [e.g., *Coutand et al.*, 2002; *Strecker et al.*, 2003; *Kalmetieva et al.*, 2009] or if this is a gradient due to a (partial) locking of the PFT. Finally, the relative displacement rates between the northernmost stations ALA1 and ALA3 is $1.2 \pm 0.7 \text{ mm yr}^{-1}$ to the direction of an azimuth of -66° over a distance of slightly more than 3 km. Although for both ALA2-ALA1 and ALA1-ALA3 segments the velocity differences are hardly distinguishable from the uncertainties, they do not conflict with the right-lateral strike-slip shift of the Pamir relative to the Tien Shan and the total trend of their convergence.

4. Interaction of the Pamir and Tien Shan

The last two large earthquakes occurred nearly two decades before the beginning of the GPS time series (the 1974, $m_b = 6.4$ Markansu earthquake [Jackson et al., 1979] or at the outer extent of the study area, just east of the Alai Valley (the 2008, magnitude 6.6 Nura earthquake [Sippl et al., 2014; Teshebaeva et al., 2014]). We therefore assume that the GPS observations represent the interseismic phase of the current seismic cycle, where the faults are either locked or exhibit creeping. Using the full GPS data set, we model the Pamir and Southwest Tien Shan mountain belts as flat, uniformly strained bodies [Zubovich and Mukhamediev, 2010] (also see Appendix A for mathematical details), estimate the strain rate uniformity of these belts and define how the deformation on the WAGP relate to them. We thereby applied an iterative inversion procedure: First, we calculated the rotation and strain rate parameters separately for the Pamir and Southwest Tien Shan using two GPS data subsets. The resulting best fit parameters were used to forward model the horizontal velocity vectors. Then, we discarded the point with the largest residual between the modeled data and the observations. The procedure was repeated until the remaining data points showed residuals below a certain threshold. For the Pamir region we selected 10 GPS points with residuals below 1.3 mm yr^{-1} (black dots in Figure 5) and for the Southwest Tien Shan region 24 GPS points with residuals below 1 mm yr^{-1} (Figure 6). The stricter criterion for the Southwest Tien Shan data is justified by the larger amount of available GPS data and smaller data uncertainties. In addition, we propagated the GPS data uncertainties through the inversion (using the best fit model parameters) by adding a random Gaussian noise (normalized by the single data uncertainties) to the input data and repeated this procedure 1000 times, in order to obtain a statistical model parameter uncertainty estimation following [Metzger et al., 2011].

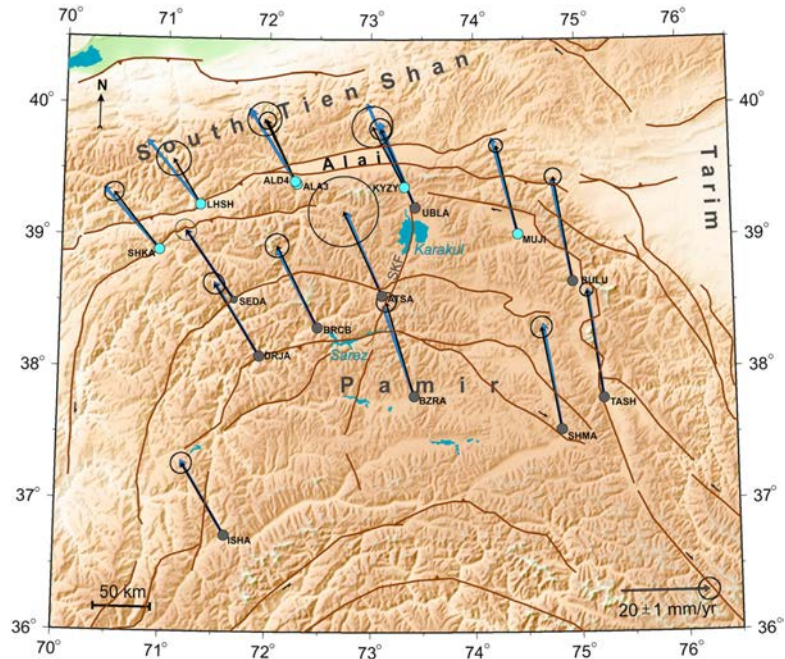


Figure 5. Observed (in black, with 95% confidence ellipses) and modeled (blue) GPS velocities of the Pamir region in a Eurasian-fixed reference frame. Black dots mark the GPS points used for the inversion.

For the Pamir region, the best fit model nicely matches the input GPS observations in terms of azimuth and amplitudes (Figure 5). This leads to the conclusion that the interior of the Pamir is uniformly strained within data uncertainties. This observation does not support the findings based on microseismicity of *Schurr et al.* [2014] about the NNE-SSW trending Sarez-Karakul sinistral normal fault system (SKF on Figure 5). However, the recent 2015 magnitude 7.2 earthquake with the epicenter near Lake Sarez most probably reactivated exactly this fault (U.S. Geological Survey). One explanation might be that the deep seismic processes observed by *Schurr et al.* [2014] did not yet reach the Earth’s surface.

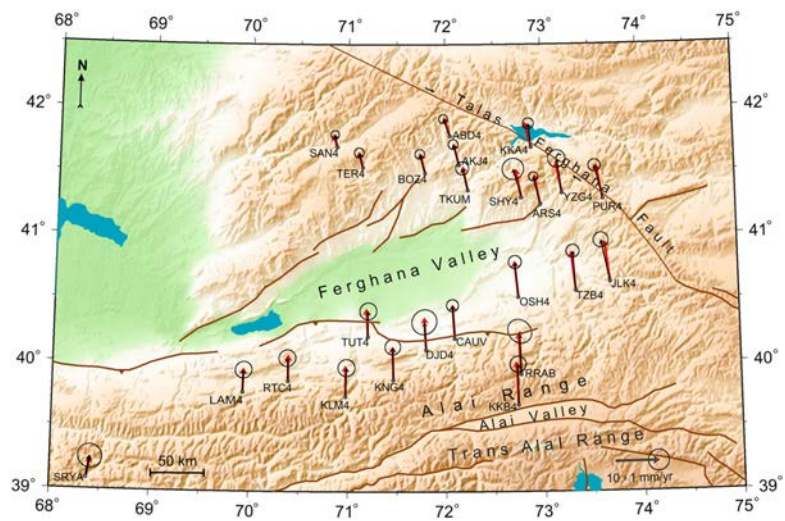


Figure 6. Observed (in black, with 95% confidence levels) and modeled (red) GPS velocities in the Southwest Tien Shan in a Eurasian-fixed reference frame.

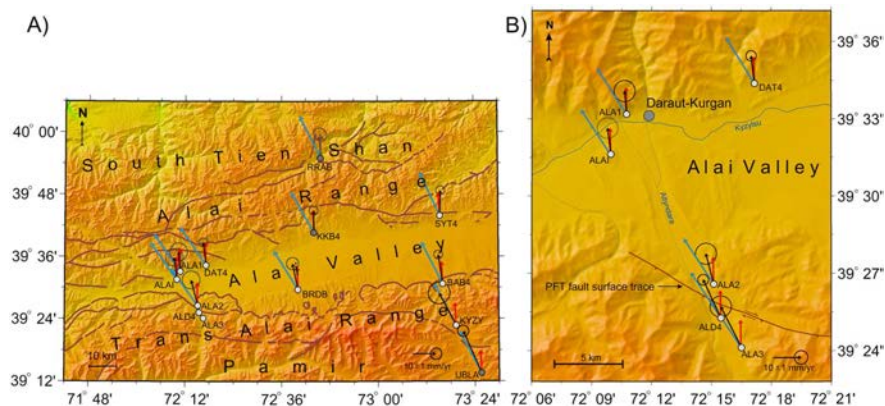


Figure 7. (a) Observed (black, with 95% confidence ellipses) and modeled (red for the Southwest Tien Shan and blue for the Pamir model parameters) velocities in the Alai Valley with respect to stable Eurasia. The stations KKB4, RRAB, and UBLA (black dots) were used as input data for the Southwest Tien Shan and Pamir model inversion, respectively. (b) Close up of the western Alai Valley with WAGP stations.

The best fit strain rate parameters for the Pamir have a maximal strain rate $E1 = 26.6 \pm 1.8 \times 10^{-9} \text{ year}^{-1}$ and a minimal strain rate $E2 = -10.2 \pm 3.8 \times 10^{-9} \text{ year}^{-1}$ with an $E2$ axis azimuth of $17.5 \pm 2.4^\circ$ in NNE-SSW direction (positive strain rates represent extension and negative rates are shortening). The extension rate is thus nearly 2.5 times larger than the orthogonal shortening rate, which can indicate gravitation-driven, lateral mass outflux of the Pamir as proposed by, e.g., *Burtman [2013]*, *Stübner et al. [2013]*, and *Schurr et al. [2014]*. The faster ESE-WNW lengthening with respect to the NNE-SSW shortening could be a sign of crustal thinning of the Pamir but that is apparently compensated by the subducting Tien Shan below the Pamir. The angular velocity of the Pamir rotation with respect to Eurasia is estimated with $0.93 \pm 0.11^\circ \text{ Myr}^{-1}$ counterclockwise around a pole at $61.2 \pm 1.7^\circ$ east and $33.1 \pm 0.6^\circ$ north.

The Pamir GPS data points, which were not used for the inversion but forward modeled (cyan dots, Figure 5), are located along the active northern perimeter of the Pamir, where strain is not uniform anymore. The closer the data points are to the Pamir's margin, the higher the difference between the observed data and the model. This indicates that the northern frontal strip of the Pamir is deformed more rapidly than its internal parts. It might be possible that one or more active fault strands south of the PFT system (e.g., the Main Pamir Trust [*Sobel et al., 2013*]) absorb parts of the strain rate along the Pamir's front. Another explanation could be that the Pamir's front has a greater capability to be strained than its interior, due to the decreasing crustal thickness toward the north. In addition, the farther the Northern Pamir data points (except SHKA) are to the west, the smaller the east component of the observed velocities are compared to the model.

For the Southwest Tien Shan region the fit between model and observations is very good (Figure 6). We find a maximum strain rate $E1 = -0.7 \pm 1.1 \times 10^{-9} \text{ year}^{-1}$ and a minimal strain rate $E2 = -22.1 \pm 1.5 \times 10^{-9} \text{ year}^{-1}$ with an azimuth of $-19.8 \pm 2.4^\circ$. We thus observe a NNW shortening in the Tien Shan without any lengthening in ENE direction. The angular velocity of the Southwest Tien Shan with respect to Eurasia is estimated with $0.62 \pm 0.05^\circ \text{ Myr}^{-1}$ counterclockwise around a pole at $62.6 \pm 0.8^\circ$ east and $39.0 \pm 0.3^\circ$ north. This result agrees well with calculations of *Zubovich and Mukhamediev [2010]*, where the field of horizontal velocity gradient was determined by a method of superimposed triangulations, as well as with the previously derived angular velocity of the Fergana Valley of $0.73 \pm 0.08^\circ \text{ Myr}^{-1}$ [*Zubovich et al., 2010*]. From this we conclude that the mountain parts of the Southwest Tien Shan covered by the GPS data presented here and the Fergana basin are in fact one uniform strain unit.

We also forward modeled the GPS points in the Alai Valley including WAGP stations and using the best fit model parameters both for the Pamir and for the Southwest Tien Shan (Figure 7). The Southwest Tien Shan model nicely predicts the data of the GPS points north of the valley, but it clearly overestimates the southern points located at the foot of the Trans Alai Range. The GPS velocities acquired close to the PFT system differ from the modeled velocities both in amplitude and azimuth. This could mean that the uniformly deformed, differently rotating moving Pamir and Tien Shan interact with each other along the PFT and

thereby produce strike-slip and thrust displacements. A partial or complete locking of the faults enforces these displacements to be nonuniformly distributed around the PFT.

5. Conclusion

In this paper we present the first observations of the Western Alai GPS profile (WAGP, Figure 4 and Table 1), a profile of four continuous GPS stations installed in 2013 across the West of the Alai Valley, and the surface trace of the Pamir Frontal Thrust (PFT), where the highest deformation rates in the Pamir-Tien Shan region are revealed. These new GPS data help to better localize areas of high strain and identify the nature of slip of the local strand of the PFT system. In addition, the data nicely complement the existing GPS networks in the Pamir and the Southwest Tien Shan, which we present here in a combined reference frame.

Inversions of block rotation/strain models show that the inner part of both the Southwest Tien Shan (including the Ferghana Valley) and the Pamir behave as uniformly strained blocks rotating in horizontal plane with respect to Eurasia counterclockwise with the angular velocities of $0.62 \pm 0.05^\circ \text{ Myr}^{-1}$ and $0.93 \pm 0.11^\circ \text{ Myr}^{-1}$, respectively (Figures 5 and 6). This agrees well with previous results using different methods and data sets [Zubovich and Mukhamediev, 2010; Zubovich *et al.*, 2010]. The Southwest Tien Shan exceeds a NNE-SSW shortening of $-22.1 \pm 1.5 \times 10^{-9} \text{ year}^{-1}$ without any extension in perpendicular direction. The best fit model parameters for the Pamir region show that its shortening in a NNE-SSW direction of $-10.2 \pm 3.8 \times 10^{-9} \text{ year}^{-1}$ is nearly 2.5 times lower than its lateral extension. This is further evidence for gravitational-driven lateral mass outflux of the Pamir as it was suggested before [Burtman, 2013; Stübner *et al.*, 2013; Schurr *et al.*, 2014]. A faster ESE-WNW lengthening than NNE-SSW shortening could lead to crustal thinning of the Pamir, but that is apparently compensated by subduction of the Tien Shan below the Pamir. The GPS data observed in and near the Alai Valley, which marks the Southwest Tien Shan and the Pamir border area, agree poorly with the model predictions. We conclude that along the PFT we find a zone of increased deformation, which is bounded by the northern rim of the Alai Valley on the north and in the south enters 30–50 km into the Pamir.

The 20 km long WAGP reveals a maximum displacement rate of $9.3 \pm 0.8 \text{ mm yr}^{-1}$ between the outermost stations. Considering the fact that the southernmost station is located only 3 km from the fault surface trace, this agrees well with the $10\text{--}15 \text{ mm yr}^{-1}$ measured earlier across the eastern end of Alai Valley [Zubovich *et al.*, 2010]. The spatial resolution of the data points, however, does not give clear evidence if the total deformation on the PFT is accommodated by a single, locked fault or if the PFT is creeping freely and additional active strands without clear surface expressions exist. To answer this question and assess the locking degree of the PFT we extend the WAGP particularly toward the south and densify the station spacing with additional GPS points. From the deformation rates provided by the stations directly north and south of the PFT, however, we can separate the fault slip into a stronger right-lateral, fault-parallel component of at least $5.6 \pm 0.8 \text{ mm yr}^{-1}$ and a less dominant fault-perpendicular shortening of at least $2.2 \pm 0.8 \text{ mm yr}^{-1}$.

Appendix A: Inverting 2-D Linear Velocity Field

In the following, vectors and second-order tensors are designated by bold Latin small and uppercase letters. Symbols \cdot , \mathbf{x} , and \otimes stand for the scalar, vector, and tensor (dyadic) products, correspondingly. Superscripts T and $^{-1}$ denote the transpose and inverse tensor.

Let a linear velocity field $\mathbf{v}(\mathbf{x})$ be realized in a plane material domain Ω , i.e.,

$$\mathbf{v}(\mathbf{x}) = \mathbf{x} \cdot \mathbf{G} + \mathbf{b}, \quad \mathbf{x} \in \Omega, \quad (\text{A1})$$

where \mathbf{v} is the horizontal velocity of a material point possessing the radius vector \mathbf{x} , and the second-order tensor \mathbf{G} and the vector \mathbf{b} are constants throughout Ω . By differentiating \mathbf{v} with respect to \mathbf{x} it is apparent that \mathbf{G} is the velocity gradient (i.e., $\mathbf{G} = \text{grad } \mathbf{v}$) which can be uniquely decomposed into symmetric and antisymmetric parts by

$$\mathbf{G} = \mathbf{E} + \mathbf{W} \quad (\mathbf{E} = \mathbf{E}^T, \quad \mathbf{W} = -\mathbf{W}^T). \quad (\text{A2})$$

Here \mathbf{E} is the constant strain rate tensor of the homogeneously deformed domain Ω ; \mathbf{W} is the spin associated with the angular velocity vector \mathbf{w} by equation

$$\mathbf{x} \cdot \mathbf{W} = \mathbf{x} \times \mathbf{w}, \quad (\mathbf{w} = \omega \mathbf{n}), \quad (\text{A3})$$

which is valid for arbitrary vector \mathbf{x} . In equation (A3) \mathbf{n} is a unit vector orthogonal to the deformation plane and ω is the angular velocity of the domain which is positive for counterclockwise rotation when looking from the end of \mathbf{n} .

Information about the real horizontal velocity field $\mathbf{v}^{\text{real}}(\mathbf{x})$ in Ω is represented by the velocity vectors $\mathbf{v}^{(i)}$ specified at the set of K discrete points (GPS stations) $\mathbf{x}^{(i)} \in \Omega$, $i = 1, \dots, K$. The problem is to determine \mathbf{G} and \mathbf{b} in equation (A1) in such a way as to find the best fit between $\mathbf{v}^{\text{real}}(\mathbf{x})$ and the model field $\mathbf{v}(\mathbf{x})$. For this purpose one can minimize the residual functional J ,

$$J = \sum_{i=1}^K (\mathbf{v}^{(i)} - \mathbf{x}^{(i)} \cdot \mathbf{G} - \mathbf{b}) \cdot (\mathbf{v}^{(i)} - \mathbf{x}^{(i)} \cdot \mathbf{G} - \mathbf{b}) \rightarrow \min \quad (\text{A4})$$

for which the following equations should be solved

$$\frac{\partial J}{\partial \mathbf{G}} = 0, \quad \frac{\partial J}{\partial \mathbf{b}} = 0. \quad (\text{A5})$$

The solution of equation (A5) can be expressed as

$$\mathbf{G} = \mathbf{C}^{-1} \cdot \mathbf{A}, \quad \mathbf{b} = \mathbf{v}^0 - \mathbf{x}^0 \cdot \mathbf{C}^{-1} \cdot \mathbf{A}, \quad (\text{A6})$$

where

$$\mathbf{x}^0 = \frac{1}{K} \sum_{i=1}^K \mathbf{x}^{(i)}, \quad \mathbf{v}^0 = \frac{1}{K} \sum_{i=1}^K \mathbf{v}^{(i)} \quad (\text{A7})$$

$$\mathbf{A} = \sum_{i=1}^K (\mathbf{x}^{(i)} \otimes \mathbf{v}^{(i)}) - K \mathbf{x}^0 \otimes \mathbf{v}^0, \quad \mathbf{C} = \sum_{i=1}^K (\mathbf{x}^{(i)} \otimes \mathbf{x}^{(i)}) - K \mathbf{x}^0 \otimes \mathbf{x}^0. \quad (\text{A8})$$

The desired result for the model field $\mathbf{v}(\mathbf{x})$,

$$\mathbf{v}(\mathbf{x}) = \mathbf{v}^0 + (\mathbf{x} - \mathbf{x}^0) \cdot \mathbf{C}^{-1} \cdot \mathbf{A}, \quad (\text{A9})$$

exists if $\det \mathbf{C} \neq 0$, i.e., the GPS stations are not located along a straight line.

The seeking strain rate \mathbf{E} and the angular velocity ω are determined from the first relation in equation (A6) by using equations (A2) and (A3). The \mathbf{E} 's eigenvalues E_1 and E_2 ($E_1 \geq E_2$) and orientation of principal axes are found from \mathbf{E} by conventional methods.

Acknowledgments

We thank Edward Sobel and Lothar Ratschbacher for constructive reviews of this paper. The data for this paper are available by contacting the corresponding author.

References

- Abdrakhmatov, K. Y., et al. (1996), Relatively recent construction of the Tien Shan inferred from GPS measurements of present-day crustal deformation rates, *Nature*, *384*, 450–453.
- Arrowsmith, J. R., and M. R. Strecker (1999), Seismotectonic range-front segmentation and mountain-belt growth in the Pamir-Alai region, Kyrgyzstan (India-Eurasia collision zone), *Geol. Soc. Am. Bull.*, *111*(11), 1665–1683.
- Burtman, V. S. (2013), The geodynamics of the Pamir-Punjab syntaxis, *Geotectonics*, *47*(1), 31–51.
- Burtman, V. S., and P. Molnar (1993), Geological and geophysical evidence for deep subduction of continental crust beneath the Pamir, *Geol. Soc. Am. Spec. Pap.*, *281*, 1–76.
- Coutand, I., M. R. Strecker, J. R. Arrowsmith, G. Hillel, R. C. Thiede, A. Korjenkov, and M. Omuraliev (2002), Late Cenozoic tectonic development of the intramontane Alai Valley (Pamir–Tien Shan region, central Asia): An example of intracontinental deformation due to the Indo-Eurasia collision, *Tectonics*, *21*, 1053–1071, doi:10.1029/2002TC001358.
- Fielding, E., B. Isacks, M. Barazangi, and C. Duncan (1994), How flat is Tibet?, *Geology*, *22*, 163–167.
- Herring, T. A. (2004), *GLOBK: Global Kalman Filter VLBI and GPS Analysis Program Version 4.1*, Mass. Inst. of Technol., Cambridge.
- Herring, T. A., R. W. King, and S. C. McClusky (2009), *Introduction to GAMIT/GLOBK, Release 10.35*, Mass. Inst. of Technol., Cambridge.
- Ischuk, A., et al. (2013), Kinematics of the Pamir and Hindu Kush regions from GPS geodesy, *J. Geophys. Res. Solid Earth*, *118*, 2408–2416, doi:10.1002/jgrb.50185.
- Jackson, J., P. Molnar, H. Patton, and T. Fitch (1979), Seismotectonic aspects of the Markansu Valley, Tadjikistan, earthquake of August 11, 1974, *J. Geophys. Res.*, *84*, 6157–6167.
- Kalmetieva, Z. A., A. V. Mikolaichuk, B. D. Moldobekov, A. V. Meleshko, M. M. Jantaev, and A. V. Zubovich (2009), *Atlas of Earthquakes in Kyrgyzstan*, CAIAG, Bishkek, ISBN 978-9967-25-829-7.
- Mechie, J., et al. (2012), Crustal and uppermost mantle structure along a profile across the Pamir and southern Tien Shan as derived from project TIPAGE wide-angle seismic data, *Geophys. J. Int.*, *188*, 385–407, doi:10.1111/j.1365-246X.2011.05278.x.

- Metzger, S., S. Jónsson, and H. Geirsson (2011), Locking depth and slip-rate of the Húsavík Flatey fault, North Iceland, derived from continuous GPS data 2006–2010, *Geophys. J. Int.*, *192*, 441–455, doi:10.1111/j.1365-246X.2011.05176.x.
- Mohadjer, S., et al. (2010), Partitioning of India-Eurasia convergence in the Pamir-Hindu Kush from GPS measurements, *Geophys. Res. Lett.*, *37*, L04305, doi:10.1029/2009GL041737.
- Reigber, C., G. W. Michel, R. Galas, D. Angermann, J. Klotz, J. Y. Chen, A. Papschev, R. Arslanov, V. E. Tzurkov, and M. C. Ishanov (2001), New space geodetic constraints on the distribution of deformation in Central Asia, *Earth Planet. Sci. Lett.*, *191*(1–2), 157–165, doi:10.1016/S0012-821X(01)00414-9.
- Schmidt, J., B. R. Hacker, L. Ratschbacher, K. Stübner, M. Stearns, A. Kylander-Clark, J. M. Cottle, A. A. G. Webb, G. Gehrels, and V. Minaev (2011), Cenozoic deep crust in the Pamir, *Earth Planet. Sci. Lett.*, *312*(3–4), 411–421, doi:10.1016/j.epsl.2011.10.034.
- Schöne, T., C. Zech, K. Unger-Shayesteh, V. Rudenko, H. Thoss, H.-U. Wetzel, A. Gafurov, J. Illigner, and A. Zubovich (2013), A new permanent multi-parameter monitoring network in Central Asian high mountains—From measurements to data bases, *Geosci. Instrum., Methods Data Syst.*, *2*, 97–111, doi:10.5194/gid-2-301-2012.
- Schurr, B., L. Ratschbacher, C. Sippel, R. Gloaguen, X. Yuan, and J. Mechie (2014), Seismotectonics of the Pamir, *Tectonics*, *33*, 1501–1518, doi:10.1002/2014TC003576.
- Sippel, C., et al. (2013a), Geometry of the Pamir-Hindu Kush intermediate-depth earthquake zone from local seismic data, *J. Geophys. Res. Solid Earth*, *118*, 1438–1457, doi:10.1002/jgrb.50128.
- Sippel, C., B. Schurr, J. Timpel, S. Angiboust, J. Mechie, X. Yuan, F. M. Schneider, S. V. Sobolev, L. Ratschbacher, and C. Haberland (2013b), Deep burial of Asian continental crust beneath the Pamir imaged with local earthquake tomography, *Earth Planet. Sci. Lett.*, *384*, 165–177.
- Sippel, C., L. Ratschbacher, B. Schurr, C. Krumbiegel, H. Rui, L. Pingren, and U. Abdybaev (2014), The 2008 Nura earthquake sequence at the Pamir-Tian Shan collision zone, southern Kyrgyzstan, *Tectonics*, *33*, 2382–2399, doi:10.1002/2014TC003705.
- Sobel, E., and T. Dumitru (1997), Thrusting and exhumation around the margins of the western Tarim basin during the India-Asia collision, *J. Geophys. Res.*, *102*, 5043–5063.
- Sobel, E., J. Chen, L. Schönbohm, R. Thiede, D. Stockli, M. Sudo, and M. Strecker (2013), Oceanic-style subduction controls late Cenozoic deformation of the Northern Pamir orogen, *Earth Planet. Sci. Lett.*, *363*, 204–218.
- Storchak, D. A., D. Di Giacomo, I. Bondár, E. R. Engdahl, J. Harris, W. H. K. Lee, A. Villaseñor, and P. Bormann (2013), Public release of the ISC-GEM global instrumental earthquake catalogue (1900–2009), *Seismol. Res. Lett.*, *84*(5), 810–815, doi:10.1785/0220130034.
- Strecker, M. R., G. E. Hilley, J. R. Arrowsmith, and I. Coutand (2003), Differential structural and geomorphic mountain-front evolution in an active continental collision zone: The Northwest Pamir, Southern Kyrgyzstan, *Bull. Geol. Soc. Am.*, *115*(2), 166–181.
- Stübner, K., et al. (2013), The giant Shakh-dara migmatitic gneiss dome, Pamir, India-Asia collision zone, I: Geometry and kinematics, *Tectonics*, *32*, 948–979, doi:10.1002/tect.20057.
- Teshebaeva, K., H. Sudhaus, H. Ehtler, B. Schurr, and S. Roessner (2014), Strain partitioning at the eastern Pamir-Alai revealed through SAR data analysis of the 2008 Nura earthquake, *Geophys. J. Int.*, *198*(2), 760–774.
- Thompson, J. A., D. W. Burbank, T. Li, J. Chen, and B. Bookhagen (2015), Late Miocene northward propagation of the northeast Pamir thrust system, northwest China, *Tectonics*, *34*, 510–534, doi:10.1002/2014TC003690.
- van Hinsbergen, D. J. J., P. Kapp, G. Dupont-Nivet, P. C. Lippert, P. G. DeCelles, and T. H. Torsvik (2011), Restoration of Cenozoic deformation in Asia and the size of Greater India, *Tectonics*, *30*, TC5003, doi:10.1029/2011TC002908.
- Zubovich, A. V., and S. A. Mukhamediev (2010), A method of superimposed triangulations for calculation of velocity gradient of horizontal movements: Application to the Central Asian GPS network, *Geodyn. Tectonophys.*, *1*(2), 169–185.
- Zubovich, A. V., et al. (2010), GPS velocity field for the Tien Shan and surrounding regions, *Tectonics*, *29*, TC6014, doi:10.1029/2010TC002772.

3.1.3 Cyclic fault slip under the magnifier: Co- and postseismic response of the Pamir front to the 2015 M_w 7.2 Sarez, Central Pamir, earthquake

Published as: A. Zubovich, S. Metzger, T. Schöne, J. Kley, O. Mosienko, C. Zech, B. Moldobekov, A. Sharshebaev (2022), Cyclic fault slip under the magnifier: Co- and postseismic response of the Pamir front to the 2015 M_w 7.2 Sarez, Central Pamir, earthquake, *Tectonics*, **41**, e2022TC007213. doi:10.1029/2022TC007213

Supporting information: available online

Data publication: S. Metzger, N. Kakar, A. Zubovich, M. Borisov, S. Saif, A. H. Panjsheri, J. R. Rahmani, M. Y. Zaryab, M. T. Rezai, Z. Deng, R. Bendick, S.-K. Kufner, J. Okoiev, (2021), Survey mode GNSS data, acquired 2014–2019 in the Afghan Hindu Kush and across northern Pamir margin, Central Asia. *GFZ Data Services*, doi:10.5880/GFZ.4.1.2021.003.

Scientific application: This work is a follow-up of *Zubovich et al. (2016)*, presenting longer time-series and a spatial extension of the initial profile. The main observable in the dense GNSS time-series across the Pamir's northern front are the co-seismic effects in the intermediate field of the 2015 Pamir earthquake (at ~ 150 km distance). We show that the concept of a co-seismic damage zone needs to be revisited: Not only the near-field, but also the intermediate field exhibits independent activation, leading to (in this case) temporary fault unloading of adjacent faults.

Methodological advances: The GNSS observation profile across the Pamir frontal thrust of *Zubovich et al. (2016)* has been densified (~ 2.5 km) and elongated, which allows to detect co- and interseismic fault kinematics in unprecedented resolution and validate similar, but remote observations of co-seismic triggering from InSAR and sparse, but similar observations from the West Pamir.

Individual Contributions: AZ was responsible for the cGNSS, I for the sGNSS network. cGNSS and sGNSS data were processed independently by OS and ZD, and analyzed independently by me and AZ. I processed and interpreted all InSAR data. JK contributed with geological data and interpretation. I and AZ were the leading authors in the writing process, supported by all co-authors.

Tectonics®

RESEARCH ARTICLE

10.1029/2022TC007213

Key Points:

- The 2015 Sarez earthquake unlocked the Aramkungey fault at 150 km distance but in the following 0.5–2.5 years the locking began again
- 10–20 mm Alai coseismic displacements toward the Sarez earthquake epicenter led to a slight decrease in the load state of this area
- The Sarez coseismic deformations attenuated faster in the decompaction strip around the Aramkungey fault with a width of at least 7.5 km

Supporting Information:

Supporting Information may be found in the online version of this article.

Correspondence to:

A. Zubovich,
a.zubovich@caiag.kg

Citation:

Zubovich, A., Metzger, S., Schöne, T., Kley, J., Mosienko, O., Zech, C., et al. (2022). Cyclic fault slip under the magnifier: Co- and postseismic response of the Pamir front to the 2015 M_w 7.2 Sarez, Central Pamir, earthquake. *Tectonics*, 41, e2022TC007213. <https://doi.org/10.1029/2022TC007213>

Received 12 JAN 2022

Accepted 5 JUL 2022

Author Contributions:

Data curation: O. Mosienko

Cyclic Fault Slip Under the Magnifier: Co- and Postseismic Response of the Pamir Front to the 2015 M_w 7.2 Sarez, Central Pamir, Earthquake

A. Zubovich¹ , S. Metzger² , T. Schöne², J. Kley³ , O. Mosienko¹, C. Zech², B. Moldobekov¹, and A. Shsarshebaev¹

¹Central-Asian Institute for Applied Geosciences, Bishkek, Kyrgyzstan, ²Helmholtz Centre Potsdam, GFZ German Research Centre for Geosciences, Potsdam, Germany, ³Georg-August-University Göttingen, Geoscience Centre, Structural Geology & Geodynamics, Göttingen, Germany

Abstract The constant increase of geodetic instrumentation over the past decades enables us to not only detect ever smaller tectonic signals but also to monitor their evolution in time and space. We present spatial and temporal slip variations observed on a fault affected by a large, intermediate-field earthquake: the 2015 M_w 7.2 Sarez, Central Pamir, earthquake ruptured the sinistral, NE-trending Sarez-Karakul fault system. 120–170 km North of the main rupture, the thin-skinned, E-trending Pamir thrust system bounding the Pamir to the North was co-seismically activated. We derived co-seismic offsets and post-seismic rates observed by two dense, high-rate Global Positioning System (GPS) profiles crossing the Pamir thrust system at different longitudes. The continuous GPS observations of the western profile focus on the dextral, NW-striking Aramkungey fault segment that connects two thrust faults with opposite dip. We compare inter-, co- and post-seismic displacement rates by complementing the continuous data with survey-mode GPS data and East rates derived from satellite radar interferometric displacement time-series. All the GPS stations were shifted toward the epicenter against the direction of the interseismic load with an increased gradient in the Aramkungey fault segment. During the postseismic stage, the fault-parallel and fault-perpendicular rates were affected differently, suggesting gradual re-locking of the Aramkungey fault after its unlocking by right-lateral co-seismic slip.

Plain Language Summary The 2015 M_w 7.2 Sarez earthquake, occurred in the Central Pamir, caused m-scale displacement of the Earth's surface. This earthquake also affected another system near the northern Pamir front at 120–170 km distance from the epicenter where the Pamir thrust system separates the Pamir from the Alay valley (a testimony of an ancient ocean) and the adjacent Tien Shan mountain range to the North. Time-series analysis of accurate positioning data (GPS) showed 10–20 mm displacements of the Alai crust surface toward the earthquake epicenter with an increased level of deformation near the western segment of the system—in the zone of the Aramkungey right strike-slip fault. As a result of the earthquake, this fault was unlocked, but then gradually began to be relocked, accelerating the strain accumulation in the following 4.5 years.

1. Introduction

It is generally assumed that faults are either locked and accumulate strain elastically, which is then released instantly in an earthquake, or that they behave more plastically by accommodating constant (or transient) slow slip. They may also accommodate a mixture of both. If lithospheric strain is released in large earthquakes, stress-release continues during the post-seismic period. The postseismic phase includes (a) afterslip on the ruptured fault (e.g., Marone et al., 1991; Perfettini et al., 2010), (b) poro-elastic rebound due to pore fluid pressure changes (e.g., Jónsson et al., 2003; Peltzer et al., 1998) and (c) viscoelastic mantle relaxation (e.g., Nur & Mavko, 1974; Wang et al., 2012). These processes can last months to decades depending on earthquake magnitude and rheological properties, with relocking taking place simultaneously (Bürgmann & Dresen, 2008). Eventually, the seismic cycle returns to the interseismic stage, where strain is being accumulated in a quasi-linear fashion.

Unlike oceanic subduction zones with a well-defined plate interface, the geometry of intercontinental faults is often unknown and slip rates are significantly slower thus leading to an underestimation of the regional seismic hazard potential. In the plate interior, the lithosphere is fractured in a most complex way, probably pre-stressed and can be triggered by small transient stress perturbations (Calais et al., 2016). Consequently,

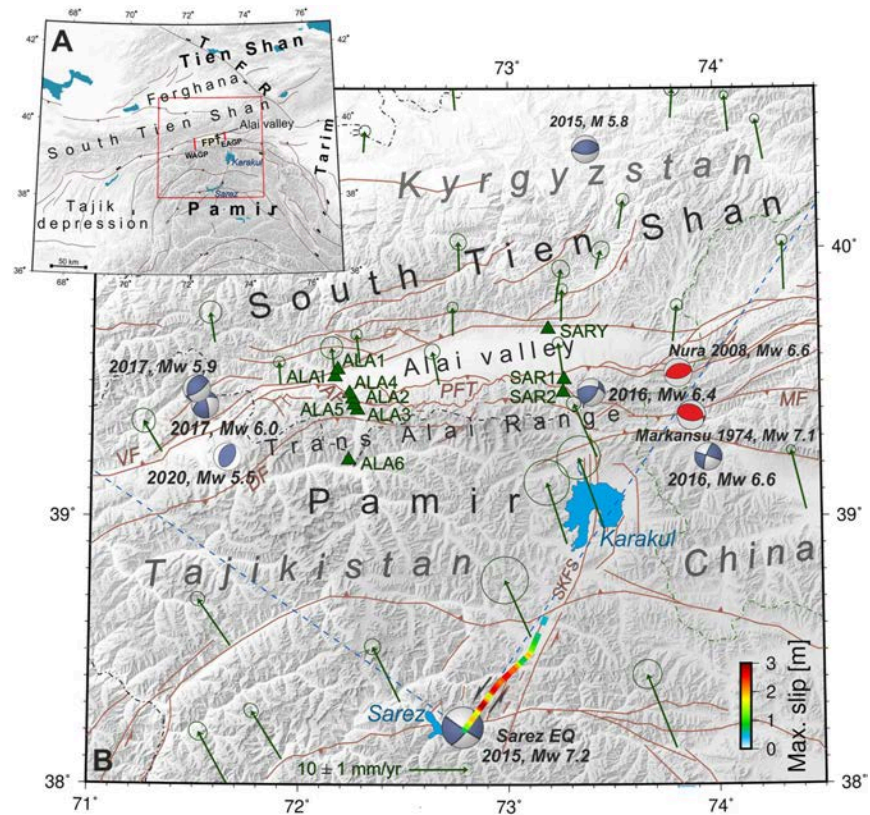


Figure 1. (a) Tectonic map of the Alai valley and its enclosing mountain ranges, the South Tien Shan and the north-advancing Pamir, at the northwestern tip of the India-Asia collisional belt. (b) The western and eastern Alai GPS profiles (green triangles) are located in a tensional quadrant of the sinistral 2015 M_w 7.2 Sarez earthquake (dashed blue lines), focal mechanism from USGS, color-coded co-seismic slip of Metzger et al., (2017). Violet focal mechanisms represent all $M_w \geq 5.5$ earthquakes (GEOFON, 2006), labeled by year and magnitude, that occurred during GPS data acquisition; red mechanisms relate to earthquakes mentioned in the text. Green arrows indicate interseismic GPS rates (Zubovich et al., 2010, 2016). Mapped faults (in brown) from Mohadjer et al. (2016); AF—Aramkungey fault, DF—Darvaz fault, MF—Markansu fault, PFT—Pamir frontal thrust, SKFS—Sarez-Karakul fault system, VF—Vakhsh fault.

continental earthquakes are often unexpected and most fatal, as they often also initiate secondary effects, like landslides or flooding due to blocked rivers. Continental collision zones often behave more like intercontinental than plate-boundary faults; large earthquakes can create highly complex fracture patterns due to dynamics and/or static stress changes (Xu et al., 2020).

The Pamir and the Tien Shan in Central Asia belong to the tectonically most active regions of the India-Eurasian collision zone and are known to host devastating earthquakes (Figure 1a). Examples in the northern Tien Shan are the 1,911 moment magnitude M_w 8.0 Kebin earthquake (Kulikova & Krüger, 2015) and the 1946 Chatkal earthquake with a body wave magnitude of M_B 7.5 (Kulikova, 2016), and in the South Tien Shan the 1949 M_w 7.6 Khait earthquake (Evans et al., 2009; Kulikova, 2016). The 1911 M_B 7.3 (Kulikova et al., 2016) and 2015 M_w 7.2 Sarez earthquakes (Metzger et al., 2017; Sangha et al., 2017) ruptured the center of the Pamir and the 1974 M_w 7.1 Markansu earthquake its northwestern rim (ISC-GEM catalog, Di Giacomo et al., 2015).

A prerequisite for seismic hazard assessment are accurate fault-slip estimates and space-based positioning data (e.g., Global Positioning System [GPS]) are most helpful to constrain them with mm-accuracy. The data is either collected episodically or continuously, and there is a trade-off between spatio-temporal data density and measurement cost: many regional GPS networks comprise either a low station density (~ 100 km) or rare measurements (\sim once a year). To improve our understanding of fault slip behavior over the full seismic cycle and detect complex

rupture patterns in this tectonically active region in Central Asia we need high-resolution data both in space and time.

We present new GPS data acquired in continuous- (cGPS) and survey-mode (sGPS) from the Alai valley in southwestern Kyrgyzstan that separates the Pamir in the South and the Tien Shan in the North (Figure 1b). Two ~N-S oriented GPS profiles cross both the Alai valley and the Pamir thrust system representing the active front of the north-advancing Pamir orogen with dense instrumentation. The 4–6 years long GPS time-series provide inter-, co- and postseismic rate estimates in the context of the 2015 M_w 7.2 Sarez earthquake. This event ruptured the Sarez-Karakul fault system (Figure 1b), a sinistral, NE-trending fault not directly connected to the Pamir thrust system. Our observations provide new insights on the kinematic response of a fault activated by a nearby large earthquake. After a brief introduction to the tectonic setting and the instrumental setup we present the coseismic offsets and post-seismic rate changes caused by the event, compare them to interseismic East rates obtained by satellite radar interferometric (InSAR) time-series and discuss the implications for the faults at the Pamir front.

2. Tectonic Setting

The E-W trending Alai valley is a 150 km long, asymmetric intermountain depression of up to 25 km width that is embedded between the two largest orogenic belts of Eurasia: the Tien Shan in the North and the Pamir in the South (Figure 1). While the Tien Shan is an intraplate orogen, the Pamir belongs to the Alpine-Himalayan belt that was formed as a result of the closure of the Tethys paleo-ocean (van Hinsbergen et al., 2012). During the late Oligocene/early Miocene (~25–20 Ma) the former Tarim-Tajik basin was separated by the Pamir. In mid-Miocene (~16–12 Ma) N-S-shortening localized along the Pamir thrust system, consequently forming the Trans Alai range, followed by basin annihilation as already observed West and East of the Alai valley (Coutand et al., 2002). The Cenozoic infill of the Alai valley exhibits a southward increase in thickness from 3.5 to 5.5 km (Coutand et al., 2002).

The south-dipping Pamir thrust system delimits the Pamir to the North and comprises the Main Pamir thrust, located within the Trans Alai Range (e.g., Gubin, 1940; Nikonov, 1988), and the Pamir frontal thrust (PFT) that separates the Alai valley from the Trans Alai range with a clear morphological expression (e.g., Arrowsmith & Strecker, 1999; Strecker et al., 1995; Sobel & Dumitru, 1997) (Figure 1). The PFT in our study region was formed ~0.7 Ma ago and has remained active since then (Coutand et al., 2002; Strecker et al., 2003). It is divided in three segments that are separated by two transfer zones (Figure 2), all exhibiting kinematic variations of absorbing plate convergence (Arrowsmith & Strecker, 1999). The eastern segment witnesses no Quaternary tectonic activity; fan surfaces are smooth and intact (Arrowsmith & Strecker, 1999; Strecker et al., 2003). Quaternary deformation and background seismicity is offset further South to the E-trending Markansu fault (Schurr et al., 2014). The eastern transfer zone shows evidence for major Quaternary deformation but significant displacement is scarcely found (Arrowsmith & Strecker, 1999). The central segment contains thrust faults, covered in some places by late-Holocene landslides (Arrowsmith & Strecker, 1999). Movement along the fault with a southward dip of 30°–45° is mainly dip-slip with a Holocene slip rate of up to 6 mm/yr (Strecker et al., 2003). The western transfer zone is tectonically the most complex of all segments and consists of en-echelon faults (Arrowsmith & Strecker, 1999). NW-striking, dextral strike-slip faults alternate with SW-trending thrust faults. The westernmost dextral Aramkungey fault (Figures 1b, 3a, and 3b) (Nikonov, 1988) exhibits a dip-slip along-strike across the Altyndara valley (see next paragraph) and accommodates an interseismic slip rate of at least 6.0 ± 0.8 mm/yr (Zubovich et al., 2016) and a Holocene slip rate of 2.5–6 mm/yr (Arrowsmith & Strecker, 1999). At the western segment of the PFT, the Alai valley narrows to 3 km before the Pamir and Tien Shan unite orographically. Holocene displacements emphasize thrusting, but the fault surface trace is often buried by landslide sediments (Strecker et al., 2003).

Although the surface trace of the NW-SE-striking Aramkungey fault is not continuously evident, it very probably connects two thrust faults striking WSW-ENE to E-W (Figure 3): A western one emplacing Lower Cretaceous strata on Pliocene to Quaternary and an eastern one emplacing Lower Cretaceous on Upper Cretaceous strata. While the western thrust dips south and has a little deformed succession of the Alai valley foreland in its footwall, the eastern thrust has a more internal (southern) position and dips north, functioning as a “passive” backthrust that borders the large Pik Sverdlova (Figure 3b) triangle zone (Voigt et al., 2020). From west to east, the Aramkungey fault thus mediates a southward step of proven active deformation by about 7.5 km and a change in the

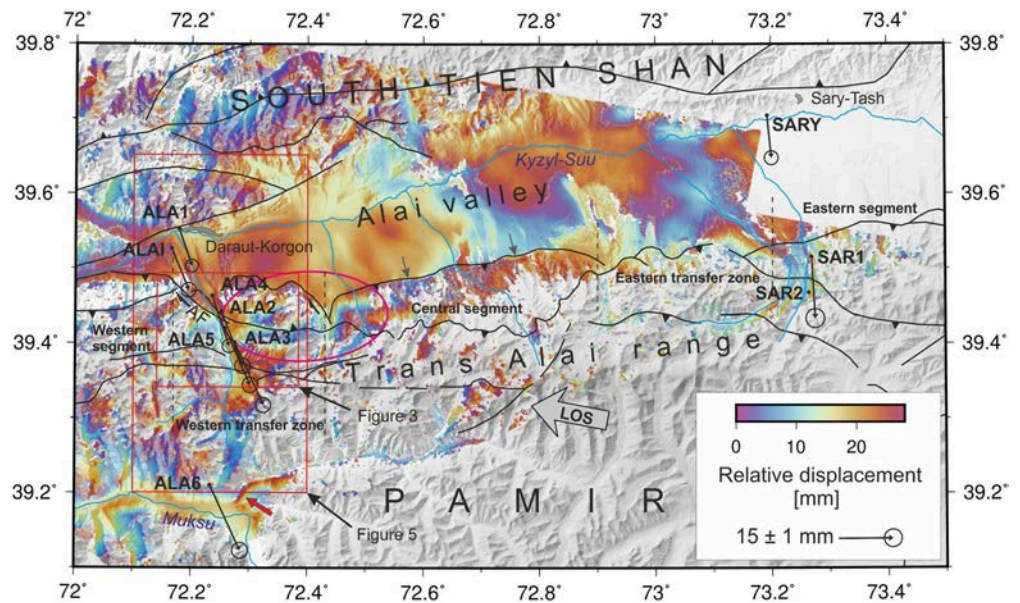


Figure 2. Coseismic displacement from the 2015 M_w 7.2 Sarez earthquake observed by cGPS (black arrows with two-sigma-confidence ellipses) and interseismic satellite radar interferometric. Wrapped interferometric co-seismic fringes in descending view mode (LOS), pointing away from the satellite (Metzger et al., 2017). Gray and red arrows mark sharp interferometric offsets, the pink ellipse highlights deformation fringes, vertical dashed lines separate the Pamir frontal thrust segments, the red rectangles mark the extent of Figures 3 and 5.

thrusting direction from North to South (Figure 3b). No strata older than Lower Cretaceous are exposed anywhere North of the thrust fault labeled “TJ” in Figure 3a. This indicates a thin-skinned structural style where all thrust faults branch from a gently south-dipping basal décollement near the base of the Lower Cretaceous succession. As the Aramkungey fault separates two parts of the thrust wedge sliding on the décollement, it should itself also terminate on this low-angle thrust plane (Figure 3b) at a maximum depth of 2–3 km below the surface.

Both West and East of the Aramkungey fault (Komansu fault scarp, Arrowsmith & Strecker, 1999), the active deformation front is located further north. However, deformed and uplifted strata North of the Aramkungey fault must also be underlain by a décollement fault. Whether this fault (approximate trace dashed in Figure 3a) is presently active together with the Aramkungey fault or the deformation front has stepped back onto the Aramkungey fault from a more external position is unknown.

A detailed seismotectonic analysis of Schurr et al. (2014) revealed a predominant dextral slip along E(SE) trending planes of the PFT, arranged in sub-vertical clusters underneath a décollement layer. Trenching data provide evidence of at least two full ruptures of the central PFT segment within the last 5,000 years and a few partial ruptures at the western end of the segment (Patyniak et al., 2021). In instrumental times the 1974 M_w 7.1 Markansu earthquake and the 2008 M_w 6.6 Nura earthquake (Figure 1) ruptured thrust faults East of the eastern PFT segment (Sippl et al., 2014) (Figure 1b). Slip might also occur on faults below the sedimentary layer further North, or historic surface expressions might have been eroded (Patyniak et al., 2021).

GPS data suggest that the eastern Trans Alai range accommodates more than a third (10–15 mm/yr) of the India-Asian convergence and 5–6 mm/yr dextral shear. The western Trans Alai Range accommodates a similar amount of shortening (12–13 mm/yr) but increased dextral shear (8–9 mm/yr) (Zubovich et al., 2010). At least 7.0 ± 0.8 mm/yr shortening and 7.0 ± 0.8 mm/yr shear are accommodated at the PFT (Zubovich et al., 2016) with the largest portion of slip being attributed to the dextral Aramkungey fault between the two stations ALA3 and ALA2 in 5 km distance (3.8 ± 0.8 mm/yr, respectively, 4.7 ± 0.8 mm/yr) (Figure 1). These rates are in agreement with the kinematics derived from structural and stratigraphic field data (e.g., Coutand et al., 2002) and the gravitational, westward mass outflux of the West Pamir into the lower Tajik depression (Ischuk et al., 2013; Metzger et al., 2020; Schurr et al., 2014; Zubovich et al., 2016). Highest slip rates are observed on the Vakhsh and Darvaz

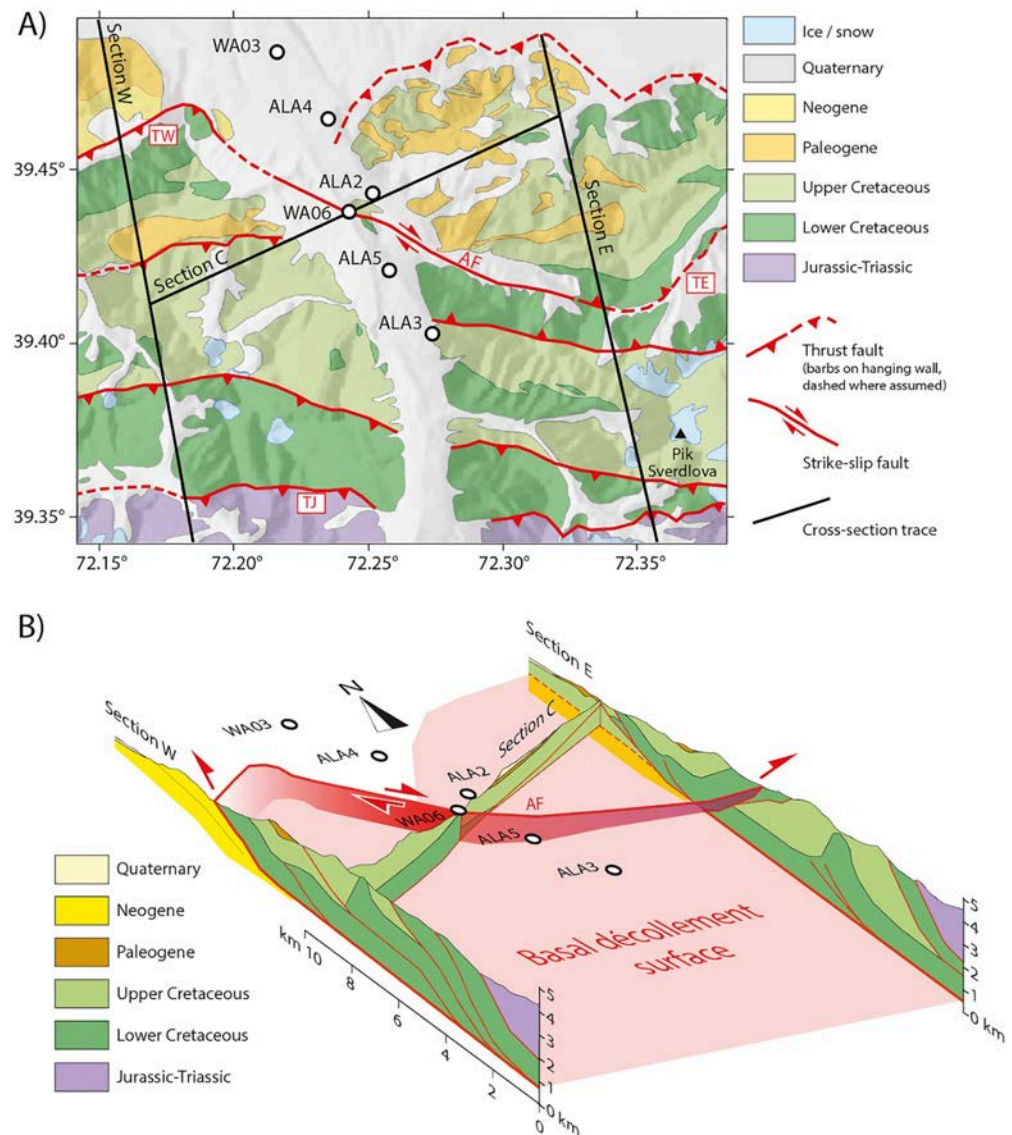


Figure 3. (a) Simplified geological map of the frontal Pamir thrust belt around the Aramkungey fault, based on 1:50,000 maps (Zaalaian Exploration Team, 1993) and own observations (see Figure 2 for spatial extent). Only major faults are shown. The Aramkungey fault (AF) connects a north-vergent thrust fault in the West (TW) with a south-vergent backthrust in the East (TE). (b) Two transverse cross-sections “W” and “E” and central section “C” crossing the Aramkungey fault, shown as a fence diagram. Section locations in Figure 3a. The Aramkungey fault is expected to terminate on the basal décollement surface of the thrust belt.

faults (Figure 1) forking from the PFT at the western end of the Alai valley toward WSW and SW, respectively, squeezing out the intervening triangular block to the southwest. The dextral-transpressive Vakhsh thrust accommodates $22 \pm 5/4$ mm/yr of slip, and the sinistral-transpressive Darvaz fault accommodates ~ 18 mm/yr of slip (Metzger et al., 2020; Mohadjer et al., 2010). The East Pamir, in contrast, moves northwards nearly en-bloc and we do not observe an eastward escape toward the Tarim basin (Avouac et al., 1993; Reigber et al., 2001). The NE-trending, sinistral Sarez-Karakul fault system in the central Pamir presumably accommodates this kinematic difference of East and West Pamir by 3–4 mm/yr of sinistral slip (Metzger et al., 2017).

During our GPS data collection, the region was struck by several M_6+ earthquakes, of which three are relevant to our analysis: the 7 December 2015, $M_w 7.2$ Sarez, Central Pamir, earthquake ruptured an 80 km-long segment of

the Sarez-Karakul fault system with as much as ~ 3 m of sinistral slip (Figure 1) (Metzger et al., 2017). High-rate GPS stations in NE-Afghanistan (250 km from the epicenter) and the western Alai valley (Metzger et al., 2017) observed cm-displacement and survey GPS data in the West Pamir also support the assumption of co-seismic activation (Metzger et al., 2020). Six, respectively 12 months later, the M_w 6.4 Sary-Tash thrust event (Funning & Garcia, 2019; Vajedian et al., 2017) and the M_w 6.6 Aketao (Muji) dextral-slip earthquake (e.g., Wang et al., 2017; Feng et al., 2017) ruptured the Pamir's northern rim. It is debated, if they form a sequence or not (Bloch et al., 2021; Jin et al., 2022; Li et al., 2019).

3. The Alai GPS Network and Data Processing

To better understand the kinematic behavior of the PFT in 2013 we installed four continuously-operated GPS stations along a N-S oriented profile in the western Alai valley (WAGP, Figure 1) (Zubovich et al., 2016). In 2014 this profile was densified and elongated by six sGPS markers and in 2015 by another three cGPS stations. The WAGP stretches over 40 km from the southernmost Tien Shan across the Alai valley and the Trans Alai range and thus covers the surface expressions of the full Pamir thrust system, with the smallest inter-station distance (~ 2.5 km) across the Aramkungey fault. A second N-S profile with three cGPS stations was installed in the eastern Alai valley (EAGP). It has a total length of 27 km and crosses the PFT.

The WAGP was designed such that we can quantify the relative convergence between the South Tien Shan and the North Pamir with a particular focus on the slip mechanism on the PFT fault strand as well as eventual shortening within the Trans Alai Range and the sediments of the Alai valley. If compared to data from the WAGP, the sparse EAGP allows to identify slip variations along the PFT.

The limiting factor of the network design was the terrain that impedes (direct) visibility between the stations to enable data transfer, and solar power supply, particularly during winter time. Primary, independent stations (ALAI/ALA6/SARY) that collect data from secondary stations via wireless ethernet transmission are built as Remotely-Operated Multi-Parameter Stations (Figure S1 in Supporting Information S1) (Schöne et al., 2013; Zech et al., 2021). All stations are operating autonomously and automatically and maintenance is limited to summer and autumn. They are equipped with Septentrio AsteRx2e GPS receivers and NavXperience antennas. Three stations (ALAI, ALA2 and ALA4) are installed in alluvial conglomerates. To improve their stabilization, the metal antenna mounts were cemented into a buried cube of 70 cm length. The antenna mounts of all other stations were anchored to bedrock. More information on the instrument setup and communication can be found in the supplementary material. The stations sample at 1 Hz and transmit the raw data automatically to our data storage facilities during daytime. Data loss occurred mostly in the first year (see the full time-series in Figures S3a and S3b in Supporting Information S1).

The sGPS markers were measured annually from 2014 to 2019 in the time period between July and September (Metzger, Kakar, et al., 2021). All but two markers were installed by drilling and glueing a 10 cm-long stainless-steel bolt of 1 cm diameter into bedrock. Two markers (WA02 and WA03) were installed in alluvial conglomerates; they consist of a 1.5 m-long and 2 cm-wide steel rod, hammered and cemented into the ground (Figures S2a and S2b in Supporting Information S1). Each point was measured at minimum for 48 hr using Topcon PG-A1 antennas fixed on a vertical rod 15 cm above ground (Figures S2c and S2d in Supporting Information S1). The rod was centered in a triangular instrument table that was horizontally adjusted by three extendable screws. The quasi-four-legged setup was a challenge to stabilize and might have caused repeatability noise. The data was sampled at 30 s using Topcon GB-1000 receivers; power supply was ensured by car batteries and solar panels.

We processed the data with the GAMIT software using standard parameters (Herring et al., 2009, 2018) to obtain daily positions (Figure S3 in Supporting Information S1). We included data from all CAIAG/GFZ and IGS regional GPS stations (in the area from 66° to 80° in longitude and from 34° to 45° in latitude) as well as the Eurasian reference stations of the IGS network (43 in total) (Johnston et al., 2017) available at <https://cddis.nasa.gov> and <http://garner.ucsd.edu>. The time series were derived by combining the daily GAMIT solutions with the GLOBK software (Herring et al., 2009, 2015).

Table 1
cGPS Locations, Epicentral Distances and Co-Seismic cGPS Displacements Caused by the 2015 M_w 7.2 Sarez Earthquake

Station	Coordinates		Epicent. distance (km)	Displacement (mm)			
	Lon. (°)	Lat. (°)		East	North	Up	Horizontal
SARY	73.19371	39.70529	169.7	1.3 ± 0.6	-11.8 ± 0.9	3.0 ± 5.8	12.4
SAR1	73.26953	39.51603	151.0	1.0 ± 0.9	-16.9 ± 0.9	3.4 ± 6.1	17.2
SAR2	73.26478	39.46850	145.8				
ALA1	72.17914	39.55298	157.8	3.6 ± 0.7	-10.1 ± 0.8	2.6 ± 9.5	11.9
ALAI	72.16589	39.52653	155.4	4.8 ± 0.6	-11.0 ± 0.9	3.1 ± 5.8	12.7
ALA4	72.23589	39.46355	146.8	5.5 ± 0.6	-14.4 ± 0.8	-3.6 ± 2.0	15.4
ALA2	72.25173	39.44326	144.2	6.1 ± 0.7	-15.2 ± 0.8	2.8 ± 7.8	15.9
ALA5	72.25779	39.42136	141.7	6.9 ± 0.6	-15.8 ± 0.9	3.7 ± 5.3	17.0
ALA3	72.27453	39.40224	139.2	7.8 ± 0.6	-17.2 ± 0.9	2.4 ± 4.0	19.4
ALA6	72.23272	39.21072	120.7	8.0 ± 0.7	-18.0 ± 0.9	3.5 ± 6.7	19.7

Note. Station SAR2 was out of service during the event.

4. The Seismic Cycle, Observed by GPS and InSAR

The 2015 M_w 7.2 Sarez and the 2016 M_w 6.4 Sary-Tash earthquakes (Figure 1) caused significant seismic offsets in our GPS time-series (see time-series in Figures S3 and S4 in Supporting Information S1), providing insight into the full seismic cycle of a fault activated by a nearby large earthquake. We analyzed the co- and postseismic GPS rates and compared them to interseismic rates constrained before the Sarez earthquake, and rates derived from satellite interferometric radar (InSAR) time-series starting at least 8 months after the Sarez earthquake.

4.1. Coseismic Offsets

The cGPS time-series show that the 2015 M_w 7.2 Sarez earthquake caused static offsets at all stations in the Alai valley, located at 120–170 km distance from the epicenter. The observed offsets are on cm-level or less, hence, it is crucial to properly estimate the offset overlaid by secular fault loading. We therefore first calculated baselines between our network stations and other regional stations unaffected by the earthquake (Wdowinski et al., 1997) to reduce the systematic noise (Figure S5 in Supporting Information S1). We then built linear regressions of data acquired 60 days before and 60 days after the earthquake to determine the coseismic offset. This time window represents a good trade-off to limit daily scatter but suppress the influence of seasonal effects. Daily solutions with large deviations or uncertainties were excluded from the regression. For each station of the Alai network we created 25 baselines, extracted the individual, and calculated the mean offset for each component while excluding anomalous results (Table 1, exemplary baseline plots are shown in Figure S5 of the Supporting Information S1). The corresponding uncertainties were derived by the standard deviation of the individual offsets.

We found that the EAGP stations moved 12–17 mm southwards during the Sarez earthquake; the WAGP stations moved 3–8 mm eastward and 10–18 mm southward (Figure 2 and Table 1). The stations closest to the epicenter observed the largest co-seismic offsets. Largely within the respective uncertainty ranges (5–12 mm), all stations were coseismically uplifted by 2.4–3.7 mm, except for station ALA4 that exhibits subsidence of -3.6 ± 2.0 mm. The offsets are also presented along profiles that cross the Pamir front perpendicular to the Pamir front strike (Figure 4).

In the same fashion we searched for potential offsets caused by the other nearby M_w 5.5+ events (Table S1 in Supporting Information S1) and identified the 2016 M_w 6.4 Sary-Tash earthquake as a second event, detected by station SARY on the EAGP profile only, where we measured a southward offset of 8.1 ± 1.2 mm and an eastward offset of 4.8 ± 1.3 mm. The other two EAGP stations were not operating at that time. We conclude that in the western Alai valley the co-seismic response to the Sary-Tash earthquake is below the cGPS detection threshold.

We also estimated the co-seismic offsets using a trajectory model that accounts for a linear trend, (semi-)annual oscillation and offsets (Figures S3a and S3b in Supporting Information S1) (Metzger et al., 2013). This independent

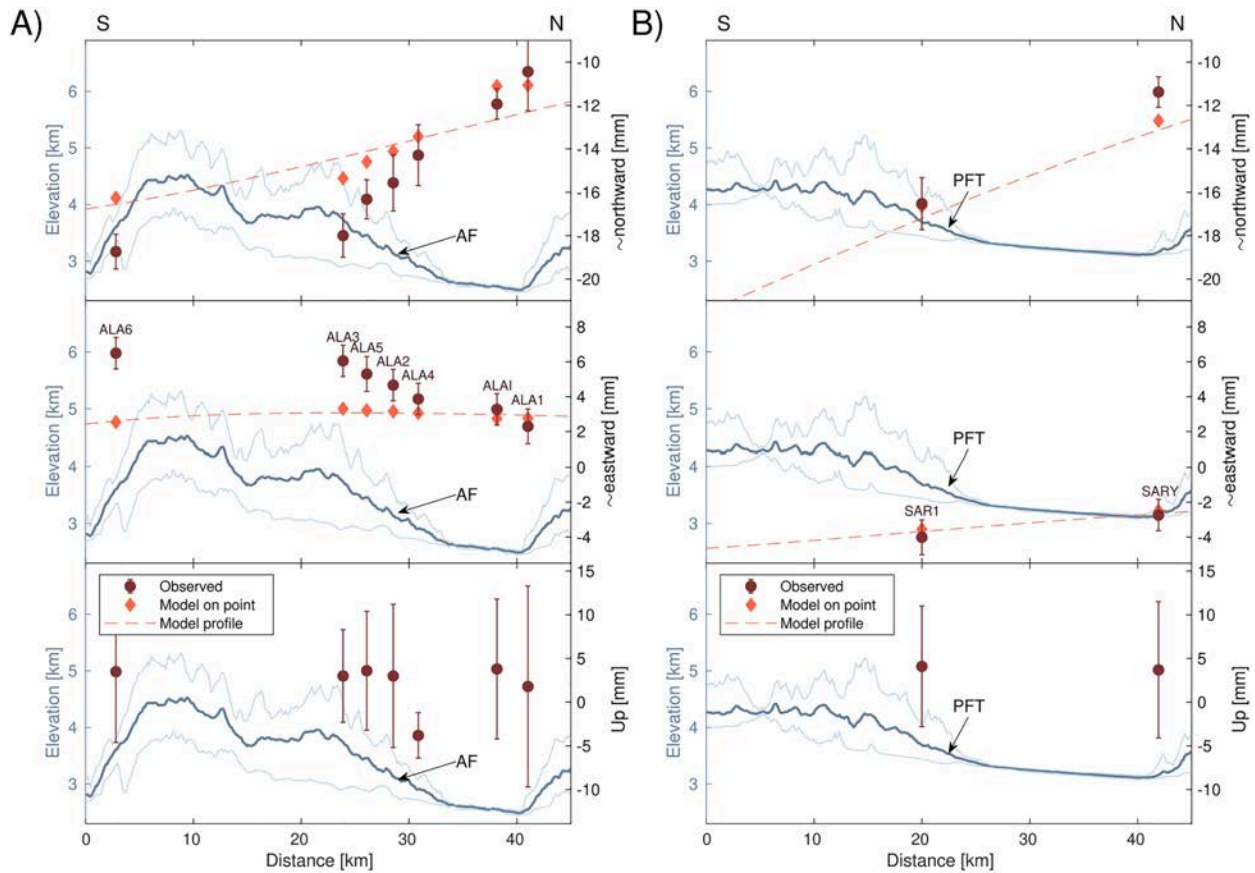


Figure 4. Co-seismic cGPS offsets (dark red circles) along (a) the WAGP and (b) the eastern Alai valley, in comparison to horizontal model predictions on-site (diamonds) and along a straight N-S profile (dashed line) (Metzger et al., 2017). The offsets are rotated by 5°, resp. 15° counterclockwise and correspond to ~northward (or PFT-perpendicular), ~eastward (or PFT-parallel) and vertical offsets. Minimum, median and maximum elevation of a 10 km wide swath is indicated in blue. AF: Aramkungey fault, PFT: Pamir frontal thrust.

approach resulted in a consistently higher eastward offset of 1–3 mm and lower southward offset of ~2 mm (Figure S6 in Supporting Information S1). This systematic bias is caused by the (unmodeled) visco-elastic relaxation component that affects the data only in the 1–2 months following the earthquake with amplitudes just at the detection threshold (Figures S3c and S3d in Supporting Information S1). But—as we show later—both methods do reproduce the local, residual deformation pattern. In the following, we only show the offsets derived from the baseline estimates.

4.2. Post-Seismic Rates Following the 2015 Sarez Earthquake

To better understand the crustal response to the 7 December 2015 M_w 7.2 Sarez earthquake we analyzed two postseismic phases of the cGPS time-series, starting from July 2016, respectively, 2018 and lasting two years each. We excluded data collected in the first 7 months after the event, because they either were contaminated by postseismic relaxation during the first 1–2 months following the earthquake (Figures S3c and S3d in Supporting Information S1), the 26 June 2016 M_w 6.6 Sary-Tash earthquake (Table 1, Figure S2 in Supporting Information S1) and/or the stations were temporarily out of service.

We used the GLOBK software (Herring et al., 2009, 2015) to uniformly constrain the apriori daily positions derived from GAMIT (Herring et al., 2018) and selected a subset of stable stations using the *glorg* program. We then estimated the rates and their uncertainties from our time-series of the cGPS observations, while excluding outliers and removing seasonal variations. The resulting rate uncertainties were normalized by their length of

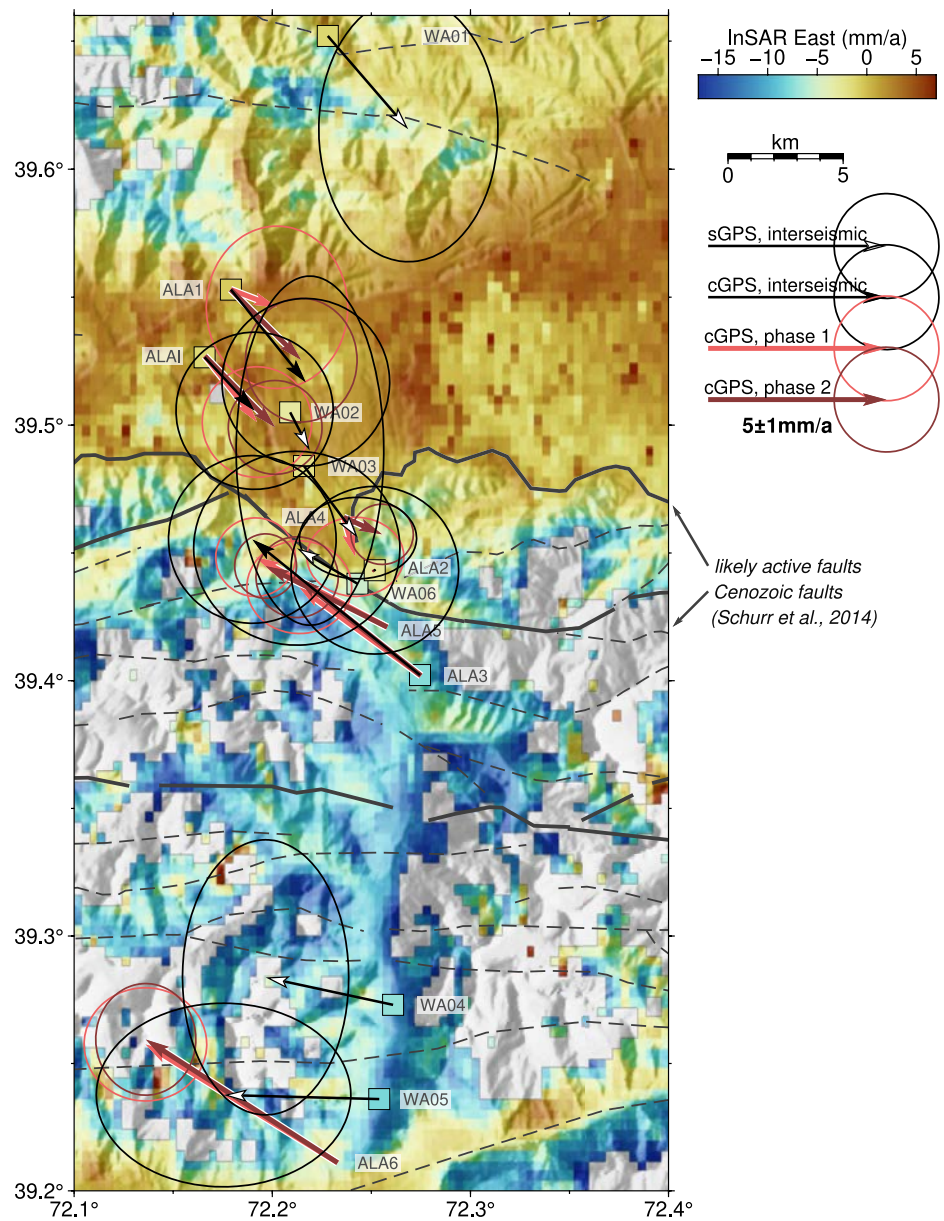


Figure 5. Interseismic sGPS and inter- (Zubovich et al., 2016) and post-seismic cGPS rates of phase 1 and 2 of the western Alai valley, all relative to station ALA2. Background map and color-coded squares are interseismic GPS, respectively interseismic satellite radar interferometric East rates relative to stable Eurasia (Metzger, Lazecky, & Maghsoudi, 2021).

2 years (Geirsson et al., 2006). The rates are presented in map view (Figure 5) and in profile view (Figure 6), both relative to ALA2 (Table 2)—the central station in the profile and closest to the fault trace—to highlight the detailed kinematics at the Aramkungey fault segment.

4.3. Complementary Rates From Survey GPS and InSAR Time-Series

Interseismic rates of the WAGP prior to the Sarez earthquake have already been published (Zubovich et al., 2016); we complement them with linear sGPS rates (Metzger, Kakar, et al., 2021) and high-resolution East rates obtained from InSAR time-series analysis (Metzger, Gała, et al., 2021; Metzger, Lazecky, & Maghsoudi, 2021).

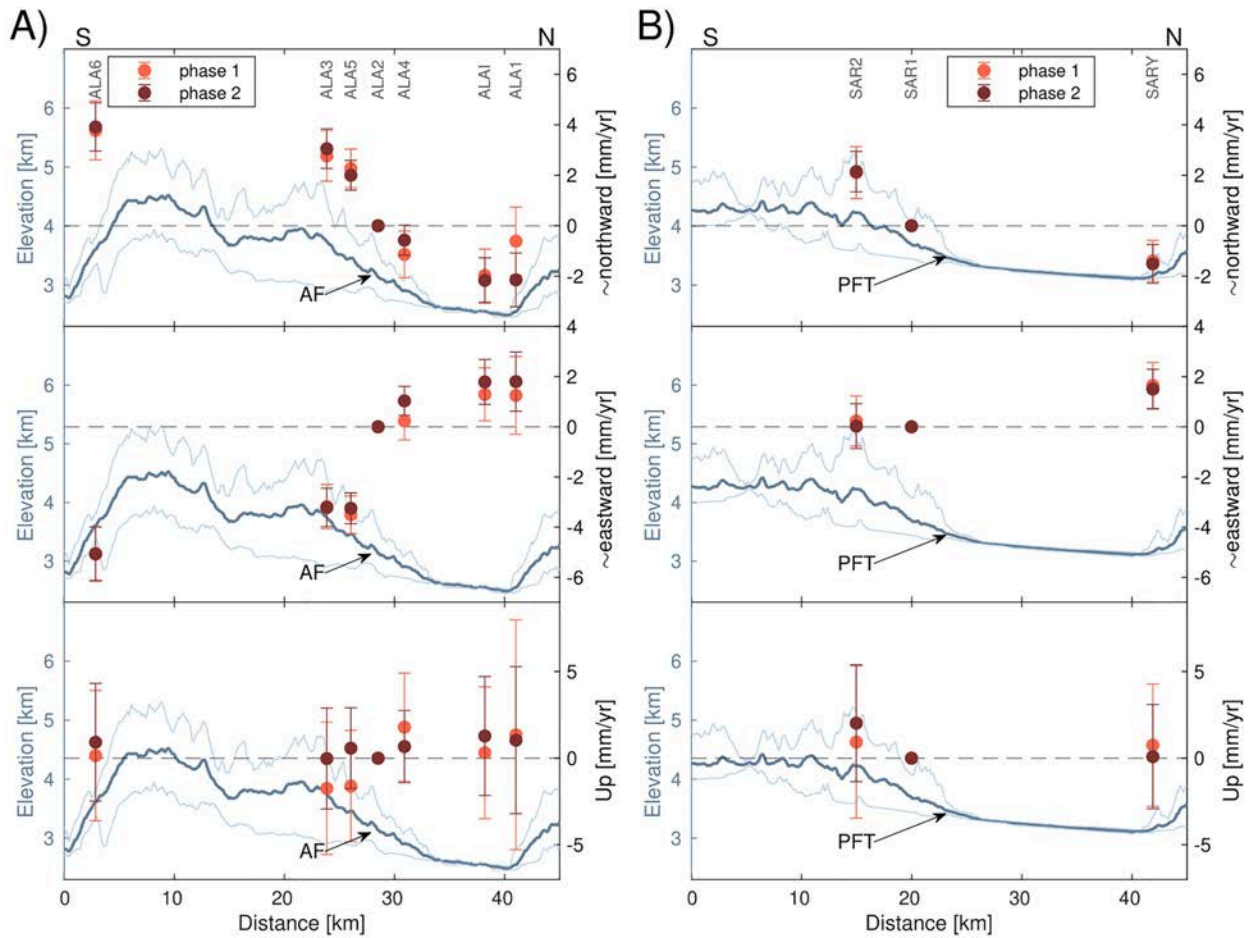


Figure 6. Post-seismic cGPS rates during phase 1 (month 8–31) and phase 2 (month 32–55) along the (a) WAGP and (b) EAGP, in comparison to minimum, median and maximum height of a 10 km wide topographic swath (in blue). Rates are relative to station (a) ALA2 and (b) SAR1, rotated counterclockwise by (a) 5°, respectively (b) 15° and thus correspond to PFT-perpendicular (~northward), PFT-parallel (~eastward), and vertical rates. AF: Aramkungey fault, PFT: Pamir frontal thrust.

Table 2
Postseismic cGPS Rates Relative to the Station SARI (EAGP) and ALA2 (WAGP) for Months 8–31 (Phase 1) and 32–55 (Phase 2) After the 2015 M_w 7.2 Sarez Earthquake

Station	Distance (km)	North (mm/yr)		East (mm/yr)		Up (mm/yr)	
		Phase 1	Phase 2	Phase 1	Phase 2	Phase 1	Phase 2
SARY	-21.1	-0.9 ± 0.9	-1.1 ± 0.8	2.0 ± 0.8	1.8 ± 0.8	0.8 ± 3.5	0.1 ± 3.0
SAR1	0.0	-	-	-	-	-	-
SAR2	5.3	2.1 ± 1.0	2.1 ± 0.9	-0.3 ± 1.0	-0.5 ± 0.8	0.9 ± 4.4	2.0 ± 3.4
ALA1	-12.2	-0.5 ± 1.6	-2.0 ± 1.2	1.3 ± 1.4	2.0 ± 1.1	1.4 ± 6.6	1.0 ± 4.2
ALAI	-9.3	-1.9 ± 1.1	-2.0 ± 0.9	1.5 ± 1.0	2.0 ± 0.9	0.3 ± 3.8	1.3 ± 3.4
ALA4	-2.3	-1.1 ± 0.8	0.5 ± 0.6	0.3 ± 0.9	1.1 ± 0.6	1.8 ± 3.1	0.7 ± 2.1
ALA2	0.0	-	-	-	-	-	-
ALA5	2.4	2.0 ± 0.8	1.7 ± 0.6	-3.7 ± 0.8	-3.4 ± 0.6	-1.6 ± 3.2	0.6 ± 2.3
ALA3	4.6	2.5 ± 0.9	2.8 ± 0.8	-3.4 ± 1.0	-3.5 ± 0.8	-1.7 ± 3.8	0.0 ± 2.9
ALA6	25.9	3.3 ± 1.1	3.5 ± 1.1	-5.4 ± 1.2	-5.4 ± 1.0	0.2 ± 3.8	0.9 ± 3.4

The sGPS positions resulting from the combined GAMIT processing were visually checked for outliers. Linear rates and corresponding uncertainties were extracted using a weighted linear regression and averaged standard deviations. All sGPS positioning data collected after the 2015 M_w 7.2 Sarez earthquake were corrected for the expected co-seismic offset using interpolated cGPS offset data (Table 1 and Figure S4 in Supporting Information S1). The standard deviations are rather large due to significant data scattering, probably caused by the rickety instrument setup (Figure S2c in Supporting Information S1), and consider these rates as inferior.

The InSAR East rates are derived from C-band (i.e., 5.6 cm wavelength) radar data of the European Copernicus Sentinel-1 radar mission (Metzger, Gagala, et al., 2021; Metzger, Lazecky, & Maghsoudi, 2021). Imagery was acquired in ascending (orbit number 100) and descending (005) view mode, starting from eight, respectively 16 months after the Sarez earthquake, both ending in June 2020. The differential interferograms usually cover 12–48 days and were automatically generated, multi-looked (downsampled) to \sim 100 m, filtered using an adaptive-phase filter and unwrapped to provide relative displacement data in two look directions of the satellite (Lazecky et al., 2020). After an additional multilooking to \sim 400 m the interferograms served as database for a small-baseline time-series analysis (Morishita et al., 2020) that automatically accounts for atmospheric signal contributions (Yu et al., 2018), suppresses interferometric noise, identifies outliers using a variety of quality markers and estimates rates using a linear fit to the time-series. The final rates were Gaussian-filtered in space (2 km) and time (\sim 2 months) (Hooper et al., 2007). We used interpolated GPS rates (Zubovich et al., 2010) to fix the North component, extract the East rate component and tie the rates to a Eurasian stable reference frame (Figure 6) (Ou, 2020). Rate uncertainties are \sim 1.5 mm/yr. More details on the processing and results can be found in Metzger, Gagala, et al. (2021).

5. Discussion

Our analysis and interpretation of along-strike slip behavior of the Pamir frontal thrust and the dextral-transpressive Aramkungey segment in particular lean on different data types with different sampling rates covering various time spans of the seismic cycle embracing the 2015 M_w 7.2 Sarez earthquake. Co-, post- and interseismic signals are at mm- to cm-scale and thus close to the noise level; isolating the tectonic signal from unwanted instrumental, atmospheric, seasonal or near-surface effects is most crucial and the data treatment differs for each data type or sampling rate. We only consider observations to be significant for interpretation if they are supported either by adjacent stations or independent data covering the same period. We rank the cGPS observations as being most reliable, followed by InSAR rates and, finally, the interseismic sGPS rates.

5.1. Static Displacements

The static, co-seismic cGPS displacements (Figure 3) image the detailed response of the Earth's crust to the Sarez earthquake in 120–170 km distance. All stations are located in the same tensional quadrant of the rupture mechanism (Figure 1b) and were pulled toward the earthquake epicenter and its NE-striking rupture plane (Metzger et al., 2017), that is the WAGP stations toward SSE, the EAGP stations toward South. The epicentral drag of all stations is similar and stations closest to the epicenter exhibit the highest offset. Amplitudes agree to the first order with co-seismic offset predictions based on a homogeneous half-space model (Metzger et al., 2017).

When the offsets are displayed along profiles crossing the Pamir front and decomposed into a front-parallel and -perpendicular component, the offsets decay distinctly across the front (Figure 4). This is obvious in particular at the dense, western profile: while the southernmost two stations (ALA6, ALA3) are offset almost equally, we observe a significant offset decrease at the stations further North. The co-seismic slip model of Metzger et al. (2017) assumes a homogeneous substrate, slightly underpredicts the \sim southward offset by \sim 3 mm and fails to represent the \sim eastward offset by up to \sim 4 mm of the cGPS stations near or South of the Aramkungey fault. It also does not foresee such a rapid offset decrease. This is significant since the EAGP predictions and observations fit much better. Our observations could be explained with a co-seismic, sinistral (retrograde) reorganization of the heavily fractured fault zone, which could only be satisfyingly modeled using an inhomogeneous model setup allowing for slip on local structures, for example, the PFT and/or the Aramkungey fault. Given the sparse amount of cGPS data, the high uncertainties of the sGPS and InSAR offsets and the highly three-dimensional nature of the local fault geometry, we refrain from any rather speculative modeling attempt.

The observation of co-seismic offset across the PFT is also supported by local surface deformation observed by a co-seismic radar interferogram (Metzger et al., 2017) exhibiting a range decrease of ~ 1 fringe (corresponding to ~ 2.8 cm) on the hanging wall toward the surface trace of the PFT, just East of the Aramkungey fault segment (pink ellipse in the Figure 2). At the central PFT segment we observe sharp offsets of 5–10 mm in line-of-sight, indicating that the hanging wall of the PFT was displaced away from the satellite relative to the footwall over remarkable tens of km (marked by gray arrows in Figure 2). We rule out atmospheric errors as the sharp offsets are also observed on a second, independent interferogram with a different view angle (Metzger et al., 2017). We also rule out a bias caused by a poor digital elevation model as the signal cannot be reproduced in, for example, postseismic interferograms (Bloch et al., 2021).

Most interestingly, the sign of the offset seems to flip along-strike. We can limit the occurrence of these offsets to the time window of 19 days before and 5 days after the Sarez earthquake, which are the acquisition dates of the two radar images forming the interferogram. Thus, the PFT activation observed in the interferogram must have occurred during the earthquake (as constrained by cGPS time-series) and/or in the subsequent 5 days. These signals could be explained by the lowering of the hanging fault wall, relative to the footwall, due to its greater displacement toward the epicenter. Faults in the region are generally assumed to exhibit co- (Teshebaeva et al., 2014) or interseismic (Metzger et al., 2020) slip on low-friction décollements (e.g., Chen et al., 2004; Hamburger et al., 1992; Schurr et al., 2014).

Co-seismic activation of neighboring faults has already been reported using InSAR data (e.g., Fialko et al., 2002; Elliott et al., 2016; Wright et al., 2001). A particularly impressive example is the complex fracture pattern caused by the 2019 M_w 7.1 Ridgecrest earthquake that induced slip and creep on the conjugate Garlock fault as observed by radar interferograms (Ramos et al., 2020; Xu et al., 2020). Both GPS and InSAR data testimony that the Pamir thrust system was co-seismically activated and exhibits retrograde mm-slip along tens of km. Conjugate slip can be triggered either dynamically by the seismic waves passing by (Velasco et al., 2008), or mechanically, in our case by pulling the upper crust material toward the epicenter inducing slip along neighboring faults with low friction properties.

If we assume that the PFT accommodates at least 9 mm/yr of slip during the interseismic period, our observations indicate that the Sarez earthquake set back the system's stress level equal to ~ 1 year of constant loading.

The northernmost stations of the WAGP (ALAI and ALA1) are clearly positioned North of the Pamir frontal thrust, but nevertheless exhibit a slightly different offset. If their difference is significant, this could either be due to co-seismic relaxation of a fault hidden under the alluvial sediments (Coutand et al., 2002), or caused by a relaxation of the latter that are under constant, interseismic N-S-compression.

Except for station ALA4, located at the footwall closest to the Aramkungey fault, all stations of the WAGP exhibit a co-seismic uplift between 2.4 and 3.7 mm, which lies within the respective measurement uncertainties (Figure 4). If this consistency in uplift is to be trusted, it would mean that the whole Northern Pamir Front was slightly uplifted by the earthquake, possibly, due to partial compressional stress release (Figure 2).

5.2. Post-Seismic Displacements

Postseismic rate changes across the Pamir front are subtle in map view (Figure 5) and, again, better visualized if the rates are plotted along profiles and decomposed into front-parallel (\sim eastward) and front-perpendicular (\sim northward) components (Figure 6). As the rates are derived from baselines to a station roughly at the center of the profile and closest to the fault trace,—ALA2 in the WAGP, and SAR1 in the EAGP—all rates are plotted relative to these. The slip sense of the Aramkungey fault flipped from sinistral (during the co-seismic phase) to dextral. Both, front-parallel and -perpendicular WAGP rate changes show a slight, absolute increase from phase 1 to phase 2 to a final 6 mm/yr of \sim N-S-shortening, and 7 mm/yr of dextral shear, suggesting an increase in strain accumulation. Interestingly, dextral shear varies more across the Aramkungey fault than shortening. The two stations closest to the Aramkungey fault on the southern side—ALA3 and ALA5, at only ~ 2.5 km distance—exhibit the same front-parallel motion. In phase 1, the stations ALA2 and ALA4, closest to the fault on the northern side, behave similarly to the southern stations, suggesting that the Aramkungey fault is either completely unlocked by the Sarez earthquake and its sides slide freely relative to each other, or the fault locking has only yet affected a corridor up to 2.5 km width.

Jin et al. (2022) used forward and inverse models, a subset of the GPS time-series presented here, and post-seismic InSAR data to quantify the individual spatio-temporal contribution of afterslip, poro-elastic rebound and visco-elastic relaxation following the Sarez earthquake. It appears that the postseismic deformation affected only the near-field (10–100 km), ceased after ~ 5 years, and was mostly caused by afterslip at the northernmost rupture segment. Visco-elastic contributions were below the geodetic detection threshold, which can be explained with a relatively strong lithosphere containing amalgamated blocks and deep-rooted faults that accommodate most of the internal deformation (Avouac & Tapponnier, 1993; Hubbard & Shaw, 2009). These findings are supported by a GPS trajectory model (Metzger et al., 2013) indicating that an additional viscoelastic relaxation term would improve the data fit during the first ~ 1 – 2 months following the Sarez earthquake (Figure S3 in Supporting Information S1), so we may exclude viscoelastic behavior while interpreting the velocities estimated 8+ months later.

Elastic screw dislocation models predict that the steepness of the rate gradient across a locked strike-slip fault relates to the locking depth such that 50% of the rate change across the fault occurs within a corridor sized twice the locking depth (Savage & Burford, 1973). For the Aramkungey fault this would suggest a locking depth of 1–2 km or less, which is approximately half of the distance to the basal décollement.

Sliding can not occur across the fault due to its verticality, so in this direction distributed elastic strain arises in an unconsolidated volume in a strip no less than 7.5 km (distance ALA3-ALA4) wide around the fault, explaining the gentler gradient. During phase 2, the behavior of ALA2 and ALA4 slightly changes, which suggests the expansion of the deformation zone toward North.

The strongest rate variation between the two postseismic phases is observed at the northernmost station of the western profile, ALA1, with a significant front-perpendicular rate increase of 1.5 mm/yr, but no significant change in the front-parallel direction. If significant, this may suggest that one of the thrust faults hidden in the sediments of the Alai valley was active during the first post-seismic phase with a reverse sense of slip.

Both Alai GPS profiles were affected by similarly-sized offsets (Figure 4, Table 1), but the EAGP time-series do not show significant non-linear, post-seismic effects (Figure 6b). This might indicate that the eastern PFT is not affected by the westward escape of the West Pamir, and is kinematically decoupled from the western PFT.

In the vertical rates we observe—within uncertainties—an increased uplift of WAGP stations located in the PFT footwall and an opposite behavior in the EAGP. If this pattern is real, it might represent postseismic alluvial sediment compression in the western Alai valley.

5.3. Transition to the Interseismic Stage

Once postseismic rates equal interseismic rates, a fault system has returned to the interseismic stage of the seismic cycle. This is best checked by overlying postseismic and interseismic rates (acquired prior to the Sarez earthquake (Zubovich et al., 2016)) in map view (Figure 5). We complement those with postseismic sGPS rates acquired between 2014 and 2019, and high-resolution InSAR East rates. To highlight the kinematics near the Aramkungey fault and mitigate potential reference frame shifts, we plot the rate vectors relative to station ALA2, the cGPS station located closest to the Aramkungey fault surface trace. cGPS stations ALA4, ALA5 and ALA6 were installed only shortly before the Sarez earthquake and lack interseismic rate estimates. Given the relatively large uncertainties of the interseismic rates we focus on general trends in space and time rather than a quantitative interpretation of each station. The sGPS rates are in general agreement (within uncertainties) with the other data sets, and serve as supporting information.

The stations far North from the Aramkungey fault seem to have returned to the interseismic stage rather quickly, at least in the post-seismic phase 2 (Figure 5). The stations next to the Aramkungey fault (ALA3, maybe ALA4 and ALA5) have probably not yet fully returned to the interseismic stage where we observe a larger rate change across the fault. Rate differences across the fault before and after the earthquake show that the relative rate ALAI-ALA3 temporarily dropped to 78%, and then reached 85% in phase 1 and 2, and the relative rate ALA2-ALA3 temporarily dropped to 70%, respectively 73% of the pre-event rate difference. Thus, near the Aramkungey fault and 4.5 years after the earthquake pre-event strain conditions have not yet been fully recovered.

The InSAR East rates exhibit average surface deformation between 8 months to 4.5 years after the Sarez earthquake (Figure 5). The rates show the westward motion of the Trans Alai range with respect to the Alai valley and the adjacent South Tien Shan. Average rate differences between the Trans Alai and the Alai valley deposits are

~6–8 mm/yr, which is at the lower boundary of observed interseismic fault slip rates of the Pamir frontal thrust (Metzger et al., 2020; Zubovich et al., 2016), agreeing to the postseismic cGPS rates. Further East, at the longitude of the WAGP, dextral slip on the Pamir front has been constrained to be of ~7 mm/yr (Metzger et al., 2020). The InSAR rates show a sharp eastward rate change across the Aramkungey fault, supporting a shallow locking depth of 1–2 km or less. As the input interferograms were strongly filtered (Lazecký et al., 2020) we cannot resolve potential shallow fault creep. East and West of the Aramkungey fault, mapped faults (Schurr et al., 2014) also show significant rate changes, which could indicate that these strands are also active. The InSAR rate map also shows a strong gradient at the southern end of the Trans Alai range and the WAGP. Most probably, these are strong near-surface effects due to slope processes and seasonal water load of the Muksu river valley draining the ~70 km-long Fedchenko glacier, one of the largest glaciers on Earth. It is worth noting, however, that these slopes also seemed to be activated during the Sarez earthquake as observed in the coseismic interferogram (red arrow in Figure 2).

6. Conclusion

As a follow-up of Zubovich et al. (2016) we densified and elongated the western Alai continuous GPS profile and installed the eastern profile to monitor the kinematics of the Pamir thrust system. The improved western profile extends far South into the Trans Alai range and is most densely spaced (~2.5 km) near the surface trace of the Aramkungey fault, a dextral-transpressive fault segment that links two right-stepping thrust segments with opposite dip and unites with the basal décollement of the thin-skinned Pamir thrust system. In addition, survey GPS data were collected over six consecutive years to further densify the network and extend it northward into the South Tien Shan. The Alai GPS network captured co-seismic displacement during and post-seismic rate changes following the 2015 M_w 7.2 Sarez earthquake. 4–6 years-long, continuous high-rate GPS time-series provide insight in the kinematic response of a fault exposed to a large earthquake occurring at 120–170 km distance. These time-series exhibit co-seismic station offsets of 10–20 mm toward the epicenter of the Sarez earthquake in agreement with its slip mechanism, indicating a slight load decrease of the Pamir frontal thrust. In the western transfer PFT segment, the offsets rapidly decay across $a > 7.5$ km-wide zone around the Aramkungey fault. Further east we observed interferometric offsets of 5–10 mm in line-of-sight tracing a 20–30 km-long, central segment of the PFT. Both observations suggest a co-seismic activation of the PFT during the Sarez earthquake.

Postseismic cGPS rates show that relocking of the Aramkungey fault, unlocked by the Sarez earthquake in a retrograde fashion, began already ~0.5–2.5 years after this event and increased in the following ~2.5–4.5 years, but did not yet reach the full level observed before the earthquake. This is most apparent at the stations closest to the Aramkungey fault, where the profile-parallel and profile-perpendicular post-seismic rate change patterns differ. The front-parallel rates suggest either creep movements along the Aramkungey fault, or initial locking in the upper part. The front-parallel rates indicate a continued accumulation of elastic deformation, slightly reduced by the Sarez event and the following, postseismic processes. The findings are supported by InSAR East rates that, on top, highlight retrograde slip activity on the northernmost fault strands of the Pamir frontal thrust system, again suggesting rather shallow slip.

We rule out a significant kinematic contribution to the north-advance of the Pamir of the thick-skinned structures buried underneath the (western) Alai valley sediments. The major shortening and dextral shear is accommodated by the Pamir thrust system under the Trans Alai range.

The comparison of East and West Alai GPS profile rates confirms that the eastern and western segments of the Pamir thrust system are kinematically decoupled due to the westward escape of the West Pamir. Our study showcases an example of co-seismic retrograde activation of neighboring faults during a large earthquake. At the latest since the well-observed 2019 M_w 7.1 Ridgecrest earthquake we know that such events evoke complex faulting patterns reaching out to conjugate faults at the boundary between near- and far-field. The implications of this to the overall fault loading states and consequent seismic hazard assessment will be a key question in future research.

Data Availability Statement

Interferometric data were processed on JASMIN, the UK's collaborative data analysis environment. They are originally based on Copernicus Sentinel data. The cGPS data are archived at Zenodo (<https://zenodo.org/record/6555931>). Some figures were created using GMT (Wessel et al., 2013) and scientific color maps (Crameri, 2020). The cGPS reference data are made available by the IGS (Johnston et al., 2017). We also would like to thank our colleagues who helped with the installation and maintenance of the ROMPS stations as well as with the data acquisition, namely Julia Illigner, Nico Stolarczuk, Torsten Queisser, Matthias Köppl (all GFZ Potsdam), and Abdysamat Shakirov, Mikhail Borisov, Joldosh Okoev (all CAIAG).

Acknowledgments

We thank the editors and two anonymous reviewers for comments and suggestions that improved the quality of this manuscript.

References

- Arrowsmith, J. R., & Strecker, M. R. (1999). Seismotectonic range-front segmentation and mountain-belt growth in the Pamir-Alai region, Kyrgyzstan (India-Eurasia collision zone). *The Geological Society of America Bulletin*, 111(11), 1665–1683. [https://doi.org/10.1130/0016-7606\(1999\)111<1665:SRFSAM>2.3.CO;2](https://doi.org/10.1130/0016-7606(1999)111<1665:SRFSAM>2.3.CO;2)
- Avouac, J. P., & Tapponnier, P. (1993). Kinematic model of active deformation in central Asia. *Geophysical Research Letters*, 20(10), 895–898. <https://doi.org/10.1029/93GL00128>
- Avouac, J. P., Tapponnier, P., Bai, M., You, H., & Wang, G. (1993). Active thrusting and folding along the northern Tien Shan and late Cenozoic rotation of the Tarim relative to Dzungaria and Kazakhstan. *Journal of Geophysical Research*, 98(B4), 6755–6804. <https://doi.org/10.1029/92JB01963>
- Bloch, W., Metzger, S., Schurr, B., Yuan, X., Ratschbacher, L., Reuter, S., et al. (2021). The 2015–2017 Pamir earthquake sequence: Fore-, main-, and aftershocks, seismotectonics and fault interaction. *Earth and Space Science Open Archive*. <https://doi.org/10.1002/essoar.10508392.2>
- Bürgmann, R., & Dresen, G. (2008). Rheology of the lower crust and upper mantle: Evidence from rock mechanics, geodesy, and field observations. *Annual Review of Earth and Planetary Sciences*, 36(1), 531–567. <https://doi.org/10.1146/annurev.earth.36.031207.124326>
- Calais, E., Camelbeeck, T., Stein, S., Liu, M., & Craig, T. J. (2016). A new paradigm for large earthquakes in stable continental plate interiors. *Geophysical Research Letters*, 43(20), 10621–10637. <https://doi.org/10.1002/2016GL070815>
- Chen, S., Tang, L., Jin, Z., Jia, C., & Pi, X. (2004). Thrust and fold tectonics and the role of evaporites in deformation in the Western Kuqa Foreland of Tarim Basin, Northwest China. *Marine and Petroleum Geology*, 21(8), 1027–1042. <https://doi.org/10.1016/j.marpetgeo.2004.01.008>
- Coutand, I., Strecker, M. R., Arrowsmith, J. R., Hilley, G. E., Thiede, R. C., Korjenkov, A., & Omuraliev, M. (2002). Late Cenozoic tectonic development of the intramontane Alai Valley, (Pamir-Tien Shan region, central Asia): An example of intracontinental deformation due to the Indo-Eurasia collision. *Tectonics*, 21(6), 1053–3-19. <https://doi.org/10.1029/2002TC001358>
- Crameri, F. (2020). Scientific colour maps (version 6.0.4). <https://doi.org/10.5281/zenodo.4153113>
- Di Giacomo, D. D. I., Bondár, I., Storchak, D. A., Engdahl, E. R., Bormann, P., & Harris, J. (2015). ISC-GEM: Global Instrumental Earthquake Catalogue (1900–2009): III. Re-computed MS and mb, proxy MW, final magnitude composition and completeness assessment. *Physics Earth Planetary Interiors*, 239, 33–47. <https://doi.org/10.1016/j.pepi.2014.06.005>
- Elliott, J. R., Jolivet, R., Gonzalez, P. J., Avouac, J. P., Hollingsworth, J., Searle, M. P., & Stevens, V. L. (2016). Himalayan megathrust geometry and relation to topography revealed by the Gorkha earthquake. *Nature Geoscience*, 9(2), 174–180. <https://doi.org/10.1038/ngeo2623>
- Evans, S. G., Nicholas, J. R., Ischuk, A., Delaney, K. B., Morozova, G. S., & Tutubalina, O. (2009). Landslides triggered by the 1949 Khait earthquake, Tajikistan, and associated loss of life. *Engineering Geology*, 109(3–4), 195–212. <https://doi.org/10.1016/j.enggeo.2009.08.007>
- Feng, W., Tian, Y., Zhang, Y., Samsonov, S., Almeida, R., & Liu, P. (2017). A slip gap of the 2016 M_w 6.6 Muji, Xinjiang, China, earthquake inferred from Sentinel-1 TOPS interferometry. *Seismological Research Letters*, 88(4), 1054–1064. <https://doi.org/10.1785/0220170019>
- Fialko, Y., Sandwell, D., Agnew, D., Simons, M., Shearer, P., & Minster, B. (2002). Deformation on nearby faults induced by the 1999 Hector Mine earthquake. *Science*, 297(5588), 1858–1862. <https://doi.org/10.1126/science.1074671>
- Funning, G. J., & Garcia, A. (2019). A systematic study of earthquake detectability using Sentinel-1 Interferometric Wide-Swath Data. *Geophysical Journal International*, 216(1), 332–349. Figure S23, supplementary material. <https://doi.org/10.1093/gji/ggy426>
- Geirsson, H., Árnadóttir, T., Völksen, C., Jiang, W., Sturkell, E., Villemin, T., et al. (2006). Current plate movements across the Mid-Atlantic Ridge determined from 5 years of continuous GPS measurements in Iceland. *Journal of Geophysical Research*, 111(B9), B09407. <https://doi.org/10.1029/2005JB003717>
- GEOFON Data Centre. (2006). *Moment tensor solution for the 2016 M_w 6.4 Sary-Tash, Kyrgyzstan earthquake*. GFZ German Research Centre for Geosciences. Retrieved from <http://geofon.gfz-potsdam.de/eqinfo/event.php?id=gfz2016mmgj>
- Gubin, I. E. (1940). Geological boundary between Pamir and Alai, M.-L. (Gosgeolizdat) (p. 48).
- Hamburger, M. W., Sarewitz, D. R., Pavlis, T. L., & Popandopulo, G. A. (1992). Structural and seismic evidence for intracontinental subduction in the Peter the First range, central Asia. *The Geological Society of America Bulletin*, 104(4), 397–408. <https://doi.org/10.1130/0016-7606>
- Herring, T. A., Floyd, M. A., King, R. W., & McClusky, S. C. (2015). *GLOBK reference manual, Global Kalman filter VLBI and GPS analysis program, release 10.6*. Department of Earth, Atmospheric, and Planetary Sciences Massachusetts Institute of Technology.
- Herring, T. A., King, R. W., Floyd, M. A., & McClusky, S. C. (2018). *GAMIT reference manual, reference GPS analysis at MIT, release 10.7*. Department of Earth, Atmospheric, and Planetary Sciences, Massachusetts Institute of Technology.
- Herring, T. A., King, R. W., & McClusky, S. C. (2009). *Introduction to GAMIT/GLOBK, release 10.35*. Massachusetts Institute of Technology.
- Hooper, A., Segall, P., & Zebker, H. (2007). Persistent scatterer interferometric synthetic aperture radar for crustal deformation analysis, with application to Volcán Alcedo, Galápagos. *Journal of Geophysical Research: Solid Earth*, 112(7), 1–21. <https://doi.org/10.1029/2006JB004763>
- Hubbard, J., & Shaw, J. H. (2009). Uplift of the Longmen Shan and Tibetan plateau, and the 2008 Wenchuan ($M = 7.9$) earthquake. *Nature*, 458(7235), 194–197. <https://doi.org/10.1038/nature07837>
- Ischuk, A., Bendick, R., Rybin, A., Molnar, P., Khan, S. F., Kuzikov, S., et al. (2013). Kinematics of the Pamir and Hindu Kush regions from GPS geodesy. *Journal of Geophysical Research: Solid Earth*, 118(5), 2408–2416. <https://doi.org/10.1002/jgrb.50185>
- Jin, Z., Fialko, Y., Zubovich, A., & Schöne, T. (2022). Lithospheric deformation due to the 2015 $M7.2$ Sarez (Pamir) earthquake constrained by 5 years of space geodetic observations. *Journal of Geophysical Research: Solid Earth*, 127(4), e2021JB022461. <https://doi.org/10.1029/2021JB022461>
- Johnston, G., Riddell, A., & Hausler, G. (2017). The International GNSS Service. In P. J. G. Teunissen & O. Montenbruck (Eds.), *Springer handbook of global navigation satellite systems* (1st ed., pp. 967–982). Springer International Publishing. <https://doi.org/10.1007/978-3-319-42928-1>

- Jónsson, S., Segall, P., Pedersen, R., & Björnsson, G. (2003). Post-earthquake ground movements correlated to pore-pressure transients. *Nature Geoscience*, 424(6945), 179–183. <https://doi.org/10.1038/nature0177>
- Kulikova, G. (2016). *Source parameters of the major historical earthquakes in the Tien-Shan region from the late 19th to the early 20th century*. PhD Thesis. Potsdam University. Retrieved from https://publishup.uni-potsdam.de/opus4-ubp/frontdoor/deliver/index/docId/8837/file/kulikova_diss.pdf
- Kulikova, G., & Krüger, F. (2015). Source process of the 1911 M8.0 Chon-Kemin earthquake: Investigation results by analogue seismic records. *Geophysical Journal International*, 3, 1891–1911. <https://doi.org/10.1093/gji/ggv091>
- Kulikova, G., Schurr, B., Krüger, F., Brzoska, E., & Heimann, S. (2016). Source parameters of the Sarez-pamir earthquake of 1911 February 18. *Geophysical Journal International*, 205(2), 1086–1098. <https://doi.org/10.1093/gji/ggv069>
- Lazecký, M., Spaans, K., González, P. J., Maghsoudi, Y., Morishita, Y., Albino, F., et al. (2020). LiCSAR: An automatic InSAR tool for measuring and monitoring tectonic and volcanic activity. *Remote Sensing*, 12(15), 2430. <https://doi.org/10.3390/RS12152430>
- Li, T., Schoenbohm, L. M., Chen, J., Yuan, Z., Feng, W., Li, W., et al. (2019). Cumulative and coseismic (during the 2016 M_w 6.6 Aketao earthquake) deformation of the dextral-slip Muji Fault, northeastern Pamir orogen. *Tectonics*, 38(11), 3975–3989. <https://doi.org/10.1029/2019TC005680>
- Marone, C. J., Scholtz, C. H., & Bilham, R. (1991). On the mechanics of earthquake afterslip. *Journal of Geophysical Research*, 96(B5), 8441–8452. <https://doi.org/10.1029/91JB00275>
- Metzger, S., Gagala, Ł., Ratschbacher, L., Schurr, B., Lazecky, M., & Maghsoudi, Y. (2021). Tajik depression and greater Pamir neotectonics from InSAR rate maps. *Journal of Geophysical Research: Solid Earth*, 126(12), e2021JB022775. <https://doi.org/10.1029/2021JB022775>
- Metzger, S., Ischuk, A., Deng, Z., Ratschbacher, L., Perry, M., Kufner, S. K., et al. (2020). Dense GNSS profiles across the northwestern tip of the India-Asia collision zone: Triggered slip and westward flow of the Peter the First Range, Pamir, into the Tajik Depression. *Tectonics*, 39, e2019TC005797. <https://doi.org/10.1029/2019TC005797>
- Metzger, S., Jónsson, S., Danielsen, G. J. K., Hreinsdóttir, S., Jouanne, F., Giardini, D., & Villemin, T. (2013). Present kinematics of the Tjörnes Fracture Zone, North Iceland, from campaign and continuous GPS measurements. *Geophysical Journal International*, 192(2), 441–455. <https://doi.org/10.1093/gji/ggs032>
- Metzger, S., Kakar, N., Zubovich, A., Borisov, M., Saif, S., Panjsheri, A. H., et al. (2021). *Survey mode GNSS data, acquired 2014–2019 in the Afghan Hindu Kush and across northern Pamir margin, Central Asia*. GFZ Data Services. <https://doi.org/10.5880/GFZ.4.1.2021.003>
- Metzger, S., Lazecky, M., & Maghsoudi, Y. (2021). *High-resolution rate maps from the Tajik basin and the Pamir*. GFZ Data Services. <https://doi.org/10.5880/GFZ.4.1.2021.005>
- Metzger, S., Schurr, B., Ratschbacher, L., Sudhaus, H., Kufner, S.-K., Schöne, T., et al. (2017). The 2015 M_w 7.2 Sarez strike-slip earthquake in the Pamir interior: Response to the underthrusting of India's western promontory. *Tectonics*, 36(11), 2407–2421. <https://doi.org/10.1002/2017TC004581>
- Mohadjer, S., Bendick, S. R., Ischuk, A., Kuzikov, S., Kostuk, A., Saydullaev, U., et al. (2010). Partitioning of India/Eurasia convergence in the Pamir-Hindu Kush from GPS measurements. *Geophysical Research Letters*, 37(4), L04305. <https://doi.org/10.1029/2009GL041737>
- Mohadjer, S., Ehlers, T. A., Bendick, R., Stübner, K., & Strube, T. (2016). A quaternary fault database for central Asia. *Natural Hazards and Earth System Sciences*, 16(2), 529–542. <https://doi.org/10.5194/nhess-16-529-2016>
- Morishita, Y., Lazecky, M., Wright, T. J., Weiss, J. R., Hooper, A., Elliott, J. R., & Hooper, A. (2020). LiCSBAS: An open-Source InSAR time series analysis package integrated with the LiCSAR automated Sentinel-1 InSAR processor. *Remote Sensing*, 12(3), 5–8. <https://doi.org/10.3390/rs12030424>
- Nikonov, A. A. (1988). Reconstruction of the main parameters of old large earthquakes in Soviet Central Asia using the paleoseismogeological method. *Tectonophysics*, 147(3–4), 297–312. [https://doi.org/10.1016/0040-1951\(88\)90191-6](https://doi.org/10.1016/0040-1951(88)90191-6)
- Nur, A., & Mavko, G. (1974). Postseismic viscoelastic rebound. *Science*, 183(4121), 204–206. <https://doi.org/10.1126/science.183.4121.204>
- Ou, Q. (2020). *Crustal deformation and seismic hazard of the NE Tibetan Plateau*, PhD Thesis. University of Oxford.
- Patyniak, M., Landgraf, A., Dzhumabaeva, A., Baikulov, S., Williams, A. M., Weiss, J. R., et al. (2021). The Pamir Frontal Thrust fault: Holocene full-segment ruptures and implications for complex segment interactions in a continental collision zone. *Journal of Geophysical Research: Solid Earth*, 126(12), e2021JB022405. <https://doi.org/10.1029/2021JB022405>
- Peltzer, G., Rosen, P., Rogez, F., & Hudnut, K. (1998). Poroelastic rebound along the Landers 1992 earthquake surface rupture. *Journal of Geophysical Research*, 103(B12), 30131–30145. <https://doi.org/10.1029/98JB02302>
- Perfettini, H., Avouac, J.-P., Tavera, H., Kositsky, A., Nocquet, J.-M., Bondoux, F., et al. (2010). Seismic and aseismic slip on the Central Peru megathrust. *Nature*, 465(7294), 78–81. <https://doi.org/10.1038/nature09062>
- Ramos, M. D., Neo, J. C., Thakur, P., Huang, Y., & Wei, S. (2020). Stress changes on the Garlock fault during and after the 2019 ridgecrest earthquake sequence. *Bulletin of the Seismological Society of America*, 110(4), 1752–1764. <https://doi.org/10.1785/0120200027>
- Reigber, C., Michel, G. W., Galas, R., Angermann, D., Klotz, J., Chen, J. Y., et al. (2001). New space geodetic constraints on the distribution of deformation in Central Asia. *Earth and Planetary Science Letters*, 191(1–2), 157–165. [https://doi.org/10.1016/S0012-821X\(01\)00414-9](https://doi.org/10.1016/S0012-821X(01)00414-9)
- Sangha, S., Peltzer, G., Zhanga, A., Menga, L., Liang, C., Lundgren, P., & Fielding, E. (2017). Fault geometry of 2015, M_w 7.2 Murghab, Tajikistan earthquake controls rupture propagation: Insights from InSAR and seismological data. *Earth and Planetary Science Letters*, 462, 132–141. <https://doi.org/10.1016/j.epsl.2017.01.018>
- Savage, J. C., & Burford, R. O. (1973). Geodetic determination of relative plate motion in central California. *Journal of Geophysical Research*, 78(5), 832–845. <https://doi.org/10.1029/JB078i005p00832>
- Schöne, T., Zech, C., Unger-Shayesteh, K., Rudenko, V., Thoss, H., Wetzel, H.-U., et al. (2013). A new permanent multi-parameter monitoring network in Central Asian high mountains—From measurements to data bases. *Geoscientific Instrumentation, Methods and Data Systems*, 2, 97–111. <https://doi.org/10.5194/gid-2-301-2012>
- Schurr, B., Ratschbacher, L., Sippl, C., Gloaguen, R., Yuan, X., & Mechie, J. (2014). Seismotectonics of the Pamir. *Tectonics*, 33(8), 1501–1518. <https://doi.org/10.1002/2014TC003576>
- Sippl, C., Ratschbacher, L., Schurr, B., Krumbiegel, C., Rui, H., Pingren, L., & Abdybachaev, U. (2014). The 2008 Nura earthquake sequence at the Pamir-Tian Shan collision zone, southern Kyrgyzstan. *Tectonics*, 33(12), 2382–2399. <https://doi.org/10.1002/2014TC003705>
- Sobel, E., & Dumitru, T. (1997). Thrusting and exhumation around the margins of the western Tarim basin during the India-Asia collision. *Journal of Geophysical Research*, 102(B3), 5043–5063. <https://doi.org/10.1029/96JB03267>
- Strecker, M. R., Frisch, W., Hamburger, M. W., Ratschbacher, L., Semiletkin, S., Zamoruyev, A., & Sturchio, N. (1995). Quaternary deformation in the eastern Pamirs, Tadzhikistan and Kyrgyzstan. *Tectonics*, 14(5), 1061–1079. <https://doi.org/10.1029/95TC00927>
- Strecker, M. R., Hillel, G. E., Arrowsmith, J. R., & Coutand, I. (2003). Differential structural and geomorphic mountain-front evolution in an active continental collision zone: The northwest Pamir, southern Kyrgyzstan. *The Geological Society of America Bulletin*, 115(2), 166–181. [https://doi.org/10.1130/0016-7606\(2003\)115<0166:DSAGMF>2.0.CO;2](https://doi.org/10.1130/0016-7606(2003)115<0166:DSAGMF>2.0.CO;2)

- Teshebaeva, K., Sudhaus, H., Ehtler, H., Schurr, B., & Roessner, S. (2014). Strain partitioning at the eastern Pamir-Alai revealed through SAR data analysis of the 2008 Nura earthquake. *Geophysical Journal International*, 198(2), 760–774. <https://doi.org/10.1093/gji/ggu158>
- Vajedian, S., Motagh, M., Wetzel, H.-U., & Teshebaeva, K. (2017). Coupling of Sentinel-1, Sentinel-2 and ALOS-2 to assess coseismic deformation and earthquake-induced landslides following the 26 June, 2016 earthquake in Kyrgyzstan. *Geophysical Research Abstracts*, 19, EGU2017-18464-1. <https://meetingorganizer.copernicus.org/EGU2017/EGU2017-18259.pdf>
- van Hinsbergen, D. J., Lippert, P. C., Dupont-Nivet, G., McQuarrie, N., Doubrovine, P. V., Spakman, W., & Torsvik, T. H. (2012). Greater India Basin hypothesis and a two-stage Cenozoic collision between India and Asia. *Proceedings of the National Academy of Sciences*, 109(20), 7659–7664. <https://doi.org/10.1073/pnas.1117262109>
- Velasco, A. A., Hernandez, S., Parsons, T., & Pankow, K. (2008). Global ubiquity of dynamic earthquake triggering. *Nature Geoscience*, 1(6), 375–379. <https://doi.org/10.1038/ngeo204>
- Voigt, T., Kley, J., & Wehner, C. (2020). A mountain of folds: Triangle zone in the fold-and-thrust belt of the external Pamir, Kyrgyzstan. EGU General Assembly, EGU2020-22109. <https://doi.org/10.5194/egusphere-egu2020-22109>
- Wang, K., Hu, Y., & He, J. (2012). Deformation cycles of subduction earthquakes in a viscoelastic Earth. *Nature*, 484(7394), 327–332. <https://doi.org/10.1038/nature11032>
- Wang, S., Xu, C., Wen, Y., Yin, Z., Jiang, G., & Fang, L. (2017). Slip model for the 25 November 2016 M_w 6.6 Aketao earthquake, Western China, revealed by Sentinel-1 and ALOS-2 observations. *Remote Sensing*, 9(4), 325. <https://doi.org/10.3390/rs9040325>
- Wdowinski, S., Bock, Y., Zhang, J., Fang, P., & Genrich, J. (1997). Southern California permanent GPS geodetic array: Spatial filtering of daily positions for estimating coseismic and postseismic displacements induced by the 1992 Landers earthquake. *Journal of Geophysical Research: Solid Earth*, 102(B8), 18057–18070. <https://doi.org/10.1029/97JB01378>
- Wessel, P., Smith, W. H. F., Scharroo, R., Luis, J. F., & Wobbe, F. (2013). Generic mapping Tools: Improved version released. *Eos, Transactions American Geophysical Union*, 94(45), 409–410. <https://doi.org/10.1002/2013EO450001>
- Wright, T., Fielding, E. J., & Parsons, B. (2001). Triggered slip: Observations of the 17 August 1999 Izmit (Turkey) earthquake using radar interferometry. *Geophysical Research Letters*, 28(6), 1079–1082. <https://doi.org/10.1029/2000GL011776>
- Xu, X., Sandwell, D. T., & Smith-Konter, B. (2020). Coseismic displacements and surface fractures from Sentinel-1 InSAR: 2019 ridgecrest earthquakes. *Seismological Research Letters*, 91(4), 1997–1985. <https://doi.org/10.1785/0220190275>
- Yu, C., Li, Z., Penna, N. T., & Crippa, P. (2018). Generic atmospheric correction model for interferometric synthetic aperture radar observations. *Journal of Geophysical Research: Solid Earth*, 123(10), 9202–9222. <https://doi.org/10.1029/2017JB015305>
- Zaalaiian Exploration Team. (1993). Geological structure and minerals of Alai area. Report on exploration works of a 1:50,000 scale in the area of the sheets J-43-3-A-r, B, B, F, J-43-14-A, B-a, 6, F, J-43-15-A, B, B, 1987–1993.
- Zech, C., Schöne, T., Illigner, J., Stolarczuk, N., Queißer, T., Köppl, M., et al. (2021). Hydrometeorological data from a remotely operated multi-parameter station network in central Asia. *Earth System Science Data*, 13(3), 1289–1306. <https://doi.org/10.5194/essd-13-1289-2021>
- Zubovich, A. V., Schöne, T., Metzger, S., Mosienko, O., Mukhamediev, S., Sharshbaev, A., & Zech, C. (2016). Tectonic interaction between the Pamir and Tien Shan observed by GPS. *Tectonics*, 35(2), 283–292. <https://doi.org/10.1002/2015TC004055>
- Zubovich, A. V., Wang, X. Q., Scherba, Y. G., Schelochkov, G. G., Reilinger, R., Reigber, C., et al. (2010). GPS velocity field of the Tien Shan and surrounding regions. *Tectonics*, 29(TC6014), 1–23. <https://doi.org/10.1029/2010TC002772>

3.1.4 Dense GNSS profiles across the northwestern tip of the India-Asia collision zone: Triggered slip and westward flow of the Peter the First Range, Pamir, into the Tajik Depression

Published as: [S. Metzger](#), A. Ischuk, Z. Deng, L. Ratschbacher, M. Perry, S.-K. Kufner, R. Bendick, M. Moreno (2020), Dense GNSS profiles across the northwestern tip of the India-Asia collision zone: Triggered slip and westward flow of the Peter the First Range, Pamir, into the Tajik Depression, *Tectonics*, **39**, e2019TC005797. [doi:10.1029/2021JB022775](https://doi.org/10.1029/2021JB022775)

Supporting information: available online

Data publication: [S. Metzger](#), A. Ischuk, A. Akhmedov, Z. Ilyasova, M. Moreno, S. Murodkulov, Z. Deng (2019), Survey-mode GPS data in the West Pamir, Tajikistan, Central Asia, 2013–2016, *GFZ Data Services*, [doi:10.5880/GFZ.4.1.2019.007](https://doi.org/10.5880/GFZ.4.1.2019.007)

Scientific application: This work presents the first observations to quantify the (very) high continental recent fault-slip rates at the two major fault zones in the Western Pamir. On top, our sGNSS data observed inter-mediate field fault activation following the 2015 Pamir earthquake, which so far was only seen in spatially dense radar interferograms and lead to the follow-up publication focusing on the northern rim of the Pamir [Zubovich et al. \(2022\)](#).

Methodological advances: Thorough analysis of sparse, survey GNSS data, considering superimposed tectonic signals. Combination of deformation rates and structural information from geological cross sections.

Individual Contributions: The study was designed, conducted and written by me. I, AI,MP, RB and MM collected/supported the GNSS survey data, ZD pre-processed the GNSS data, SK provided published seismological data to support the interpretation. LR assisted in the tectonic interpretation. All authors commented on the writing.

Tectonics

RESEARCH ARTICLE

10.1029/2019TC005797

Key Points:

- New survey-GNSS data record gravity-driven, lateral material flow out of the Pamir Plateau and shortening of the Tajik Basin deposits
- The Vakhsh fault accommodates $15 + 4/-2$ mm/yr shortening and 16 ± 3 mm/yr dextral shear, the Darvaz fault ~ 15 mm/yr sinistral shear
- The 2015 $M_w 7.2$ Sarez earthquake may have triggered ~ 2 cm of slip on the Darvaz fault reverse to its interseismic loading sense

Supporting Information:

- Supporting Information S1
- Data Set S1
- Data Set S2

Correspondence to:

S. Metzger,
metzger@gfz-potsdam.de

Citation:

Metzger, S., Ischuk, A., Deng, Z., Ratschbacher, L., Perry, M., Kufner, S.-K., et al. (2020). Dense GNSS profiles across the northwestern tip of the India-Asia collision zone: Triggered slip and westward flow of the Peter the First Range, Pamir, into the Tajik Depression. *Tectonics*, 39, e2019TC005797. <https://doi.org/10.1029/2019TC005797>

Received 31 JUL 2019

Accepted 24 JAN 2020

Accepted article online 26 JAN 2020

©2020. The Authors.

This is an open access article under the terms of the Creative Commons Attribution License, which permits use, distribution and reproduction in any medium, provided the original work is properly cited.

Dense GNSS Profiles Across the Northwestern Tip of the India-Asia Collision Zone: Triggered Slip and Westward Flow of the Peter the First Range, Pamir, Into the Tajik Depression

Sabrina Metzger¹ , Anatoly Ischuk² , Zhiguo Deng¹ , Lothar Ratschbacher³ , Mason Perry⁴ , Sofia-Katerina Kufner¹ , Rebecca Bendick⁴ , and Marcos Moreno⁵ 

¹HelmholtzZentrum Potsdam, Deutsches GeoForschungsZentrum, Potsdam, Germany, ²Institute of Geology, Earthquake Engineering and Seismology, Academy of Sciences, Dushanbe, Tajikistan, ³Geologie, TU Bergakademie Freiberg, Freiberg, Germany, ⁴Department of Geosciences, University of Montana, Missoula, MT, USA, ⁵Departamento de Geofisica, Universidad de Concepción, Concepción, Chile

Abstract At the northwestern tip of the India-Asia collision zone, the Pamir orocline overrides the Tajik Depression and the Tarim Basin and collides with the Tian Shan. Currently, the Pamir's northern edge exhibits localized shortening rates of 13–19 mm/yr. While the eastern Pamir and the Tarim Basin move northward nearly en block, north-south shortening decreases westward along the Pamir front into the Tajik Depression. In the northeastern Tajik Depression, the wedge-shaped crustal sliver of the Peter the First Range is squeezed between the dextral-transpressive Vakhsh and the sinistral-transpressive Darvaz faults. Global Navigation Satellite System (GNSS) data collected along two densely surveyed profiles detail the kinematics of north-south shortening and westward lateral extrusion in the northwestern Pamir. The 2016 campaign data suggest a short-duration dextral-slip activation of the Darvaz fault, which we interpret as a far-field effect triggered by the 2015, $M_w 7.2$ Sarez, Central Pamir earthquake. 2013–2015 interseismic GNSS velocities and kinematic modeling show that the Darvaz fault zone accommodates ~ 15 mm/yr sinistral shear and ~ 10 mm/yr fault-normal extension below a locking depth of $9.0 + 0.4/-1.1$ km. The Vakhsh fault shows shortening rates of $15 + 4/-2$ mm/yr and dextral shear rates of 16 ± 3 mm/yr. Jointly, these faults accommodate NW-SE shortening and southwestward material flow out of the Peter the First Range into the Tajik Depression. Together with seismic and geologic data, our and published geodetic surveys showcase the prolonged interaction of shortening and lateral material flow out of a plateau margin.

Plain Language Summary The Pamir Mountains, Central Asia, are the result of the northward indentation of the Indian continent into Eurasia. In average, the Pamir Plateau is $\sim 3,000$ m higher than the adjacent Tajik Depression to the west. We present time-series of high-precision point positioning data that show in great detail how the upper crust of the Pamir is flowing out into the lower lying Tajik Depression. This westward transport occurs on shallow-dipping, low-friction sedimentary layers that reach surface at the beginning of the Tian Shan Mountains further north. These sediments accommodate a total slip of around 2 cm, which is extremely high for continent-continent plate boundaries. In addition, our data observed a few centimeters of slip on the Darvaz fault that most probably was triggered by a large earthquake occurring in some 200 km distance. Such phenomena have so far rarely been observed.

1. Introduction

The Pamir at the northwestern tip of the India-Asia collision zone (Figure 1a) is a seismically active orogen, producing magnitude M_6-7 earthquakes approximately every 10 years. Over the last 50 years, those occurred mainly along the Pamir's northern perimeter (Figure 1b). Seismicity in the Pamir interior is less frequent, as recorded in both long-term, global (Storchak et al., 2013) and temporary, local catalogs (Schurr et al., 2014). Modern geodetic observations show that the Pamir thrust system along the Pamir's leading edge has the highest shortening rates of the whole India-Asia collision zone, accommodating 13–19 mm/yr across a ~ 75 km N-S distance (Ischuk et al., 2013; Zubovich et al., 2010, 2016). This corresponds to $\sim 50\%$ of the total shortening rate between India and Asia (DeMets et al., 2010).

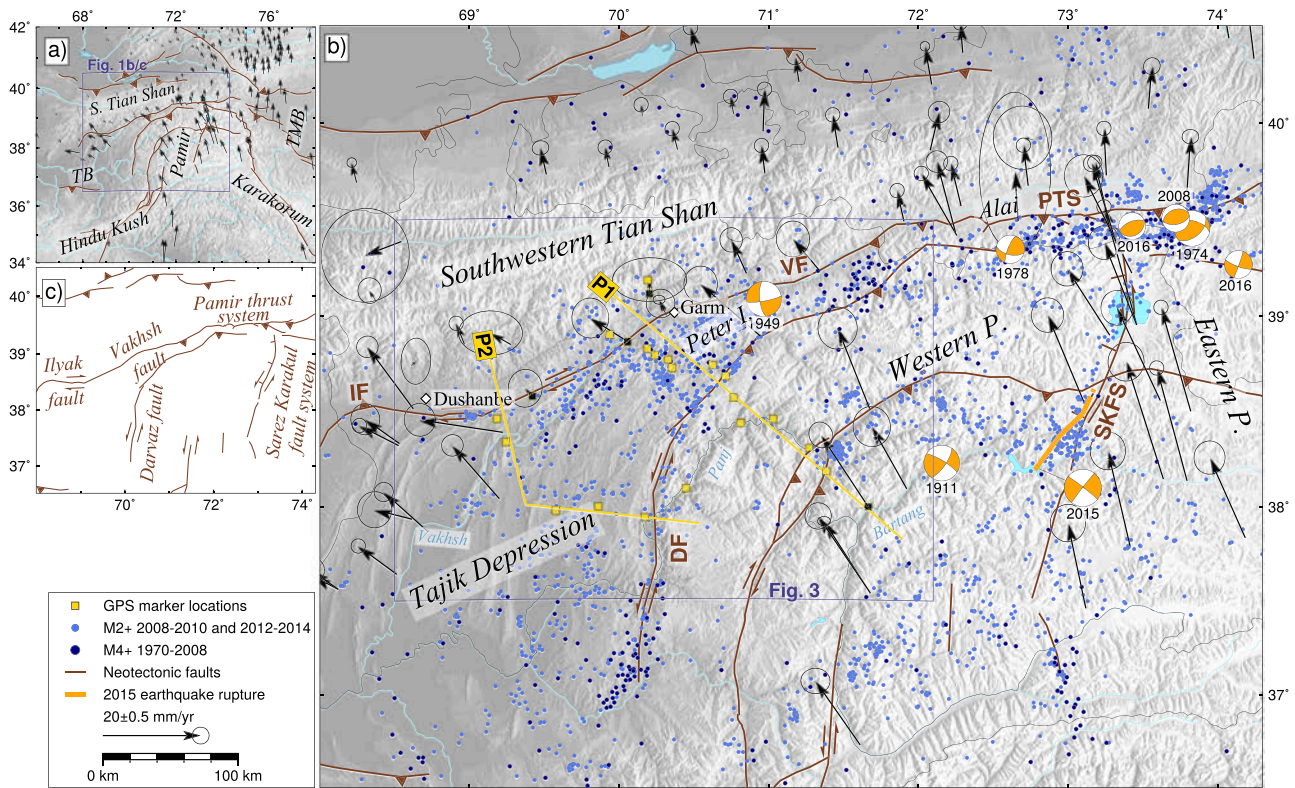


Figure 1. (a) Tectonic setting and main tectonic structures of the Pamir (in brown, Schurr et al., 2014) and published GNSS rates (Eurasia-fixed arrows, Ischuk et al., 2013; Mohadjer et al., 2010; Zubovich et al., 2010). TB = Tajik Basin; TMB = Tarim Basin. (b) Close-up of (a), highlighting the main active faults and their slip sense. (c) Close up of (a), highlighting (re)measured GNSS sites installed in 2013 (yellow squares) or earlier (black) along Profiles P1 and P2, seismicity observed by a regional network (2008–2010 and 2012–2014, bright blue, Kufner et al., 2018) and by teleseismics (1970–2008, dark blue, Engdahl et al., 1998), focal mechanisms of instrumentally recorded M6–7 earthquakes (Dziewonski et al., 1981; Ekström et al., 2012; Kulikova et al., 2015; Sippl et al., 2014) and the rupture extent of the M_w 7.2 Sarez earthquake (orange line, Metzger et al., 2017). DF = Darvaz fault; VF = Vakhsh fault; PTS = Pamir thrust system; SKFS = Sarez-Karakul fault system.

The eastern Pamir, that is, the Pamir east of the Sarez-Karakul fault system, and the Tarim Basin advance toward stable Asia at nearly the same rate (Zubovich et al., 2010), allowing little shear along the eastern margin of the Pamir. In contrast, the western Pamir—west of the Sarez-Karakul fault system—moves both north and west, involving lateral extrusion (cf. Ratschbacher et al., 1991) of material from the Pamir Plateau into the Tajik Depression (Ischuk et al., 2013). The latter hosts the Tajik Basin that was inverted in the Neogene to form the thin-skinned Tajik-basin fold-thrust belt, which is detached along a basal décollement in Jurassic evaporites (Figure 1b) (e.g., Bourgeois et al., 1997; Chapman et al., 2017; Nikolaev, 2002).

While today's shortening at the northern edge of the Pamir is mainly accommodated across the Pamir thrust system (Zubovich et al., 2010, 2016), two fault systems accommodate the more complicated relative motion between the western Pamir and southwestern Tian Shan, confining the northeastward narrowing Tajik Basin (Figure 1c): The N to NE striking, sinistral-transpressive Darvaz fault zone separates the Pamir from the Tajik Basin (Leith & Alvarez, 1985; Trifonov, 1978); the WSW striking, dextral-transpressive Vakhsh fault zone constitutes the leading thrust of the Tajik-basin fold-thrust belt in the northwestern Pamir and marks the boundary to the southwestern Tian Shan. How exactly surface motion is partitioned between these two faults is unclear (Ischuk et al., 2013). The Vakhsh fault transitions westward into the approximately east striking, dextral Ilyak fault zone (Babaev, 1975; Leith & Simpson, 1986) and continues eastward along the southern border of the Alai valley as a south dipping décollement along Jurassic evaporites (Nikolaev, 2002; Skobelev & Florenskiy, 1974). In between the Vakhsh and Darvaz fault zones, the wedge-shaped Peter the First Range hosts focused seismicity, indicating its NW-SE shortening and NE-SW lengthening (Hamburger et al., 1992; Kufner et al., 2018) (Figures 1b and 2).

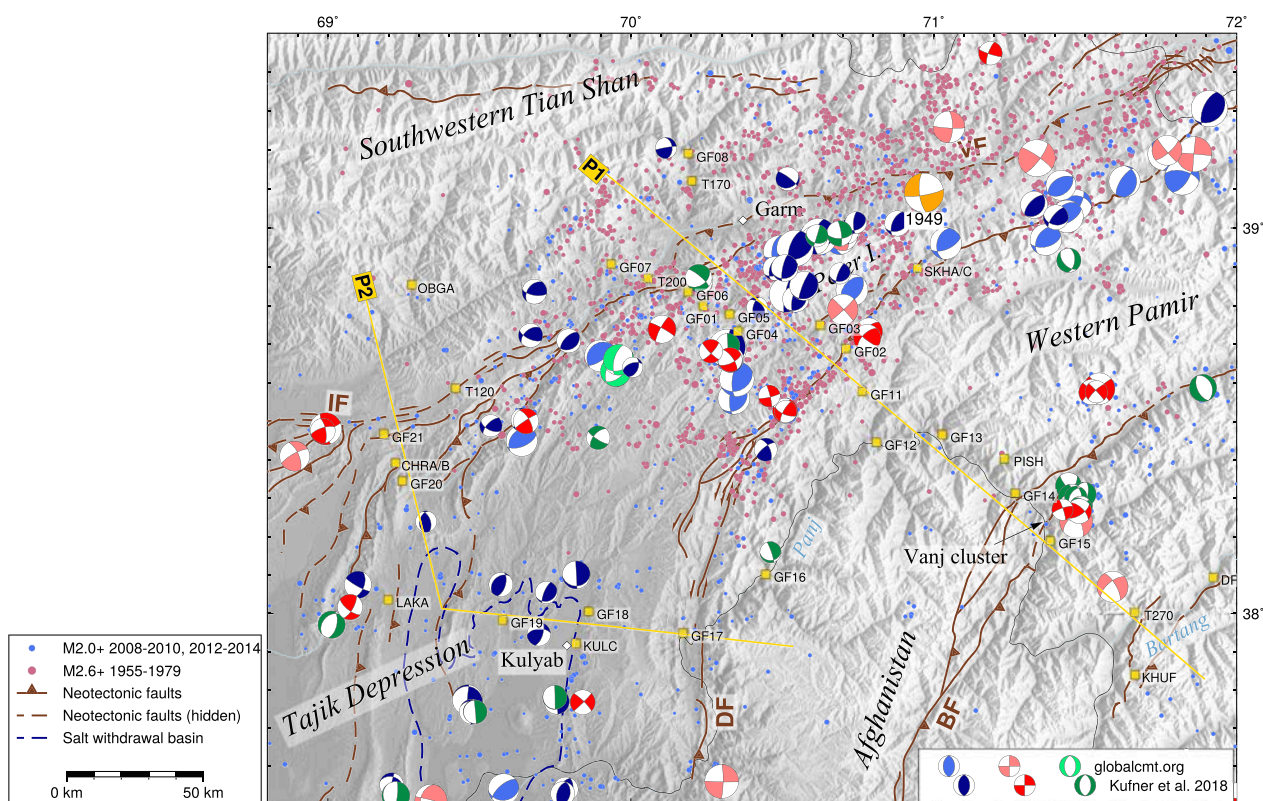


Figure 2. Seismic setting of the western Pamir, Tajik Depression, and southwestern Tian Shan. Crustal seismicity (Hamburger et al., 1992; Kufner et al., 2018), focal mechanisms (Dziewonski et al., 1981; Ekström et al., 2012; Kufner et al., 2018; Kulikova, 2016), and GNSS markers (yellow squares).

The long-term history of bulk N-S shortening and westward material flow at the northwestern Pamir-Tibet plateau margin is evident from the geologic record in the Pamir interior and shortening in the Tajik-basin fold-thrust belt (Chapman et al., 2017; Nikolaev, 2002; Rutte et al., 2017; Stübner et al., 2013; Worthington et al., 2019). Paleogene fold nappes in the Central Pamir record crustal thickening but accompanying along-strike flow lineations imply orogen-parallel material transport. Dextral wrenching and fold-axis parallel, E-W extension in upper crustal thrust sheets, and the pinch and swell geometry of the Pamir gneiss domes record Neogene orogen-parallel material transport at shallower crustal levels. Whereas currently and over most of the Neogene, the Pamir crust has been collapsing into the Tajik Depression, lateral material transport thickened the crust in the western Hindu Kush of Afghanistan in the Paleogene (Robert et al., 2017; Rutte et al., 2017).

Herein, we present Global Navigation Satellite System (GNSS) time series acquired between 2013 and 2016 along two densely spaced profiles—P1 and P2—ranging from the western Pamir Plateau across the north-eastern Tajik-basin fold-thrust belt of the Peter the First Range into the southwestern Tian Shan (Figure 1b). We first review the regional tectonics (section 2), focusing on the regional seismicity, large earthquakes that were instrumentally observed in the region, geologic evidence of Quaternary fault-slip on the Vakhsh and the Darvaz fault zones, and recent rate estimates by geodetic measurements. In section 3, we introduce the new campaign GNSS data collected across the Vakhsh and Darvaz fault zones (Metzger et al., 2019). We detail the GNSS data collection, the data processing, and the rate estimation from the resulting time series. This includes measures for the effect of the 2015, M_w 7.2 Sarez, Central Pamir, earthquake (Metzger et al., 2017; Sangha et al., 2017) on the rate estimates (section 4). We also assess the slip type and slip rate of the Darvaz and Vakhsh fault zones using kinematic modeling. In section 5, we integrate the geodetic, geologic, and seismic data and propose a conceptual model of the kinematic relationships between the western Pamir Plateau, the Tajik Depression, and the southwestern Tian Shan.

2. Neotectonic Setting

In the Pamir, northward displacement and crustal shortening is currently accommodated along the Vakhsh fault system and the Pamir thrust system in the north (e.g., Zubovich et al., 2010, 2016), the sinistral Darvaz fault zone in the west and northwest (Ischuk et al., 2013; Mohadjer et al., 2010), the dextral Aksu-Murghab (Ruzhentsev, 1963, 1968; Schurr et al., 2014; Strecker et al., 1995), and Karakorum (Chevalier et al., 2015; Sridevi et al., 2004) fault systems in the southeast, and the Kongur Shan-Tashkorgan normal fault system in the Chinese eastern Pamir (Chen et al., 2011; Liu, 1993), which also has a weak dextral component (Chevalier et al., 2015; Fan et al., 1994). Under the Pamir, Asian lithosphere forms a subduction arc that is retreating north and westward as traced by intermediate-depth (60–300 km) seismicity (Schneider et al., 2013; Sippl et al., 2013; Sippl et al., 2013). Kufner et al. (2016) suggested that Asian slab retreat is forced by indentation of the Indian lithosphere, bulldozing into the cratonic lithosphere of the Tajik-Tarim Basin at mantle depth.

In the Pamir interior, the active displacement field is composed of bulk northward movement combined with E-W extension (Ischuk et al., 2013; Zhou et al., 2016). The crust hosts both sinistral strike-slip faulting on NE striking or conjugate planes and—to a lesser degree—normal faulting on approximately north striking planes (Schurr et al., 2014). The only NE striking sinistral-transtensive fault system of the Pamir interior, which has a clear morphologic expression and is seismically active, is the Sarez-Karakul fault system that stretches from south of Lake Sarez to north of Lake Karakul (Figure 1b) (Rutte et al., 2017; Schurr et al., 2014; Strecker et al., 1995). The E-W extension is driven by westward gravitational collapse of thickened Pamir-Plateau crust into the Tajik Depression (Rutte et al., 2017; Schurr et al., 2014; Stübner et al., 2013), causing NW-SE shortening of the ~7–12 km thick sedimentary rocks of the Tajik Basin (Leith & Alvarez, 1985; Nikolaev, 2002). In the western Pamir Plateau, distributed strike-slip faulting accommodates shear between the northward moving Pamir and the Tajik Depression. The Darvaz fault splays off from the Pamir thrust system in a WSW direction and then curves south (Figures 1b and 1c). Farther southeast, the Badakhshan fault runs in parallel to the Darvaz fault. Offset morphologic features in central Badakhshan, Afghanistan, suggest dextral-transpressive slip (Schurr et al., 2014; Stübner et al., 2013), but neither geodetic nor seismic data constrain its kinematics.

2.1. Recent Crustal Seismicity

Crustal microseismicity (i.e., events with local magnitude smaller 4; hereafter called seismicity) is focused along the perimeter of the Pamir, where it coincides with the Pamir thrust system in the north, the Peter the First Range in the northwest and the eastern Tajik Basin in the west (Figure 1b) (Kufner et al., 2018; Schurr et al., 2014). The interior of the Pamir also hosts seismicity following the Sarez-Karakul fault system (Schurr et al., 2014). The Badakhshan fault does not feature instrumentally recorded earthquakes.

In the Peter the First Range, seismicity is mostly located along the Darvaz fault and in between the Darvaz and the Vakhsh faults (Figure 1b) (Hamburger et al., 1992). Along the Darvaz fault seismicity clusters along its northern and southern segments. Three event catalogs, one combined from Schurr et al. (2014) and Kufner et al. (2018) with events recorded in 2008–2010 and in 2012–2014, respectively, one including events from the Soviet/US-CSE network operated during 1955–1979 (Hamburger et al., 1992), and events from teleseismic data recorded between 1970 and 2008 (Engdahl et al., 1998) all show the same seismically active features and areas of quiescence (Figure 2). In the Tajik Depression, seismicity is less prominent but distributed at the base and above the sedimentary cover at ~11 km. Sparse events occur in the basement down to 40 km depth, plus activity at the southern end of the Darvaz fault and where the Darvaz and the Vakhsh faults run in parallel, at ~71.5°E (Figure 1b).

Focal mechanisms available from the regional and global catalogs exhibit a nodal plane parallel to the curved outline of the Pamir (Figure 2) (Dziewonski et al., 1981; Ekström et al., 2012; Kufner et al., 2018; Schurr et al., 2014). The mechanisms along the Darvaz fault zone are mostly strike-slip but rotate to thrusting farther northeast. Earthquakes along the Ilyak fault zone have strike-slip mechanisms. Farther northeast, where the Ilyak transitions into the Vakhsh fault, thrusting becomes dominant and the epicenters are mostly located on the southeastern, downdip side of the fault. Even farther to the east, the global (M4.5+) CMT catalog (Storchak et al., 2013) contains a few strike-slip events that have similarities to the 1949, M_w 7.6 Khait earthquake. A series of NW-SE aligned strike-slip events links the Darvaz and the

Vakhsh fault just close to our GNSS profile P1. The Tajik Depression west of the southern Darvaz fault hosts mostly thrust earthquakes with one subhorizontal nodal plane, likely indicating E-W oriented slip along a horizontal interface. There, features like the 800 m high Hoja Mumin diapir 20 km SW of Kulyab (Dooley et al., 2015) are attributed to salt tectonics (Figure 2).

Over the last 110 years, the Pamir region was struck by four M7+ crustal earthquakes: The 1949 Khait earthquake occurred at the northwestern perimeter of the Pamir, the 1974 Markansu earthquake at the northeastern perimeter and the 1911/2015 Sarez earthquakes in the Central Pamir (Figure 1b). The 1949, M_w 7.6 Khait earthquake affected the area where the Darvaz and Vakhsh faults run in parallel (Figure 1b). This earthquake shows a NE-striking, sinistral and a NW striking dextral focal plane, probably rupturing a fault of ~60 km length (Kondorskaya & Shebalin, 1982; Kulikova, 2016; Storchak et al., 2013) either on the Vakhsh fault or in the southern Tian Shan (Schurr et al., 2014). We did not find reports on surface ruptures, but many landslides occurred (e.g., Evans et al., 2009), mostly in the area ~20 km northwest of the instrumentally derived epicenter (Figure 1b). The 1974, M_w 7.1 Markansu earthquake activated the Pamir frontal thrust (Sippl et al., 2014).

The 1911, M_s ~7.7 Lake Sarez earthquake was observed by a few analog, teleseismic stations and was located—with large uncertainties—~80 km west of the southern Sarez-Karakul fault system (Kulikova et al., 2015). Kulikova et al. (2015) and Schurr et al. (2014) argued that this earthquake ruptured the Sarez-Karakul fault system. The 2015, M_w 7.2 Sarez, Central Pamir, earthquake has a strike-slip focal mechanism comparable to the 1911 Lake Sarez earthquake (USGS, 2015). Surface displacement maps from satellite imagery and neotectonic field mapping traced the rupture surface along the Sarez-Karakul fault system. The earthquake nucleated near Lake Sarez and propagated northeastward (Sangha et al., 2017). Metzger et al. (2017) observed coseismic slip of up to 3 m and modeled the source as a subvertical ~80 × 25 km fault plane comprising three segments. In addition, continuous GNSS stations in the eastern Alai valley (Figure 1b), ~120 km from the epicenter, and in northeastern Afghanistan, ~250 km from the epicenter, recorded horizontal offsets of a few millimeters up to 2 cm (see supporting information Figure S3 in Metzger et al., 2017). Stations on profile P1 are in a similar distance from the epicenter and thus might have been affected by the event as well (section 4.1).

2.2. Quaternary Deformation Rates

Quaternary faults in the western Pamir parallel the topographic margin of the Pamir Plateau (Burtman & Molnar, 1993; Trifonov, 1978). Neotectonic mapping located their activity primarily along the Darvaz fault zone. Offset geomorphologic markers—i.e., 20 m of late Holocene landforms, 120–150 m of early Holocene terraces and alluvial fans and 300 m of late Pleistocene landforms—suggest a sinistral slip rate of 10–15 mm/yr along the southern Darvaz fault at ~37.8°N (Trifonov, 1978). Farther north, at 38.5–38.7°N, the ~21 m displacement of a ~1,500 or 2,200 yr old, man-made defense structure suggests 10–40 mm/yr of sinistral slip (Kuchai & Trifonov, 1977). Offsets of Holocene (~160 m) and late Pleistocene (~800 m) valleys in the same area suggest 5–16 and 4–12 mm/yr, respectively (Nikonov, 1975, 1977; Trifonov, 1983).

Farther northeast, at ~39°N and ~71°20'E, Trifonov (1983) mapped 50–170 m sinistral and ~10 m vertical offsets of moraines, implying to 3–4 to ~8 mm/yr sinistral-transpressive slip rates since the last glacial maximum, assumed at ~20 ka (Burtman & Molnar, 1993). The mapped fault segments strike approximately E-W but an association with either the Vakhsh or the Darvaz fault is unclear. Where the Darvaz fault enters the Trans-Alai Range, at ~71.4°E, it seems to become inactive.

Neotectonic deformation along the Vakhsh fault comprises a 9–12 km wide belt of thrust and reverse faults along the northern slope of Peter the First Range (Burtman & Molnar, 1993). Trifonov (1983) reported 10–15 m of dextral offsets of dry valleys at 70.5°E, east of Garm. Furthermore, ^{14}C ages of 670 ± 40 , 1470 ± 100 , and 2000 ± 100 yr from swamp deposits dammed by tectonic scarps suggest recent tectonic activity.

The Tajik Basin shortens NW-SE, indicated by Quaternary, right-lateral displacements along the major faults at its northern rim (Zakharov, 1948, 1955, 1958). Dextral displacements of Holocene landforms (~15 m) occurred along approximately east striking faults (Legler & Przhivalgovskaya, 1979), and of late Pleistocene terraces (~90 m) along approximately NE striking faults (Trifonov, 1983). These faults are likely part of the Ilyak fault system and the faults of the Tajik-basin fold-thrust belt that are dragged right-laterally

into the Ilyak fault zone. Within the fold-thrust belt, sinistral offsets of late Pleistocene and Holocene landforms occurred along N-NE striking, oblique-reverse faults (Nikonov, 1970; Trifonov, 1983).

2.3. Geodetic Deformation Rates

The estimated geodetic slip rate for the Darvaz fault from a sparse regional geodetic array is 10 ± 1 mm/yr (Ischuk et al., 2013). Given the interstation distance of 250 km, it is unclear whether this deformation is accommodated by the Darvaz fault or within the Tajik-basin fold-thrust belt. Zhou et al. (2016) estimated ~ 7 mm/yr of N-S shortening either on the Vakhsh fault, the Darvaz fault, or on any structure in-between. Farther north, where the Darvaz fault approaches the Vakhsh fault and links with the Pamir thrust system, continuous GNSS stations indicate a minimum of 5.6 ± 0.8 mm/yr dextral shear and 2.2 ± 0.8 mm/yr N-S shortening on one of the fault strands of the Pamir thrust system (Zubovich et al., 2016).

Slip on the Vakhsh fault near the Garm region, the northwestern Peter the First Range (Figure 1b) was observed using leveling and laser-ranging techniques since 1948/1950 and 1968, respectively. A 317° trending, 6 km long triangulation and leveling network revealed a relative rate of 16 ± 1 mm/yr between the Peter the First Range and the southern Tian Shan (Guseva, 1986; Konolpatsev, 1971). Given the fault strike, this corresponds to ~ 6 mm/yr of dextral shear along and ~ 15 mm/yr of shortening across the Vakhsh fault, but this may only capture a portion of the full strain accumulation across the fault and could point to (post-seismic) fault creep. The rates were confirmed by an independent network measured in 1972 and 1980, spanning less than 1 km across the fault scarp: The relative horizontal rate was 15.9 ± 0.5 mm/yr with respect to the markers in the southern Tian Shan (Guseva, 1986). A remeasurement of the original profile using laser-ranging devices in 1974–1984 resulted in a more complicated pattern, with ~ 8 mm/yr of convergence across the Vakhsh fault, and ~ 4 mm/yr of shortening within the northernmost 4 km of Peter the First Range. If the pattern changes are significant, they might reflect the return from the postseismic (afterslip or creeping) stage after the 1949, $M_w 7.6$ Khait earthquake to the (locked) interseismic stage.

The leveling data acquired over 5 to 29 years showed no uplift on the northwestern side of the Vakhsh river in the southwestern Tian Shan, but 7–9 mm/yr of relative uplift on its southeastern side that rapidly decreased to 1–4 mm/yr southeastward (Guseva, 1986), suggesting a listric geometry for the Vakhsh fault with a rapidly decreasing southeast dip (Burtman & Molnar, 1993). Another 1 km profile across the Vakhsh thrust revealed even higher uplift rates, 18.6–21.6 mm/yr. A 200 m long dense leveling profile in a tunnel dug across the Vakhsh thrust yielded a relative uplift rate of 14.6 ± 0.3 mm/yr between 1973 and 1976, pointing to a steeply S dipping fault. Using borehole data across the Vakhsh thrust, Guseva (1986) determined a 48° dip.

3. GNSS Data Collection, Processing, and Rate Estimation

3.1. Marker Installation and Instrument Setup

In 2013, we installed 21 GNSS markers in the northwestern Pamir with a focus on the Vakhsh and the Darvaz faults (Figure 1b). We placed the network such that it forms two profiles (P1 and P2), crossing these faults subperpendicularly. The network also included four stations of the survey of Ischuk et al. (2013), where we prolonged the time series. Profile P1 crosses the Peter the First Range and includes 14 points. It has a length of ~ 230 km and extends from ~ 50 km NW of Garm to ~ 40 km SE of the Panj-Bartang river junction (Figure 2). Profile P2 is located ~ 100 km farther southwest and covers the Pamir foothills and the northeastern Tajik Basin from the Panj river to 50 km ESE of Dushanbe with a total length of ~ 200 km. It contains seven new data points, of which one was destroyed in 2014. The profile has a kink to better image fault-parallel and fault-perpendicular rates (section 4.2). Average interstation distances are 10 km and 15 km for P1 and P2, respectively.

The GNSS markers are 10 cm long stainless steel bolts of 1 cm diameter that were drilled and glued into the bedrock. The minimalistic design contains only a small dimple to fix the tip of the tripod (Figure S1a in the supporting information).

We used three Trimble Zephyr Geodetic Model 1 antennas (TRM 41249.00) and three Trimble R7 receivers to acquire the data. The antennas were installed on top of portable, short-braced aluminum tripods (Figure S1b), locked to the ground with rocks to stabilize the set up (Figures S1b and S1c). The antenna was aligned to true North. We recorded data for 40–48 hr per campaign (i.e., two consecutive nights) with a

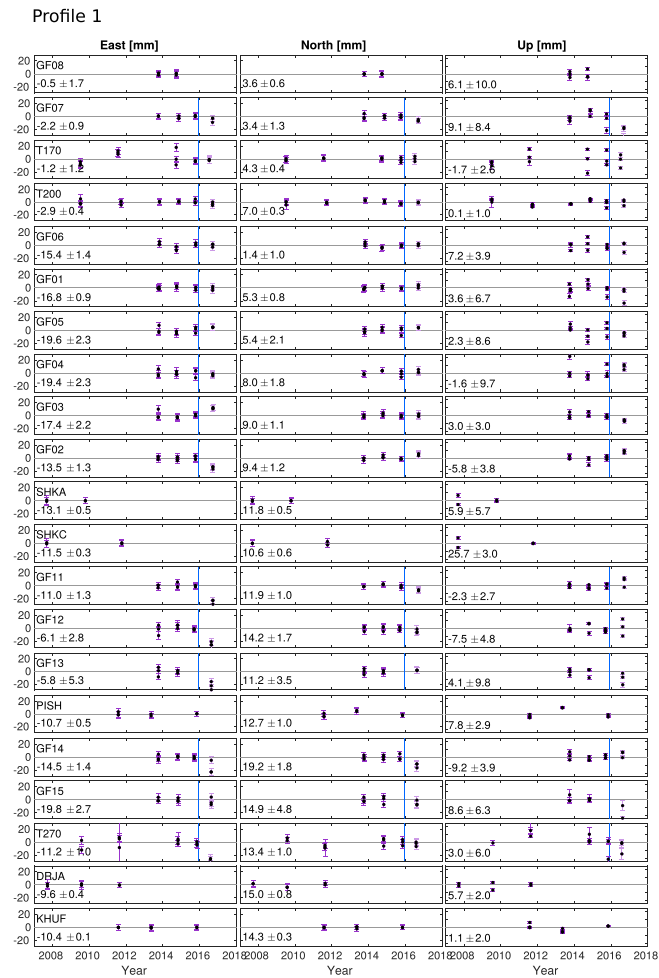


Figure 3. East (left column), north (center), and vertical (right) GNSS time series residuals after removing a linear velocity fitting the data until 2015. The stations are sorted along Profiles P1 (here) and P2 (continued figure). The vertical blue line marks the M_w 7.2 Sarez earthquake. Rates obtained from data acquired before the earthquake are indicated in each subfigure.

sampling rate of 30 s. To minimize seasonal loading signals, we collected the data in fall (September to November) of the years 2013 to 2016. The slope steepness near the measurement sites in the northwestern Pamir reaches 45° leading to limited space aperture (Figures S1c and S1d).

3.2. Data Processing

The raw data were converted into daily, receiver-independent exchange format (RNX) files, which were published in Metzger et al. (2019). They were processed together with 24 reference stations of the International Global Navigation Satellite System Service (IGS) network and RNX data of Ischuk et al. (2013) and Zhou et al. (2016), using the Earth Parameter and Orbit System software (Deng et al., 2016). The processing includes ionosphere-free linear combination, undifference carrier phase and pseudo-range observables, IGS08 absolute phase center variations (Schmid et al., 2016) and the FES2004 ocean tide loading model (Lyard et al., 2006). Apriori zenith hydrostatic delay is obtained using the Global Pressure and Temperature model (GPT2) and the Vienna mapping function in a grid file database. Station coordinates and tropospheric wet zenith delays are estimated using random-walk parameters for every two hours

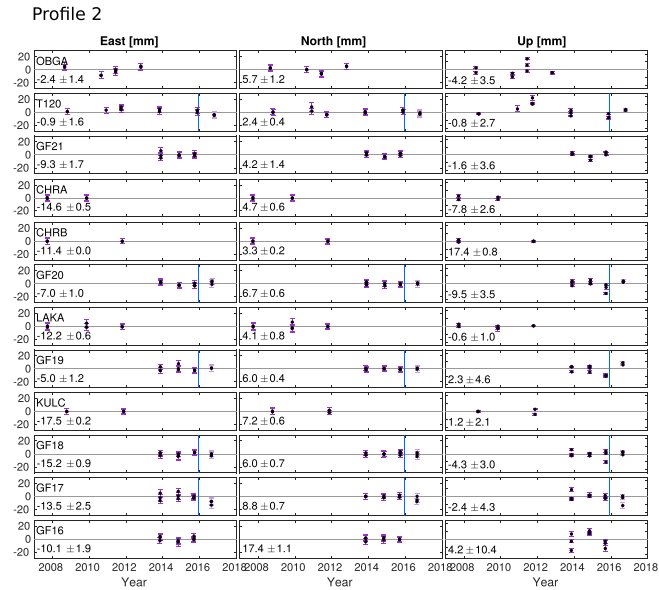


Figure 3. (continued)

(Gendt et al., 2013). In order to ensure consistency in the processing, we applied reprocessed GNSS precise satellite orbits as well as clock products obtained by the Earth Parameter and Orbit System software using the same parameter setup as for the station coordinate estimation (Gendt et al., 2013). Additionally, station coordinates were estimated in network mode and aligned to the IGS 2nd combined daily coordinate product (ITRF14), reducing the impact of the Earth rotation parameter (Altamimi et al., 2016; Rebischung et al., 2016). As a quality measure, daily observation files with continued observations shorter than 1 hr were excluded. With very few exceptions, the data quality is very good and the positions are consistent. The standard deviation of the daily positions per measurement is 2.1 mm (Figure 3). In the vertical direction, the standard deviation is 4 times larger (8.1 mm).

3.3. Rate Estimates

From the daily positions, we built time series and estimated the interseismic deformation rates individually for each station and component. By a visual inspection, we excluded outliers and then applied a two-parameter, linear rate estimation using a least squares inversion (Figure 3). All data points were weighted with their instrumental error. Following (Geirsson et al., 2006), we normalized the estimated rate uncertainty σ by the total observation period ΔT between the first and the last measurement of the time series, with N being the total number of positioning data points, and the daily position y_i being predicted by model point \hat{y}_i ,

$$\sigma = \frac{\sum_{i=1}^N (y_i - \hat{y}_i)^2}{\sqrt{N-2}} \cdot \frac{1}{\Delta T}.$$

This means that for time series with a short observation period of 2 or 3 years the rate uncertainty can be rather large. The average misfit of the rate estimation is 0.8 mm/yr in North, 0.5 mm/yr in East and 2.0 mm/yr in the vertical component, which is good, given the steep topography and limited space aperture. The derived rates and uncertainties are provided both in the ITRF14 no-net-rotation (NNR) reference frame (Altamimi et al., 2016) and in a Eurasian-fixed reference frame (Table 1) (Altamimi et al., 2017) in the supporting information (GNSSratesITRF14_NNR.txt, GNSSratesITRF14_EU.txt). The data show no apparent bias in the residuals apart from a distinct offset between data collected until the 2015 campaign and after (Figure 3), which will be discussed in section 4.1.

Table 1

Eurasian-Stable Rates v and 1σ Uncertainties (Altamimi et al., 2017) for East, North, and Vertical Components, Obtained From a Combined Network Solution of New and Updated Data (Ischuk et al., 2013; Zhou et al., 2016; Zubovich et al., 2010)

Name	Lon. (°)	Lat. (°)	Rates 2013–2015 (mm/yr)						Rates 2013–2016 (mm/yr)						ΔT (yr)
			vE	vN	vU	σE	σN	σU	vE	vN	vU	σE	σN	σU	
GF01	70.2383	38.7988	-16.8	5.4	3.6	0.9	0.8	6.7	-17.0	6.1	0.2	0.7	0.7	5.0	3/2
GF02	70.7105	38.6884	-13.5	9.4	-5.8	1.3	1.2	3.8	-17.6	11.0	-0.9	1.7	0.9	3.0	3/2
GF03	70.6252	38.7486	-17.4	9.0	3.0	2.2	1.1	3.0	-14.0	9.2	-0.6	1.8	0.7	2.1	3/2
GF04	70.3533	38.7334	-19.4	8.1	-1.6	2.3	1.8	9.7	-20.1	8.8	3.1	1.3	1.2	6.0	3/2
GF05	70.3262	38.7770	-19.6	5.4	2.3	2.3	2.1	8.6	-18.1	6.7	-0.3	1.4	1.3	4.9	3/2
GF06	70.1889	38.8340	-15.4	1.4	7.2	1.4	1.0	3.9	-15.4	1.4	7.2	1.4	1.0	3.9	3/3
GF07	69.9355	38.9064	-2.2	3.4	9.1	0.9	1.4	8.4	-3.5	1.6	-0.4	0.9	1.0	6.1	3/2
GF08	70.1893	39.1908	-0.5	3.6	6.1	1.7	0.6	10.0	-0.5	3.6	6.1	1.7	0.6	10.0	1/1
GF11	70.7643	38.5774	-11.0	11.9	-2.3	1.3	1.0	2.7	-17.9	10.0	1.3	2.7	0.9	2.7	3/2
GF12	70.8109	38.4467	-6.1	14.2	-7.5	2.8	1.7	4.8	-12.8	13.0	-5.6	3.1	1.2	4.4	3/2
GF13	71.0280	38.4664	-5.8	11.2	4.1	5.3	3.5	9.8	-13.9	12.0	-1.7	2.4	1.0	4.1	3/1
GF14	71.2691	38.3146	-14.5	19.2	-9.2	1.5	1.8	3.9	-19.5	15.6	-6.9	2.5	1.7	2.7	3/2
GF15	71.3850	38.1908	-19.8	14.9	8.6	2.7	4.8	6.3	-20.8	13.0	-6.7	1.4	1.6	4.6	3/1
GF16	70.4449	38.1034	-10.1	17.4	4.2	1.9	1.1	10.5	-10.1	17.4	4.2	1.9	1.1	10.5	2
GF17	70.1721	37.9496	-13.5	8.9	-2.4	2.5	0.7	4.3	-16.4	7.6	-4.0	1.8	0.9	3.3	3/2
GF18	69.8604	38.0061	-15.2	6.0	-4.3	0.9	0.8	3.0	-15.2	6.0	-4.3	0.9	0.8	3.0	3
GF19	69.5762	37.9839	-5.0	6.0	2.3	1.2	0.4	4.6	-5.0	6.0	2.3	1.2	0.4	4.6	3
GF20	69.2454	38.3459	-7.0	6.7	-9.5	1.0	0.6	3.5	-7.0	6.7	-9.5	1.0	0.6	3.5	3
GF21	69.1845	38.4673	-9.3	4.2	-1.6	1.7	1.4	3.6	-9.3	4.2	-1.6	1.7	1.4	3.6	2
T120 ^a	69.4213	38.5852	-0.9	2.4	-0.8	1.6	0.4	2.7	-0.9	2.4	-0.8	1.6	0.4	2.7	8
T170 ^a	70.2012	39.1204	-1.2	4.3	-1.7	1.2	0.4	2.6	-1.2	4.3	-1.7	1.2	0.4	2.6	7
T200 ^a	70.0563	38.8691	-2.9	7.0	0.1	0.4	0.3	1.0	-2.9	7.0	0.1	0.4	0.3	1.0	7
T270 ^a	71.6630	38.0032	-11.2	13.4	3.0	1.0	1.0	6.0	-13.7	13.2	2.4	1.7	0.8	4.8	7/6

Note. ΔT indicates time series length, if the 2016 data acquisitions are excluded or included, respectively. The full network solution (with additional rates of 51 locations) is available in the supporting information (GNSSratesITRF14_EU.txt and GNSSratesITRF14_NNR.txt).

^aExtended time series of Ischuk et al. (2013).

The obtained rates were then compared to an independent processing run using the GAMIT/GLOBK software package (Herring et al., 2018a, 2018b). In this run, we combined positions of 25 regional continuous and IGS stations with 66 campaign stations throughout the region using GAMIT to calculate initial daily positions, which were then edited, averaged, and weighted over ~ 2 week long intervals. Then, GLOBK's Kalman filter (Herring et al., 2015) was used to estimate linear horizontal velocities from the position averages within the ITRF08 reference frame (Altamimi et al., 2012), incorporating a random walk noise model to account for systematic errors. The mean difference between the two data sets is 1.7 ± 2.3 mm/yr in the east direction and -0.3 ± 1.2 mm/yr in the north direction.

4. Results and Interpretation

4.1. Potential Influence of the 2015, $M_w 7.2$ Sarez Earthquake on the Time Series

Some GNSS positions of the 2016 campaign show a clear offset from the (assumed) linear rate trend provided by the measurements acquired prior to 2016 (in Figure 3 and Table S1). This is most prominent at stations T270, GF11, GF12, GF13, GF14, and GF02, with 5–20 mm offsets toward the west. Station GF03 exhibits an 11 mm offset toward the east. Together, these stations suggest dextral motion on the Darvaz fault, which is opposite the sense of interseismic loading. This signal is not a measurement bias, for example, from seasonal variations, which are to be expected to be in the order of a few millimeters (Dong et al., 2002) or neglected firmware updates. We also rule out artifacts caused by instrument types or setup (Table S1). Therefore, we interpret the signal to reflect real ground displacements. Stations with large offsets between the 2015 and 2016 campaigns are located near the Darvaz fault, with amplitudes generally decreasing from SE to NW and an abrupt sign change across the Darvaz fault (Figure 4 and Table S1). Station GF15 is an exception but was not measured in 2015. The displacement pattern resembles either a dextral slip event or transient creep on the Darvaz fault with fault slip of centimeters to decimeters.

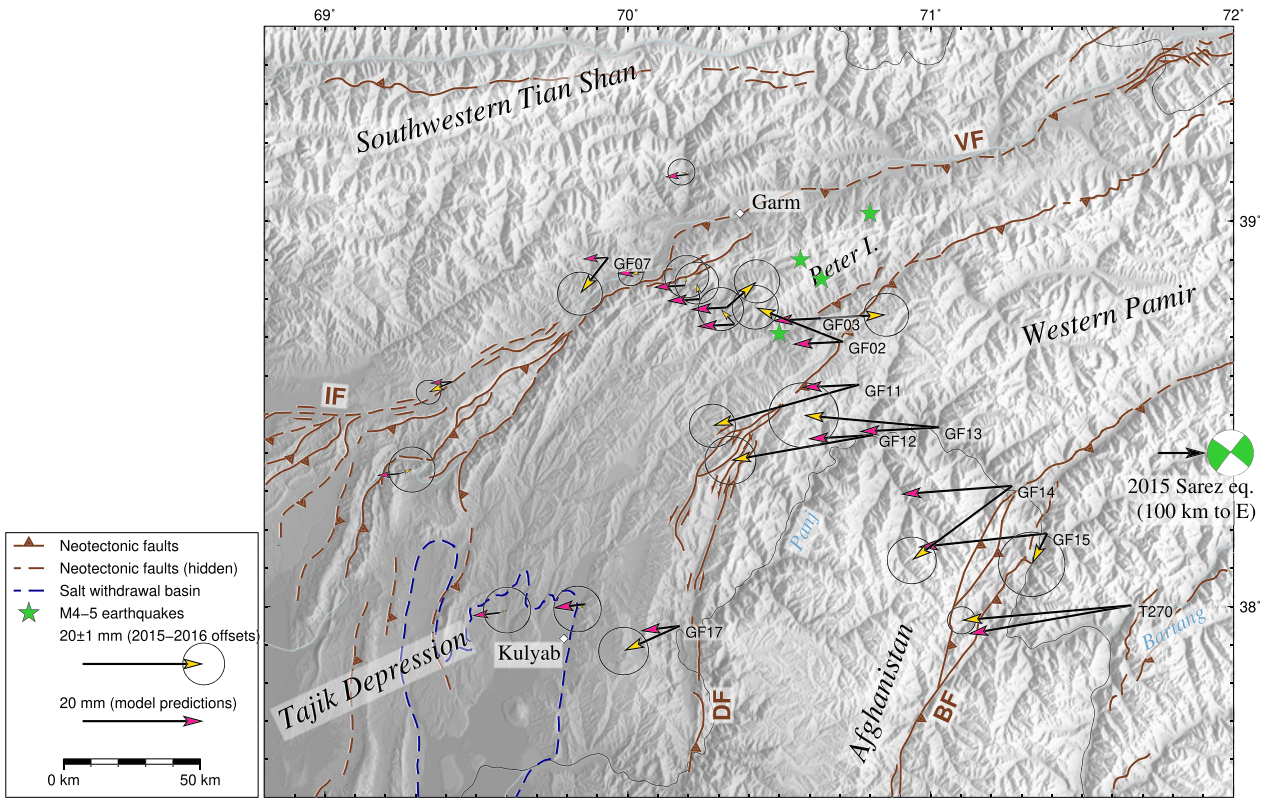


Figure 4. GNSS positioning differences between the 2015 and 2016 data surveys (yellow arrows, 2σ confidence level) in comparison to the coseismic displacements (pink arrows) of the M_w 7.2 Sarez earthquake (green focal mechanism) as predicted using the slip model of Metzger et al. (2017). Green stars mark the M4–5 earthquakes that occurred between the 2015 and 2016 surveys (see also Tables S1 and S2 in the supporting information).

Several instrumentally recorded earthquakes occurred between the two measurement periods in fall 2015 and 2016. To understand their effect on our time series, we investigated if these events could have caused a coseismic displacement of the order of a few centimeters on the mentioned stations. We consider both, the 7 December 2015, M_w 7.2 Sarez earthquake discussed above (Metzger et al., 2017; Sangha et al., 2017) and a series of crustal M4–5 earthquakes near the Darvaz fault (Figure 4 and Table S2) (GEOFON Data Centre, 1993). For the largest event of this series, the M5.1, 1 July 2016 earthquake, we checked, if satellite radar interferometry (Sentinel-1, acquired on 27 May and 14 July 2016) shows a signal comparable to the GNSS-derived offsets, but did not find one. We forward modeled a series of slip events with random source-parameter combinations following scaling laws (Mai & Beroza, 2000) to see if they cause a displacement pattern similar to the observed GNSS offsets. We used rectangular dislocations in an elastic half-space (Okada, 1985) and refer to section 4.3 for more modeling details. None of the synthetic models predict more than 1 cm offset, unless the source is located only a few hundred meters deep. But according to these models, a shallow source would not have affected stations at distance of 100 km, like station GF14 and T270. We therefore suggest that the offset signal was caused by the M_w 7.2 Sarez earthquake. This hypothesis is also supported by satellite radar interferometry (Metzger et al., 2018) and 1 Hz-GNSS data acquired across the Pamir thrust system in the Alai valley (Zubovich et al., 2016) (Figure 1b): The coseismic interferograms show a distinct surface rupture of a strand of the Pamir thrust system of a few millimeters to centimeters. The 1 Hz-GNSS stations recorded coseismic static displacement of a couple of centimeters, with a slip-sense opposite to the expected loading direction, in a similar distance to the earthquake epicenter as the stations presented here (Metzger et al., 2018). Using the distributed slip model of Metzger et al. (2017), we predict the expected displacement in the region of the Darvaz fault (Figure 4). The results match the amplitudes, but do not explain the rapid signal decay across the Darvaz fault or the eastward offset of station GF03. Instead the offset azimuth remains constant and the amplitudes decay quasi-linear with increasing distance to the Sarez

rupture. The GNSS observations on the sinistral-transpressive Darvaz fault and the dextral-transpressive Pamir thrust system show a pattern which is opposite to the interseismic loading sense, suggesting fault loading, probably triggered by the Sarez earthquake. We thus decided to exclude the data acquired in 2016 from the analysis of the interseismic deformation rates below.

4.2. Interseismic Rates 2013–2015

Based on the acquisitions between 2013 and 2015 we present horizontal and vertical interseismic GNSS rates relative to stable Eurasia (Altamimi et al., 2017) in map view (Figure 5). We also decompose the rates along profiles P1 and P2, into profile-perpendicular and profile -parallel components, where the former roughly represent shortening/extension and the latter shear across the Darvaz and or Vakhsh or Ilyak faults (Figure 6). In doing so, we projected all GNSS points and seismologic data in a 120 km wide profile swath onto the profiles.

The western Pamir-Plateau stations move at ~ 17 mm/yr toward northwest relative to Eurasia (Figure 5a). When crossing the Darvaz fault the rates of the profile P1 stations decrease slightly and the displacement vectors rotate from NW toward WNW (GF04, GF01, GF05, and GF06). Across the Vakhsh fault, the rates drop to 5 mm/yr N (T200, GF07, T170, and GF08). Along profile P2, the stations exhibit an increasingly more westerly orientated motion when crossing the Darvaz fault from east to west (GF16, GF17, GF18, and KULC). This westerly displacement vanishes across the Ilyak fault (T120 and OBGA). The slow rate at GF19 stands out from the adjacent stations GF18, KULK, and LAKA. This station—located within the salt withdrawal basin near Kulyab—might be influenced by the active salt tectonics. Overall, the strongest internal deformation is observed in the Tajik-basin fold-thrust belt and along its northern margin, whereas the western Pamir-Plateau and the southwestern Tian Shan exhibit minor internal deformation.

Vertical velocities obtained from stations with more than two measurement campaigns (Figure 5b) are less significant but suggest that the southwestern Tian Shan north of Dushanbe is subsiding 5–10 mm (e.g., station OBGA) while the southwestern Tian Shan farther east appears stable (T170 and T200). In the Peter the First Range, uplift is gradually increasing toward the Vakhsh fault (GF05, GF01, and GF06). In the western Pamir Plateau, the values are more heterogeneous and vary between ± 10 mm/yr. Stations in the Tajik Depression show mostly subsidence.

Along profile P1, the most significant feature of the profile-perpendicular and profile-parallel rate (Figures 6c and 6e) is the rate change across the Vakhsh fault, which amounts to ≥ 17 mm/yr in the profile-parallel direction (shortening) and ≥ 13 mm/yr in the profile-perpendicular direction (consistent dextral slip sense). The profile-perpendicular rate gradient is steeper than in profile-parallel direction and could be classified as an offset. In classic screw dislocation models the steepness of the rate change across a fault is inverse proportional to the locking depth (Segall, 2010); thus, a step function suggests that a fault is freely creeping. Consequently, shear and shortening might be partitioned in the upper part of the Vakhsh, with its most shallow section dominated by strike-slip and the deeper part by shortening. Along the Darvaz fault, the data suggest a locked fault that accommodates ~ 10 mm/yr of profile-parallel extension and ~ 15 mm/yr of sinistral (profile-perpendicular) shear (Figures 6c and 6e). The Badakhshan fault may accommodate 5–10 mm/yr dextral shear, but the uncertainties are large and the station spacing is large.

The geodetic data are in agreement with the focal mechanisms of Kufner et al. (2018) that suggest thrusting with a dextral component along the Vakhsh fault and predominantly sinistral shear along the Darvaz fault (Figures 2 and 6a). The abundant seismicity underneath Peter the First Range reaches in excess 20 km. Below 5–10 km it probably outlines steeply NW dipping faults in the crystalline basement rocks underneath the Tajik-basin deposits (Kufner et al., 2018). Along the southeastern margin of the Peter the First Range the seismicity delineates a near-vertical structure along the Darvaz fault; it then significantly decreases toward SE (Figure 6a). Local, vertically aligned seismicity occurs near the Badakhshan fault, but in map view, it is apparent that this seismicity is associated with a small cluster and not outlining a major fault zone (Figure 2).

In general, the rate changes along profile P2 are harder to interpret than along profile P1, as the station distances are larger. Both the Ilyak fault and the Darvaz fault seem to be less active than along profile P1 (Figures 6d and 6f). The Ilyak fault accommodates ~ 5 mm/yr of shortening and 8–15 mm/yr of dextral slip, which is in agreement with the dextral focal mechanisms (Figure 6b) associated with earthquakes occurring

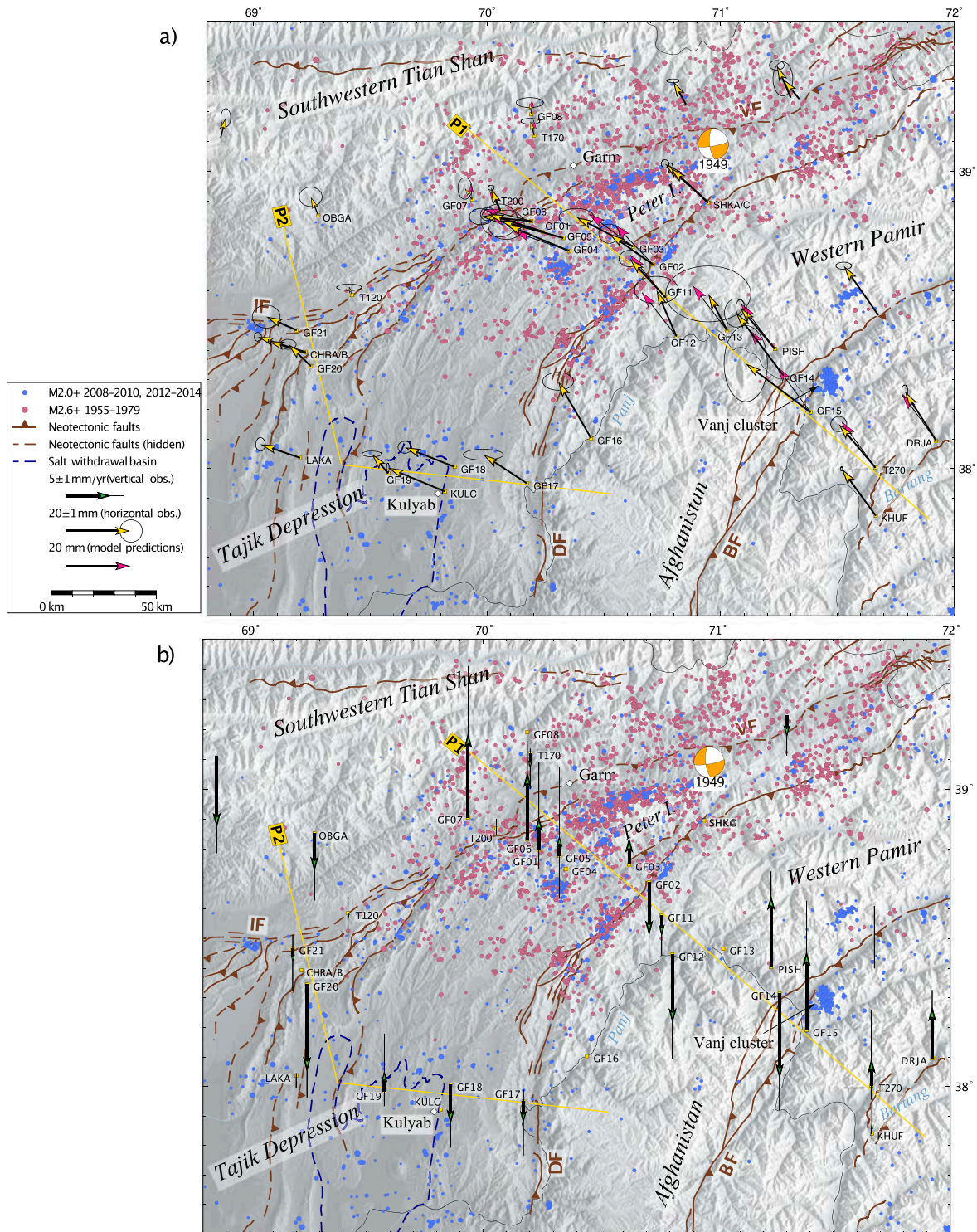


Figure 5. Horizontal and (b) vertical GNSS rates measured between 2013 and 2015 with 2σ uncertainties in a Eurasian reference frame (Altamimi et al., 2017). Pink arrows in (a) are the modeled rates (see section 4.3). Note the different rate scale in (a) and (b). Yellow lines mark Profiles P1 and P2, crustal seismicity of Hamburger et al. (1992) in red, and Kufner et al. (2018) in blue.

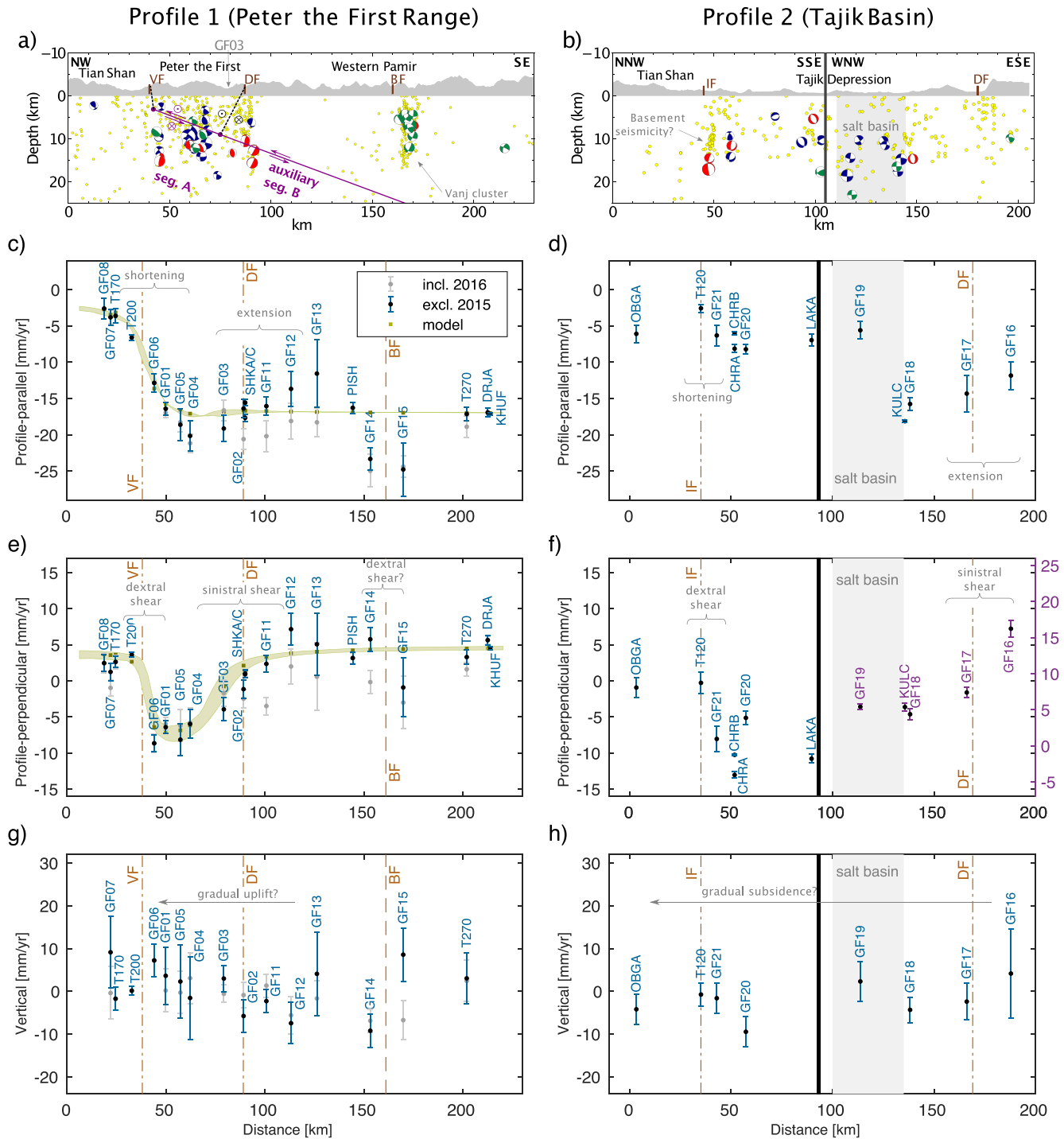


Figure 6. (a) and (b) Topography (enhanced by factor 10) and seismicity of a 120 km wide swath (Kufner et al., 2018) along Profiles P1 and P2, respectively. Violet lines mark model Segment A and auxiliary Segment B including slip sense, dashed lines symbolize the locking depths of the Vakhsh fault and the Darvaz fault (section 4.3). Note in (b) that the Vanj cluster is not along the Badakhshan fault (BF). IF = Ilyak fault; VF = Vakhsh fault. The GNSS velocities with 1σ uncertainties along Profile P1 (c, e, and g) and Profile 2 (d, f, and h) are resolved in profileparallel (c and d), pro fileperpendicular (e and f), and vertical components (g and h). The gray velocities include the 2016 campaign data; the blue rates exclude them. In (c) and (e) the slip model predictions are plotted for each GNSS data point (olive green squares) and—within 2σ uncertainties—for profile P1 (olive green band).

in the basement rocks below the Tajik-basin strata (Kufner et al., 2018). The rate change between station GF16 and GF17, at ~ 20 km profile-perpendicular distance across the Darvaz fault zone, suggests 8 ± 1 mm/yr sinistral shear and 2 ± 2 mm/yr extension along the Darvaz fault zone. Also along profile P2, the Darvaz fault is outlined by focused seismicity: The only constrained focal mechanism is in agreement with its sinistral kinematics (Figure 6b).

The vertical rates along profile P1 imply a gradual increasing uplift of a few millimeters of the stations NW of the Darvaz and a gradual subsidence of 5–7 mm/yr on the SE side of the fault (Figure 6g). The stations SE of the Badakhshan fault show uplift of 0–10 mm/yr. The stations along profile P2 indicate a gradual change from uplift of 0–5 mm/yr in the western Pamir Plateau to subsidence of 0–10 mm/yr in the Tajik Depression (Figure 6h).

4.3. Kinematic Modeling

To numerically assess the kinematic parameters of the Darvaz and the Vakhsh faults, we simulated fault slip using rectangular dislocations in an elastic half-space (Okada, 1985) with a rigidity of 30 GPa. The complex geologic structure of the Peter the First Range would be best represented with a three-dimensional model. However, since the GNSS data are aligned along profiles P1 and P2, with the highest station density along profile P1, a three-dimensional model would rely on strongly constrained geometric model parameters. Consequently, we simplified the geometry to two dimensions by focusing on the rates observed along profile P1, which is sub-perpendicular to the Darvaz and the Vakhsh faults. We neglected the curved fault geometry while assuming infinite fault length and down-dip extent. We tested fault geometries with up to five segments, also to come up with the potential slip partitioning in the upper part of the Vakhsh fault (section 4.2; Figures 6c and 6e), but the amount of data was too sparse to stabilize the results. The best data fit—using the smallest number of free model parameters—was obtained with a 10° SE dipping plane representing the Vakhsh thrust, following the basal décollement in the Jurassic evaporites. This geometry corresponds on first order to the geologic cross sections of Chapman et al. (2017) and Hamburger et al. (1992) and the seismicity (Kufner et al., 2018) (Figure 6a). Our modeling setup implies that the Darvaz fault is locked until it merges with the basal décollement. Free parameters are the fault strike and location, the locking depth, that is, the depth of the upper edge of the dipping plane (Figure 6a). We further solved for dip-slip, along-strike slip and fault strike on two subsegments—Segments A and B—with the down-dip extent of Segment A as another free parameter (Figure 6a). Including two parameters for a reference frame correction we solve for ten free parameters. The best fit model parameters were first constrained by a Monte Carlo type, simulated annealing approach (Cervelli et al., 2001) that over time gradually favors parameter combinations producing low misfits. This approach minimizes the chance to get trapped in a local minimum of the multidimensional parameter space. Then, we used the outcome of the annealing as a starting point for a classical nonlinear least squares inversion. The model parameter uncertainties were assessed in 500 additional runs using bootstrapping, in which the input of one GNSS station is randomly replaced by another (Efron, 1979).

The preferred model has a fault strike of $049^\circ + 6^\circ/-8^\circ$, which is similar to the average strike of the Darvaz and the Vakhsh faults along profile P1. Slip only occurs below $3.1 + 0.5/-0.8$ km, meaning that the upper part of the Vakhsh fault is locked (outlined by the dashed line in Figure 6a). Under the Peter the First Range, Segment A accommodates 16 ± 3 mm/yr of profile-parallel dextral shear and $15 + 4/-2$ mm/yr of profile-perpendicular shortening. Segment B begins near station GF03 (Figure 6a) and shear flips to a sinistral $1 + 2/-3$ mm/yr rate but with a constant $16 + 1/-1$ mm/yr shortening rate. Segment B represents the northwestward (block) motion of the western Pamir-Plateau crust; its geometry is quite arbitrary, except that the intersection between Segments A and B places the connection between the Darvaz fault and the basal décollement of the Vakhsh thrust at $9.0 + 0.4/-0.8$ km (dashed lines in Figure 6a). Thus, the difference in shear between Segments A and B is interpreted to be accommodated by the Darvaz fault; the along-strike slip difference is $15 + 4/-5$ mm/yr. Apart from a few stations near the Badakhshan fault, which we do not include in our model and which also exhibits large rate uncertainties, the fit between the observations and the model is good (Figure 5a). In the Peter the First Range, the shear and shortening rates are systematically underrepresented by a few millimeters (olive green squares in Figure 5a). The model slightly underestimates the profile-parallel rates of GF03-05

and is unable to reproduce the abrupt rate decrease, in particular the profile-perpendicular rates between T200 and GF06 across the Vakhsh fault. This shows that near the surface, the locking regime must be more complex than our preferred model can predict; this is in accordance with our inference (section 4.2) of slip partitioning and possible creep in the shallow section of the Vakhsh fault.

The parameter uncertainty analysis reveals strong correlation among several parameters, manifested by elongated and curved scatter plots of best fit parameters obtained from bootstrapping (Figure S2): A deeper locking depth of the Vakhsh fault calls for a shorter width of Segment A, higher dextral shear rates on Segment A and (in opposite sense) Segment B, and a more easterly fault strike. Even within the 2σ uncertainties (95% confidence), the model fails to fit the profile-parallel rate of GF04 and the profile-perpendicular rate of GF06 (olive green band in Figures 6c and 6e).

5. Discussion

Given the low temporal resolution of survey mode GNSS data, we cannot uniquely link the offsets observed on GNSS stations between the 2015 and the 2016 campaigns to the 2015 M_w 7.2 Sarez earthquake or other nearby earthquakes (see section 4.1). If we include the 2016 data for the estimation of the GNSS rates, the observed fault slip rates on the Darvaz drop to a few mm of shortening and ≤ 9 mm/yr of sinistral slip (gray data in Figure 6a), which is less than what the neotectonic slip rates suggest. If true, the estimated slip rates presented in section 4.2 would reflect an upper bound only and/or the Darvaz fault would be less active than presumed. We also tried to correct the 2016 positions using the surface displacement predicted by the coseismic slip model of the 2015 Sarez earthquake of that exhibits sinistral slip of up to 3 m on a subvertical, NE striking, 80 km long fault (Figure S3) (Metzger et al., 2017). This increases the slip rates only slightly and the quasi-linear decay of the predicted displacements from ENE to WSW (Figure 4) does not explain the observed offsets satisfyingly. Therefore, we suggest that the Darvaz fault was activated during the 2015 Sarez earthquake and produced dextral coseismic slip of a few centimeters, opposite to its interseismic slip.

Triggered slip phenomena are not yet well studied, as the focus of the scientific community lies on the activity of the main event. But due to an increased spatial resolution, e. g. using Synthetic Aperture Radar interferometry (Price & Sandwell, 1998; Wei et al., 2011; Wright et al., 2001) or high instrumental sensitivity, for example, using creep meters (Bodin et al., 1994; Victor et al., 2018), we begin to observe coseismic response on adjacent or even remote faults. A recent observation of such activity is the 2019 Ridgecrest seismic sequence that ruptured an unmapped fault of the Eastern California Shear Zone dextrally, and simultaneously triggered sinistral activity along the Garlock fault that strikes subperpendicular to the unmapped fault (Barnhart et al., 2019). If the triggered fault (in our case the Darvaz fault) is farther than a few fault lengths away from the main fault (in our case the Sarez-Karakul fault zone), Coulomb failure stress changes become insignificant (Tingay et al., 2008). Then, transient dynamic unclamping or triggering can be evoked by the surface waves passing through, as it has been observed on faults separated by up to 5 km (Freed, 2005). This is often the case along disconnected structures at immature fault systems (e.g., Gombert, 1996). Another reason may be sudden pore pressure changes (Brodsky, 2003; Brodsky & Prejean, 2005). Significantly, the Darvaz fault (this study) and the Pamir thrust system (Metzger et al., 2018) slipped opposite to their loading sense, which would indicate that the coseismic mass movements outweigh the local stress field, even 150–200 km away from the epicenter of the Sarez earthquake in the southern Sarez-Karakul fault segment. In other words, the surface displacement predicted by the homogeneous half-space model of Metzger et al. (2017) (pink arrows in Figure 4) dominate the sense of displacement until they hit a structural discontinuity—the Darvaz fault or the evaporitic décollement underneath Peter the First Range—and then quickly drop below significance.

As we were not able to correct the 2016 campaign data for the (potential) coseismic displacement due to the Sarez earthquake, we omitted them for the interseismic slip rate estimates. The observed ~ 15 mm/yr sinistral slip across the Darvaz fault zone, measured on profile P1, is consistent with the 4–16 mm/yr of offset in the Holocene and Pleistocene (e.g., Burtman & Molnar, 1993). Farther south—along profile P2—we observed 8 ± 1 mm/yr sinistral shear, which is less than the 10–15 mm/yr offset measured by Trifonov, (1978, 1983). The GNSS data further suggest extension of ~ 10 mm/yr across the northern part of the Darvaz fault (profile P1),

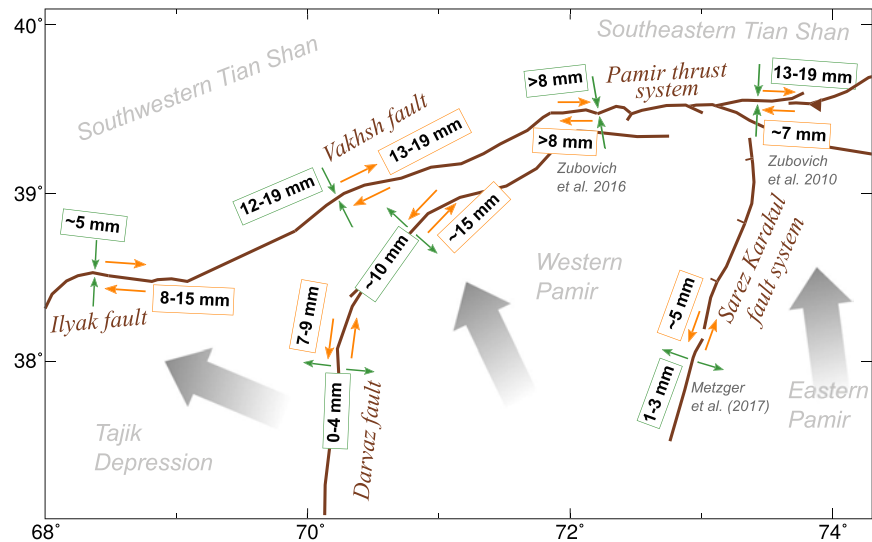


Figure 7. Same as Figure 1b, indicating the kinematics in the western Pamir and Tajik Depression. The gray arrows indicate the main direction of motion with respect to stable Eurasia observed by GNSS, the orange arrows indicate shear, the green arrows shortening or extension. The values are deduced from models and/or GNSS observations of Zubovich et al. (2010, 2016), Metzger et al. (2017), and this study. Rates of Zubovich et al. (2016) represent a lower limit, given the limited profile length toward south.

which has not been observed in neotectonic studies. Along the southern part of the Darvaz fault, geologic mapping indicated sinistral transtension (Kuchai & Trifonov, 1977; Trifonov, 1978, 1983), which corresponds to our GNSS results. No neotectonic slip rates are available for the Vakhsh fault. However, the geologic and geodetic findings agree on the slip sense.

While the sparse and widely distributed published GNSS rates (Ischuk et al., 2013; Mohadjer et al., 2010; Zhou et al., 2016) are in general agreement with our findings, the leveling results of Guseva (1986) and Konolpatsev (1971) acquired across the Vakhsh fault near Garm are systematically lower with 8–16 mm/yr shortening and ~6 mm/yr dextral shear, compared to our 12–19 mm/yr shortening and 13–19 mm/yr dextral shear. This might be explained by the shorter measurement profile and/or the possibility that their data were affected by postseismic deformation following the 1949, M_w 7.6 Khait earthquake.

The seismicity along our GNSS Profile 1 (Figure 6a) shows significant, vertically aligned activity underneath Peter the First Range and along the Darvaz fault. This activity extends into the basement rocks underneath the evaporitic décollement, which is mimicked in our kinematic model by the Segments A and B. The updip end of Segment B ends just between these two highly active zones, probably because we have not included an additional (subvertical) segment to account for slip underneath Peter the First Range. Our model also likely underestimates the magnitude of the rate changes for the profile-parallel and profile-perpendicular GNSS components across the Vakhsh fault. This might be due to slip partitioning in the upper segment of the fault zone or even due to a three-dimensional rotation of the Peter the First Range that also includes vertical motions.

We combine our findings with other geodesy-based results (Zubovich et al., 2010, 2016; Metzger et al., 2017) to create a conceptual model for the northeastern Tajik Basin and the western and northern Pamir, highlighting the kinematics of the key structures, that is, the Vakhsh and Darvaz faults, the Pamir thrust system and the Sarez-Karakul fault system (Figure 7). The Pamir is shortening approximately N-S and is flowing westward at the same time, that is, experiencing lateral extrusion from the Pamir Plateau toward the Tajik Depression. In the Pamir interior this combined N-S shortening and E-W extension is mostly accommodated by the NE striking Sarez-Karakul fault system (Figure 1b), which interseismically exhibits ~5 mm/yr sinistral shear and 1–3 mm/yr of extension (see Figure S11 in Metzger et al., 2017); however, the entire western Pamir Plateau shows this deformation pattern. The due west motion of the Tajik

Depression upper crust commences west of the Darvaz fault zone, which shows sinistral shear of ~ 15 mm/yr and ~ 10 mm/yr E-W extension. Along the northwestern rim of Peter the First Range, the SE dipping Vakhsh fault separates the Tajik Depression from the southwestern Tian Shan; the latter marks the nearly rigid backstop for the material flow out of the Pamir Plateau. The Vakhsh fault absorbs dextral shear of 16 ± 3 mm/yr and $15 + 4/-2$ mm/yr of NW-SE shortening. Along the Ilyak fault farther west, N-S shortening drops to ~ 5 mm/yr but dextral shear remains high (8–15 mm/yr). On the Pamir thrust system farther east, dextral shortening (and thus Pamir-Plateau mass outflow) decreases to ~ 7 mm/yr, while the Pamir's northward advance keeps constant at a rate of 13–19 mm/yr (Zubovich et al., 2016, 2010). The Peter the First Range, an upper-crustal wedge of strongly shortened Tajik-basin strata squeezed between the Vakhsh and the Darvaz faults, extrudes as a southwestward widening crustal sliver. Although the lateral extrusion of the upper-crustal wedge is facilitated by the low-frictional properties of the evaporitic basal décollement, subdécollement seismicity indicates a thick-skinned sliver extrusion, demonstrated to be active within the adjacent Tian Shan from the late Miocene to Recent (Käbner et al., 2016).

6. Conclusion

New GNSS campaign data collected over 4 years (2013–2016) in the western Pamir and the adjacent Tajik Depression along two profiles crossing the Vakhsh and the Darvaz faults zone show steady interseismic motions from 2013–2015 and static offsets of up to 2 cm between the 2015 and the 2016 measurements, consistent with dextral fault slip on the Darvaz fault, opposite to its interseismic and long-term slip history. We propose that the 2015, $M_w 7.2$ Sarez earthquake triggered the dextral movements along the Darvaz fault.

Velocities obtained from data prior to the 2016 observations show that the W(SW) striking Ilyak and Vakhsh faults and the Pamir thrust system constitute the highly active boundary zone between in the Pamir, the Tajik Depression, and the nearly stable foreland, the southwestern Tian Shan. From W to E, these structures accommodate shortening of ~ 5 mm/yr (Ilyak fault), $15 + 4/-2$ mm/yr (Vakhsh fault), and 13–19 mm/yr (Pamir thrust system). Dextral shear rates are high at the northern edge of the Tajik Depression (8–15 mm/yr along the Ilyak fault; 16 ± 3 mm/yr along the Vakhsh fault) but decrease eastward to ~ 7 mm/yr along the Pamir thrust system. For the Darvaz fault we obtained 10–15 mm/yr sinistral slip and ~ 10 mm/yr of approximately E-W extension. We further surmise that the Pamir Plateau and the hanging wall of the Vakhsh thrust in the Peter the First Range are still growing vertically by a few millimeters per year, while the Tajik Depression is subsiding.

Our geodetic data indicate, in accordance with the geologic and seismic record that the eastern Tajik Depression, including the Peter the First Range, is collapsing (lateral extruding) toward the west. The southwestern Tian Shan acts as a backstop and deforms little. The gravity-driven mass-outflow from the Pamir Plateau to its west induces shortening of the Tajik-basin deposits, forming the Tajik-basin fold-thrust belt, facilitated by the near-horizontal, evaporitic basal décollement of the fold-thrust belt. The Ilyak fault marks a major tear fault, disconnecting the shortening in the Tajik basin fold-thrust belt from the weakly deforming Tian Shan backstop. Thus, combining the geodetic results with the geologic and thermochronologic constraints from the Pamir Plateau, Tajik Basin, and Tian Shan foreland, it appears that northward displacement and westward lateral extrusion of the Pamir Plateau into the Tajik Depression have been active since the late Miocene.

Acknowledgments

We thank Zukhra Ilyasova, Akram Akhmedov, and Shorukh Murodkulov for helping us collecting the GNSS data. The GNSS RNX files are published via GFZ Data Services (Metzger et al., 2019). Some figures were produced using the Generic Mapping Tools (GMT) public domain software (Wessel et al., 2013). We thank Richard Walker an anonymous reviewer for their valuable comments.

References

- Altamimi, Z., Métivier, L., & Collilieux, X. (2012). ITRF2008 plate motion model. *Journal of Geophysical Research*, *117*, 1–14. <https://doi.org/10.1029/2011JB008930>
- Altamimi, Z., Métivier, L., Reischung, P., Rouby, H., & Collilieux, X. (2017). ITRF2014 plate motion model. *Geophysical Journal International*, *209*(3), 1906–1912. <https://doi.org/10.1093/gji/ggx136>
- Altamimi, Z., Reischung, P., Métivier, L., & Collilieux, X. (2016). ITRF2014: A new release of the International Terrestrial Reference Frame modeling nonlinear station motions. *Journal of Geophysical Research: Solid Earth*, *121*, 6109–6131. <https://doi.org/10.1002/2016JB013098>
- Babaev, A. M. (1975). *Recent tectonics of the zone of orogenesis of the Gissar-Alai and Tajik Depression* (p. 149). Dushanbe: Donish (in Russian).
- Barnhart, W. D., Hayes, G. P., & Gold, R. D. (2019). The July 2019 Ridgecrest, California earthquake sequence: Kinematics of slip and stressing in cross fault ruptures. *Geophysical Research Letters*, *46*, 11,859–11,867. <https://doi.org/10.1029/2019gl084741>
- Bodin, P., Bilham, R., Behr, J., Gombert, J., & Hudnut, K. W. (1994). Slip triggered on southern California faults by the 1992 Joshua Tree, Landers, and Big Bear earthquakes. *Bulletin of the Seismological Society of America*, *84*(3), 806–816. [https://doi.org/10.1016/0148-9062\(95\)94487-7](https://doi.org/10.1016/0148-9062(95)94487-7)

- Bourgeois, O., Cobbold, P. R., Rouby, D., Thomas, J.-C. J., & Shein, V. (1997). Least squares restoration of Tertiary thrust sheets in map view, Tajik depression, central Asia. *Journal of Geophysical Research*, *102*(B12), 27,553–27,573. <https://doi.org/10.1029/97JB02477>
- Brodsky, E. E. (2003). A mechanism for sustained groundwater pressure changes induced by distant earthquakes. *Journal of Geophysical Research*, *108*(B8), 1–10. <https://doi.org/10.1029/2002jb002321>
- Brodsky, E. E., & Prejean, S. G. (2005). New constraints on mechanisms of remotely triggered seismicity at Long Valley Caldera. *Journal of Geophysical Research*, *110*, 1–14. <https://doi.org/10.1029/2004JB003211>
- Burtman, V. S., & Molnar, P. (1993). Geological and geophysical evidence for deep subduction of continental crust beneath the Pamir. *Geological Society of America, Special Paper*, *281*, 1–76.
- Cervelli, P., Murray, H. M., Segall, P., Aoki, Y., & Kato, T. (2001). Estimating source parameters from deformation data, with an application to the March 1997 earthquake swarm off the Izu Peninsula. *Journal of Geophysical Research*, *106*(B6), 11,217–11,237. <https://doi.org/10.1029/2000JB900399>
- Chapman, J. B., Carrapa, B., Ballato, P., DeCelles, P. G., Worthington, J., Oimahmadov, I., et al. (2017). Intracontinental subduction beneath the Pamir Mountains: Constraints from thermokinematic modeling of shortening in the Tajik fold-and-thrust belt. *GSA Bulletin*, *129*(11–12), 1450–1471. <https://doi.org/10.1130/B31730.1>
- Chen, J., Schoenbohm, L. M., Yuan, Z., Li, W., Li, T., Owen, L. A., et al. (2011). Holocene slip rate along the northern Kongur extensional system, Chinese Pamir. *AGU Fall Meeting*, T43F–T2447F.
- Chevalier, M. L., Pan, J., Li, H., Liu, D., & Wang, M. (2015). Quantification of both normal and right-lateral late Quaternary activity along the Kongur Shan extensional system, Chinese Pamir. *Terra Nova*, *27*(5), 379–391. <https://doi.org/10.1111/ter.12170>
- DeMets, C., Gordon, R. G., Argus, D. F., & Stein, S. (2010). Geologically current plate motions. *Geophysical Journal International*, *181*(1), 1–80. <https://doi.org/10.1111/j.1365-246X.2009.04491.x>
- Deng, Z., Gendt, G., & Schöne, T. (2016). Status of the IGS-TIGA tide gauge data reprocessing at GFZ. *International Association of Geodesy Symposia*, (January 1994, 33–40. https://doi.org/10.1007/1345_2015_156
- Dong, D., Fang, P., Bock, Y., Cheng, M. K., & Miyazaki, S. (2002). Anatomy of apparent seasonal variations from GPS-derived site position time series. *Journal of Geophysical Research*, *107*(B4), ETG 9-1–ETG 9-16. <https://doi.org/10.1029/2001JB000573>
- Dooley, T. P., Jackson, M. P. A., & Hudec, M. R. (2015). Breakout of squeezed stocks: Dispersal of roof fragments, source of extrusive salt and interaction with regional thrust faults. *Basin Research*, *27*(1), 3–25. <https://doi.org/10.1111/bre.12056>
- Dziewonski, A. M., Chou, T.-A., & Woodhouse, J. H. (1981). Determination of earthquake source parameters from waveform data for studies of global and regional seismicity. *Journal of Geophysical Research*, *86*, 2825–2852. <https://doi.org/10.1029/JB086iB04p02825>
- Efron, B. (1979). Bootstrap methods: Another look at the Jackknife. *The Annals of Statistics*, *7*(1), 1–26. <https://doi.org/10.1214/aos/1176344552>
- Ekström, G., Nettles, M., & Dziewonski, A. M. (2012). The global CMT project 2004–2010: Centroid-moment tensors for 13,017 earthquakes. *Physics of the Earth and Planetary Interiors*, *200–201*, 1–9. <https://doi.org/10.1016/j.pepi.2012.04.002>
- Engdahl, E. R., van der Hilst, R., & Buland, R. (1998). Global teleseismic earthquake relocation with improved travel times and procedures for depth determination. *Bulletin of the Seismological Society of America*, *88*, 722–743.
- Evans, S. G., Roberts, N. J., Ischuk, A., Delaney, K. B., Morozova, G. S., & Tutubalina, O. (2009). Landslides triggered by the 1949 Khait earthquake, Tajikistan, and associated loss of life. *Engineering Geology*, *109*, 195–212. <https://doi.org/10.1016/j.enggeo.2009.08.007>
- Fan, G., Ni, J. F., & Wallace, T. C. (1994). Active tectonics of the Pamirs and Karakorum. *Journal of Geophysical Research*, *99*(B4), 7131–7160.
- Freed, A. M. (2005). Earthquake triggering by static, dynamic, and postseismic stress transfer. *Annual Reviews of Earth and Planetary Science*, *33*, 335–367. <https://doi.org/10.1146/annurev.earth.33.092203.122505>
- Geirsson, H., Árnadóttir, T., Völkens, C., Jiang, W., Sturkell, E., Villemin, T., et al. (2006). Current plate movements across the Mid-Atlantic ridge determined from 5 years of continuous GPS measurements in Iceland. *Journal of Geophysical Research*, *111*, B09407. <https://doi.org/10.1029/2005JB003717>
- Gendt, G., Deng, Z., Ge, M., Nischan, T., Uhlemann, M., Beeskov, G., et al. (2013). GFZ analysis center of IGS - Annual report for 2013. Retrieved from ftp://ftp.gfz-potsdam.de/GNSS/DOCS/IGS_repro2/GFZ_igs_annual_report_2013_iss1-0.pdf (last accessed date: Jan 29, 2020).
- GEOFON Data Centre. (1993). GEOFON Seismic Network. Deutsches GeoForschungsZentrum GFZ. <https://doi.org/10.14470/TR560404>
- Gomberg, J. (1996). Stress/strain changes and triggered seismicity following the M_w 7.3 Landers, California earthquake. *Journal of Geophysical Research*, *101*, 751–764. <https://doi.org/10.1029/95JB03251>
- Guseva, T. G. (1986). Contemporary movements of the Earth's crust in the transition zone from the Pamir to the Tian Shan (in Russian). Moscow Institute of Physics of the Earth. Academi Nauk, 171.
- Hamburger, M. W., Sarewitz, D. R., Pavlis, T. L., & Popandopulo, G. A. (1992). Structural and seismic evidence for intracontinental subduction in the Peter the First Range, Central Asia. *Geological Society of America Bulletin*, *104*, 397–408.
- Herring, T. A., Floyd, M. A., King, R. W., & McClusky, S. C. (2015). GLOBK reference manual, Release 10.6, Technical Report, Department of Earth, Atmospheric, and Planetary Sciences, Massachusetts Institute of Technology.
- Herring, T. A., King, R. W., Floyd, M. A., & McClusky, S. C. (2018a). Introduction to GAMIT/GLOBK, Release 10.7, Technical Report, Department of Earth, Atmospheric, and Planetary Sciences, Massachusetts Institute of Technology.
- Herring, T. A., King, R. W., Floyd, M. A., & McClusky, S. C. (2018b). GAMIT reference manual, release 10.7, Technical Report, Department of Earth, Atmospheric, and Planetary Sciences, Massachusetts Institute of Technology.
- Ischuk, A., Bendick, R., Rybin, A., Molnar, P., Khan, S. F., Kuzikov, S., et al. (2013). Kinematics of the Pamir and Hindu Kush regions from GPS geodesy. *Journal of Geophysical Research: Solid Earth*, *118*, 2408–2416. <https://doi.org/10.1002/jgrb.50185>
- Kälfner, A., Ratschbacher, L., Jonckheere, R., Enkelmann, E., Khan, J., Sonntag, B.-L., et al. (2016). Cenozoic intracontinental deformation and exhumation at the northwestern tip of the India-Asia collision—southwestern Tian Shan, Tajikistan, and Kyrgyzstan. *Tectonics*, *35*, 2171–2194. <https://doi.org/10.1002/2015TC003897>
- Kondorskaya, N., & Shebalin, N. (chief editors). (1982). New catalog of strong earthquakes in the U.S.S.R. from ancient times through 1977. Report SE31, World Data Center A for Solid Earth Geophysics, 609. <https://doi.org/ftp://ftp.ngdc.noaa.gov/hazards/publications/Wdce-31.pdf>
- Konolpatsev, I. M. (1971). Measurements of crustal movements in the Garm area, 1948–1970 (in Russian). *Geotektonika*, *5*, 111–116.
- Kuchai, V., & Trifonov, V. (1977). Young left-lateral strike-slip along the zone of the Darvaz Fault (in Russian). *Geotektonika*, *3*, 91–105.
- Kufner, S.-K., Schurr, B., Ratschbacher, L., Murodkulov, S., Abdulhameed, S., Ischuk, A., et al. (2018). Seismotectonics of the Tajik Basin and surrounding Mountain Ranges. *Tectonics*, *37*, 2404–2424. <https://doi.org/10.1029/2017tc004812>

- Kufner, S.-K., Schurr, B., Sippl, C., Yuan, X., Ratschbacher, L., Ischuk, A., et al. (2016). Deep India meets deep Asia: Lithospheric indentation, delamination and break-off under Pamir and Hindu Kush (Central Asia). *Earth and Planetary Science Letters*, 435, 171–184. <https://doi.org/10.1016/j.epsl.2015.11.046>
- Kulikova, G. (2016). Source parameters of the major historical earthquakes in the Tien-Shan region from the late 19th to the early 20th century. PhD Thesis. Potsdam University.
- Kulikova, G., Schurr, B., Krüger, F., Brzoska, E., & Heimann, S. (2015). Source parameters of the Sarez-Pamir earthquake of 1911 February 18. *Geophysical Journal International*, 205(2), 1086–1098. <https://doi.org/10.1093/gji/ggw069>
- Legler, B. A., & Przhivalgovskaya, I. A. (1979). *The interaction of the Indian and Asian lithospheric plates and the tectonics of the Tadjik Depression (in Russian) In: Structure of lithospheric plates* (pp. 125–188). Akademi Nauk, USSR, Moscow: Institute of Oceanology.
- Leith, W., & Alvarez, W. (1985). Structure of the Vakhsh fold-and-thrust belt, Tadjik SSR: Geologic mapping on a Landsat image base. *Bulletin of the Geological Society of America*, 96(7), 875–885. [https://doi.org/10.1130/0016-7606\(1985\)96<875:SOTVFB>2.0.CO;2](https://doi.org/10.1130/0016-7606(1985)96<875:SOTVFB>2.0.CO;2)
- Leith, W., & Simpson, D. W. (1986). Earthquakes related to active salt doming near Kulyab, Tadjikistan, USSR. *Geophysical Research Letters*, 13(10), 1019–1022. <https://doi.org/10.1029/GL013i010p01019>
- Liu, Q. (1993). Paleoclimat et contraintes chronologiques sur les mouvements recent dans l'Ouest du Tibet: Failles du Karakorum et de Longmu Co–Gozha Co. lacs en pull-apart de Longmu Co et de Sumxi Co. PhD Thesis. Universite Paris VII.
- Lyard, F., Lefevre, F., Letellier, T., & Francis, O. (2006). Modelling the global ocean tides: Modern insights from FES2004. *Ocean Dynamics*, 56(5–6), 394–415. <https://doi.org/10.1007/s10236-006-0086-x>
- Mai, M. P., & Beroza, G. C. (2000). Source scaling properties from finite-fault-rupture models. *Bulletin of the Seismological Society of America*, 90(3), 604–615. <https://doi.org/10.1785/0119990126>
- Metzger, S., Ischuk, A., Akhmedov, A., Ilyasova, Z., Moreno, M., Murodkulov, S., & Deng, Z. (2019). Survey mode GPS data in the West Pamir, Tajikistan, Central Asia, 2013–2016. *GFZ Data Services*. <https://doi.org/10.5880/GFZ.4.1.2019.007>
- Metzger, S., Ischuk, A., Zubovich, A., Deng, Z., Schöne, T., Schurr, B., et al. (2018). Observations from four high-resolution GPS profiles across the active margin of the Pamir, Central Asia: Can we discriminate interseismic fault-slip rates, slip partitioning, and even coseismically triggered slip? *Geophysical Research Abstracts*, 20, EGU2018-16410–1.
- Metzger, S., Schurr, B., Ratschbacher, L., Sudhaus, H., Kufner, S.-K., Schöne, T., et al. (2017). The 2015 M_w 7.2 Sarez strike-slip earthquake in the Pamir interior: Response to the underthrusting of India's western promontory. *Tectonics*, 36, 2407–2421. <https://doi.org/10.1002/2017TC004581R>
- Mohadjer, S., Bendick, S. R., Ischuk, A., Kuzikov, S., Kostuk, A., Saydullaev, U., et al. (2010). Partitioning of India/Eurasia convergence in the Pamir-Hindu Kush from GPS measurements. *Geophysical Research Letters*, 37. <https://doi.org/10.1029/2009GL041737>
- Nikolaev, V. G. (2002). Afghan-Tajik depression: Architecture of sedimentary cover and evolution. *Russian Journal of Earth Sciences*, 4(6), 399–421.
- Nikonov, A. A. (1970). Differential analysis of the Quaternary tectonics of the Afghan-Tajik Depression (in Russian). *Geotektonika*, 1, 101–107.
- Nikonov, A. A. (1975). An analysis of tectonic movements along the Hindu Kush-Darvaz-Karakul fault zone in late Pliocene and Quaternary time (in Russian). *Bulletin MOIP (of the Moscow Society for the Investigation of Nature). Geology Section*, 50, 5–23.
- Nikonov, A. A. (1977). *Holocene and contemporary movements of the earth's crust (in Russian)* (p. 240). Moscow: Nauka.
- Okada, Y. (1985). Surface deformation due to shear and tensile faults in a half-space. *Bulletin of the Seismological Society of America*, 75(4), 1135–1154. [https://doi.org/10.1016/0148-9062\(86\)90674-1](https://doi.org/10.1016/0148-9062(86)90674-1)
- Price, E. J., & Sandwell, D. T. (1998). Small-scale deformations associated with the 1992 Landers, California, earthquake mapped by synthetic aperture radar interferometry phase gradients. *Journal of Geophysical Research*, 103(B11), 27,001–27,016. <https://doi.org/10.1029/98jb01821>
- Ratschbacher, L., Merle, O., Davy, P., & Cobbold, P. (1991). Lateral extrusion in the Eastern Alps, Part 1: Boundary conditions and experiments scaled for gravity. *Tectonics*, 10(2), 245–256.
- Rebeschung, P., Altamimi, Z., Ray, J., & Garayt, B. (2016). The IGS contribution to ITRF2014. *Journal of Geodesy*, 90(7), 611–630. <https://doi.org/10.1007/s00190-016-0897-6>
- Robert, A. M. M., Fernández, M., Jiménez-Munt, I., & Vergés, J. (2017). Lithospheric structure in Central Eurasia derived from elevation, geoid anomaly and thermal analysis. *Geological Society, London, Special Publications*, 427(1), 271–293. <https://doi.org/10.1144/SP427.10>
- Rutte, D., Ratschbacher, L., Schneider, S., Stübner, K., Stearns, M. A., Gulzar, M. A., & Hacker, B. R. (2017). Building the Pamir-Tibetan Plateau—Crustal stacking, extensional collapse, and lateral extrusion in the Central Pamir: 1. Geometry and kinematics. *Tectonics*, 36, 342–384. <https://doi.org/10.1002/2016TC004293>
- Ruzhentsev, S. V. (1963). Strike-slip faults of the southeastern Pamir (in Russian) In: *Faults and horizontal movements of the Earth's crust. Moscow, Nauka, Trudy Geological Institute, Akademi Nauk, USSR*, 80, 113–127.
- Ruzhentsev, S. V. (1968). *Tectonic development of the southeastern Pamir and the role of horizontal movements in the formation of its Alpine structure (in Russian)* (p. 202). Moscow: Nauka.
- Sangha, S., Peltzer, G., Zhang, A., Meng, L., Lian, C., Lundgren, P., & Fielding, E. (2017). Fault geometry of 2015, M_w 7.2 Murghab, Tajikistan earthquake controls rupture propagation: Insights from InSAR and seismological data. *Earth and Planetary Science Letters*, 462, 132–141. <https://doi.org/https://doi.org/10.1016/j.epsl.2017.01.018>
- Schmid, R., Dach, R., Collilieux, X., Jäggi, A., Schmitz, M., & Dilssner, F. (2016). Absolute IGS antenna phase center model igs08.atx: Status and potential improvements. *Journal of Geodesy*, 90(4), 343–364. <https://doi.org/10.1007/s00190-015-0876-3>
- Schneider, F. M., Yuan, X., Schurr, B., Mechie, J., Sippl, C., Haberland, C., et al. (2013). Seismic imaging of subducting continental lower crust beneath the Pamir. *Earth and Planetary Science Letters*, 375, 101–112. <https://doi.org/10.1016/j.epsl.2013.05.015>
- Schurr, B., Ratschbacher, L., Sippl, C., Gloaguen, R., Yuan, X., & Mechie, J. (2014). Seismotectonics of the Pamir. *Tectonics*, 33, 1501–1518. <https://doi.org/10.1002/2014TC003576>
- Segall, P. (2010). *Earthquake and volcano deformation*. Princeton: Princeton University Press. <https://doi.org/10.1515/9781400833856>
- Sippl, C., Ratschbacher, L., Schurr, B., Krumbiegel, C., Rui, H., Pingren, L., & Abdybachev, U. (2014). The 2008 Nura earthquake sequence at the Pamir-Tian Shan collision zone, southern Kyrgyzstan. *Tectonics*, 33, 2382–2399. <https://doi.org/10.1002/2014TC003705>
- Sippl, C., Schurr, B., Tjypel, J., Angiboust, S., Mechie, J., Yuan, X., et al. (2013). Deep burial of Asian continental crust beneath the Pamir imaged with local earthquake tomography. *Earth and Planetary Science Letters*, 384, 165–177. <https://doi.org/10.1016/j.epsl.2013.10.013>
- Sippl, C., Schurr, B., Yuan, X., Mechie, J., Schneider, F. M., Gadoev, M., et al. (2013). Geometry of the Pamir-Hindu Kush intermediate-depth earthquake zone from local seismic data. *Journal of Geophysical Research: Solid Earth*, 118, 1438–1457. <https://doi.org/10.1002/jgrb.50128>

- Skobelev, S. F., & Florenskiy, P. V. (1974). Holocene tectonic deformation and rock slides in the Vakhsh overthrust zone. *Geotectonics*, 5, 316–317.
- Sridevi, J., Bhatt, B. C., Yang, Z., Bendick, R., Gaur, V. K., Molnar, P., et al. (2004). GPS measurements from the Ladakh Himalaya, India: Preliminary tests of plate-like or continuous deformation in Tibet. *GSA Bulletin*, 116(11–12), 1385–1391. <https://doi.org/10.1130/B25357.1>
- Storchak, D. A., Di Giacomo, D., Bondár, I., Engdahl, E. R., Harris, J., Lee, W. H. K., et al. (2013). Public release of the ISC-GEM global instrumental earthquake catalogue (1900–2009). *Seismological Research Letters*, 84(5), 810–815. <https://doi.org/10.1785/0220130034>
- Strecker, M. R., Frisch, W., Hamburger, M. W., Ratschbacher, L., Semiletkin, S., Zamoruyev, A., & Sturchio, N. (1995). Quaternary deformation in the eastern Pamirs, Tadjikistan and Kyrgyzstan. *Tectonics*, 14(5), 1061–1079. <https://doi.org/10.1029/95TC00927>
- Stübner, K., Ratschbacher, L., Rutte, D., Stanek, K., Minaev, V., Wiesinger, R., Gloaguen, R., & Project TIPAGE members (2013). The giant Shakh dara migmatitic gneiss dome, Pamir, India-Asia collision zone, 1: Geometry and kinematics. *Tectonics*, 32, 948–979. <https://doi.org/10.1002/tect.20057>
- Tingay, M., Heidbach, O., Davies, R., & Swarbrick, R. (2008). Triggering of the Lusi mud eruption: Earthquake versus drilling initiation. *Geology*, 36(8), 639–642. <https://doi.org/10.1130/G24697A.1>
- Trifonov, V. (1978). Late Quaternary tectonic movements of western and central Asia. *Bulletin of the Geological Society of America*, 89(7), 1059–1072.
- Trifonov, V. (1983). Late Quaternary tectogenesis (in Russian): Moscow. *Nauka*, 224.
- USGS. (2015). M 7.2–104 km W of Murghob, Tajikistan.
- Victor, P., Oncken, O., Sobiesiak, M., Kemter, M., Gonzalez, G., & Ziegenhagen, T. (2018). Dynamic triggering of shallow slip on forearc faults constrained by monitoring surface displacement with the IPOC Creepmeter Array. *Earth and Planetary Science Letters*, 502, 57–73. <https://doi.org/10.1016/j.epsl.2018.08.046>
- Wei, M., Sandwell, D., Fialko, Y., & Bilham, R. (2011). Slip on faults in the Imperial Valley triggered by the 4 April 2010 M_w 7.2 El Mayor-Cucapah earthquake revealed by InSAR. *Geophysical Research Letters*, 38, 1–6. <https://doi.org/10.1029/2010GL045235>
- Wessel, P., Smith, W. H. F., Scharroo, R., Luis, J. F., & Wobbe, F. (2013). Generic mapping tools: Improved version released. *Eos, Transactions American Geophysical Union*, 94, 409–410. <https://doi.org/10.1002/2013EO450001>
- Worthington, J. R., Ratschbacher, L., Stübner, K., Khan, J., Malz, N., Schneider, S., et al. (2019). The Alchur dome, South Pamir, western India–Asia collisional zone: Detailing the Neogene Shakh dara–Alchur syn-collisional gneiss-dome complex and connection to lithospheric processes. *Tectonics*, 39. <https://doi.org/10.1029/2019TC005735>
- Wright, T., Fielding, E. J., & Parsons, B. (2001). Triggered slip: Observations of the 17 August 1999 Izmit (Turkey) earthquake using radar interferometry. *Geophysical Research Letters*, 28(6), 1079–1082. <https://doi.org/10.1029/2000GL011776>
- Zakharov, S. A. (1948). On the east-west strike-slip faults on the south front of the Gissar Range (in Russian). *Reports of the Tadjik Filial Akademi Nauk of the USSR*, 5, 3–5.
- Zakharov, S. A. (1955). On the relationship of the Tadjik Depression and the Gissar Range (in Russian). *Izvestiya, Branch of Natural Sciences of the Tadjik SSR*, 9, 15–20.
- Zakharov, S. A. (1958). *Sediment structure of the Mesozoic and Cenozoic of the Tadjik Depression (in Russian)* (p. 230). Donish: Stalinabad.
- Zhou, Y., He, J., Oimahmadov, I., Gadoev, M., Pan, Z., Wang, W., et al. (2016). Present-day crustal motion around the Pamir Plateau from GPS measurements. *Gondwana Research*, 35, 144–154. <https://doi.org/10.1016/j.gr.2016.03.011>
- Zubovich, A., Schöne, T., Metzger, S., Mosienko, O., Mukhamediev, S., Sharshabaev, A., & Zech, C. (2016). Tectonic interaction between the Pamir and Tien Shan observed by GPS. *Tectonics*, 35, 283–292. <https://doi.org/10.1002/2015TC004055>
- Zubovich, A. V., Wang, X., Scherba, Y. G., Schelochkov, G. G., Reilinger, R., Reigber, C., et al. (2010). GPS velocity field of the Tien Shan and surrounding regions. *Tectonics*, 29, TC6014. <https://doi.org/10.1029/2010TC002772>

3.1.5 Tajik depression and Greater Pamir neotectonics from InSAR rate maps

Published as: [S. Metzger](#), Ł. Gała, L. Ratschbacher, M. Lazecký, Y. Maghsoudi, B. Schurr (2021), Tajik depression and Greater Pamir neotectonics from InSAR rate maps, *Journal of Geophysical Research: Solid Earth*, **126**, e2021JB022775. doi:[10.1029/2021JB022775](https://doi.org/10.1029/2021JB022775)

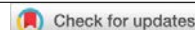
Supporting information: available online

Data publication: [S. Metzger](#), M. Lazecký, Y. Maghsoudi, (2021), High-resolution rate maps from the Tajik basin and the Pamir, *GFZ Data Services*. doi:[10.5880/GFZ.4.1.2021.005](https://doi.org/10.5880/GFZ.4.1.2021.005)

Scientific application: This work provided a detailed spatio-temporal kinematic insight in basin inversion, orogenic collapse, and other deformation effects of continental collision and provided one of the first Sentinel-1 large-scale deformation maps in a remote and topographically challenging region.

Methodological advances: The reference-framing of individually processed radar acquisition units (tiles) into a large, continent-stable reference frame is not straightforward, particularly, if the long-wavelength signals are to be preserved, resulting in a multi-stage complex data processing and analysis.

Individual Contributions: The study was designed, conducted and written by me. ML, YM and I created the LiCSAR interferograms. LG and LR contributed with a re-analysis of their earlier, only partially published work (structural geologic data), which was relevant for the data validation and interpretation that was done as a team effort of me, LG, LR and BS. All authors commented on the writing.



JGR Solid Earth

RESEARCH ARTICLE

10.1029/2021JB022775

Tajik Depression and Greater Pamir Neotectonics From InSAR Rate Maps



Key Points:

- East- and up-rate maps exhibit tectonic and anthropogenic processes with mm-accuracy in high spatial resolution (400 m)
- Rate map quality depends on interferometric data coherence and the availability of stabilizing Global Navigation Satellite System data
- Major tectonic signal is E–W shortening in the Tajik fold-thrust belt due to the westward collapse of the Pamir-Plateau crust

Supporting Information:

Supporting Information may be found in the online version of this article.

Correspondence to:

S. Metzger,
metzger@gfz-potsdam.de

Citation:

Metzger, S., Gała, Ł., Ratschbacher, L., Lazecký, M., Maghsoudi, Y., & Schurr, B. (2021). Tajik depression and Greater Pamir neotectonics from InSAR rate maps. *Journal of Geophysical Research: Solid Earth*, 126, e2021JB022775. <https://doi.org/10.1029/2021JB022775>

Received 13 JUL 2021

Accepted 28 NOV 2021

Author Contributions:

Conceptualization: Sabrina Metzger, Łukasz Gała, Lothar Ratschbacher
Data curation: Sabrina Metzger, Milan Lazecký, Yasser Maghsoudi
Formal analysis: Sabrina Metzger, Łukasz Gała, Lothar Ratschbacher, Milan Lazecký, Yasser Maghsoudi
Funding acquisition: Sabrina Metzger, Bernd Schurr
Investigation: Sabrina Metzger, Łukasz Gała, Lothar Ratschbacher, Milan Lazecký, Yasser Maghsoudi, Bernd Schurr
Methodology: Sabrina Metzger, Łukasz Gała

© 2021. The Authors.

This is an open access article under the terms of the [Creative Commons Attribution License](#), which permits use, distribution and reproduction in any medium, provided the original work is properly cited.

Sabrina Metzger¹ , Łukasz Gała^{2,3} , Lothar Ratschbacher² , Milan Lazecký⁴ , Yasser Maghsoudi⁴ , and Bernd Schurr¹

¹Lithosphere Dynamics, Helmholtz Center, Research Center for Geosciences, Potsdam, Germany, ²Geologie, Technische Universität Bergakademie Freiberg, Freiberg, Germany, ³Now at Hellenic Petroleum, Marousi, Greece, ⁴COMET, School of Earth and Environment, University of Leeds, Leeds, UK

Abstract Using E–W and vertical deformation-rate maps derived from radar interferometric time-series, we analyze the deformation field of an entire orogenic segment, that is, the Tajik depression and its adjoining mountain belts, Tian Shan, Pamir, and Hindu Kush. The data-base consists of 900+ radar scenes acquired over 2.0–4.5 years and global navigation satellite system measurements. The recent, supra-regional kinematics is visualized in an unprecedented spatio-temporal resolution. We confirm the westward collapse of the Pamir-Plateau crust, inverting the Tajik basin into a fold-thrust belt (FTB) with shortening rates decaying westward from ~15 to 2 mm/yr. Vertical rates in the Hindu Kush likely record slab-dynamic effects, that is, the progressive break-off of the Hindu Kush slab. At least 10 mm/yr of each, uplift and westward motion occur along the western edge of the Pamir Plateau, outlining the crustal-scale ramp along which the Pamir Plateau overrides the Tajik depression. The latter shows a combination of basin-scale tectonics, halokinesis, and seasonal/weather-driven near-surface effects. Abrupt ~6 mm/yr horizontal-rate changes occur across the kinematically linked dextral Ilyak strike-slip fault, bounding the Tajik FTB to the north, and the Babatag backthrust, the major thrust of the FTB, located far west in the belt. The sharp rate decay across the Ilyak fault indicates a locking depth of ≤1 km. The Hoja Mumin salt fountain is spreading laterally at ≤350 mm/yr. On the first-order, the modern 20–5 and fossil (since ~12 Ma) 12–8 mm/yr shortening rates across the FTB correspond.

Plain Language Summary The Tian-Shan-Pamir-Tibet-Himalaya mountain belts result from the Cenozoic collision of the Asian and Indian continents. Currently, the Pamir is colliding with the Tian Shan and collapsing westward into its foreland depression, creating the Tajik-basin fold-thrust belt (FTB). We use ~5-years of regularly acquired satellite radar imagery and pointwise positioning data to monitor the surface-deformation of the whole region. The resulting rate maps visualize crustal-scale tectonic and near-surface processes with an accuracy of a few millimeters and a spatial resolution of ~400 m. The FTB formed above a low-friction décollement, detached from the underlying basement, and terminates in the west and north along a kinematically linked thrust–strike-slip fault system. In the eastern FTB, salt rises forming a salt fountain that spreads up to 350 mm/yr. In agricultural areas, subsidence of >10 mm/yr is partially due to anthropogenically caused water-level changes.

1. Introduction

At the western end of the India-Asian collision zone, the Tian Shan, Pamir, and Hindu Kush frame the Tajik depression, hosting the Tajik basin (Figure 1a). Deformation rates derived from pointwise Global Navigation Satellite System (GNSS) data along the northern and western margins of the Pamir reach ~20 mm/yr (Metzger et al., 2020; Zubovich et al., 2010), being among the highest measured inside a continent. The accommodating crustal structures—thrusts and strike-slip faults—host abundant seismicity (e.g., Kufner et al., 2018; Schurr et al., 2014), including six magnitude M7 and 18 M6.5 earthquakes during the past 115 years. All of these occurred in the center and along the northeastern and northwestern rims of the Pamir. Geologic, geophysical, and geodetic observations indicate that the Pamir has moved northward, building an orocline with 65–75-km-thick crust beneath the Pamir Plateau (Mechie et al., 2012; Schneider et al., 2019). At the same time, the Pamir-Plateau crust has collapsed and has laterally (westward) extruded, thickening the crust west of the collision zone (Rutte et al., 2017; Stübner et al., 2013). Over the last ~12 Ma, westward extrusion into the Tajik depression has inverted the Tajik basin, forming the Tajik fold-thrust belt (FTB; Figures 1a and 1b; e.g., Abdulhameed et al., 2020;

Project Administration: Sabrina Metzger

Resources: Sabrina Metzger, Milan Lazecký, Yasser Maghsoudi

Software: Sabrina Metzger, Łukasz Gagala, Milan Lazecký, Yasser Maghsoudi

Supervision: Sabrina Metzger

Validation: Sabrina Metzger, Łukasz Gagala, Lothar Ratschbacher, Milan Lazecký, Yasser Maghsoudi, Bernd Schurr

Visualization: Sabrina Metzger, Łukasz Gagala, Lothar Ratschbacher

Writing – original draft: Sabrina Metzger, Łukasz Gagala, Lothar Ratschbacher

Writing – review & editing: Sabrina Metzger, Łukasz Gagala, Lothar Ratschbacher, Milan Lazecký, Yasser Maghsoudi, Bernd Schurr

Gagała et al., 2020; Kufner et al., 2018; Nikolaev, 2002; Schurr et al., 2014; Stübner et al., 2013). Structural geometries, GNSS velocities, and seismicity inside the Tajik depression suggest that the Tajik FTB is thin-skinned, formed above an evaporitic décollement at 6–12 km depth (e.g., Bekker, 1996; Bourgeois et al., 1997; Gagała et al., 2020; Schurr et al., 2014). Although the distribution and age of deformation is known geologically, the relative short observation period used to record seismicity by high-resolution temporary networks (Kufner et al., 2018; Schurr et al., 2014), the sparse GNSS data (e.g., Ischuk et al., 2013; Metzger et al., 2020), and the paucity of detailed neotectonic observations (Trifonov, 1978) limit the quantification of how far the deformation field of the Pamir is influencing the Tajik depression and how the individual structures in the FTB are contributing to its active shortening. In addition, the geodetically derived rates might be influenced by salt tectonics (Ischuk et al., 2013; Metzger et al., 2020), anthropogenic effects (e.g., Mukhabbatov et al., 2020), disturbances by the recent large earthquakes (Metzger et al., 2020), and the mantle processes below the Hindu Kush and Pamir (Kufner et al., 2021; Sippl et al., 2013). Herein, we used a sampling method with high spatio-temporal resolution and large areal coverage—Interferometric Synthetic Aperture Radar (InSAR)—to assess the distribution of active deformation within the Tajik FTB and the surrounding mountain ranges.

Since the launch of the European Sentinel-1 radar satellite mission in 2014, InSAR data have become easily accessible and tectonically active regions are monitored every 6–12 days worldwide. The data—usually provided in single tiles—cover $\sim 240 \times 200$ km on ground (Figure 1c) and allow the detection of rate changes of ~ 1 mm/yr (e.g., Weiss et al., 2020). Herein, we present relative displacement-rate maps derived from InSAR time-series analysis for the Tajik FTB and the adjoining Pamir and Hindu Kush with a spatial resolution of ~ 400 m. We derive 13 individual rate maps in two independent view angles, tied to available GNSS rates in a Eurasia-fixed reference frame (Figure 1d), and decomposed into horizontal (E-W) and vertical rates (Figures 2 and 3).

Linking the rate maps to land-cover data, seismicity, and geologic structures formed over the last ~ 12 Ma, we observe and discuss the following first-order features: (a) In the Tajik and Ferghana depressions, the vertical rates outline stripes with >15 mm/yr subsidence, with the strongest signal following the major river valleys; this subsidence is partially an artifact, partially caused by water extraction for irrigation. (b) In the Pamir, the horizontal rates outline a 3-D orogen-margin geometry with crustal material flowing laterally (westward) out of the N-S collision zone; the flow rates increase from east to west from the eastern to the western Pamir and decrease westward across the Tajik FTB, dissipating over its salt-rooted structures. (c) At the Tajik FTB's eastern edge and the adjacent western Pamir, high vertical and horizontal rates record passive roof uplift above a crustal-scale ramp, caused by the indentation of the leading edge of the Pamir. (d) In the northern and western Tajik FTB, the kinematically linked dextral Ilyak strike-slip fault and the Babatag thrust accommodate abrupt rate changes, marking the northern and western edge of the active Tajik FTB. (e) In the southeastern Tajik FTB, the rates trace active salt-tectonic structures. (f) In the Hindu Kush, large-wavelength displacement-rate changes likely record slab-dynamic processes in the mantle.

2. Tectonic Setting

The Tajik FTB and the bounding mountain belts of the Tian Shan, Pamir, and Hindu Kush formed due to the northward advance of the western promontory of India (e.g., Bloch, Schurr, et al., 2021; Burtman & Molnar, 1993; Kufner et al., 2016; Schwab et al., 2004). Currently, the Pamir-Plateau crust moves northward, collides with the Tian Shan, and collapses and extrudes westward into the Tajik depression, forming the Tajik FTB (Figures 1a and 1b; Kufner et al., 2018; Schurr et al., 2014). The Tajik FTB comprises a series of westward-convex, \sim N-trending folds and thrusts (e.g., Bourgeois et al., 1997; Chapman et al., 2017; Gagała et al., 2020) that bend in the north into the dextral Ilyak fault (Leith & Simpson, 1986); a similar—less pronounced—bending occurs in the south but no bounding strike-slip fault—akin to the Ilyak fault—has developed (Figures 2 and 3). The bending of the thrusts and folds into the Ilyak fault is compatible with the $<50^\circ$, paleomagnetically determined, anti-clockwise vertical-axis rotations in the northern Tajik FTB (Pozzi & Feinberg, 1991; Thomas et al., 1994). The Tajik FTB, southwestern Tian Shan, and Hindu Kush reflect partitioning of the \sim N4°E-oriented India-Asia convergence (DeMets et al., 1994) into \sim N-S shortening accompanied by dextral slip in the Tian Shan and along the Ilyak fault, \sim E-W shortening in the Tajik FTB, and \sim NW-SE shortening in the Afghan platform in the foothills of the Hindu Kush (Käßner et al., 2016; Kufner et al., 2018, 2021; McNab et al., 2019).

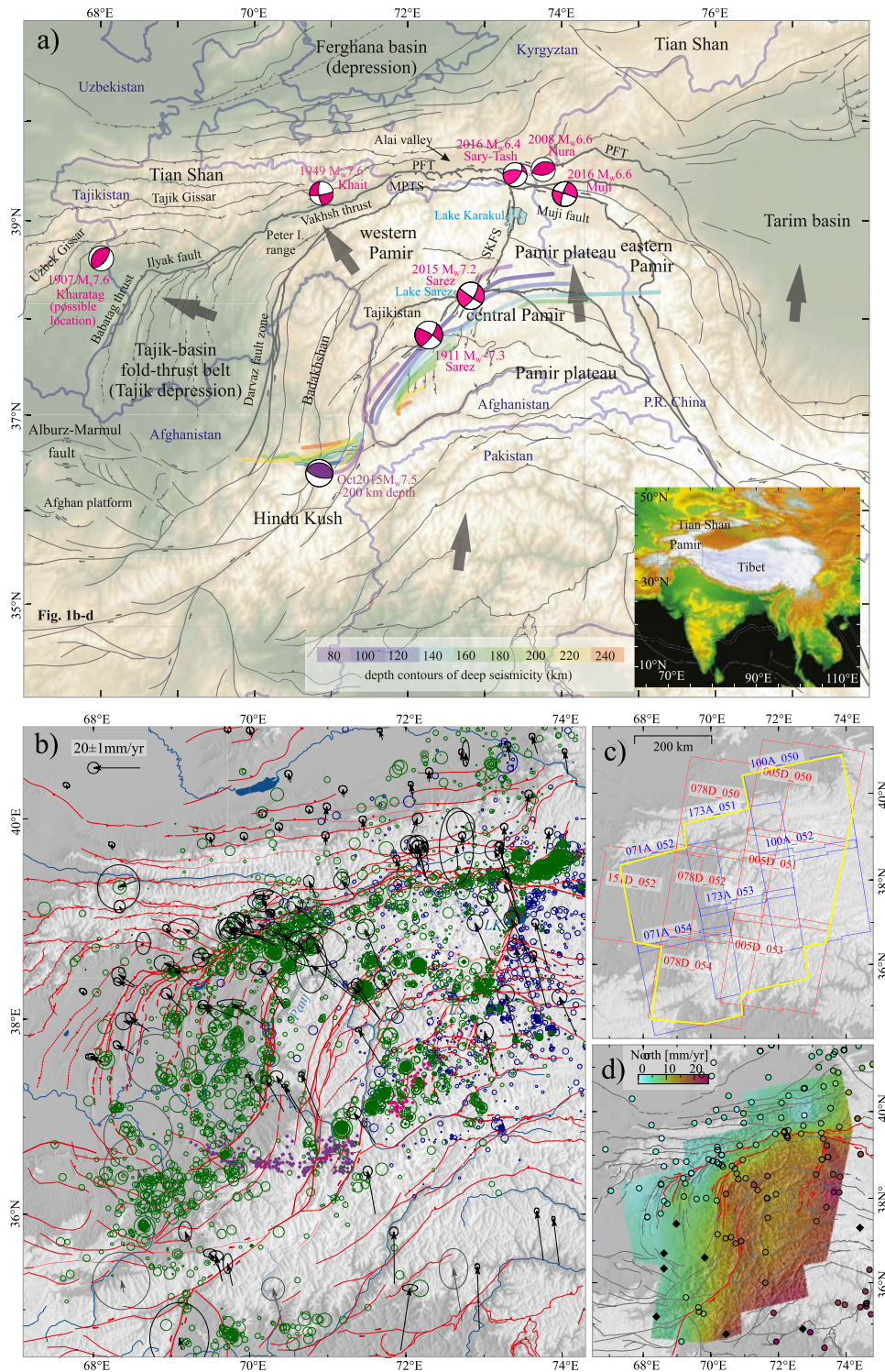


Figure 1.

Total ~E-W shortening reaches ~148 km in the north-central Tajik FTB, with decaying values toward south (~93 km) and toward northeast into the narrow corridor between the Pamir and Tian Shan (>22 km; Gagala et al., 2020). The southeastern part of the Tajik FTB showcases salt tectonics (Bekker, 1996; Gagala et al., 2020), for example, at the Hoja Mumin salt fountain with vertical extrusion rates of ~170 mm/yr (Leith & Simpson, 1986). The southwestern Tian Shan—the Uzbek and Tajik Gissar—constitute the thick-skinned foreland buttresses to the Tajik FTB (Figure 1a; Gagala et al., 2020). To the east, along the front of the Pamir, the Tian Shan is separated from the Pamir Plateau by the Main Pamir Thrust System with its leading fault, the Pamir Frontal Thrust; the western part of the Pamir Frontal Thrust—in the Peter I. Range—is the dextral-transpressive Vakhsh thrust that transitions westward into the Ilyak fault (Figure 1a). In the Pamir, the ~NNW-striking, sinistral-transpressive Sarez-Karakul fault system separates the western and eastern Pamir (Figure 1a). The eastern Pamir is dominated by en-bloc northward advance, whereas the western Pamir has a distinct westward flow component (Ischuk et al., 2013; Kufner et al., 2018; Metzger et al., 2020).

Abdulhameed et al. (2020) estimated—based on low-temperature thermochronologic data that incorporate dates from Chapman et al. (2017) and Jepson et al. (2018)—that major shortening started at ~12 Ma, spread immediately across the entire FTB, and declined at ~9 Ma in the western FTB; younger reactivation concentrated in the internal (eastern) FTB with the thickest evaporites. The youngest ages (~7–2 Ma) occur along the Vakhsh thrust, that is, the active erosional front of the northeastern Tajik FTB belt, where it narrows between the converging Tian Shan and Pamir, and along the eastern edge of the FTB—at the western flank of the Pamir Plateau, dominated by the sinistral-transpressive Darvaz fault zone (Figure 1a). The onset of shortening at ~12 Ma yields 12–8 mm/yr average long-term shortening rates in the north-central and southern Tajik FTB (see total shortening values above).

GNSS survey profiles across the Pamir's northern and western margins provide insights into the large-scale deformation and fault kinematics (Figure 1b). The highest differential velocities are observed across the Pamir Frontal Thrust (13–19 mm/yr shortening, ~7 mm/yr dextral shear; Zubovich et al., 2010). Across the Vakhsh thrust, shortening is $15 \pm 4/2$ mm/yr, while dextral shear increases to 16 ± 3 mm/yr; the Ilyak fault accommodates 8–15 mm/yr of dextral shear and ~5 mm/yr of shortening (Metzger et al., 2020). Kinematic modeling indicates a rather shallow fault-locking depth at the Vakhsh fault of <5 km (Metzger et al., 2020). The rates across the Darvaz fault zone decay from north to south, that is, from ~15 to 7–9 mm/yr sinistral shear and from ~10 to 4–0 mm/yr extension. The Sarez-Karakul fault system accommodates 5 ± 2 mm/yr sinistral slip (Metzger et al., 2017). The sparse GNSS data in the Tajik depression show that it is shortening ~ENE-WSW (Figure 1b; Ischuk et al., 2013; Metzger et al., 2020; Mohadjer et al., 2010). The interior of the Tian Shan exhibits minor dextral shear and shortening (Figure 1b). The recent kinematics of the Uzbek Gissar and the Afghan platform is largely unresolved. In the Hindu Kush, two relatively short GNSS profiles across the NE-to NNE-striking, poorly mapped faults indicate sinistral-transpressive motion of $\geq 2.5 \pm 1.8$ mm/yr in the central Hindu Kush and $\geq 7.3 \pm 1.0$ mm/yr in the northeastern Hindu Kush (Badakhshan, Figures 1a and 1b; Kufner et al., 2021; Perry et al., 2018).

Abundant crustal seismicity highlights the most active faults, that is, the Pamir Frontal Thrust, the Vakhsh thrust, the Darvaz fault zone, and the Sarez-Karakul fault system (Figures 1a and 1b; Kufner et al., 2018; Schurr et al., 2014; Sippl, et al., 2013). The earthquake focal mechanisms fit the observed fault kinematics (Figure 3; Kufner et al., 2018; Schurr et al., 2014). Seismicity is abundant beneath the Peter I. Range that is squeezed between converging Vakhsh and Darvaz faults, and north of the eastern Pamir, where the 2008 M_w 6.6 Nura (He et al., 2018; Sippl et al., 2014; Teshebaeva et al., 2014) and the 2016 M_w 6.4 Sary-Tash earthquakes (Bloch, Metzger, et al., 2021; Funning & Garcia, 2019; Vajedian et al., 2017) ruptured the northern Main Pamir

Figure 1. Tectonic setting of the Greater Pamir, Global Navigation Satellite System (GNSS) velocities, and Interferometric Synthetic Aperture Radar (InSAR) data coverage. (a) Major Cenozoic tectonic structures (completed from Abdulhameed et al., 2020; Käbner et al., 2016; Schurr et al., 2014) of the western edge of the India-Asia collision zone. Inset locates the study area in the India-Asia collision zone. Transparent gray arrows give bulk kinematics. Historical M6-7 earthquakes—potentially influencing our analysis—are plotted as red and purple focal mechanisms (the purple mechanism refers to a mantle earthquake; references in text and GEOFON data center). The Kharatag earthquake is poorly located. Contours give depth of the intermediate-depth earthquakes of the Hindu Kush and Pamir slabs (after Schurr et al., 2014). PFT: Pamir Frontal Thrust, MPTS: Main Pamir Thrust System, SKFS: Sarez-Karakul fault system. (b) Eurasian-fixed GNSS rates (Metzger et al., 2020), major Cenozoic faults and folds (red lines), background seismicity—scaled by size from Kufner et al. (2018, 2021) as green and from Bloch, Metzger, et al. (2021) as blue circles—, and river systems. Intermediate-depth earthquakes (>200 km depth) highlight the mantle portion of the Pamir slab (pink dots) and the Hindu Kush slab (purple dots; Kufner et al., 2021). (c) Interferometric database containing six frames acquired in ascending line-of-sight (LOS) (blue) and seven frames in descending LOS (red) view direction. Yellow polygon marks region where the LOS rates were decomposed into east and vertical components using interpolated north rates, shown in (d), based on available GNSS rates (circles), including eight artificial (interpolated) rates to stabilize the sparsely occupied regions (black squares).

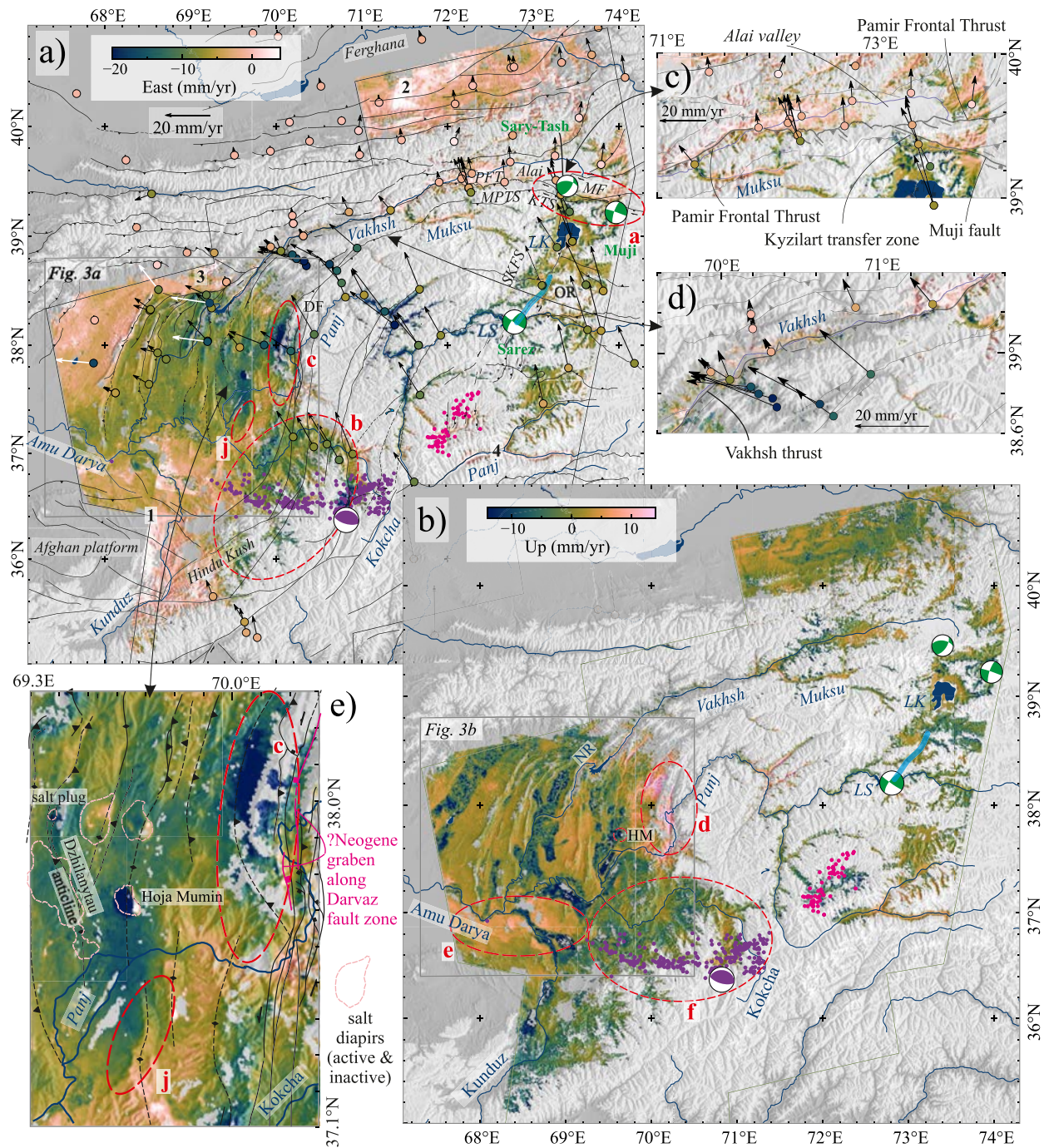


Figure 2. (a) East and (b) vertical InSAR rates, plotted on topography and simplified fault map. (c–e) highlight areas with specific short-wavelength features discussed in the text. Salt diapirs are from Figure 11 in Gaglia et al. (2020); the salt plug and the Hoja Mumin salt fountain are active. East rates are compared to GNSS rates (vectors and color-coded circles); color scales are saturated. White arrows mark GNSS rates in the Tajik depression that were excluded as outliers. Focal mechanisms indicate crustal (dark green, $M > 6$) and slab break-off (at 200 km, purple, $M_w 7.5$) earthquakes that occurred during the data acquisition period (references in text). Purple and pink dots outline the intermediate-depth earthquakes (>200 km depth) of the Hindu Kush and Pamir slabs, respectively. The transparent, light blue lines in (a and b) represent the modeled rupture trace of the 2015 $M_w 7.2$ Sarez earthquake (Metzger et al., 2017). Markers “1” to “4” locate artifacts, that is, frame-overlap jumps in the corners and edges of frames. Markers “a” to “j” locate features that we discuss in detail in the text. DF: Darvaz fault zone, IF: Ilyak fault, KTS: Kyzylart transfer zone, MF: Muji fault, OF: Officers Range, PFT: Pamir Frontal Thrust, PTS: Pamir Thrust System, SKFS: Sarez-Karakul fault system; HM: Hoja Mumin salt fountain, LK: Lake Karakul, LS: Lake Sarez, NR: Nurak reservoir.

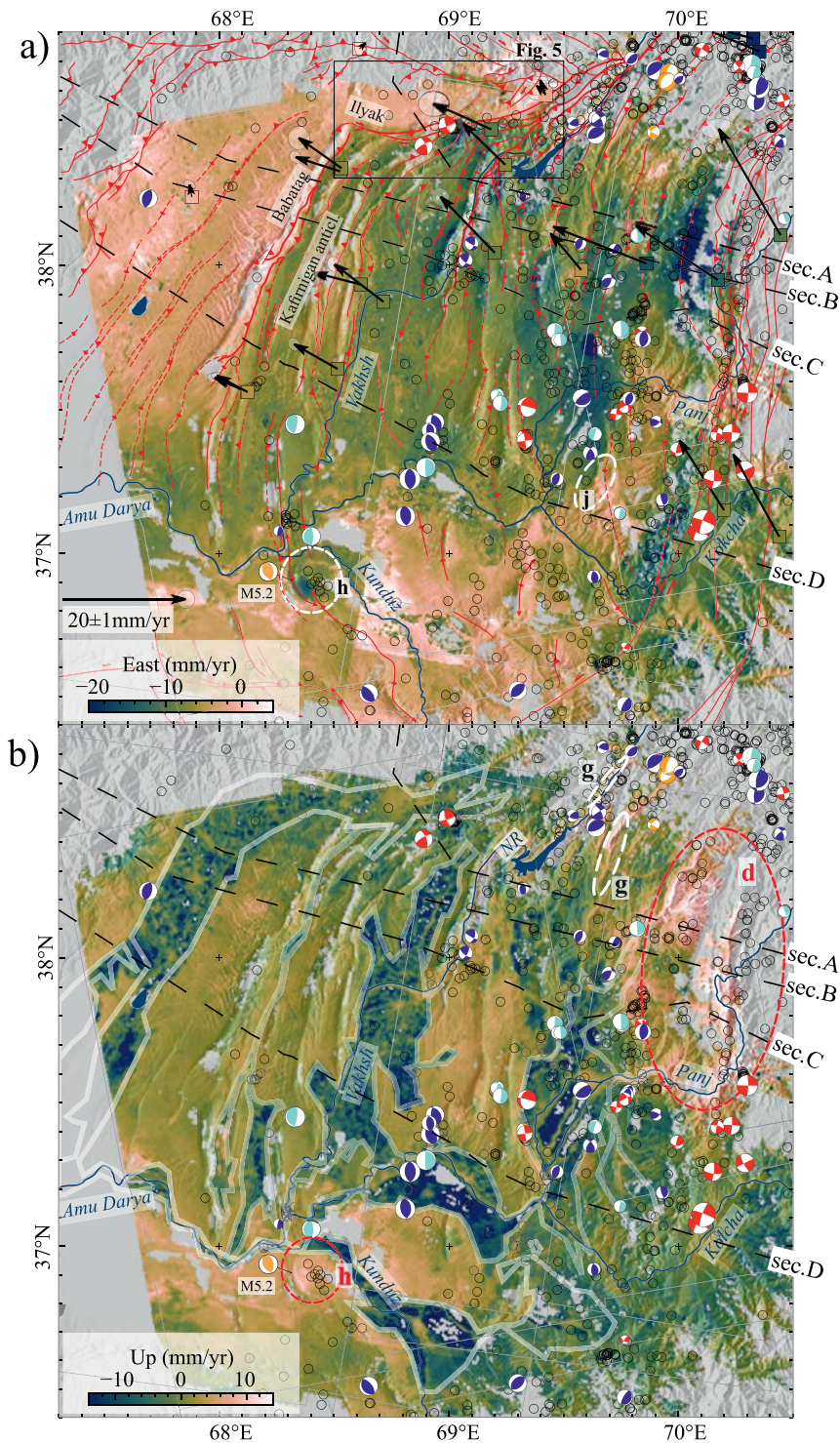


Figure 3. InSAR rates in the Tajik depression, compared to background seismicity (circles and focal mechanisms; Ekström et al., 2012; Kufner et al., 2018, 2021), and plotted on detailed fault-fold map. The focal mechanisms are colored according to fault type: red, strike-slip; orange, normal; blue, thrust; turquoise, thrusts with one sub-horizontal fault plane. Thin gray lines mark extent of interferometric frames. (a) East rates are compared to GNSS rates (color-coded squares and arrows). (b) Vertical rates; white frames mark agricultural land use, based on MDA US BaseVue (2013) Landsat 8 data. Cross sections A to D are shown in Figures 4a and 4b. Markers “d”, “h”, and “j” locate features that we discuss in detail in the text. NR: Nurak reservoir.

Thrust System, and the 2016 M_w 6.6 Aketao/Muji earthquake (Feng et al., 2017; Wang et al., 2017) ruptured the Muji fault (Figure 1a). Sparse seismicity occurs in the western Tajik depression; in its eastern part, it is intense but diffuse with focal mechanisms indicating overall \sim E-W shortening (Figure 3; Kufner et al., 2018). Most events occur at 5–25 km depth, that is, in general below the evaporite décollement, with the overlying sedimentary stack deforming mostly aseismic (Gagała et al., 2020). The Ilyak fault appears to be mostly aseismic, apart from a cluster of seismicity southeast of Dushanbe (Figure 3; Section 4.3.2). In the Hindu Kush, crustal seismicity is also sparse, suggesting that crustal faults are locked, with diffuse strain accumulation (Kufner et al., 2021).

In the context of our data analysis, a few large earthquakes stand out (Figure 1a): the 2015 M_w 7.2 Sarez earthquake ruptured the central Pamir along the Sarez-Karakul fault system (Elliott et al., 2020; Metzger et al., 2017; Sangha et al., 2017); this event was in sequence with the two 2016 M_6 earthquakes at the northern rim of the Pamir mentioned above (Bloch, Metzger, et al., 2021). The 1949 M_w 7.6 Khait earthquake likely affected the Tian Shan region north of Peter I. Range, causing a series of landslides (Evans et al., 2009; Kulikova, 2016). In 1907, the poorly located M_s 7.6 ± 0.3 Kharatag earthquake occurred somewhere at the northern rim of the Tajik depression (Kondorskaya & Shebalin, 1982) or farther east in the Peter I. Range (Kulikova, 2016; Storchak et al., 2013). The Hindu Kush-Pamir region also hosts frequent intermediate-depth earthquakes at 80–300 km depth, which are related to the ongoing indentation of Indian cratonic lithosphere beneath the Pamir and the subduction and break-off of marginal Indian lithosphere below the central Hindu Kush (Figures 1a, 1b and 2a, 2b, Kufner et al., 2016, 2017, 2021; Sippl et al., 2013). In 2015, during the InSAR data acquisition, the Hindu Kush hosted a M_w 7.5 earthquake at \sim 200 km depth, related to slab break-off (Kufner et al., 2017).

3. Data Processing

3.1. InSAR Time-Series Analysis

We used data from the Sentinel-1 satellites operating in C-Band with a wavelength of \sim 5.55 cm. The data were published as automatically pre-processed, differential interferograms as follows (Lazecký et al., 2020): each radar scene was automatically combined with three preceding and three subsequent scenes in time, resulting in six interferometric products with temporal baselines of a couple of weeks to months each (assuming no time gaps). The interferograms were created with the GAMMA SAR software (Wegmüller & Werner, 1997; Wegmüller et al., 2016) and multi-looked (downsampled) to \sim 100 m spatial resolution. They were filtered using an adaptive phase filter (Goldstein & Werner, 1998), assuming that short-baseline interferograms contain no sudden phase changes—e.g., due to fault creep—that are naturally smeared by strong filtering. Pixels with low coherence values were masked and the data were unwrapped automatically using SNAPHU v2 (Chen & Zebker, 2002). The unwrapped interferograms were resampled and geocoded using the 1-arc-second, void-filled digital elevation model of the Shuttle Radar Topography Mission (Farr et al., 2007). Each radar scene spatially overlaps along-track with other data frames of the same acquisition time and along-range with time-independent acquisitions (Figure 1c).

Interferometric time-series analysis allows to single out the small, secular tectonic and/or anthropogenic signals from the interferometric noise. This is done frame-wise (Figure 1c) by spanning a network of all interferometric scenes of one radar frame (Figure S1 of the Supporting Information S1). We used a modified small-baseline approach (NSBAS, Doin et al., 2011; López-Quiroz et al., 2009), as implemented in the python code LiCSBAS v1.3 (Morishita et al., 2020) that directly integrates the above interferograms. Tropospheric noise was suppressed using synchronous tropospheric delay maps, which are based on extrapolated weather data of the European Centre for Medium-Range Weather Forecasts in a horizontal resolution of 0.125° , updated every six hours (Yu et al., 2018). We automatically excluded interferograms from further processing, if they contained sparse or noisy data or did not pass a phase-loop closure test (Biggs et al., 2007; De Zan et al., 2015) indicating severe unwrapping errors. The most stable pixel over time for each frame was selected as a reference pixel (red stars in Figures S2a and S2b in Supporting Information S1). The whole interferometric network was then inverted for incremental displacements between the acquisition dates, with the mean (i.e., linear) displacement velocity being derived from the cumulative displacements by least squares (Morishita et al., 2020). Network gaps were overcome by adding a linear constraint with a scaling factor to the Green's functions (Doin et al., 2011). The standard deviation of the inverted rates was obtained by percentile bootstrapping (Efron & Tibshirani, 1986). The uncertainties are usually underestimated, particularly if the network is not fully connected (Morishita et al., 2020; uncertainty

investigations are discussed in Section 4.1). The resulting rate maps are masked by several quality assessment criteria, such as interferometric coherence, amount of data, rate standard deviation, time period covered, number of network gaps, or unwrapping errors, or root-mean-square of rate residuals. Finally, the maps were high-pass filtered in time and low-pass filtered in space using a Gaussian filter kernel (Hooper et al., 2007).

We processed six overlapping frames in ascending flight mode and seven frames in descending flight mode of three adjacent satellite tracks (Figure 1c). The assembled data set covers 270,000 km² in both view angles, stretching N–S from the Ferghana depression to the Hindu Kush and W–E from the Tajik depression to the eastern Pamir (Figure 2). When the mission's second satellite became fully operational at the end of 2016, the regular acquisition repeat time increased from 24 to 12 days, which drastically increased the interferogram quality. In the Pamir, many frames show co- or post-seismic displacements related to the 2015 M_w 7.2 Sarez earthquake (Fialko et al., 2021; Metzger et al., 2017). In this region, we used only data acquired one year or more after the earthquake (Figure S1 in Supporting Information S1). Overall, each frame contains 255–500 interferograms of 82–175 radar images spanning 2–6 years (Table S1 in Supporting Information S1). To increase the processing speed, the interferograms were four-times multi-looked (i.e., 4×4 block complex-value averaged) to a ground resolution of ~ 350 m in range and ~ 450 m in azimuth. After quality assessment, the remaining 50–110 scenes spanned a network of 90–350 interferograms (Table S1 in Supporting Information S1). The rates resulting from the time-series analysis were masked using standard threshold parameters, that is, an average coherence of >0.05 , a rate standard deviation of <100 mm/yr, <10 network gaps, and a spatio-temporal consistency of at least 5 mm. Some of these parameters were modified individually after visual inspection (Table S2 in Supporting Information S1). After the multi-looked and atmospheric-correction procedures, we repeated each processing step iteratively, removed poor interferograms, or corrected unwrapping errors manually. This improved the data quality, in particular in the rugged western Pamir, where the rates are most difficult to retrieve. The spatio-temporal filter was set to three times the average sampling interval in time and 2 km in space. Topography-related phase signals were suppressed using a linear correction term estimated between 200 and 10,000 m elevation.

The completeness of the resulting rate maps correlates with topographic roughness (Figures S2a and S2b in Supporting Information S1). While the Tajik depression and the arid eastern Pamir Plateau exhibit a relative high coverage, the deeply incised western Pamir, Tian Shan, and Hindu Kush are mostly void, apart from flat-bottom, formerly glaciated valleys (Stübner et al., 2017). The obtained deformation rates range between ± 15 mm/yr in line-of-sight (LOS) relative to their respective local reference points (Figures S2a and S2b in Supporting Information S1). Due to data sparsity, the standard rate deviation of the descending frame 005D_053 (Figure S2b in Supporting Information S1) is significantly larger than those of the other frames; we excluded this frame from further processing. The rate uncertainties are between 0.5 and 3.0 mm/yr, with higher uncertainties in the descending acquisition geometry (Figure S3 in Supporting Information S1). The highest uncertainties are observed in the Panj valley in the western Pamir and south of the Hindu Kush, where either the topography or a poorly resolved elevation model foster unwrapping errors. We excluded the area south of the Hindu Kush from further processing, as it also lacks stabilizing GNSS information. The lowest uncertainties are found near the reference points. These uncertainties only reflect a lower boundary, as they do not consider atmospheric disturbances or systematic biases caused by spatial subsampling and saw-blade like soil-moisture variations (see Figure 2 in Mira et al., 2021), which are problematic to correctly unwrap and cause bias in interferogram networks with short temporal baselines (Ansari et al., 2021; De Zan et al., 2014; Mathey et al., 2021), as we further discuss in Section 4.3.1. Such biases can be suppressed to some extent if long-baseline interferograms are included in the interferometric network, and full resolution data are processed, which was not applicable in our case. However, we qualitatively estimated the spatial footprint of these biases by the phase-loop closure technique: for each frame, we calculated the mean of closed phase loops, that is, the sum of the interferometric phase difference $\varphi_{ij} + \varphi_{jk} - \varphi_{ik}$, between three acquisition epochs i , j , and k , which is supposed to be zero (De Zan et al., 2015). If several of these loops are averaged, a systematic phase bias becomes apparent (Figure S4 in Supporting Information S1). For each frame, we calculated the sum of 70–90 phase loops acquired during 2017–2020. Significantly, mostly negative phase bias—correlated with the slow decrease of soil-moisture (see Section 4.3.1)—is observed in the Tajik and Ferghana depressions, and the extent of the affected regions is spatially well defined.

The outcome of our time-series analysis cannot only be used to derive linear rates, but also to monitor temporal rate anomalies, induced by seasonal processes (Figure S5 and S6 in Supporting Information S1), transients, or

smaller earthquakes (see discussion in Sections 4.2 and 4.3.2). Thus, the noise level and temporal information in InSAR time-series nearly reach the one of daily GNSS time-series, but clearly outperform them in terms of spatial coverage.

3.2. Reference Frame and LOS Rate Decomposition

We collapsed all LOS rate maps with their individual stable reference points (Figures S2a and S2b in Supporting Information S1) into a supra-regional Eurasia-fixed reference frame (Figures S2c and S2d in Supporting Information S1), using published horizontal survey-mode GNSS data (Figure 1b; Ischuk et al., 2013; Kufner et al., 2021; Metzger et al., 2019, 2020, 2021a; Mohadjer et al., 2010; Zubovich et al., 2016). During this first processing step, we identified and excluded four GNSS rates in the Tajik depression and one in the eastern Pamir as outliers (white arrows in Figure 2a; see also sensitivity tests in Section 4.1). Next, we tied each rate map into the Eurasia-fixed reference frame: we applied a linear ramp to each map to optimize (a) the fit to the horizontal GNSS rates within a search radius of ~ 4 km (or 10 pixels), and (b) the along-track overlap of the data frames (Ou, 2020) by inverting an over-determined, weighted design matrix, where the GNSS rates were collapsed into LOS (more details are provided in the Supporting Information S1). After removal of the GNSS outliers, we added eight artificial data points (black squares in Figure 1d) to stabilize the frames covering the southern Hindu Kush, where GNSS data are sparse and which could not have been referenced otherwise. Their positions were placed at the edges of the respective radar frames, their rates were interpolated from the adjacent stations, and their uncertainties were doubled (gray arrows in Figure 1b). The individual rate maps of the descending tracks 078 and 005 were not fitted to match the along-track overlay, because the data in the overlap area were either too sparse or the deviation was abnormally large (Figure S2b in Supporting Information S1; see also the sensitivity tests in Section 4.1). The resulting rates (Figures S2c and S2d in Supporting Information S1) contain significant offsets across-track, which are mostly due to the sudden LOS change (Figure S7 in Supporting Information S1). The westward motion of the western Pamir dominates the ascending rate maps (Figure S2c in Supporting Information S1) with positive values and the descending rate maps (Figure S2d in Supporting Information S1) with negative values. Due to the right-looking acquisition geometry of the Sentinel-1 satellite, the data are sensitive to about 40%, 10%, and 50% of the full east, north, and vertical displacement signals. If observations are available from ascending and descending LOS, they can be decomposed (Wright et al., 2004) into east and subvertical components by making use of the Pythagorean trigonometric identity between the LOS, east, and the subvertical direction (see sketch in Figure S8 in Supporting Information S1). The minor north component in the subvertical signal can be suppressed by subtracting interpolated north rates based on independent GNSS rates (Figure 1d; Ou, 2020; Supporting Information S1).

The resulting east rates agree with the corresponding GNSS data (Figure 2a) and range between -20 to $+10$ mm/yr in the ITRF2014 Eurasia-fixed reference frame (Altamimi et al., 2017). The vertical rates are in a data-centered reference frame and embrace ± 18 mm/yr (Figure 2b). The rates are most coherent in the Tajik and Ferghana depressions and—to some extent—in the eastern Pamir and the Alai valley. Rates in the western Pamir could only be extracted along the Panj-river valley and some of its tributaries. We still observe long-wavelength extrema at the corners and edges of some frames, for example, in the NW-corner of frames 071A_054 and 100A_050 or the SW-corner of 078D_052 (Figure 1c; markers “1” and “2” in Figure 2a). They are probably due to multiple unwrapping errors in disconnected, high-topography regions (Figures S2a and S2b in Supporting Information S1). The spatial data coverage decreased further after decomposition (Figure S2 in Supporting Information S1) to regions covered by both view angles only. The decomposed rate uncertainties—now including the GNSS data uncertainties—are in the range of 0.6–2.6 mm/yr (Figures S9 and S10 in Supporting Information S1). In a similar study on Anatolia—with slightly more data—the uncertainties are in the range of 2–3 mm/yr for wavelengths of 50–150 km and a 5-year-long time-series (Figure S7 in Weiss et al., 2020). For our slightly sparser data set, we assume that local rate changes are significant if >1.5 mm/yr, and long wavelength signals are significant if >3 –5 mm/yr. These estimates are probably still too optimistic for the Panj-river valley, where the interferometric networks are short in time and repeatedly sub-divided, impeding the correct assessment of linear rates (Figure S1 in Supporting Information S1), or where too few GNSS data points are available (Hindu Kush). There, the decomposed rate uncertainties are higher than in the rest of the data set and reach 4.5 mm/yr. The individual ascending and descending rate maps and the final decomposed east and vertical rate maps, both stable to Eurasia (Altamimi et al., 2017) are available as geo-referenced TIF-files in Metzger, Lazecký, and Maghsoudi (2021).

4. Results and Discussion

4.1. Rate Map Quality Assessment

Interferometric radar analysis is challenged by several factors. Seasonal vegetation changes and (ground) water dynamics introduce a bias, if only short temporal baseline interferograms are used (Figure S4 in Supporting Information S1; Ansari et al., 2021; Mathey et al., 2021), or if the network density is not equally distributed throughout the seasons. Heavy snowfall causes interferometric decorrelation, which may apply in particular for the western Pamir. The partially incomplete digital elevation model (Farr et al., 2007) of the deeply incised western Pamir and southern Hindu Kush contains topographic artifacts, which makes interferograms prone to unwrapping errors. Given these obstacles, our LiCSBAS rate maps contain isolated data patches due to spatial and temporal decorrelation (Figure S2 in Supporting Information S1), which challenges the combination of the observed rates of several independent acquisition frames into one single reference frame. We overcame this to some extent by tying the rates to the GNSS reference frame, but some sharp jumps along frame boundaries remain; these are in the Afghan platform, the western Ferghana depression, the Dushanbe trough north of the Ilyak fault, and the upper Panj-river valley (markers “1” to “4” in Figure 2a, respectively). Also, the east rates of ~ 0 mm/yr observed in the Muksu-river valley in the northern Pamir (Muksu in Figure 2a)—conflicting with the higher rates in the surrounding regions—are difficult to interpret. Thus, abundant GNSS data are fundamental to correctly transform LOS rate maps with spatial gaps into a supra-regional reference frame. For example, the sparse GNSS data in the Hindu Kush do not suffice to stabilize the observed, disconnected LOS rates correctly—particularly in the region south of the Hindu Kush—and we can only speculate if the long-wavelength signals are rooted in tectonics (Figures 2a and S2 in Supporting Information S1).

To further test the stability of the decomposed, Eurasian-fixed rate maps, we performed the steps described in Section 3.2 three more times, using different referencing strategies. First, we included the five GNSS-rates identified and excluded as outliers in Section 3.3; then, we fitted also the along-track overlaps of frames 078 and 005, that originally exhibit a poor fit; finally, we combined the previous two procedures. A visual comparison of these tests shows that—apart from obvious sharp rate changes along frame boundaries—only long-wavelength patterns in the rate maps are affected (Figure S11 in Supporting Information S1). The inclusion of the GNSS-rate outliers increases the westward motion of the region west of the Babatag fault by up to 4 mm/yr (models A in Figure S11 in Supporting Information S1), but introduces an obvious misfit between the InSAR and all other GNSS rates in the Tajik basin; it has no significant effect on the vertical rates. Fitting frames 078 and 005 along-track effects the southern Tajik basin strongest (models B in Figure S11 in Supporting Information S1), increasing the westward rate by 9 mm/yr and the subsidence by 8 mm/yr in the fold-thrust-belt; in the Hindu Kush, it yields unrealistic increase of east and uplift-rates by 13 and 6 mm/yr, respectively. Given the poor GNSS–InSAR misfit and the unrealistic rates for the Hindu Kush, we stick to the reference-frame strategy detailed in Section 3.2.

The independent LiCSBAS rate maps offer reliable data to identify km-scale mass movements, which are abundant in this region, but these signals should be confirmed by optical imagery and/or fieldwork. We encourage the reader to make use of the supplementary material (Metzger, Lazecký, & Maghsoudi, 2021) for their own specific analyses. When interpreting our results, one must consider the different time periods of data collection (Figure S1 in Supporting Information S1). Each individual LOS rate map might be differently affected by moderate-sized earthquake signals or season-dependent near-surface dynamics. The Tajik depression yielded the highest data resolution in space and time, where we have both, dense data and distinct tectonic and non-tectonic signals that can be correlated with independent structural data in high-resolution. We therefore discuss the observations from the Pamir and Hindu Kush in a reconnaissance way and focus on the Tajik depression, in particular the Tajik FTB.

4.2. Pamir and Hindu Kush

In the Eurasia-fixed reference frame, the InSAR rates exhibit westward motion in the order of ≥ 10 mm/yr in the western Pamir and the Tajik FTB with a good match to the GNSS-derived east rates (Figure 2a). We assign the large-scale west-directed surface displacements to the westward collapse and lateral extrusion of the Pamir-Plateau crust. North of the Pamir-Tian Shan collision boundary, the Ferghana depression appears to lack horizontal motion (i.e., it is relatively stable in reference to Eurasia), as all significant features in the rate maps also appear in the phase-bias map (Figure S4 in Supporting Information S1) or collocate with radar-frame boundaries (marker “2” in Figure 2a) and hence are artifacts. Along the northern front of the Pamir in the southern Alai valley

(Figures 1a, 2a and 2c), sharp rate changes record the westward-increasing dextral shear at the leading edge of the Pamir, indicating its escape toward the west in addition to the dominant N–S shortening showcased by GNSS data (Zubovich et al., 2010, 2016). The east-rate map also indicates that part of the active deformation steps back south of the eastern Alai valley from the Pamir Frontal Thrust and connects to the ~WNW-striking Muji fault (Figures 1a, 2a and 2c). It remains indistinguishable whether the recorded velocities reflect post-seismic activation following the 2016 Sary-Tash and Muji earthquakes (Bie et al., 2018; Feng et al., 2017) or are a long-term signal. Afterslip can be excluded, since we removed data acquired in (at least) the first six months after these two M6 events, but a slight non-linear signal is still observable in individual time-series (e.g., Figures S6g–S6j in Supporting Information S1). In any case, the indicated rates support the transfer of the top-to-west normal slip along the Kongur Shan extensional system of the eastern Pamir (e.g., Robinson et al., 2004, 2007; just outside and southeast of the eastern boundary of Figure 2a) via the Muji fault and the Kyzylart transfer zone (marker “a” in Figure 2a) to the Pamir Thrust System and in particular to the deformation front along the Pamir Frontal Thrust (Sippl et al., 2014). The existence of this dextral transfer zone, consisting of the Muji fault and the faults of the Kyzylart transfer zone, that transfer ~E–W crustal extension along the Kongur Shan system to the dextral strike-slip component along the Pamir front, is also implied by the slight divergence of the GNSS velocity field between the eastern Pamir (e.g., Lake Karakul area in Figure 2a) and the Tarim block (Zubovich et al., 2010). North of the transfer zone the GNSS vectors parallel those in the Tarim basin, albeit with lower rates than in the Tarim basin, reflecting the shortening across the multiple faults of the Pamir Thrust System (Figures 2a and 2c). The dextral transfer zone (Muji fault and faults of the Kyzylart transfer zone) implies that the eastern Pamir is involved in the partitioning of convergence into ~N–S shortening and ~E–W extension, here with a westward flow component smaller than that of the western Pamir.

At the northwestern rim of the Pamir, along the Vakhsh valley, sharp east-rate changes of 12–24 mm/yr either imply high landslide activity or—more likely—a shallow locking depth of the evaporite-rooted, dextral-transpressive Vakhsh thrust (Figures 2a and 2d); the estimated dextral strike-slip rates are 16 ± 3 mm/yr (Metzger et al., 2020). If the Vakhsh thrust is nearly freely creeping, the 1949 M_w 7.6 Khait earthquake likely did not rupture the Vakhsh thrust but a structure in the crystalline basement of the Tian Shan.

On first order—and given that the east rates measured in the valleys of the Panj and its tributaries are significant, the west rates appear to increase from 5–15 mm/yr westward motion in the eastern Pamir (east of the Sarez-Karakul fault system) to 15–20 mm/yr in the western Pamir; this conforms with the intense western Pamir seismicity with focal mechanisms that show strike-slip and normal fault solutions with ~E-trending T-axes (Schurr et al., 2014). A minor westward rate increase occurs across the distributed segments of the Sarez-Karakul fault system, for example, near Lake Sarez (Figures 1a and 2a). The implied extensional deformation component accommodated by the Sarez-Karakul fault system agrees with the geologic observations of major range-bounding normal faults northeast of Lake Sarez (Officers Range, marker “OR” in Figure 2a; Rutte et al., 2017; Schurr et al., 2014) but contrasts with focal mechanism solutions, which record nearly pure sinistral strike-slip (Metzger et al., 2017; Schurr et al., 2014). However, we consider the rates in this area somewhat uncertain, as some short wavelength rate changes correlate with slopes and the systematic bias map (Figure S4 in Supporting Information S1). We suspect that this is not a topographic artifact but rather caused by seasonal, permafrost-related sagging of (or pore-pressure changes in) unconsolidated material (e.g., Rouyet et al., 2019); we extensively mapped such features that formed as a result of the 2015 Sarez earthquake (the light-blue lines in Figures 2a and 2b show the modeled rupture trace from Metzger et al., 2017).

The northeastern Hindu Kush of Badakhshan (Figure 1a), with reliable data along the Kokcha-river valley (marker “b” in Figure 2a), exhibits nearly as high westward rates (7–12 mm/yr) as the eastern Tajik FTB (8–15 mm/yr) and the western Pamir (marker “c” in Figure 2a, 16–26 mm/yr). No modern structural information is available for the faults and folds mapped in the northeastern Hindu Kush, but the highest rate changes coincide with thrust-cored folds along the southeastern margin of the Tajik FTB, involving Pliocene strata (Figure 3a; Doeblich & Wahl, 2006; own unpublished mapping). In contrast, the western Hindu Kush—including the Afghan platform—appears to be horizontally mostly stable with respect to Eurasia (west of marker “b” in Figure 2a, 0 ± 2 mm/yr).

We observe strong and accelerating uplift of 10–17 mm/yr in the westernmost Pamir (along the Panj valley and west of it) and easternmost Tajik FTB where its eastern erosional edge is cut by the Darvaz fault zone (marker “d” in Figures 2 and 3b, time-series in Figures S5a and S5b in Supporting Information S1); this area coincides with the area of rapid westward motion (marker “c” in Figure 2a; see interpretation below). The acceleration started

~1 year (Figure S5a and S5b in Supporting Information S1) after the Sarez and the slab-break-off earthquakes 200–250 km farther east and south, respectively (Figures 1a, 2a and 2b).

A N–S gradient—with uplift rates of 4–6 mm/yr—occurs at the southern margin of the Tajik depression at its transition to the Afghan platform (marker “e” in Figure 2b). This area south of the Amu Darya–Panj-river valley, marks the interaction and transition from the ~E–W shortening of the Tajik FTB to the ~NW–SE shortening within the Afghan platform, implied by earthquake focal mechanism (e.g., Supplementary Figure S5 in Kufner et al., 2021; McNab et al., 2019), and the appearance of ~E-striking faults, for example, the dextral-oblique thrust in the Alburz-Marmul fault zone (Figure 1a).

The whole northeastern Hindu Kush and southwestern Pamir are located above steeply dipping lithospheric slabs; their position in the mantle is outlined by depth contours of intermediate-depth seismicity in Figure 1a and the intermediate-depth earthquake epicenters in Figures 1b, 2a and 2b (e.g., Kufner et al., 2016, 2017, 2021; Zhan & Kanamori, 2016). The Pamir slab starts to bend down from west to east beneath the eastern Tajik FTB (Figures 6 and 7 in Schneider et al., 2019; crustal-scale cross section in Figure 18c of Gagala et al., 2020) and likely laterally terminates in the south where strong uplift (marker “d” in Figure 2b) gives way to subsidence in the northeastern Hindu Kush (marker “f” in Figure 2b). The Hindu Kush slab is subducting northward, dips steeply north to vertical, and is in the process of stretching and tearing in its eastern part (Kufner et al., 2017, 2021). The boundary between the mantle parts of the two slabs is outlined by the intermediate-depth earthquakes in the southwestern-most Pamir (Hindu Kush slab: purple dots; Pamir slab: pink dots in Figures 2a and 2b). It is difficult to assess, whether these deep-seated processes are reflected in our rate maps. InSAR radar satellite antennas are most sensitive to vertical motions, but subtle rate changes across several tens—if not hundreds of kilometers—are challenging to correctly retrieve. Our observation of clearly linear, regional, 0–4 mm/yr subsidence in the northeastern Hindu Kush (marker “f” in Figure 2b; Figure S5i in Supporting Information S1) above and north of the Hindu Kush slab, and in particular the marked contrast to the 10–17 mm/yr uplift in the easternmost Tajik FTB (marker “d” in Figure 2b) likely record these lithosphere processes. This regional subsidence remains—or even increases—despite the different reference framing strategies discussed in Section 4.1 (Figure S11 in Supporting Information S1). The region where the crust of the Tajik depression bends down, forming the footwall of the western Pamir (crustal-scale buckling in profile along latitude 38°N in Figure 6 of Schneider et al., 2019; Gagala et al., 2020), likely constitutes a crustal-scale antiform above a ramp, causing uplift. In the southwestern Pamir, the steeply ~SE-dipping to vertical, back-rolling Pamir slab (Kufner et al., 2016) possibly induces subsidence (Figure 2b). The north-dipping to subvertical, back-rolling Hindu Kush slab possibly induces the subsidence in the Hindu Kush (marker “f” in Figure 2b): there, subsidence of up to 4 mm/yr changes to uplift at the western end of the slab where it is intact (boundary between markers “e” and “f”) and subsidence possibly changes to modest uplift at the slab's eastern end, where the break-off has progressed most (Kufner et al., 2021). We interpret the general ≥ 10 mm/yr subsidence south of marker “f” and south of the eastern part of marker “e” as a tectonic signal caused by the Hindu Kush slab; there, Kufner et al. (2021) tomographically mapped its down-bending toward a subvertical position in the mantle marked by the purple earthquakes. In contrast to these long-wavelength features, we interpret the pronounced stripes of 20–40 mm/yr subsidence crossing and extending to the south of marker “e” along the Kunduz-river valley as anthropogenically caused (Figure 2b; see Section 4.3.1 for equivalent subsidence along the valleys of the Tajik depression).

4.3. Active Structures in the Tajik Fold-Thrust Belt

The rates in the Tajik FTB are interpreted in combination with seismicity (Kufner et al., 2018) and the structural geometries, derived from surface, seismic, and borehole data (Gagala et al., 2020). In addition to the map view (Figure 3), we projected the horizontal and vertical rates onto four geologic cross-sections within 5 km swaths (Figures 4a and 4b; cross-section traces in Figure 3), and into a detailed east-rate map and an oblique-crossing profile of the Ilyak fault (Figure 5; frame in Figure 3a). In addition, we compared the rates to topographic profiles and percentage of arable land, both computed within 5 km swaths (Figures 4a and 4b).

4.3.1. Non-Tectonic Signal

Herein, we outline the non-tectonic signal, that is systematic subsidence, by land classification data based on Landsat 8 optical imagery (MDA US BaseVue, 2013); land classified as arable correlates well with the systematic soil-moisture bias map (Figure S4 in Supporting Information S1). We marked the major agricultural areas

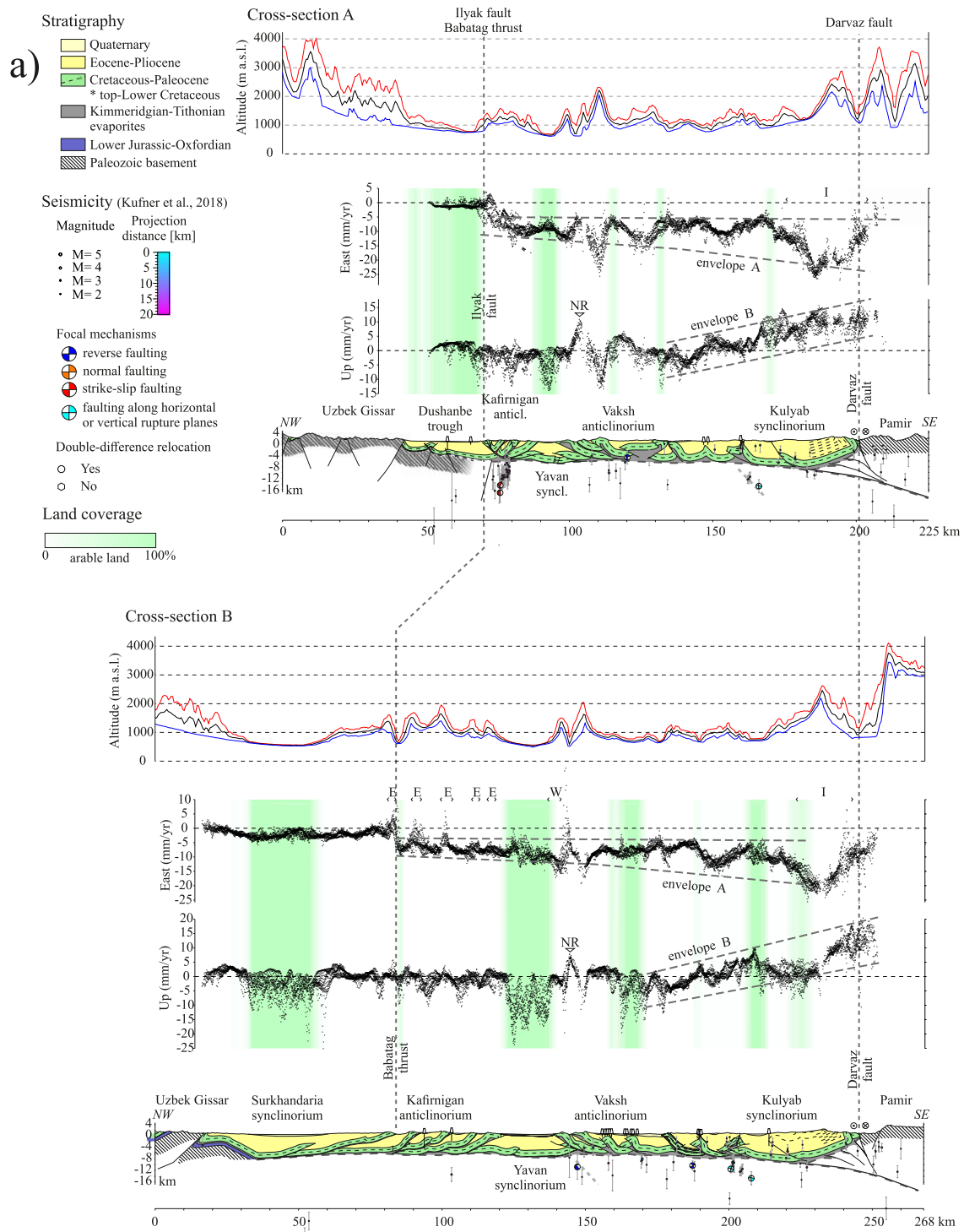


Figure 4. Topographic profiles (max., mean, min. values within 5-km swath), InSAR horizontal and vertical rates, and background seismicity (Kufner et al., 2018) projected onto geologic cross-sections A to D through the Tajik depression (Gagała et al., 2020; see Figure 3 for location) with the main structural features named (compare Figures 1–3). Markers E (east), H (location marker), I (location marker), NR (Nurak reservoir), and W (west), and envelopes A and B locate features that we discuss in detail in the text.

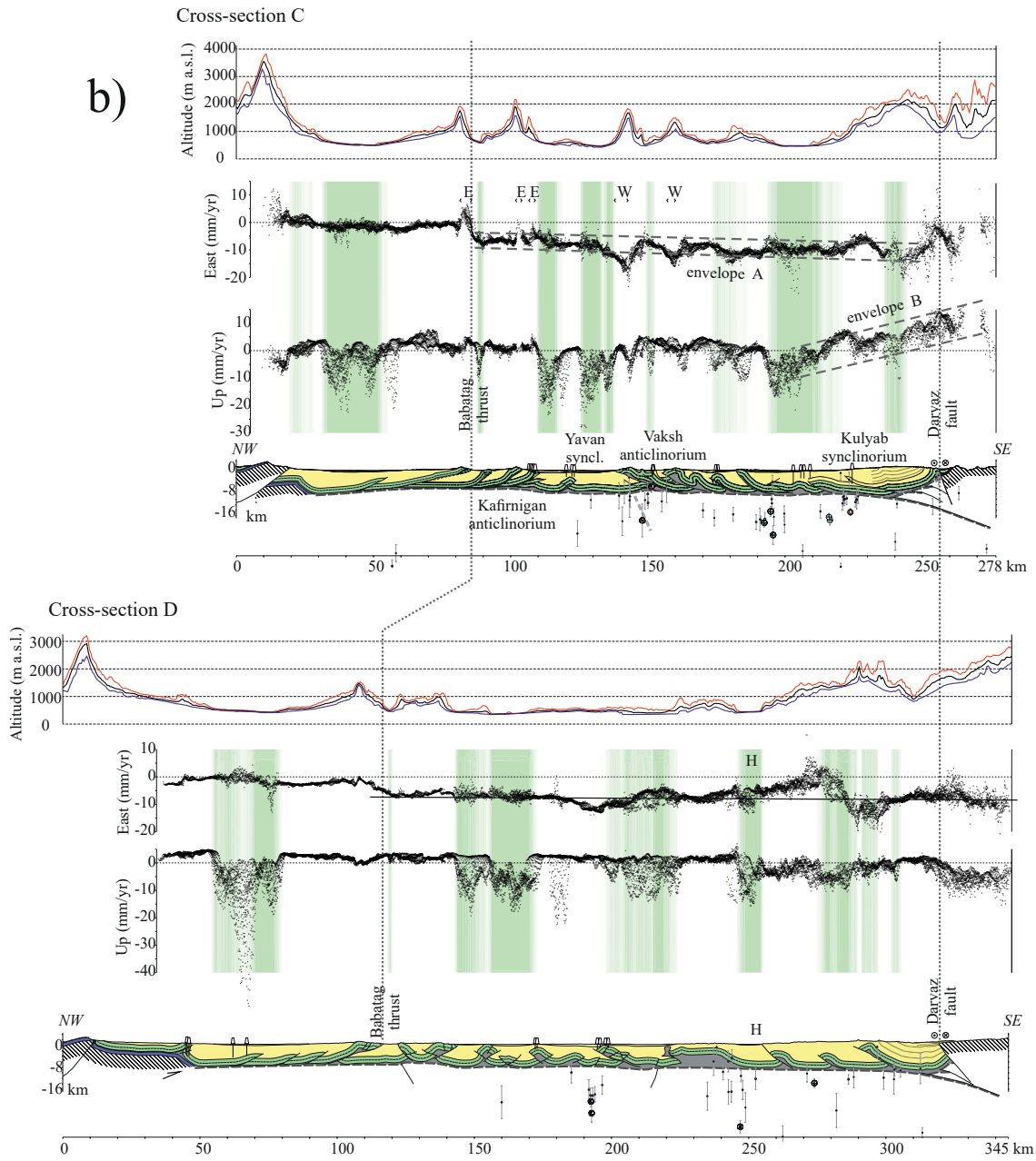


Figure 4. Continued.

by polygons framed thick-white (Figure 3b) respectively shaded in green (Figures 4a and 4b). The vertical rate maps of Figures 2b and 3b outline stripes with >15 mm/yr subsidence as the most outstanding feature of the Tajik depression; the strongest subsidence signal follows the major river valleys of the Tajik depression, which host intense agriculture. The observed subsidence is most likely caused by precipitation-induced soil-moisture changes that alter the dielectric properties and thus the vertical propagation of the incoming radar waves (Ansari et al., 2021; De Zan et al., 2014). Rainfall and/or snowmelt causes rapid pore filling and simultaneous soil uplift (Gabriel et al., 1989), which often leads to unwrapping errors in interferograms. The consequent slow dehumidification (see Figure 2 in Mira et al., 2021), on the other hand, is correctly imaged in interferograms, thus biasing the vertical rates derived from the time-series analysis toward the negative. This bias is likely strongly enhanced

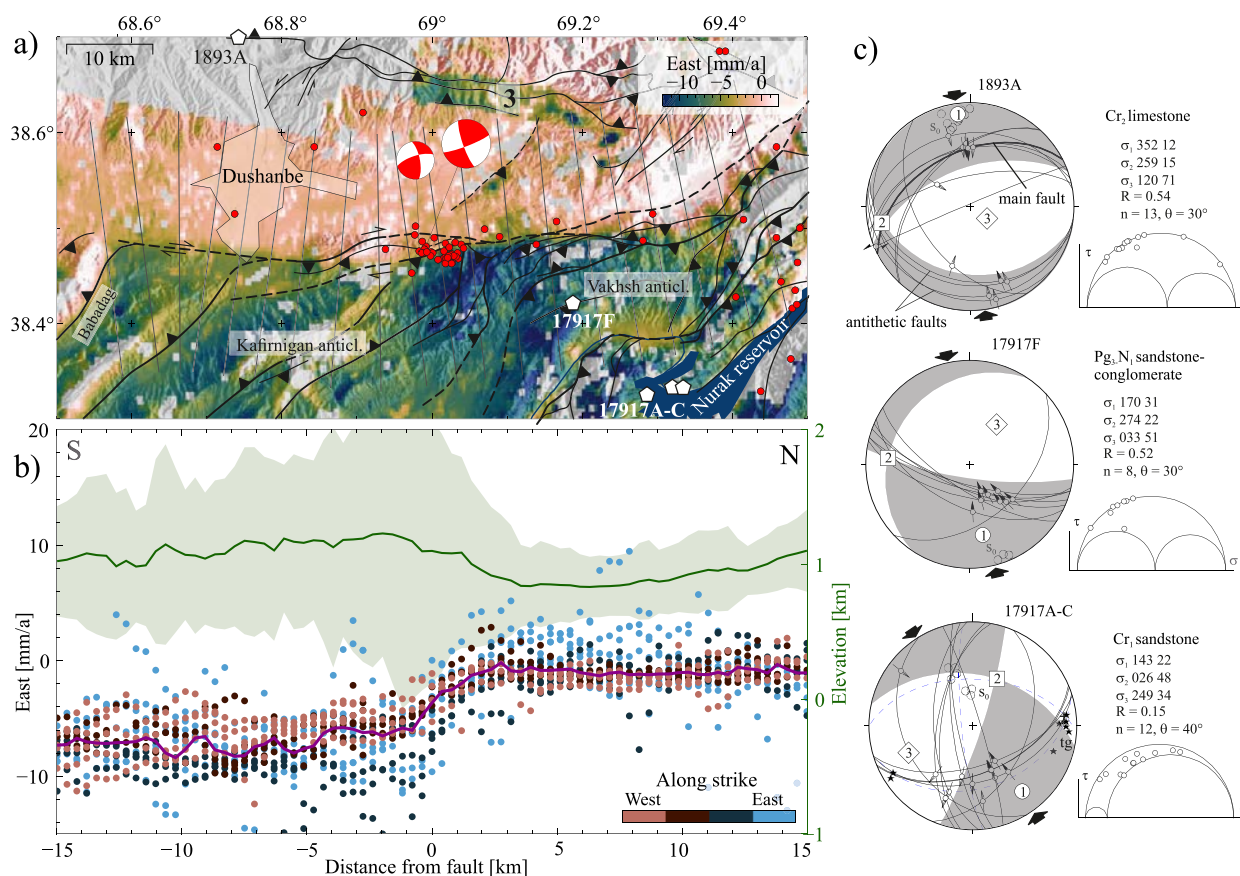


Figure 5. East rates across the Ilyak fault in (a) map view and (b) as across-fault profile. Background seismicity and focal mechanisms (Kufner et al., 2018) are plotted in red. The profiles in (b) are centered along the maximum rate change and are color-coded along strike, indicating different slip behavior. Median rates are plotted in purple, median topography and its deviation is indicated in green. (c) Sites that characterize structural data from selected deformation zones north and south of the Ilyak fault, which is badly exposed, mostly due to its anthropogenic overprint. Pure top-to-south thrusting emplaced the crystalline basement of the Tian Shan onto Cretaceous limestone (1893A); the two sites in the Vakhsh anticlinorium characterize that part of the Tajik FTB where the overall \sim N-striking thrusts bend into the Ilyak fault zone; they have dextral-transpressive top-to-(N)NW kinematics. Structural data are plotted in lower hemisphere, equal area stereograms. Arrows around the stereograms indicate sub-horizontal maximum stress orientations determined from fault-slip analysis (following Sperner & Ratschbacher, 1994). Faults are drawn as great circles and shear directions and striae (slickenlines) as arrows pointing in the direction of the displacement of the hanging wall. Confidence levels of slip-sense determination are expressed in the arrowhead style: solid, certain; open, reliable; half, unreliable. Lithology and strata age (Cr₁: Lower Cretaceous, Cr₂: Upper Cretaceous, Pg₃-N₁: Oligocene-Miocene), and reduced stress-tensor calculations are plotted on the right (principal stress orientations: σ_1 , σ_2 , σ_3 ; θ fracture angle used for calculation; R is the shape factor of the stress-ellipsoid, $(\sigma_2 - \sigma_3)/(\sigma_1 - \sigma_3)$; n: number of data used for calculation; dimensionless Mohr diagram visualizes normal versus shear stress relations for each fault (circles), tg: tensions gashed plotted as poles to the planes, s_0 : bedding. Transparent beach balls outline compressional (gray) and extensional (white) dihedra.

by water extraction due to the extensive irrigation in the summer months, during which most of the used radar scenes were acquired; a more detailed study of these signals lies beyond the scope of this work. In the horizontal rates, the agricultural areas often coincide with a high measurement scatter, although without any systematic component. A second conspicuous vertical signal—but this time positive—correlates with major rivers and related to water level increase during hinterland snow melt (e.g., markers “g” in Figure 3b).

The distinct, patchy subsidence in the region between the fossil and active (Hoja Mumin) salt diapirs in the southeastern Tajik FTB and the Nurak water reservoir (markers “HM” and “NR” in Figure 2b) are likely an effect of salt tectonics (Figure 11 of Gagala et al., 2020). But it is also correlating with arable land that has not been properly classified in the Landsat 8 data. The highest deformation rates occur at the Hoja Mumin salt fountain (Figure 2e), where we observed local uplift of \sim 50 mm/yr at its top, surrounded by up to \sim 120 mm/yr of subsidence and lateral outflow of \sim 350 mm/yr to the west and \sim 170 mm/yr to the east. These rates confirm the recent activity of this salt fountain, as documented by Leith and Simpson (1986), Dooley et al. (2015), and Gagala

et al. (2020). We also observed localized uplift surrounding the shores of the Nurak reservoirs (and smaller reservoirs downstream; marker “NR” in Figure 2b and cross-sections A and B in Figure 4a) that is probably related to elastic rebound caused by reservoir-volume changes, as it was confirmed elsewhere (e.g., Cavalié et al., 2007; Neelmeijer et al., 2018).

4.3.2. Tectonic Signal

The unambiguous horizontal tectonic signal consists of long-wavelength trends. Foremost, the bulk of the Tajik FTB accommodates westward motion (map view in Figures 2a and 3a, cross-sectional view in Figures 4a and 4b). Characteristically, the east rates are not affected by the vergence of the fold-thrust structures in the Tajik FTB; in particular, the Yavan synclinorium—the zone of vergence change—is showing similar horizontal rates as the bounding Kafirnigan and Vakhsh anticlinoria. Therefore, the Yavan synclinorium must be—at least at present—entirely detached from its original substratum. Chapman et al. (2017) postulated that the east-vergent western Tajik FTB is part of the greater Tian Shan orogenic system, distinct from the eastern Tajik FTB whose shortening is linked to the Pamir, with the Yavan synclinorium being a remnant foreland common to both fold-thrust systems; again—at least at present—the west-directed rates indicate the detachment of the entire Tajik FTB as part of the outward-growing Pamir orogenic system.

The west-directed rates decay away from the Pamir: Figure 3a shows—in average—higher westward displacements in the part of the Tajik FTB adjacent to the Pamir than away from it. Cross-sections A, B and C in Figures 4a and 4b illustrate this pattern (envelope ‘A’ in the horizontal displacement profiles), while in the southernmost cross-section D this trend is not convincing. We interpret this decrease by the gradual dissipation of the west-directed motion across the FTB-internal, salt-rooted thrusts and folds; however, this absorption of displacement by FTB-internal structures is subordinate to the coherent westward displacement of the whole Tajik FTB. The rates decrease and become less systematic toward south (cross-sections A–C vs. D; Figures 4a and 4b), suggesting active, northward-increasing, anti-clockwise vertical-axis rotations in the Tajik FTB, in agreement with the sense of past rotations evidenced by paleomagnetic data (Pozzi & Feinberg, 1991; Thomas et al., 1994).

In detail, the horizontal displacement profiles often show a saw-blade pattern (Figures 4a and 4b). These short-wavelength perturbations stand out across the Kafirnigan anticlinorium, where positive spikes—reaching up to 10 mm/yr above the regional background—are centered over scarp slopes of east-facing hogback ridges (“E” markers placed over the horizontal displacement profiles in cross-section B and C; Figures 4a and 4b). Figure 6a highlights these short-wavelength anomalies in a high-pass filtered map of horizontal rates that suppresses the regional component: the east-facing scarp slopes (“E” markers) show narrow but pronounced positive, the west-facing slopes negative, albeit less pronounced horizontal displacement anomalies. The divisions between the local positive and negative anomalies follow the crests of the topographic ridges, suggesting divergent ground motions across the ridge crests. We interpret the short-wavelength saw-blade patterns—superimposed on the regional displacement profiles—as related to gravitationally induced mass movements (slope sagging or creep) and rule out topographic artifacts, as these perturbations also vary along elevation isolines. Due to the homoclinal structure of the hogback ridges in the Kafirnigan anticlinorium, the east-facing scarp slopes incise older strata, including mass-movement prone Cenomanian-Campanian shale, marl, limestone, and evaporites, while the west-facing ones follow in general sandstone- and conglomerate-dominated Oligocene-Neogene strata with less mass-movement susceptibility; this likely causes the faster ground motion on eastern than western slopes. Figure 6b provides structural evidence for northwest-directed mass movement, albeit without age control: along a steeply west-dipping slope in the ~NW-dipping strata of the Karshi anticline—east of the Babatag anticline, an Upper Cretaceous shale-gypsum sequence shows dominantly ~NW-directed normal faulting, with the fault planes, shear zones, and numerous tension gashes infiltrated/lubricated by gypsum.

Across the frontal anticline of the Vakhsh anticlinorium, where the hogback ridges face west due to the change of the structural polarity across the Yavan synclinorium, this relationship seems to be reversed: there, the west-facing scarp slopes (“W” markers in cross-sections B and C of Figures 4a, 4b and 6a) correlate with negative displacement spikes. This indicates that a local west-directed displacement component adds up to the regional displacement. We propose the same explanation as for the Kafirnigan anticlinorium, that is, variable susceptibility of the slopes to mass movements; however, the relationship is more diffuse in the Vakhsh than in the Kafirnigan anticlinorium, possibly due to the complex surface geology, in particular the presence of incised hanging-wall anticlines.

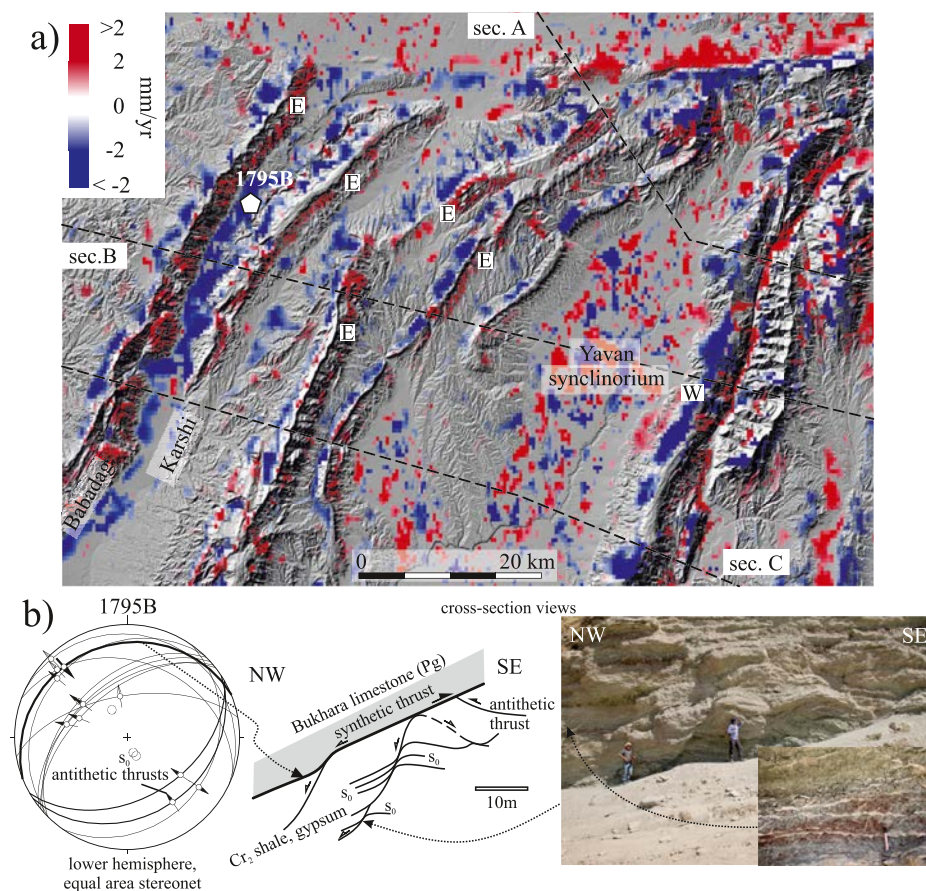


Figure 6. High-pass filtered horizontal displacement map that suppresses the regional component for the northern part of the Kafirigan anticlinorium superposed over a shaded relief map. Kernel size is 7 pixels, that is, ~ 2800 m. The east-facing scarp slopes of east-facing hogback ridges (“E” markers) show narrow but pronounced positive, the west-facing scarp slopes negative, less pronounced horizontal displacement anomalies. Sign change follows the crests of the topographic hogback ridges, suggesting divergent ground motions. These short-wavelength patterns—superimposed on the regional displacement profiles—are likely related to active gravitationally induced mass movements. (b) Structural evidence for NW-directed mass movement: along a steeply west-dipping slope in the NW-dipping strata of the Karshi anticline (site 1795B), an Upper Cretaceous shale-gypsum sequence shows dominantly west-directed normal faulting, with the faults planes and numerous tension gashes infiltrated by gypsum. See text for discussion.

An abrupt ~ 5 mm/yr change in the east rates occurs across the Ilyak fault and the Babatag thrust (Figures 2a, 3a, 4a and 5). The Babatag thrust accommodates an abrupt arrest of the Tajik FTB’s westward motion. It is the most prominent structure of the Tajik FTB in terms of the amount of shortening with total displacement exceeding 20 km over the past ~ 12 Ma in its northern segment; total displacement drops to ~ 10 km in the south (Gagała et al., 2020). The horizontal velocity contrast across this thrust is ~ 5 mm/yr all along strike, although the velocity gradient in the north (cross-sections B and C; Figures 4a and 4b) is higher than in the south (cross-section D). The absolute numbers indicate a passive hanging wall and actively underthrusting footwall. The dip of the Babatag thrust—constrained by boreholes—is $\sim 15^\circ$ (Gagała et al., 2020), hence, the horizontal underthrusting at ~ 5 mm/yr should resolve in ~ 1.3 mm/yr vertical displacement of the hanging wall; such an uplift anomaly is not evident, probably due to its low value compared to the noise. Recent activity of the Babatag thrust may independently be indicated by geomorphology: Figure S12 in Supporting Information S1 shows a series of 500-m-wide swath profiles along selected stream trunks. Most of the profiles display knickpoints, possibly indicating topographic perturbations due to slip along the Babatag thrust; the most affected stream profiles (2, 3, 5 in Figure S12 in Supporting Information S1) face an exposed portion of the Babatag thrust where it overrides Quaternary alluvia.

However, due to the resolution of the current-state of geologic mapping in this area (scale 1:200,000), we cannot assess the effect of lithological changes on the position of the knickpoints in detail.

Cross-section A in Figure 4a shows and Figure 5 details the transition of the Tajik FTB to the Dushanbe trough, which is involved in the moderate \sim N–S shortening of the Tian Shan to the north (Gagała et al., 2020; Käbner et al., 2016). Figure 5 shows the structures, seismicity, and east-rate changes across the Ilyak fault southeast of Dushanbe, where the fault exhibits a horizontal rate change within a corridor of ≤ 4 km. In an elastic screw dislocation model, 50% of the fault's relative motion should occur in a corridor of twice its locking depth (Savage & Burford, 1973); this would suggest that the fault is locked at < 1 km depth, if not—given the spatial sampling of ~ 350 , respectively ~ 450 m and the strong filtering of the original interferograms—freely creeping as suggested by InSAR LOS rate maps produced by higher spatial sampling (Wilkinson et al., 2021). Dextral slip varies along strike and decreases from ~ 10 mm/yr in the east to ~ 5 mm/yr in the west (Figures 5a and 5b). Seismicity is sparse except for an area ~ 20 -km west of Dushanbe, where the focal mechanisms suggest dextral shear (Figure 5a; Kufner et al., 2018). This is where the fault changes strike and several thrusts of the Kafirnigan anticlinorium enter the Ilyak fault, forming transpressive shear lenses, imbricating Lower Cretaceous to Pliocene rocks.

We have no direct structural information on the Ilyak fault, mostly due its strong anthropogenic overprint. The data at the three sites shown in Figure 5c characterize the northern edge of the Dushanbe trough and the Vakhsh anticlinorium south and north of the Ilyak fault, respectively. Pure top-to-south thrusting emplaced the crystalline basement of the Tian Shan on Cretaceous limestone of the Tajik basin at station 1893A at the northern rim of the Dushanbe trough; the age of thrusting is unknown but younger than ~ 10 Ma (Käbner et al., 2016). The lack of a strike-slip signal confirms that the band of westward displacement signal, coinciding with a series of thrusts farther east, is a radar frame artifact (marker “3” in Figures 2a and 5a). The \sim NE-striking fault east of Dushanbe, well-expressed topographically and forming a clear boundary between agricultural and pastoral land, appears to accommodate west-directed rates of up to 5 mm/yr, highlighting FTB-internal deformation. The two sites (Figure 5c) in the Vakhsh anticlinorium south of the Ilyak fault characterize that part of the Tajik FTB where the overall \sim N-striking thrusts progressively bend into the Ilyak fault zone. Characteristically, the thrusts have dextral-transpressive top-to-(N)NW kinematics; these faults accommodate horizontal rate changes of a few mm/yr. Our data neither support nor disprove the hypothesis that the 1907 $M_s 7.6 \pm 0.3$ Kharatag earthquake occurred on a locked fault ~ 100 km west of Dushanbe (Figure 1a; Kondorskaya & Shebalin, 1982).

An obvious but small active structure is a \sim N-striking fault south of the conjunction of Vakhsh, Panj, and Kunduz rivers that exhibits frequent seismicity and where the hanging wall exhibits increased west-directed motion (marker “h” in Figures 3a and 3b). Its surface trace reaches a length of ~ 15 km but may be connected with a similar structure north of the Amu Darya, also hosting a cluster of seismicity and two focal mechanism solutions that indicate slip along \sim N-striking sub-horizontal planes (Kufner et al., 2018). The original time-series of a pixel selected in the hanging wall captured about ~ 3 cm of slip toward ascending LOS after a 2017, January 9, $M_w 5.2$ earthquake (event 201701090559A, Ekström et al., 2012; Figure S5j in Supporting Information S1). Our kinematic observations agree with the double couple solution from the Global Centroid Moment Tensor catalog that reports thrusting on a $\sim 46^\circ$ -dipping plane on a \sim SSE-striking fault (marked in orange and labeled by magnitude; Figure 3). The epicenter, however, is ~ 15 km west of the cluster of earthquakes (Kufner et al., 2018). We consider the structure to be part of the southernmost Kafirnigan anticlinorium, where it bends from a \sim N to a \sim SE strike, marking the southern margin of the Tajik FTB.

Extremely rapid westward motion occurs west of the Darvaz fault zone, at the eastern erosional edge of the Tajik FTB, where westward rates reach 16–26 mm/yr (marker “c” in Figures 2a and 2e; markers “I” in Figure 4a); these high rates can be observed from the Peter I. Range in the north all the way to west of the Kokcha river in Badakhshan in the south, interrupted by a relatively stable area and with only locally retrievable signal along the Panj valley. Vertical uplift rates also increase toward the Darvaz fault reaching 10–17 mm/yr (marker “d” in Figure 2b; envelopes B in Figures 4a and 4b; see Section 4.2). The area of rapid uplift coincides with high topography, developed in often weakly consolidated Neogene coarse-grained terrestrial strata (Figure 4, topographic swath profiles). From our uncertainty analyses (Figures S3, S4, S8, S10, and S11 in Supporting Information S1), we can exclude atmospheric or near-surface contributions to these rates, thus they are of tectonic origin. Both the high horizontal rates and the Pamir-ward—probably temporarily—increase of the vertical uplift rates support the earlier given interpretation (Section 4.2) of a tectonic stack above a ramp, caused by ongoing indentation of the leading edge of the Pamir below this marginal part of the Tajik depression, resulting in a passive roof uplift; the

temporary increase possibly correlates in time with the $M_w 7.2/7.5$ Sarez/slab break-off earthquakes (Figure S5a and S5b in Supporting Information S1). The rapid westward motion and the uplift, however, appear inconsistent with the modern sinistral kinematics of the Darvaz fault (Kufner et al., 2018; Metzger et al., 2020). We favor an interpretation of slip partitioning, with top-to-WNW thrusting of the Pamir's buried leading edge being kinematically decoupled by the sinistral Darvaz fault from the Pamir hinterland. We envision a similar displacement partitioning as described for the deformation at the northern edge of the Pamir, east of the Alai valley (Section 4.2): there, dominant northward motion is accommodated by the large thrusts of the Pamir Thrust System (with the recent Nura and Sary-Tash earthquakes) and subordinate dextral strike-slip faults, the Muji fault and the Kyzylart transfer zone (with the recent Muji earthquake), that accommodate the westward escape of the Pamir. In this scenario, the thrusts and strike-slip faults at the eastern edge of the Tajik FTB would partition deformation in northward motion along the Darvaz fault zone (and little-studied parallel faults in the western Pamir of Badakhshan) and westward motion along the thrusts.

If significant, the westward increase of the horizontal rates west of the Darvaz fault zone (marker “c” in Figures 2a and 2e) would imply ongoing extension along the eastern border of the displacement anomaly and concomitant shortening along its western border, a pattern typical for gravity-driven deformation. Past extension is indeed evidenced by likely Neogene graben fills in the Darvaz fault zone (Figure 2e; Gagala et al., 2020), but we are lacking structural and geomorphic data to confirm that such a process is operating today. We interpret the eastern edge of the Tajik FTB as the western margin of the province with strike-slip and normal fault focal mechanisms that indicate ~E–W extension across the western Pamir (Schurr et al., 2014). The westward increasing rates may indicate the zone where the crust of the topographically high western Pamir Plateau acquires a component of westward gravitational sliding being transferred from the crustal ramp to the salt-décollement of the Tajik FTB.

There is a conspicuous westward horizontal rate increase of up to 7 mm/yr across a ~NNE-trending watershed between the Panj and the Kokcha rivers that seems to be a true kinematic signal (marker “j” in Figures 2a, 2e and 3a); toward east, rates increase again to ~8 mm/a westward movement (southern extension of marker “c” in Figures 2a and 2e), which we interpreted above as due to a component of westward gravitational sliding along the western margin of the Pamir Plateau. The boundary of increased westward motion at marker “j” coincides with the transition from the west-vergent thrust-folds with thick Neogene hanging-wall strata to the area in the southeastern Tajik FTB that is governed by salt-tectonics (marker “H” in cross-section D of Figure 4b). The box-shaped antiform with a >25-km wavelength, cored by up to 5-km-thick evaporites and a salt diapir at its western tip west of marker “H”, may indicate a zone of enhanced westward flow feeding the various thrust detachment folds with thick evaporite cores farther west. This indicates that parts of the buried salt structures of the southeastern Tajik FTB—besides the Hoja Mumin salt fountain—are active; the strong anthropogenic overprint prohibits an interpretation of the vertical displacements but as in the area between the Nurak reservoir and Hoja Mumin salt fountain, the subsidence signal features a distinct, patchy pattern.

5. Conclusions

Our research shows that interferometric rate-map creation for an entire orogenic segment is challenging given the extreme changes in—for example—topography, precipitation, and vegetation. Aided by the high velocities at the western margin of the India-Asia collision zone, our rate maps offer insights into the horizontal and vertical displacement field that pointwise sampling methods (e.g., GNSS) cannot provide. Combined with seismicity and—in particular—geologic and thermochronologic data, it provides an efficient approach to integrate the short- and long-term rate observations into a detailed orogenic evolution.

The interferometric rate maps of the greater Pamir area exhibit large-scale tectonic features, ground subsidence due to water level changes, salt tectonics, and mass movements. Rate interpretation is limited by data sparsity of the underlying interferometric network in time and space. Single interferograms of poor quality—containing unwrapping errors across disconnected regions, for example—might significantly influence the 13 derived relative rate maps in LOS. The GNSS data play a key role to correctly tie the rate maps to a supra-regional, Eurasian-fixed reference frame and the decomposition of the LOS rates into east and vertical rates, particularly for long-wavelength signals. Our GNSS data quality is somewhat limited, as the database contains only horizontal rates, derived from repeated, annual surveys in difficult terrain and confined by topography. The temporal resolution and accuracy of spatio-temporally filtered InSAR time-series (in LOS) nearly equals daily GNSS solutions

and are able to reproduce ephemeral and seasonal processes. We discussed the most conspicuous tectonic and anthropogenic features, and linked them to the seismicity, and the geologic structures formed over the last ~12 Ma.

The displacement-rate maps highlight the 3-D geometry of large parts of the northwestern orogenic margin of the India-Asia collision zone, with crustal material flowing laterally (westward) out of the N-S convergence zone. The west-directed lateral extrusion rates increase from east to west from the eastern to the western Pamir and decrease from ~20 to 5 mm/yr westward across the Tajik fold-thrust belt (Tajik FTB), dissipating over the salt-rooted structures. On the first-order, the modern shortening rates across the Tajik FTB (20–5 mm/yr) correspond to the 12–8 mm/yr long-term shortening rates (148–93 km shortening over 12 Myr) in the north-central and southern Tajik FTB, determined from line-length restoration and thermochronology. Characteristically, the modern westward rates are not affected by the vergence of the Tajik FTB structures, in particular the Yavan synclinorium—the zone of vergence change; therefore, the entire Tajik FTB is detached from its original substratum. The modern kinematics thus shows that the Tajik FTB is a depression-wide, thin-skinned belt developed above an evaporitic décollement, whose evolution is governed by the westward growth of the Pamir orocline. A short-wavelength saw-blade pattern—superimposed on the regional horizontal displacement profiles—is interpreted as related to mass movements on steeply dipping slopes of structurally controlled hogback ridges.

Abrupt ~6 mm/yr changes in the horizontal rates occur across the kinematically linked dextral Ilyak strike-slip fault bounding the Tajik FTB to the north and the Babatag thrust, the major thrust of the FTB, located far west in the belt. The dextral slip or creep rates on the Ilyak fault are of 5–10 mm/yr, decreasing toward west; the locking depth of the fault is ≤ 1 km.

The vertical and horizontal rates of the southeastern Tajik FTB are laterally diverse with a distinct, patchy displacement signal, in particular in the region with salt tectonics, where upright detachment anticlines and bivergent thrust sheets pointing at an unconfined detachment. The highest velocities occur at the Hoja Mumin salt fountain, where we observed local uplift of ~50 mm/yr at its top, surrounded by up to ~120 mm/yr of subsidence and lateral outflow of ~350 mm/yr to the west and ~170 mm/yr to the east.

The vertical rate map outlines stripes with >15 mm/yr subsidence as the most outstanding feature of the Tajik depression; the strongest subsidence signal follows the major river valleys of the Tajik depression, which host intense agriculture. The subsidence is caused by a combination of a bias related to soil-moisture changes (slow dehumidification) and probably water extraction for the extensive irrigation. In addition, we observed strong uplift of 10–17 mm/yr in the western Pamir and the easternmost Tajik FTB where its eastern erosional edge is cut by the broad Darvaz fault zone. Both the high horizontal rates and the Pamir-ward increase of the vertical uplift rates support the existence of a crustal-scale antiform above a ramp caused by ongoing indentation of the leading edge of the Pamir below this marginal part of the Tajik depression, resulting in a passive roof uplift.

Further interferometric rate studies of high relevance in the Tajik FTB could address the anthropogenic impact on the vertical rates and detail the recent activity in a classic salt-tectonic province. The provided rate maps should be a starting point for this research.

Data Availability Statement

Qi Ou advised us on how to tie multiple InSAR rate maps to GNSS data. Some figures were created using GMT (Wessel et al., 2013) and fair data-representation colormaps (Crameri, 2020). LiCS interferograms (Looking into the Continents from Space, <https://comet.nerc.ac.uk/comet-lics-portal/>) contain modified Copernicus Sentinel data analyzed by COMET, the Centre for the Observation and Modelling of Earthquakes, Volcanoes and Tectonics, using JASMIN, the UK's collaborative data analysis environment (<http://jasmin.ac.uk>). Atmospheric phase delay maps were provided by the Generic Atmospheric Correction Online Service for InSAR (<http://www.gacos.net>). GNSS rate tables are published as mentioned in the text. The individual and the final, decomposed rate maps and uncertainties are provided in Metzger, Lazecky, and Maghsoudi (2021).

Acknowledgments

Funded by the Helmholtz Center, German Research Center for Geosciences, Potsdam, the German Research Council (DFG) grant RA 442/40, and the German Ministry of Science and Education within the CaTeNA project (support 3G0878A). We thank Rishav Mallick and an anonymous reviewer for their suggestions on how to improve the manuscript. Open access funding enabled and organized by Projekt DEAL.

References

- Abdulhameed, S., Ratschbacher, L., Jonckheere, R., Gagala, L., Enkelmann, E., Käfner, A., et al. (2020). Tajik basin and Southwestern Tian Shan, Northwestern India-Asia collision zone: 2. Timing of basin inversion, Tian Shan mountain building, and relation to Pamir-Plateau advance and deep India-Asia indentation. *Tectonics*, 39(5), e2019TC005873. <https://doi.org/10.1029/2019TC005873>
- Altamimi, Z., Métivier, L., Rebischung, P., Rouby, H., & Collilieux, X. (2017). ITRF2014 plate motion model. *Geophysical Journal International*, 209(3), 1906–1912. <https://doi.org/10.1093/gji/ggx136>
- Ansari, H., De Zan, F., & Parizzi, A. (2021). Study of systematic bias in measuring surface deformation with SAR interferometry. *IEEE Transactions on Geoscience and Remote Sensing*, 59(2), 1285–1301. <https://doi.org/10.1109/TGRS.2020.3003421>
- Bekker, Y. A. (1996). Tectonics of the Afghan–Tadjik depression (russ.). *Geotektonika*, 30(1), 76–82.
- Bie, L., Hicks, S., Garth, T., Gonzalez, P., & Rietbrock, A. (2018). “Two go together”: Near-simultaneous moment release of two asperities during the 2016 M_w 6.6 Muji, China earthquake. *Earth and Planetary Science Letters*, 491, 34–42. <https://doi.org/10.1016/j.epsl.2018.03.033>
- Biggs, J., Wright, T., Lu, Z., & Parsons, B. (2007). Multi-interferogram method for measuring interseismic deformation: Denali Fault, Alaska. *Geophysical Journal International*, 170(3), 1165–1179. <https://doi.org/10.1111/j.1365-246X.2007.03415.x>
- Bloch, W., Metzger, S., Schurr, B., Yuan, X., Ratschbacher, L., Reuter, S., et al. (2021). The 2015–2017 Pamir earthquake sequence: Fore-, main-, and aftershocks, seismotectonics and fault interaction. *Earth and Space Science Open Archive*. preprint published on Oct 20, 2021. <https://doi.org/10.1002/essoar.10508392.1>
- Bloch, W., Schurr, B., Yuan, X., Ratschbacher, L., Reuter, S., Kufner, S.-K., et al. (2021). Structure and stress field of the lithosphere between Pamir and Tarim. *Geophysical Research Letters*, 48, e2021GL095413. <https://doi.org/10.1029/2021gl095413>
- Bourgeois, O., Cobbold, P. R., Rouby, D., Thomas, J.-C., & Shein, V. (1997). Least squares restoration of Tertiary thrust sheets in map view, Tajik depression, central Asia. *Journal of Geophysical Research*, 102(B12), 27553–27573. <https://doi.org/10.1029/97JB02477>
- Burtman, V. S., & Molnar, P. (1993). Geological and geophysical evidence for deep subduction of continental crust beneath the Pamir. *Geological Society of America Special Paper*, 281, 1–76. <https://doi.org/10.1130/spe281-pl>
- Cavalié, O., Doin, M.-P., Lasserre, C., & Briole, P. (2007). Ground motion measurement in the Lake Mead area, Nevada, by differential synthetic aperture radar interferometry time series analysis: Probing the lithosphere rheological structure. *Journal of Geophysical Research*, 112(B3), 1–18. <https://doi.org/10.1029/2006JB004344>
- Chapman, J. B., Carrapa, B., Ballato, P., DeCelles, P. G., Worthington, J., Oimahmadov, I., et al. (2017). Intracontinental subduction beneath the Pamir Mountains: Constraints from thermokinematic modeling of shortening in the Tajik fold-and-thrust belt. *GSA Bulletin*, 129(11–12), 1450–1471. <https://doi.org/10.1130/B31730.1>
- Chen, C. W., & Zebker, H. A. (2002). Phase unwrapping for large SAR interferograms: Statistical segmentation and generalized network models. *IEEE Transactions on Geoscience and Remote Sensing*, 40(8), 1709–1719. <https://doi.org/10.1109/TGRS.2002.802453>
- Cramer, F. (2020). *Scientific color maps (Version 6.0.4)*. <https://doi.org/10.5281/zenodo.4153113>
- De Zan, F., Parizzi, A., Prats-Iraola, P., & López-Dekker, P. (2014). A SAR interferometric model for soil moisture. *IEEE Transactions on Geoscience and Remote Sensing*, 52(1), 418–425. <https://doi.org/10.1109/TGRS.2013.2241069>
- De Zan, F., Zonno, M., & López-Dekker, P. (2015). Phase Inconsistencies and Multiple Scattering in SAR Interferometry. *IEEE Transactions on Geoscience and Remote Sensing*, 53(12), 6608–6616. <https://doi.org/10.1109/TGRS.2015.2444431>
- DeMets, C., Gordon, R. G., Argus, D. F., & Stein, S. (1994). Effect of recent revisions to the geomagnetic reversal time scale on estimates of current plate motions. *Geophysical Research Letters*, 21(20), 2191–2194. <https://doi.org/10.1029/94GL02118>
- Doeblich, J. L., & Wahl, R. R. (Compilers) (2006). *Geological and mineral resource map of Afghanistan; Version 2* (pp. 2006–1038). U.S. Geol. Surv. Open File Rep.
- Doin, M.-P., Lodge, F., Guillaso, S., Jolivet, R., Lasserre, C., Ducret, G., et al. (2011). Presentation of the small baseline NSBAS processing chain on a case example: The Etna deformation monitoring from 2003 to 2010 using Envisat data. In *Proceedings of the ESA Fringe 2011 workshop* (pp. 19–23).
- Dooley, T. P., Jackson, M. P. A., & Hudec, M. R. (2015). Breakout of squeezed stocks: Dispersal of roof fragments, source of extrusive salt and interaction with regional thrust faults. *Basin Research*, 27(1), 3–25. <https://doi.org/10.1111/br.12056>
- Efron, B., & Tibshirani, R. (1986). Bootstrap methods for standard errors, confidence intervals, and other measures of statistical accuracy. *Statistical Science*, 1, 54–75. <https://doi.org/10.1214/ss/1177013815>
- Ekström, G., Nettles, M., & Dziewonski, A. M. (2012). The global CMT project 2004–2010: Centroid-moment tensors for 13,017 earthquakes. *Physics of the Earth and Planetary Interiors*, 200–201, 1–9. <https://doi.org/10.1016/j.pepi.2012.04.002>
- Elliott, A., Elliott, J., Hollingsworth, J., Kulikova, G., Parsons, B., & Walker, R. (2020). Satellite imaging of the 2015 M7.2 earthquake in the central Pamir, Tajikistan, elucidates a sequence of shallow strike-slip ruptures of the Sarez-Karakul fault. *Geophysical Journal International*, 221(3), 1696–1718. <https://doi.org/10.1093/gji/ggaa090>
- Evans, S. G., Roberts, N. J., Ischuk, A., Delaney, K. B., Morozova, G. S., & Tutubalina, O. (2009). Landslides triggered by the 1949 Khait earthquake, Tajikistan, and associated loss of life. *Engineering Geology*, 109(3–4), 195–212. <https://doi.org/10.1016/j.enggeo.2009.08.007>
- Farr, T. G., Rosen, P. A., Caro, E., Crippen, R., Duren, R., Hensley, S., et al. (2007). The shuttle radar topography mission. *Review of Geophysics*, 45, RG2004. <https://doi.org/10.1029/2005RG000183>
- Feng, W., Tian, Y., Zhang, Y., Samsonov, S., Almeida, R., & Liu, P. (2017). A slip gap of the 2016 M_w 6.6 Muji, Xinjiang, China, earthquake inferred from Sentinel-1 TOPS interferometry. *Seismological Research Letters*, 88(4), 1054–1064. <https://doi.org/10.1785/0220170019>
- Fialko, Y., Jin, Z., Zubovich, A., & Schöne, T. (2021). Lithospheric deformation due to the 2015 M7.2 Sarez (Pamir) earthquake constrained by 5 years of space geodetic observations. *Earth and Space Science Open Archive*. Preprint published on Oct 1, 2021. <https://doi.org/10.1002/essoar.10508106.1>
- Funning, G. J., & Garcia, A. (2019). A systematic study of earthquake detectability using Sentinel-1 Interferometric Wide-Swath data. *Geophysical Journal International*, 216(1), 332–349. Figure S23 in the supporting information. <https://doi.org/10.1093/gji/ggy426>
- Gabriel, A. K., Goldstein, R. M., & Zebker, H. A. (1989). Mapping small elevation changes over large areas: Differential radar interferometry. *Journal of Geophysical Research*, 94(B7), 9183–9191. <https://doi.org/10.1029/JB094iB07p09183>
- Gagala, L., Ratschbacher, L., Ringenbach, J. C., Kufner, S.-K., Schurr, B., Dedow, R., et al. (2020). Tajik Basin and Southwestern Tian Shan, Northwestern India-Asia collision zone: 1. Structure, kinematics, and salt tectonics in the Tajik fold-and-thrust belt of the Western Foreland of the Pamir. *Tectonics*, 39(5), e2019TC005871. <https://doi.org/10.1029/2019TC005871>
- Goldstein, R. M., & Werner, C. L. (1998). Radar interferogram filtering for geophysical applications. *Geophysical Research Letters*, 25(21), 4035–4038. <https://doi.org/10.1029/1998GL900033>

- He, P., Hetland, E. A., Niemi, N. A., Wang, Q., Wen, Y., & Ding, K. (2018). The 2016 Mw6.5 Nura earthquake in the Trans Alai range, northern Pamir: Possible rupture on a back-thrust fault constrained by Sentinel-1A radar interferometry. *Tectonophysics*, 749, 62–71. <https://doi.org/10.1016/j.tecto.2018.10.025>
- Hooper, A., Segall, P., & Zebker, H. (2007). Persistent scatterer interferometric synthetic aperture radar for crustal deformation analysis, with application to Volcán Alcedo, Galápagos. *Journal of Geophysical Research*, 112(7), 1–21. <https://doi.org/10.1029/2006JB004763>
- Ischuk, A., Bendick, R., Rybin, A., Molnar, P., Khan, S. F., Kuzikov, S., et al. (2013). Kinematics of the Pamir and Hindu Kush regions from GPS geodesy. *Journal of Geophysical Research: Solid Earth*, 118(5), 2408–2416. <https://doi.org/10.1002/jgrb.50185>
- Jepson, G., Glorie, S., Konopelko, D., Gillespie, J., Danišik, M., Evans, N. J., et al. (2018). Thermochronological insights into the structural contact between the Tian Shan and Pamirs, Tajikistan. *Terra Nova*, 30, 95–104. <https://doi.org/10.1111/ter.12313>
- Käbner, A., Ratschbacher, L., Jonckheere, R., Enkelmann, E., Khan, J., Sonntag, B.-L., et al. (2016). Cenozoic intracontinental deformation and exhumation at the northwestern tip of the India-Asia collision—Southwestern Tian Shan, Tajikistan, and Kyrgyzstan. *Tectonics*, 35(9), 2171–2194. <https://doi.org/10.1002/2015TC003897>
- Kondorskaya, N., & N. Shebalin (Eds.), (chief Eds.), (1982). *New catalog of strong earthquakes in the U.S.S.R. From ancient times through 1977, Report SE31* (Vol. 609). World Data Center A for Solid Earth Geophysics.
- Kufner, S.-K., Kakar, N., Bezada, M., Bloch, W., Metzger, S., Yuan, X., et al. (2021). The Hindu Kush slab break-off as revealed by deep structure and crustal deformation. *Nature Communications*, 12, 1685. <https://doi.org/10.1038/s41467-021-21760-w>
- Kufner, S.-K., Schurr, B., Haberland, C., Zhang, Y., Saul, J., Ischuk, A., & Oimahmadov, I. (2017). Zooming into the Hindu Kush slab break-off: A rare glimpse on the terminal stage of subduction. *Earth and Planetary Science Letters*, 461, 127–140. <https://doi.org/10.1016/j.epsl.2016.12.043>
- Kufner, S.-K., Schurr, B., Ratschbacher, L., Murodkulov, S., Abdulhameed, S., Ischuk, A., et al. (2018). Seismotectonics of the Tajik Basin and surrounding mountain ranges. *Tectonics*, 37(8), 2404–2424. <https://doi.org/10.1029/2017TC004812>
- Kufner, S.-K., Schurr, B., Sippl, C., Yuan, X., Ratschbacher, L., son of Mohammad Akbar, A., et al. (2016). Deep India meets deep Asia: Lithospheric indentation, delamination and break-off under Pamir and Hindu Kush (central Asia). *Earth and Planetary Science Letters*, 435, 171–184. <https://doi.org/10.1016/j.epsl.2015.11.046>
- Kulikova, G. (2016). *Source parameters of the major historical earthquakes in the Tien-Shan region from the late 19th to the early 20th century*, PhD Thesis. Potsdam University. <https://publishup.uni-potsdam.de/opus4-ubp/frontdoor/index/index/docId/8837>
- Lazecký, M., Spaans, K., González, P. J., Maghsoudi, Y., Morishita, Y., Albino, F., et al. (2020). LiCSAR: An automatic InSAR tool for measuring and monitoring tectonic and volcanic activity. *Remote Sensing*, 12(15), 2430. <https://doi.org/10.3390/RS12152430>
- Leith, W., & Simpson, D. W. (1986). Earthquakes related to active sail doming near Kulyab, Tadjikistan, USSR. *Geophysical Research Letters*, 13(10), 1019–1022. <https://doi.org/10.1029/GL013i010p01019>
- López-Quiroz, P., Doin, M.-P., Tupin, F., Briole, P., & Nicolas, J. M. (2009). Time series analysis of Mexico City subsidence constrained by radar interferometry. *Journal of Applied Geophysics*, 69, 1–15. <https://doi.org/10.1016/j.jappgeo.2009.02.006>
- Mathey, M., Doin, M.-P., André, P., Walpersdorf, A., Baize, S., & Sue, C. (2021). Spatial heterogeneity of uplift pattern in the Western European Alps revealed by InSAR time series analysis, accepted to *Geophysical Research Letters*, 10.1029/2021GL095744R. *Earth Space Science Open Archive*. <https://doi.org/10.1002/essoar.10507009.1>
- McNab, F., Sloan, R. A., & Walker, R. T. (2019). Simultaneous orthogonal shortening in the Afghan-Tajik Depression. *Geology*, 47(9), 862–866. <https://doi.org/10.1130/G46090.1>
- MDA US BaseVue (2013). *Global land cover data*. available on ESRI ArcGIS Living Atlas. Retrieved from <https://livingatlas.arcgis.com>
- Mechie, J., Yuan, X., Schurr, B., Schneider, F., Sippl, C., Ratschbacher, L., et al. (2012). Crustal and uppermost mantle velocity structure along a profile across the Pamir and southern Tien Shan as derived from project TIPAGE wide-angle seismic data. *Geophysical Journal International*, 188(2), 385–407. <https://doi.org/10.1111/j.1365-246X.2011.05278.x>
- Metzger, S., Ischuk, A., Akhmedov, A., Ilyasova, Z., Moreno, M., Murodkulov, S., & Deng, Z. (2019). *Survey mode GPS data in the West Pamir, Tajikistan, central Asia, 2013–2016*. GFZ Data Services. <https://doi.org/10.5880/GFZ.4.1.2019.007>
- Metzger, S., Ischuk, A., Deng, Z., Ratschbacher, L., Perry, M., Kufner, S.-K., et al. (2020). Dense GNSS profiles across the northwestern tip of the India-Asia collision zone: Triggered slip and westward flow of the Peter the First Range, Pamir, into the Tajik depression. *Tectonics*, 39(2), e2019TC005797. <https://doi.org/10.1029/2019TC005797>
- Metzger, S., Kakar, N., Zubovich, A., Borisov, M., Saif, S., Panjsheri, A. H., et al. (2021). *Survey mode GNSS data, acquired 2014–2019 in the Afghan Hindu Kush and across northern Pamir margin, central Asia*. GFZ Data Services. <https://doi.org/10.5880/GFZ.4.1.2021.003>
- Metzger, S., Lazecký, M., & Maghsoudi, Y. (2021). *High-resolution rate maps from the Tajik basin and the Pamir*. GFZ Data Services. <https://doi.org/10.5880/GFZ.4.1.2021.005>
- Metzger, S., Schurr, B., Ratschbacher, L., Sudhaus, H., Kufner, S.-K., Schöne, T., et al. (2017). The 2015 M_w 7.2 Sarez strike-slip earthquake in the Pamir interior: Response to the underthrusting of India's western promontory. *Tectonics*, 36(11), 2407–2421. <https://doi.org/10.1002/2017TC004581R>
- Mira, N. C., Catalão, J., Nico, G., & Mateus, P. (2021). Soil moisture estimation using atmospherically corrected C-band InSAR data. *IEEE Transactions on Geoscience and Remote Sensing*, 99, 1–9. <https://doi.org/10.1109/TGRS.2021.3109450>
- Mohadjer, S., Bendick, R., Ischuk, A., Kuzikov, S., Kostuk, A., Saydullaev, U., et al. (2010). Partitioning of India-Eurasia convergence in the Pamir-Hindu Kush from GPS measurements. *Geophysical Research Letters*, 37(4), L04305. <https://doi.org/10.1029/2009GL041737>
- Morishita, Y., Lazecký, M., Wright, T. J., Weiss, J. R., Elliott, J. R., & Hooper, A. (2020). LiCSBAS: An open-source InSAR time series analysis package integrated with the LiCSAR automated Sentinel-1 InSAR processor. *Remote Sensing*, 12(3), 5–8. <https://doi.org/10.3390/RS12030424>
- Mukhabbatov, H. M., Zhiltsov, S. S., & Markova, E. A. (2020). Tajikistan water resources and water management issues. In Zonn, I. S., Zhiltsov, S. S., Kostianoy, A. G., & Semenov, A. V. (eds.), *Water resources management in Ventral Asia* (Vol. 105, pp. 111–124), Hdb. Env. Chem. https://doi.org/10.1007/698_2020_602
- Neelmeijer, J., Schöne, T., Dill, R., Klemann, V., & Motagh, M. (2018). Ground deformations around the Toktogul Reservoir, Kyrgyzstan, from Envisat ASAR and Sentinel-1 Data—A case study about the impact of atmospheric corrections on InSAR time series. *Remote Sensing*, 10(3), 462. <https://doi.org/10.3390/rs10030462>
- Nikolaev, V. G. (2002). Afghan-Tajik depression: Architecture of sedimentary cover and evolution. *Russian Journal of Earth Sciences*, 4(6), 399–421. <https://doi.org/10.2205/2002es000106>
- Ou, Q. (2020). *Crustal strain and seismic hazard of the NE Tibetan Plateau*. PhD Thesis, University of Oxford. Retrieved from <https://ora.ox.ac.uk/objects/uuid:139c5ffd-5f50-4ca8-b56f-39da3c91d914>
- Perry, M., Kakar, N., Ischuk, A., Metzger, S., Bendick, R., Molnar, P., & Mohadjer, S. (2018). Little Geodetic evidence for localized Indian subduction in the Pamir-Hindu Kush of central Asia. *Geophysical Research Letters*, 46(1), 109–118. <https://doi.org/10.1029/2018GL080065>

- Pozzi, J. P., & Feinberg, H. (1991). Paleomagnetism in the Tajikistan: Continental shortening of European margin in the Pamirs during Indian Eurasian collision. *Earth and Planetary Science Letters*, 103(1–4), 365–378. [https://doi.org/10.1016/0012-821X\(91\)90173-F](https://doi.org/10.1016/0012-821X(91)90173-F)
- Robinson, A. C., Yin, A., Manning, C. E., Harrison, T. M., Zhang, S.-H., & Wang, X.-F. (2004). Tectonic evolution of the northeastern Pamir: Constraints from the northern portion of the Cenozoic Kongur Shan extensional system, western China. *GSA Bulletin*, 116(7–8), 953–973. <https://doi.org/10.1130/B25375.1>
- Robinson, A. C., Yin, A., Manning, C. E., Harrison, T. M., Zhang, S.-H., & Wang, X.-F. (2007). Cenozoic evolution of the eastern Pamir: Implications for strain-accommodation mechanisms at the western end of the Himalayan-Tibetan orogen. *GSA Bulletin*, 119(7–8), 882–896. <https://doi.org/10.1130/B25981.1>
- Rouyet, L., Lauknes, T. R., Christiansen, H. H., Strand, S. M., & Larsen, Y. (2019). Seasonal dynamics of a permafrost landscape, Adventdalen, Svalbard, investigated by InSAR. *Remote Sensing of Environment*, 231, 111236. <https://doi.org/10.1016/j.rse.2019.111236>
- Rutte, D., Ratschbacher, L., Schneider, S., Stübner, K., Stearns, M. A., Gulzar, M. A., & Hacker, B. R. (2017). Building the Pamir-Tibetan Plateau—Crustal stacking, extensional collapse, and lateral extrusion in the central Pamir: 1. Geometry and kinematics. *Tectonics*, 36(3), 342–384. <https://doi.org/10.1002/2016TC004293>
- Sangha, S., Peltzer, G., Zhang, A., Meng, L., Lian, C., Lundgren, P., & Fielding, E. (2017). Fault geometry of 2015, Mw7.2 Murghab, Tajikistan earthquake controls rupture propagation: Insights from InSAR and seismological data. *Earth and Planetary Science Letters*, 462, 132–141. <https://doi.org/10.1016/j.epsl.2017.01.018>
- Savage, J. C., & Burford, R. O. (1973). Geodetic determination of relative plate motion in central California. *Journal of Geophysical Research*, 78(5), 832–845. <https://doi.org/10.1029/JB078i005p00832>
- Schneider, F. M., Yuan, X., Schurr, B., Mechie, J., Sippl, C., Kufner, S.-K., et al. (2019). The crust in the Pamir: Insights from receiver functions. *Journal of Geophysical Research: Solid Earth*, 124, 9313–9331. <https://doi.org/10.1029/2019JB017765>
- Schurr, B., Ratschbacher, L., Sippl, C., Gloaguen, R., Yuan, X., & Mechie, J. (2014). Seismotectonics of the Pamir. *Tectonics*, 33(80), 1501–1518. <https://doi.org/10.1002/2014TC003576>
- Schwab, M., Ratschbacher, L., Siebel, W., McWilliams, M., Minaev, V., Lutkov, V., et al. (2004). Assembly of the Pamirs: Age and origin of magmatic belts from the southern Tien Shan to the southern Pamirs and their relation to Tibet. *Tectonics*, 23, TC4002. <https://doi.org/10.1029/2003TC001583>
- Sippl, C., Ratschbacher, L., Schurr, B., Krumbiegel, C., Rui, H., Pingren, L., & Abdybachev, U. (2014). The 2008 Nura earthquake sequence at the Pamir-Tian Shan collision zone, southern Kyrgyzstan. *Tectonics*, 33(12), 2382–2399. <https://doi.org/10.1002/2014TC003705>
- Sippl, C., Schurr, B., Yuan, X., Mechie, J., Schneider, F. M., Gadoev, M., et al. (2013). Geometry of the Pamir-Hindu Kush intermediate-depth earthquake zone from local seismic data. *Journal of Geophysical Research: Solid Earth*, 118(4), 1438–1457. <https://doi.org/10.1002/jgrb.50128>
- Sperner, B., & Ratschbacher, L. (1994). A Turbo Pascal program package for graphical presentation and stress analysis of calcite deformation. *Zeitschrift der Deutschen Geologischen Gesellschaft*, 145, 414–423.
- Storchak, D. A., Di Giacomo, D., Bondár, I., Engdahl, E. R., Harris, J., Lee, W. H. K., et al. (2013). Public release of the ISC-GEM global instrumental earthquake catalogue (1900–2009). *Seismological Research Letters*, 84, 810–815. <https://doi.org/10.1785/0220130034>
- Stübner, K., Grin, E., Hidy, A. J., Schaller, M., Gold, R. D., Ratschbacher, L., & Ehlers, T. (2017). Middle and Late Pleistocene glaciations in the southwestern Pamir and their effects on topography. *Earth and Planetary Science Letters*, 466, 181–194. <https://doi.org/10.1016/j.epsl.2017.03.012>
- Stübner, K., Ratschbacher, L., Rutte, D., Stanek, K., Minaev, V., Wiesinger, R., & Gloaguen, R. (2013). The giant Shakh-dara migmatitic gneiss dome, Pamir, India-Asia collision zone, 1. Geometry and kinematics. *Tectonics*, 32, 948–979. <https://doi.org/10.1002/tect.20057>
- Teshebaeva, K., Sudhaus, H., Ehtler, H., Schurr, B., & Roessner, S. (2014). Strain partitioning at the eastern Pamir-Alai revealed through SAR data analysis of the 2008 Nura earthquake. *Geophysical Journal International*, 198(2), 760–774. <https://doi.org/10.1093/gji/ggu158>
- Thomas, J.-C., Chauvin, A., Gapais, D., Bazhenov, M. L., Perroud, H., Cobbold, P. R., & Burtman, V. S. (1994). Paleomagnetic evidence for Cenozoic block rotations in the Tadjik depression (central Asia). *Journal of Geophysical Research*, 99(B8), 15141–15160. <https://doi.org/10.1029/94JB00901>
- Trifonov, V. G. (1978). Late Quaternary tectonic movements of western and central Asia. *GSA Bulletin*, 89(7), 1059–1072. [https://doi.org/10.1130/0016-7606\(1978\)89<1059:lqtmow>2.0.co;2](https://doi.org/10.1130/0016-7606(1978)89<1059:lqtmow>2.0.co;2)
- Vajedian, S., Motagh, M., Wetzel, H.-U., & Teshebaeva, K. (2017). Coupling of Sentinel-1, Sentinel-2 and ALOS-2 to assess coseismic deformation and earthquake-induced landslides following the 26 June, 2016 earthquake in Kyrgyzstan. *Geophysical Research Abstracts*, 19, EGU2017-18464-1.
- Wang, S., Xu, C., Wen, Y., Yin, Z., Jiang, G., & Fang, L. (2017). Slip model for the 25 November 2016 Mw6.6 Aketao earthquake, Western China, revealed by Sentinel-1 and ALOS-2 observations. *Remote Sensing*, 9, 325. <https://doi.org/10.3390/rs9040325>
- Wegmüller, U., & Werner, C. (1997). Gamma SAR processor and interferometry software. *ERS symposium on space at the service of our environment, Florence, Italy*.
- Wegmüller, U., Werner, C., Strozzi, T., Wiesmann, A., Frey, O., & Santoro, M. (2016). Sentinel-1 support in the GAMMA software. *Procedia Computer Science*, 100, 1305–1312. <https://doi.org/10.1016/j.procs.2016.09.246>
- Weiss, J. R., Walters, R. J., Morishita, Y., Wright, T. J., Lazecky, M., Wang, H., et al. (2020). High-resolution surface velocities and strain for Anatolia From Sentinel-1 InSAR and GNSS data. *Geophysical Research Letters*, 47(17), e2020GL087376. <https://doi.org/10.1029/2020GL087376>
- Wessel, P., Smith, W. H. F., Scharroo, R., Luis, J. F., & Wobbe, F. (2013). Generic Mapping Tools: Improved version released. *EOS Transactions AGU*, 94, 409–410. <https://doi.org/10.1002/2013EO450001>
- Wilkinson, R., Daout, S., Parsons, B., Walker, R., Pierce, J., & Ischuk, A. (2021). A time series InSAR study of faulting around Dushanbe (Tajikistan). *Fringe 2021, 11th international workshop on "advances in the science and applications of SAR interferometry and sentinel-1 InSAR"*, 31 May–4 June 2021. Retrieved from <https://www.youtube.com/watch?v=u1-ok689wWw>
- Wright, T. J., Parsons, B. E., & Lu, Z. (2004). Toward mapping surface deformation in three dimensions using InSAR. *Geophysical Research Letters*, 31, L01607. <https://doi.org/10.1029/2003GL018827>
- Yu, C., Li, Z., Penna, N. T., & Crippa, P. (2018). Generic atmospheric correction model for interferometric synthetic aperture radar observations. *Journal of Geophysical Research: Solid Earth*, 123(10), 9202–9222. <https://doi.org/10.1029/2017JB015305>
- Zhan, Z., & Kanamori, H. (2016). Recurring large deep earthquakes in Hindu Kush driven by a sinking slab. *Geophysical Research Letters*, 43(14), 7433–7441. <https://doi.org/10.1002/2016GL069603>
- Zubovich, A. V., Schöne, T., Metzger, S., Mosienko, O., Mukhamediev, S., Sharshbaev, A., & Zech, C. (2016). Tectonic interaction between the Pamir and Tien Shan observed by GPS. *Tectonics*, 35(2), 283–292. <https://doi.org/10.1002/2015TC004055>
- Zubovich, A. V., Wang, X. Q., Scherba, Y. G., Schelochkov, G. G., Reilinger, R., Reigber, C., et al. (2010). GPS velocity field of the Tien Shan and surrounding regions. *Tectonics*, 29, TC6014. <https://doi.org/10.1029/2010TC002772>

3.1.6 The Hindu Kush slab break-off as revealed by deep structure and crustal deformation

Published as: S.-K. Kufner, N. Kakar, W. Bloch, S. Metzger, X. Yuan, J. Mechie, L. Ratschbacher, S. Murodkulov, Z. Deng, B. Schurr (2021), The Hindu Kush slab break-off as revealed by deep structure and crustal deformation, *Nature Communications*, **12**, 1685. doi:[10.1038/s41467-021-21760-w](https://doi.org/10.1038/s41467-021-21760-w)

Supporting information: available online

Scientific application: Using a new tomographic approach, this work tackles the question of the geometry of an ongoing slab break-off underneath the Hindu Kush, to find out whether the downgoing slab is of Indian or Eurasian provenance and how the dynamics at depth are translated into the crustal kinematics.

Methodological advances: This joint inversion of local and remote earthquakes was a multi-disciplinary study. The paper presented the first sGNSS rates and a high-quality crustal earthquake catalog of the remote Hindu Kush.









Individual Contributions: The study was designed and conducted by SK under the guidance of MB. The seismic and geodetic data was collected by NK and SM. The seismic analysis was conducted by SK. with support from WB, XY and JM. The sGNSS data was pre-processed by ZD and analyzed and interpreted by me. The manuscript was written by SK with input from all authors.

ARTICLE


<https://doi.org/10.1038/s41467-021-21760-w>

OPEN

The Hindu Kush slab break-off as revealed by deep structure and crustal deformation

Sofia-Katerina Kufner ^{1,2,7}✉, Najibullah Kakar ^{3,4}, Maximiliano Bezada ², Wasja Bloch ¹,
Sabrina Metzger ¹, Xiaohui Yuan ¹, James Mechie ¹, Lothar Ratschbacher⁵, Shokhrukh Murodkulov⁶,
Zhiguo Deng¹ & Bernd Schurr ¹

Break-off of part of the down-going plate during continental collision occurs due to tensile stresses built-up between the deep and shallow slab, for which buoyancy is increased because of continental-crust subduction. Break-off governs the subsequent orogenic evolution but real-time observations are rare as it happens over geologically short times. Here we present a finite-frequency tomography, based on jointly inverted local and remote earthquakes, for the Hindu Kush in Afghanistan, where slab break-off is ongoing. We interpret our results as crustal subduction on top of a northwards-subducting Indian lithospheric slab, whose penetration depth increases along-strike while thinning and steepening. This implies that break-off is propagating laterally and that the highest lithospheric stretching rates occur during the final pinching-off. In the Hindu Kush crust, earthquakes and geodetic data show a transition from focused to distributed deformation, which we relate to a variable degree of crust-mantle coupling presumably associated with break-off at depth.

¹GFZ German Research Centre for Geosciences, Potsdam, Germany. ²University of Minnesota, Minneapolis, MI, USA. ³Norwegian Afghanistan Committee, Kabul, Afghanistan. ⁴University of Potsdam, Potsdam, Germany. ⁵TU Bergakademie Freiberg, Freiberg, Germany. ⁶Tajik Academy of Sciences, Dushanbe, Tajikistan. ⁷Present address: British Antarctic Survey, Cambridge, United Kingdom. ✉email: sofner@bas.ac.uk

At the closing of a plate tectonic cycle, subduction transitions to continental collision and subducted lithosphere detaches and is recycled into the mantle. This process has a strong influence on the magmatic, tectonic and basin-formation history of an orogen. Understanding the dynamics during the final detachment and linking these deep mantle processes to deformation in the crust are key aspects in understanding mountain-building processes^{1,2}. The fraction and composition of the lithosphere returned into the mantle, in turn, influences the mantle chemical composition and contributes to global plate tectonics³. Yet, much of our understanding of slab detachment hinges on numerical modelling or on geological data of past events as the final pinching-off is supposed to happen ephemerally^{4,5}. The Hindu Kush in Afghanistan, located at the western margin of the India-Asia collision zone (Fig. 1), is one of the few places where an ongoing detachment of lithosphere in a continental setting has been proposed, as frequent seismicity occurs at depths that are unusual for an intracontinental setting (Fig. 1a; 60–300 km depth—intermediate-depth seismicity). At the same time, these earthquakes offer the unique opportunity to

study the deep structure of a mountain range through seismic tomography.

In body-wave tomography, the resolution largely depends on the number of crossing rays in the subsurface and the number and distribution of seismic stations within the study region. A good tool to image large-scale upper mantle structures is teleseismic tomography, which uses earthquakes located outside the study region. Different velocity models derived from teleseismic data exist for the Hindu Kush^{6–10}, consistently showing a high-velocity zone (HVZ) in the upper mantle. These anomalies have been interpreted either as a detaching slab of Indian origin^{6–8,10,11} or as highly thickened, dense lithosphere, foundering drop-like into the more buoyant asthenosphere^{9,12}. Each scenario imposes a distinctive shallow crustal deformation field¹³ and may also influence the temperature and hence velocity structure of the crust in a characteristic way. However, because of the near-vertically incident rays at shallow levels, teleseismic data alone have a low resolution in the crust. Further, only large anomalies in the mantle can be resolved. Ref. ⁶ for instance, used a dense local seismic network (station spacing between 30 and

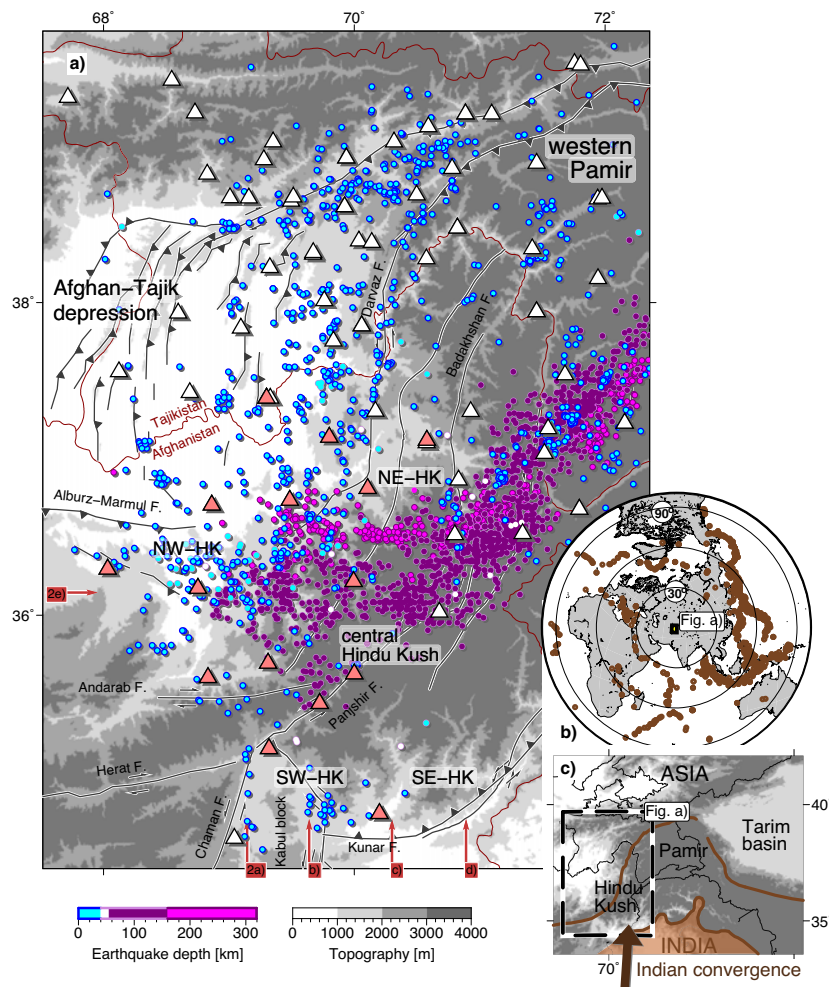


Fig. 1 Geographic setting and data input for seismic tomography. a Tectonic setting, local earthquakes used as inversion input, colour-coded by depth (circles), and seismic stations (triangles) with the campaign stations of the recent Afghanistan network (active 2017–2019) in light red. Faults (in black with white background) simplified after refs. ^{30,44,62} and references therein. Political boundaries in dark red. NE/NW/SE/SW-HK abbreviate north-east/north-west/south-east/south-west Hindu Kush. Starting points of profiles shown in Fig. 2 are highlighted in red. **b** Teleseismic earthquakes used as inversion input. **c** Study region in the context of the Indian-Asian collision zone where India converges at ~ 34 mm/year^{63,64} northward towards Asia. The Cenozoic Indus-Yarlung suture (southern brown line) separates Indian from Asian rocks. The northern brown line represents the late Paleozoic-Triassic suture separating cratonic Asia in the north from the accreted Gondwana terranes in the south.

60 km), but still showed that a ~30 km thick anomaly at 200 km depth would be unresolvable using teleseismic data alone.

In the Hindu Kush, the crust above the mantle velocity anomalies comprises the Cenozoic Afghan-Tajik depression fold-thrust belt in the north and major strike-slip faults in the central Hindu Kush that dissect the crystalline basement rocks (Fig. 1a,^{14–18}). The crust is highly thickened¹⁹ and partly subducting to at least 150 km depth^{20,21}. Neotectonic and geomorphological studies reveal regionally distributed tectonic activity^{16,22} and positioning measurements of the global navigation satellite systems (GNSS)²³ show little horizontal shortening in the north-east Hindu Kush (NE-HK; Fig. 1a). The connection between this crustal deformation field and processes in the upper mantle is largely unknown.

Here, we present new data on crustal deformation and lithospheric-scale seismic images derived from finite-frequency coupled local and teleseismic P-wave tomography, which allow bridging interpretations on crustal vs. mantle deformation. Our approach combines local and teleseismic travel time data with their complementary depth coverage to obtain a well-resolved velocity image of both the crust and mantle. Resolution at depth is further sharpened through the use of sensitivity kernels at different frequency ranges rather than rays in the inversion^{24–26}. We used data recorded by a recent, temporarily operated seismic network in Afghanistan, which covers for the first time the entire Hindu Kush region, overlying the deep mantle anomalies, as well as data from past deployments (Fig. 1a, Supplementary Table 1). Based on the tomograms, shallow earthquake fault plane solutions and new and existing GNSS data, we propose Indian subduction and ongoing slab break-off beneath the Hindu Kush and provide insight into coupling between deep processes and the crustal deformation field.

Results

Seismic imaging and slab model. Our P-wave velocity model (Fig. 2) illuminates the crustal and mantle structure in the Hindu Kush, Afghan-Tajik depression and western Pamir from the surface to up to ~600 km depth. Details on the inversion strategy can be found in the ‘Methods’. The mantle beneath the Hindu Kush is dominated by a prominent HVZ, which forms an east-striking, north-dipping slab (Fig. 2a–d). Its depth penetration, dip angle and thickness change along strike. The HVZ depth extent is shallowest (~350 km down-dip length), most gently dipping (~30° dip) and thickest (~200 km wide) in the west (Fig. 2a). It gradually penetrates deeper and thins in the upper 200 km towards the central Hindu Kush, where the HVZ ultimately reaches 600 km depth and dips nearly vertically or even appears gently overturned (Fig. 2d). The zone of intermediate-depth seismicity overlies the upper part of the HVZ, featuring a similar along-strike steepening and deepening towards the central Hindu Kush. The frequency of large magnitude earthquakes also increases towards the central Hindu Kush. All intermediate-depth earthquakes with magnitude >6.5 that struck the Hindu Kush in the last 30 years belong to the near-vertically dipping and highly thinned portion of the HVZ (Fig. 2c–e).

Compared to global averages²⁷, the Hindu Kush crust is characterized by a high-velocity upper crust (6.0–6.4 km/s; 0–5 km depth) and a domain of low-velocity middle/lower crust (crustal LVZ; 6.1–6.9 km/s; 30–60 km depth; Fig. 2 and Supplementary Fig. 2a). Beneath the central Hindu Kush, a mantle low-velocity zone (LVZ; 7.3–7.6 km/s; 80–160 km depth) extends this middle/lower crustal low-velocity domain down to ~160 km depth. The zone of intermediate-depth seismicity is sandwiched between the HVZ and the overlying LVZ (Fig. 2c, d). East of 71°E, we image a similar pair of high/low-velocity zones

and a deep earthquake zone, separated from the Hindu Kush anomalies (Fig. 2g–j). These anomalies have been attributed to the Pamir deep seismic zone^{6,28,29} and will not be discussed in this paper.

Resolution tests. We conducted resolution tests to evaluate the performance of our combined local and teleseismic tomography approach (hereafter termed ‘joint inversion’) and to verify the robustness of the imaged velocity anomalies (see ‘Methods’ for details on the synthetic inversion procedure). First, the comparison of the joint inversion results for real and synthetic data with either only local or only teleseismic data shows that only the joint inversion can resolve both the crustal and mantle structure satisfactorily in terms of amplitude and geometry (Fig. 3a–c; further comparison in Supplementary Note 1), ultimately offering the least ambiguous basis for a tectonic interpretation.

Second, using the joint inversion approach, we tested different geometric configurations for the Hindu Kush mantle anomaly to discriminate between proposed processes responsible for the loss of mantle lithosphere (Fig. 3d). Subducted Asian lithosphere²³ and subducted Indian lithosphere^{6–8,11} are represented by a south- and north-dipping anomaly, respectively (Fig. 3b, d-i). For the north-dipping scenario, we further tested different slab thicknesses (Fig. 3d-iii, d-iv). A vertical HVZ represents a hypothetical mantle drip^{9,12} (Fig. 3d-ii). In addition, a model with a shallower slab termination and a neutral zone in the upper mantle is designed to evaluate whether vertical smearing strongly affects the inversion results (Fig. 4). All synthetic models feature the same crustal structure. Beneath the Hindu Kush, the crust consists of an upper crustal HVZ (0–15 km depth) and a middle/lower crustal LVZ. This pattern of velocity anomalies is inverted in the Afghan-Tajik depression crust (low-velocity sediments, high-velocity basement; see ref. ³⁰ for detailed interpretation). In addition to the synthetic models of Figs. 3 and 4, a checkerboard test, which is a more generic proxy for ray coverage, is included in Supplementary Fig. 3.

The recovered anomalies in all synthetic test scenarios can be clearly distinguished from each other. However, only the north-dipping slab scenario, which includes a low-velocity zone overlying the slab to ~160 km depth (Fig. 3c) resembles the real data observations. Tests with different slab-thicknesses (Fig. 3d-iii, d-iv) illustrate that the thinning of the slab at 160–250 km depth is not a model artefact and that a slab of ~50 km thickness could still be resolved at upper mantle depths. The robustness of the W-E asymmetric slab-penetration depth is confirmed through the comparison shown in Fig. 4: a slab that terminates at 600 km depth along the entire W-E range covered here and a slab that terminates at ~360 km depth can be distinguished from each other. Thus, we can exclude that the varying depth penetration of the slab in the real data is an artefact of velocity smearing.

We note that the intensity of the recovered anomalies as well as the depth resolution varies locally (Fig. 4c), which is attributed to varying ray coverage and event distribution. Depth resolution is up to 600 km in the west (69°E) and east (71°E), whereas it is shallower in the centre (70°E). However, comparison of the synthetic models (Fig. 4-ii, iii) with the real data (Fig. 4-i) shows that all velocity anomalies introduced in the section above, specifically the tearing of the slab and the successive deepening of the slab, are within the resolution capacity of the tomographic inversion. Furthermore, global tomographies with larger resolution depth do not show a deeper penetration depth of the Hindu Kush slab either^{7,8}.

Interpretation of the lithospheric structure. Based on the real data inversion and synthetic tests, we conclude that the mantle

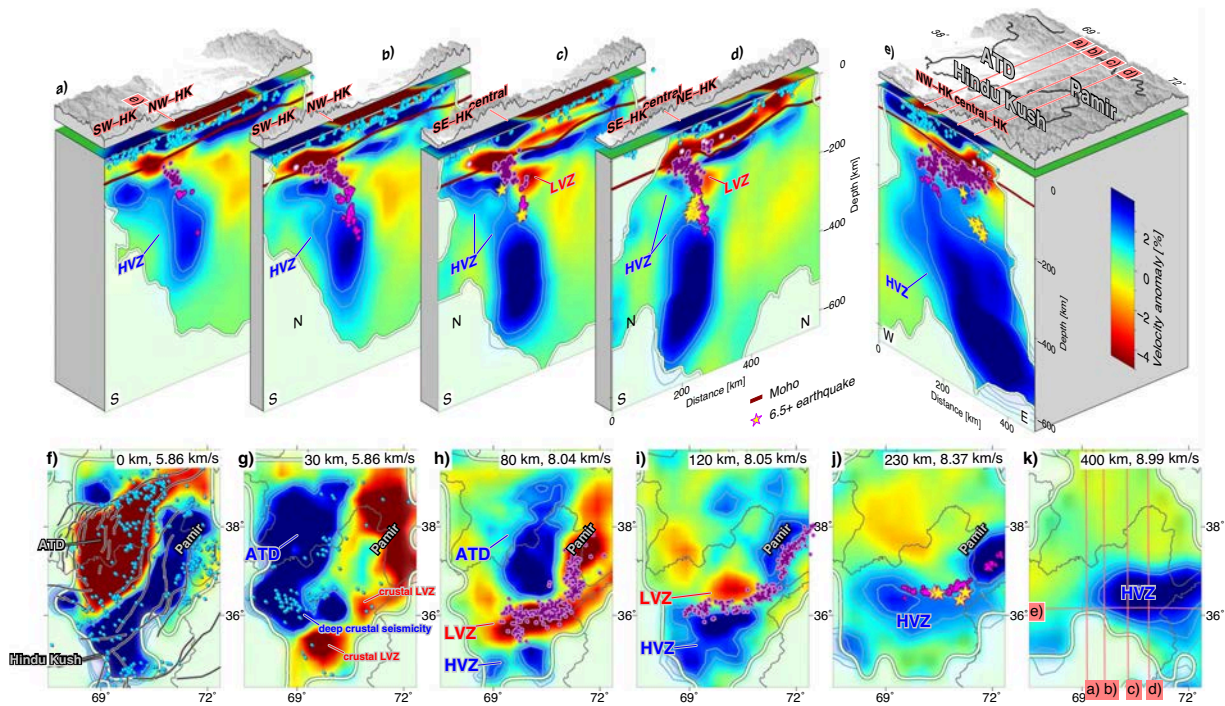


Fig. 2 P-wave velocity tomographic model. a–e Cross-sections with the topography on top; velocity anomaly is colour-coded by the percentage of variation relative to the initial 1D velocity model used in the inversion (Supplementary Fig. 1). The 1.0/1.5/2.0% velocity-anomaly contours are highlighted. The white line marks the resolution limit (see ‘Methods’). The dark red line represents the crust–mantle boundary (Moho) constrained from receiver functions¹⁹. Local earthquakes within 15 km of the profile (circles) are colour-coded with depth as in Fig. 1a. Crustal events include those obtained from manual picking of the events recorded by the recent network in Afghanistan and those used in the inversion (see ‘Methods’). Yellow stars represent magnitude 6.5+ earthquakes from USGS within the last 30 years projected from ± 35 km swaths to account for the larger location uncertainties compared to the local catalogue. LVZ Hindu Kush low-velocity zone, HVZ Hindu Kush high-velocity zone, ATD Afghan–Tajik depression. Other abbreviations as in Fig. 1a. **f–k** Depth sections; section–depth and absolute P-wave velocity at this depth are given in the top right of each plot. Political boundaries in grey, faults in black with a white background as in Fig. 1a. Local earthquakes are plotted from ± 5 km depth swaths in the crust and ± 10 km depth swaths in the mantle. All other features as in panels (a)–(e).

HVZ beneath the Hindu Kush has a slab-like shape, dipping to the north, overlain by a region of focused intermediate-depth seismicity and an LVZ. The HVZ likely represents cold lithosphere subducted or foundered from shallower depths as velocity anomalies in the mantle are mostly due to temperature differences³¹. Together with the focused seismicity and the clear dip direction, this configuration agrees best with the scenario of a north-dipping Indian lithospheric slab beneath the Hindu Kush. The gradual eastward thinning, deepening and steepening of the subducted slab (Fig. 2a–e) then indicates the process of slab break-off^{6,32–34}, with the break-off being most advanced beneath the central Hindu Kush²⁰. Such a configuration explains uniformly down-dip extensional focal mechanisms⁶ and the accumulation of the largest earthquakes during the most advanced stage of break-off due to the largest strain rates occurring in the critically thinned portion of the slab⁴. Thus, the slab-penetration depth of ~ 600 km beneath the central Hindu Kush probably results from slab-stretching and break-off and does not represent the initial subduction length.

As the mantle LVZ overlies the lithospheric slab and geometrically connects with a region of over-thickened crust (as indicated by the seismic velocities resolved here and from receiver functions¹⁹), it likely represents crustal material pulled to mantle depths together with descending mantle lithosphere^{20,21}. This requires coupling between the subducting crust and mantle lithosphere and explains why subduction of crustal material may be feasible despite its buoyancy³⁵. The thickness of the LVZ is less

than the total crustal thickness (~ 20 – 30 km vs. 65 km;¹⁹), suggesting that only a part of the crust is pulled down. These are likely the lower and part of the middle crust as the upper crust has the lowest density and would more strongly resist subduction⁴.

The LVZ, which we interpret as subducted crust terminates at ~ 160 km depth. Nevertheless, below ~ 160 km, subducted lower crust may be present, but eclogitized, making it indistinguishable from subducted mantle lithosphere²⁸. In contrast, middle crust with the andesitic or granitic composition that undergoes high- or ultrahigh-pressure metamorphic mineral transitions retains its buoyancy to ~ 160 km depth^{28,36} and hence should retain its low-density, low-velocity character (e.g., velocities below ~ 7.5 km/s³⁷). Therefore, the middle crust is unlikely to subduct to depths greater than ~ 160 km. Just above the detachment point, the low velocities accumulate in a drop-like volume (Fig. 2c, d). This may represent ascending buoyant middle crust, possibly associated with melt generation while slab break-off is advancing^{5,20}. In such a slab break-off and crustal-subduction scenario, the upper part of the intermediate-depth seismicity (~ 60 – 160 km; purple in Fig. 2) would mostly originate in the subducted crust as the earthquakes are geometrically located mostly within the LVZ overlying the mantle slab (Fig. 2). The earthquakes could then be due to phase transitions (i.e., eclogitization), which may lead to transformational faulting^{38,39}. Isolated events may occur in the mantle lithosphere⁴⁰. By contrast, the deepest, most vigorous seismicity occurs in high-velocity material (160 – 300 km; pink in

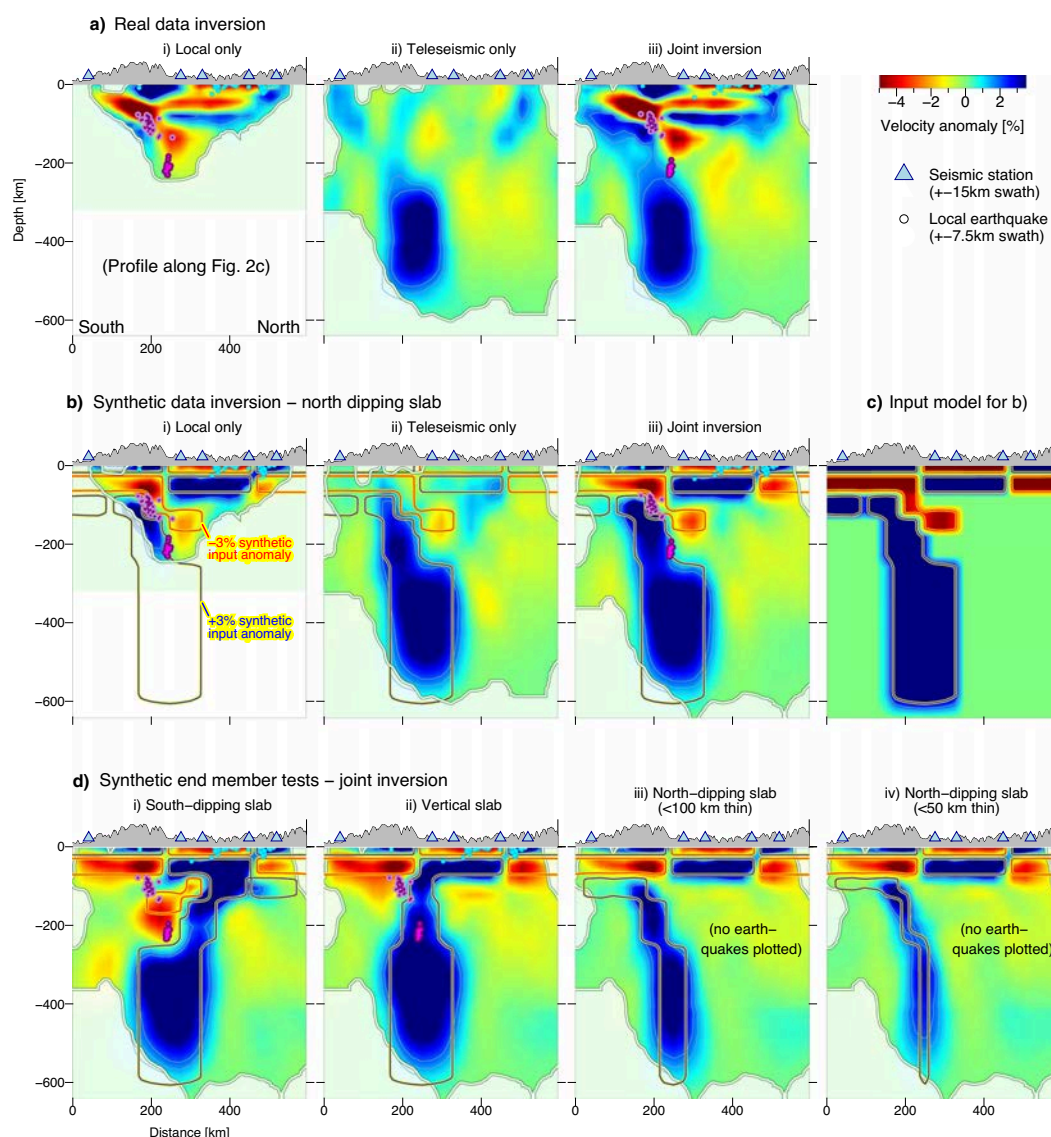


Fig. 3 Data subset inversion and end member synthetic test for mantle anomaly geometry. **a** Real data subset inversion for local only, teleseismic only and joint dataset. **b** Synthetic data subset inversion as in **(a)**. The blue/red contours represent the $\pm 3\%$ velocity anomaly outline of the synthetic input model. **c** The synthetic input model used in **(b)**, featuring a gradual increase of the velocity anomaly from 0 to 5%. **d** Synthetic models based on the combined dataset, testing different end-member scenarios for the geometry of the mantle anomaly. Local earthquakes, resolution limit and topography are plotted as in Fig. 2. All cross-sections are along with the profile of Fig. 2c.

Fig. 2), interpreted as mantle lithosphere. These earthquakes may result directly from slab break-off: under high strain rates^{12,20,34} and relatively cold temperatures strain can localize along zones of reduced grain size due to shear-heating^{41,42}. The resulting earthquakes indicate zones of active deformation.

Crustal structure and deformation field. To illuminate the relation between the slab break-off in the upper mantle and the crustal deformation field, we scrutinized all seismic data from the stations in Afghanistan to identify seismicity in the crust. This evaluation step was conducted manually and generated an event catalogue as complete as possible for our station deployment period (see details on crustal seismicity processing in the ‘Methods’). It extends the event catalogue used for tomography, as the latter is subject to location quality restrictions and declustering (see details in the ‘Methods’).

We found that crustal seismicity shows a zonation in map view relative to the deep mantle slab (Fig. 5a, b). Crustal earthquakes in the central and north-eastern Hindu Kush (NE-HK in Fig. 5b) above the middle/lower crustal low-velocity domain and above the actively detaching part of the slab are sparse to absent. This observation seems to be consistent over longer observation periods as well (Supplementary Fig. 4). Interestingly, despite sparse crustal seismicity, GNSS rates indicate sinistral-transpressional displacement across this region (2.5 ± 1.8 mm/year sinistral displacement in the central Hindu Kush (GNSS1 in Figs. 5b) and 7.3 ± 1.0 mm/year in the NE-HK (GNSS2 in Fig. 5b); see ‘Methods’ for background on GNSS rates). This deformation is likely related to large-scale Indian northward motion, but displacement does not seem to be localized across one single fault. A broader area of deformation is also supported by neotectonic and geomorphological studies, which show tectonic activity to be

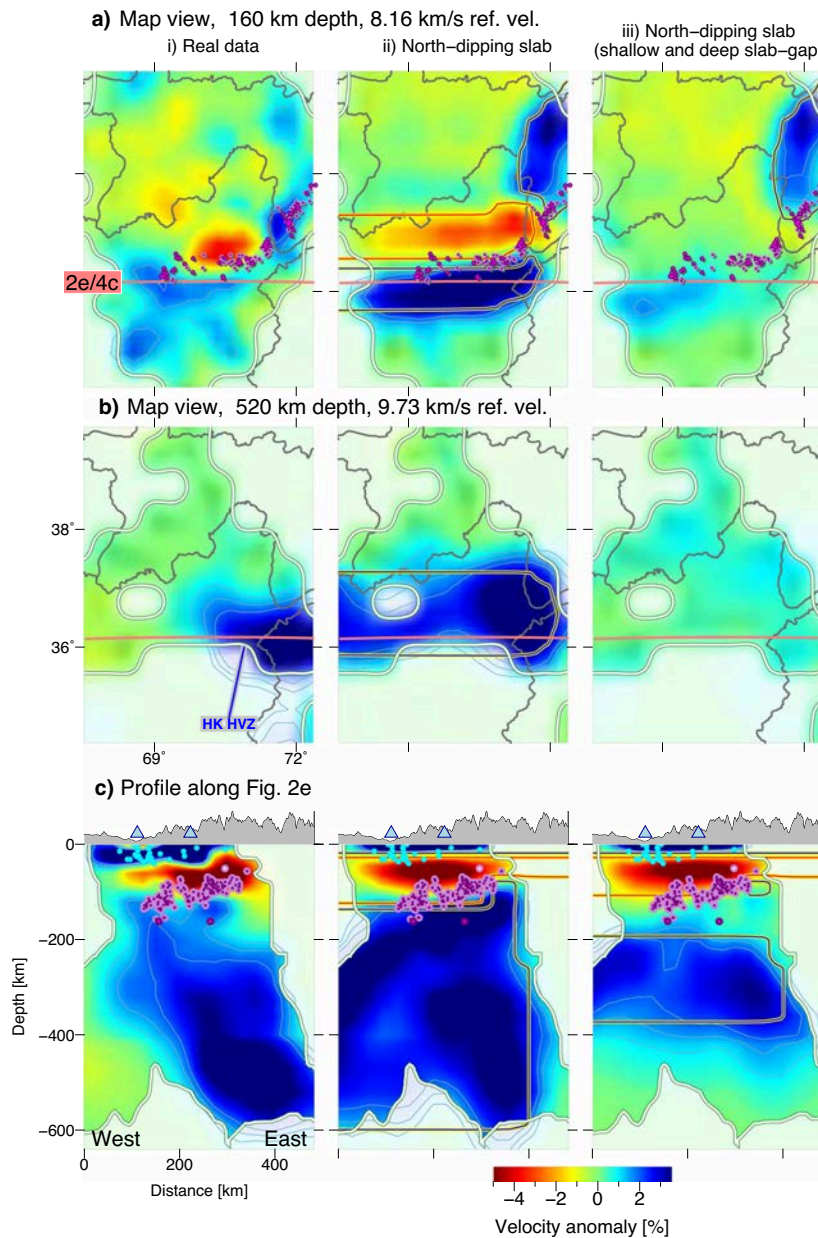


Fig. 4 End member synthetic test for mantle anomaly resolution and depth extent. **a, b** Map view sections. **c** Profile along Fig. 2e. **i** Real data inversion results as in Figs. 2 and 3a for comparison. **ii** North-dipping slab scenario as in Fig. 3b. **iii** A model with similar geometry to (ii) but no mantle high-velocity zone exists between 100 and 180 km depth and deeper than 360 km depth. Local earthquakes, resolution limit and topography are plotted as in Fig. 2.

distributed across the central Hindu Kush^{16,22}. Together with the sparse crustal seismicity, this suggests that distributed, partly aseismic deformation may dominate in the central and NE-HK, overlying the middle/lower crustal low-velocity zone and the detaching part of the slab.

Outside the region of sparse seismicity, crustal earthquakes indicate an overall approximately NW-SE compressional stress regime (Fig. 5b and Supplementary Fig. 5) and cluster mostly along the transitions from low to high topography, i.e., in the north-western Hindu Kush along its margin to the Afghan-Tajik depression (NW-HK in Fig. 5b) and along the southern margin of the eastern Hindu Kush (SE-HK in Fig. 5b). Other clusters occur along strike-slip faults, in particular, the faults rimming the Kabul block (SW-HK in Fig. 5b) and west of the Badakhshan

fault. Domains of prevailing thrusting in the north-western (NW-HK) and south-eastern (SE-HK) foothills of the Hindu Kush are separated by a corridor of sinistral strike-slip deformation, grossly connecting the Chaman fault zone (SW-HK) in the south with the strike-slip faults of the NE-HK in the north. These faults likely accommodate the relative movements between the Pamir and Hindu Kush⁴³. Crustal earthquakes are dominantly shallower than 10 km, which is the typical cut-off depth observed in adjacent crustal blocks^{30,44}. An exception is a cluster of deeper events (up to 30 km depth) occurring at the southern margin of the Afghan-Tajik depression (NW-HK in Fig. 5b). Strikingly, this deep crustal seismicity ceases at the longitude at which we propose slab break-off to initiate at mantle depths.

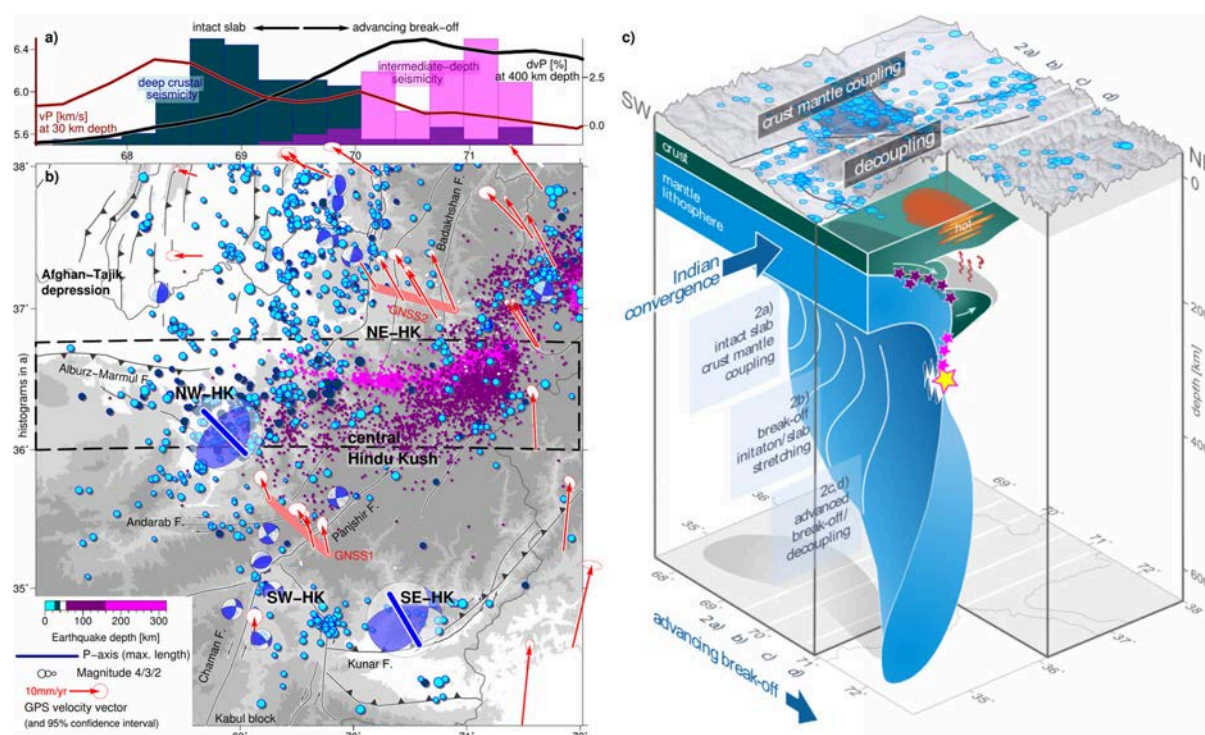


Fig. 5 Crustal event catalogue, GNSS rates and tectonic interpretation. **a** Histograms of deep crustal seismicity (25–40 km depth, 2012–2019; this study), intermediate-depth seismicity related to break-off (160–300 km depth, 2012–2019; this study and ref. 20), and tomography results for P-wave velocity (v_P) at 30 km and P-wave velocity anomaly (dv_P) at 400 km depth along the longitudinal transect highlighted in **(b)**. Positive dv_P values east of 69.5°E indicate the presence of the stretched and tearing slab at depth. This longitudinal range is characterized by middle/lower crustal low-velocities. **b** Crustal event catalogue shallower than 40 km depth, scaled by event magnitude (see Supplementary Fig. 4 for details). Intermediate-depth seismicity (this study and ref. 20) is plotted for orientation. The depth from 40 to -60 km is mostly aseismic. Compression (P)-axes and focal mechanisms of crustal earthquakes from single event solutions (small beach-balls) and strain inversion (large beach balls; see Supplementary Fig. 5 for details). GNSS rates with 95% confidence ellipses relative to Asia, re-evaluated based on refs. 23,59. GNSS1-2 highlight the locations of dense GNSS station profiles across the Hindu Kush. NE/NW/SE/SW-HK, north-east/north-west/south-east/south-west Hindu Kush. **c** Interpretation sketch illustrating the process of slab break-off and the crustal response. The slab experiences stretching and steepening during advancing break-off resulting in a greater penetration depth. Parts of the Indian crust are pulled to depth together with the slab and are buoyantly exhuming (white arrows) providing a heat input to the upper plate crust from below (wavy red arrows). Seismicity related to break-off is highlighted in pink; shallower intermediate-depth seismicity, possibly triggered by phase-transition reactions in the subducted crust, is in purple. The degree of crust-mantle coupling in the upper plate, the Hindu Kush orogen, decreases alongside the advance of slab break-off at depth. This is expressed in a change in crustal deformation style.

Discussion

The most conspicuous features in the crustal seismicity pattern are the clusters of deeply reaching (0–30 km) earthquakes above the western end of the intermediate-depth earthquake zone (NW-HK in Figs. 2 and 5b) and the scarcity of earthquakes in the central Hindu Kush above the middle/lower crustal LVZ and above the region of most intense intermediate-depth seismicity. We suggest that these observations reflect a variable intensity and style of crustal deformation within the Hindu Kush orogen, which changes laterally, potentially dependent on or accelerated by the advancement of slab break-off at depth.

Our tomographic images show an LVZ in the mantle, which we interpret as the subducted continental crust, overlying the high-velocity slab (Fig. 2). Subduction of continental crust requires coupling between the crust of the incoming plate and its mantle lithosphere^{35,45,46}. If the deeper slab sinks faster than the shallow slab, the slab must be extending, ultimately leading to the detachment of the deeper slab^{5,35,46}. Break-off may be preceded by slab steepening and roll-back, which leads to the decoupling at the interface between the down-going and overriding plate that allows for asthenosphere inflow as well as the rise of crust previously attached to the sinking slab^{5,35,46}. Our observations of the

central Hindu Kush slab agree well with this numerically predicted scenario. The LVZ above the mantle slab may represent crust previously attached to the sinking slab, which is now rising (schematically shown in Fig. 5c). The mantle slab shows a thinning and an overturned curvature that matches a geometry expected for north-directed subduction, followed by roll-back and break-off. In contrast, the western Hindu Kush slab does not exhibit thinning or overturning, nor a pronounced LVZ, suggesting that it is not yet notably detaching (Fig. 5c).

The question then arises how crustal deformation in the upper plate, i.e., in the Hindu Kush orogen, is related to these deep mantle processes. Numerical simulations^{47,48} suggest that deformational style in an orogen strongly depends on whether the upper crust is coupled to or decoupled from the underlying mantle. Generally, deformation in the crust is coupled to the mantle motion if the orogen is cold and no decoupling horizon exists. In contrast, heating of the crust, e.g., by continuous shortening or other processes, may produce a low-viscosity layer that decouples crust from the mantle and where the crustal flow is controlled by stresses transmitted horizontally. Upper crustal motion is then only coupled to mantle motion at the flanks of the orogen. Crustal low-velocity zones in orogens, that are mostly

interpreted as regions of hot crust or partial melt, support the concept of crustal decoupling^{28,49,50}.

In the Hindu Kush, we observe a middle/lower crustal LVZ as well, but not along its entire extent: in the western Hindu Kush, the middle crust shows relatively high seismic velocities (Fig. 5a), indicative of cold temperatures. The GNSS rates (this study and ref. 51) indicate an N-S shortening rate of ~10 mm/year between the station north of the Andarab fault in the central Hindu Kush and the stations showing due west displacement in the Afghan-Tajik depression, north of the Alburz-Marmul fault (Fig. 5b). Shortening across the entire Hindu Kush may be significantly larger (Fig. 5b, e.g., comparing GPS rates south of the Kunar fault and within the Tajik basin; disregarding the station in the Kabul block, that has a debated tectonic provenance¹⁸). This shortening appears to be accommodated by the deformation recorded by the deeply reaching thrust earthquakes (up to 30 km depth) in the NW-HK, which may define a retro-wedge. Thus, we suggest that the interior of the crust of the SW-HK remains strong and the ongoing convergence between India and the Afghan-Tajik depression is largely taken up by localized crustal shortening along the margins of the Hindu Kush, i.e., in the NW-HK and the SE-HK.

In the central Hindu Kush, low middle/lower crustal seismic velocities are observed above a domain of thickened crust (Figs. 5a and 2c, d). Therefore, the middle/lower crust probably behaves in a ductile manner causing decoupling from tectonic processes below. This explains why we do not observe deep crustal seismicity in the central Hindu Kush. Upper crustal seismicity is also reduced and clusters mainly at the southern flanks of the orogen. Further, neotectonics and geomorphic data^{16,22} suggest a region of distributed deformation, which matches well with an underlying zone of ductile deformation.

The changeover from presumed upper plate coupling (high-velocity crust and crustal seismic deformation) to decoupling (low-velocity crust and absence of crustal seismic deformation) coincides spatially with the presumed onset of slab break-off at mantle depths (Fig. 5a). This correlation suggests a causal relationship, which may be provided by heat input associated with break-off from below (see the sketch in Fig. 5c). Heating through crustal shortening and thickening alone, as e.g., suggested for the Tibetan crust⁵⁰, seems unlikely given the comparatively smaller size of the Hindu Kush orogen. Furthermore, it would not necessarily explain the variable along-strike crustal structure in the orogen. Instead, processes particular to advanced break-off may provide an additional heat source. The Hindu Kush lower crust could be heated by a partially molten subducted continental crust that is buoyantly exhuming and possibly relaminating to the hanging wall⁵². Both the drop-like LVZ in the mantle and the thick central Hindu Kush crust support such a scenario. In addition, asthenospheric inflow induced by slab roll-back and opening of a slab window maybe another heat source^{5,35,46}. Lastly, partial loss of gravitational force across the rapidly extending^{12,20,34} or in parts already severed slab may further contribute to the observed partitioning of hanging wall deformation. Hence, we suggest that the variable along-strike crustal deformation within the Hindu Kush orogen is influenced by processes induced by the break-off at depth.

Methods

Tomographic model

Input data. Local earthquake phase arrivals and cross-correlated teleseismic P-wave delay times measured at seismic stations from four different temporary deployment periods were integrated into this study (2008–2010, 2012–2014, 2015–2017 and 2017–2019). Together with permanent stations in the greater Pamir-Hindu Kush region, these deployments sum up to a network of 79 stations, interconnected through 19 common stations (either permanent or re-deployed campaign sites),

which were operating in at least two of the four-time periods listed above (Supplementary Table 1, Supplementary Fig. 6).

Teleseismic input data were calculated via waveform cross-correlation at two different central frequencies (1 Hz and 0.5 Hz). Events with a magnitude larger than 5.0 at epicentral distances from 30° to 90° relative to the network centre (69.94°E/37.02°N) were considered. All cross-correlation results were visually inspected, removing noisy or wrongly cross-correlated traces. Local data were assembled through the first onset picking. The P-wave first onset was picked either using a semi-automatic processing chain⁵³ or manually (see Supplementary Table 1 for details). No local rays with epicentral distances greater than 5° or a back-azimuthal gap larger than 210° were included in the inversion. On average, each station has 820 observations (550 local picks and 269 teleseismic delays, respectively; Supplementary Figs. 7a, b). Only stations that have both teleseismic and local picks were included in the analysis. Based on the local earthquake data, tomography models for the stations used here were published for 2008–2010 and 2012–2014 (refs. 20,28; Supplementary Figs. 2b, c). These datasets are included in this study as groomed subsets (see Supplementary Table 1 for details). Events were de-clustered to reduce the total number of earthquakes while maintaining a representative ray-path geometry. Further, de-clustering turned out to be important to avoid introducing artefacts due to a trade-off between the relocation of closely spaced local events and the inversion for velocity anomalies.

A teleseismic tomography was calculated using data from the 2008–2010 and 2012–2014 deployments (ref. 6; Supplementary Fig. 2d). In the model presented here, the data registered by these networks are included but input teleseismic delays were newly derived via cross-correlation and are independent of the previous study. Data associated with the 2017–2019 deployment are used here for the first time.

Inversion procedure and synthetic travel times. We modified the inversion scheme of ref. 26 to calculate a P-wave velocity model. Inversion and 3D ray-tracing were performed in a 715 × 890 km wide study region using approximated Born kernels²⁵ and a graph theory method for ray tracing (software package StingRay^{54,55}). The inversion was performed based on sensitivity kernels surrounding the rays obtained in StingRay. Sensitivity kernels for teleseismic rays were calculated based on the two different filter bands used during cross-correlation for each event (1 Hz and 0.5 Hz central frequency). The local input data were considered to have 1 Hz central frequency. Regularization was achieved through damping and smoothing constraints, which are applied by minimizing the whole model norm and roughness in each iteration. Damped teleseismic event terms and station terms were included in the inversion. Poorly sampled domains in the model space were damped to prevent the creation of artificial anomalies. The quality of sampling of a specific grid node was determined through the hit-quality, a normalized measure for the number of rays crisscrossing the volume that surrounds a model node. After each inversion step, relocation of the local events was implemented by searching for the minimum root mean square travel time between observed and theoretical travel times in a cube and finer sub-cubes around the initial location. Modifications in the inversion procedure compared to ref. 26 included the extension of the ray-tracing grid above zero elevation and the input of absolute local travel times. Both favour a more accurate recovery of the absolute velocity structure in the shallow part of the study region.

We chose a two-step approach for the joint inversion, which yielded the largest data variance reduction for the entire dataset. First, a model based only on local earthquake data was calculated. This model and 3D relocated hypocentres were used as input for a joint inversion. The inversion grid (Supplementary Fig. 1) was designed in spherical coordinates, encompassing all local earthquakes and guided by the station spacing in the more densely covered regions and increased spacing in the external domains. Vertical grid spacing was increased based on ray coverage. Ray tracing was performed on a rectangular grid spanning the same domain with 5 km node spacing. Smaller ray tracing grid spacing did not significantly change the ray-tracing results. The initial 1D P-wave velocity model features regionally adequate crustal velocities including a Moho at 60 km depth²⁸ and standard radial Earth velocities from AK135²⁷ in the mantle (Supplementary Fig. 1b). Input event locations were derived by relocating the entire dataset in subsets in the 1D velocity model specified above in simulps⁵⁶, including both P and S-wave travel times and using a vP/vS ratio of 1.72 obtained from a Wadati-diagram, aiming to obtain the most accurate input locations. For both local and joint inversion, the best set of damping and smoothing parameters was determined from trade-off curves aiming to find the parameter set that yields the best compromise between data and model variance (Supplementary Fig. 8). Local and joint inversions converged after four iterations. The final data variance reduction in the local model was 72%. Data variance reduction of the final joint model, which was terminated after the seventh iteration, was 82%. Station terms are small (~±0.15 s) and show no correlation to topography (Supplementary Fig. 7c). As for the local data only inversion, we relocated the local earthquakes after each joint inversion step, but the mean hypocentre change (0.6 km in depth) is much smaller than during the local inversion (average of 5 km depth change), indicating little change in the shallow structure. For comparison and quality control, we calculated a model based on teleseismic data only, which features the same model geometry as the joint model. In all figures shown herein, the final inversion results are interpolated onto a 5 km grid (horizontally and vertically) based on interpolation among eight surrounding grid nodes⁵⁶.

For quality control and resolution assessment, synthetic tests were performed featuring the same station-event geometry as the real data. Synthetic travel times were calculated in the StingRay software in the study region and TauP (<https://www.seis.sc.edu/taup/>) outside the study region using a finer ray-tracing grid (3 km) than for the inversion. Station elevations were set to zero. Gaussian noise was added to the synthetic travel times (0.1 s standard deviation (std)) and hypocentre locations were disturbed prior to inversion (4 and 2 km std vertically and horizontally, respectively).

Local earthquake processing. Continuous waveform data from the most recent temporary seismic network (TIPTIMON II; 4C; 2017–2019; 15 stations) and 13 nearby permanent stations were scanned using a short time average-long time average trigger. Trigger alerts were associated with possible events using a grid search approach and relocated in hypo71 based on the 1D velocity model of ref. 20. All events shallower than 75 km in this initial event catalogue were taken as a basis for manual P and S wave phase picking. The thus derived crustal event catalogue was relocated in our 3D P-velocity model, including P and S picks (assuming a v_P/v_S ratio of 1.72), using the simulps and Nonlinloc software (<http://alomax.free.fr/nlloc/>) to obtain absolute location errors. We restrict our final earthquake catalogue to events with location errors smaller than 20 km. The final catalogue then contains 472 events shallower than 40 km depth with average horizontal and vertical location errors of 3.2 (std of 2.6) and 4.0 km (std of 2.5; Supplementary Fig. 4c). These are more events than used for the tomography, as only a selected high-quality subset was included in the inversion (see 'Methods'). Local magnitudes (ML) were calculated in Seiscomp3 (<https://www.seiscomp3.org/about.html>) based on the updated events. Catalogue magnitude completeness is $ML \sim 2.3$ (Supplementary Fig. 4b).

We determined fault plane solutions from first motion polarities and S to P amplitude ratios using the HASH software⁵⁷. P polarities were manually read from the unfiltered broadband-integrated vertical displacement seismogram. S to P ratios were obtained from the Cartesian sum of all three traces⁵⁸. We extracted take-off angles and back-azimuths from the 3D velocity model translated into Nonlinloc travel time tables. Only solutions with 8 or more picks, back-azimuthal coverage larger than 180°, and mechanism types that remained stable upon perturbing the input data were included in the final dataset. To further account for model errors in Moho depth, only solutions, whose mechanism type remained stable in 1D velocity models with either a shallow (30 km) or deep (60 km) Moho, were accepted in the final catalogue.

Crustal fault plane solutions were further inverted to estimate the regional stress field using the software slick (<https://www.usgs.gov/software/slick-package>). Slick performs a linear inversion to minimize the number of rotations around an arbitrary axis necessary to rotate the input focal mechanisms to fit a uniform stress tensor. Based on the hypocentre location, we subdivided our data into two sub-regions (Supplementary Fig. 5a) aiming to fulfil the assumption of a uniform stress field. The north-west Hindu Kush (NW-HK) encompasses events between the Andarab and Alburz-Marmul faults (27 available mechanisms). The southern Hindu Kush (SW/SE-HK) includes events at the eastern edge of the Kabul block, along the Panjshir fault and events around the Kunar fault (23 available mechanisms). We accessed the robustness of the solution via a bootstrap test. The data were resampled 500 times while the selected fault slip direction is flipped in 10% of these cases. The spread of the results obtained from bootstrap inversions provides a measure of inversion robustness. Both stress tensors indicate NW-SE compression with the southern Hindu Kush featuring a component of sinistral strike-slip in addition to thrusting (Supplementary Fig. 5 and Fig. 5b).

GNSS rates. We reprocessed the original GNSS survey data of refs. 23,59,51 together with 24 reference stations of the International GNSS service network using the Earth Parameter and Orbit System software⁶⁰. This software accounts for phase centre variations, ocean tide loading, ionospheric, hydrostatic and tropospheric delays. Derived positions were aligned with the International Terrestrial Reference Frame 2014⁶¹. We then removed outliers in the time-series by visual inspection and estimated the linear rates using a least-square approach; uncertainties were scaled by the length of the time-series. The Badakhshan GNSS surveys took place between 2015 and 2018 (GNSS profile 2 in Fig. 5b), the Panjshir surveys between 2016 and 2018 (GNSS profile 1 in Fig. 5b). Minimum displacement rates across the profiles are derived by the rate differences between the outermost profile points, assuming fault strikes of 45°E (Panjshir fault; GNSS profile 1) and 20°E (Badakhshan fault; GNSS profile 2).

Data availability

The data that supports the findings of this study (the velocity model, local earthquake locations, the manually derived crustal earthquake catalogue, focal mechanisms and reprocessed GPS data) are attached as supplementary files to this manuscript. Raw data of the temporary networks used in this study (FDSN codes: 7B 2008–2010, <https://doi.org/10.14470/2O097102>; 6C 2013–2014, <https://doi.org/10.14470/1P7568352842>; 5C 2012–2014, <https://doi.org/10.14470/OP7567352807>; 4C 2017–2019, <https://doi.org/10.14470/9P7562848989>) are archived at the GEOFON Data Centre and can be obtained via the GEOFON website <https://geofon.gfz-potsdam.de/waveform/archive/network.php?ncode=7B&year=2008>, <https://geofon.gfz-potsdam.de/waveform/archive/network.php?ncode=6C&year=2013>, <https://geofon.gfz-potsdam.de/waveform/archive/network.php?ncode=5C&year=2012>, <https://geofon.gfz-potsdam.de/waveform/archive/network.php?ncode=4C&year=2017>. Data of 4C (2017–2019) are restricted until 8/2023 in accordance with GEOFON data policies for temporary networks. Permanent station waveform data can be obtained through the IRIS DMC (<https://ds.iris.edu/SeismiQuery/>). Figures 1–5 show results derived through processing the raw seismic data. Source data are provided with this paper.

Code availability

Software used for the derivation of the crustal earthquake catalogue, including rupture mechanisms, is open source: seiscomp3 (<https://www.seiscomp.de/seiscomp3/>), Nonlinloc (<http://alomax.free.fr/nlloc/>), simulps (e.g., <http://faldersons.net/Software/Simulps/Simulps.html>), HASH (<https://www.usgs.gov/software/hash-12>), slick (www.usgs.gov/software/slick-package), and further software specified in ref. 51. The code for finite-frequency tomography is subject to ongoing development and research and therefore not publicly available but may be accessed upon request. The two sets of ray tracers implemented in the code are open source (www.seis.sc.edu/taup/), respectively available upon request (pages.uoregon.edu/drt/Stingray/_index.html). The Earth Parameters & Orbit System software used for GPS processing has been developed at GFZ and can be used by other institutions after signing mutual agreements.

Received: 8 August 2020; Accepted: 4 February 2021;

Published online: 16 March 2021

References

- Braun, J. The many surface expressions of mantle dynamics. *Nat. Geosci.* (2010) <https://doi.org/10.1038/ngeo1020>.
- Cloetingh, S. & Willett, S. D. Linking deep earth and surface processes. *Eos Trans. Am. Geophys. Union* (2013) <https://doi.org/10.1002/2013eo050002>.
- Magni, V. Crustal recycling evolution. *Nat. Geosci.* (2017) <https://doi.org/10.1038/ngeo3015>.
- Duret, T., Schmalholz, S.M. & Gerya, T.V. Dynamics of slab detachment. *Geochem. Geophys. Geosyst.* (2012) <https://doi.org/10.1029/2011GC004024>.
- Freeburn, R., Bouilhol, P., Maunder, B., Magni, V. & van Hunen, J. Numerical models of the magmatic processes induced by slab breakoff. *Earth Planet. Sci. Lett.* (2017) <https://doi.org/10.1016/j.epsl.2017.09.008>.
- Kufner, S.-K. et al. Deep India meets deep Asia: lithospheric indentation, delamination and break-off under Pamir and Hindu Kush (Central Asia). *Earth Planet. Sci. Lett.* (2016) <https://doi.org/10.1016/j.epsl.2015.11.046>.
- Van Der Voo, R., Spakman, W. & Bijwaard, H. Tethyan subducted slabs under India. *Earth Planet. Sci. Lett.* (1999) [https://doi.org/10.1016/S0012-821X\(99\)00131-4](https://doi.org/10.1016/S0012-821X(99)00131-4).
- Villaseñor, A., Spakman, W. & Engdahl, E.R. Influence of regional travel times in global tomographic models. in EGS-AGU-EUG Joint Assembly April (2003).
- Koulakov, I. High-frequency P and S velocity anomalies in the upper mantle beneath Asia from inversion of worldwide traveltimes data. *J. Geophys. Res. Solid Earth* **116**, 1–22 (2011).
- Negredo, A.M., Replumaz, A., Villaseñor, A. & Guillot, S. Modeling the evolution of continental subduction processes in the Pamir-Hindu Kush region. *Earth Planet. Sci. Lett.* (2007) <https://doi.org/10.1016/j.epsl.2007.04.043>.
- Burtman, V. & Molnar, P. Geological and geophysical evidence for deep subduction of continental crust beneath the Pamir. *Geol. Soc. Am. Spec. Pap.* **281**, 1–78 (1993).
- Molnar, P. & Bendick, R. Seismic moments of intermediate-depth earthquakes beneath the Hindu Kush: active stretching of a blob of sinking thickened mantle lithosphere? *Tectonics* (2019) <https://doi.org/10.1029/2018TC005336>.
- Göğüş, O.H. & Pysklywec, R.N. Near-surface diagnostics of dripping or delaminating lithosphere. *J. Geophys. Res. Solid Earth* (2008) <https://doi.org/10.1029/2007JB005123>.
- Treloar, P.J. & Izatt, C.N. Tectonics of the Himalayan collision between the Indian plate and the Afghan block: a synthesis. *Geol. Soc. Spec. Publ.* (1993) <https://doi.org/10.1144/GSL.SP.1993.074.01.06>.
- Bourgeois, O., Cobbold, P.R., Rouby, D., Thomas, J.C. & Shein, V. Least squares restoration of tertiary thrust sheets in map view, Tajik depression, central Asia. *J. Geophys. Res. B Solid Earth* (1997) <https://doi.org/10.1029/97jb02477>.
- Ruleman, C.A., Crone, A.J., Machette, M.N., Haller, K.M. & Rukstales, K.S. Map and database of probable and possible quaternary faults in Afghanistan. USGS Afghanistan Proj. Prod. No. 150, Open-File Rep. 2007-1103 (2007).
- Käbner, A. et al. Proterozoic-Mesozoic history of the central Asian orogenic belt in the Tajik and southwestern Kyrgyz Tian Shan: U-Pb, 40Ar/39Ar, and

- fission-track geochronology and geochemistry of granitoids. *Bull. Geol. Soc. Am.* (2017) <https://doi.org/10.1130/B31466.1>.
18. Siehl, A. Structural setting and evolution of the Afghan orogenic segment—a review. *Geolog. Soc. Spec. Publ.* (2017). <https://doi.org/10.1144/SP427.8>.
 19. Schneider, F. M. et al. The crust in the Pamir: insights from receiver functions. *J. Geophys. Res. Solid Earth* **124**, (2019).
 20. Kufner, S.-K. et al. Zooming into the Hindu Kush slab break-off: a rare glimpse on the terminal stage of subduction. *Earth Planet. Sci. Lett.* (2017) <https://doi.org/10.1016/j.epsl.2016.12.043>.
 21. Roecker, S.W. Velocity structure of the Pamir–Hindu Kush region: possible evidence of subducted crust. *J. Geophys. Res.* (1982) <https://doi.org/10.1029/JB087iB02p00945>.
 22. Mahmood, S.A. & Gloaguen, R. Appraisal of active tectonics in Hindu Kush: insights from DEM derived geomorphic indices and drainage analysis. *Geosci. Front.* (2012) <https://doi.org/10.1016/j.gsf.2011.12.002>.
 23. Perry, M. et al. Little geotectonic evidence for localized Indian subduction in the Pamir–Hindu Kush of Central Asia. *Geophys. Res. Lett.* (2019) <https://doi.org/10.1029/2018GL080065>.
 24. Dahlen, F.A., Hung, S.H. & Nolet, G. Fréchet kernels for finite-frequency traveltimes-I. *Theory. Geophys. J. Int.* (2000) <https://doi.org/10.1046/j.1365-246X.2000.00070.x>.
 25. Schmandt, B. & Humphreys, E. Complex subduction and small-scale convection revealed by body-wave tomography of the western United States upper mantle. *Earth Planet. Sci. Lett.* (2010) <https://doi.org/10.1016/j.epsl.2010.06.047>.
 26. Bezada, M.J. et al. Evidence for slab rollback in westernmost Mediterranean from improved upper mantle imaging. *Earth Planet. Sci. Lett.* (2013) <https://doi.org/10.1016/j.epsl.2013.02.024>.
 27. Kennett, B.L.N., Engdahl, E.R. & Buland, R. Constraints on seismic velocities in the Earth from traveltimes. *Geophys. J. Int.* (1995) <https://doi.org/10.1111/j.1365-246X.1995.tb03540.x>.
 28. Sippl, C. et al. Deep burial of Asian continental crust beneath the Pamir imaged with local earthquake tomography. *Earth Planet. Sci. Lett.* (2013) <https://doi.org/10.1016/j.epsl.2013.10.013>.
 29. Schneider, F. M. et al. Seismic imaging of subducting continental lower crust beneath the Pamir. *Earth Planet. Sci. Lett.* **375**, 101–112 (2013).
 30. Kufner, S.-K. et al. Seismotectonics of the Tajik basin and surrounding mountain ranges. *Tectonics* (2018) <https://doi.org/10.1029/2017TC004812>.
 31. Sobolev, S.V. et al. Upper mantle temperatures and lithosphere-asthenosphere system beneath the French Massif Central constrained by seismic, gravity, petrologic and thermal observations. *Tectonophysics* (1997) [https://doi.org/10.1016/S0040-1951\(97\)00019-X](https://doi.org/10.1016/S0040-1951(97)00019-X).
 32. Koulikov, I. & Sobolev, S. V. A tomographic image of Indian lithosphere break-off beneath the Pamir-Hindukush region. *Geophys. J. Int.* **164**, 425–440 (2006).
 33. Lister, G., Kennett, B., Richards, S. & Forster, M. Boudinage of a stretching slablet implicated in earthquakes beneath the Hindu Kush. *Nat. Geosci.* **1**, 196–201 (2008).
 34. Zhan, Z. & Kanamori, H. Recurring large deep earthquakes in Hindu Kush driven by a sinking slab. *Geophys. Res. Lett.* (2016) <https://doi.org/10.1002/2016GL069603>.
 35. Duretz, T. & Gerya, T.V. Slab detachment during continental collision: Influence of crustal rheology and interaction with lithospheric delamination. *Tectonophysics* (2013) <https://doi.org/10.1016/j.tecto.2012.12.024>.
 36. Chapman, T., Clarke, G.L. & Daczko, N.R. The role of buoyancy in the fate of ultra-high-pressure eclogite. *Sci. Rep.* (2019) <https://doi.org/10.1038/s41598-019-56475-y>.
 37. Zhao, Z. et al. Delamination and ultra-deep subduction of continental crust: Constraints from elastic wave velocity and density measurement in ultrahigh-pressure metamorphic rocks. *J. Metamorph. Geol.* (2011) <https://doi.org/10.1111/j.1525-1314.2011.00941.x>.
 38. John, T. et al. Generation of intermediate-depth earthquakes by self-localizing thermal runaway. *Nat. Geosci.* (2009) <https://doi.org/10.1038/ngeo419>.
 39. Incel, S. et al. Laboratory earthquakes triggered during eclogitization of lawsonite-bearing blueschist. *Earth Planet. Sci. Lett.* (2017) <https://doi.org/10.1016/j.epsl.2016.11.047>.
 40. Mechie, J. et al. Crustal and uppermost mantle velocity structure along a profile across the Pamir and southern Tien Shan as derived from project TIPAGE wide-angle seismic data. *Geophys. J. Int.* **188**, 385–407 (2012).
 41. Kelemen, P. B. & Hirth, G. A periodic shear-heating mechanism for intermediate-depth earthquakes in the mantle. *Nature* (2007) <https://doi.org/10.1038/nature05717>.
 42. Thielmann, M., Rozel, A., Kaus, B. J. P. & Ricard, Y. Intermediate-depth earthquake generation and shear zone formation caused by grain size reduction and shear heating. *Geology* <https://doi.org/10.1130/G36864.1> (2015).
 43. Metzger, S. et al. The 2015 Mw7.2 Sarez strike-slip earthquake in the Pamir interior: response to the underthrusting of India’s western promontory. *Tectonics* **36**, (2017).
 44. Schurr, B. et al. Seismotectonics of the Pamir. *Tectonics* **33**, 1–41 (2014).
 45. Magni, V., Faccenna, C., Van Hunen, J. & Funicello, F. Delamination vs. break-off: the fate of continental collision. *Geophys. Res. Lett.* (2013) <https://doi.org/10.1002/grl.50090>.
 46. Duretz, T., Gerya, T.V. & May, D.A. Numerical modelling of spontaneous slab breakoff and subsequent topographic response. *Tectonophysics* (2011) <https://doi.org/10.1016/j.tecto.2010.05.024>.
 47. Royden, L. Coupling and decoupling of crust and mantle in convergent orogens: implications for strain partitioning in the crust. *J. Geophys. Res. B Solid Earth* (1996) <https://doi.org/10.1029/96jb00951>.
 48. Jamieson, R.A. & Beaumont, C. On the origin of orogens. *Bull. Geol. Soc. Am.* (2013) <https://doi.org/10.1130/B30855.1>.
 49. Yuan, X. et al. Subduction and collision processes in the Central Andes constrained by converted seismic phases. *Nature* (2000) <https://doi.org/10.1038/35050073>.
 50. Nelson, K.D. et al. Partially molten middle crust beneath southern Tibet: synthesis of project INDEPTH results. *Science* (80-) (1996) <https://doi.org/10.1126/science.274.5293.1684>.
 51. Ischuk, A. et al. Kinematics of the Pamir and Hindu Kush regions from GPS geodesy. *J. Geophys. Res. Solid Earth* (2013) <https://doi.org/10.1002/jgrb.50185>.
 52. Hacker, B.R., Kelemen, P.B. & Behn, M.D. Differentiation of the continental crust by remelting. *Earth Planet. Sci. Lett.* (2011) <https://doi.org/10.1016/j.epsl.2011.05.024>.
 53. Sippl, C. et al. Geometry of the Pamir-Hindu Kush intermediate-depth earthquake zone from local seismic data. *J. Geophys. Res. Solid Earth* (2013) <https://doi.org/10.1002/jgrb.50128>.
 54. Hammond, W.C. & Toomey, D.R. Seismic velocity anisotropy and heterogeneity beneath the mantle electromagnetic and tomography experiment (MELT) region of the East Pacific rise from analysis of P and S body waves. *J. Geophys. Res. Solid Earth* (2003) <https://doi.org/10.1029/2002jb001789>.
 55. Toomey, D.R., Solomon, S.C. & Purdy, G.M. Tomographic imaging of the shallow crustal structure of the East Pacific Rise at 9°30'N. *J. Geophys. Res.* (1994) <https://doi.org/10.1029/94jb01942>.
 56. Evans, J.R., Eberhart-Phillips, D. & Thurber, C.H. User’s manual for SIMULPS12 for imaging Vp and Vp/Vs; a derivative of the Thurber tomographic inversion SIMUL3 for local earthquakes and explosions. *US Geol. Surv.* 94–431, (1994).
 57. Hardebeck, J.L. & Shearer, P. M. A new method for determining first-motion focal mechanisms. *Bull. Seismol. Soc. Am.* (2002) <https://doi.org/10.1785/0120010200>.
 58. Bloch, W., Schurr, B., Kummerow, J., Salazar, P. & Shapiro, S.A. From slab coupling to slab pull: stress segmentation in the subducting Nazca plate. *Geophys. Res. Lett.* (2018) <https://doi.org/10.1029/2018GL078793>.
 59. Metzger, S. et al. Dense GNSS profiles across the northwestern tip of the India-Asia collision zone: triggered slip and westward flow of the Peter the first range, Pamir, into the Tajik depression. *Tectonics* **39**, (2020).
 60. Deng, Z., Gendt, G. & Schöne, T. Status of the IGS-TIGA tide gauge data reprocessing at GFZ. in International Association of Geodesy Symposia (2016). https://doi.org/10.1007/1345_2015_156.
 61. Altamimi, Z., Sillard, P. & Boucher, C. ITRF2000: a new release of the International Terrestrial Reference Frame for earth science applications. *J. Geophys. Res. Solid Earth* (2002) <https://doi.org/10.1029/2001jb000561>.
 62. Mohadjer, S., Ehlers, T.A., Bendick, R., Stübner, K. & Strube, T.A. Quaternary fault database for central Asian Nat. *Hazards Earth Syst. Sci. Discuss.* (2015) <https://doi.org/10.5194/nhessd-3-5599-2015>.
 63. Molnar, P. & Stock, J.M. Slowing of India’s convergence with Eurasia since 20 Ma and its implications for Tibetan mantle dynamics. *Tectonics* (2009) <https://doi.org/10.1029/2008TC002271>.
 64. DeMets, C., Gordon, R. G. & Argus, D. F. Geologically current plate motions. *Geophys. J. Int.* **181**, 1–80 (2010).

Acknowledgements

We thank the Department of Geology of Kabul University, the Afghanistan Geological Survey, the Norwegian Afghanistan Committee and the Tajik Academy of Sciences for installing and maintaining the Afghan and Tajik campaign sites, respectively. The Geophysical Instrument Pool Potsdam (GIPP) provided seismic instruments for the temporary networks; these (FDSN codes: 7B 2008–2010; 6C 2009–2010 and 2013–2014; 5C 2012–2014; 4C 2017–2019) are archived at the GEOFON Data Centre and can be obtained via the GEOFON website (<https://geofon.gfz-potsdam.de/waveform/archive/index.php?type=t>). Permanent station waveform data can be obtained through the IRIS DMC (<https://ds.iris.edu/SeisQuery/>). This study was supported by GFZ expedition funds, and the TIPIMON and CATENA projects, funded by the German Ministry of Science and Education (support codes 03G0809A/B and 3G0878A/B). NK was supported by an alumni scholarship from the ‘UNESCO International Training Course for Seismology’ at GFZ Potsdam. SK was supported by a postdoc fellowship of the ‘German Academic Exchange Service (DAAD)’ at the University of Minnesota. Tomographic inversion used the HPC units of the Minnesota Supercomputing Institute. Figures and

calculations used the Generic Mapping Tools (gmt.soest.hawaii.edu/), matplotlib (matplotlib.org), obspy (obspy.org) and Matlab (mathworks.com/products/matlab.html). M. Dziggel (GFZ) helped in preparing Fig. 5c and A. Gaete (GFZ) helped with first onset picking of teleseismic waveforms.

Author contributions

S.-K.K., in interaction with M.B., calculated the tomography. N.K., in interaction with S.-K.K., W.B., and B.S. produced the crustal earthquake catalogue, focal mechanisms and crustal travel time data. S.-K.K. and M.B. contributed to the teleseismic waveform cross-correlations. N.K., S. Metzger and Z.D. contributed to the collection and processing of the GNSS data. S.K., N.K., B.S., X.Y., S. Murodkulov, L.R., and J.M. contributed to the seismological experimental design and execution, with N.K. and S. Murodkulov leading the field deployments in Afghanistan and Tajikistan. All authors contributed to the interpretation and writing of the manuscript.

Funding

Open Access funding enabled and organized by Projekt DEAL.

Competing interests

The authors declare no competing interests.

Additional information

Supplementary information The online version contains supplementary material available at <https://doi.org/10.1038/s41467-021-21760-w>.

Correspondence and requests for materials should be addressed to S.-K.K.

Peer review information *Nature Communications* thanks Ana Negredo, James Ni, and the other, anonymous, reviewer(s) for their contribution to the peer review of this work. Peer reviewer reports are available.

Reprints and permission information is available at <http://www.nature.com/reprints>

Publisher's note Springer Nature remains neutral with regard to jurisdictional claims in published maps and institutional affiliations.



Open Access This article is licensed under a Creative Commons Attribution 4.0 International License, which permits use, sharing, adaptation, distribution and reproduction in any medium or format, as long as you give appropriate credit to the original author(s) and the source, provide a link to the Creative Commons license, and indicate if changes were made. The images or other third party material in this article are included in the article's Creative Commons license, unless indicated otherwise in a credit line to the material. If material is not included in the article's Creative Commons license and your intended use is not permitted by statutory regulation or exceeds the permitted use, you will need to obtain permission directly from the copyright holder. To view a copy of this license, visit <http://creativecommons.org/licenses/by/4.0/>.

© The Author(s) 2021

3.2 Oceanic subduction: Afterslip, visco-poro-elastic relaxation, earthquake coupling

3.2.1 Characterizing afterslip and ground displacement rate increase following the 2014 Iquique-Pisagua M_w 8.1 earthquake, Northern Chile

Published as: F. Hoffmann, [S. Metzger](#), M. Moreno, Z. Deng, C. Sippl, F. Ortega-Culaciati, O. Oncken (2018), Characterizing afterslip and ground displacement rate increase following the 2014 Iquique-Pisagua M_w 8.1 earthquake, Northern Chile, *Journal of Geophysical Research: Solid Earth*, **123**, 4171–4192. [doi:10.1002/2017JB014970](https://doi.org/10.1002/2017JB014970)

Supporting information: available online

Scientific application: We provide constraints for the temporal variation of the coupling degree of a subduction zone in different stages of the seismic cycle and how these variations affect adjacent fault segments.

Methodological advances: We used continuous GNSS time-series to correct the seasonal effects in the temporally sparse survey GNSS time-series, and a multi-parameter time-series decomposition to provide geodetic deformation data of the full seismic cycle embracing a large megathrust earthquake.

Individual Contributions: The study was designed, conducted and written by FH and me. Together with MM I acted as PhD supervisor of FH. MM, FH and CO collected the GNSS data, ZD pre-processed the GNSS data to positioning time-series, I wrote the multi-parameter time-series decomposition code, FH extracted the signals, ran the inversion models and designed the figures. I calculated the Coulomb failure stress change models and forward-calculated the viscoelastic response, CS provided the seismic data and OO contributed to the interpretation of the results. All authors commented on the manuscript.

Journal of Geophysical Research: Solid Earth

RESEARCH ARTICLE

10.1002/2017JB014970

Special Section:

Slow Slip Phenomena and
Plate Boundary Processes

Key Points:

- GPS rates south of 21°S accelerate in the second year following the Iquique-Pisagua event potentially reflecting coupling increase
- Afterslip lasts about 2 years before the interface relocks again almost entirely
- GPS velocity patterns and modeled interface afterslip rates suggest a seismotectonic barrier at 21°S

Supporting Information:

- Supporting information S1

Correspondence to:

S. Metzger,
metzger@gfz-potsdam.de

Citation:

Hoffmann, F., Metzger, S., Moreno, M., Deng, Z., Sippl, C., Ortega-Culaciati, F., & Oncken, O. (2018). Characterizing afterslip and ground displacement rate increase following the 2014 Iquique-Pisagua M_w 8.1 earthquake, Northern Chile. *Journal of Geophysical Research: Solid Earth*, 123. <https://doi.org/10.1002/2017JB014970>

Received 11 SEP 2017

Accepted 23 MAR 2018

Accepted article online 25 MAR 2018

©2018. American Geophysical Union.
All Rights Reserved.

Characterizing Afterslip and Ground Displacement Rate Increase Following the 2014 Iquique-Pisagua M_w 8.1 Earthquake, Northern Chile

 Felix Hoffmann¹ , Sabrina Metzger¹ , Marcos Moreno^{1,2} , Zhiguo Deng¹ , Christian Sippl¹ , Francisco Ortega-Culaciati³ , and Onno Oncken^{1,4} 

¹German Research Centre for Geosciences (GFZ), Potsdam, Germany, ²Departamento de Geofísica, Facultad de Ciencias Físicas y Matemáticas, Universidad de Concepción, Concepción, Chile, ³Departamento de Geofísica, Universidad de Chile, Santiago, Chile, ⁴Institut für Geologische Wissenschaften, Freie Universität Berlin, Berlin, Germany

Abstract The 2014 Iquique-Pisagua M_w 8.1 earthquake ruptured only parts of the 1877 Northern Chile-Southern Peru seismic gap. Here we present a comprehensive analysis of 152 continuous and campaign Global Positioning System time series that captured more than a decade of interseismic loading prior to the event and 2 years of afterslip. In high spatiotemporal resolution, our data document upper plate response not only at the coseismically affected latitudes but also at the adjacent Loa plate segment to the south. Using a combination of elastic and viscoelastic half-space models of different stages of the seismic cycle, we found that the highly coupled, former seismic gap contains a narrow low coupling zone at 21°S latitude. Just after the 2014 earthquake, this zone acts as a barrier impeding afterslip to continue southward. Possible reasons for this impediment could involve crustal heterogeneities or coupling discontinuities at the plate interface. After 2 years, afterslip cumulates to a maximum of ~89 cm and becomes negligible. Global Positioning System observations south of the inferred seismotectonic barrier reveal a deformation rate increase in the second year after the event. Our slip models suggest that this could be caused by a downdip coupling increase, perhaps bringing the highly coupled southern Loa segment closer to failure. Taken together, our results reveal (1) the interaction between different areas undergoing stress release and stress buildup in a major seismic gap, (2) constraints for the temporal variation of coupling degree in different stages of the seismic cycle, and (3) the influence of large earthquakes at adjacent segments.

1. Impact of the 2014 Earthquake on the 1877 Seismic Gap

The convergent plate boundary of western South America is characterized by megathrust events with short recurrence intervals. Almost all segments south of Peru broke within the last century and generated large subduction earthquakes such as the 1960 Valdivia M_w 9.5 earthquake (Kanamori, 1977) or the 2010 Maule M_w 8.8 earthquake (e.g., Moreno et al., 2010). The segment between 18 and 23°S latitude, known as Northern Chile-Southern Peru seismic gap, has not ruptured since 1877 (M_w 8.6 Iquique earthquake) but is capable of generating a M_w ~9 earthquake (e.g., Kelleher, 1972; Figure 1). With an estimated recurrence interval of ~100 years (Comte & Pardo, 1991) and two recent earthquakes in the adjoining segments, namely, the 1995 Antofagasta M_w 8.1 event in the south (Ruegg et al., 1996) and the 2001 Arequipa M_w 8.3 event in the north (Ruegg et al., 2001), this gap was considered to be the most mature seismic gap along the South American plate boundary south of Peru. Despite the occurrence of several smaller earthquakes in the area during the last century (Comte & Pardo, 1991; Engdahl & Villasenor, 2002) and the 2007 Tocopilla M_w 7.8 event (e.g., Motagh et al., 2010), the slip deficit remained nearly unchanged and recent geodetic studies report high plate coupling rates (e.g., Li et al., 2015; Métois et al., 2013). A megathrust event leading to a closure of the seismic gap has been expected for more than 30 years (e.g., Kelleher, 1972; Nishenko, 1985). For this reason, the region has been particularly well monitored for more than two decades already: first by the South American Geodynamic Activities project that started in 1993 (e.g., Klotz et al., 1999, 2001) and the International Associated Laboratories "Montessus de Ballore" project in the 1990's (Chlieh et al., 2004; Métois et al., 2013). Since 2007 the area has constantly been monitored by the Integrated Plate Boundary Observatory Chile (IPOC), an international effort to measure ground deformation with multipurpose instrumentation (Moreno et al., 2017) extended with University NAVSTAR Consortium data (Simons et al., 2010).

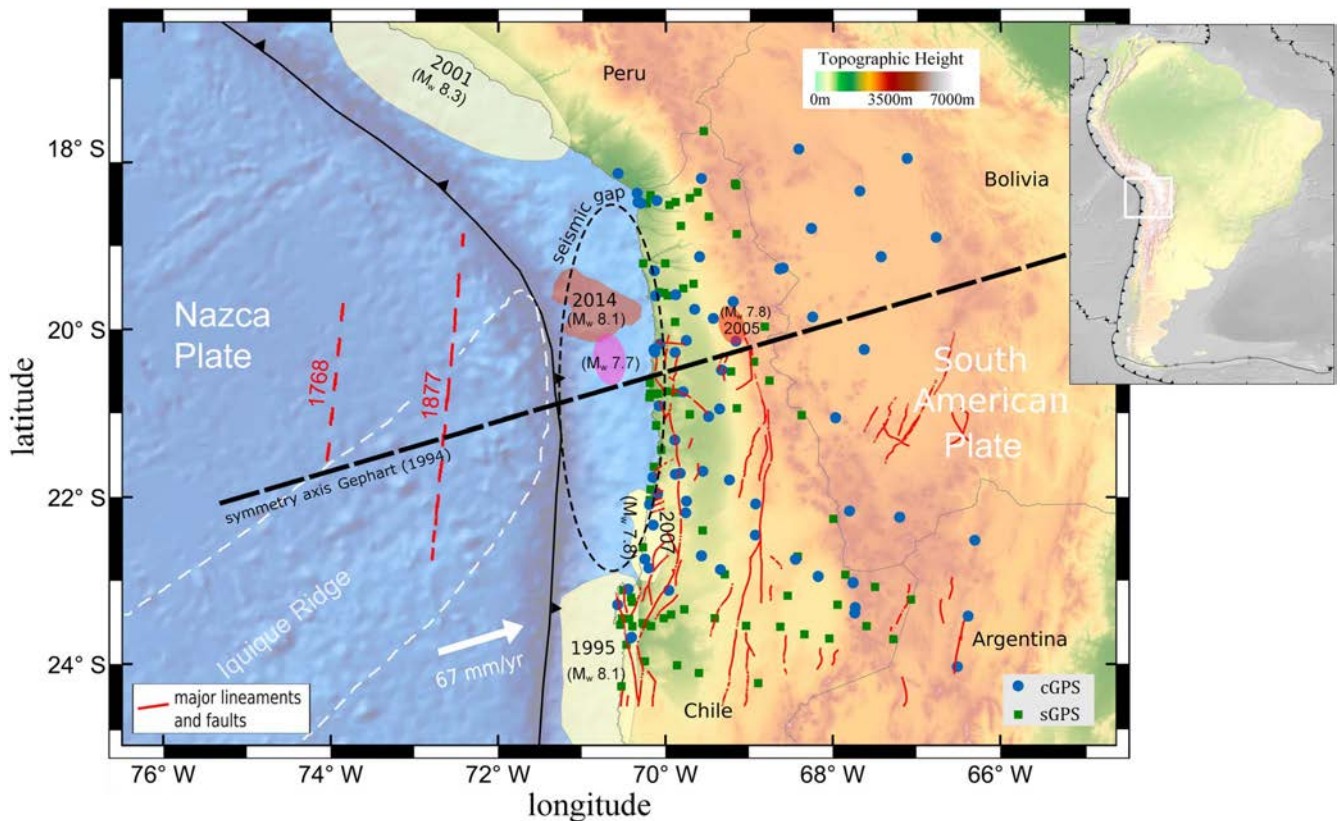


Figure 1. Topographic and geographic map of the Northern Chile-Southern Peru seismic gap region. Its relative location on the South American continent is shown in the inset. Rupture zones of past relevant earthquakes are indicated as shaded areas (source: U.S. Geological Survey): the 1995 Antofagasta, the 2001 Arequipa, the 2007 Tocopilla event (yellow), the 2005 Tarapacá event (orange), and the 2014 Iquique-Pisagua event (red) including its largest aftershock (magenta). The Northern Chile-Southern Peru Seismic gap is highlighted with a dashed ellipse. Inferred along-strike extents of the two last megathrust events in the gap area are indicated with dashed red lines (Comte & Pardo, 1991). The blue circles (continuous Global Positioning System (GPS) stations, cGPS) and green squares (survey-mode GPS stations, sGPS) mark the location of GPS stations used in this study. The Iquique Ridge is marked as dashed white line (Geersen et al., 2015). Major geologic faults and lineaments are highlighted in red (Reutter et al., 1994). The topographic symmetry axis of the Andes is indicated as black dashed line (Gephart, 1994).

On 1 April 2014, the Iquique-Pisagua M_w 8.1 megathrust event with a rupture length of about 100 km broke the plate interface in the central northern part of the gap close to the town of Pisagua (e.g., Ruiz et al., 2014; Schurr et al., 2014; see Figure 1). The mainshock nucleated in a zone of intermediate interseismic coupling and initially ruptured downdip toward a patch of higher coupling (Hayes et al., 2014; Schurr et al., 2014). Aftershocks are concentrated at the southern edge of the rupture zone (Meng et al., 2015) with the largest one being a M_w 7.7 event that occurred 2 days after and 100 km SSE of the main event (Duputel et al., 2015). Both events led to a cumulative failure of the plate interface of about 200 km length, which reflects only a partial release of the slip deficit accumulated since 1877 (Schurr et al., 2014).

In this study, we present new Global Positioning System (GPS) data acquired before and after the Iquique-Pisagua earthquake. From the acquired time series, we extract interseismic and postseismic deformation rates to analyze the temporal and spatial evolution of deformation following the earthquake. We further investigate deformation rate changes on the unbroken southern segment of the seismic gap. Interpreting surface displacements is one of the key elements in understanding the behavior of subduction zones. After a large earthquake, lithospheric stress is released in three principal processes: (1) continued slip of the fault referred to as afterslip (e.g., Marone et al., 1991; Perfettini et al., 2010), (2) poroelastic rebound due to pore fluid pressure changes (e.g., Jónsson et al., 2003; Peltzer et al., 1998), and (3) viscoelastic relaxation of the mantle (e.g., Nur & Mavko, 1974; Wang et al., 2012), while the fault simultaneously relocks during the postseismic stage. These postseismic processes may take place simultaneously and vary in duration between months to decades depending on the magnitude of the event as well as on the rheology of the

deformed material and/or the frictional properties of the slipping interface. In our analysis, we assume after-slip to be the driving mechanism controlling early postseismic deformation, although we recognize that other processes may contribute to the GPS-derived surface displacements. Of particular interest to us is the assessment of slip behavior in the postseismic stage across different tectonic segments, especially toward the southern edge of the pre-2014 seismic gap. The rupture zone of the Iquique-Pisagua event only covers less than one third of the 1877 rupture as inferred by Comte and Pardo (1991). This means that the southern segment of the Northern Chile-Southern Peru seismic gap now has accumulated a slip deficit for more than 140 years (Figure 1). For the regional earthquake hazard assessment, it is important to understand how the 2014 earthquake affects this segment of the gap. Thanks to the dense spatial coverage of GPS observations in Northern Chile (Figure 1), we can characterize regional crustal deformation in great detail. In order to evaluate spatial and temporal changes in plate coupling, we compare GPS rates before and after the Iquique-Pisagua event on the northern and southern part of the 1877 seismic gap. We first isolate tectonic GPS rates from nontectonic contributions (section 2) then use a combination of elastic and viscoelastic slip models to analyze the interseismic and postseismic stage of the Iquique-Pisagua earthquake (sections 3 and 4), discuss the interpretation of the model results (section 5), and finally draw conclusions (section 6).

2. GPS Observations and Model Approach

2.1. GPS Data Processing

The geodetic instrumentation of the IPOC (Moreno et al., 2017) and International Associated Laboratories network (Chlieh et al., 2004; Métois et al., 2013) includes GPS sites that are operated continuously (cGPS) and in survey mode (sGPS), the latter of which are also referred to as campaign GPS sites. We include data from 75 cGPS stations and 77 sGPS sites covering a latitudinal range of 17–24°S from the coast to 450 km inland (Figure 1). The sGPS sites are not strictly measured periodically but at least once every 3 years for at least 48 consecutive hours, thus delivering less accurate positioning than the cGPS stations. But since the sGPS time series extend further back in time compared to the cGPS time series, they are most helpful to estimate interseismic rates prior to the 2014 Iquique-Pisagua earthquake (Figure S1 in the supporting information).

All GPS data are organized in units of 24-h periods and were processed using the Earth Parameter and Orbit System software (Deng et al., 2016). We calibrated the positions using absolute antenna phase centers provided by the International Global Navigation Satellite System Service (Schmid et al., 2007) and compensated tidal effects using the Finite Element Solution tide model 2004 (Lyard et al., 2006). We estimated station coordinates and tropospheric wet zenith delays using random-walk parameters for every hour (Gendt et al., 2013). Finally, we estimated coordinates in network mode and aligned them to the International Global Navigation Satellite System Service combined coordinate product reducing the impact of the Earth rotation parameter (Rebischung et al., 2015). The GPS processing results are compatible with the International Terrestrial Reference Frame 2014 (Altamimi et al., 2016), which is based on a kinematic model without taking into account the nondeformational rotation of South America. We compute our final horizontal velocity field relative to the stable South American Plate by applying an Euler pole rotation (21.44°S, 125.18°W, 0.12°/Myr⁻¹, Moreno et al., 2011) comparable to the NNR-Nuvel-1A model (DeMets et al., 1994). Examples of cGPS (Figure S2) and sGPS (Figure S3) time series and more details of GPS data processing (Text S1 and Figure S4) and reference frame realization (Figure S5) are provided in the supporting information.

2.2. Extracting the Tectonic GPS Signal

Our GPS time series cover a time interval of more than a decade (1999–2016 for sGPS and 2003–2016 for cGPS; Figure S1) and include a variety of tectonic and other signals occurring at the convergent plate boundary. We excluded 3 months of data preceding the Iquique-Pisagua event 2014 from our time series as they were affected by preseismic transients (Bedford et al., 2015; see also section 3.1). The recorded ground displacements are the sum of tectonic, atmospheric, instrumental, and other signal contributions, like interseismic shortening, coseismic displacements, instrumental failure (e.g., antenna replacements), postseismic transients, and seasonal oscillations:

$$\delta_{\text{GPS}}(t) = \delta_{\text{interseismic}}(t) + \delta_{\text{coseismic}}(t) + \delta_{\text{AntennaOffset}}(t) + \delta_{\text{postseismic}}(t) + \delta_{\text{seasonal}}(t) \quad (1)$$

Following the approach of Metzger et al. (2013) and Bevis and Brown (2014), we simulate these signal types in our GPS displacement time series with (Figure 2)

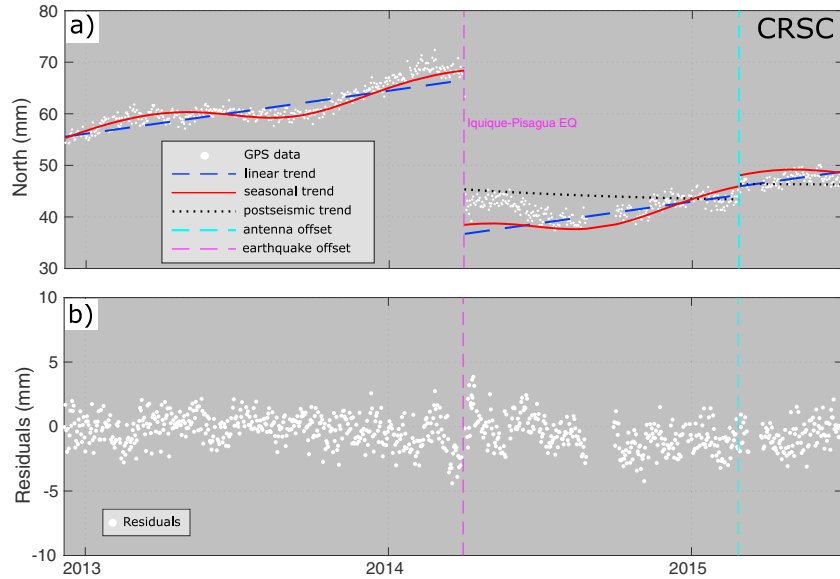


Figure 2. (a) Time series of station CRSC (see Figure 6 for location) and its decomposition into various model trajectories highlighted in different colors. (b) The model residuals of (a) (based on equation (2)). GPS = Global Positioning System.

$$\begin{aligned} \delta_{\text{GPS}}(t) = & [A + B \cdot (t - t_r)] + \left[\sum_{\text{eq}=1}^{n_{\text{eq}}} C_{\text{eq}} \cdot H(t - t_{\text{eq}}) \right] + \left[\sum_{\text{ao}=1}^{n_{\text{ao}}} D_{\text{ao}} \cdot H(t - t_{\text{ao}}) \right] \\ & + \left[\sum_{p=1}^{n_p} E_p \cdot \log \left(1 + \frac{t - t_{\text{eq}}}{T} \right) \right] + [F_1 \cdot \sin(2\pi \cdot t) + F_2 \cdot \cos(2\pi \cdot t) + F_3 \cdot \sin(4\pi \cdot t) + F_4 \cdot \cos(4\pi \cdot t)] \quad (2) \end{aligned}$$

The constant A corrects the time series for any initial offset, and the linear term B represents a constant plate velocity in each stage of the seismic cycle (Wang et al., 2012) with respect to a predefined reference time t_r . Discontinuities can arise either from coseismic displacements (eq) or antenna offsets (ao). The mathematical approach to model such data offsets is a Heaviside function $H(t)$, where n_{eq} earthquakes (or n_{ao} antenna offsets, respectively) induce a step with amplitude C_{eq} (D_{ao}) at times t_{eq} (t_{ao}). The challenge is to distinguish artificial steps in the displacement function from earthquake-induced ground motion. Postseismic relaxation observed after n_p large earthquakes is represented by a logarithmic transient E_p with a nonlinear parameter T . Bevis and Brown (2014) showed that the logarithm is nearly insensitive to T ; hence, this component can be linearized by setting T equal to 1 year. The most rapid deformation within the first weeks after the earthquake might not be perfectly represented by this simplification (Figure 2b). However, we demonstrate in section 3.1 that the linear term is most important for our velocity analysis. The last term in equation (2) represents an elastic loading response of the crust to seasonal changes in the water cycle (e.g., Heki, 2001; Van Dam et al., 2001). We apply a Fourier second-order series for terms F_1 to F_4 that represent two annual and two semiannual intervals (Dong et al., 2002).

To estimate all parameters mentioned above and to exclude irrelevant signal contributions (instrumental offsets and seasonal loading) from further analysis, we modeled the cGPS time series component wise using a least squares inversion (Figure 2). To exclude coseismic and postseismic signals related to other events than the 2014 Iquique-Pisagua earthquake, we developed a semiautomated earthquake selection procedure that extracts relevant earthquakes from the U.S. National Earthquake Information Center catalog. We used a distance-magnitude filter to identify all events that could potentially have affected our GPS time series, that is, that occurred within a radius of 20 to 2,500 km and with an incremental magnitude of 5 to 8.

All remaining offsets in the time series were then visually checked and manually classified as antenna offsets. The average rms (root-mean-square) error of all stations is 1.2 mm for the east, 1.0 mm for the north and 2.0 for the vertical component; stationwise, it ranges from 0.9 mm (LVRA) to 1.9 mm (PCAL) in the east component, 0.8 mm (ANT2) to 2.4 mm (PICN) in the north component and 1.5 mm (MCLA) to 2.7 mm (UTAR) in the

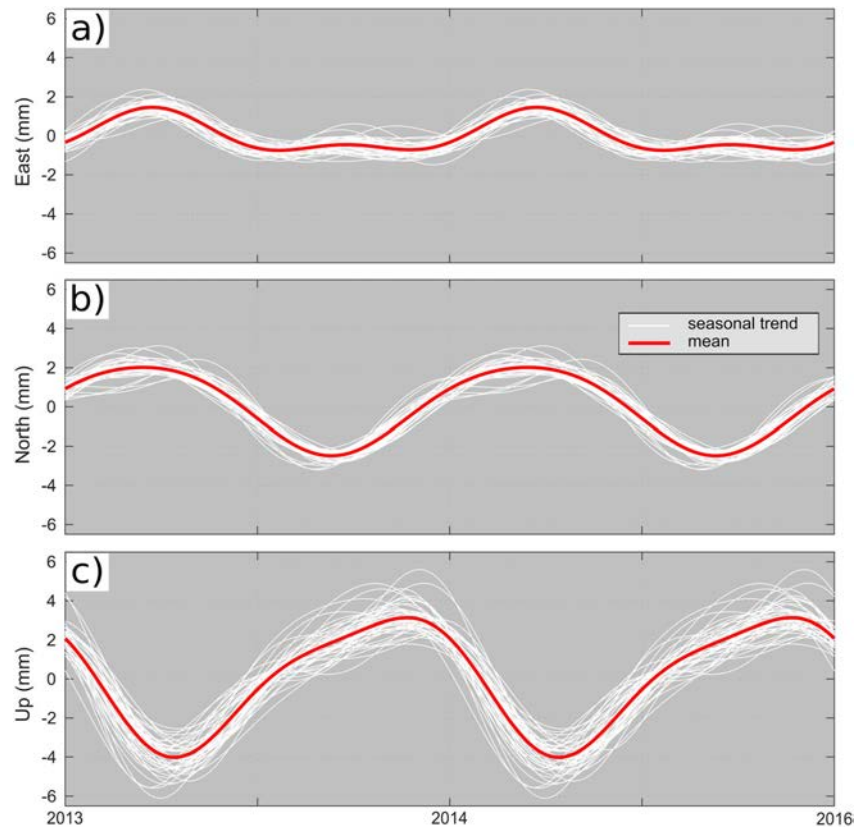


Figure 3. Modeled seasonal signal on the (a) east, (b) north, and (c) up components of 50 continuous Global Positioning System stations. Stations with significant data gaps (Figure S1b) were excluded from the analysis.

vertical component (Table S1). The residuals of the time series inversion are close to 0, thus indicating that our approach in equation (2) seems reasonable for approximating the observed GPS ground motion signal (Figure S2). We then subtracted the nontectonic signal contributions, the seasonal trend, and the antenna offsets, from the time series for each station individually (Figure S2). We further find that the seasonal changes are surprisingly consistent over the whole cGPS network (Figure 3). The east component contains a clear biannual signal with one peak in February/March and a second lower peak in September, whereas the north component exhibits a clear annual signal with a peak in February/March and a low in September. The vertical component also exhibits a one-peak annual trend, in which the highs and lows are shifted in respect to horizontal components to October/November (peak) and May/June (low).

The campaign GPS data have a much lower temporal resolution and have been collected irregularly and in different seasons (Figure S3). Thus, the extraction of the tectonic signal is more challenging here. We used the seasonal parameters estimated from the cGPS data to correct the campaign data and applied a seasonal model derived from the mean of each parameter F_1 to F_4 in equation (2) (Tables S2 and S3 and Figure S6).

2.3. Data Time Windows and Model Strategy

In order to better understand the different stages of the Northern Chile seismic cycle, we split the GPS data into an interseismic part prior to and a postseismic part after the 2014 Iquique-Pisagua earthquake. The interseismic interval is covered by three to eight GPS campaigns between 1999 and end of 2013 and by cGPS observations spanning a time interval from 2003 to end of 2013 (data from 2014 were cut due to observed GPS transients, see also section 3.1 and Figure S1). The postseismic interval contains another two to three campaign GPS surveys, covering a time period of 3 weeks after the mainshock until April 2016 and daily solutions from 3 April 2014 to April 2016. To not contaminate the afterslip analysis with the largest aftershock

occurring on 3 April, we excluded the cGPS solutions of the first 2 days after the mainshock. To analyze the temporal evolution of the postseismic response to the earthquake, we further subdivided the postseismic part into three periods that best match the timing of the campaign GPS surveys (Figure S1a). The intervals comprise days 2–16, days 17–334, and days 335–717 after the mainshock and are henceforth called Periods 1, 2, and 3, respectively.

We invert the observed GPS surface displacements for estimating slip (respectively backslip) on the subduction interface using elastic and viscoelastic half-space models (Okada, 1992). For the interseismic model, we assume elastic deformation (Okada, 1992) to be the dominant driver (e.g., Chlieh et al., 2011; Métois et al., 2016). For the postseismic models of Periods 1–3, we combine the elastic afterslip model with viscoelastic mantle relaxation using the PyLith software (Aagaard et al., 2013). In the viscoelastic finite element modeling approach, we use four different material blocks to discriminate between an elastic crust and lithospheric mantle and a viscoelastic asthenospheric mantle (Text S2 and Figure S7). The model geometry of the subducting slab is based on the SLAB 1.0 model (Hayes, Wald, & Johnson, 2012) and the elastic-visco-elastic boundary is based on the continental Moho of Tassara and Echaurren (2012). We fixed the Young's modulus to 100, 120, and 160 GPa for the continental, oceanic, and mantle layers, respectively (Li et al., 2015), and use the linear Maxwell rheology in the viscoelastic body. The Poisson's ratio is set to 0.265 and 0.30 for the continental and oceanic crust (Christensen, 1996).

In general, Maxwell viscosity is preferably applied for long-term viscosity estimates, whereas Burgers viscosity resolves short-term rheologic transients typical for the early postseismic stage (e.g., Li et al., 2015; Trubienko et al., 2013). We decided to use Maxwell rheology to reduce complexity and computational cost. When using predetermined time windows like here, the effective viscosity is defined as the best fitting Maxwell viscosity (Li et al., 2017). This approach has been successfully applied for GPS data in Chile before (Bedford et al., 2016; Li et al., 2017), but we cannot exclude the possibility that this simplification creates artifacts in our slip models as discussed in section 5. To simulate the viscous response to coseismic stress perturbation, we used the slip model of Schurr et al. (2014) and estimated the viscoelastic deformation in the respective model Periods 1–3 (Tables S7, S9, and S11). We tested different values of the Maxwell viscosity of the continental mantle and kept all other parameters constant, including the oceanic mantle viscosity, which we fixed to 10^{20} Pa s (Hu et al., 2014; Li et al., 2015). Continental viscosity was varied between 10^{18} Pa s (highly viscous) and 10^{20} Pa s (nearly elastic) in our tests and was finally constrained to 2×10^{19} Pa s, based on the best data fit (rms, see examples for Period 2 in Figures S8 and S9). Using these fixed viscosities, we removed the predicted viscoelastic signal component from our GPS observations in advance and thus account for the viscous mantle relaxation. In a second step, we subtracted the interseismic loading component from each postseismic period to finally invert for the afterslip signal only (more details can be found in section 4.1).

The elastic model geometry of the plate interface slip is also based on the SLAB1.0 subduction zone model (Hayes et al., 2012), from which we utilized the region from 17.5 to 26°S latitude. Slip is modeled as along strike and updip dislocations on 1,016 triangular fault patches with an average area of 170 km² and constrained to a maximum depth of 65 km, assumed to represent the Moho depth (Chlieh et al., 2011; Husen et al., 2000). We invert Green's functions describing slip at depth on the interface geometry to best fit the observed GPS displacements in a least squares approach (Okada, 1992). We do not constrain the rake, thus allowing backslip to occur. For regularization of the inversion, we applied a Laplacian smoothing, making the solution more stable while minimizing slip variations of neighboring patches based on an input smoothing weight. The strength of the regularization is determined by considering the trade-off between misfit and slip roughness (Figure S10). In the interseismic backslip model, three additional model parameters describe an Euler pole that accounts for the motion of the Central Andean sliver (Bevis et al., 2001). The sliver motion is collinear to the plate convergence and causes back-arc shortening in the Subandean (Chlieh et al., 2011). This model modification allows to better describe the abnormally high interseismic GPS rates (with respect to the overall convergence rate in Northern Chile) that cannot be explained by an elastic response of the plate interface alone (e.g., Métois et al., 2013, 2014). The Green's functions are inverted with the MATLAB routine "lsqin," a subspace trust-region-reflective algorithm based on the interior-reflective Newton method (Coleman & Li, 1996). To avoid physically unreasonable slip rates and additionally improve model resolution, we apply constraints for minimum slip (Du et al., 1992) based on the constant plate velocity of 67 mm/year (Angermann et al., 1999). The respective minimum slip for interseismic and postseismic models corresponds

to the “negative” backslip rates of -61 mm/year that would equal a locked (fully coupled) interface dipping $25-30^\circ$ (e.g., Husen et al., 2000).

3. Interseismic Period

3.1. Constraining GPS Rates

The interseismic ground displacements in our GPS network were affected by two major earthquakes in Northern Chile (Figure S11): the 2005 Tarapacá M_w 7.8 earthquake (Delouis & Legrand, 2007; Ruiz et al., 2014) and the 2007 Tocopilla M_w 7.8 earthquake (Motagh et al., 2010; Weiss et al., 2016). We therefore excluded all data between November 2007 and January 2008, when GPS rates were dominated by afterslip from the Tocopilla event (e.g., Delouis et al., 2009) and data in May and June 2005 due to the Tarapacá event. We further excluded all GPS data in the 3 months before the Iquique-Pisagua main rupture on 1 April, 2014, where clear transient signals appear in the time series (Figure S12). These distinct features reflect either a slow slip event preceding the mainshock (e.g., Ruiz et al., 2014; Yagi et al., 2014) or represent a surface expression of precursors of seismic slip (e.g., Bedford et al., 2015; Schurr et al., 2014). We split the interseismic GPS data into three parts to investigate on rate differences in the interseismic stage: (A) a pre-Tarapacá interval with data before June 2005, (B) a time interval between the Tarapacá and the Tocopilla event from July 2005 to October 2007, and (C) a post-Tocopilla interval with all data from February 2008 to end of December 2013.

In all three parts of the time series, we removed data points with a position error above the 99.5th percentile and/or each point whose position differs from its neighbor by more than 3 times the standard deviation of the first derivative of the time series. For each of the three interseismic subsets of continuous time series longer than 1 year, we estimate the interseismic rate by extracting the linear trend from the signal as explained in section 2.2. From the sGPS data, we derived the interseismic rates using linear regression. The rate differences of the 1d-horizontal velocities between the pre-Tarapacá (A), the inter-earthquake (B), and post-Tocopilla (C) periods do not exceed 5 mm/year (Table S4). We use the mean of all three periods, equally weighted as interseismic velocity for further analysis. The resulting velocity may not fully account for interseismic transients observed in the epicenter regions of the Tarapacá and Tocopilla events (e.g., Weiss et al., 2016). Uncertainties of the resulting cGPS rate model parameters are calculated from the mean instrumental error in each model interval. Given the low number of observations, calculating campaign GPS errors is more challenging. Following Geirsson et al. (2006), we correct the rms fit by the number of model parameters (two in the linear case) and normalize it by the full length of the time series.

The resulting interseismic rates (Tables S5 and S6) were corrected for the Andean sliver motion (see sections 2.2 and 3.2 and Figure 4a). They exhibit a consistent ENE motion that is collinear to the plate convergence over the entire area of interest in Northern Chile, even in the far field of the network. The interseismic observations are characterized by a gradual rate decrease of about 7 mm per 100 km from coastal stations to stations on the Andean Plateau. Maximum horizontal GPS velocities of up to 35.3 ± 3.1 mm/year (station MEJS) occur at coastal stations at the southern edge of our GPS network at a minimum distance of ~ 80 km to the trench, whereas minimal horizontal GPS velocities of 14.1 ± 5.2 mm/year (PAJA) occur on the Andean Plateau at a longitude of about 67°W and ~ 490 km distance to the trench (Figure 4a). The rates also exhibit a north-south gradient from coastal stations close to the border to Peru that show significantly slower GPS rates of 20.3 ± 1.2 mm/year (LYAR) to coastal stations in the south like the aforementioned station MEJS. The vertical GPS data (Figure 4b) exhibit uplift for most of the coastal stations with a maximum of 9.0 ± 1.4 mm/year (PB05) at sGPS stations near Mejillones peninsula at 23°S latitude and a maximum of 5.9 ± 2.1 mm/year (PSGA) at cGPS stations close to the epicenter of the Iquique-Pisagua earthquake 2014. Further inland, the vertical displacements show a more inhomogeneous deformation pattern with subsidence rates of less than 2 mm/year south of 22°S .

3.2. Model Results

The weights for the model approach of 50 cGPS and 51 sGPS stations are defined as the square of the inverse error. Given the inhomogeneous distribution of cGPS and sGPS stations, we additionally tested different weighting ratios $w = w_{\text{sGPS}}/w_{\text{cGPS}}$ between campaign and continuous data by performing a least rms error analysis (Cavalié et al., 2013). A weighting ratio of $w = 2.5$ generates the best data fit (Figure S13a). Based on a similar approach, we increased the uncertainty (i.e., decreased the weights) of our vertical GPS

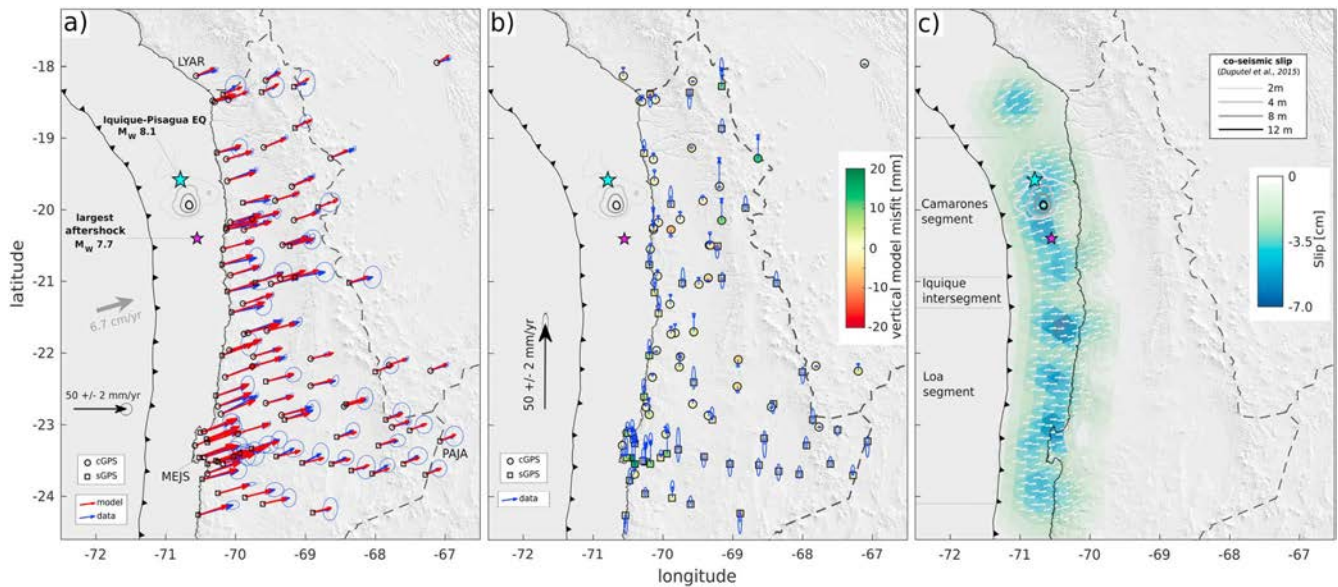


Figure 4. (a) Modeled (red) and observed (blue) Global Positioning System (GPS) displacements with 1-sigma uncertainties plotted in a stable South America reference frame, (b) corresponding vertical GPS observations (blue) with corresponding misfit indicated in colors (data minus model), and (c) modeled interseismic backslip on triangular fault patches on the subduction interface (white arrows indicate rake). Other features represent the coast line (solid line), the fault trench (solid line with triangles), political boundaries (dashed lines), and the coseismic slip model and aftershock location (Duputel et al., 2015). Inferred segment boundaries are marked with gray lines following the nomenclature of Métois et al. (2016). cGPS = continuous Global Positioning System; sGPS = survey-mode Global Positioning System.

components by a factor of 5 for cGPS and a factor of 10 for sGPS data (Figure S13b). The different weighting is necessary as in general, GPS data are more sensitive to horizontal motion and the vertical instrumental error might be underrepresented, especially for episodic GPS data acquisitions. Our interseismic backslip model locates the Euler pole representing the motion of the Andean sliver in central Ecuador (1.20°S , 77.31°W + $0.30^{\circ}/\text{Myr}^{-1}$). Amplitudes and azimuths of the resulting sliver motion are in agreement with Métois et al. (2013; 54.5°S , 37.5°W , $-0.15^{\circ}/\text{Myr}^{-1}$), whose model was based on a different station network (Figure S14). However, the Euler pole of Métois et al. (2013) is located to the south of Chile, thus opposite of our pole, suggesting smaller sliver motion southward, where the active eastern front is lacking. In our case, the sliver rotation would be anticlockwise with a main NNE component of ground motion, which is in agreement with the preferred convergence direction in Northern Chile. The shortening of the Andean sliver accounts for 12–14 mm/year of the measured ground motion, which is consistent with other studies (e.g., Brooks et al., 2011; Métois et al., 2013). This rate corresponds to about 19% of the total convergence rate, which hence has to be reduced from 67 mm/year (Angermann et al., 1999) to 54 mm/year in Northern Chile for modeling if only data from the Chilean forearc are considered (Figure 4a). The backslip model yields an estimate for the degree of coupling of the plate interface in the decade before the Iquique-Pisagua earthquake. The coupling degree can easily be inferred from the slip rate: the higher the rate of backslip, the higher the degree of coupling. Coupling maps (e.g., Li et al., 2015; Métois et al., 2016) are given in ratios between 0 and 1, with 0 referring to freely slipping fault patches and implying that the interface moves with the full rate of the subducting Nazca Plate (54 mm/year after removal of 13 mm/year of sliver motion). Slip is generally considered as interface motion toward the trench and assumed to be positive. Therefore, backslip is directed away from the trench and assumed to be negative (Savage, 1983). Similar to previous plate interface coupling studies in Northern Chile (e.g., Chlieh et al., 2011; Li et al., 2015; Métois et al., 2016), our interseismic backslip model demonstrates a heterogeneous coupling distribution ranging from almost free slipping to full coupling of the plates with rates of up to 61 mm/year effectively realistic (Figure 4c). The backslip pattern in Northern Chile exhibits several highly coupled patches with rates >50 mm/year along the Chilean coastline at an intermediate depth of 30 to 40 km. These patches are separated from each other by low coupling areas of backslip rates less than 30 mm/year.

Most prominently, the central segment between 19.3 and 21°S latitude referred to as the Camarones segment (Figure 4c), where the Iquique-Pisagua earthquake ruptured, is clearly separated by lowly coupled zones to the north and south. The low coupling corridor at 21°S is referred to as Iquique low coupling zone (or Iquique interseismic segment) and was confirmed by others with slightly different extents (e.g., Li et al., 2015; Métois et al., 2016). Our interseismic backslip model generally compares well to previous coupling maps that detect highest coupling rates at a depth range of 20–40 km (e.g., Béjar-Pizarro et al., 2013; Chlieh et al., 2011; Li et al., 2015; Métois et al., 2016). But in contrast to these maps, our results show very low backslip rates at shallower depths <15 km, which could be explained by a lack of sensitivity in this depth range.

For sensitivity analysis, we perform a checkerboard test, in which we generate rectangular slip and backslip patches of size $\sim 80 \times 80$ km in a checkerboard pattern of ± 1 m slip on our interface geometry. This interface slip is forward modeled to yield ground deformation for our GPS network and inverted again. Inversion results can then be compared to the checkerboard geometry. The interseismic model is generally well resolved south of 19°S and in a depth range below 20 km and is less sensitive for the very north of our study area and the shallow interface parts (Figure S15b). Overall, we fit the GPS observations very well with a rms misfit of only 1.8 mm/year in horizontal direction (Figure S16a) and 1.7 mm/year in vertical direction (Figure S17a). In the north of the GPS network, the Euler rotation seems somewhat overpredicted, which causes a slightly underpredicted backslip rate. Our model fit the vertical data generally well, with a few exceptions at sGPS coastal stations to the south (Figures 4b and S18a).

4. Postseismic Period

4.1. Constraining Static GPS Displacements

We used the Euler pole obtained from the interseismic model (section 3.2) to correct the postseismic data for the sliver motion. Unlike for the estimation of the interseismic rates, where we extracted linear rates, we extracted static displacements for the three consecutive intervals, Periods 1–3, directly from the GPS time series (Tables S7–S12). Outlier detection and calculation of individual uncertainties for cGPS in the postseismic stage is the same as in section 3.1. For sGPS data, we increased the instrumental error by adding the overall rms position error of all (usually 3–5) daily solutions of one campaign. To further account for the instrument setup error, we lowered the relative weights for sGPS data with respect to cGPS data in the inversion (details in section 4.2). From the postseismic static displacements, we subtracted the viscoelastic response signal determined by the independent viscous model (section 2.3) in all three periods to account for the postseismic mantle relaxation (Tables S7, S9, and S11 and Figure S19). We still allow backslip to occur to assess possible rate changes on the interface in adjoining segments of the ruptured Camarones segment. Additionally, we subtracted the interseismic backslip rates, assuming that they are constant in time (Table S13) to account for relocking and extract the afterslip signal. For stations that were not active before 2014, we predicted an average relocking velocity based on our interseismic slip model (Figure 4c).

In Period 1 (days 2–16), stations north of 21°S exhibit trenchward (WSW) motion of up to 46.0 ± 1.2 mm some 80 km southeast of the inferred maximum slip (station CGTC, Figure 5a and Table S7). This motion is oriented opposite to the interseismic ground displacement direction prior to the event. Stations south of 21°S remain more or less unaffected by this early postseismic motion and continue to move in the direction of plate convergence (2.3 ± 1.2 mm, PB03). The latitudinal displacement gradient is not symmetric around the peak slip region at 20°S: from there, the displacement decrease is ~ 14 mm within the first 100 km northward, whereas the decrease is faster, ~ 18 mm within the first 100 km, southward (Figure 5a). The vertical GPS data (Figure 5d) exhibit subsidence of all stations, with a maximum of 25.4 ± 2.3 mm (PSGA) at stations that are located close to the epicenter of the aftershock.

In Period 2 (days 17–334), the displacement pattern slightly changes: the maximum trenchward displacement has shifted about 50 km away from the coast and reaches 58.9 ± 2.2 mm at cGPS station PB11 (Figure 5b and Table S9). The asymmetric surface deformation pattern becomes more prominent, with a displacement decrease of ~ 34 mm northward and a decrease of ~ 46 mm southward within the first 100 km (Figure 5b). Moreover, the abrupt displacement sign change of stations from north to south of 21°S is more obvious. GPS station PB01 is the southernmost station that moves toward the rupture zone (11.8 ± 1.3 mm), whereas GPS station PB02, located only ~ 40 km south of PB01, moves opposite (16.7 ± 1.3 mm) before the relocking signal is subtracted. All stations south of 21°S move collinear with the plate convergence vector

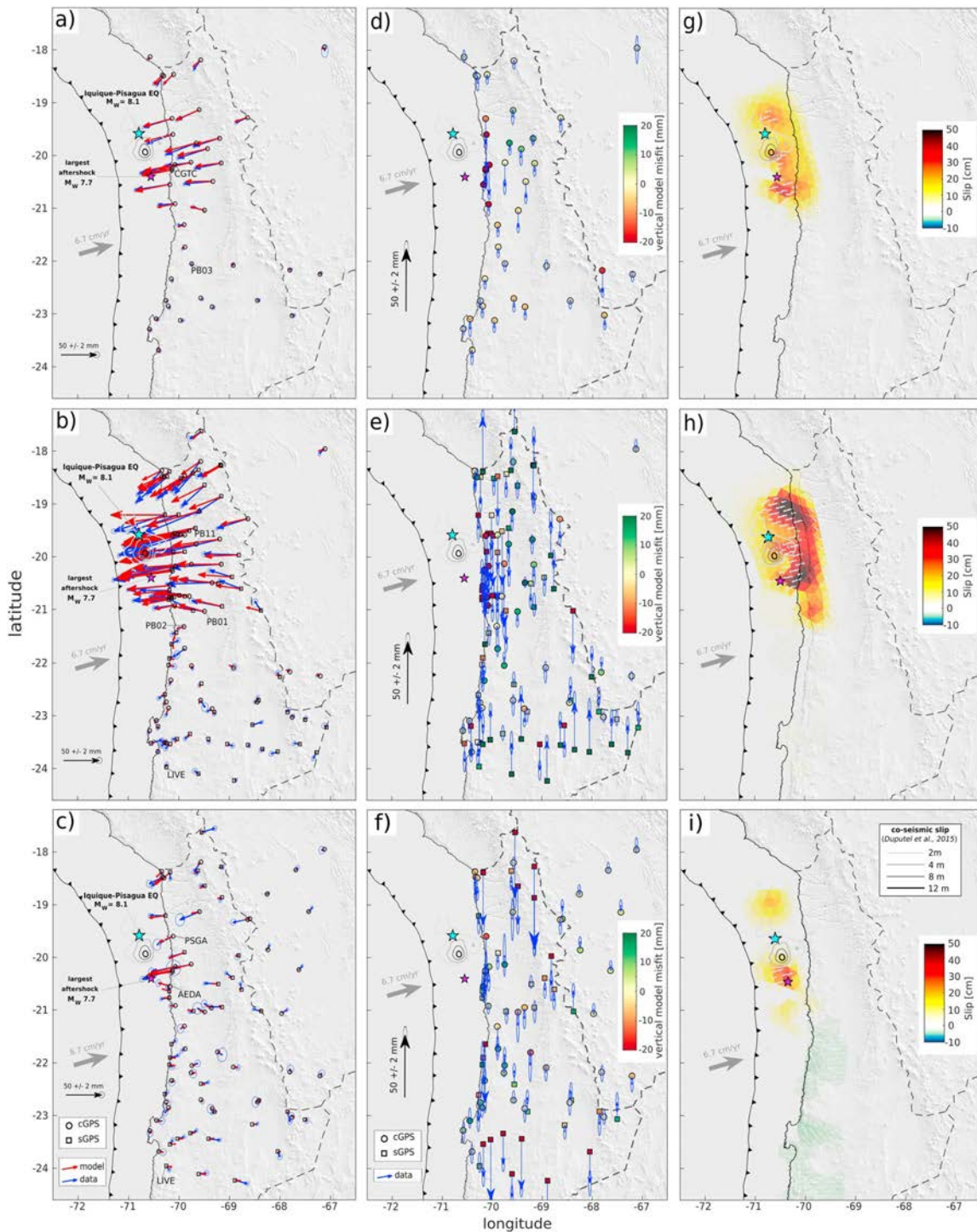


Figure 5. (a–c) Predicted displacements (red) in comparison to the Global Positioning System observations (blue) with 1-sigma uncertainties, after subtracting the reloading signal (average interseismic rate) and the viscoelastic response for (a) 2–16 days (Period 1), (b) 17–334 days (Period 2), and (c) 335–717 days (Period 3) after the mainshock. (d–f) Vertical GPS observations (blue) and color-coded model residuals for the corresponding postseismic Periods 1–3. (g–i) Predicted post-seismic afterslip on the plate interface during the corresponding postseismic Periods 1–3. For other features see Figure 4. cGPS = continuous Global Positioning System; sGPS = survey-mode Global Positioning System.

with a maximum of 28.9 ± 2.0 mm at station LIVE, which nearly corresponds to its interseismic rate of 31.7 ± 5.5 mm for 1 year. The vertical GPS data (Figure 5e) close to the main rupture exhibit subsidence of up to 23.9 ± 2.6 mm (PSGA), whereas stations toward the south of the epicenter region show uplift of 33.0 ± 2.8 mm (PRO2). This spatial sign change may represent the hinge line of postseismic uplift to subsidence at a latitudinal range of ~ 21 – 22° S. In general, the vertical displacement pattern seems more coherent for cGPS than sGPS observations. Uplift rates of sGPS data toward the south may be systematically overestimated compared to cGPS rates.

During Period 3 (days 335–717), most of the stations north of 21° S have significantly reduced their trenchward motion and relocking dominates over the afterslip component of the signal. For example, the cGPS station (PSGA) closest to the mainshock exhibits a displacement of 5.0 ± 3.7 mm toward ENE before subtracting relocking (Figure 5c and Table S11). Stations south of 20.5° S feature ENE displacement that increases southward from 15.4 ± 2.2 mm (AEDA) to 35.8 ± 1.4 mm (LIVE) before subtracting relocking velocity (Figure 5c). The vertical GPS data (Figure 5f) is relatively inhomogeneous. Coastal stations close to the main rupture still mostly exhibit subsidence with a maximum of -19.3 ± 6.1 mm (PSGA), whereas few stations south of 21° S (8.5 ± 2.2 , PB03) and in Bolivia (3.7 ± 1.7 , BMWS) experience uplift. The sGPS rates seem less coherent with generally higher subsidence rates toward the south (-10.3 ± 3.0 mm, PRO3) compared to cGPS rates (-6.6 ± 3.1 mm, JRGN).

If we analyze the temporal evolution of displacement by using a moving window of 30 days, we illustrate for how long each GPS station was affected by the Iquique–Pisagua earthquake (Figure 6). As reported before, stations south of 21° S seem not at all affected by the mainshock. Stations south of PB01 have an eastward trend collinear with the plate convergence over all investigated periods. But just 40 km north, at 21° S, the adjacent stations CRSC, CLLA, and PB01 are clearly affected by coseismic and postseismic response to the mainshock (Figure 6). The majority of GPS stations north of 21° S turn their sense of motion from trenchward to landward after about 1 year, thus slowly converging to interseismic relocking. This turnover of ground displacement motion back to interseismic relocking with surface motion collinear to the plate convergence vector is almost completed after 2 years. After April 2016, westward directed motion induced by afterslip is dominated by eastward directed motion induced by relocking and we assume interface afterslip to become negligible with less than 5 cm/year 2 years after the Iquique–Pisagua event.

4.2. Model Results

The slip models of the different postseismic stages yield a more detailed picture of the temporal evolution of afterslip (Figures 5g–5i). For the postseismic models, we first calculated the data weights based on GPS uncertainties and then introduced the weighting factor $w = w_{\text{sGPS}}/w_{\text{cGPS}}$ (Figure S13a), similar as for the interseismic model (section 3.2). Period 1 only contains cGPS data (42 stations), but for Period 2 (38 cGPS and 64 sGPS stations, $w = 2.0$) and Period 3 (33 cGPS and 43 sGPS stations, $w = 1.5$), we defined different relative weights to account for a difference in spatial distribution of cGPS and sGPS stations. Similar to the postseismic modeling approach, we increased the uncertainty of the vertical GPS component by a factor of 5 for cGPS and 10 for sGPS data to more realistically represent the vertical data error (Figures S13c and S13d).

While subtracting averaged interseismic rates from postseismic data before inverting for postseismic slip, we assume that the relocking rates remain constant before and after the Iquique–Pisagua event 2014. This may lead to an overestimation of afterslip rates and also the viscoelastic relaxation component of the signal, if interseismic loading signal does not resemble prevailing backslip during the postseismic period.

In Period 1, afterslip with a magnitude of 15–25 cm surrounds the rupture area of the Iquique–Pisagua earthquake downdip at ~ 30 – 35 -km depth (Figure 5g). Maximum slip of up to 38 cm occurs 50 km south of the mainshock at ~ 30 km depth, near the epicenter of the largest aftershock. In a latitudinal range of 20.7 – 21° S, our model indicates a transition from highest slip rates to backslip-dominated interface motion. We think that this pattern is caused by the sharp latitudinal sign change of displacement and might be linked to a seismotectonic barrier at 21° S. This sharp transition moreover suggests that stations south of this zone are not affected by afterslip (Figure 5g).

In Period 2, afterslip occurs downdip of the main rupture at 30–50-km depth, surrounding the hypocenter and reaching peak values of 51 cm (Figure 5h). One-peak slip patch is located 50 km south of the epicenter, again at the location of the largest aftershock, and a second high afterslip patch appears 40–50 km to the

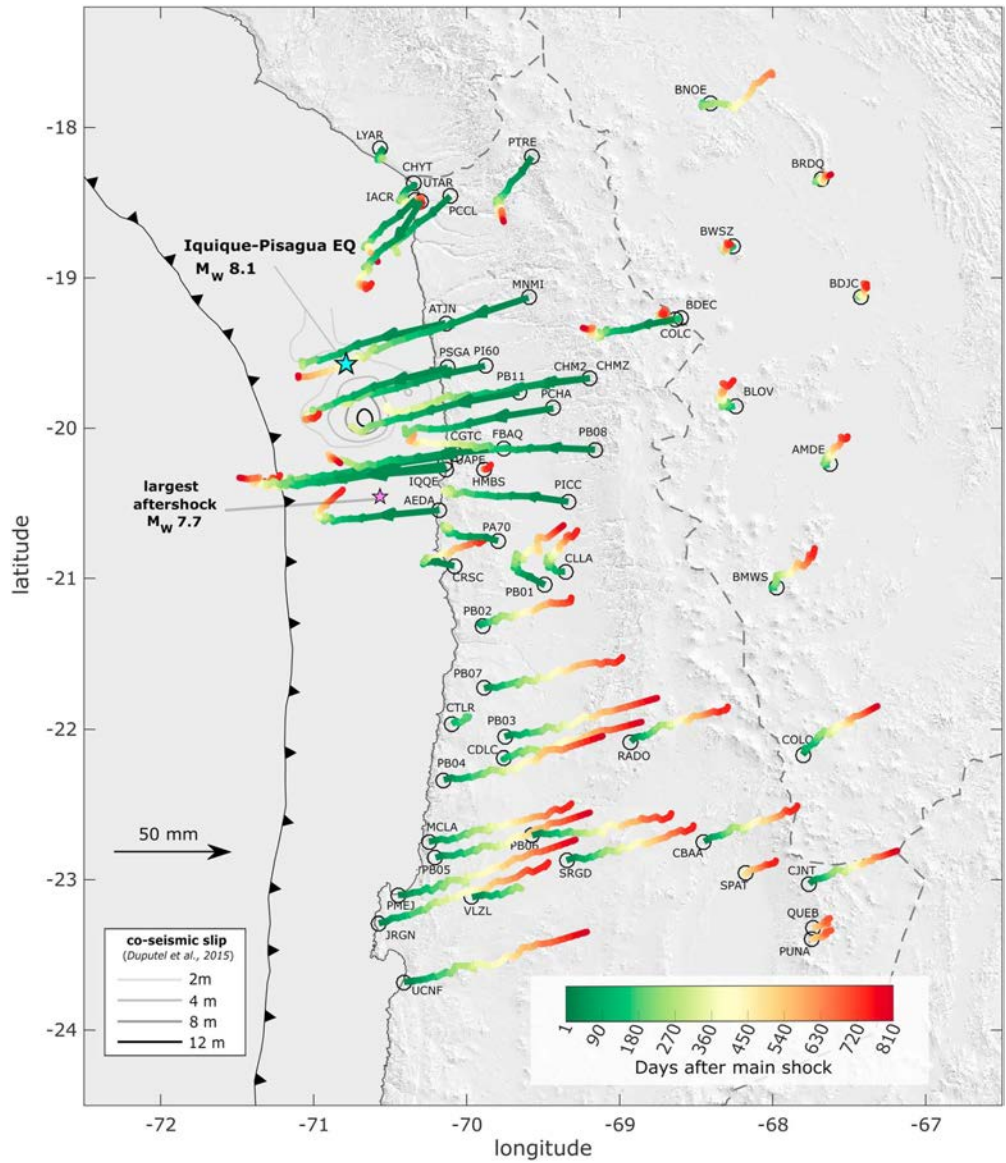


Figure 6. Postseismic ground displacement color coded by days after the mainshock (sampled every 30 days). For other features see Figure 4.

north of the main rupture at ~35–40-km depth. The updip area of our slip model exhibits significantly less slip, only 10 to 20 cm. The geometry of afterslip extent during the first year after the earthquake is surprisingly similar to the afterslip pattern of the first 2 weeks, except for the larger magnitudes. Afterslip in Period 2 involves deeper parts of the interface and is shifted ~20 km northward compared to Period 1 as visible at the aftershock peak slip. A relatively sharp transition from slip to backslip-dominated interface motion is again detected at 20.7–21°. At this latitude, slip extends about ~40 km further south underneath the Chilean coast, thus at relatively poorly resolved, deeper parts of the interface. No difference to interseismic interface motion can be observed south of this latitudinal range as inferred by a lack of slip/backslip southward.

In Period 3, afterslip has significantly decreased and converges to 0 in the center of the inferred rupture zone of the Iquique-Pisagua mainshock (Figure 5i). This reflects the transition from an afterslip-dominated stress

regime to relocking as described by Wang et al. (2012). One isolated afterslip patch is located ~50 km north of the epicenter with 10–15-cm slip. Surprisingly, peak slip occurs consistently at the area of the largest aftershock 50 km south of the mainshock, with slip of 35 cm in Period 3. The spatial transition from afterslip at the Camarones segment to interseismic relocking at the southern Loa segment becomes more diffuse in Period 3 but is shifted northward compared to Period 2 (nomenclature from Métois et al., 2016). Most prominently, south of 21°S, we observe increasing backslip rates in an interface depth range of 40–60 km. After having subtracted averaged interseismic loading rates from our observations, we expect interface slip in adjoining seismotectonic segments that are not affected by afterslip to be close to 0. In contrast, backslip rates up to –2.5 cm south of 21°S indicate a coupling increase of the subduction interface in the second year after the megathrust event. Peak backslip rates are located at 45–50-km depth underneath Mejillones peninsula at ~23°S.

Overall, a cumulative peak afterslip of $89.0 \pm 1.2/-0.4$ cm is observed within the first 2 years after the Iquique-Pisagua earthquake, occurring between 30 and 45 km depth and embracing the rupture area downdip (Figure S20). We estimated the error of the maximum slip using a simplified Monte-Carlo approach calculating the standard deviation of 50 inversions in which we added normally distributed noise to the GPS data (Figure S21). A sharp transition between afterslip to the north and backslip (increased interseismic coupling) to the south is observed in a latitudinal range of 21–21.5°S. Most interestingly, the pattern complements the high backslip pattern observed in the interseismic phase at these latitudes (Figure 4c).

The model resolution based on our checkerboard approach (section 3.2) for all three periods is generally good (Figures S15c and S15d). An exception is the southern part of Period 1, where we have rather poor resolution south of 23°S mainly due to the lack of GPS stations there as we only use cGPS data. But the expected afterslip area south of the mainshock epicenter, toward the largest aftershock, is well resolved below a depth of ~15 km. However, potential shallow afterslip above 15 km might not be resolvable with our model geometry.

The postseismic models fit the horizontal data of all three stages reasonably with a rms residual of 1.7 mm (Period 1), 4.2 mm (Period 2), and 2.4 mm (Period 3) (Figures S16b–S16d). The strongest horizontal misfit is observed in Period 2 at coastal stations close to the main rupture and to the north. Further tests have shown that the misfit cannot be significantly improved by changing model parameters (i.e., depth constraints or smoothing value). The overall direction of deviation is toward the south, implying a northward shifted model slip. One reason for the northward shift of slip could be the unfavorable spatial resolution of our model geometry that is poorly resolved at shallow parts of the interface as well as north of 19°S due to a lack of Peruvian GPS data. Thus, potential shallow afterslip may be shifted deeper and northward to better fit the observations. A more physical explanation for the deviation could involve rheologic inhomogeneity in the crust, which are not taken into account in our half-space model. The relatively high misfit and systematic underprediction of the southward displacement in Period 2 may be a consequence of our simplified model rheology. To better fit the data, a more complex geometry involving a three-dimensional model setup may be needed (e.g., Klein et al., 2016; Li et al., 2015). Another cause for local (point-wise) misfit of the GPS vectors as, for example, observed for stations VIRI or COLC in Period 3 could be upper crustal faulting, as has been observed in many parts of Northern Chile and Bolivia (e.g., Allmendinger & González, 2010; Lamb, 2000). González et al. (2015) even argued that the Iquique-Pisagua mainshock could have been triggered by a reactivated trench-oblique upper plate reverse fault (the M_w 6.7 foreshock on 16 March 2014). However, we do not observe a spatially coherent, long-wavelength misfit pattern in the far field as potentially caused by viscous relaxation (Wang et al., 2012). Thus, we believe that our model predictions for the viscoelastic component represent the amount of mantle relaxation contributing to the measured postseismic ground deformation signal well.

The vertical displacement predictions fit the data worse than the horizontal predictions and exhibit a rms residual of 3.5 mm (Period 1), 5.2 mm (Period 2) and 2.0 mm (Period 3; Figures S17b–S17d). The model clearly fails to properly predict the highly complex vertical displacement and, again, a three-dimensional model would probably improve the fit, for example, by including a complex crustal structure that accounts for features like local low-viscosity channels (e.g., Klein et al., 2016; Figures 5d–5f and S18b–S18d). Another reason for the poorly vertical fit is the relatively large data uncertainty of the vertical data, particularly for episodic measurements that can be explained by the acquisition geometry allowing more sensitivity to

horizontal measurements. Another systematic overrepresentation of vertical data is apparent close to the rupture area of the mainshock, whereas the up component toward the south is clearly underrepresented. Nevertheless, our model is capable of resolving the hinge line between postseismic uplift and subsidence at coastal stations between 20 and 21°S in Periods 1 and 2. In Period 3, this hinge line may have shifted offshore.

5. Discussion

5.1. Spatial Correlation of Afterslip and Aftershocks

The afterslip pattern of the Iquique-Pisagua earthquake is comparable with the postseismic deformation of other megathrust events of the last decade. Similar to the 2005 Nias M_w 8.7 Sumatra event (Hsu et al., 2006) or the 2010 Maule M_w 8.8 Chile earthquake (Bedford et al., 2013), afterslip surrounds the region of maximum coseismic slip and occurs mostly in the downdip area of the rupture (Figures 5g–5i). To shed light on this and better understand the relation between afterslip and aftershocks, we analyzed the location of aftershocks of the first year after the earthquake. For this we utilized a recently compiled seismicity catalog from the IPOC permanent station network that covers the years 2007–2014 (Sippl et al., 2018). The catalog contains a total of 101 k events and has good spatial coverage of the Northern Chile–Southern Peru seismic gap, with a completeness magnitude of 2.7–2.9. Events were detected using the multistep procedure of phase picking and relocation outlined in Sippl et al. (2013), the last step of which is double-difference relocation using event pair cross correlations.

In the first 2 weeks after the Iquique-Pisagua mainshock, modeled peak afterslip occurs north and southeast of the rupture area (Figure 5g), near the epicenter of the large aftershock, where interseismic backslip (coupling) is highest (Figure 4c). This suggests that in the first few days after the mainshock, afterslip neutralizes incomplete coseismic stress drop, as it was also reported after the 2010 Maule earthquake (Bedford et al., 2013). In the same period, aftershocks mostly occur in the rupture area. The distribution of aftershocks in the first days following the mainshock may thus be controlled by the redistribution of stress during the coseismic phase (Figure 7a; e.g., King et al., 1994).

The early stage of afterslip is characterized by the presence of both, normal and thrust faulting earthquakes, but after 2 weeks only thrust mechanisms dominate in the aftershock sequence. This may reflect a minor temporal change of the compressional axis of about 6° and pre-megathrust stress conditions were restored a few weeks later (Cesca et al., 2016). Aftershock locations in the first year after the mainshock until the end of 2014 seem to flank the highest coseismic rupture areas (slip above 8 m) but also border the regions of high afterslip (Figure 7b). In a band-like geometry, aftershocks separate the northern peak afterslip patch from the southern one. Modeled afterslip mostly occurs deeper than ~35 km and reaches the assumed transition zone from (brittle) crust to the hydrated mantle wedge (e.g., Bloch et al., 2014). Given the clear spatial correlation between peak afterslip and the absence of aftershocks in Period 2 (Figure 7b), we infer that postseismic stress release is mostly transferred from aseismic (rate-strengthening) peak afterslip areas to adjacent intermediate afterslip regions close to the coseismic rupture zone. The updip area exhibits relatively low afterslip, which agrees with the observation of the low degree of interseismic coupling in the shallower parts of the interface, where slip deficit is assumed to be almost 0 (Li et al., 2015). This possibly indicates interseismic creep on the updip portion of the plate interface. On the other hand, our checkerboard tests (Figure S15) show that the shallow parts of the interface are poorly resolved, and the relatively intense updip seismic activity indicates rate-weakening behavior. North of 19°S, the seismicity in the downdip high afterslip area decays rapidly (Figure 7b). Thus, the aseismic area in the north seems to release stress while creeping, which potentially reflects a transient increase of pore fluid pressure (Kodaira et al., 2004). Moreover, this region spatially correlates with low coupling in shallow to intermediate crustal depths of 10–30 km (Figure 4c), probably indicating the border to another seismotectonic segment (Li et al., 2015; Métois et al., 2013). This could also explain the relatively low GPS displacement rates north of 19°S in the interseismic (Figure 4a) and postseismic period (Figures 5g–5i) that are probably caused by a low-coupled segment to the north that is separated from the Camarones segment where the mainshock ruptured. Moreover, the distance to the trench increases toward the north, which also contributes to a slowing down of the GPS velocities there.

South of 21°S, the high-afterslip zone also exhibits a significant decrease of seismicity. The rupture area of the mainshock terminates near a low coupling zone (Iquique intersegment, Métois et al., 2013) at 20°S

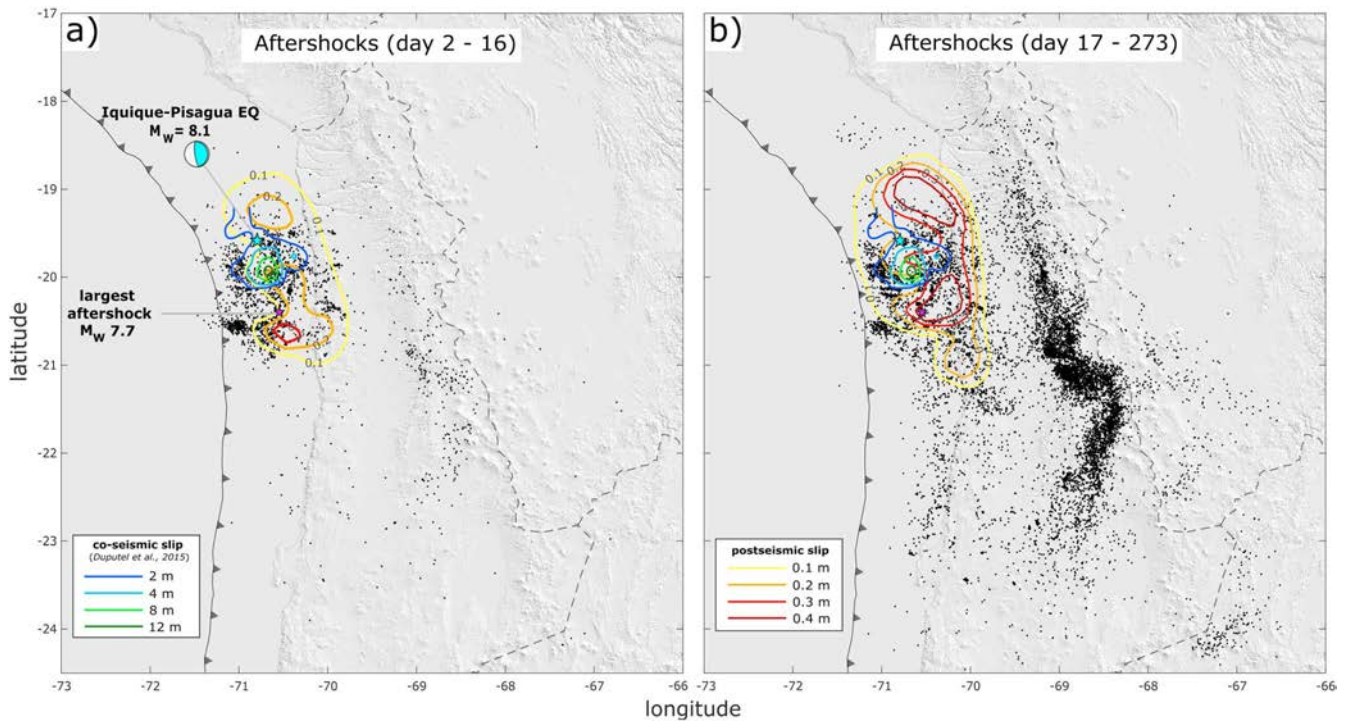


Figure 7. Aftershock distribution (Sippl et al., 2018) during (a) Period 1 and (b) Period 2 in comparison to coseismic slip (blue/green isolines) (Duputel et al., 2015) and modeled afterslip (yellow/red isolines) in the respective intervals. Each coseismic slip represents an increment of 2 m, each afterslip contour an increment of 0.1 m. Note that in (b) only aftershocks until the end of 2014 are included. For other features see Figure 4.

(Duputel et al., 2015; Ruiz et al., 2014; Schurr et al., 2014), but afterslip extends further south across to 21°S, probably due to the effects of the large aftershock (Figure 8a). Low coupling zones are assumed to behave in a rate-strengthening way, increasing their frictional strength, thus decreasing the likelihood of slip propagation (e.g., Scholz, 1998). But the afterslip also affects this interseismically low coupled zone and terminates abruptly at ~21.2°S (Figure 8a), where the seismicity likewise decreases sharply. Similar to above, the coupling differences may reflect a seismotectonic barrier.

In Period 2, a N-S oriented, left-stepping, band-like structure of seismicity becomes more prominent at 80–120 km depth and 250–300 km east of the trench (Figure 7b) and is most densely populated between 20° and 22.5°S. The spatial extent of this band correlates neither with the shallow seismicity described above nor with the coseismic or postseismic slip on the plate interface. The occurrence of this intermediate-depth seismicity is most likely caused by the metamorphic dehydration of the oceanic lithosphere effecting hydraulic embrittlement due to the release of fluids (Bloch et al., 2014; Rietbrock & Waldhauser, 2004; Yoon et al., 2009). The observed kink in the seismic band spatially correlates with the southern limit of the afterslip zone at 21°S. South of the kink, the dehydration-related seismicity occurs slightly deeper, which probably reflects heterogeneity in the subducting oceanic plate (e.g., Geersen et al., 2015) or crustal rheology.

We additionally generated a simple Coulomb failure stress (ΔCFS) change model based on our viscoelastic model geometry and the coseismic shear (σ_s) and normal stress (σ_n) changes on the interface:

$$\Delta\text{CFS} = \sigma_s - \sigma_n \mu \quad (3)$$

with $\mu = 0.1$ as the coefficient of friction (Lamb, 2006). In our model, positive ΔCFS outlines the main rupture area updip and downdip (Figure 8b), indicating that those interface regions were brought closer to failure and are more prone to aftershocks during the postseismic stage. For the updip part, where we lack model resolution, aftershock locations are in good spatial agreement with positive ΔCFS . For the downdip area, aftershocks occur in both, positively and negatively loaded ΔCFS regions. The negative ΔCFS of up to -4 Mpa spatially coincides with the high coseismic slip regions of the rupture area of the Iquique-Pisagua

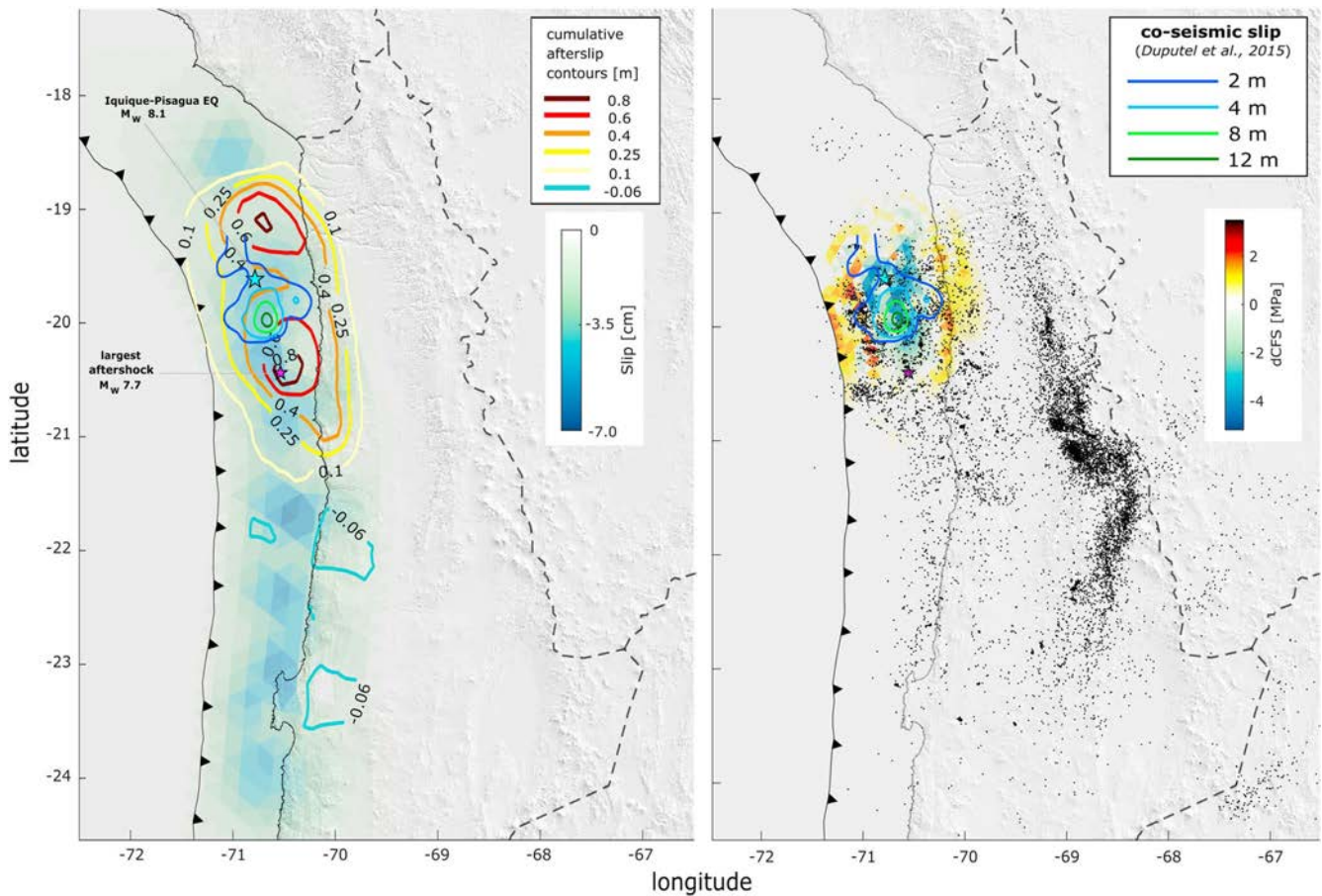


Figure 8. (a) Comparison of interseismic backslip, coseismic slip (Duputel et al., 2015) and cumulative afterslip (see also Figure S20). (b) Comparison of coseismic slip, estimated Coulomb failure stress changes based on slip model of Schurr et al. (2014), and aftershocks from April to December 2014 (Sippl et al., 2018). For other features see Figure 4.

mainshock, where significantly fewer aftershocks occur. The largest aftershock is located at the southern edge of the negative ΔCFS region. This may be associated to premainshock stress conditions and potentially reflects interseismic stress buildup preceding the mainshock, for example, due to the foreshock on 16 March 2014 (e.g., González et al., 2015).

5.2. Seismotectonic Barrier at 21°S

In all our observations, we find that the region at 21°S acts as a barrier or apparent discontinuity of physical properties. Throughout the whole investigated period, the GPS stations south of 21°S move permanently in the interseismic ENE direction, indicating that the plate interface remains strongly coupled (Figures 4a, 5a–5c, and 8a). In the postseismic stage, we observe sharp GPS rate changes near 21°S that coincide with the southern termination of the narrow, low-coupled zone (Iquique low coupling zone) (Figure 8a; Métois et al., 2016). Afterslip intrudes into this possibly rate-strengthening zone south of 21°S, which we interpret as postseismic stress transfer into a very heterogeneous subduction interface (e.g., Kaneko et al., 2010; Marone et al., 1991) at the border to a region undergoing stress buildup (south of 21°S). This transition zone also shows peak seismicity at the upper plate both before and after the 2014 earthquake (Meng et al., 2015; Figure 7b) and potentially indicates a seismotectonic barrier, which is less coupled with respect to adjacent segments. The barrier may thus be a consequence of mechanical variations in the coupling between the interface and the upper plate. Geersen et al. (2015) attribute the heterogeneous coupling to seamounts on the subducting plate that prevented the Iquique-Pisagua rupture to migrate southward. According to them, the so-called Iquique

Ridge at 19.5–21°S (Figure 1) favors aseismic conditions with smaller earthquakes and creep rather than large ruptures due to extensive fracturing at the plate boundary (Geersen et al., 2015; Wang & Bilek, 2011). Another explanation for the presence of the barrier could be a postulated abrupt change of slab dip at ~21°S, interpreted as slab bending in recent studies (e.g., León-ríos et al., 2016). In the numerical model of Kaneko et al. (2010), two rate-weakening zones were separated by a narrow rate-strengthening block. This is comparable to the tectonic setting of our study, where two highly coupled zones are separated by the narrow Iquique low coupling zone at 21°S (Figure 8a). Whenever one of the rate-weakening zones ruptured individually in this experiment, stress was transferred to the opposite zone that, in turn, was brought closer to failure than expected from the original recurrence interval (Kaneko et al., 2010). These results focus our attention to the southern Loa segment at 21–23°S.

However, the origin of the seismotectonic barrier might also be related to the upper plate rather than to the plate interface. Loveless et al. (2009) reported that the preferred orientation of surface cracks north and south of 21°S changes from NNW to NE, indicating two distinct stress regimes in the upper crust. This zone is also the southern limit of E-W trending faults (Figure 1) responsible for along-strike shortening of the Coastal Cordillera (Allmendinger & González, 2010; Allmendinger et al., 2005). These authors have related this kinematic observation to the location of the symmetry axis of the Andean orocline (Gephart, 1994; Figure 1) as well as of the Benioff Zone. This finding is also supported by numerical analysis and analog simulation in Boutelier and Oncken (2010) and Boutelier et al. (2014), both of which suggest that bending in conjunction with specific plate interface properties have a key role in the kinematic response. The seismotectonic barrier correlates spatially with the boundary between a strongly faulted upper plate domain in the North and an unfaulted upper plate in the South (Allmendinger & González, 2010). From these observations together with the observed sharp gradient in surface motion, we additionally speculate that there could be an associated strength change of the forearc crust.

The seismotectonic barrier at 21°S potentially prevented the Northern Chile-Southern Peru seismic gap region to rupture in a single event as in the 1877 Iquique M_w 8.6 earthquake (e.g., Comte & Pardo, 1991). Although there is also some discordance about the actual size of the 1877 event (Métois et al., 2013), this earthquake was certainly larger than the 2014 event and either extended the barrier, or the barrier was only formed in the postseismic and interseismic stage following the 1877 event. The 2014 earthquake could only partially release the slip deficit accumulated since 1877 (Métois et al., 2013; Schurr et al., 2014). Consequently, for further analysis the seismic gap region should be split into two parts separated by the seismotectonic barrier at 21°S. Moreover, our results suggest that the seismotectonic behavior may be more strongly affected by upper plate strength variations along the Chilean margin than previously surmised.

5.3. GPS Rate Change South of 21°S

GPS rates south of 21°S reflect the crustal response to the occurrence of the 2014 earthquake at this unbroken adjacent segment. Here we find a significant rate change of up to 10 mm/year over different postseismic periods after the Iquique-Pisagua earthquake. To illustrate this, we extracted the linear trend from the time series of Periods 2 and 3 as described in section 2.2 and calculated the rate changes with respect to the interseismic rates observed before the earthquake (Figure 9). In the first year after the mainshock, stations south of 21°S latitude experienced a rate decrease compared to the preearthquake rates, whereas in the second year those stations (consistently sGPS and cGPS) show a rate increase (Figure 9). This rate increase may not be dependent on the distance between station and trench as maximum acceleration is observed at inland stations at distances of 130 to 170 km away from the trench and not at coastal stations that are closer to the trench. We interpret this change of behavior between the first and the second year following the Iquique-Pisagua earthquake as response to decreasing afterslip rates and the dominant effect of interseismic deformation at the southern Loa segment. Hence, the rate decrease in the first year could be explained by the interaction of (1) far-field afterslip on the interface and (2) viscoelastic relaxation. Both mechanisms cause GPS stations to move toward the rupture zone, opposite to the ongoing interseismic coupling locking (Bedford et al., 2016; Wang et al., 2012). Therefore, the observed rate decrease in the first year could be the consequence of relaxation processes. This confirms that the viscoelastic relaxation decays fast, being more dominant in the first year after the event. But what causes the rate increase in the second year after the earthquake, which is comparable to what was reported from adjoining segments of the 2003 Tokachi-Oki M_w 8.0, Japan earthquake (Heki & Mitsui, 2013)? One explanation may be given by recent studies of Melnick et al. (2017) and Klein et al. (2016)

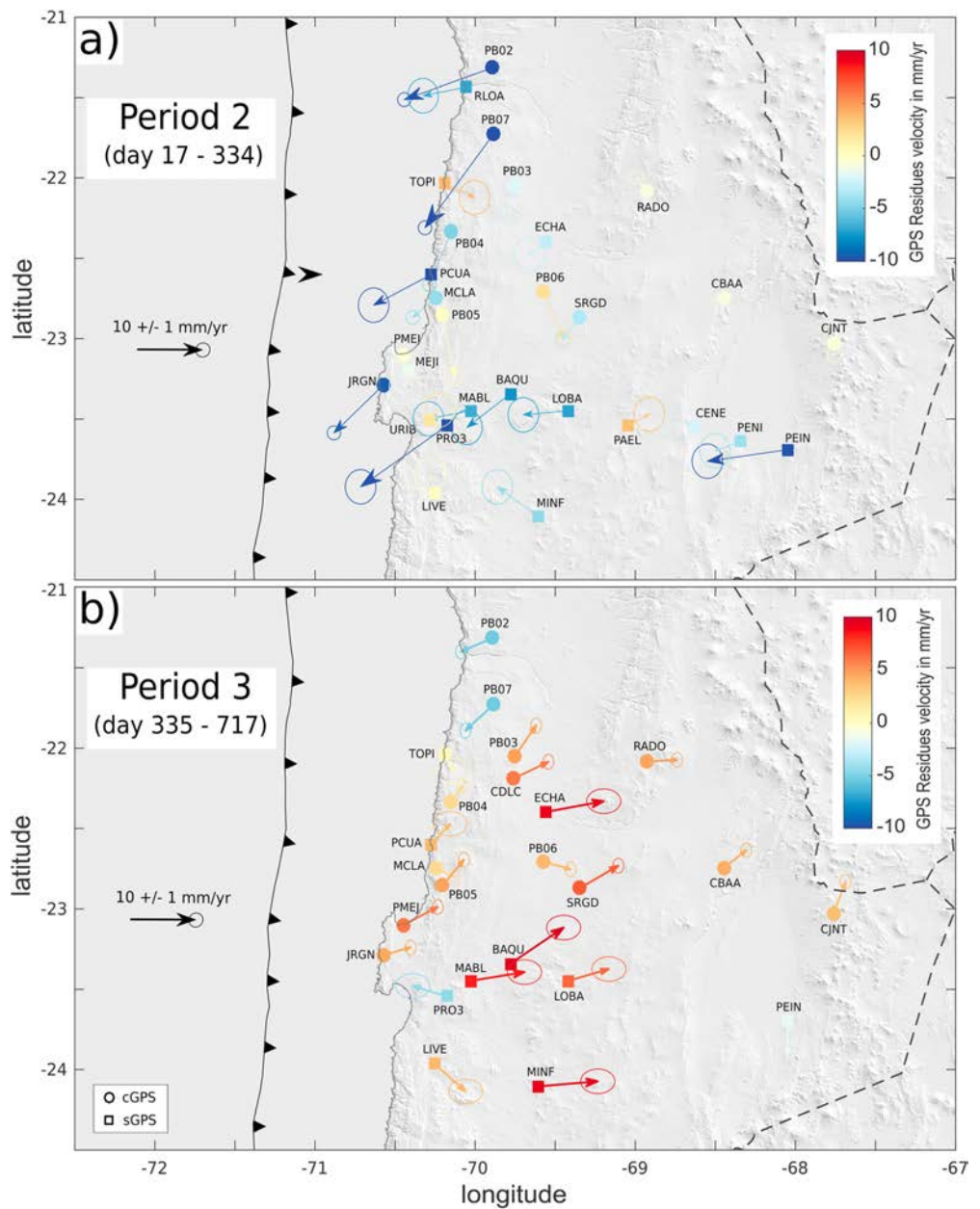


Figure 9. Rate changes during (a) Period 2 and (b) Period 3 after the Iquique-Pisagua earthquake with respect to the pre-event displacement rates. The vectors are color coded by the amplitude of the rate change; the symbols mark continuous (circle) and campaign (square) GPS rates. GPS = Global Positioning System.

that documented GPS rate increase after the 2010 Maule earthquake at the adjacent unbroken segments. Likewise, we propose that the observed rate increase south of 21°S can be an effect of continental-scale, viscoelastic mantle relaxation (Klein et al., 2016) that induces an increase of fault shear stresses more than 200 km away from the rupture zone. The increase of interseismic rates can also be mechanically related to the elastic flexural bending response of both plate segments to the uncoupling after a large earthquake in one of the segments. This uncoupling may increase the interseismic stress accumulation at adjacent clamped (locked) segments (Melnick et al., 2017). Our models confirm these temporal variations of

interseismic rate after a large earthquake and suggest a significant increase in backslip rate of up to 10 mm/year (Figure 9) and thus increased interface coupling in the second year after the earthquake (Figure 5i). The observation that maximum rate increase occurs not at coastal stations, but 40 to 80 km inland potentially reflects downdip changes of interface coupling deeper than 40 km at the downdip limit of the seismogenic zone. Similar to the potential triggering of the 2015 Illapel M_w 8.2 earthquake (Tilmann et al., 2016) by the 2010 Maule M_w 8.8 event as bimodal megathrust occurrence (Klein et al., 2016; Melnick et al., 2017), we suggest that the Iquique-Pisagua event can bring the Loa segment closer to failure due to increased shear stress at the downdip limitation of the fault.

Another, more speculative hypothesis locates the source of surface displacement rate increase to the upper crust, particularly if we assume that our elastic models somewhat overestimate the coupling degree. This would be the case, if we underestimate the viscoelastic relaxation or the interseismic loading prior to the earthquake. Given the complexity of our time series that cover the full seismic cycle including two major earthquakes (the 2005 Tarapacá and 2007 Tocopilla event) that affect velocities in our pre-Iquique-Pisagua earthquake interval, our extracted loading rates may be underestimated. In this case, we should detect a time-dependent increase of upper crust weakening and the current slip deficit would be released aseismically. Another realistic explanation for coupling increase in our models involves our simplified model rheology with a homogeneous, linear Maxwell viscosity that does not account for complex rheologic features like low-viscosity wedges (e.g., Klein et al., 2016). However, the consistency and uniformity of the change of the interseismic velocity field, observed in both, sGPS and cGPS data, suggest an increase of shortening rate at the Loa segment independent of our modeling strategy. Longer postseismic time series will provide valuable data to our findings and to further investigate the temporal variations of coupling degree.

Acknowledgments

We thank all institutions that made GPS data available in the frame of the IPOC Network (www.ipoc-network.org; <http://doi.org/10.5880/GFZ.1.1.2017.001> for cGPS data; <http://doi.org/10.5880/GFZ.4.1.2017.003> for sGPS data). Data used in this study come from different institutions—German Research Centre for Geosciences, Institut de Physique du Globe de Paris, Centro Sismológico Nacional, Universidad de Chile, Departamento de Geofísica, Proyecto Fondecyt 11140904 (CONICYT, Chile), and Universidad Católica del Norte, Antofagasta, Chile. We additionally acknowledge the French-Chilean International Associated Laboratory (LIA) “Montessus de Ballore” and the USA-Chilean Central Andean Tectonic Observatory Geodetic Array projects for giving access to data of several of their continuous GPS stations in Chile. We particularly thank Daniel Carrizo, Edmundo Norabuena, Diana Comte, Jorge Jara, Eduardo Contreras-Reyes, Mohamed Chlieh, Arthur Delorme, Joachim F. Genrich, Emilie Klein, Ismael Ortega, Sophie Peyrat, Efrain Rivera, Sergio Ruiz, Maria Carolina Valderas Bermejo, Klaus Dieter Bataille, Mark Simons, Anne Socquet, Christophe Vigny, and Jean-Pierre Vilotte who all contributed to the GPS data acquisition. Francisco Ortega-Culaciati acknowledges support from Proyecto Fondecyt 11140904, CONICYT, CHILE. We also thank Juan Carlos Baez (CNS Chile) and Klaus Bataille (University of Concepción, Chile) for GPS equipment. Felix Hoffmann is a member of the Helmholtz graduate research school GeoSim. Marcos Moreno has been supported by the German Science Foundation (DFG) grant MO 2310/3-1. This paper has benefitted from discussions with Jonathan Bedford. We thank two anonymous reviewers and the Associate Editor for their fruitful and useful corrections and suggestions that improved much the clarity of this study.

6. Conclusion

Based on 152 GPS time series, we have derived an interseismic backslip model of the (former) Northern Chile-Southern Peru seismic gap and three consecutive postseismic models documenting 2 years of afterslip motion following the 2014 M_w 8.1 Iquique-Pisagua earthquake. Prior to the earthquake, we find a heterogeneously locked plate interface with two highly coupled patches in the central part of the gap that are separated by a narrow, low-coupling zone at 21°S (Iquique low coupling zone), probably acting as a seismotectonic barrier. Consequently, the rupture area of the 1877 M_w 8.6 Iquique earthquake should be analyzed as two distinct patches.

The postseismic models exhibit peak afterslip at the location of the largest aftershock and show a relatively sharp gradient from trenchward to landward motion at ~21°S latitude. Based on this strong displacement gradient as well as mapped changes in upper plate faulting and crack orientations, we speculate that crustal strength heterogeneity may contribute to cause this seismotectonic barrier.

Cumulative afterslip reaches $89.0 \pm 1.2/-0.4$ cm, outlines the main rupture area downdip and dissolves after 2 years. The Loa segment south of 21°S is unaffected by afterslip but yields a significant rate increase toward interseismic ground displacement direction of up to 10 mm/year in the second year following the earthquake. We interpret this as an increase in downdip interface coupling due to shear stress increase as a consequence of regionally induced deformation (viscoelastic and/or elastic bending) after the 2014 earthquake. The Iquique-Pisagua earthquake may have initiated a superinterseismic phase in the southern sector with a bimodal occurrence of megathrust events (Loveless, 2017; Melnick et al., 2017). In this case, the risk of another earthquake in this unbroken part between 21 and 23°S has increased. An opposing interpretation suggests time-dependent crustal weakening involving aseismic slip release in the Loa segment. Longer deformation time series are needed to distinguish between these hypotheses and an increased observational attention to this segment is recommended.

References

- Aagaard, B., Knepley, M., & Williams, C. A. (2013). A domain decomposition approach to implementing fault slip in finite-element models of quasi-static and dynamic crustal deformation. *Journal of Geophysical Research: Solid Earth*, 118, 3059–3079. <https://doi.org/10.1002/jgrb.50217>
- Allmendinger, R. W., Gonzáles, G., Yu, J., Hoke, G., & Isacks, B. (2005). Trench-parallel shortening in the Northern Chilean Forearc: Tectonic and climatic implications. *Geological Society of America Bulletin*, 117(1), 89–104. <https://doi.org/10.1130/B25505.1>

- Allmendinger, R. W., & González, G. (2010). Tectonophysics invited review paper: Neogene to quaternary tectonics of the coastal cordillera, northern Chile. *Tectonophysics*, 495(1–2), 93–110. <https://doi.org/10.1016/j.tecto.2009.04.019>
- Altamimi, Z., Rebischung, P., Métivier, L., & Collilieux, X. (2016). ITRF2014: A new release of the International Terrestrial Reference Frame modeling nonlinear station motions. *Journal of Geophysical Research: Solid Earth*, 121, 6109–6131. <https://doi.org/10.1002/2016JB013098>
- Angermann, D., Klotz, J., & Reigber, C. (1999). Space-geodetic estimation of the Nazca-South America Euler vector. *Earth and Planetary Science Letters*, 171(3), 329–334. [https://doi.org/10.1016/S0012-821X\(99\)00173-9](https://doi.org/10.1016/S0012-821X(99)00173-9)
- Bedford, J., Moreno, M., Baez, J.-C., Lange, D., Tilmann, F., Rosenau, M., et al. (2013). A high-resolution, time-variable afterslip model for the 2010 Maule $M_w = 8.8$, Chile megathrust earthquake. *Earth and Planetary Science Letters*, 383, 26–36. <https://doi.org/10.1016/j.epsl.2013.09.020>
- Bedford, J., Moreno, M., Li, S., Oncken, O., Baez, J. C., Bevis, M., et al. (2016). Separating rapid relocking, afterslip, and viscoelastic relaxation: An application of the postseismic straightening method to the Maule 2010 cGPS. *Journal of Geophysical Research: Solid Earth*, 121, 7618–7638. <https://doi.org/10.1002/2016JB013093>
- Bedford, J., Moreno, M., Schurr, B., Bartsch, M., & Oncken, O. (2015). Investigating the final seismic swarm before the Iquique-Pisagua 2014 M_w 8.1 by comparison of continuous GPS and seismic foreshock data. *Geophysical Research Letters*, 42, 3820–3828. <https://doi.org/10.1002/2015GL063953>
- Béjar-Pizarro, M., Socquet, A., Armijo, R., Carrizo, D., Genrich, J., & Simons, M. (2013). Andean structural control on interseismic coupling in the North Chile subduction zone. *Nature Geoscience*, 6(6), 462–467. <https://doi.org/10.1038/ngeo1802>
- Bevis, M., & Brown, A. (2014). Trajectory models and reference frames for crustal motion geodesy. *Journal of Geodesy*, 88(3), 283–311. <https://doi.org/10.1007/s00190-013-0685-5>
- Bevis, M., Kendrick, E., Smalley, R. Jr., Brooks, B., Allmendinger, R., & Isacks, B. (2001). On the strength of interplate coupling and the rate of back arc convergence in the Central Andes: An analysis of the interseismic velocity field. *Geochemistry, Geophysics, Geosystems*, 2, 1067. <https://doi.org/10.1029/2001GC000198>
- Bloch, W., Kummerow, J., Salazar, P., Wigger, P., & Shapiro, S. A. (2014). High-resolution image of the North Chilean subduction zone: Seismicity, reflectivity and fluids. *Geophysical Journal International*, 197(3), 1744–1749. <https://doi.org/10.1093/gji/ggu084>
- Boutelier, D. A., & Oncken, O. (2010). Role of the plate margin curvature in the plateau buildup: Consequences for the central Andes. *Journal of Geophysical Research*, 115, B04402. <https://doi.org/10.1029/2009JB006296>
- Boutelier, D., Oncken, O., & Cruden, A. R. (2014). Trench-parallel shortening in the forearc caused by subduction along a seaward-concave plate boundary: Insights from analogue modelling experiments. *Tectonophysics*, 611, 192–203. <https://doi.org/10.1016/j.tecto.2013.11.028>
- Brooks, B. A., Bevis, M., Whipple, K., Arrowsmith, J. R., Foster, J., Zapata, T., et al. (2011). Orogenic-wedge deformation and potential for great earthquakes in the central Andean backarc. *Nature Geoscience*, 4(6), 380–383. <https://doi.org/10.1038/ngeo201143>
- Cavalié, O., Pathier, E., Radiguet, M., Vergnolle, M., Cotte, N., Walpersdorf, A., et al. (2013). Slow slip event in the Mexican subduction zone: Evidence of shallower slip in the Guerrero seismic gap for the 2006 event revealed by the joint inversion of InSAR and GPS data. *Earth and Planetary Science Letters*, 367, 52–60. <https://doi.org/10.1016/j.epsl.2013.06.020>
- Cesca, S., Grigoli, F., Heimann, S., Dahm, T., Kriegerowski, M., Sobiesiak, M., et al. (2016). The M_w 8.1 2014 Iquique, Chile, seismic sequence: A tale of foreshocks and aftershocks. *Geophysical Journal International*, 204(3), 1766–1780. <https://doi.org/10.1093/gji/ggv544>
- Chlieh, M., De Chabalier, J. B., Rugg, J. C., Armijo, R., Dmowska, R., Campos, J., & Feigl, K. L. (2004). Crustal deformation and fault slip during the seismic cycle in the North Chile subduction zone, from GPS and InSAR observations. *Geophysical Journal International*, 158(2), 695–711. <https://doi.org/10.1111/j.1365-246X.2004.02326.x>
- Chlieh, M., Perfettini, H., Tavera, H., Avouac, J. P., Remy, D., Nocquet, J. M., et al. (2011). Interseismic coupling and seismic potential along the Central Andes subduction zone. *Journal of Geophysical Research*, 116, B12405. <https://doi.org/10.1029/2010JB008166>
- Christensen, N. (1996). Poisson's ratio and crustal seismology. *Journal of Geophysical Research*, 101, 3139–3156. <https://doi.org/10.1029/95JB03446>
- Coleman, T. F., & Li, Y. (1996). A reflective Newton method for minimizing a quadratic function subject to bounds on some of the variables. *SIAM Journal on Optimization*, 6(4), 1040–1058. <https://doi.org/10.1137/S1052623494240456>
- Comte, D., & Pardo, M. (1991). Reappraisal of great historical earthquakes in the northern Chile and southern Peru seismic gaps. *Natural Hazards*, 4(1), 23–44. <https://doi.org/10.1007/BF00126557>
- Delouis, B., & Legrand, D. (2007). M_w 7.8 Tarapaca intermediate depth earthquake of 13 June 2005 (northern Chile): Fault plane identification and slip distribution by waveform inversion. *Geophysical Research Letters*, 34, L01304. <https://doi.org/10.1029/2006GL028193>
- Delouis, B., Pardo, M., Legrand, D., & Monfret, T. (2009). The M_w 7.7 Tocopilla earthquake of 14 November 2007 at the southern edge of the northern Chile seismic gap: Rupture in the deep part of the coupled plate interface. *Bulletin of the Seismological Society of America*, 99(1), 87–94. <https://doi.org/10.1785/0120080192>
- DeMets, C., Gordon, R. G., Argus, D. F., & Stein, S. (1994). Effect of recent revisions to the geomagnetic reversal time scale on estimates of current plate motions. *Geophysical Research Letters*, 21, 2191–2194. <https://doi.org/10.1029/94GL02118>
- Deng, Z., Gendt, G., & Schöne, T. (2016). Status of the TIGA tide gauge data reprocessing at GFZ. In C. Rizos, & P. Willis (Eds.), *IAG 150 Years: Proceedings of the IAG Scientific Assembly in Potsdam, Germany, 2013, (International Association of Geodesy Symposia; 143)* (pp. 33–40). Potsdam, Germany: Springer International. https://doi.org/10.1007/1345_2015_156
- Dong, D., Fang, P., Bock, Y., Cheng, M. K., & Miyazaki, S. (2002). Anatomy of apparent seasonal variations from GPS-derived site position time series. *Journal of Geophysical Research*, 107(B4), 2075. <https://doi.org/10.1029/2001JB000573>
- Du, Y., Aydin, A., & Segall, P. (1992). Comparison of various inversion techniques as applied to the determination of a geophysical deformation model for the 1983 Borah Peak earthquake. *Bulletin of the Seismological Society of America*, 82(4), 1840–1866.
- Duputel, Z., Jiang, J., Jolivet, R., Simons, M., Rivera, L., Ampuero, J.-P., et al. (2015). The Iquique earthquake sequence of April 2014: Bayesian modeling accounting for prediction uncertainty. *Geophysical Research Letters*, 42, 7949–7957. <https://doi.org/10.1002/2015GL065402>
- Engdahl, E. R., & Villasenor, A. (2002). Global seismicity: 1900–1999. *Int. Geophys.*, 81, 665–690. [https://doi.org/10.1016/S0074-6142\(02\)80244-3](https://doi.org/10.1016/S0074-6142(02)80244-3)
- Geersen, J., Ranero, C. R., Barckhausen, U., & Reichert, C. (2015). Subducting seamounts control interplate coupling and seismic rupture in the 2014 Iquique earthquake area. *Nature Communications*, 6(1), 8267–8211. <https://doi.org/10.1038/ncomms9267>
- Geirsson, H., Árnadóttir, T., Völkens, C., Jiang, W., Sturkell, E., Villemin, T., et al. (2006). Current plate movements across the Mid-Atlantic Ridge determined from 5 years of continuous GPS measurements in Iceland. *Journal of Geophysical Research*, 111, B09407. <https://doi.org/10.1029/2005JB003717>
- Gendt, G., Deng, Z., Ge, M., Nischan, T., Uhlemann, M., Beeskow, G., et al. (2013). GFZ ANALYSIS CENTER OF IGS—Annual Report for 2013 (pp. 1–10).
- Gephart, J. W. (1994). Topography and subduction geometry in the Central Andes: Clues to the mechanics of a noncollisional orogen. *Journal of Geophysical Research*, 99, 12,279–12,288. <https://doi.org/10.1029/94JB00129>

- González, G., Salazar, P., Loveless, J. P., Allmendinger, R. W., Aron, F., & Shrivastava, M. (2015). Upper plate reverse fault reactivation and the unclamping of the megathrust during the 2014 northern Chile earthquake sequence. *Geology*, *43*(8), 671–674. <https://doi.org/10.1130/G36703.1>
- Hayes, G. P., Herman, M. W., Barnhart, W. D., Furlong, K. P., Riquelme, S., Benz, H. M., et al. (2014). Continuing megathrust earthquake potential in Chile after the 2014 Iquique earthquake. *Nature*, *512*(7514), 295–298. <https://doi.org/10.1038/nature13677>
- Hayes, G. P., Wald, D. J., & Johnson, R. L. (2012). Slab1.0: A three-dimensional model of global subduction zone geometries. *Journal of Geophysical Research*, *117*, B01302. <https://doi.org/10.1029/2011JB008524>
- Heki, K. (2001). Seasonal modulation of interseismic strain buildup in northeastern Japan driven by snow loads. *Science*, *293*(5527), 89–92. <https://doi.org/10.1126/science.1061056>
- Heki, K., & Mitsui, Y. (2013). Accelerated Pacific plate subduction following interplate thrust earthquakes at the Japan trench. *Earth and Planetary Science Letters*, *363*, 44–49. <https://doi.org/10.1016/j.epsl.2012.12.031>
- Hsu, Y.-J., Simons, M., Avouac, J.-P., Galetzka, J., Sieh, K., Chlieh, M., et al. (2006). Frictional afterslip following the 2005 Nias-Simeulue earthquake, Sumatra. *Science*, *312*(5782), 1921–1926. <https://doi.org/10.1126/science.1126960>
- Hu, Y., Bürgmann, R., Freymueller, J. T., Banerjee, P., & Wang, K. (2014). Contributions of poroelastic rebound and a weak volcanic arc to the postseismic deformation of the 2011 Tohoku earthquake. *Earth, Planets and Space*, *66*(1), 106. <https://doi.org/10.1186/1880-5981-66-106>
- Husen, S., Kissling, E., & Flueh, E. R. (2000). Local earthquake tomography of shallow subduction in North Chile: A combined onshore and offshore study. *Journal of Geophysical Research*, *105*, 28,183–28,198. <https://doi.org/10.1029/2000JB900229>
- Jónsson, S., Segall, P., Pedersen, R., & Björnsson, G. (2003). Post-earthquake ground movements correlated to pore-pressure transients. *Nature Geoscience*, *4*(2), 179–183. <https://doi.org/10.1038/nature01777>
- Kanamori, H. (1977). The energy release in great earthquakes. *Journal of Geophysical Research*, *82*, 2981–2987. <https://doi.org/10.1029/JB082i020p02981>
- Kaneko, Y., Avouac, J.-P., & Lapusta, N. (2010). Towards inferring earthquake patterns from geodetic observations of interseismic coupling. *Nature Geoscience*, *3*(5), 363–369. <https://doi.org/10.1038/ngeo843>
- Kelleher, J. A. (1972). Rupture zones of large South American earthquakes and some predictions. *Journal of Geophysical Research*, *77*, 2087–2103. <https://doi.org/10.1029/JB077i011p02087>
- King, G. C. P., Stein, R. S., & Lin, J. (1994). Static stress changes and the triggering of earthquakes. *Bulletin of the Seismological Society of America*, *84*(3), 935–953.
- Klein, E., Fleitout, L., Vigny, C., & Garaud, J. D. (2016). Afterslip and viscoelastic relaxation model inferred from the large-scale post-seismic deformation following the 2010 M_w 8.8 Maule earthquake (Chile). *Geophysical Journal International*, *205*(3), 1455–1472. <https://doi.org/10.1093/gji/ggw086>
- Klotz, J., Angermann, D., Michel, G. W., Porth, R., Reigber, C., Reinking, J., et al. (1999). GPS-derived deformation of the Central Andes including the 1995 Antofagasta $M_w = 8.0$ earthquake. *Pure and Applied Geophysics*, *154*(3–4), 709–730. <https://doi.org/10.1007/s000240050249>
- Klotz, J., Khazaradze, G., Angermann, D., Reigber, C., Perdomo, R., & Cifuentes, O. (2001). Earthquake cycles dominates contemporary crustal deformation in central and southern Andes. *Earth and Planetary Science Letters*, *193*(3–4), 437–446. [https://doi.org/10.1016/S0012-821X\(01\)00532-5](https://doi.org/10.1016/S0012-821X(01)00532-5)
- Kodaira, S., Iidaka, T., Kato, A., Park, J., Iwasaki, T., & Kaneda, Y. (2004). High Pore Fluid Pressure May Cause Silent Slip in the Nankai Trough. *Science*, *304*(5675), 1295–1298. <https://doi.org/10.1126/science.1096535>
- Lamb, S. (2000). Active deformation in the Bolivian Andes, South America. *Journal of Geophysical Research*, *105*, 25,627–25,653. <https://doi.org/10.1029/2000JB900187>
- Lamb, S. (2006). Shear stresses on megathrusts: Implications for mountain building behind subduction zones. *Journal of Geophysical Research*, *111*, B07401. <https://doi.org/10.1029/2005JB003916>
- León-ríos, S., Ruiz, S., Maksymowicz, A., & Leyton, F. (2016). Diversity of the 2014 Iquique's foreshocks and aftershocks: Clues about the complex rupture process of a M_w 8.1 earthquake. *Journal of Seismology*, *20*(4), 1059–1073. <https://doi.org/10.1007/s10950-016-9568-6>
- Li, S., Moreno, M., Bedford, J., Rosenau, M., Heidbach, O., Melnick, D., & Oncken, O. (2017). Postseismic uplift of the Andes following the 2010 Maule earthquake: Implications for mantle rheology. *Geophysical Research Letters*, *44*, 1768–1776. <https://doi.org/10.1002/2016GL071995>
- Li, S., Moreno, M., Bedford, J., Rosenau, M., & Oncken, O. (2015). Revisiting viscoelastic effects on interseismic deformation and locking degree: A case study of the Peru-North Chile subduction zone. *Journal of Geophysical Research: Solid Earth*, *120*, 4522–4538. <https://doi.org/10.1002/2015JB011903>
- Loveless, J. P. (2017). Super-interseismic periods: Redefining earthquake recurrence. *Geophysical Research Letters*, *44*, 1329–1332. <https://doi.org/10.1002/2017GL072525>
- Loveless, J. P., Allmendinger, R. W., Pritchard, M. E., Garroway, J. L., & González, G. (2009). Surface cracks record long-term seismic segmentation of the Andean margin. *Geology*, *37*(1), 23–26. <https://doi.org/10.1130/G25170A.1>
- Lyard, F., Lefevre, F., Letellier, T., & Francis, O. (2006). Modelling the global ocean tides: Modern insights from FES2004. *Ocean Dynamics*, *56*(5–6), 394–415. <https://doi.org/10.1007/s10236-006-0086-x>
- Marone, C. J., Scholtz, C. H., & Bilham, R. (1991). On the mechanics of earthquake afterslip. *Journal of Geophysical Research*, *96*, 8441–8452. <https://doi.org/10.1029/91JB00275>
- Melnick, D., Moreno, M., Quinteros, J., Baez, J. C., Deng, Z., Li, S., & Oncken, O. (2017). The super-interseismic phase of the megathrust earthquake cycle in Chile. *Geophysical Research Letters*, *44*, 784–791. <https://doi.org/10.1002/2016GL071845>
- Meng, L., Huang, H., Bürgmann, R., Ampuero, J. P., & Strader, A. (2015). Dual megathrust slip behaviors of the 2014 Iquique earthquake sequence. *Earth and Planetary Science Letters*, *411*, 177–187. <https://doi.org/10.1016/j.epsl.2014.11.041>
- Métois, M., Socquet, A., Vigny, C., Carrizo, D., Peyrat, S., Delorme, A., et al. (2013). Revisiting the North Chile seismic gap segmentation using GPS-derived interseismic coupling. *Geophysical Journal International*, *194*(3), 1283–1294. <https://doi.org/10.1093/gji/ggt183>
- Métois, M., Vigny, C., & Socquet, A. (2016). Interseismic coupling, Megathrust earthquakes and seismic swarms along the Chilean subduction zone (38°–18°S). *Pure and Applied Geophysics*, *173*(5), 1431–1449. <https://doi.org/10.1007/s00024-016-1280-5>
- Métois, M., Vigny, C., Socquet, A., Delorme, A., Morvan, S., Ortega, I., & Valderas-Bermejo, C. M. (2014). GPS-derived interseismic coupling on the subduction and seismic hazards in the Atacama region, Chile. *Geophysical Journal International*, *196*(2), 644–655. <https://doi.org/10.1093/gji/ggt418>
- Metzger, S., Jónsson, S., Danielsen, G., Hreinsdóttir, S., Joanne, F., Giardini, D., & Villemin, T. (2013). Present kinematics of the Tjörnes fracture zone, North Iceland, from campaign and continuous GPS measurements. *Geophysical Journal International*, *192*(2), 441–455. <https://doi.org/10.1093/gji/ggs032>
- Moreno, M., Bedford, J., Baez, J.-C., Klotz, J., Hoffmann, F., Deng, Z., et al. (2017). Survey mode GPS data in the IPOC Region, Central Andes, Chile, GFZ Data Services. <https://doi.org/10.5880/GFZ.4.1.2017.003>

- Moreno, M., Melnick, D., Rosenau, M., Bolte, J., Klotz, J., Echter, H., et al. (2011). Heterogeneous plate locking in the south-central Chile subduction zone: Building up the next great earthquake. *Earth and Planetary Science Letters*, 305(3–4), 413–424. <https://doi.org/10.1016/j.epsl.2011.03.025>
- Moreno, M., Rosenau, M., & Oncken, O. (2010). 2010 Maule earthquake slip correlates with pre-seismic locking of Andean subduction zone. *Nature*, 467(7312), 198–202. <https://doi.org/10.1038/nature09349>
- Motagh, M., Schurr, B., Anderssohn, J., Cailleau, B., Walter, T. R., Wang, R., & Villotte, J. P. (2010). Subduction earthquake deformation associated with 14 November 2007, M_w 7.8 Tocopilla earthquake in Chile: Results from InSAR and aftershocks. *Tectonophysics*, 490(1–2), 60–68. <https://doi.org/10.1016/j.tecto.2010.04.033>
- Nishenko, S. P. (1985). Seismic potential for large and great interplate earthquakes along the Chilean and southern Peruvian margins of South America: A quantitative reappraisal. *Journal of Geophysical Research*, 90, 3589–3615. <https://doi.org/10.1029/JB090iB05p03589>
- Nur, A., & Mavko, G. (1974). Postseismic viscoelastic rebound. *Science*, 183(4121), 204–206. <https://doi.org/10.1126/science.183.4121.204>
- Okada, Y. (1992). Internal deformation due to shear and tensile faults in a half-space. *Bulletin of the Seismological Society of America*, 97(B5), 7137–7140. <https://doi.org/10.1029/92JB00178>
- Peltzer, G., Rosen, P., Rogez, F., & Hudnut, K. (1998). Poroelastic rebound along the Landers 1992 earthquake surface rupture. *Journal of Geophysical Research*, 103, 30,131–30,145. <https://doi.org/10.1029/98JB02302>
- Perfettini, H., Avouac, J.-P., Tavera, H., Kositsky, A., Nocquet, J.-M., Bondoux, F., et al. (2010). Seismic and aseismic slip on the Central Peru megathrust. *Nature*, 465(7294), 78–81. <https://doi.org/10.1038/nature09062>
- Reibischung, P., Ray, J., Benoist, C., Metivier, L., & Altamimi, Z. (2015). Error analysis of the IGS repro2 station position time series (13 pp.). Abstract G23B-1065 Presented at the 2015 AGU Fall Meeting, San Francisco, CA.
- Reutter, K.-J., Scheuber, E., & Wigger, P. (Eds.) (1994). *Tectonics of the southern Central Andes* (334 pp.). Heidelberg: Springer-Verlag. <https://doi.org/10.1007/978-3-642-77353-2>
- Rietbrock, A., & Waldhauser, F. (2004). A narrowly spaced double-seismic zone in the subducting Nazca Plate. *Geophysical Research Letters*, 31, L10608. <https://doi.org/10.1029/2004GL019610>
- Ruegg, J. C., Campos, J., Armijo, R., Barrientos, S., Briole, P., Thiele, R., et al. (1996). The $M_w = 8.1$ Antofagasta (North Chile) earthquake of July 30, 1995: First results from teleseismic and geodetic data. *Geophysical Research Letters*, 23, 917–920. <https://doi.org/10.1029/96GL01026>
- Ruegg, J. C., Olcay, M., & Lazo, D. (2001). Co-, post- and pre(?) seismic displacements associated with the $M_w 8.4$ southern Peru earthquake of 23 June 2001 from continuous GPS measurements. *Seismological Research Letters*, 72(6), 673–678. <https://doi.org/10.1785/gssrl.72.6.673>
- Ruiz, S., Métois, M., Fuenzalida, A., Ruiz, J., Leyton, F., Grandin, R., et al. (2014). Intense foreshocks and a slow slip event preceded the 2014 Iquique $M_w 8.1$ earthquake. *Science*, 345(6201), 1165–1169. <https://doi.org/10.1126/science.1256074>
- Savage, J. C. (1983). A dislocation model of strain accumulation and release at a subduction zone. *Journal of Geophysical Research*, 88(B6), 4984–4996. <https://doi.org/10.1029/JB088iB06p04984>
- Schmid, R., Steigenberger, P., Gendt, G., Ge, M., & Rothacher, M. (2007). Generation of a consistent absolute phase-center correction model for GPS receiver and satellite antennas. *Journal of Geodesy*, 81(12), 781–798. <https://doi.org/10.1007/s00190-007-0148-y>
- Scholz, C. H. (1998). Earthquakes and friction laws. *Nature*, 391(6662), 37–42. <https://doi.org/10.1038/34097>
- Schurr, B., Asch, G., Hainzl, S., Bedford, J., Hoechner, A., Palo, M., et al. (2014). Gradual unlocking of plate boundary controlled initiation of the 2014 Iquique earthquake. *Nature*, 512(7514), 299–302. <https://doi.org/10.1038/nature13681>
- Simons, M., Galetzka, J. E., Genrich, J. F., Ortega, F., Comte, D., Glass, B., et al. (2010). Central Andean tectonic observatory geodetic Array, UNAVCO, GPS Data Set. <https://doi.org/10.7283/T50P0X37>
- Sippl, C., Schurr, B., Asch, G., & Kummerow, J. (2018). Seismicity structure of the Northern Chile forearc from >100 000 double-difference relocated hypocenters. *Journal of Geophysical Research: Solid Earth*, 123. <https://doi.org/10.1002/2017JB015384>
- Sippl, C., Schurr, B., Yuan, X., Mechie, J., Schneider, F. M., Gadoev, M., et al. (2013). Geometry of the Pamir-Hindu Kush intermediate-depth earthquake zone from local seismic data. *Journal of Geophysical Research: Solid Earth*, 118, 1438–1457. <https://doi.org/10.1002/jgrb.50128.7>
- Tassara, A., & Echaurren, A. (2012). Anatomy of the Andean subduction zone: Three-dimensional density model upgraded and compared against global-scale models. *Geophysical Journal International*, 189(1), 161–168. <https://doi.org/10.1111/j.1365-246X.2012.05397.x>
- Tilmann, F., Zhang, Y., Moreno, M., Saul, J., Eckelmann, F., Palo, M., et al. (2016). The 2015 Illapel earthquake, Central Chile: A type case for a characteristic earthquake? *Geophysical Research Letters*, 43, 574–583. <https://doi.org/10.1002/2015GL066963>
- Trubienko, O., Fleitout, L., Garaud, J. D., & Vigny, C. (2013). Interpretation of interseismic deformations and the seismic cycle associated with large subduction earthquakes. *Tectonophysics*, 589, 126–141. <https://doi.org/10.1016/j.tecto.2012.12.027>
- Van Dam, T., Wahr, J., Milly, P. C. D., Shmakin, A. B., Blewitt, G., Lavallée, D., & Larson, K. M. (2001). Crustal displacements due to continental water loading. *Geophysical Research Letters*, 28, 651–654. <https://doi.org/10.1029/2000GL012120>
- Wang, K., & Bilek, S. L. (2011). Do subducting seamounts generate or stop large earthquakes? *Geology*, 39(9), 819–822. <https://doi.org/10.1130/G31856.1>
- Wang, K., Hu, Y., & He, J. (2012). Deformation cycles of subduction earthquakes in a viscoelastic Earth. *Nature*, 484(7394), 327–332. <https://doi.org/10.1038/nature11032>
- Weiss, J. R., Brooks, B. A., Foster, J. H., Bevis, M., Echalar, A., Caccamise, D., et al. (2016). Isolating active orogenic wedge deformation in the southern Subandes of Bolivia. *Journal of Geophysical Research: Solid Earth*, 121, 6192–6218. <https://doi.org/10.1002/2016JB013070>
- Yagi, Y., Okuwaki, R., Enescu, B., Hirano, S., Yamagami, Y., Endo, S., & Komoro, T. (2014). Rupture process of the 2014 Iquique Chile earthquake in relation with the foreshock activity. *Geophysical Research Letters*, 41, 4201–4206. <https://doi.org/10.1002/2014GL060274>
- Yoon, M., Buske, S., Shapiro, S. A., & Wigger, P. (2009). Reflection image spectroscopy across the Andean subduction zone. *Tectonophysics*, 472(1–4), 51–61. <https://doi.org/10.1016/j.tecto.2008.03.014>

3.2.2 Role of poroelasticity during the early postseismic deformation of the 2010 Maule megathrust earthquake

Published as: C. Peña, S. Metzger, O. Heidbach, J. Bedford, B. Bookhagen, M. Moreno, O. Oncken, F. Cotton (2022), Role of poroelasticity during the early postseismic deformation of the 2010 Maule megathrust earthquake, *Geophysical Research Letters*, **49**, e2022GL098144. doi:[10.1029/2022GL098144](https://doi.org/10.1029/2022GL098144)

Supporting information: available online

Scientific application: By combining InSAR (high-resolution in space) and GNSS (high-resolution in time) data we show the importance of accounting for poroelastic effects after large megathrust earthquakes. If those are neglected, afterslip processes tend to be overestimated and, thus, the updated seismic hazard underestimated.

Methodological advances: We used a multi-parameter model approach that includes afterslip, visco-elastic and poro-elastic relaxation processes to validate multi-disciplinary observations (GNSS and InSAR). The heritage radar data from the ALOS satellite showing postseismic deformation has (to my knowledge) not been published elsewhere.

Individual Contributions: The study was designed, conducted and written by CP, supervised by OH. I prepared the InSAR observations and wrote the respective manuscript sections, JB prepared the GNSS observations. All authors commented on the interpretation and the manuscript.



Geophysical Research Letters®



RESEARCH LETTER

10.1029/2022GL098144

Key Points:

- A poro-viscoelastic deformation model improves the geodetic data misfit by 14% compared to an elastic model that only accounts for afterslip
- Poroelastic deformation mainly produces surface uplift and landward displacement patterns on the coastal forearc region
- Neglecting poroelastic effects may locally alter the afterslip amplitude by up to $\pm 40\%$ near the region of maximum coseismic slip

Supporting Information:

Supporting Information may be found in the online version of this article.

Correspondence to:

C. Peña,
carlosp@gfz-potsdam.de

Citation:

Peña, C., Metzger, S., Heidbach, O., Bedford, J., Bookhagen, B., Moreno, M., et al. (2022). Role of poroelasticity during the early postseismic deformation of the 2010 Maule megathrust earthquake. *Geophysical Research Letters*, 49, e2022GL098144. <https://doi.org/10.1029/2022GL098144>

Received 29 MAR 2022

Accepted 11 APR 2022

Author Contributions:

Conceptualization: Carlos Peña, Sabrina Metzger, Oliver Heidbach

Data curation: Carlos Peña, Sabrina Metzger, Jonathan Bedford, Bodo Bookhagen

Formal analysis: Carlos Peña, Sabrina Metzger, Oliver Heidbach, Jonathan Bedford, Bodo Bookhagen, Marcos Moreno, Onno Oncken, Fabrice Cotton

Funding acquisition: Carlos Peña, Oliver Heidbach, Bodo Bookhagen, Fabrice Cotton

Investigation: Carlos Peña, Sabrina Metzger, Oliver Heidbach

© 2022. The Authors.

This is an open access article under the terms of the [Creative Commons Attribution License](#), which permits use, distribution and reproduction in any medium, provided the original work is properly cited.

Role of Poroelasticity During the Early Postseismic Deformation of the 2010 Maule Megathrust Earthquake

Carlos Peña^{1,2} , Sabrina Metzger¹ , Oliver Heidbach^{1,3}, Jonathan Bedford¹ , Bodo Bookhagen² , Marcos Moreno⁴, Onno Oncken^{1,5}, and Fabrice Cotton^{1,2}

¹Helmholtz Centre Potsdam, GFZ German Research Centre for Geosciences, Potsdam, Germany, ²Institute of Geosciences, University of Potsdam, Potsdam, Germany, ³Institute of Applied Geosciences, Technical University Berlin, Berlin, Germany, ⁴Departamento de Geofísica, University of Concepción, Concepción, Chile, ⁵Department of Earth Sciences, Freie Universität Berlin, Berlin, Germany

Abstract Megathrust earthquakes impose changes of differential stress and pore pressure in the lithosphere-asthenosphere system that are transiently relaxed during the postseismic period primarily due to afterslip, viscoelastic and poroelastic processes. Especially during the early postseismic phase, however, the relative contribution of these processes to the observed surface deformation is unclear. To investigate this, we use geodetic data collected in the first 48 days following the 2010 Maule earthquake and a poro-viscoelastic forward model combined with an afterslip inversion. This model approach fits the geodetic data 14% better than a pure elastic model. Particularly near the region of maximum coseismic slip, the predicted surface poroelastic uplift pattern explains well the observations. If poroelasticity is neglected, the spatial afterslip distribution is locally altered by up to $\pm 40\%$. Moreover, we find that shallow crustal aftershocks mostly occur in regions of increased postseismic pore-pressure changes, indicating that both processes might be mechanically coupled.

Plain Language Summary Large earthquakes modify the state of stress and pore pressure in the upper crust and mantle. These changes induce stress relaxation processes and pore pressure diffusion in the postseismic phase. The two main stress relaxation processes are postseismic slip along the rupture plane of the earthquake and viscoelastic deformation in the rock volume. These processes decay with time, but can sustain over several years or decades, respectively. The other process that results in volumetric crustal deformation is poroelasticity due to pore pressure diffusion, which has not been investigated in detail. Using postseismic surface displacement data acquired by radar satellites after the 2010 Maule earthquake, we show that poroelastic deformation may considerably affect the vertical component of the observed geodetic signal during the first months. Poroelastic deformation also has an impact on the estimation of the postseismic slip, which in turn affects the energy stored at the fault plane that is available for the next event. In addition, shallow aftershocks within the continental crust show a good, positive spatial correlation with regions of increased postseismic pore-pressure changes, suggesting they are linked. These findings are thus important to assess the potential seismic hazard of the segment.

1. Introduction

In the aftermath of large earthquakes, the Earth surface displays time-dependent deformation patterns on different spatiotemporal scales that may last several of years or decades due to the relaxation of coseismically imposed stress and pore pressure changes in the lithosphere-asthenosphere system (e.g., Hergert & Heidbach, 2006; Hughes et al., 2010; K. Wang et al., 2012, and references therein). These relaxation processes are aseismic post-seismic slip on the fault interface (afterslip), poroelastic processes in the upper crust, and viscoelastic relaxation in the lower crust and upper mantle (e.g., Agata et al., 2019; Barbot, 2018; Hughes et al., 2010; Liu et al., 2020; Peña et al., 2020; Sun & Wang, 2015). Afterslip distributions can be used as a proxy to gain valuable insights into the mechanical behavior of the fault interface and to quantify the remaining slip budget (Avouac, 2015, and references therein). To do so, it is compulsory to decipher the relative contribution of each postseismic process to the surface deformation. In particular, the contribution of poroelastic processes is not fully understood.

In the long-term (years to decades) and at larger spatial scales (100s of km) it is widely accepted that afterslip and viscoelastic relaxation prevail (e.g., Barbot, 2018; Peña et al., 2021, 2020; Sun et al., 2014; K. Wang et al., 2012). Conversely, poroelastic processes seem to contribute primarily in the early postseismic phase (days to months),

Methodology: Carlos Peña, Sabrina Metzger, Oliver Heidbach
Project Administration: Carlos Peña, Oliver Heidbach
Software: Carlos Peña, Jonathan Bedford
Supervision: Carlos Peña, Oliver Heidbach, Fabrice Cotton
Validation: Carlos Peña, Sabrina Metzger, Jonathan Bedford, Bodo Bookhagen, Onno Oncken
Writing – review & editing: Carlos Peña, Sabrina Metzger, Oliver Heidbach, Jonathan Bedford, Bodo Bookhagen, Marcos Moreno, Onno Oncken, Fabrice Cotton

especially in the near field close to the area of high coseismic slip. Here, the contribution of poroelastic processes to the surface deformation has been shown to be up to 30% compared to those due to linear viscoelastic relaxation (e.g., Hu et al., 2014; Hughes et al., 2010; Masterlark et al., 2001). However, previous studies often neglect both poroelastic and viscoelastic relaxation, assuming that afterslip is the dominant process and that the crust and upper mantle respond in a purely elastic fashion (e.g., Aguirre et al., 2019; Rolandone et al., 2018; Tsang et al., 2019). Recently K. McCormack et al. (2020) and Yang et al. (2022) investigated the poroelastic effects on afterslip inversions during the first ~ 1.5 months following the 2012 M_w 7.8 Nicoya, Costa Rica, and 2015 M_w 8.3 Illapel, Chile, earthquakes, using Global Navigation Satellite System (GNSS) data. They show that the resulting amplitude of afterslip may be affected by more than $\pm 50\%$ in regions of $\sim 40 \times 40 \text{ km}^2$ when neglecting poroelasticity. Yet, their models ignore viscoelastic relaxation. For the same 2015 Illapel event and similar postseismic 3D GNSS data, Guo et al. (2019) find that linear viscoelastic effects may increase and reduce the resulting inverted afterslip at shallower and deeper segments, respectively, but they do not consider the potential effect of poroelastic and non-linear viscoelastic processes. Hence, the relative contributions of postseismic processes to the early postseismic phase at subduction zones are still elusive.

The postseismic deformation associated with the 2010 M_w 8.8 Maule earthquake in central-southern Chile (Figure 1) has been studied extensively using afterslip only (e.g., Aguirre et al., 2019; Bedford et al., 2013), combining afterslip and linear viscoelastic relaxation (e.g., Bedford et al., 2016; Klein et al., 2016; Li et al., 2018), and afterslip and non-linear viscoelastic relaxation (Peña et al., 2019, 2020; Weiss et al., 2019). In this work, we investigate for the first time the relative contribution of afterslip, poroelastic and non-linear viscoelastic processes of the early postseismic deformation of the 2010 Maule earthquake. We use a model approach that combines a 4D forward model of poroelastic and non-linear viscoelastic relaxation with an afterslip inversion. We use displacements observed by continuous 3D GNSS sites and Interferometric Synthetic-Aperture Radar (InSAR) during the first 48 days after the main shock. We find that particularly in the near field poroelastic processes significantly affect the afterslip estimates and could explain the observed postseismic uplift signal.

2. Geodetic Observations

3D GNSS displacements time-series are obtained using the processing strategy explained in Bedford et al. (2020). Data are retrieved in the International Terrestrial Reference Frame 2014 and then rotated to a Stable South American reference frame. Seasonal signals and offsets caused by aftershocks are removed using sparse linear regression of a modified trajectory model (Bedford & Bevis, 2018). We do not remove the interseismic component because it is negligible compared to the surface deformation in the first 48 days. We select only stations that account for at least 38 daily solutions, resulting in 20 GNSS sites (Figure 1). We linearly interpolate gaps in the time series up to 10 days assuming linear behavior (e.g., Bedford et al., 2013; Moreno et al., 2012).

To increase the spatial coverage, we complete the GNSS data with InSAR line-of-sight (LOS) displacement. We used an image pair of the L-Band (23.6 cm wavelength) ALOS PALSAR satellite mission from the Japanese Space Agency. The scenes were acquired on descending pass in ScanSAR wide-beam mode on the 1st of March (Scene ID: ALPSRS218444350) and 16th of April (ALPSRS225154350), thus spanning day 2–48 following the earthquake. The differential interferogram was created after co-registration and burst synchronization using the GAMMA software (Wegmüller & Werner, 1997; Werner et al., 2011). To increase the coherence, we multi-looked the original interferogram 3, resp., 16 times in range/azimuth to a spatial resolution of 30/50 m. We removed the topographic phase using a 90 m digital elevation model from the Shuttle Radar Topography Mission (Farr et al., 2007). We further improved the signal-to-noise ratio with an adaptive phase filter (Goldstein & Werner, 1998) and unwrapped the phase using Minimum Cost Flow (Costantini, 1998). The geocoded LOS displacements were quad-tree subsampled (Jónsson et al., 2002; Welstead, 1999) to a total number of 586 data samples using the Kite software (Isken et al., 2017) from the open-source seismology toolbox Pyrocko (Heimann et al., 2017). Uncertainties were estimated using the full variance-covariance matrix (Sudhaus & Jónsson, 2009). Finally, we removed the long-wavelength orbital signal by minimizing the misfit between the LOS InSAR displacements (averaged on a $15 \times 15 \text{ km}^2$ window at each GNSS position) and the GNSS data (collapsed into LOS) using a linear ramp (e.g., Cavalié et al., 2013). The GNSS and deramped InSAR data are then used for the afterslip inversion.

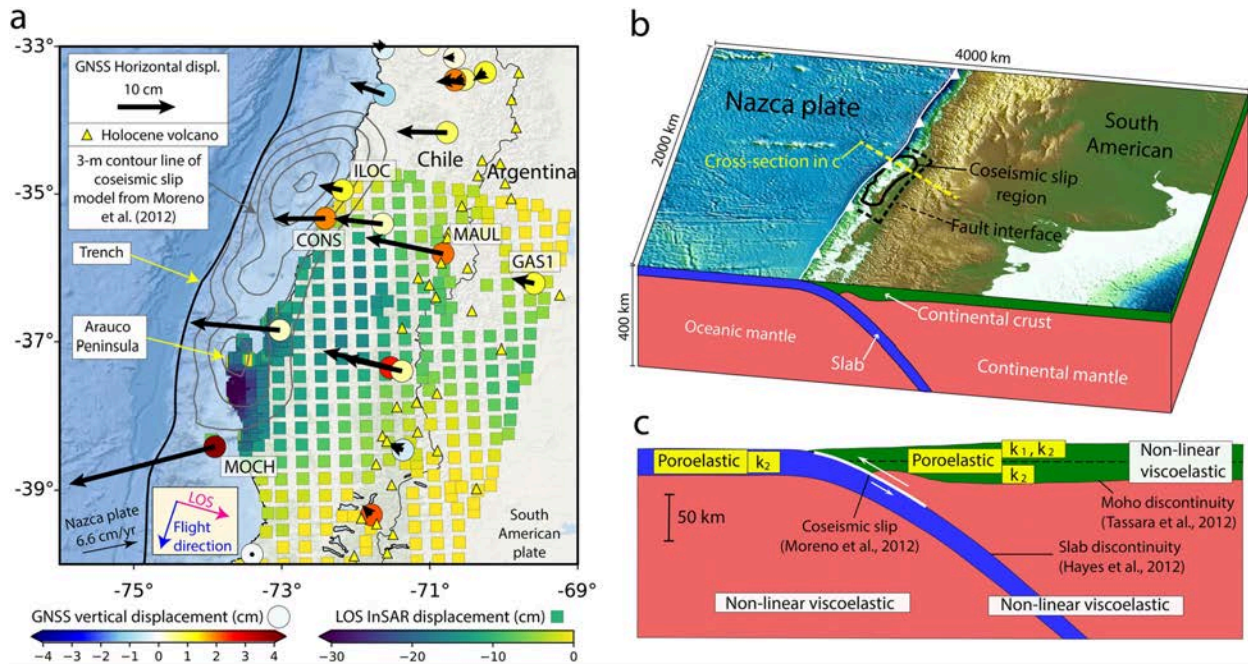


Figure 1. (a) Cumulative postseismic Interferometric Synthetic-Aperture Radar and Global Navigation Satellite System surface displacements between the days 2 and 48 after the 2010 Maule M_w 8.8 earthquake. Negative line-of-sight values indicate relative motion away from the satellite. (b) 3D view and (c) cross-section of the model illustrating layers and rheology with k as permeability described in Section 3.

3. Model Setup

We use the model workflow of Peña et al. (2020), where the postseismic surface displacements produced by 4D forward simulation are first subtracted from the geodetic data. The remaining signal is then inverted for afterslip. Here, we extend the forward model part of Peña et al. (2020) by adding poroelasticity to the model (Figure 1c).

We simulate the postseismic non-linear rock viscous deformation under high-temperature and high-pressure conditions as:

$$\dot{\epsilon}_{cr} = A\sigma^n \exp\left(\frac{-Q}{RT}\right) \quad (1)$$

where $\dot{\epsilon}_{cr}$ is the creep strain rate, A is a pre-exponent parameter, σ the differential stress, n the stress exponent, Q the activation energy for creep, R the gas constant and T the absolute temperature (e.g., Hirth & Kohlstedt, 2003). The poroelastic response is simulated following the approach of H. F. Wang (2000), where the constitute equations of mass conservation and Darcy's law describe the coupled displacement (u) and pore-fluid pressure (p) in Cartesian coordinates (x) expressed in index notation as follows:

$$G\nabla^2 u_i + \frac{G}{(1-2\nu)} \frac{\partial^2 u_k}{\partial x_i \partial x_k} = \alpha \frac{\partial p}{\partial x_i} \quad (2)$$

$$\alpha \frac{\partial \epsilon_{kk}}{\partial t} + S_e \frac{\partial p}{\partial t} = \frac{k}{\mu_f} \nabla^2 p \quad (3)$$

Here, G and ν are the shear modulus and the drained Poisson ratio, respectively, α is the Biot-Willis coefficient, t the elapsed time since the main shock, S_e the constrained storage coefficient, $\epsilon_{kk} = \partial u_k / \partial x_k$ is the volumetric strain, k the intrinsic permeability and μ_f the pore-fluid viscosity (H. F. Wang, 2000). The subscript i represents the three orthogonal spatial directions, while the subscript k denotes the summation over these three components (Hughes et al., 2010).

The onset of the poroelastic and viscoelastic postseismic deformation is driven by the coseismically induced response (e.g., Hughes et al., 2010; K. McCormack et al., 2020; Masterlark et al., 2001). We prescribe the coseismic slip model of Moreno et al. (2012) as displacement boundary conditions on the fault interface (Peña et al., 2020). The lateral and bottom model boundaries are free to displace parallel to their faces. We also apply stress-free and no-flow boundary conditions in the surface layer (e.g., Hughes et al., 2010; Tung & Masterlark, 2018). The resulting numerical problem is solved with the commercial finite element software ABAQUS™, version 6.14.

Given the high uncertainty of rock permeability, temperature, and viscous creep parameters, we consider end-member scenarios for the crust and upper mantle (Figure 1c; Tables S1 and S2 in Supporting Information S1). We consider two scenarios with lower and upper bounds of permeability of $1 \times 10^{-16} \text{ m}^2$ and $1 \times 10^{-14} \text{ m}^2$ for the continental crust in the upper 15 km (Völker et al., 2011), while we set a permeability of $1 \times 10^{-16} \text{ m}^2$ for the lower crust, as obtained from crustal-scale studies in Chile (e.g., Husen & Kissling, 2001; Koerner et al., 2004) and other regions (e.g., Ingebritsen & Manning, 2010). We adopt quartzite and diabase creep parameters for the continental crust, and wet olivine with 0.01 and 0.005% of water for the upper mantle (e.g., Hirth & Kohlstedt, 2003; Peña et al., 2020). We do not further explore rock property changes for the oceanic crust and mantle due to the lack of offshore measurements to constrain our results. We thus set a permeability of $1 \times 10^{-16} \text{ m}^2$ for the oceanic plate (Fisher, 1998), and assign diabase and wet olivine with 0.005% of water creep parameters for the slab and oceanic mantle, respectively (Peña et al., 2020).

During the afterslip inversion, we determine the relative weights of InSAR and GNSS data sets by identifying the optimal misfit value between the observed and modeled surface displacement that does not substantially vary the misfit of each individual data set (e.g., Cavalié et al., 2013; Melgar et al., 2017). We find that the relative weights for GNSS and InSAR are 1 and 0.6, respectively (Figure S2 in Supporting Information S1). This agrees with the tendency of lowering the InSAR data weight when including GNSS and InSAR along with land-leveling (Moreno et al., 2012) and strong motion data (Melgar et al., 2017) that found relative weights of about 0.5 and 0.3 for GNSS and InSAR data, respectively. Furthermore, we neglect the postseismic processes coupling as it does not change the results beyond the GNSS data uncertainty (Figure S3 in Supporting Information S1).

4. Model Results Compared to Geodetic Observations

All GNSS horizontal postseismic displacements show trench-ward motion (Figure 1). The maximum cumulative surface displacement reaches 24.5 cm at station MOCH, while the maximum cumulative InSAR LOS displacement is observed at the Arauco Peninsula with 32.5 cm. The volcanic arc region also exhibits significant long-wavelength deformation, reaching ~ 15 and ~ 2 cm in the horizontal and vertical components at the station MAUL, respectively. Along the coastline, the observations exhibit strong vertical variations. The northern part subsides by up to 1 cm, while the two GNSS sites (ILOC and CONS) near the region of maximum coseismic slip yield uplift of 1–2 cm. A maximum uplift of 6.5 cm is measured at station MOCH further south.

The combined result of the forward poro-viscoelastic model and the afterslip inversion display a lowest mean absolute data error of 5.4 cm (Figure 2a; Table S3 in Supporting Information S1), while by neglecting poroelasticity the data misfit slightly increases to 5.5 cm (Figure 2b). Despite this small data fit improvement, our *F*-test results show that our poro-viscoelastic model is statistically better than a (non-linear) viscoelastic-only model considering a significance level of 0.05 (Figure 2a and Supporting Information S1). The data fit of the poro-viscoelastic model is 14% better than the one from a pure elastic model (Figures 2c and 2f). In particular, the inclusion of viscoelasticity can substantially improve the data fit in the volcanic and back-arc regions and, to some extent, at the coast (Figures 2d and 2e).

We also show that afterslip processes dominate the near-field deformation (Figures 3a, 3d, and 3g), while non-linear viscoelastic relaxation the surface deformation at volcanic and back arc regions (Figures 3b, 3e, and 3i). The largest poroelastic effects are found close to the region of maximum coseismic slip, while the resulting surface poroelastic response exhibit varying patterns (Figure 3f). Onshore, the poroelastic response exhibits landward and uplift surface deformation, while offshore and particularly close to the trench it is the opposite (Figure 3f). The cumulative poroelastic landward displacements reach up to 0.75 cm, lowering the cumulative displacement of station ILOC by $\sim 15\%$ (Figures 3c and 3h). We also find that the poroelastic response exhibits a maximum coastal uplift of 1.3 cm (Figures 3c and 3f), which is in good agreement with the observations.

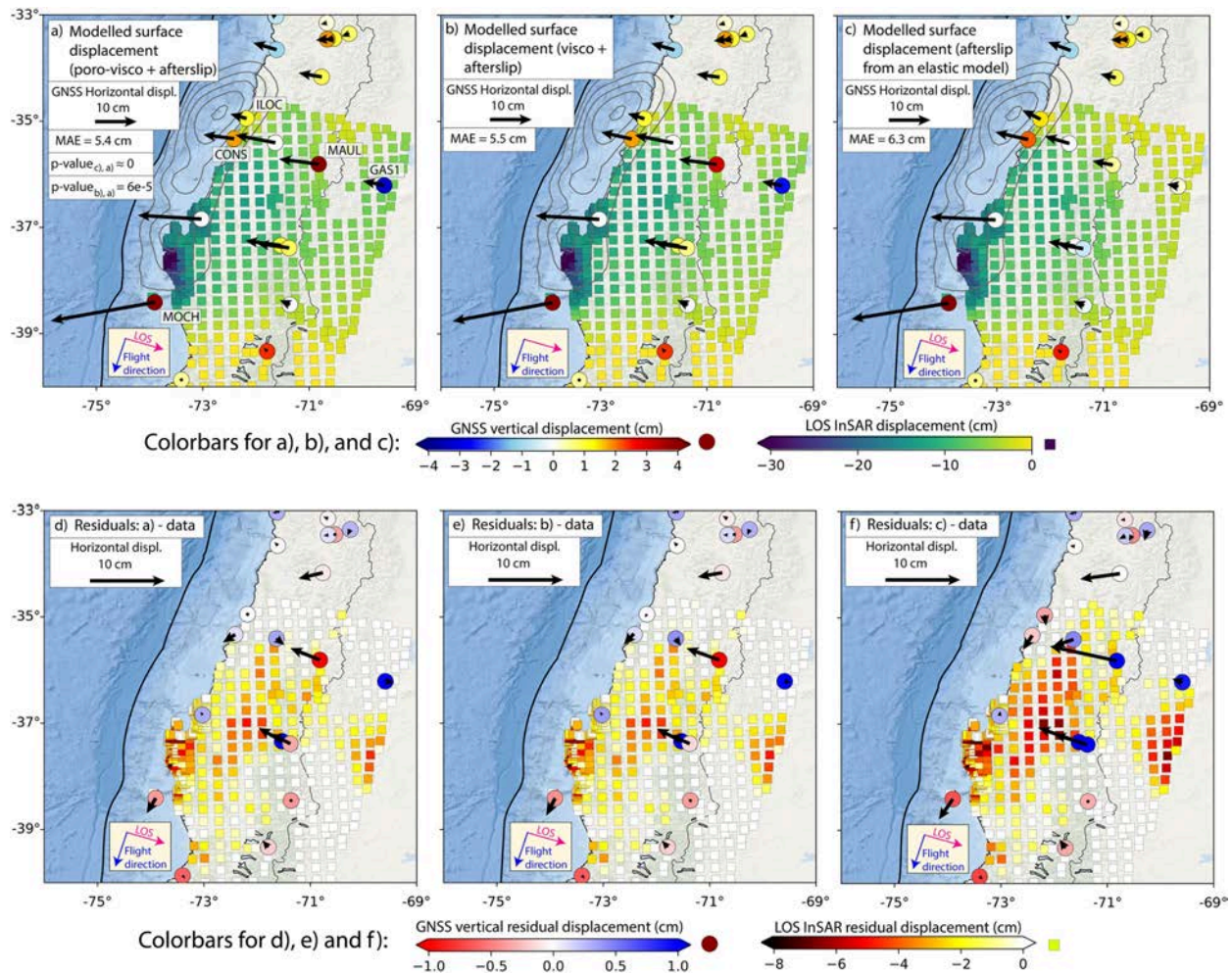


Figure 2. Predicted displacements from forward modeling in combination with an afterslip inversion considering (a) poroelasticity and non-linear viscoelasticity, (b) non-linear viscoelasticity-only, and (c) elasticity-only. MAE represents the mean absolute error. The p -values in panel (a) are obtained by computing the F -values from panels (b and c) (null hypothesis) with respect to panel (a). (d–f) show the residual displacements between the model in panels (a and c) and the geodetic data.

5. Spatial Distributions of Afterslip

We further compare afterslip distributions resulting from a poro-viscoelastic, poroelastic and elastic models. Overall, these models predict most of the afterslip occurring outside regions of high coseismic slip (Figures 4a and 4c), with maximum afterslip amplitude in the southern segment at 37.7°S at 20 km depth. In the northern segment, however, the afterslip predicted by the poro-viscoelastic model differs. It is notably reduced by more than 30 cm close to the trench and by 20–30 cm at 20–50 km depths (Figure 4d). At 20–50 km depth, afterslip resolution and bootstrapping tests report robust results (Figure S4 and S5 in Supporting Information S1; Bedford et al., 2013; Peña et al., 2020). We find a general reduction of the afterslip by 16% if poro-viscoelastic effects are incorporated. Viscoelastic effects dominate the prediction as the poroelastic effects (Figure 4e) are significantly smaller than those from the combined model (Figure 4d). However, poroelastic effects alter the afterslip distribution by up to ± 25 cm in regions of $\sim 50 \times 50$ km² (Figure 4e), representing up to $\pm 40\%$ of deviation from the elastic-only model (Figure 4f). These effects are strongest near the region of maximum coseismic slip, where poroelastic effects contribute most to the observed surface displacements (Figure 3c).

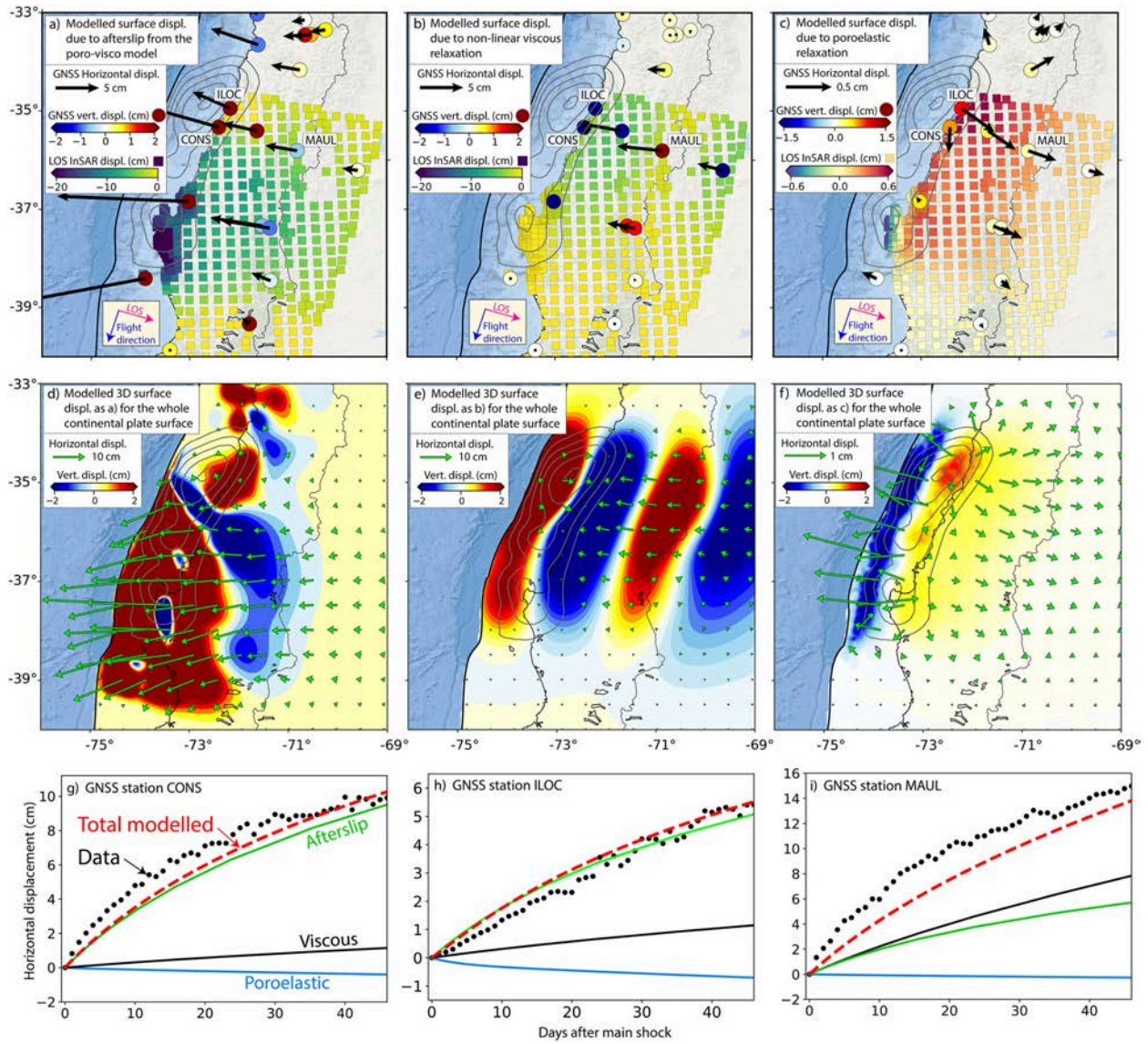


Figure 3. Decomposition of the predicted cumulative and temporal 3D surface displacements from the model that inverts for afterslip considering poro-viscoelasticity. Individual contribution due to (a) afterslip, (b) viscoelastic, and (c) poroelastic processes at the observation sites and (d–f) in full 3D-resolution. Individual Global Navigation Satellite System horizontal time-series decomposition at stations (g) CONS, (h) ILOC, and (i) MAUL. Temporal evolution of afterslip is modeled with a logarithmic function as $A(t) = A_0 \log((t + t_c)/t_c)$, where A_0 is the cumulative afterslip calculated from the inversion approach, t is the time after the main shock, t_c is the characteristic time of relaxation, and t_c the critical time, which is introduced to avoid the singularity at $t = 0$ (Avouac et al., 2015).

6. Discussion

Poroelastic processes in the upper crust are a fundamental aspect of rock mechanics (e.g., Beeler et al., 2000; Oncken et al., 2021; Warren-Smith et al., 2019). Yet, they have been commonly ignored in postseismic deformation studies. We show that following the Maule event, poroelastic processes affect horizontal GNSS observations by up to 15% (Figure 3c). Moreover, poroelastic processes locally alter the estimated afterslip by up to $\pm 40\%$ near the region of maximum coseismic slip compared to the results of a purely elastic model. Similar patterns have been also reported for the 2012 Nicoya Costa Rica (K. McCormack et al., 2020) and the 2015 Illapel Chile (Yang et al., 2022) earthquakes. Nonetheless, in the work by K. McCormack et al. (2020) and Yang et al. (2022) the poroelastic effects on both the geodetic signal and afterslip amplitudes are generally larger than in our study.

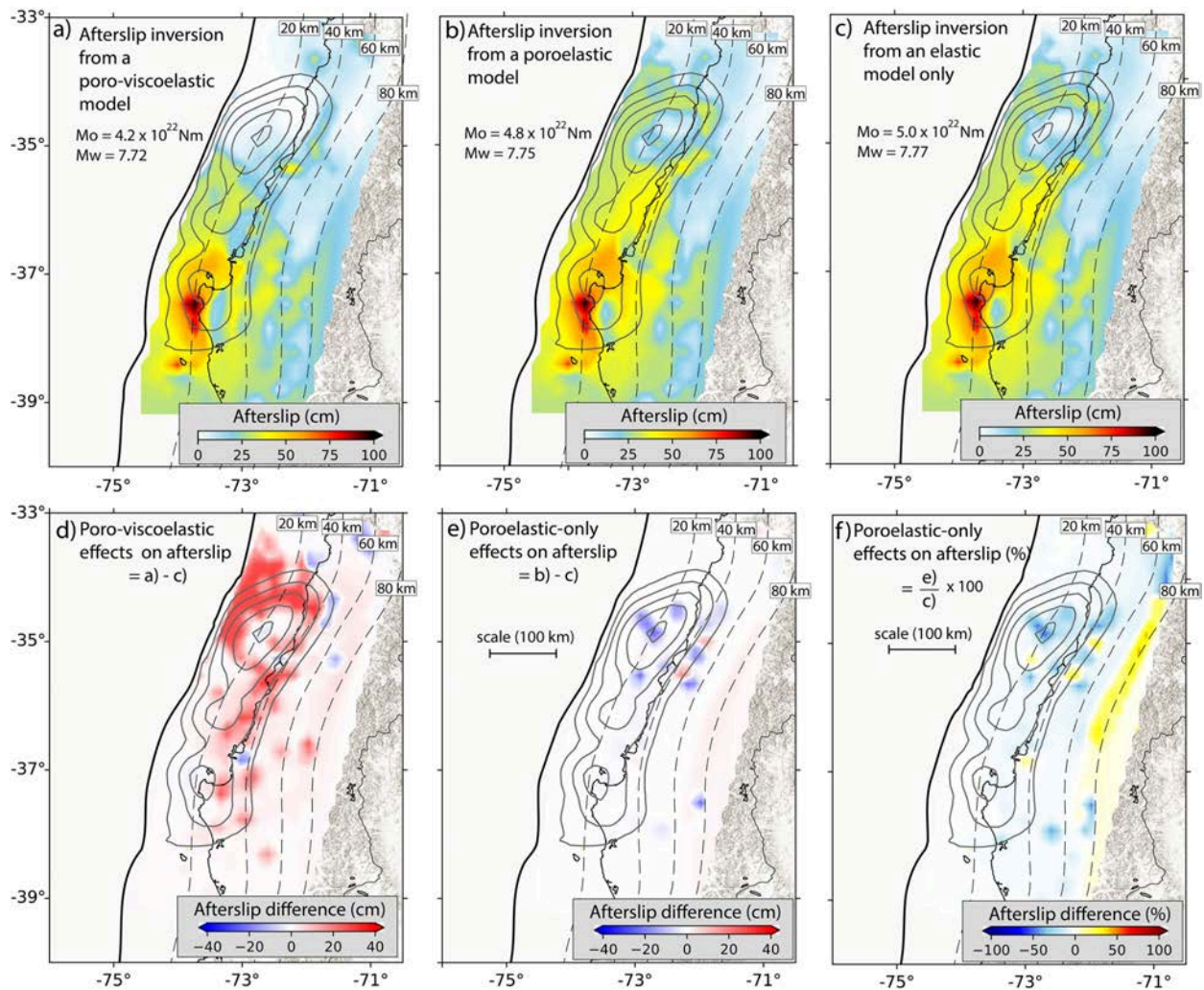


Figure 4. Afterslip distributions from (a) the poro-viscoelastic, (b) the poroelastic-only, and (c) the elastic-only models. Gray contour lines show coseismic slip as in Figure 1. Dashed lines represent the plate interface depth from Hayes et al. (2012). (d and e) exhibit afterslip differences between panels (a and b) and (b and c), respectively, while (f) as (e) but in percent.

This might be because these studies neglect viscoelastic relaxation, which also has a significant impact on the afterslip distributions (Figure 4d). In particular, the inclusion of non-linear viscoelasticity considerably reduces the afterslip at shallower segments close to the region of largest coseismic slip (Figures 4a and 4d), thus better explaining the absence of shallow aftershocks (e.g., Lange et al., 2012) (Figure S6 in Supporting Information S1).

Our poro-viscoelastic model considers rock parameters that agree with previous studies investigating non-linear viscoelastic (Peña et al., 2020, 2021; Weiss et al., 2019) and poroelastic processes (e.g., Koerner et al., 2004). The permeability of 10^{-14} m^2 used here, however, is about two orders of magnitude higher than that the one used by studies investigating the postseismic deformation of the 2011 Tohoku-Oki (Hu et al., 2014) and the 2004 Sumatra-Andaman megathrust events (Hughes et al., 2010). Nevertheless, these authors either focused on a longer observation period (~ 2 years, Hu et al., 2014) or investigated the stress transfer due to pore-pressure changes (Hughes et al., 2010). This relatively high permeability may be because of upper crustal fractures augmenting permeability locally (e.g., Gomila et al., 2016) or a transient response increasing permeability due to the pass of the seismic waves (e.g., Manga et al., 2012), or both processes.

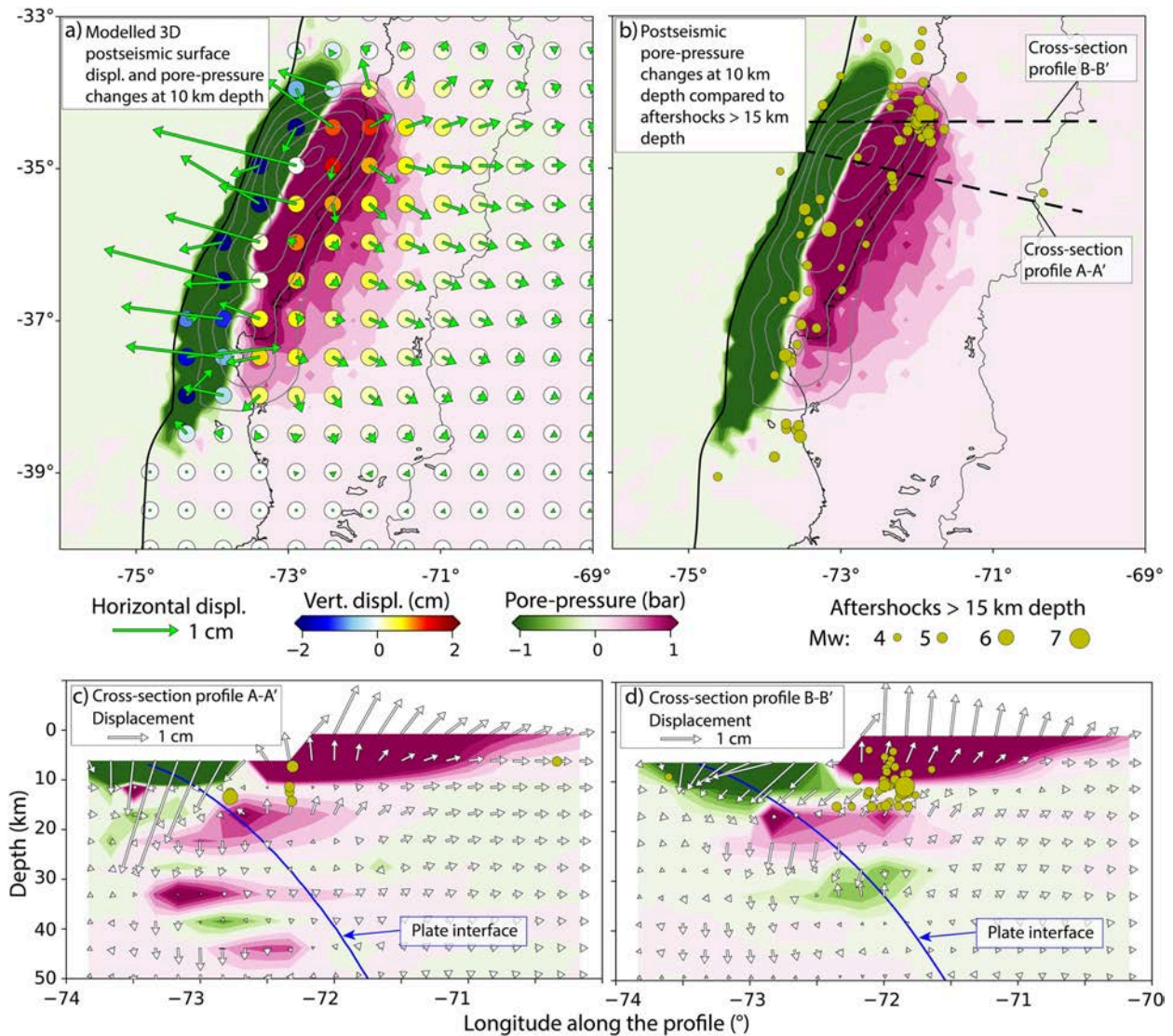


Figure 5. Cumulative postseismic pore-pressure changes, displacement, and $M_w \geq 4$ aftershock distribution in the upper 15 km (USGS-NEIC catalog) during the first 48 days following the main shock.

Our results show that the predicted poroelastic vertical displacement is about two times higher than the horizontal displacement (Figure 3f), which is in good agreement with previous studies (Hu et al., 2014; Hughes et al., 2010; Masterlark et al., 2001; K. McCormack et al., 2020). Poroelastic vertical surface displacement patterns can also explain a major part of the observed uplift near the maximum coseismic slip region (Figure 3c). The modeled surface uplift and subsidence pattern is produced by increase and decrease of postseismic pore-pressure changes in the upper crust following the main shock, respectively (Figures 5a and 5c). We also find that shallow aftershocks, especially above ~11 km depth, mostly occur beneath the coastal forearc, where our model predicts pore-pressure increase (Figures 5b–5d). An increase of shallow seismic activity following megathrust earthquakes has been observed in many subduction zones (e.g., Soto et al., 2019; Toda et al., 2011), but the mechanisms of these aftershocks are not well understood. Our results indicate that increased postseismic pore-pressure changes may be a plausible triggering process, as they reduce the effective fault normal stress more efficiently than afterslip and viscous processes (e.g., Hughes et al., 2010; Miller et al., 2004).

Given that the vertical surface displacement is highly sensitive to poroelastic effects (Figure 3f), additional geodetic vertical deformation data derived from, for example, offshore pressure gauges (Wallace et al., 2016) or multiple radar look directions (Weiss et al., 2020; Wright et al., 2004) could be used in future studies to better understand crustal poroelastic processes. Moreover, a homogenous spatial distribution of permeability may not be a realistic representation of the upper crust (e.g., Manga et al., 2012). Additional water-level observations could directly constrain spatial variations of crustal poroelastic properties (K. A. McCormack & Hesse, 2018).

7. Conclusion

We use a 4D forward model that considers poroelasticity and non-linear viscoelasticity to invert for the afterslip during the first 48 days of postseismic deformation following the 2010 Maule earthquake. Compared to a purely elastic model inverting for afterslip only, our model approach fits the observed postseismic geodetic data 14% better and yields a reduction of the total predicted afterslip of 16%. The latter is primarily due to the implementation of viscoelasticity. Close to the area of maximum coseismic slip, poroelastic effects play a local, but significant role by dragging the horizontal GNSS observations by up to 15% in the opposite direction and altering the afterslip amplitude by up to $\pm 40\%$ in regions of $\sim 50 \times 50 \text{ km}^2$. Poroelastic effects on postseismic slip budgets may be higher and may play a key role in triggering upper crustal aftershocks. However, additional vertical geodetic and water-level are needed to validate these hypotheses and to improve our knowledge of poroelastic processes in the upper crust.

Data Availability Statement

Global Navigation Satellite System data are available through Bedford et al. (2020). We use the model geometry that is available in Peña et al. (2020). We use Kite software (Isken et al., 2017) from the open-source seismology toolbox Pyrocko (Heimann et al., 2017). The ALOS-2/PALSAR-2 data were provided by the Japanese Aerospace Exploration Agency (JAXA) and are available from <https://earth.jaxa.jp/en/data/2496/index.html>.

References

- Agata, R., Barbot, S. D., Fujita, K., Hyodo, M., Inuma, T., Nakata, R., et al. (2019). Rapid mantle flow with power-law creep explains deformation after the 2011 Tohoku mega-quake. *Nature Communications*, 10(1), 1385. <https://doi.org/10.1038/s41467-019-08984-7>
- Aguirre, L., Bataille, K., Novoa, C., Peña, C., & Vera, F. (2019). Kinematics of subduction processes during the earthquake cycle in Central Chile. *Seismological Research Letters*, 90(5), 1779–1791. <https://doi.org/10.1785/0220180391>
- Avouac, J.-P. (2015). From geodetic imaging of seismic and aseismic fault slip to dynamic modeling of the seismic cycle. *Annual Review of Earth and Planetary Sciences*, 43(1), 233–271. <https://doi.org/10.1146/annurev-earth-060614-105302>
- Barbot, S. (2018). Asthenosphere flow modulated by megathrust earthquake cycles. *Geophysical Research Letters*, 45, 6018–6031. <https://doi.org/10.1029/2018GL078197>
- Bedford, J., & Bevis, M. (2018). Greedy automatic signal decomposition and its application to daily GPS time series. *Journal of Geophysical Research: Solid Earth*, 123, 6992–7003. <https://doi.org/10.1029/2017JB014765>
- Bedford, J., Moreno, M., Baez, J. C., Lange, D., Tilmann, F., Rosenau, M., et al. (2013). A high-resolution, time-variable after slip model for the 2010 Maule Mw = 8.8, Chile megathrust earthquake. *Earth and Planetary Science Letters*, 383, 26–36. <https://doi.org/10.1016/j.epsl.2013.09.020>
- Bedford, J., Moreno, M., Deng, Z., Oncken, O., Schurr, B., John, T., et al. (2020). Trajectory models for daily displacement time series in the five years preceding the 2010 Maule Mw 8.8, Chile, and 2011 Tohoku-oki Mw 9.0, Japan earthquakes. GFZ Data Services. <https://doi.org/10.5880/GFZ.4.1.2020.001>
- Bedford, J., Moreno, M., Li, S., Oncken, O., Baez, J. C., Bevis, M., et al. (2016). Separating rapid relocking, afterslip, and viscoelastic relaxation: An application of the postseismic straightening method to the Maule 2010 cGPS. *Journal of Geophysical Research: Solid Earth*, 121(10), 7618–7638. <https://doi.org/10.1002/2016JB013093>
- Beeler, N. M., Simpson, R. W., Hickman, S. H., & Lockner, D. A. (2000). Pore fluid pressure, apparent friction, and Coulomb failure. *Journal of Geophysical Research*, 105(B11), 25533–25542. <https://doi.org/10.1029/2000JB900119>
- Cavalié, O., Pathier, E., Radiguet, M., Vergnolle, M., Cotte, N., Walpersdorf, A., et al. (2013). Slow slip event in the Mexican subduction zone: Evidence of shallower slip in the Guerrero seismic gap for the 2006 event revealed by the joint inversion of InSAR and GPS data. *Earth and Planetary Science Letters*, 367, 52–60. <https://doi.org/10.1016/j.epsl.2013.02.020>
- Costantini, M. (1998). A novel phase unwrapping method based on network programming. *IEEE Transactions on Geoscience and Remote Sensing*, 36(3), 813–821. <https://doi.org/10.1109/36.673674>
- Farr, T. G., Rosen, P. A., Caro, E., Crippen, R., Duren, R., Hensley, S., et al. (2007). The shuttle radar topography mission. *Review of Geophysics*, 45(2), RG2004. <https://doi.org/10.1029/2005RG000183>
- Fisher, A. T. (1998). Permeability within basaltic oceanic crust. *Reviews of Geophysics*, 36(2), 143–182. <https://doi.org/10.1029/97RG02916>
- Goldstein, R. M., & Werner, C. L. (1998). Radar interferogram filtering for geophysical applications. *Geophysical Research Letters*, 25(21), 4035–4038. <https://doi.org/10.1029/1998GL900033>

Acknowledgments

This work has received funding from the Initiative and Networking Fund of the Helmholtz Association through the project “Advanced Earth System Modelling Capacity.” Carlos Peña appreciates the scholarship granted to him by the University of Potsdam through the Bridge Program. Marcos Moreno acknowledges support from the ANID PIA Anillo ACT192169, Millennium Scientific Initiative grant NC160025 (CYCLO), and National Research Center for Integrated Natural Disaster Management (CIGIDEN), CONICYT/FONDAP/15110017. We would like to thank the Editor Lucy Flesch and two anonymous reviewers for their constructive comments and suggestions to improve our work. Open access funding enabled and organized by Projekt DEAL.

- Gomila, R., Arancibia, G., Mitchell, T. M., Cembrano, J. M., & Faulkner, D. R. (2016). Palaeopermeability structure within fault-damage zones: A snap-shot from microfracture analyses in a strike-slip system. *Journal of Structural Geology*, 83, 103–120. <https://doi.org/10.1016/j.jsg.2015.12.002>
- Guo, R., Zheng, Y., Xu, J., & Shahid Riaz, M. (2019). Transient viscosity and afterslip of the 2015 Mw 8.3 Illapel, Chile, earthquake. *Bulletin of the Seismological Society of America*, 109(6), 2567–2581. <https://doi.org/10.1785/0120190114>
- Hayes, G. P., Wald, D. J., & Johnson, R. L. (2012). Slab1.0: A three-dimensional model of global subduction zone geometries. *Journal of Geophysical Research*, 117, B01302. <https://doi.org/10.1029/2011JB008524>
- Heimann, S., Kriegerowski, M., Isken, M., Cesca, S., Daout, S., Grigoli, F., et al. (2017). *Pyrocko - an open-source seismology toolbox and library*. GFZ Data Services. <https://doi.org/10.5880/GFZ.2.1.2017.001>
- Hergert, T., & Heidbach, O. (2006). New insights into the mechanism of the postseismic stress relaxation exemplified by the 23 June Mw = 8.4 earthquake in southern Peru. *Geophysical Research Letters*, 30(2), L02307. <https://doi.org/10.1029/2005GL024858>
- Hirth, G., & Kohlstedt, D. (2003). Rheology of the upper mantle and the mantle wedge: A view from the experimentalists. *Inside the subduction Factory*, 138, 83–105. <https://doi.org/10.1029/138GM06>
- Hu, Y., Bürgmann, R., Freymueller, J., Banerjee, P., & Wang, K. (2014). Contributions of poroelastic rebound and a weak volcanic arc to the postseismic deformation of the 2011 Tohoku earthquake. *Earth Planets and Space*, 66(1), 106. <https://doi.org/10.1186/1880-5981-66-106>
- Hughes, K. L., Masterlark, T., & Mooney, W. D. (2010). Poroelastic stress-triggering of the 2005 Mw 8.7 Nias earthquake by the 2004 Mw 9.2 Sumatra–Andaman earthquake. *Earth and Planetary Science Letters*, 293(3–4), 289–299. <https://doi.org/10.1016/j.epsl.2010.02.043>
- Husen, S., & Kissling, E. (2001). Postseismic fluid flow after the large subduction earthquake of Antofagasta, Chile. *Geology*, 229(9), 847–850. [https://doi.org/10.1130/0091-7613\(2001\)029<0847:PPFATL>2.0.CO;2](https://doi.org/10.1130/0091-7613(2001)029<0847:PPFATL>2.0.CO;2)
- Ingebritsen, S. E., & Manning, C. E. (2010). Permeability of the continental crust: Dynamic variations inferred from seismicity and metamorphism. *Geofluids*, 10, 193–205. <https://doi.org/10.1111/j.1468-8123.2010.00278.x>
- Isken, M., Sudhaus, H., Heimann, S., Steinberg, A., Daout, S., & Hannes, V.-B. (2017). *Kite - software for rapid earthquake source optimisation from InSAR surface Displacement*. GFZ Data Services. <https://doi.org/10.5880/GFZ.2.1.2017.002>
- Jónsson, S., Zebker, H. A., Segall, P., & Amelung, F. (2002). Fault slip distribution of the 1999 Mw7.2 Hector Mine earthquake, California, estimated from satellite radar and GPS measurements. *Bulletin of the Seismological Society of America*, 92(4), 1377–1389. <https://doi.org/10.1785/0120000922>
- Klein, E., Fleitout, L., Vigny, C., & Garaud, J. D. (2016). Afterslip and viscoelastic relaxation model inferred from the large-scale postseismic deformation following the 2010 Mw 8.8 Maule earthquake (Chile). *Geophysical Journal International*, 205(3), 1455–1472. <https://doi.org/10.1093/gji/ggw086>
- Koerner, A., Kissling, E., & Miller, S. A. (2004). A model of deep crustal fluid flow following the Mw = 8.0 Antofagasta, Chile, earthquake. *Journal of Geophysical Research*, 109(B6), B06307. <https://doi.org/10.1029/2003JB002816>
- Lange, D., Tilmann, F., Barrientos, S. E., Contreras-Reyes, E., Methe, P., Moreno, M., et al. (2012). Aftershock seismicity of the 27 February 2010 Mw 8.8 Maule earthquake rupture zone. *Earth and Planetary Science Letters*, 317–318, 413–425. <https://doi.org/10.1016/j.epsl.2011.11.034>
- Li, S., Bedford, J., Moreno, M., Barnhart, W. D., Rosenau, M., & Oncken, O. (2018). Spatiotemporal variation of mantle viscosity and the presence of cratonic mantle inferred from 8 years of postseismic deformation following the 2010 Maule, Chile, earthquake. *Geochemistry, Geophysics, Geosystems*, 19(9), 3272–3285. <https://doi.org/10.1029/2018GC007645>
- Liu, S., Shen, Z., Bürgmann, R., & Jónsson, S. (2020). Thin crème brûlée rheological structure for the Eastern California Shear Zone. *Geology*, 49(2), 216–221. <https://doi.org/10.1130/G47729.1>
- Manga, M., Beresnev, I., Brodsky, E. E., Elkhoury, J. E., Elsworth, D., Ingebritsen, S. E., et al. (2012). Changes in permeability caused by transient stresses: Field observations, experiments, and mechanisms. *Reviews of Geophysics*, 50(2), RG2004. <https://doi.org/10.1029/2011RG000382>
- Masterlark, T., DeMets, T. C., Wang, H. F., Sanchez, O., & Stock, J. (2001). Homogeneous vs heterogeneous subduction zone models: Coseismic and postseismic deformation. *Geophysical Research Letters*, 28(21), 4047–4050. <https://doi.org/10.1029/2001GL013612>
- McCormack, K., Hesse, M. A., Dixon, T. H., & Malservisi, R. (2020). Modeling the contribution of poroelastic deformation to postseismic geodetic signals. *Geophysical Research Letters*, 47(8), e2020GL086945. <https://doi.org/10.1029/2020GL086945>
- McCormack, K. A., & Hesse, M. A. (2018). Modeling the poroelastic response to megathrust earthquakes: A look at the 2012 Mw 7.6 Costa Rican event. *Advances in Water Resources*, 114, 236–248. <https://doi.org/10.1016/j.advwatres.2018.02.014>
- Melgar, D., Riquelme, S., Xu, X., Baez, J. C., Geng, J., & Moreno, M. (2017). The first since 1960: A large event in the Valdivia segment of the Chilean Subduction zone, the 2016 Mw 7.6 Melinka earthquake. *Earth and Planetary Science Letters*, 474, 68–75. <https://doi.org/10.1016/j.epsl.2017.06.026>
- Miller, S., Collettini, C., Chiaraluce, L., Cocco, M., Barchi, M., & Kaus, B. J. P. (2004). Aftershocks driven by a high-pressure CO₂ source at depth. *Nature*, 427(6976), 724–727. <https://doi.org/10.1038/nature02251>
- Moreno, M., Melnick, D., Rosenau, M., Baez, J., Klotz, J., Oncken, O., et al. (2012). Toward understanding tectonic control on the Mw 8.8 2010 Maule Chile earthquake. *Earth and Planetary Science Letters*, 321–322, 152–165. <https://doi.org/10.1016/j.epsl.2012.01.006>
- Oncken, O., Angiboust, S., & Dresen, G. (2021). Slow slip in subduction zones: Reconciling deformation fabrics with instrumental observations and laboratory results. *Geosphere*, 18(1), 104–129. <https://doi.org/10.1130/GES02382.1>
- Peña, C., Heidbach, O., Moreno, M., Bedford, J., Ziegler, M., Tassara, A., & Oncken, O. (2019). Role of lower crust in the postseismic deformation of the 2010 Maule earthquake: Insights from a model with power-law rheology. *Pure and Applied Geophysics*, 176(9), 3913–3928. <https://doi.org/10.1007/s00024-018-02090-3>
- Peña, C., Heidbach, O., Moreno, M., Bedford, J., Ziegler, M., Tassara, A., & Oncken, O. (2020). Impact of power-law rheology on the viscoelastic relaxation pattern and afterslip distribution following the 2010 Mw 8.8 Maule earthquake. *Earth and Planetary Science Letters*, 542, 116292. <https://doi.org/10.1016/j.epsl.2020.116292>
- Peña, C., Heidbach, O., Moreno, M., Melnick, D., & Oncken, O. (2021). Transient deformation and stress patterns induced by the 2010 Maule earthquake in the Illapel segment. *Frontiers of Earth Science*, 9, 644834. <https://doi.org/10.3389/feart.2021.644834>
- Rolandone, F., Nocquet, J.-M., Mothes, P. A., Jarrin, P., Vallée, M., Cubas, N., et al. (2018). Areas prone to slow slip events impede earthquake rupture propagation and promote afterslip. *Science Advances*, 4(1), eaao6596. <https://doi.org/10.1126/sciadv.aao6596>
- Soto, H., Sippl, C., Schurr, B., Kummerow, J., Asch, G., Tilmann, F., et al. (2019). Probing the northern Chile megathrust with seismicity: The 2014 Mw 8.1 Iquique earthquake sequence. *Journal of Geophysical Research: Solid Earth*, 124(12), 12935–12954. <https://doi.org/10.1029/2019JB017794>
- Sudhaus, H., & Jónsson, S. (2009). Improved source modelling through combined use of InSAR and GPS under consideration of correlated data errors: Application to the June 2000 Kleifarvatn earthquake, Iceland. *Geophysical Journal International*, 176(2), 389–404. <https://doi.org/10.1111/j.1365-246X.2008.03989.x>

- Sun, T., & Wang, K. (2015). Viscoelastic relaxation following subduction earthquakes and its effects on afterslip determination. *Journal of Geophysical Research: Solid Earth*, *120*(2), 1329–1344. <https://doi.org/10.1002/2014JB011707>
- Sun, T., Wang, K., Iinuma, T., Hino, R., He, J., Fujimoto, H., et al. (2014). Prevalence of viscoelastic relaxation after the 2011 Tohoku-oki earthquake. *Nature*, *514*(7520), 84–87. <https://doi.org/10.1038/nature13778>
- Toda, S., Lin, J., & Stein, R. S. (2011). Using the 2011 Mw 9.0 off the Pacific coast of Tohoku Earthquake to test the Coulomb stress triggering hypothesis and to calculate faults brought closer to failure. *Earth Planets and Space*, *63*(7), 39–730. <https://doi.org/10.5047/eps.2011.05.010>
- Tsang, L. L. H., Vergnolle, M., Twardzik, C., Sladen, A., Nocquet, J.-M., Rolandone, F., et al. (2019). Imaging rapid early afterslip of the 2016 Pedernales earthquake, Ecuador. *Earth and Planetary Science Letters*, *524*, 115724. <https://doi.org/10.1016/j.epsl.2019.115724>
- Tung, S., & Masterlark, T. (2018). Delayed poroelastic triggering of the 2016 October Visso earthquake by the August Amatrice earthquake, Italy. *Geophysical Research Letters*, *45*(5), 2221–2229. <https://doi.org/10.1002/2017GL076453>
- Völker, D., Grevemeyer, I., Stüpp, M., Wang, K., & He, J. (2011). Thermal control of the seismogenic zone of southern central Chile. *Journal of Geophysical Research*, *116*(B10), B10305. <https://doi.org/10.1029/2011JB008247>
- Wallace, L. M., Webb, S. C., Ito, Y., Mochizuki, K., Hino, R., Henrys, S., et al. (2016). Slow slip near the trench at the Hikurangi subduction zone, New Zealand. *Science*, *352*(6286), 701–704. <https://doi.org/10.1126/science.aaf2349>
- Wang, H. F. (2000). *Theory of linear poroelasticity: With applications to geomechanics*. Princeton University Press.
- Wang, K., Hu, Y., & He, J. (2012). Deformation cycles of subduction earthquakes in a viscoelastic Earth. *Nature*, *484*(7394), 327–332. <https://doi.org/10.1038/nature11032>
- Warren-Smith, E., Fry, B., Wallace, L., Chon, E., Henrys, S., Sheehan, A., et al. (2019). Episodic stress and fluid xure cycling in subducting oceanic crust during slow slip. *Nature Geoscience*, *12*(6), 475–481. <https://doi.org/10.1038/s41561-019-0367-x>
- Wegmüller, U., & Werner, C. (1997). Gamma SAR processor and interferometry software. In *Proceedings of the 3rd ERS Scientific Symposium on space at the service of our environment*. (pp. 1686–1692).
- Weiss, J. R., Qiu, Q., Barbot, S., Wright, T. J., Foster, J. H., Saunders, A., et al. (2019). Illuminating subduction zone rheological properties in the wake of a giant earthquake. *Science Advances*, *5*(12), eaax6720. <https://doi.org/10.1126/sciadv.aax6720>
- Weiss, J. R., Walters, R. J., Morishita, Y., Wright, T. J., Lazecky, M., Wang, H., et al. (2020). High-resolution surface velocities and strain for Anatolia from Sentinel-1 InSAR and GNSS data. *Geophysical Research Letters*, *47*(17), e2020GL087376. <https://doi.org/10.1029/2020GL087376>
- Welstead, S. T. (1999). *Fractal and wavelet image compression techniques* (p. 232). SPIE Opt. Eng.
- Werner, C., Wegmüller, U., Frey, O., & Santoro, M. (2011). *Interferometric processing of PAL SAR wide-beam Scan SAR data, Fringe 2011, 8th International workshop on "advances in the Science and applications of SAR Interferometry"*.
- Wright, T. J., Parsons, B. E., & Lu, Z. (2004). Toward mapping surface deformation in three dimensions using InSAR. *Geophysical Research Letters*, *31*(1), L01607. <https://doi.org/10.1029/2003GL018827>
- Yang, H., Guo, R., Zhou, J., Yang, H., & Sun, H. (2022). Transient poroelastic response to megathrust earthquakes: A look at the 2015 Mw 8.3 Illapel, Chile, event. *Geophysical Journal International*, *230*(2), 908–915. [ggac099. https://doi.org/10.1093/gji/ggac099](https://doi.org/10.1093/gji/ggac099)

References From the Supporting Information

- Christensen, N. (1996). Poisson's ratio and crustal seismology. *Journal of Geophysical Research*, *101*(B2), 3139–3156. <https://doi.org/10.1029/95JB03446>
- Li, S., Moreno, M., Bedford, J., Rosenau, M., & Oncken, O. (2015). Revisiting viscoelastic effects on interseismic deformation and locking degree: A case study of the Peru-North Chile subduction zone. *Journal of Geophysical Research: Solid Earth*, *120*(6), 4522–4538. <https://doi.org/10.1002/2015JB011903>
- Lin, Y. N., Kositsky, A. P., & Avouac, J.-P. (2010). PCAIM joint inversion of InSAR and ground-based geodetic time series: Application to monitoring magmatic inflation beneath the Long Valley Caldera. *Geophysical Research Letters*, *37*(23), L23301. <https://doi.org/10.1029/2010GL045769>
- Masterlark, T. (2003). Finite element model predictions of static deformation from dislocation sources in a subduction zone: Sensitivities to homogeneous, isotropic, Poisson-solid, and half-space assumptions. *Journal of Geophysical Research*, *108*(B11), 2540. <https://doi.org/10.1029/2002JB002296>
- Press, W., Teukolsky, A., Vetterling, W., & Flannery, B. (2002). *Numerical recipes in C: The art of Scientific computing*, Cambridge Univ Press.
- Ranalli, G. (1997). Rheology and deep tectonics. *Annali di Geofisica*, *40*(3), 671–780. <https://doi.org/10.4401/ag-3893>
- Tassara, A., Götz, H. J., Schmidt, S., & Hackney, R. (2006). Three-dimensional density model of the Nazca plate and the Andean continental margin. *Journal of Geophysical Research*, *111*(B9), B09404. <https://doi.org/10.1029/2005JB003976>
- Williamson, A. L., & Newman, A. V. (2018). Limitations of the resolvability of finite-fault models using static land-based geodesy and open-ocean tsunami waveforms. *Journal of Geophysical Research: Solid Earth*, *123*(10), 9033–9048. <https://doi.org/10.1029/2018JB016091>

3.2.3 Chilean megathrust earthquake recurrence linked to frictional contrast at depth

Published as: M. Moreno, S. Li, D. Melnick, J. R. Bedford, J. C. Baez, M. Motagh, M., S. Metzger, S. Vajedian, C. Sippl, B. D. Gutknecht, E. Contreras-Reyes, Z. Deng, A. Tassara, O. Oncken, O. (2018), Chilean megathrust earthquake recurrence linked to frictional contrast at depth. *Nature Geoscience*, **11**, 285–290. [doi:10.1038/s41561-018-0089-5](https://doi.org/10.1038/s41561-018-0089-5)

Supporting information: available online

Scientific application: We show that, at subduction zones, the seismic cycle of the (relatively shallow) megathrust earthquakes is mechanically controlled by the occurrence of more frequent, deep events of moderate size by a contrast in frictional strength.

Methodological advances: This integrative study combines geodetic and seismic observations, kinematic slip inversions, seismic reflection data and mechanical modelling.

Individual Contributions: MM and SL conceived the original idea, which was elaborated with JB, DM and OO, MM and SL performed all numerical simulations. JB performed the slip inversions. MMo and SV processed the InSAR data. JB and ZD processed the GNSS data. I performed the GNSS time series analysis (Figure S1) and prepared the InSAR observations for the modeling (subsampling and noise estimation, Figure S4). BC performed the stress-anomaly model. CS processed the seismological data. EC performed the processing of seismic reflection data. DM installed cGNSS stations. The manuscript was written by MM with contributions from DM, JB, SL, CS, me, OO, EC and AT.

Chilean megathrust earthquake recurrence linked to frictional contrast at depth

M. Moreno^{1,2*}, S. Li^{1,3}, D. Melnick^{4,5}, J. R. Bedford¹, J. C. Baez⁶, M. Motagh^{1,7}, S. Metzger¹, S. Vajedian⁷, C. Sippl¹, B.D. Gutknecht⁸, E. Contreras-Reyes⁹, Z. Deng¹, A. Tassara^{5,10} and O. Oncken¹

Fundamental processes of the seismic cycle in subduction zones, including those controlling the recurrence and size of great earthquakes, are still poorly understood. Here, by studying the 2016 earthquake in southern Chile—the first large event within the rupture zone of the 1960 earthquake (moment magnitude (M_w) = 9.5)—we show that the frictional zonation of the plate interface fault at depth mechanically controls the timing of more frequent, moderate-size deep events ($M_w < 8$) and less frequent, tsunamigenic great shallow earthquakes ($M_w > 8.5$). We model the evolution of stress build-up for a seismogenic zone with heterogeneous friction to examine the link between the 2016 and 1960 earthquakes. Our results suggest that the deeper segments of the seismogenic megathrust are weaker and interseismically loaded by a more strongly coupled, shallower asperity. Deeper segments fail earlier (~60 yr recurrence), producing moderate-size events that precede the failure of the shallower region, which fails in a great earthquake (recurrence >110 yr). We interpret the contrasting frictional strength and lag time between deeper and shallower earthquakes to be controlled by variations in pore fluid pressure. Our integrated analysis strengthens understanding of the mechanics and timing of great megathrust earthquakes, and therefore could aid in the seismic hazard assessment of other subduction zones.

Models of recent, large, subduction-zone earthquakes have revealed spatial relations between zones of high pre-seismic locking on the interface and regions of large coseismic slip, mechanically indicative of so-called asperities^{1–5}. Although such relationships can be interpreted as evidence for heterogeneous fault friction properties^{3,6}, little is known about the physical controls on the spatial distribution of creep, locking and slip on a seismogenic interface. Possible hypotheses include the varying degrees of geometric complexity^{7,8}, the nature and thickness of the trench sediments⁹, variable fluid release at different depths^{10–13}, differential loading along the plate interface associated with the geologic structure of the upper plate^{14–16} and fault zone rheology^{17,18}. Each of these proposed physical mechanisms may independently influence dynamic, mechanical, and hydraulic properties of the subduction interface and consequently its frictional strength (stress required to initiate earthquake slip) and kinematics.

The lack of precision and completeness in deformation records between great earthquakes, and the rarity in recording major events affecting the same segment have restricted the characterization of the earthquake cycle to short snapshots. Thus, our understanding of the cycle in terms of frictional conditions along the plate interface is limited. The 25 December 2016 southern Chile earthquake¹⁹ (moment magnitude (M_w) = 7.6; Fig. 1) is the first sign of seismic reactivation within the segment that failed during the 1960 megathrust earthquake—the largest recorded by modern seismology^{20,21}. Therefore, exploring the relationship between both events could provide insights into the persistence of asperities and a better understanding of slip

behaviour (locking, creeping and seismic slip) with respect to spatiotemporal variations in frictional properties on the plate interface.

The 2016 Southern Chile earthquake

The first-order kinematics of the 2016 event¹⁹ resembles previous Chilean megathrust events (that is, 1985 Central Chile²², 1995 Antofagasta²³, 2007 Tocopilla²⁴) in that most slip occurred along the deeper portions of the seismogenic region of the megathrust, within the transitional rheological separation to aseismic sliding^{25,26}. Furthermore, such deeper, zone-C events²⁶ with $M_w = 7–8$ are more frequent than great ($M_w > 8.5$) shallower events in subduction zones²⁷ and thus play an important role in the process of stress build-up and release of seismic energy.

The 2016 earthquake ruptured the deeper portion of an area thought to represent a locked asperity, based on decadal-scale geodetic monitoring²⁸ (Fig. 1). Kinematic models suggest that this patch previously released its full slip deficit in 1960 with over 10 m of slip²⁹. We report near-fault, static surface displacements of the 2016 mainshock recorded by nine continuous GPS stations and synthetic aperture radar (SAR) differential interferograms (Fig. 1b and Supplementary Figs. 1–4). The largest recorded horizontal and vertical displacements occurred at Guafo Island (located ~20 km from the epicentre). To derive the slip distribution, we jointly inverted the GPS and InSAR data. Our preferred slip solution (Fig. 1) suggests a simple rupture composed of a single slip patch with a maximum slip of 2.9 m at 22 km depth. This amount is consistent with the release of ~80% of the total plate motion accumulated there since 1960.

¹GFZ Helmholtz Centre Potsdam, German Research Centre for Geosciences, Telegrafenberg, Potsdam, Germany. ²Departamento de Geofísica, Facultad de Ciencias Físicas y Matemáticas, Universidad de Concepción, Concepción, Chile. ³Department of Earth and Environmental Sciences, University of Iowa, Iowa City, IA, USA. ⁴Instituto de Ciencias de la Tierra, TAQUACH, Universidad Austral de Chile, Valdivia, Chile. ⁵Millennium Nucleus The Seismic Cycle Along Subduction Zones, Valdivia, Concepción, Chile. ⁶Centro Sismológico Nacional, Universidad de Chile, Facultad de Ciencias Físicas y Matemáticas, Santiago, Chile. ⁷Institute of Photogrammetry and GeoInformation, Leibniz Universität Hannover, Hannover, Germany. ⁸Institut für Planetare Geodäsie, Technische Universität Dresden, Dresden, Germany. ⁹Departamento de Geofísica, Facultad de Ciencias Físicas y Matemáticas, Universidad de Chile, Santiago, Chile. ¹⁰Departamento de Ciencias de la Tierra, Facultad de Ciencias Químicas, Universidad de Concepción, Concepción, Chile. *e-mail: marcos@gfz-potsdam.de

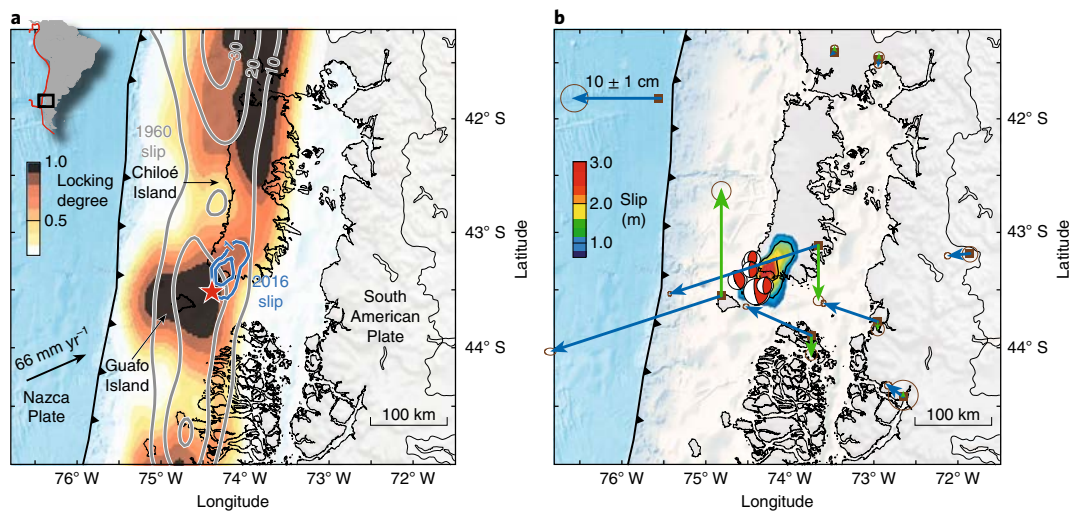


Fig. 1 | The 1960 and 2016 earthquakes. **a**, The 2016 earthquake affected the southern half of the rupture zone of the 1960 event. White-grey lines show the rupture zone (10 m) of the 1960 earthquake²⁹. The red star shows the epicentre of the 2016 event. Blue contours (1 m) depict the slip of the 2016 event. Background colours show the distribution of locking degree²⁸. **b**, Slip distribution derived from our joint inversion is shown by a coloured grid. Horizontal and vertical GPS coseismic displacements are shown by blue and green arrows, respectively. Focal mechanisms of the aftershock sequence are plotted in red.

This is in agreement with the degree of pre-2016 locking, implying that the 2016 earthquake released most of the elastic strain accumulated over 56 years in this area. The epicentre and aftershocks of this event were located just up-dip of the zone of highest coseismic slip, similar to the location of the background seismicity recorded before 2016³⁰ (Fig. 2a). Interestingly, the aftershock sequence featured relatively low magnitudes ($M_w < 5.5$) and event numbers rapidly decayed with time (Supplementary Fig. 6), suggesting the regions surrounding the mainshock were below the critical conditions for failure.

The seismogenic zone in this area has been inferred to be shallow and controlled by a hot and young (13 Ma) incoming Nazca Plate³⁰. The seismic to aseismic transition along the interface has been mapped at ~30 km depth and coincides with an isotherm of ~325 °C, close to the tip of the hydrated mantle wedge at the intersection of the slab with the continental Moho³¹ (Fig. 2c). Below this limit, neither interseismic microseismicity³⁰ nor aftershocks of the 2016 event have been recorded, indicating a rheological regime where creep is dominant.

Using offshore multichannel seismic reflection data (Supplementary Fig. 7), we mapped the morphology and distribution of Tertiary forearc basins. We find that Guafo Island lies over a sedimentary basin, which has a thickness of ~750 m at the depocentre. A patch of high interseismic locking and large 1960 slip release is coincident with a region of negative anomalous gravity³² in the basin area (Fig. 2). The relation between gravity lows (basins) and concentration of coseismic slip (high locking) has been linked with elevated effective coefficients of friction and thus higher shear fault strengths (greater resistance) that cause long-term (million year timescale) topographic depressions^{14,33}. The continental basement has a local high (ridge) that delimits the eastern border of the basin. This ridge structure correlates with a relative gravity high, which coincides with the downdip end of the locked zone as well as of the downdip extents of the 1960 and 2016 coseismic ruptures. Such a gravity high has been observed globally along subduction zones³², and has been inferred to represent an expression of the long-term stability of the downdip limit of the seismogenic zone. Likewise, the ridge structure could be caused by the transformation of interseismic strain into permanent geologic strain via faulting, folding and/or buckling of the inner forearc at the transition between unstable (seismic) and stable (aseismic) sliding³².

Stress build-up along the seismogenic zone

Heterogeneity in frictional strength at the plate interface is a first-order control on earthquake rupture and frequency³⁴. The spatial correlation between the forearc structure and the kinematics of both the 1960 and 2016 events suggests a depth-varying frictional segmentation along the seismogenic zone (Fig. 2c), with the shallower segment being the highly coupled portion of the fault (higher shear strength state at depths shallower than 20 km), and the deeper segment localized in the narrow transition from unstable to stable slip (the rupture zone of 2016 event at 20–30 km depth).

Inspired by the observed correlation, we investigated the frictional structure of the seismogenic zone with a mechanical model designed to simulate the evolution of stress build-up due to the steady subduction³⁵ of a coupled asperity under the Coulomb friction failure criterion. Our model outputs the spatiotemporal evolution of tractions (stresses on the fault plane) for a heterogeneous frictional seismogenic zone under tectonic stress loading. We do not attempt to model the complex dynamics of rupture^{6,36} and subsequent healing³⁷, which are of short duration compared with the period of stress build-up of a 2016-class earthquake (56 yr assuming that the 1960 event released all stress in the 2016 zone). In our model, a higher coefficient of effective friction clamps a segment of the fault (no sliding) until the frictional forces overcome the fault strength and the coupled section begins to slide. Aseismic slip occurs around areas with a lower effective coefficient of friction, where the weaker interface fails due to a smaller resisting shear strength. The clamp model produces a deformation halo of low creep rate surrounding the coupled asperity that in turn causes higher strain rates downdip, effectively loading these areas while shielding updip portions of the asperity (Supplementary Fig. 9) due to the shadowing of stresses³⁸.

It is important to note that the size of the coupled asperity and the frictional contrast around the asperity control both the pattern of strain energy concentration at the downdip end and the rupture interval (time when a fault segment begins sliding without building extra stress) (Supplementary Fig. 9). Accordingly, larger asperities require more time to reach the critical failure state. We tested a wide range of frictional contrasts based on the distribution of locking degree to define the boundary of the coupled asperity. We found a significant spatial correlation between the shear stress accumulation after 50 yr of interseismic loading in the deeper fault portion and the

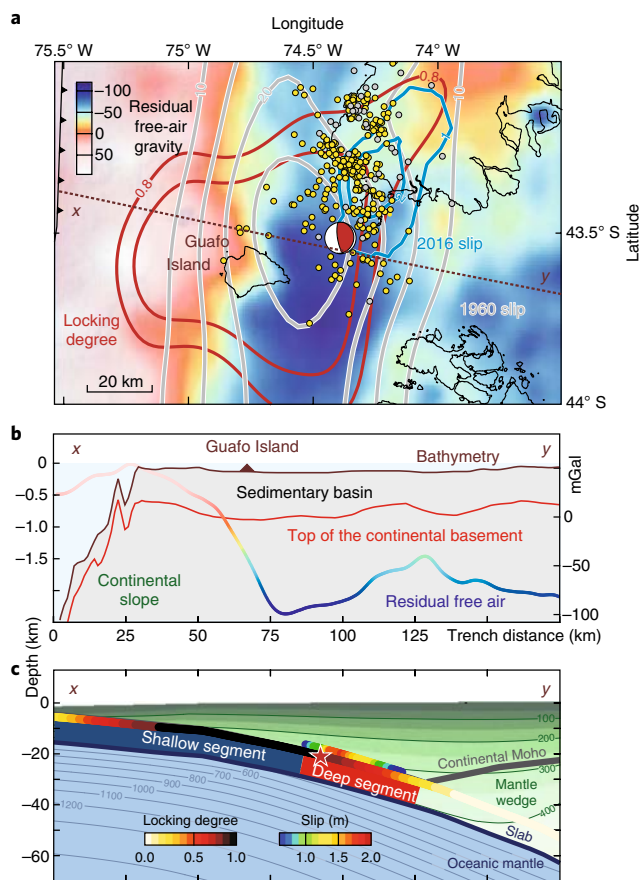


Fig. 2 | Downdip segmentation of the seismogenic zone. **a**, High locking degree (>0.8 , red contours) and large 1960 slip (white-grey 5 m contours) coincides with a region of negative free-air gravity anomaly³². The 2016 earthquake (blue 1 m contours) was located below this region. Yellow dots and the red beachball show locations of aftershocks and the mechanism of the 2016 earthquake, respectively. Grey dots show interseismic background seismicity. **b**, Cross-section xy showing the forearc morphology and gravity anomaly³². **c**, Locking and slip distribution overlaying a thermal model³¹. Shallow (<20 km depth) and deep (20–30 km depth) segments of the plate interface are shown.

slip of the 2016 earthquake when the shallow segment of the fault is clamped (Fig. 3a). This finding suggests that the shallow segment mechanically behaves like a coupled asperity that induces strain and stress accumulation in the deeper seismogenic segment. This is also supported by its kinematics, as this fault section released the highest slip during the 1960 event (slip >25 m) and its centre is fully locked (locking degree >0.9 ; Fig. 2). Our model shows that following a deeper-class earthquake, the shallower coupled segment will continue stressing and straining the transition between the shallower and deeper segments, but with a reduced ring-shaped area (Fig. 3b). After 100 yr of loading, a subsequent rupture of the entire coupled segment could also drive failure of the down-dip region, producing a $M_w > 8.5$ earthquake.

Failure lag time

Given the lag time between the 1960 and 2016 events, we further investigated the effective friction coefficients for both the shallow and deep fault segments that would favour the rupture of the deep segment after 60 ± 5 yr of interseismic loading. In doing so, we assume that tectonic stress guides the loading of the system and

seismic stress drop represents pre-earthquake stress conditions on the fault. In addition, we assume that a giant 1960-class event fully releases the accumulated elastic stresses, as proposed for the 2011 Tohoku earthquake³⁹. We focus on characterizing the downdip frictional zonation across the 2016 rupture zone, and thus we do not attempt to explore along-strike variations. The rupture times of the fault segments are assessed as the initial time when the fault cannot hold the accumulated stresses in the system, marking the onset of unstable sliding. The results indicate the range of coefficients of friction combinations (between the shallow and deep segments) that can produce the observed 56-year lag time for rupture of the deep segment (Supplementary Fig. 10). The effective friction coefficient of the deep segment needs to be <0.01 and always lower than that of the shallow segment, which ranges between 0.01 and 0.04 (Supplementary Fig. 10). This result suggests that the seismogenic zone is weak, with an effective friction coefficient of generally <0.04 , as suggested by thermal modelling studies⁴⁰.

The rupture time of the deep segment depends not only on its own effective friction coefficient but also on the transfer of stress from the shallow segment. Hence, the spatiotemporal evolution of stress build-up, and thus timing of ruptures, can be controlled by the contrast in effective friction between the shallow and deep seismogenic segments (Supplementary Fig. 11). We cannot yet directly establish the value of the friction coefficient of the shallow segment, and therefore its rupture time. We can, however, use the stress drop of the 2016 event (Supplementary Fig. 12) as a proxy for the expected stress in this region. Thus, to accumulate shear stresses in the range of the stress drop after 56 yr of steady subduction, the effective friction coefficient of the deep segment needs to be 30–40% of the value of the shallow segment (Fig. 4a). We can narrow the rupture time of the shallow segment to an optimal range of 110–140 yr of interseismic loading (Fig. 4a), similar to the recurrence time of historical $M_w > 8$ ruptures⁴¹. The proposed differential along-dip mechanical behaviour of the seismogenic zone allows an elastic slip deficit accumulation period on the shallow segment to be twice as long as on the deeper segment; such a longer period may thus result in great tsunamigenic earthquakes.

Frictional contrast and pore pressure relationship

Our model suggests that differences in lithostatic load (Supplementary Fig. 14) alone cannot produce the short-term mechanical behaviour of a coupled asperity. High normal stress couples the fault below the seismogenic limit, whereas low normal stress induces a reduction of fault resistance in the shallow segment, opposite to its mechanical behaviour (Supplementary Fig. 15). Hence, variations on the effective friction coefficient are expected to offset the normal stress¹⁴. It has long been recognized that pore fluid pressure can counteract the normal stress, weakening the absolute strength and stability of a fault^{10,42}. Likewise, gradients in fluid pressure can induce fault strength segmentation^{11,13}, with drained conditions promoting fault coupling^{12,13}.

By assuming that the pore fluid pressure gradient is the main parameter varying the frictional resistance, we estimated the values of the pore pressure ratio ($\lambda = \text{pore pressure/lithostatic stress}$) based on the predicted values of effective friction coefficient (Fig. 4b). We ignored additional factors beside pore pressure alone, such as heterogeneity of the shear zone and accumulation of damage³⁷, that may play a role in frictional variations. In absence of these additional complexities, our results suggest that λ in the deep segment has to be >0.98 to permit its rupture after ~ 56 years of loading. In contrast, in the shallow segment $\lambda = 0.95\text{--}0.96$ is needed in order to accumulate the shear traction matching the stress drop of the 2016 event. Our results not only support the anti-correlation between locking degree and λ proposed by previous studies^{10,12}, but also demonstrate that overpressure results in a faster release of shear stress, potentially causing more frequent earthquakes of moderate

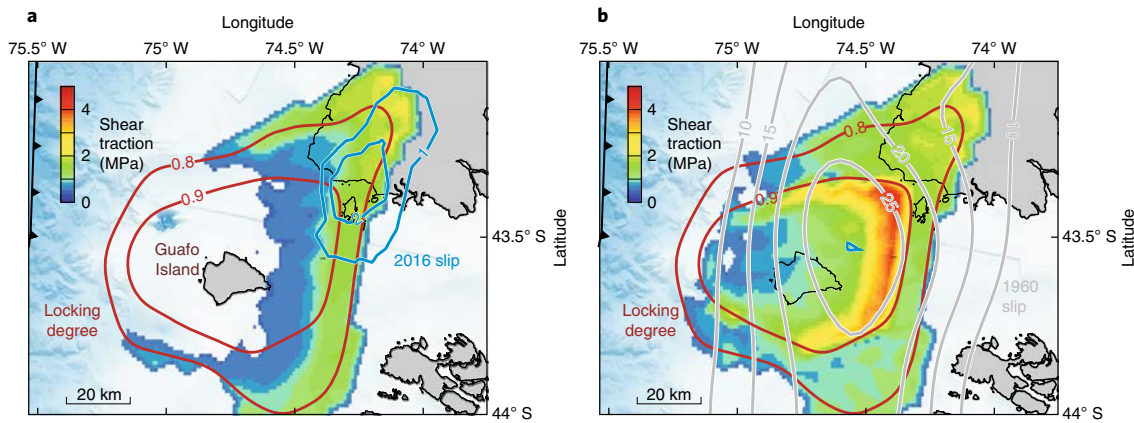


Fig. 3 | Stress build-up pattern around a clamped shallow asperity. This model incorporates an effective friction coefficient of the deep segment 0.35 times the value of the shallow segment. Red contours delimit highly locked areas (>0.8). **a**, Stress build-up after 50 years of loading. This model produces a shear traction accumulation similar in magnitude and location with the rupture zone of the 2016 earthquake (1 m blue contours). **b**, Stress build-up after 100 years of loading. Shear traction is accumulated in the downdip limit of the asperity, encircling the area with highest slip during the 1960 event (white-grey 5 m contours).

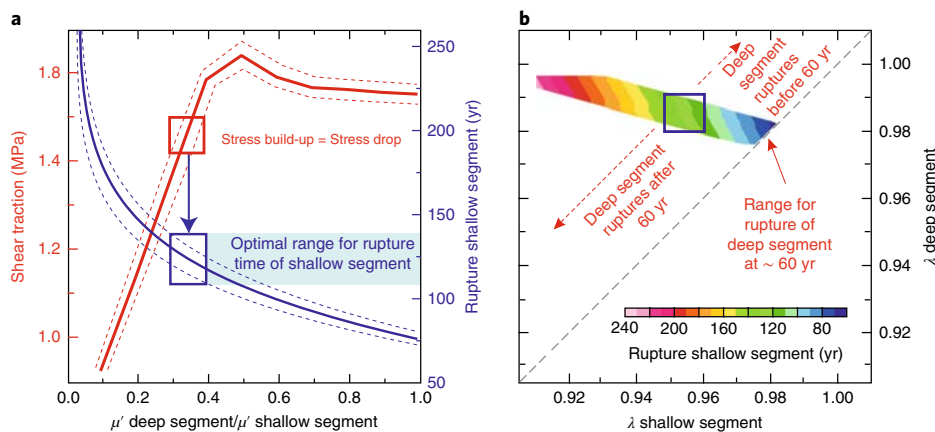


Fig. 4 | Effective friction coefficient and pore pressure ratios. **a**, Shear traction in the deep segment and rupture time of the shallow segment as functions of the effective friction coefficient (μ') ratio. Red curves show the accumulated shear traction in the deep segment after 60 ± 5 yr of loading. Blue curves show the rupture time of shallow segment with 95% confidence intervals. Stress build-up matches the 2016 stress drop when μ' of the deeper segment is 30–40% of the value of the shallower segment. This frictional contrast suggests a rupture time of 110–140 yr for the shallow segment. **b**, Estimation of pore pressure ratio (λ) for both segments. Rupture times of the shallow segment are given by the colour for possible combinations of λ that should produce the rupture of the deeper segment at 56 yr lag time. The blue square marks the range of λ combinations determined from Fig. 4a.

size. Pore fluid may thus exert similar stresses to the lithostatic load, providing an explanation for the apparent weakness of the fault in the transition between unstable and stable frictional behaviour. In our study area, this transition ends around the slab-Moho discontinuity, where temperatures are inferred to be 300–400 °C (ref. ³¹), and where serpentinite and other hydrous minerals may release fluids into the seismogenic zone maintaining pore pressure close to lithostatic values (Fig. 5).

Localized hydration at the base of the continental plate will form an effective permeability seal because of associated volumetric dilation caused by the hydrous mineral phases, forcing fluids to move upwards along the interplate fault zone and increasing pore pressure⁴³. In addition, high pore pressures within the plate interface in southern Chile may be partly attributed to its geological history. Here, the forearc basement consists of metamorphic rocks from a Permo–Triassic accretionary complex⁴⁴. Geophysical images and exhumation history suggest rock units exposed at the surface are

continuous to interplate depths^{44,45} (Fig. 5). These units are associated with duplex structures interpreted to reflect continuous basal accretion of underthrust trench sediments⁴⁴. Such duplexes are formed by low-angle thrust sheets dominated by subhorizontal foliations. These pervasive structures are locally cut by submetric vertical quartz veins interpreted as syn-exhumation tension gashes filled with silica-rich fluids pumped by seismogenic processes^{43,44}. The predominant horizontal fabrics of basally accreted material may constitute an additional permeability seal (stratigraphic fluid barrier) precluding the ascent of trapped fluids, in contrast to intrusive continental framework rocks that are usually associated with vertical cooling fabrics. Subhorizontal fabrics in southern Chile may thus play a role in restricting vertical fluid migration pathways and enhancing interplate pore pressure.

The interseismic GPS deformation field shows a landward reduction from 50 mm yr⁻¹ to 12 mm yr⁻¹ in a distance of only 100 km, indicating a high degree of crustal shortening just above the deeper

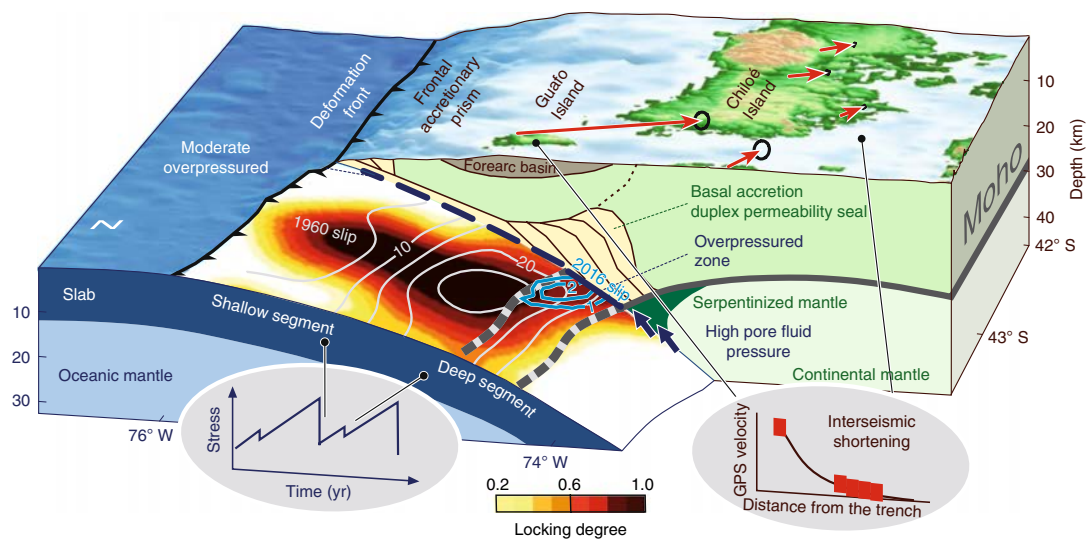


Fig. 5 | Schematic conceptual model of the frictional loading across the plate interface. The stronger shallower segment strains and stresses the deeper segment of the seismogenic zone. The deeper segment is weaker and fails at lower stress build-up in 2016-class earthquakes. Higher shear strength along the shallow segment allows longer periods (>110 yr) of stress build-up, the release of which may result in great 1960-class earthquakes that can also extend into the deeper segment. Interseismic GPS velocities indicate high crustal shortening above the deeper section of the seismogenic zone (right inset). Pore fluid pressure gradients along the plate interface are related to the geological configuration of the margin, and exert a mechanical control on the strength segmentation and timing of stress release in the seismogenic zone (left inset).

section of the seismogenic zone (Fig. 5). This observation corroborates our conceptual model of the deeper segment being interseismically strained. This mechanical behaviour appears to have a major impact on the long-term morphology of subduction margins as suggested by the relation of forearc basins with seismic asperities^{14–16} and the permanent emergence of coastlines above deeper seismogenic segments⁴⁶.

In summary, we propose that a variation in pore fluid pressure induces a downdip zonation of frictional strength along the plate interface. The frictional contrast at depth may thus control the lag time between deeper seismic ruptures (such as the 2016 event) and great shallower megathrust earthquakes (such as the 1960 event). Hence, deeper 2016-class earthquakes may be considered as a first phase of energy release that precedes failure of the shallower region during great earthquakes. Rupture of the shallow segment could drive failure of the downdip region even if the latter has experienced more-frequent smaller events, resulting in a 1960-class earthquake. Although our model assumes uniform properties along-strike, in nature the frictional contrast may vary along strike, making the failure time different at different along-strike segments. The central part of the 1960 rupture zone seems to be highly locked²⁸ in a wider along-strike segment than in the 2016 region. This suggests that either the fault strength is uniform over a larger along-strike segment or that the friction contrast at depth is relatively low, allowing a bigger area to be clamped over a longer period. Our model predicts that as interseismic strain builds up, more 2016-class events should occur along the 1960 rupture zone. These forthcoming events will allow a better understanding of along-strike frictional variations. Further development of this modelling strategy, such as incorporating variations of frictional behaviour in the strike direction, could be used to estimate the critical failure threshold of asperities and their time-dependent seismic potential.

Methods

Methods, including statements of data availability and any associated accession codes and references, are available at <https://doi.org/10.1038/s41561-018-0089-5>.

Received: 10 August 2017; Accepted: 27 February 2018;
Published online: 02 April 2018

References

- Bürgmann, R. et al. Interseismic coupling and asperity distribution along the Kamchatka subduction zone. *J. Geophys. Res.* **110**, B07405 (2005).
- Chlieh, M., Avouac, J., Sieh, K., Natawidjaja, D. & Galetzka, J. Heterogeneous coupling of the Sumatran megathrust constrained by geodetic and paleogeodetic measurements. *J. Geophys. Res.* **113**, B05305 (2008).
- Perfettini, H. et al. Seismic and aseismic slip on the Central Peru megathrust. *Nature* **465**, 78–81 (2010).
- Moreno, M., Rosenau, M. & Oncken, O. Maule earthquake slip correlates with pre-seismic locking of Andean subduction zone. *Nature* **467**, 198–202 (2010).
- Loveless, J. P. & Meade, B. Spatial correlation of interseismic coupling and coseismic rupture extent of the 2011 $M_w=9.0$ Tohoku-oki earthquake. *Geophys. Res. Lett.* **38**, L17306 (2011).
- Kaneko, Y., Avouac, J. & Lapusta, N. Towards inferring earthquake patterns from geodetic observations of interseismic coupling. *Nat. Geosci.* **3**, 363–369 (2010).
- Wang, K. & Bilek, S. Do subducting seamounts generate or stop large earthquakes? *Geology* **39**, 819–822 (2011).
- Kopp, H. Invited review paper: the control of subduction zone structural complexity and geometry on margin segmentation and seismicity. *Tectonophysics* **589**, 1–16 (2013).
- Ruff, L. Do trench sediments affect great earthquake occurrence in subduction zones? *PAGEOPH* **129**, 263–282 (1989).
- Saffer, D. M. & Tobin, H. J. Hydrogeology and mechanics of subduction zone forearcs: fluid flow and pore pressure. *Annu. Rev. Earth Planet. Sci.* **39**, 157–186 (2011).
- Audet, P. & Schwartz, S. Hydrologic control of forearc strength and seismicity in the Costa Rican subduction zone. *Nat. Geosci.* **6**, 852–855 (2013).
- Moreno, M. et al. Locking of the Chile subduction zone controlled by fluid pressure before the 2010 earthquake. *Nat. Geosci.* **7**, 292–296 (2014).
- Saffer, D. M. Mapping fluids to subduction megathrust locking and slip behavior. *Geophys. Res. Lett.* **44**, 9337–9340 (2017).
- Song, T. R. A. & Simons, M. Large trench-parallel gravity variations predict seismogenic behavior in subduction zones. *Science* **301**, 630–633 (2003).
- Wells, R. E., Blakely, R. J., Sugiyama, Y., Scholl, D. W. & Dinterman, P. A. Basin-centred asperities in great subduction zone earthquakes: a link between slip, subsidence, and subduction erosion. *J. Geophys. Res.* **108**, 2507–2537 (2003).

16. Bassett, D., Sandwell, D., Fialko, Y. & Watts, A. Upper-plate controls on co-seismic slip in the 2011 magnitude 9.0 Tohoku-oki earthquake. *Nature* **531**, 92–96 (2016).
17. Angiboust, S. et al. Probing the transition between seismically coupled and decoupled segments along an ancient subduction interface. *Geochem. Geophys. Geosyst.* **16**, 1905–1922 (2015).
18. Gao, X. & Wang, K. Rheological separation of the megathrust seismogenic zone and episodic tremor and slip. *Nature* **543**, 416–419 (2017).
19. Ruiz, S. et al. Reawakening of large earthquakes in south central Chile: the 2016 M_w 7.6 Chiloé, event. *Geophys. Res. Lett.* **44**, 6633–6640 (2017).
20. Pfalzer, G. & Savage, J. Mechanism of the Chilean earthquake of May 21 and 22, 1960. *Geol. Soc. Am. Bull.* **81**, 1001–1030 (1970).
21. Barrientos, S. & Ward, S. The 1960 Chile earthquake: inversion for slip distribution from surface deformation. *Geophys. J. Int.* **103**, 589–598 (1990).
22. Barrientos, S. Slip distribution of the 1985 Central Chile earthquake. *Tectonophysics* **145**, 225–241 (1988).
23. Pritchard, M. E. et al. Geodetic, teleseismic, and strong motion constraints on slip from recent southern Peru subduction zone earthquakes. *J. Geophys. Res.* **112**, B03307 (2007).
24. Motagh, M. et al. Subduction earthquake deformation associated with 14 November 2007, M_w 7.8 Tocopilla earthquake in Chile: results from InSAR and aftershocks. *Tectonophysics* **490**, 66–68 (2010).
25. Schurr, B. et al. The 2007 M_w 7.7 Tocopilla northern Chile earthquake sequence: Implications for along-strike and downdip rupture segmentation and megathrust frictional behavior. *J. Geophys. Res.* **117**, B05305 (2012).
26. Lay, T. et al. Depth-varying rupture properties of subduction zone megathrust faults. *J. Geophys. Res.* **117**, B04311 (2012).
27. Allen, T., Marano, K., Earle, P. & Wald, D. PAGER-CAT: a composite earthquake catalog for calibrating global fatality models. *Seismol. Res. Lett.* **80**, 57–62 (2009).
28. Moreno, M. et al. Heterogeneous plate locking in the South-Central Chile subduction zone: building up the next great earthquake. *Earth Planet. Sci. Lett.* **305**, 413–424 (2011).
29. Moreno, M. S., Bolte, J., Klotz, J. & Melnick, D. Impact of megathrust geometry on inversion of coseismic slip from geodetic data: Application to the 1960 Chile earthquake. *Geophys. Res. Lett.* **36**, L16310 (2009).
30. Lange, D. et al. Seismicity and geometry of the south Chilean subduction zone (41.5°S–43.5°S): Implications for controlling parameters. *Geophys. Res. Lett.* **34**, L06311 (2007).
31. Völker, D., Grevemeyer, I., Stipp, M., Wang, K. & He, J. Thermal control of the seismogenic zone of southern central Chile. *J. Geophys. Res.* **116**, B10305 (2011).
32. Bassett, D. & Watts, A. Gravity anomalies, crustal structure, and seismicity at subduction zones: 1. seafloor roughness and subducting relief. *Geochem. Geophys. Geosyst.* **16**, 1508–1540 (2015).
33. Fuller, C., Willett, S. & Brandon, M. Formation of forearc basins and their influence on subduction zone earthquakes. *Geology* **34**, 65–68 (2006).
34. Scholz, C. H. Earthquakes and friction laws. *Nature* **391**, 37–42 (1998).
35. Kanda, R. & Simons, M. An elastic plate model for interseismic deformation in subduction zones. *J. Geophys. Res.* **115**, B03405 (2010).
36. Perfettini, H. & Ampuero, J. P. Dynamics of a velocity strengthening fault region: Implications for slow earthquakes and postseismic slip. *J. Geophys. Res.* **113**, B09411 (2008).
37. Rice, J., Sammis, C. & Parsons, R. Off-fault secondary failure induced by a dynamic slip pulse. *Bull. Seismol. Soc. Am.* **96**, 109–134 (1995).
38. Hetland, E. A. & Simons, M. Post-seismic and interseismic fault creep ii: transient creep and interseismic stress shadows on megathrusts. *Geophys. J. Int.* **181**, 99–112 (2010).
39. Hasegawa, A., Yoshida, K. & Okada, T. Nearly complete stress drop in the 2011 M_w 9.0 off the Pacific coast of Tohoku Earthquake. *Earth Planet. Sp.* **63**, 35 (2011).
40. Gao, X. & Wang, K. Strength of stick-slip and creeping subduction megathrusts from heat flow observations. *Science* **345**, 1038–1041 (2014).
41. Cisternas, M. et al. Predecessors of the giant 1960 Chile earthquake. *Nature* **437**, 404–407 (2005).
42. K. Hubbert, M. & Rubey, W. Role of fluid pressure in mechanics of overthrust faulting: I. Mechanics of fluid-filled porous solids and its application to overthrust faulting. *Bull. Seismol. Soc. Am.* **70**, 115–166 (1959).
43. Bachmann, R. et al. Exposed plate interface in the European Alps reveals fabric styles and gradients related to an ancient seismogenic coupling zone. *J. Geophys. Res.* **114**, B05402 (2009).
44. Glodny, J. et al. Differential Late Paleozoic active margin evolution in south-central Chile (37–40°S) - the Lanalhue Fault Zone. *J. South Am. Earth Sci.* **26**, 397–4110 (2008).
45. Groß, K., Micksch, U. & Group, T. R. The reflection seismic survey of project TIPTEQ-the inventory of the Chilean subduction zone at 38.2°S. *Geophys. J. Int.* **172**, 565–571 (2007).
46. Melnick, M. Rise of the central Andean coast by earthquakes straddling the Moho. *Nat. Geosci.* **9**, 401–407 (2016).

Acknowledgements

This work is supported by the German Science Foundation (DFG) grants MO3157/2-3 (M.M., J.R.B.) and SCHU2460/3-1 (C.S.), Millennium Scientific Initiative (ICM) grant NC160025 "CYCLO - the seismic cycle along subduction zones" (D.M., A.T.), Chilean National Commission for Scientific and Technological Research (CONICYT) grant PAI-MEC 2016 (M.M.), FONDECYT 1150321 (D.M.), and Helmholtz Graduate Research School GeoSim (S.L.). ALOS original data are copyright of the Japanese Aerospace Exploration Agency and provided under proposal 1161 (M.Mo.). This study was encouraged by discussions with B. Schurr and I. Urrutia. We thank Armada de Chile for hosting our cGPS stations GUAF (Faro Guafo) and MELK (Melinka).

Author contributions

M.M. and S.L. conceived the original idea, which was elaborated with J.R.B., D.M. and O.O. M.M. and S.L. performed all numerical simulations. J.R.B. performed the slip inversions. S.M., M.Mo. and S.V. processed the InSAR data. J.C.B. and Z.D. processed the GPS data. S.M. performed the time series analysis of GPS data. B.D.G. performed the stress anomaly model. C.S. processed the seismological data. E.C. performed the processing of seismic reflection data. D.M. installed cGPS stations. The manuscript was written by M.M. with comments from D.M., J.R.B., S.L., C.S., S.M., O.O., E.C. and A.T.

Competing interests

The authors declare no competing interests.

Additional information

Supplementary information is available for this paper at <https://doi.org/10.1038/s41561-018-0089-5>.

Reprints and permissions information is available at www.nature.com/reprints.

Correspondence and requests for materials should be addressed to M.M.

Publisher's note: Springer Nature remains neutral with regard to jurisdictional claims in published maps and institutional affiliations.

Methods

GPS data processing and coseismic offset estimations from time-series. Data from all available continuous GPS stations with coseismic data were compiled and processed using the Earth Parameter and Orbit System (EPOS) software⁴⁷ in the ITRF 2014 reference frame. IGS08 phase centre variations and FES2004 ocean tide loading were used with hourly tropospheric wet zenith delays estimated as random-walk parameters and Vienna mapping functions in a grid file database. The reprocessed precise satellite orbit and clock products were generated together with station coordinates by EPOS and combined with IGS products in order to reduce the impact in estimating Earth rotation parameters.

We estimated the coseismic offset of the GPS data from the continuous stations FUTE, GUAU, MELK, MUER, PMO1, PTRO, GLLN, RMBA, TPYU installed by the National Seismological Center of Chile (CSN) and the University of Potsdam, Germany. The resulting time series were automatically cleaned for all data and/or error outliers. The coseismic offset was estimated using an iterative least-square inversion that also solves for additional signal components^{48,49} like the linear (interseismic) plate rate, antenna offsets, seasonal and semi-seasonal variations and coseismic offsets from relevant earthquakes in the vicinity, based on the NEIC (National Earthquake Information Center, <https://earthquake.usgs.gov>) earthquake catalogue and with a threshold given by the magnitude–distance relationship. The variance of the resulting coseismic offsets was estimated using the averaged data fit normalized by overall length of the time series⁵⁰. Supplementary Figure 1 shows the time series and the parameters estimated for each station used in our analysis.

InSAR data. C-band and L-band Synthetic Aperture Radar (SAR) data acquired by the European and Japanese space agencies (ESA, JAXA), respectively, were used in this study. They include a pair of ascending and descending C-band SAR data acquired in interferometric wide-swath (IW) mode from the Sentinel-1 (S1) satellite and a pair of descending L-band SAR data acquired in ScanSAR mode (full aperture) by Advanced Land Observing Satellite 2 (ALOS 2). S1 interferograms were constructed from images acquired on 12 December 2016 and 10 January 2017 for descending and 21 December 2016 and 14 January 2017 for ascending pairs, whereas the ScanSAR ALOS-2 interferogram was constructed from images covering 1 December 2016 and 12 January 2017. The S1 interferograms were processed with the GAMMA software⁵¹. The spectral diversity method⁵² was applied for precise coregistration of SAR data. ALOS-II ScanSAR processing⁵³ was done using SARscape (<http://www.sarmap.ch/wp/>). A 90 m digital elevation model that was derived from the NASA Shuttle Radar Topography Mission (SRTM) was used as the reference topography model⁵⁴ for the topography-related phase correction and geocoding of all the interferograms. The coseismic wrapped interferograms (Supplementary Fig. 2) were unwrapped using the minimum cost flow (MCF) method⁵⁵ (Supplementary Fig. 3).

The unwrapped data were visually checked for unwrapping errors, which were either corrected or excluded from the modelling (for example mountainous areas). We then subsampled the data using the quad-tree approach⁵⁶ (Supplementary Fig. 4). In parallel, we calculated the corresponding line of sight (LOS) and the centre of mass of all valid data within one subsampled cell that was used as observation coordinate. Overall, we obtained 520 data points for the Sentinel 1 ascending data set, 550 points for the Sentinel 1 descending data set and 230 data points for the ALOS descending data set.

In the modelling, we accounted for a phase jump of a multiple of 2π between the main land, Chiloé Island and Guafo Island by introducing three additional parameters for InSAR phase ambiguities between these subsets. As the first-order proxy for estimating the noise level of the data we used the inverse of the width of the subsampled quads⁵⁷.

Slip inversion. Plate interface slip was modelled using over 600 triangular patches with a mean area of 65 km² meshed to represent the undulating plate interface model⁵⁸. Slip on each patch was represented by Green's functions of dislocation in an elastic half-space⁵⁹ and two slip vectors were solved for at each patch. These two slip vectors bound the horizontal azimuthal motion of each patch between the bearings of 250 and 290 degrees. In the inversion for slip, the lower bound of slip for each slip direction was defined as zero, so that all modelled slip has a thrust component. A maximum slip for each slip direction was set at 5 m. The bounding azimuths were selected to represent a realistic direction of plate interface motion based on the focal mechanics of moment tensor inversions along this subduction margin. The inversion problem was formulated in the L2 regularization sense so that the procedure enacted the following optimization:

$$\text{minimize} \|w \times (d - G \times m)\|_2 + \beta \|m\|$$

subject to:

$$0 \leq m \leq 5$$

where d is the data vector containing the GPS, G are the Green's functions, m is the solution vector corresponding to the amounts of slip for each Green's function, w is the vector of weights for each data point, and β is the weighting of the regularization. Accordingly, this optimization is the solution of the Tikhonov

damped, bounded, weighted least squares problem. Data are first weighted by their respective errors with a uniform error of the InSAR estimated to be 6 cm from the lateral variability of the data. The data are then further weighted in the inversion so that InSAR LOS data are weighted 10 times as strongly as GPS displacements. The choice of ratio between weighting of GPS and InSAR was based upon the approach of ref. ⁶⁰. The optimization was regularized with the L2 norm of the parameter values. The favoured damping coefficient was selected using a trade-off curve between model misfit and damping coefficient (Supplementary Fig. 5). The optimization was performed using the Matlab package CVX OPT⁶¹.

Checkerboard tests were performed revealing regions of the interface that are better resolved and the sizes of kinematic heterogeneity that can be isolated (Supplementary Fig. 5). In the region containing the mainshock and aftershock seismicity, the results of the checkerboard tests confirm that the modelled slip distribution is in a relatively well resolved region of the plate interface and that the shape of the recovered slip distribution is broader than the finest scale that can be resolved.

Seismicity. We used raw waveform data from seismic networks C and C1 available on IRIS (<https://ds.iris.edu/SeisQuery/>) to detect and locate aftershock seismicity after the 25 December earthquake. Initially, we ran a recursive STA/LTA trigger algorithm over the raw data and searched for events with coherent arrivals at at least five stations. After manually picking P and S phases for these events, we also visually checked the raw waveform data at station GO07 (which is closest to the main shock) and identified additional smaller events that were missed in the first step. All events that were visible on at least four seismometer stations were also handpicked and added to the dataset. This yielded a total of 262 earthquakes detected in the time interval between the main shock and 31 January 2017, nearly all of which are located in the main shock area. We also ran the STA/LTA algorithm over the two years of data preceding the main shock, but found no significant precursory activity. However, network coverage in the region has increased only recently, which means smaller events before 2015 may have been missed. For relocation, we employed joint hypocentre determination⁶² to the manual P and S picks, keeping the velocity model fixed to the local model³⁰. Due to the relatively small number of stations at close distances and their unfavourable geometry (most stations are located to the NE of the main shock; no coverage at western azimuths), hypocentral depths are not well defined, but epicentres should be relatively reliable.

We also determined moment tensors for five of the largest aftershocks with a previously reported technique⁶³. Only these five events had sufficient signal-to-noise ratios at long periods to be thus inverted. We required the solutions to be deviatoric, and used the period band between 15 and 35 s. The epicentres for these events were fixed to their catalogue position, and inversions with different trial centroid depths were performed. The trial depth with the lowest misfit solution was then chosen as the optimal centroid depth. All five aftershocks show low-angle thrust mechanisms, and their depths are situated close to the plate interface as defined previously³⁸, giving us confidence that the aftershock seismicity is indeed situated on the plate interface. Since moment tensor inversion is less dependent on event–station geometry than hypocentral location, these centroid depths should be more reliable than the ones from the event catalogue. The aftershocks sequence is characterized by a rapid decay in the number of events (Supplementary Fig. 6).

Multichannel seismic reflection data. Multichannel seismic reflection data were acquired offshore of Guafo Island during the SPOC using R/V Sonne in 2000/2001. (Supplementary Fig. 7). The signals for the seismic reflection experiment were generated by a tuned set of 20 air guns with a total volume of 51.21. The multichannel seismic reflection data were analysed using standard processing, including re-binning, normal move out correction, stacking, deconvolution and post-stack time migration. A predictive deconvolution with two gates, for the shallow sedimentary events and the deeper crustal events, was applied before the stack.

A space and time variant frequency filter prior to a post-stack migration completed the processing flow⁶⁴. The seismic recording system is characterized by a record length of 14,332 ms, a sampling rate of 4 ms, and a LC-Filter of 3 Hz. The shots were triggered in time intervals of 60 s on full minutes UTC. At a speed of 5 knots that results in a shot point distance of 154 m. A constant hydrophone spacing of 25 m (108 channels) was chosen for the seismic processing, resulting in a common mid-point distance of 12.5 m and a maximum fold of 27 (ref. ⁶⁴). Results of the seismic reflection processing are used to characterize the depth-varying structural features (Supplementary Fig. 7). A reflective zone shows the upper limit of the continental basement, which defines the lower limits of a sedimentary basin. Guafo Island lies in the centre of this forearc basin, which has a sediment thickness of ~750 m at its depocentre (Fig. 2b).

Mechanical modelling. The purpose of this model is to estimate the spatiotemporal evolution of stress build-up along the seismogenic zone, and its relationship to the lag time between the 1960 and 2016 earthquakes. We performed 3D geomechanical simulations using the PyLith software⁶⁵. Our model consists of an elastic downgoing slab (oceanic plate) and an upper crustal unit (overriding continental plate) that sit on top of oceanic and continental asthenospheric units, respectively (Supplementary Fig. 8). We specified a Young's modulus of 100, 120

and 160 GPa, for the continental, oceanic and mantle layers, respectively²⁸. The Poisson's ratio was set to 0.265 and 0.30 for the continental and oceanic crusts⁶⁶, respectively.

To simulate the steady interseismic subduction of the oceanic plate, we implemented the previously reported Elastic Plate Model³⁵. In this model, the plate subduction is kinematically represented by the superposition of creep along the entire base of the oceanic crust and on the top of the slab below the seismogenic zone (Supplementary Fig. 8). We specified two fault interfaces with kinematic fault conditions, representing the base of the slab (Fault3) and the creeping part below the seismogenic zone (Fault2). On those interfaces, we prescribed a homogeneous constant creeping equal to the plate convergence velocity (6.6 cm yr⁻¹), but with opposite sense of movement. The seismogenic fault (Fault1) extends between 0 and 30 km depth and is divided at 20 km depth into two segments (the shallower and deeper seismogenic segments) with different coefficients of effective friction (Fig. 2). The frictional behaviour of the seismogenic zone is modelled with the Coulomb failure criterion:

$\tau = \mu' \times (\sigma_n') + c$, where τ is the shear strength of the fault, μ' is the effective friction coefficient, σ_n' is the fault normal stress and c is the cohesion. Here, fault activation occurs when the driving forces exceed τ . For simplicity, our model neglects gravity body force but specifies normal tractions consistent with overburden (lithostatic load) as initial stress state along the frictional fault. We simulate the mechanical behaviour of a coupled asperity by clamping a section of the fault, so that it has a higher friction than the non-asperity region of the fault.

In our mechanical model, tectonic forces (slab pull) load the system and fault strength controls the levels of stress that the fault can support before sliding. We do not model the complex dynamics of rupture nucleation, dynamic interaction between asperities, or rupture propagation. Rather, we focus on the static friction that needs to be overcome to begin the process of fault motion, and not the subsequent evolution of material properties during a seismic event. Therefore, our model contributes to the conceptual understanding into the level of stress that the seismogenic zone can support before breaking in medium to large earthquakes. Other significant assumptions we make include: (i) the stress drops in the earthquakes must represent almost all of the pre-earthquake shear stress on the faults, and so the faults must be able to support only a few tens of megapascals of shear stress before slipping in earthquakes; (ii) the 1960 earthquake totally released the stress in the 2016 rupture zone; (iii) frictional strength is uniform along-strike in the study area.

We tested different values of the effective friction coefficient for both fault segments; running a total time of 360 yr of steady interseismic loading. We define the onset of instable fault behaviour as the rupture time. In this study, we assumed that the fault instable behaviour occurs when the fault creep rate exceeds 3 cm yr⁻¹. We also varied this threshold value between 1 and 5 cm yr⁻¹ and found that this variation does not significantly impact the retrieved rupture times.

Supplementary Fig. 10 shows the rupture times of all tested effective friction coefficient combinations for the two segments. Results indicate that both segments must be weak with a low coefficient of effective friction (generally <0.1) to maintain a reasonable rupture time (generally <300 yr), which is consistent with previous studies^{36,67}. These results give a range of friction combinations that produces rupture of the deeper segment after 56 yr of loading (Supplementary Fig. 10). For the deep segment to rupture at 60 ± 5 yr (black circles in Supplementary Fig. 10b), the rupture time of shallow segment depends on the ratio of the effective friction coefficients between the two segments.

We estimated the change of Coulomb failure stress (CFS)⁶⁸ predicted by our optimal slip distribution (Supplementary Fig. 12). We use a homogeneous coefficient of friction $\mu = 0.5$ (ref. ⁶⁹). The CFS values (<1.5 MPa) are in keeping with those expected from such a moderate size earthquake. We estimate the optimal range effective friction coefficient combinations that induce accumulation of stress build-up similar to the stress drop at the 2016 rupture zone, and use this frictional ratio to estimate the rupture time of the shallow segment. In order to accumulate shear stresses in the range of the stress drop of the 2016 event, the effective friction coefficient of the deep segment has to be 30–40% of the value of the shallow segment (Fig. 4a). For this friction coefficient combination, the shallow segment fails after 110–140 yr of loading.

The low effective friction coefficients of our model can be interpreted to be the result of high pore fluid pressure. High pore fluid pressure acts to locally reduce the effective normal stress on faults, which are able to fail at lower shear stresses than if the fluid were absent¹⁰.

The effective friction coefficient $\mu' = \mu_0 \times (1 - \lambda)$, can be used to incorporate pore pressure into the Coulomb stress criterion, where μ_0 is a typical frictional sliding coefficient and the value of λ , so-called the pore pressure ratio, represents the degree to which pore pressure counteracts the total stress generated by the overburden stress. Considering the typical frictional sliding coefficient as 0.5 in southern Chile subduction zone⁶⁹, we derived the pore pressure ratio of the two segments by the formula of $\lambda = 1 - \mu' / \mu_0$. Figure 4b shows the parameter space of λ of the two segments that allows the deep segment ruptures after a reasonable amount of time. For the deep segment, λ has to be >0.98 to permit its rupture after 56 years of loading. It is expected that in the shallow segment $\lambda \approx 0.95$ –0.96 in order to accumulate shear traction matching the stress drop of the 2016 event.

Stress anomaly. To gain insight into the heterogeneity of the initial static stress distribution at the plate interface we make use of normal stress anomalies reported previously⁷⁰. The anomaly is derived from vertical stress (lithostatic load) and then projected into the normal of the subduction interface. Since there is no external horizontal component involved, it is more exactly expressed as normal component of the vertical stress anomaly. Using a 3D density model further developed from the gravity forward modelling reported previously⁷¹, the vertical stress effects of density anomalies at the computation depth, that is the interface of the subducting plate in the 3D model, are incorporated into the model. Density anomalies are defined as bodies of a rock density that deviate from the standard three-layer reference model used during gravity forward modelling of the 3D density model. Isostatic or flexural effects are not considered. Topographic masses add to the vertical load and therefore we added the lithostatic stress effect of topographic masses by using ETOPO1 heights and a standard density of 2,670 kg m⁻³. The sum of the results in the vertical component is then projected into the interface normal. The static stress anomaly grid was computed on a ~3 minutes grid. For the 3D model, therefore, normal stresses are carefully calculated.

Our mechanical clamping models indicate that including the normal stress anomaly (due to density contrast in the forearc) (Supplementary Fig. 14), with a constant value for the effective friction coefficient, cannot produce the coupling pattern of the asperity (Supplementary Fig. 15) and therefore variations of effective friction along the plate interface are needed to clamp the fault.

Code availability. Numerical simulations were calculated in Pylith⁶⁵, which is available on the Computational Infrastructure for Geodynamics web site (<https://geodynamics.org/cig/software/pylith/>). Codes developed in this study to simulate stress build-up under interseismic loading are available from the corresponding author upon reasonable request. The GAMMA and Sarscape software used to compute the interferograms can be accessed at www.gamma-rs.ch and www.sarmap.ch/page.php?page=sarscape, respectively.

Data availability. The GPS data that support the findings of this study are available in the GNSS data repository of the Centro Sismológico Nacional, Chile (<http://gps.csn.uchile.cl/data/>). GPS data from stations GUAJ and MELK (before 2016) are available from the corresponding author upon reasonable request. C-band Synthetic Aperture Radar imaging from the Sentinel mission is available from the Copernicus Open Access Hub (<https://scihub.copernicus.eu>). ALOS original data are copyright to the Japanese Aerospace Exploration Agency and are not publicly available.

References

- Deng, Z., Gendt, G. & Schöne, T. in *IAG 150 Years* Vol. 143 (eds Rizos, C. & Willis, P.) 33–40 (Springer, Cham, 2015).
- Metzger, S. et al. Present kinematics of the Tjörnes Fracture Zone, North Iceland, from campaign and continuous GPS measurements. *Geophys. J. Int.* **192**, 441–455 (2013).
- Bevis, M. & Brown, A. Trajectory models and reference frames for crustal motion geodesy. *J. Geod.* **88**, 283–311 (2014).
- Geirsson, H. et al. Current plate movements across the Mid-Atlantic Ridge determined from 5 years of continuous GPS measurements in Iceland. *J. Geophys. Res.* **111**, B09407 (2006).
- Wegmüller, U. & Werner, C. Gamma SAR processor and interferometry software. In *3rd ERS Symp. Space Serv. Environ.* (eds Guyenne, T. D. & Danesny, D.) 1687–1692 (ESA, Noordwijk, 1997).
- Scheiber, R. & Moreira, A. Coregistration of interferometric SAR images using spectral diversity. *IEEE Trans. Geosci. Remote Sens.* **38**, 2179–2191 (2000).
- Guarnieri, A. & Prati, C. Scansar focusing and interferometry. *IEEE Trans. Geosci. Remote Sens.* **34**, 1029–1038 (1996).
- Farr, T. & Kobrick, M. Shuttle radar topography mission produces a wealth of data. *Eos Trans. Am. Geophys.* **81**, 583–585 (2000).
- Costantini, M. A novel phase unwrapping method based on network programming. *IEEE Trans. Geosci. Remote Sens.* **36**, 813–821 (1998).
- Jónsson, S., Zebker, H., Segall, P. & Amelung, F. Fault slip distribution of the 1999 M_w 7.1 Hector Mine, California, earthquake, estimated from satellite radar and GPS measurements. *Seismol. Soc. Am. Bull.* **92**, 1377–1389 (2002).
- Sudhaus, H. & Jónsson, S. Improved source modelling through combined use of InSAR and GPS under consideration of correlated data errors: application to the June 2000 Kleifarvatn earthquake, Iceland. *Geophys. J. Int.* **176**, 389–404 (2009).
- Tassara, A. & Echaurren, A. Anatomy of the Andean subduction zone: three-dimensional density model upgraded and compared against global-scale models. *Geophys. J. Int.* **189**, 161–168 (2012).
- Okada, Y. Internal deformation due to shear and tensile faults in a half-space. *Bull. Seism. Soc. Am.* **82**, 1018–1040 (1992).
- Cavalié, O. et al. Slow slip event in the Mexican subduction zone: evidence of shallower slip in the Guerrero seismic gap for the 2006 event revealed by the joint inversion of InSAR and GPS data. *Earth Planet. Sci. Lett.* **367**, 52–60 (2013).

61. Grant, M. C. & Boyd, S. P. in *Recent Advances in Learning and Control* (eds Blondel, V. et al.) 95–110 (Springer, London, 2008).
62. Kissling, E., Ellsworth, W. L., Eberhart-Phillips, D. & Kradolfer, U. Initial reference models in local earthquake tomography. *J. Geophys. Res.* **99**, 19635–19646 (1994).
63. Nabelek, J. & Xia, G. Moment-tensor analysis using regional data: application to the 25 March, 1993, Scotts Mills, Oregon, Earthquake. *Geophys. Res. Lett.* **22**, 13–16 (1995).
64. Reichert, C., Schreckenberger, B. & SPOC Team. *Fahrtbericht SONNE-Fahrt SO-161 Leg 2 and 3 SPOC -Subduktionsprozesse vor Chile- BMBF-Forschungsvorhaben 03G0161A Valparaiso 16.10.2001–Valparaiso 29.11.2001* (Bundesanst. für Geowis. und Rohstoffe, 2002).
65. Aagaard, B., Knepley, M. & Williams, C. A domain decomposition approach to implementing fault slip in finite-element models of quasi-static and dynamic crustal deformation. *J. Geophys. Res.* **118**, 3059–3079 (2013).
66. Christensen, N. Poisson's ratio and crustal seismology. *J. Geophys. Res.* **101**, 3139–3156 (1996).
67. Li, S., Moreno, M., Rosenau, M., Melnick, D. & Oncken, O. Splay fault triggering by great subduction earthquakes inferred from finite element models. *Geophys. Res. Lett.* **41**, 385–391 (2014).
68. King, G. P., Stein, R. & Lin, J. Static stress changes and the triggering of earthquakes. *Bull. Seismol. Soc. Am.* **84**, 935–953 (1994).
69. Lamb, S. Shear stresses on megathrusts: Implications for mountain building behind subduction zones. *J. Geophys. Res.* **111**, B07401 (2006).
70. Gutknecht, B. D. et al. Structure and state of stress of the Chilean subduction zone from terrestrial and satellite-derived gravity and gravity gradient data. *Surv. Geophys.* **35**, 1417–1440 (2014).
71. Tassara, A., Götze, H., Schmidt, S. & Hackney, R. Three-dimensional density model of the Nazca plate and the Andean continental margin. *J. Geophys. Res.* **111**, B09404 (2006).

3.3 Transform zones: Seismic swarms and fault creep

3.3.1 Scaling and spatial complementarity of tectonic earthquake swarms

Published as: L. Passarelli, E. Rivalta, S. Jónsson, M. Hensch, S. Metzger, S. S. Jakobsdóttir, F. Maccaferri, F. Corbi, T. Dahm (2018), Scaling and spatial complementarity of tectonic earthquake swarms. *Earth and Planetary Science Letters*, **482**, 62–70. doi:[10.1016/j.epsl.2017.10.052](https://doi.org/10.1016/j.epsl.2017.10.052)

Supporting information: available online

Scientific application: Comparative study of a series of tectonic earthquake swarms in North Iceland using seismic and geodetic data and modeling to estimate their impact on tectonic strain release.

Methodological advances: Include geodetic observations to a seismological study to gain information on potential aseismic strain release.

Individual Contributions: The study was designed and conducted by LP, ER and SH with inputs from all other authors. My contribution was the analysis, modeling and interpretation of the geodetic data. All authors contributed to and commented on the writing.



Scaling and spatial complementarity of tectonic earthquake swarms



Luigi Passarelli^{a,*}, Eleonora Rivalta^a, Sigurjón Jónsson^b, Martin Hensch^{c,1},
Sabrina Metzger^a, Steinunn S. Jakobsdóttir^{a,b,d}, Francesco Maccaferri^a, Fabio Corbi^{a,e},
Torsten Dahm^a

^a GFZ German Research Centre for Geosciences, Telegrafenberg, 14473 Potsdam, Germany

^b King Abdullah University of Science and Technology (KAUST), Physical Sciences and Engineering Division (PSE), Thuwal, 23955-6900, Saudi Arabia

^c Icelandic Meteorological Office, Bústaðavegi 7-9, 108 Reykjavík, Iceland

^d The Icelandic Centre for Research, Borgartún 30, 105 Reykjavík, Iceland

^e Geosciences Montpellier Laboratory, Montpellier University, CC.60, Place E. Bataillon, 34095 Montpellier cédex 5, France

ARTICLE INFO

Article history:

Received 27 June 2017

Received in revised form 23 October 2017

Accepted 26 October 2017

Available online xxxx

Editor: P. Shearer

Keywords:

Tectonic Earthquake Swarms (TES)
moment, duration and migration velocity
scalings of TES
efficient tectonic strain release by TES
aseismic/seismic source mechanisms for TES
triggering mechanisms of TES
ridge transform fault earthquakes

ABSTRACT

Tectonic earthquake swarms (TES) often coincide with aseismic slip and sometimes precede damaging earthquakes. In spite of recent progress in understanding the significance and properties of TES at plate boundaries, their mechanics and scaling are still largely uncertain. Here we evaluate several TES that occurred during the past 20 years on a transform plate boundary in North Iceland. We show that the swarms complement each other spatially with later swarms discouraged from fault segments activated by earlier swarms, which suggests efficient strain release and aseismic slip. The fault area illuminated by earthquakes during swarms may be more representative of the total moment release than the cumulative moment of the swarm earthquakes. We use these findings and other published results from a variety of tectonic settings to discuss general scaling properties for TES. The results indicate that the importance of TES in releasing tectonic strain at plate boundaries may have been underestimated.

© 2017 Elsevier B.V. All rights reserved.

1. Introduction

Sequences of earthquakes without a clear triggering mainshock, referred to as earthquake swarms, have been observed in volcanic and hydrothermal areas for decades. Tectonic Earthquake Swarms (TES) is another category of swarms linked to active tectonic regions. Recent work has helped identifying some common characteristics of TES regarding their release of seismic moment in time and space (Peng and Gomberg, 2010; Vidale and Shearer, 2006). TES have typical durations of days, weeks or months and the majority of their moment release is usually delayed from the onset of the sequences (Chen and Shearer, 2011; Roland and McGuire, 2009; Passarelli et al., 2015). In addition, TES often migrate at velocities of 1 km/day to 1 km/h, affecting larger volumes of rock than might be suggested by the largest earthquake of the sequence (Vidale and Shearer, 2006; Lohman and McGuire, 2007; Roland and McGuire, 2009). Furthermore, established earthquake scaling

laws, such as the Gutenberg–Richter, Omori–Utsu or Båth laws, often do not work well for swarms. TES usually do not involve high magnitude events and are thought to release only an insignificant fraction of the accumulated tectonic strain at plate boundaries. However, the role TES play in releasing tectonic strain has rarely been quantified and remains poorly understood.

Based on deformation measurements, some TES have been linked to Slow Slip Events (SSEs) (Cheloni et al., 2017; Lohman and McGuire, 2007; Vallée et al., 2013; Villegas-Lanza et al., 2016). In addition, several destructive earthquakes, including the 2009 L'Aquila, the 2011 Tohoku and the 2014 Iquique earthquakes, followed TES linked to or driven by SSEs (Borghini et al., 2016; Kato et al., 2012; Schurr et al., 2014).

TES are puzzling for their apparent lack of “order”: no significant correlation has been found between their moment release and their duration or migration properties (Peng and Gomberg, 2010; Vidale and Shearer, 2006). Peng and Gomberg (2010) noticed that the moment/duration scaling of TES appears to branch off that for SSEs. However, they postulated that TES might commonly hide aseismic moment, and if this moment were to be detected, e.g. by deformation measurements, then the swarms would scale analogously to SSEs. This hypothesis is difficult to test, due to a lack

* Corresponding author.

E-mail address: luigi.passarelli@gfz-potsdam.de (L. Passarelli).

¹ Present address: Regierungspräsidium Freiburg, Landesamt für Geologie, Rohstoffe und Bergbau, Landeserdbendienst, Albertstraße 5, Freiburg, Germany.

of data on TES spanning different moment scales and tectonic settings. Another issue is that seismicity catalogs are generally not long enough to consider recurrence times of TES, which makes it difficult to assess their role in the long-term tectonic strain budget (Passarelli et al., 2015; Cheloni et al., 2017). Usually, historical information on earthquake swarms is not even included in the historical earthquake catalogs (Passarelli et al., 2015).

To study further the properties of TES and define their interaction behavior over longer time scales we have analyzed ~ 20 yr of seismic data containing several well-recorded and energetic TES that occurred on the Húsavík–Flatey Fault (HFF) in North Iceland. We have selected the largest TES sequences and investigated their spatial and temporal organization, before comparing their scaling to that of previously evaluated TES. Finally, we have discussed the possible physical mechanisms behind their behavior.

2. Seismicity along the Húsavík–Flatey Fault and Eyjafjarðaráll Rift

The HFF is a ~ 100 -km-long right-lateral transform fault and a part of the wider Tjörnes Fracture Zone, which links two segments of the Mid-Atlantic Ridge in Iceland, i.e. the Northern Volcanic Zone to the offshore Eyjafjarðaráll Rift (ER) and Kolbeinsey Ridge (Fig. 1a). The HFF has been active since 7–9 Myr and probably has a cumulative displacement of more than 60 km (Rögnvaldsson et al., 1998). At this latitude the divergence rate between the North American and Eurasian plates is ~ 18 mm/yr, of which 6–9 mm/yr is focused on the HFF according to interseismic backslip modeling constrained by GPS (Metzger and Jónsson, 2014; Metzger et al., 2011 and 2013). Three or four magnitude 6.5–7 historical earthquakes occurred on the HFF in the past 300 years with the last large earthquakes in 1872 (Fig. 1a), so the accumulated moment on the fault corresponds approximately to a magnitude 6.8–7.0 earthquake (Metzger and Jónsson, 2014).

Earthquake locations in North Iceland are routinely determined with data collected by the Icelandic National Seismic Network (SIL, Icelandic Meteorological Office), which has a detection threshold ranging from magnitude zero on the eastern HFF to magnitude one offshore (Hensch et al., 2013). The statistical magnitude of completeness, M_c , is slightly higher, or 0.5 on the eastern HFF and 1.5 offshore (Maccafferri et al., 2013). Typical location errors of earthquake hypocenters are of the order of a few kms with a decreasing accuracy moving westward along the HFF (Hensch et al., 2013).

We relocated all 27969 earthquakes in the SIL catalog (Böðvarsson et al., 1996) from 1997 until 15th of July 2015 that occurred within 10 km from the HFF and ER (Fig. S1). We used the relative location method by Slunga et al. (1995) and a local seismic velocity model from local earthquake tomography (LET), replacing the top 5 km of the layered LET model (Riedel et al., 2005 and 2006) with a velocity gradient (Fig. S2). We then selected 23425 events with horizontal errors < 200 m and vertical errors < 2 km (Fig. S3, Jakobsdóttir et al., 2013). The relocated events appear more focused and shallower than the automatic locations, consistent with results from previous relocation studies of North Iceland (Rögnvaldsson et al., 1998; Hensch et al., 2008).

We estimated the cumulative seismic moment release per km on the HFF and ER since 1997 and compared it to the slip deficit expected for the same time interval (Metzger et al., 2013; Metzger and Jónsson, 2014). Based on available focal mechanism solutions for the largest earthquakes we calculated the component of the slip vector parallel to the tectonic motion and the component of the fault area parallel to the plate boundary surface (Bird et al., 2002). We used a shear modulus of 30 GPa and an average seismogenic thickness of 10 km (Bird et al., 2002; Metzger and Jónsson, 2014). From this analysis, we find that the fraction of strain released by the earthquakes varies spatially by two orders

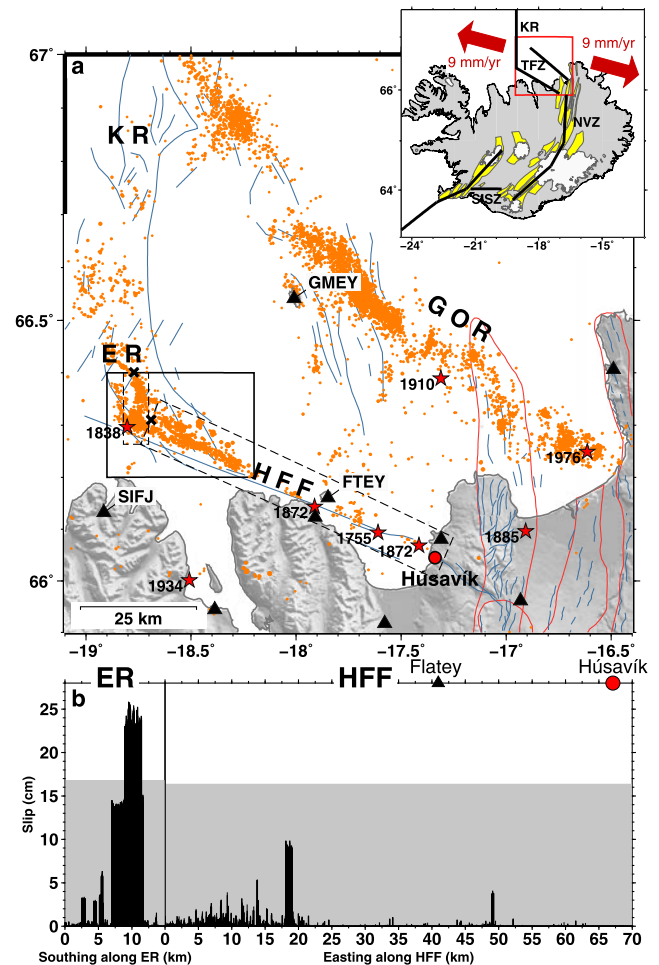


Fig. 1. Earthquake locations in North Iceland and moment release along the Eyjafjarðaráll Rift (ER) and the Húsavík–Flatey Fault (HFF). (a) Earthquakes (orange dots) in the Tjörnes Fracture Zone (TFZ) primarily occur on the HFF and the Grímsey Oblique Rift (GOR). Red stars mark approximate locations of historical $M > 6$ earthquakes, black triangles seismic and GPS (when labeled) stations, blue thin lines mapped faults and fractures, and red thin lines the outlines of fissure swarms and volcanic systems. The black rectangle marks the earthquake swarm study area shown in Fig. 2 while black dashed boxes bound the earthquakes considered in the moment release diagram in (b) with thick black crosses indicating the position of the axes origins. The town of Húsavík is indicated by a red dot. FTEY marks Flatey Island and a GPS station located there and KR stands for Kolbeinsey Ridge. Inset shows the TFZ location in North Iceland and the relative plate velocity. SISZ and NVZ stand for South Iceland Seismic Zone and North Volcanic Zone. (b) Cumulative seismic moment released by earthquakes within the rectangular dashed boxes shown in (a) around the ER and the HFF during 1997–2015 and represented as fault slip. Gray shaded areas are the slip predicted by tectonic loading at plate speed of 9 mm/yr. The slip along ER is projected on the horizontal plane and the dip angles for HFF and ER are 90° and 60° respectively. The rupture areas of earthquakes are calculated using standard scaling (Wells and Coppersmith, 1994) and the fault width is fixed at 10 km for both fault segments. The scalar seismic moment of the earthquakes is derived using the moment-magnitude scaling (Kanamori and Anderson, 1975) and the slip scales with moment assuming a rigidity of 30 GPa. Flatey Island (black triangle) and the town of Húsavík (red circle) are indicated for reference. (For interpretation of the references to color in this figure legend, the reader is referred to the web version of this article.)

of magnitude, with 30% of the strain released on the ER segment, but only 3% on the northwestern-most part of the HFF and 0.1% on the remaining part of the fault (Fig. 1b). Full locking of the eastern HFF is consistent with analysis of the stress shadow casted by the 1975–1984 Krafla rifting episode, which involved a sequence of 19 dike intrusions that compressed the easternmost portion of the fault abating the seismic activity (Rögnvaldsson et al., 1998; Maccafferri et al., 2013; Passarelli et al., 2014).

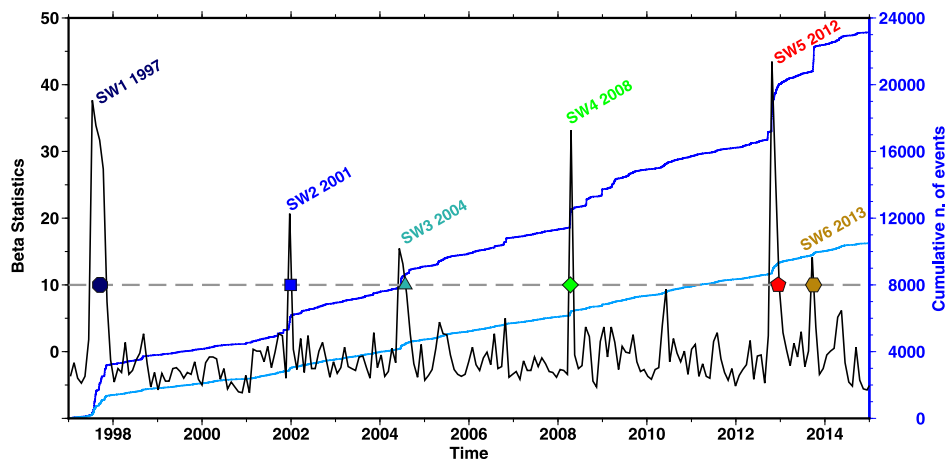


Fig. 2. Earthquake swarm identification results using beta statistics. Black line is the beta statistics calculated in 30 days non-overlapping time windows. The horizontal dashed line shows the $10\times$ standard-deviation threshold used to identify anomalies in the seismicity rate with colored symbols and labels marking selected swarms. The dark and light blue lines show the cumulative number of earthquakes in the original and declustered catalogs, respectively. (For interpretation of the references to color in this figure legend, the reader is referred to the web version of this article.)

3. Swarm activity

Several energetic seismic swarms have been recorded on the HFF since 1997 when a permanent seismic network was installed in North Iceland. We isolated the main swarms as clusters of activity exceeding the average background rate by more than 10 standard deviations (beta statistics introduced by [Matthews and Reasenber, 1988](#)). We used a declustered catalog ([Reasenber, 1985](#)) and non-overlapping time windows of 30 days ([Matthews and Reasenber, 1988](#)). We identified six time periods, robust to the choice of window length and the use of overlapping or non-overlapping time windows, that match the seismic cluster requirement ([Fig. 2](#)). Based on a spatial and temporal analysis of the seismicity around these time periods we isolated six swarms, all in the westernmost portion of the HFF and along the ER ([Fig. 3a](#)). We labeled the swarms SW1 to SW6 ([Figs. 2 and 3a](#), and [Table S1](#) in the supplementary material).

The two most energetic swarms occurred in 1997 and 2012 (SW1 and SW5) with two and four $M > 4.5$ earthquakes, respectively. These swarms consist of several temporally and spatially separated migrating event bursts, eight for SW1 (labeled A to H in [Table S1](#) and [Fig. 3c](#)) and three for SW5 (A to C, [Table S1](#)). Swarm SW3 also shows two spatially separated bursts (i.e. A to B, [Table S1](#)). In total we identified 13 bursts within the six swarms, with durations ranging from 12 h to 2 weeks, cumulatively occupying 25 km long section of the HFF and 15 km of the ER. The total seismic moment released by the selected swarms is 4.5×10^{17} Nm ([Table S1](#)), which is 99% of the entire seismic moment released along the HFF and ER during the 18-year study period ([Table S1](#)).

We further calculated best fitting focal mechanisms for the strongest events within each burst of seismicity, based on P-wave polarity readings and P, SV and SH amplitudes ([Rögnvaldsson and Slunga, 1993](#)). Our focal mechanism solutions show that analyzed events in swarms SW1A–H, SW2, 3A, 4 and 6 are all predominantly strike-slip earthquakes while event mechanisms in swarms SW3B and SW5A–C, which occurred on the ER, range from oblique strike-slip to N–S striking normal faulting ([Fig. 3a](#) and [Table S2](#)). The focal mechanisms are similar within each burst but differ slightly between consequent bursts, suggesting that the bursts occurred on distinctive approximately planar fault segments with somewhat different strikes.

The swarms cluster tightly on multiple distinct fault strands and appear spatially complementary, both in map view and

when projected on a vertical plane along the HFF surface trace ([Fig. 3a–b](#)). Later swarms have filled in the gaps left behind by earlier swarms and together over the 20-year period the swarms have illuminated most of the southern ER and northwestern HFF. This activity pattern suggests efficient strain release by the swarms (strain release of magnitude similar to, or larger than, that accumulated over the 20 yr time scale of the seismic catalog), as the subsequent seismicity appears discouraged from areas where swarms have already occurred ([Wei et al., 2013](#)). When zooming into SW1 ([Fig. 3c–d](#)), we find that the spatial complementarity also applies for the bursts of each swarm, suggesting scale invariance. The seismicity, after occupying a fault segment in a burst, jumps to another segment (not necessarily an adjacent segment) that had not ruptured before, and then to another one until an entire larger segment is activated. The same pattern is observed for SW5. Moreover, SW5 included a small burst (i.e. SW5C) immediately east of SW1 (easternmost red cluster in [Fig. 3a–b](#)), while the fault segments in-between, activated 15 yr earlier by SW1, remained silent.

We quantify the deviation of the sequences from mainshock–aftershock sequence scaling by calculating the skewness of the moment release in time ([Roland and McGuire, 2009](#); [Chen and Shearer, 2011](#)). In contrast to mainshock–aftershocks sequences, for which the moment distribution in time is highly left-skewed (most moment is released by a mainshock at the onset of the sequence resulting in skewness $\gg 8$, [Roland and McGuire, 2009](#)), during earthquake swarms the seismic moment release is often delayed from the swarm onset, resulting in a small or negative skewness. For our six swarms (SW1–6) we find $-4 < \text{skewness} < 4$ ([Fig. S4](#)), consistent with other previously published swarms ([Roland and McGuire, 2009](#); [Chen and Shearer, 2011](#)). When considering the bursts individually, three bursts show higher skewness up to 8.6 (SW1A, SW1F and SW5B). In spite of these relatively high skewness values, these bursts still deviate from mainshock–aftershock sequences since the dominant moment release was linked to at least two large events of comparable magnitude. For example, SW5B involved two $M > 5$ within 12 h from its beginning (supplementary [Figs. S5 and S6](#)).

We also checked the magnitude–frequency scaling of the individual swarms, of the entire catalog and of the catalog with swarms removed ([Fig. S7](#) in the supplement). The Gutenberg–Richter relationship is a good model in all cases, with a power law fitting well the frequency–magnitude distribution. The individual swarms have b-values in the range 0.8–1.6, somewhat increasing to the West, while the overall seismicity, both including and ex-

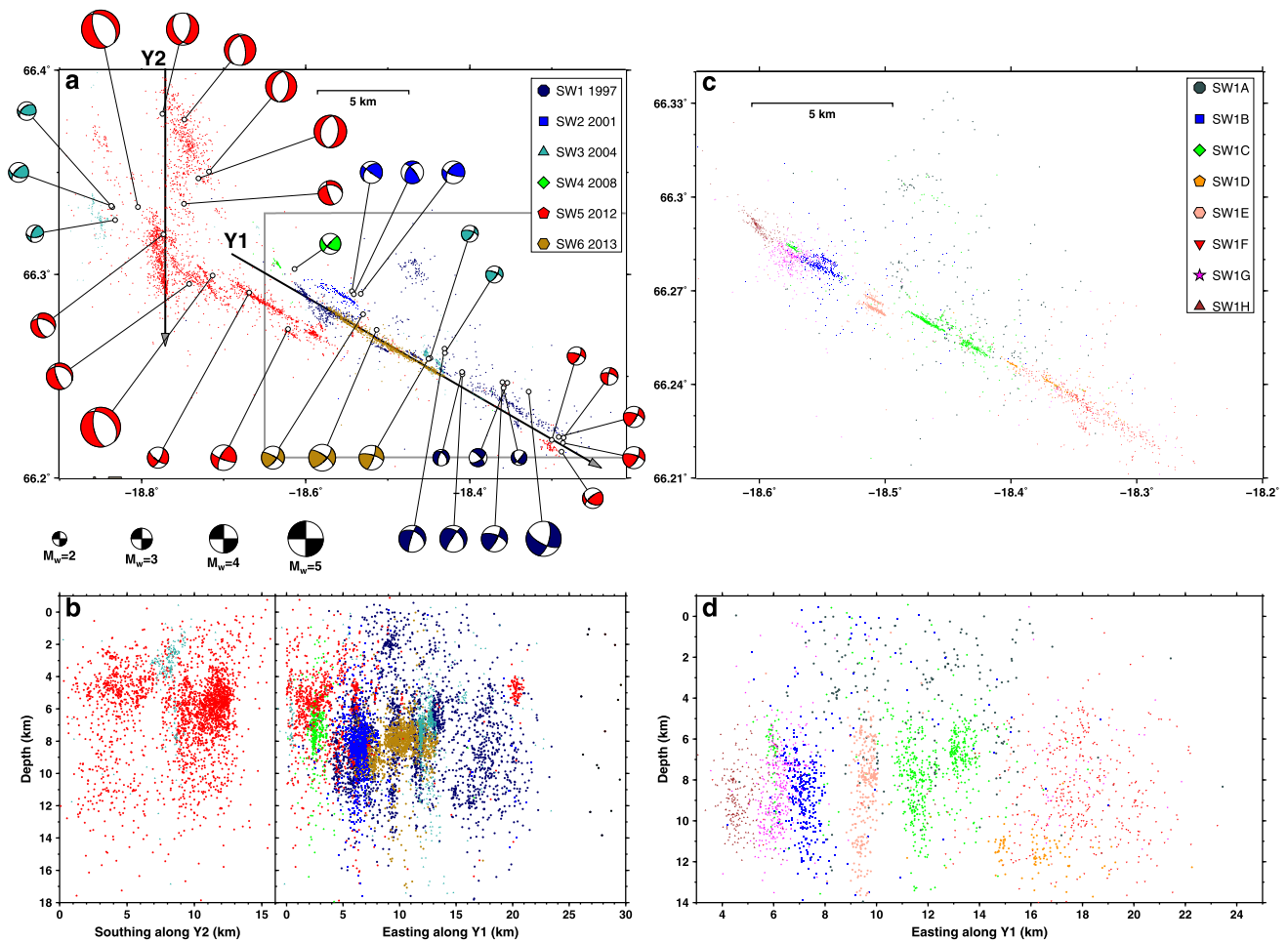


Fig. 3. Spatial complementarity of earthquake swarms on the HFF and ER. Swarm event locations 1997–2015 in (a) map view and (b) in depth cross-sections along axes Y2 and Y1. Events and focal mechanisms are sized and color-coded according to size and the swarm they belong to, respectively. The two largest earthquake swarms (SW1 and SW5) consisted of several individual bursts (Table S1). (c)–(d) same as panels (a)–(b), except for the 1997 earthquake swarm (SW1) and its eight separate bursts. The black dashed box in (a) outlines the area covered in (c). (For interpretation of the colors in this figure, the reader is referred to the web version of this article.)

cluding the TES, has b-value very close to 1 (see also [Maccaferri et al., 2013](#)).

We next look into the earthquake migration pattern within each burst. In some cases, the first earthquake locations are scattered before focusing on one fault strand of the HFF (see e.g. SW1A). In other cases, the earthquakes remain small at first and concentrate near the center of an activated fault segment and then migrate concentrically outwards with increasing average magnitude (Fig. 4, see also Figs. S5 and S6 in the supplement for all the swarms). Most of the migrations accelerate at first and then terminate abruptly (Fig. 4a–c, Fig. S5); the activity then jumps to another fault strand. While all the bursts show a sharp and unambiguous migration onset (supplementary Fig. S5 and S6 and Table S1), it is more difficult to determine the end of each migration: we take it as the time when the earthquake front reaches the maximum along-strike distance (Table S1). We then calculate the average migration velocity for the bursts as the migration distance over its duration (Table S1). Such average velocities, however, are not fully representative of the migration process, as additional details such as differences between along-rake and along-strike migrations and existence of multiple phases with different velocities are visible (Fig. 4 and S5–S6). Therefore, we also estimate the maximum and minimum migration velocity for each burst (details are in the supplementary Table S3).

The average migration velocities range from 1 km/day to 1 km/h (Table S3 in the supplement), similar to that of previously identified migrating TES ([Roland and McGuire, 2009](#)). The migration appears faster in the rake direction, i.e. faster horizontally for strike-slip segments and faster vertically for normal-faulting bursts (Fig. 4, S5, and S6, Table S3).

Accelerated or even constant-speed hypocenter migrations that then end abruptly are not consistent with diffusive processes, which advance as a square root of time and fade off slowly. Rather, the migration pattern suggests that the bursts mark a rupture process comprising a slow nucleation phase followed by a break-out phase ([Ohnaka and Shen, 1999](#); [Bouchon et al., 2013](#)). The earthquakes may be generated by brittle asperities punctuating velocity-strengthening or heterogeneously stressed fault surfaces, as previously suggested ([Kato et al., 2012](#); [Lay et al., 2012](#); [Vallée et al., 2013](#)). Under this hypothesis, we use the estimated duration, the average rupture velocity and the cumulative seismic moment of each burst to investigate the swarm scaling properties.

When comparing these dynamic parameters to the scaling previously reported for slow slip events and TES ([Gao et al., 2012](#); [Ide et al., 2007](#); [Peng and Gomberg, 2010](#)) we find that our data confirm and extend the scaling proposed by [Peng and Gomberg \(2010\)](#), according to which TES duration-moment scaling branches off the SSE scaling, with TES duration independent of seismic moment (Fig. 5a). In contrast to SSEs, whose propagation velocity

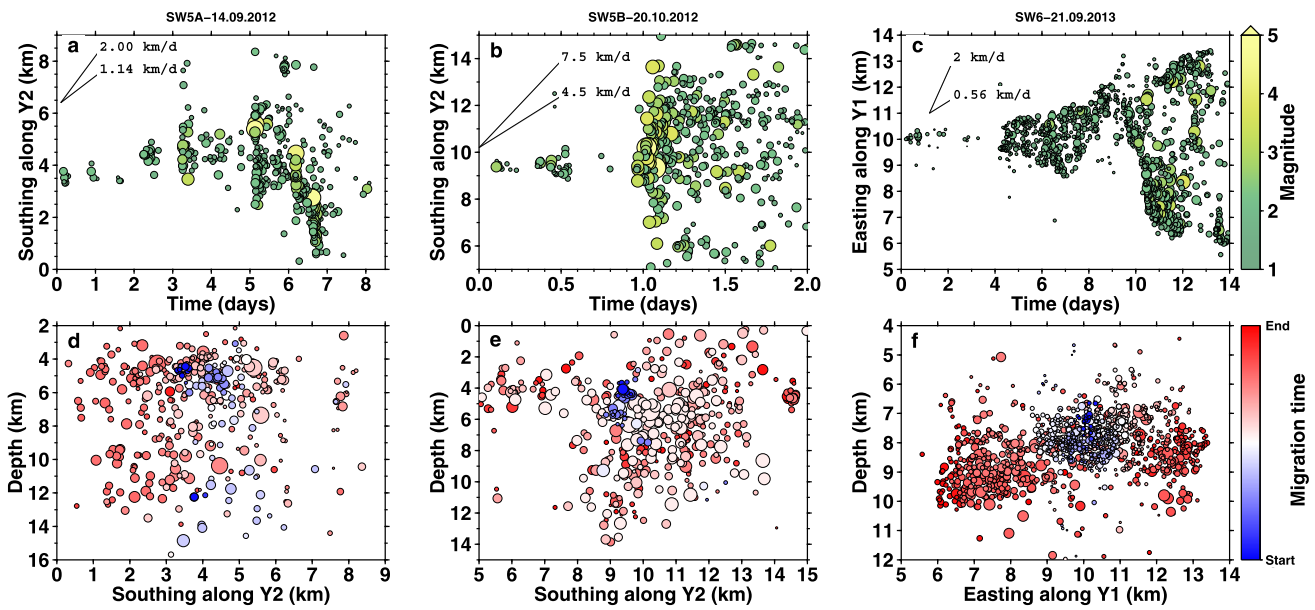


Fig. 4. Migration of selected earthquake swarms. The upper panels (a–c) show the event migration along axes Y1 or Y2 (see Fig. 2) versus time, color-coded according to event magnitude, while bottom panels (d–f) show the migration in depth cross-section along Y1 or Y2, color-coded according to time. The maximum and minimum migration velocity is indicated in the upper panels (see also Table S3). (For interpretation of the colors in this figure, the reader is referred to the web version of this article.)

scales as $M_0^{-1/2}$, the migration velocity of TES appears correlated with the seismic moment, with an approximate scaling exponent of $\sim 1/3$ (Fig. 5b). The uncertainty of the estimated scaling exponent is large but it could be reduced in future investigations with larger datasets.

TES activate larger areas compared to what might be expected from their cumulative seismic moment. This results in a static effective stress drop that is one or two orders of magnitude lower than for tectonic earthquakes (Vidale and Shearer, 2006). We calculate the effective stress drop, $\Delta\sigma$, for our TES using the rela-

tion: $M_0 = \pi \Delta\sigma W^2 L / 2$, where M_0 is the static seismic moment, and W and L are fault width and length, respectively (Kanamori and Anderson, 1975). We estimated W and L as the width and length of the area within which 80% of the swarm hypocenters are located (Table S1 and Fig. S6). The estimated $\Delta\sigma$ spans the range between 0.001 and 1 MPa (Fig. 6), lower than 1–10 MPa values for regular earthquakes (Kanamori and Anderson, 1975; Gao et al., 2012). Low effective stress drop during TES might indicate aseismic deformation behind TESs in this study (e.g. Roland and McGuire, 2009; Fischer and Hainzl, 2017).

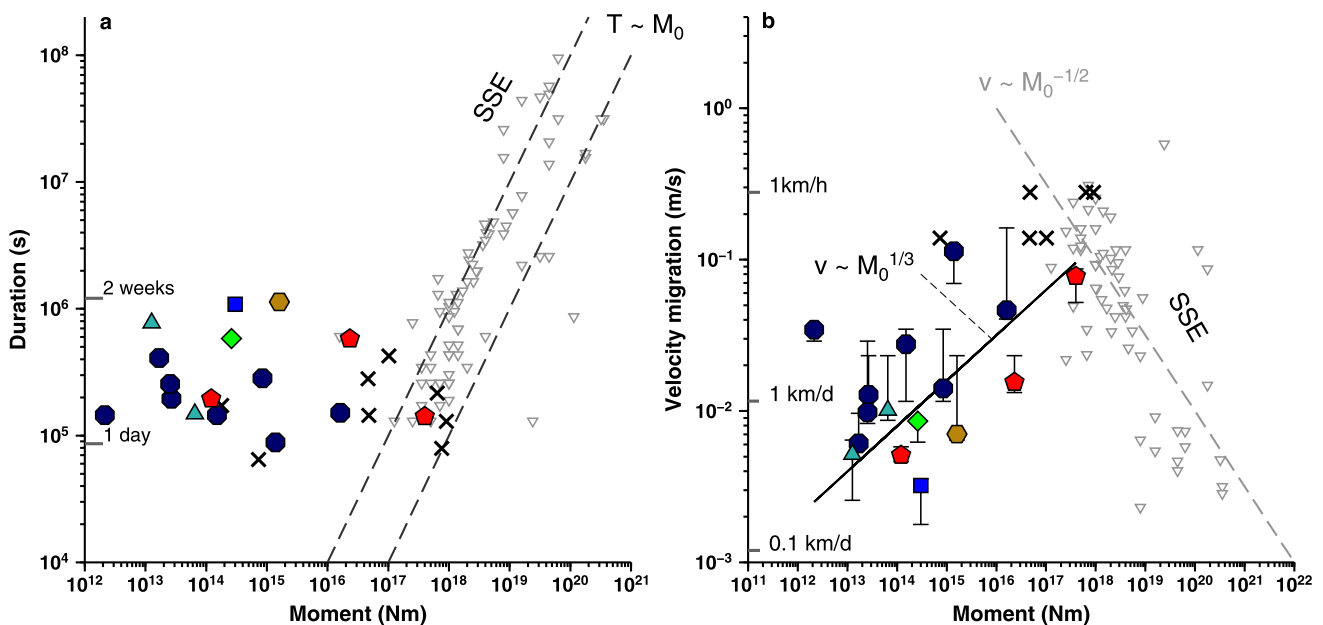


Fig. 5. Scaling of tectonic earthquake swarms. (a) Event duration versus moment and (b) migration velocity versus moment for the swarms in this study (color-coded as in Fig. 2) and swarms in Peng and Gomberg (2010) (black crosses) in comparison to SSEs (gray inverted triangles) according to Gao et al. (2012). In panel (b) the black straight line is the scaling for swarm velocity and seismic moment (closed symbols). (For interpretation of the colors in this figure, the reader is referred to the web version of this article.)

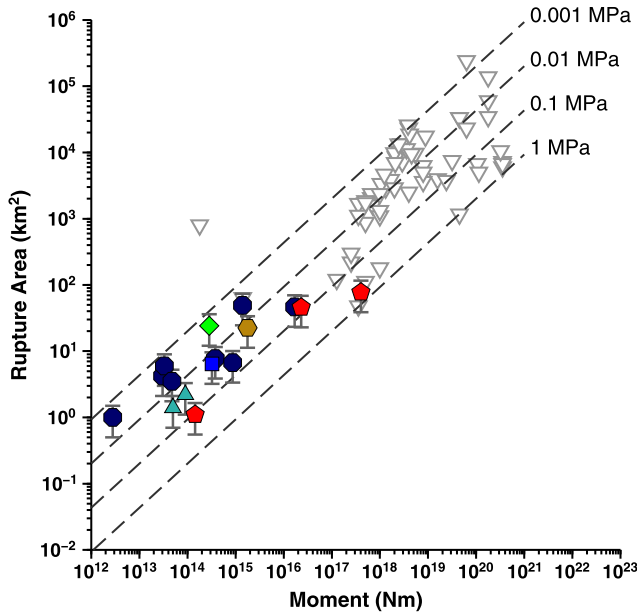


Fig. 6. Static stress drop of seismic swarms along the HFF and ER. The rupture area versus the seismic moment for the swarms in this study (color-coded as in Fig. 2). Error bars are 50% relative error on the area estimations and the rupture areas (see Table S3 and Fig. S6). Dashed lines are constant static stress drop calculated for a rectangular crack with $L = 2W$ (Kanamori and Anderson, 1975). Inverted triangles show results for SSEs from Gao et al. (2012). (For interpretation of the colors in this figure, the reader is referred to the web version of this article.)

4. Statistics of the swarm earthquakes and aseismic strain release

In order to better understand the scaling of the swarm earthquakes, their triggering mechanism and their interaction with the local tectonics, we performed additional statistical analysis on the seismicity catalog. Using the Epidemic Type Aftershock Sequence (ETAS) model (Ogata, 1988), we quantified how foreshock and aftershock productivity varies along the HFF and the ER and compared the results with previous analyses of continental and oceanic seismicity. ETAS models were designed to reproduce mainshock-aftershocks sequences so that abnormal fitted parameters can highlight any anomalies with respect to such reference behavior.

According to ETAS models, any earthquake generates offsprings at a rate according to a combination of a magnitude-dependent productivity law:

$$K(M) = k10^{\alpha(M-M_c)}, \quad (1)$$

(where K is the number of directly triggered offspring, k and α are region-dependent parameters) and the Omori–Utsu law for seismicity-rate decay after an earthquake (Ogata, 1988). The average number of aftershocks per mainshock (directly and indirectly triggered) is then given by the equation:

$$N(M) = (k/(1-n))10^{\alpha(M-M_c)}, \quad (2)$$

where b is the slope of the Gutenberg–Richter relation and $n = kb/(b - \alpha)$ is the so-called branching ratio, representing the fraction of the earthquake population that was triggered by another earthquake (Helmstetter and Sornette, 2002). Earthquake productivity is directly related to the degree of crustal “brittleness”, linked to seismogenic thickness and thus high for continental settings and low for oceanic environments, due to more important viscoelastic dissipation in the latter case. In addition, earthquake productivity is modulated by permanent or transient aseismic stressing processes affecting the seismogenic crust (Helmstetter and Sornette,

2002); this includes slow earthquakes, more important on ridge-transform faults (RTF) than in California (McGuire et al., 2005).

For this analysis we considered the entire catalog of earthquakes close to the ER and HFF with magnitudes above $M_c = 1.5$, rather than restricting the analysis to only the swarm seismicity. Following McGuire et al. (2005), we identified as mainshocks all $M_{main} > 3.2$ events that were not preceded within 2 weeks and 15 km by another $M > M_{main} - 1.2$ earthquake. The 15 km limit represents three times the rupture length of the largest events in our catalog while the magnitude threshold was chosen to avoid multiple close-in-time mainshocks, which would bias the fore- and aftershock counting. Indeed, the procedure excludes all the largest events in SW5, i.e. the four $M > 4.5$ earthquakes that occurred within 12 h, and many other earthquakes that occurred during ‘swarmy’ time periods. The identified mainshocks occurred mainly on the western portion of the HFF and along the ER, while only one mainshock event was recognized on the eastern HFF (Table S4).

The inferred parameters $\alpha \sim 0.8$ and $n \sim 0.8$ show that the HFF and ER have aftershock productivity more similar to California than to RTFs (Fig. 7a). The high aftershock productivity might be related to the thicker seismogenic crust (10–15 km, this study and Rögnvaldsson et al., 1998) of the HFF and ER ridge-transform segment when compared with other RTFs where the seismogenic thickness is in the order of 7 km or thinner (e.g. Engeln et al., 1986; Boettcher and Jordan, 2004).

In addition, we quantified the ratio of foreshocks to aftershocks, which has been used to estimate the relative importance of aseismic forcing and earthquake–earthquake triggering (McGuire et al., 2005). We find that the HFF and ER, unlike RTFs, are almost as productive in terms of aftershocks as southern California faults (reaffirming the results in Fig. 7a), but simultaneously they are as productive as RTFs in terms of foreshocks, i.e. they produce a half order of magnitude more foreshocks than what has been observed for the southern California seismicity and predicted by the ETAS model (Fig. 7b, see also McGuire et al., 2005). This supports the hypothesis that transient aseismic forcing has triggered the seismicity along the western HFF and ER. Future studies using more data should help reducing the statistical uncertainties of the parameter estimations and help separating the different effects that control earthquake productivity in Northern Iceland.

5. Constraining the aseismic strain release

Based on the analyses performed above, we conclude that TES on the HFF and ER were likely associated with significant transient aseismic slip. Now we seek to estimate the fraction of the aseismic strain release in order to further constrain the scaling relationships of our TES.

First, we check whether part of the aseismic moment release can be measured geodetically by the sparse GPS network operating in North Iceland (Fig. 1a). The closest continuously operating GPS stations (SIFJ, GMEY and FTEY, installed in 2006/7) are not of much help as they are located >15 km away from the swarms (Fig. 1a) and can therefore at best only give an upper limit of the moment potentially released by the swarms. The baselines SIFJ–GMEY and SIFJ–FTEY (Fig. S8) show no significant deformation signal associated with the TES, at an average confidence level of 2–3 mm for the horizontal and 6–9 mm for the vertical components. We checked with rectangular dislocation models in an elastic half-space (Okada, 1985) what could be the maximum moment release on the fault planes activated in the 2012 sequences without producing a significant signal in the GPS time series. The model geometry was constrained manually to fit the location and spatial extent of the earthquake swarms SW5A and SW5B. The segments were buried at 1 km depth and different slip rake angles were

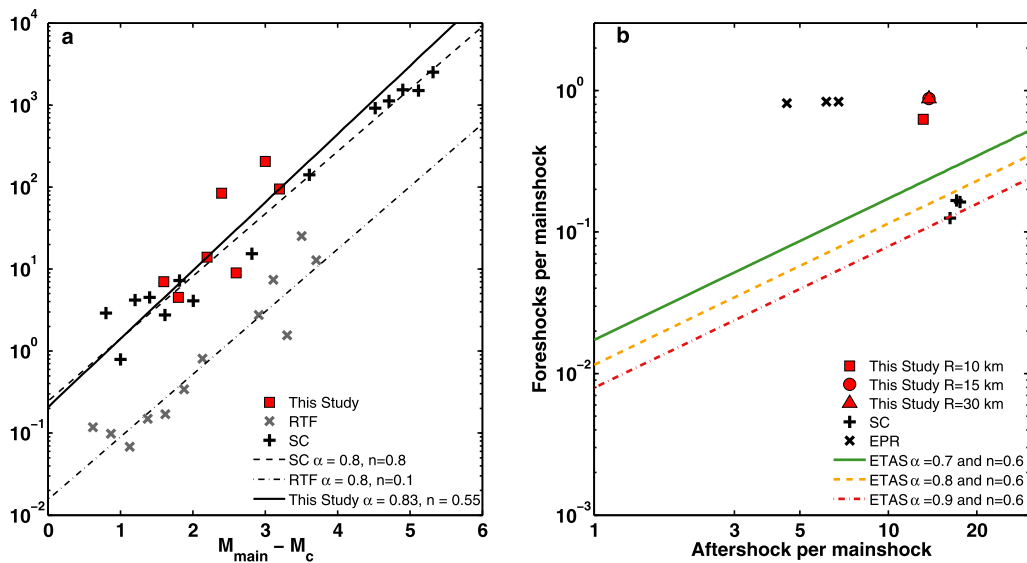


Fig. 7. Scaling of aftershock and foreshock productivity along the HFF and ER. (a) Number of aftershocks per mainshock versus the mainshock magnitude M_{main} minus the magnitude of completeness M_c . Red squares are aftershock counts along the HFF and ER above $M_c = 1.5$ within 14 days and 15 km of all $M_{main} > 3.2$ mainshocks in comparison to results from southern California (SC) and ridge-transform faults (RTFs) (Boettcher and Jordan, 2004; McGuire et al., 2005). Best fits for the slope α and the intercept $k/(n-1)$ of $\log_{10} N(M)$ from Eq. (2) yield $\alpha = 0.83, n = 0.55$ ($\alpha = 0.05$ – 1.6 at 95% confidence interval) for our data alone and $\alpha = 0.65$ – $0.85, n = 0.55$ – 0.80 (95% confidence interval) for our data together with those from southern California. (b) Number of foreshocks versus number of aftershocks per mainshock, counted during the 1 h-time window before and 5 h after each mainshocks, in comparison to results from SC and East Pacific Rise (EPR). Straight lines are ETAS predictions as derived by McGuire et al. (2005) (eq. (1)). (For interpretation of the references to color in this figure legend, the reader is referred to the web version of this article.)

tested. We found that a moment larger than about $5 \cdot 10^{17}$ Nm for SW5A and SW5B should have been seen in the GPS time series, which is larger than the seismic moment of $2.3 \cdot 10^{16}$ Nm and $4 \cdot 10^{17}$ Nm released in the swarms (supplementary Table S1). Therefore, based on the GPS data we cannot exclude the possibility that some aseismic slip took place, although most of the moment in SW5B appears to have been seismically released.

We estimated a lower limit for the stress drop of the 1997 swarm (SW1) by considering its interaction with SW5. The SW1 fault segments remained silent following the two $M > 5$ earthquakes in SW5B while a small fault patch adjacent and to the East of SW1 became active (the SW5C burst). The Coulomb Failure Stress (ΔCFS) induced on the HFF by the largest $M > 5$ event of SW5B is positive on the HFF (Jónsson et al., 2013). This suggests that SW5C may have been statically triggered, and that the stress drop of SW1 must have been larger than the Coulomb Failure Stress change (ΔCFS) caused by SW5B. The estimated ΔCFS is of the order of 0.1–0.02 MPa when it is projected onto the HFF in the 1997 SW1 swarm area (see Fig. 2 in Jónsson et al., 2013). We calculated the corresponding moment with the formula $M_o = \Delta\sigma dLW$ assuming that the fault is strained over a distance $d = 5$ km (half of fault width, Madariaga, 1979), and $L = 20$ km and $W = 10$ km are respectively the length and width of the fault segment activated in the SW1 swarm. The resulting moment $M_o > 0.2$ – $1.0 \cdot 10^{17}$ Nm ranges between the cumulative seismic moment released by SW1 and five times as much (Table S1), which suggests that SW1 may have released additional moment aseismically. Considering that the ΔCFS estimate refers only to the largest earthquake, rather than to the entire sequence, and that we neglected 15 years tectonic loading onto the SW1 segment in this calculation, we reckon this as a conservative estimate.

Finally, we estimate how much aseismic slip could potentially be hidden within the HFF and ER bursts while remaining within the limits of 20 years of tectonic strain accumulation. The total tectonic moment accumulated along HFF and ER during the time span of the seismicity catalog is $\sim 2.9 \cdot 10^{18}$ Nm, using $\mu = 30$ GPa and the same fault geometry as in Fig. 1b. Assuming that

the area illuminated by the earthquakes (Fig. 6 and supplementary Table S1 and Fig. S6) is representative of the total moment released by the bursts, we estimate such moment based on the standard relationship $M_w = 4.07 + 0.98 \cdot \log(RA)$ linking rupture area (RA) in km^2 with moment magnitude (M_w) (Wells and Coppersmith, 1994) in turn converted into seismic moment (Kanamori and Anderson, 1975). This procedure results in an estimated hidden aseismic moment between 2 and 700 times larger than the relative cumulative seismic moment, and amounts, if all swarms are taken together, to $2 \cdot 10^{18}$ Nm. This is close to the total moment accumulated during 20 years of tectonic loading. Thus, under the above assumptions, the TES and the associated aseismic slip have efficiently released the accumulated tectonic moment.

6. Discussion and conclusions

The TES have progressively activated most of the northwestern HFF and the ER during the almost 20 year of recorded seismicity showing a clear spatial complementarity. This raises several questions: Is such complementarity unique? What are the potential underlying processes leading to this behavior? What are the implications for the long-term strain release on this section of the plate boundary in North Iceland?

Some evidence for TES occupying fault patches adjacent to previous swarms or segments ruptured by large earthquakes exist (e.g. Holtkamp and Brudzinski, 2014), but to our knowledge, the spatial complementarity of the North Iceland swarms, observed on a scale of tens of km and in only 20 years, has never been described for any other regions. Similar patterns of spatial complementarity are instead found at a much longer and larger spatial scales for plate-boundary earthquakes, with major earthquakes sometimes occurring in seismic gaps left by earlier events (Schurr et al., 2014).

Given the small cumulative seismic moment released by some of our TES, the observation that they discourage other earthquakes from occurring on the same fault patch while encouraging new TES on adjacent patches, is difficult to explain without including an additional aseismic moment release. The total estimated aseismic

moment released by the TES is equal to the tectonic load accumulated in 20 years and the size of the fault patches illuminated by earthquakes in each swarm may be a proxy for such total seismic/aseismic moment release during the TES. Our analysis suggests that TES may be a manifestation of significant strain release, provoking both short and long-term stress interaction.

Aseismic stress release is consistent with both low stress drop and slow rupture velocity and linked to low fault stiffness (Segall et al., 2010) associated to velocity-strengthening rock rheology and/or low normal stress (in turn may be due to a number of reasons, including high pore pressure, geometry, stress interaction). Several of these factors likely contribute to the TES activity on the HFF. In the region around HFF deep fluid circulation is abundant, as demonstrated by widespread release of hydrothermal fluids on the ocean floor (Hensch et al., 2008) and reflected in observed anomalies of seismic velocities v_p and v_s (Riedel et al., 2005). In such conditions, the frictional strength of faults and in turn the expected level of strain release is strongly controlled by the pore pressure.

Zencher et al. (2006) demonstrated with a numerical model that fluids at near-lithostatic pore pressure might propagate upward to mid-crustal levels if a deep fluid reservoir below an impervious layer at the brittle-ductile transition becomes abruptly connected with the overlying permeable crustal layers. The model explains several observations from the South Iceland Seismic Zone, the other major transform zone in Iceland, and it might plausibly apply to the HFF. Young hot rock cooling below the brittle ductile transition is expected to release fluids that may pool at the rheological discontinuity. An intrusion of high pore pressure fluids would lower the threshold stress for rupture and eventually the strongest asperities pinning the fault would fail. Laboratory studies and numerical models show that when an unstable system fails at a low normal stress or high pore pressure, the conditions for slow slip are approached (Leeman et al., 2016). The rupture velocity may be limited by local pore-pressure drop due to inhomogeneous stress on the fault segments and by poroelastic coupling and dilatancy hardening (Segall and Rice, 1995; Segall et al., 2010), with the small-scale asperities failing as regular earthquakes (Kato et al., 2012; Gao et al., 2012). In such conditions, the ‘seismic cycle’ is short, as high stress levels are never reached on the fault.

Stress interactions with the strong Krafla rifting episode on the neighboring ridge segment, which occurred in the NVZ in 1975–1984, caused strong compression on the southeastern HFF (Rögnvaldsson et al., 1998; Maccafferri et al., 2013) while decompressing the northwestern-most part of the fault. Normal stress changes are not easily compensated by tectonic movements in a transform fault setting and may thus last for long time. Static decompression leads to increase of permeability, fluid release and circulation, so that the swarm behavior of the northwestern HFF, contrasting the locked and quiet southeastern part of the fault, might have been stimulated by static stress interaction with the NVZ.

Considering geometry and stress interaction may explain additional observations. The HFF is composed of sub-parallel fault strands that are more or less favorably oriented according to the tectonic stressing. The apparent jumps of swarms and bursts between segments may be a consequence of this structural setting.

Earthquake swarms have been observed to act as barriers to large earthquake ruptures on plate boundaries, leading to efficient rupture arrests (Holtkamp and Brudzinski, 2014). Whether this dynamics may apply to the HFF, or whether on the contrary any future large rupture may extend to the entire fault length would be critical for local seismic hazard assessments but remains unclear and challenging to determine. However, this study adds to increasing evidence that TES play a previously unrecognized role in accommodating long-term plate motion on plate boundaries. They

embody as a specific category of slow strain release that may act efficiently on shorter time scales. Evaluating them only based on the seismic moment they release seismically may be misleading.

Acknowledgements

This work received funding from the European Union through ERC Grant N. 240583. We thank Sigrún Hreinsdóttir (GNS Science) for providing the GPS time-series. The stimulating comments of two anonymous reviewers helped to improve the manuscript. Data from one seismometer was kindly provided by R.S. White from a project funded by the UK Natural Environment Research Council (NERC) SEIS-UK (loan 968). Data retrieved in this study are available in the supplementary information. The SIL earthquake catalog is available at www.vedur.is. All figures except for Fig. 7 are drawn using Generic Mapping Tools software (Wessel and Smith, 1998).

Appendix A. Supplementary material

Supplementary material related to this article can be found online at <https://doi.org/10.1016/j.epsl.2017.10.052>.

References

- Bird, P., Kagan, Y.Y., Jackson, D.D., 2002. Plate tectonics and earthquake potential of spreading ridges and oceanic transform faults. In: Stein, eds S., Freymueller, J.T. (Eds.), *Plate Boundary Zones*. American Geophysical Union, Washington, DC.
- Böðvarsson, R., Rögnvaldsson, S.T., Jakobsdóttir, S.S., Slunga, R., Stefánsson, R., 1996. The SIL data acquisition and monitoring system. *Seismol. Res. Lett.* 67, 35–46. <https://doi.org/10.1785/gssrl.67.5.35>.
- Boettcher, M.S., Jordan, T.H., 2004. Earthquake scaling relations for mid-ocean ridge transform faults. *J. Geophys. Res.* 109 (B12). <https://doi.org/10.1029/2004JB003110>.
- Borghi, A., Aoudia, A., Javed, F., Barzaghi, R., 2016. Precursory slow-slip loaded the 2009 L'Aquila earthquake sequence. *Geophys. J. Int.* 205, 776–784. <https://doi.org/10.1093/gji/ggw046>.
- Bouchon, M., Durand, V., Marsan, D., Karabulut, H., Schmittbuhl, J., 2013. The long precursory phase of most large interplate earthquakes. *Nat. Geosci.* 6 (4), 299–302. <https://doi.org/10.1038/ngeo1770>.
- Cheloni, D., D'Agostino, N., Selvaggi, G., Avallone, A., Fornaro, G., Giuliani, R., Reale, D., Sansosti, E., Tizzani, P., 2017. Aseismic transient during the 2010–2014 seismic swarm: evidence for longer recurrence of $M \geq 6.5$ earthquakes in the Pollino gap (Southern Italy)? *Sci. Rep.* 7 (1), e576. <https://doi.org/10.1038/s41598-017-00649-z>.
- Chen, X., Shearer, A., 2011. Comprehensive analysis of earthquake source spectra and swarms in the Salton Trough, California. *J. Geophys. Res.* 116. <https://doi.org/10.1029/2011JB008263>.
- Engeln, J.F., Wiens, D.A., Stein, S., 1986. Mechanisms and depths of Atlantic transform earthquakes. *J. Geophys. Res.* 91 (B1), 548–577. <https://doi.org/10.1029/JB091iB01p00548>.
- Fischer, T., Hainzl, S., 2017. Effective stress drop of earthquake clusters. *Bull. Seismol. Soc. Am.* 107 (5), 2247–2257. <https://doi.org/10.1785/0120170035>.
- Gao, H., Schmidt, D.A., Weldon II, R.J., 2012. Scaling relationships of source parameters for slow slip events. *Bull. Seismol. Soc. Am.* 102, 352–360. <https://doi.org/10.1785/0120110096>.
- Helmstetter, A., Sornette, D., 2002. Subcritical and supercritical regimes in epidemic models of earthquake aftershocks. *J. Geophys. Res.* 107 (B10). <https://doi.org/10.1029/2001JB001580>.
- Hensch, M., Guðmundsson, G.B., SIL Monitoring Group, 2013. Offshore seismicity with large azimuthal gap: challenges for the SIL network. In: Jóhannesdóttir, G., et al. (Eds.), *Proceedings of a Workshop on Earthquakes in North Iceland*. Húsavík, 6–8 June, 2013. Húsavík Academic Centre. Available at http://www.hac.is/wp-content/uploads/2014/04/lokaskjal_pretnun_net%C3%BAtg%C3%A1fa.pdf.
- Hensch, M., Riedel, C., Reinhardt, J., Dahm, T., The NICE-People, 2008. Hypocenter migration of fluid-induced earthquake swarms in the Tjörnes Fracture Zone (North Iceland). *Tectonophysics* 447 (1), 80–94. <https://doi.org/10.1016/j.tecto.2006.07.015>.
- Holtkamp, S.G., Brudzinski, M.R., 2014. Megathrust earthquake swarms indicate frictional changes which delimit large earthquake ruptures. *Earth Planet. Sci. Lett.* 390, 234–243. <https://doi.org/10.1016/j.epsl.2013.10.033>.
- Ide, S., Beroza, G.C., Shelly, D.R., Uchide, T., 2007. A scaling law for slow earthquakes. *Nature* 447, 76–79. <https://doi.org/10.1038/nature05780>.
- Jakobsdóttir, S., Guðmundsson, G.B., Hensch, M., Rivalta, E., 2013. Towards improved earthquake locations in the Tjörnes Fracture Zone. In: Jóhannesdóttir,

- G., et al. (Eds.), Proceedings of a Workshop on Earthquakes in North Iceland. Húsavík, 6–8 June, 2013. Húsavík Academic Centre. Available at http://www.hac.is/wp-content/uploads/2014/04/lokaskjal_prentun_net%C3%BAtg%C3%A1fa.pdf.
- Jónsson, S., Metzger, S., Hreinsdóttir, S., Rivalta, E., Passarelli, L., Maccaferri, F., 2013. The 2012–2013 earthquake sequences in North Iceland: geodetic constraints and associated stress changes. In: Jóhannesdóttir, G., et al. (Eds.), Proceedings of a Workshop on Earthquakes in North Iceland. Húsavík, 6–8 June, 2013. Húsavík Academic Centre. Available at http://www.hac.is/wp-content/uploads/2014/04/lokaskjal_prentun_net%C3%BAtg%C3%A1fa.pdf.
- Kanamori, H., Anderson, D.L., 1975. Theoretical basis of some empirical relations in seismology. *Bull. Seismol. Soc. Am.* 65 (5), 1073–1095.
- Kato, A., Obara, K., Igarashi, T., Tsuruoka, H., Nakagawa, S., Hirata, N., 2012. Propagation of slow slip leading up to the 2011 Mw 9.0 Tohoku–Oki earthquake. *Science* 335 (6069), 705–708. <https://doi.org/10.1126/science.1215141>.
- Lay, T., Kanamori, H., Ammon, C.J., Koper, K.D., Hutko, A.R., Ye, L., Yue, H., Rushing, T.M., 2012. Depth-varying rupture properties of subduction zone megathrust faults. *J. Geophys. Res.* 117, B04311. <https://doi.org/10.1029/2011JB009133>.
- Leeman, J., Saffer, D.M., Scuderi, M., Marone, C., 2016. Laboratory observations of slow earthquakes and the spectrum of tectonic fault slip modes. *Nat. Commun.* 7. <https://doi.org/10.1038/ncomms11104>.
- Lohman, R.B., McGuire, J.J., 2007. Earthquake swarms driven by aseismic creep in the Salton Trough, California. *J. Geophys. Res.* 112. <https://doi.org/10.1029/2006JB004596>.
- Maccaferri, F., Rivalta, E., Passarelli, L., Jónsson, S., 2013. The stress shadow induced by the 1975–1984 Krafla rifting episode. *J. Geophys. Res.* 118, 1109–1121. <https://doi.org/10.1002/jgrb.50134>.
- Madariaga, R., 1979. On the relation between seismic moment and stress drop in the presence of stress and strength heterogeneity. *J. Geophys. Res.* 84 (B5), 2243–2250.
- Matthews, M.V., Reasenber, P.A., 1988. Statistical methods for investigating quiescence and other temporal seismicity patterns. *Pure Appl. Geophys.* 126 (2), 357–372.
- McGuire, J.J., Boettcher, M.S., Jordan, T.H., 2005. Foreshock sequences and short-term earthquake predictability on East Pacific Rise transform faults. *Nature* 434 (7032), 457–461. <https://doi.org/10.1038/nature03377>.
- Metzger, S., Jónsson, S., 2014. Plate boundary deformation in North Iceland during 1992–2009 revealed by InSAR time-series analysis and GPS. *Tectonophysics* 634, 127–138. <https://doi.org/10.1016/j.tecto.2014.07.027>.
- Metzger, S., Jónsson, S., Danielsen, G., Hreinsdóttir, S., Jouanne, F., Giardini, D., Villemin, T., 2013. Present kinematics of the Tjörnes Fracture Zone, North Iceland, from campaign and continuous GPS measurements. *Geophys. J. Int.* 192 (2), 441–455. <https://doi.org/10.1093/gji/ggs032>.
- Metzger, S., Jónsson, S., Geirsson, H., 2011. Locking depth and slip-rate of the Húsavík Flatey fault, North Iceland, derived from continuous GPS data 2006–2010. *Geophys. J. Int.* 187, 564–576. <https://doi.org/10.1111/j.1365-246X.2011.05176.x>.
- Ogata, Y., 1988. Statistical models for earthquake occurrences and residual analysis for point processes. *J. Am. Stat. Assoc.* 83 (401), 9–27.
- Ohnaka, M., Shen, L., 1999. Scaling of the shear rupture process from nucleation to dynamic propagation: implications of geometric irregularity of the rupturing surfaces. *J. Geophys. Res.* 104, 817–844. <https://doi.org/10.1029/1998JB900007>.
- Okada, Y., 1985. Surface deformation due to shear and tensile faults in a half-space. *Bull. Seismol. Soc. Am.* 75 (4), 1135–1154.
- Passarelli, L., Hainzl, S., Cesca, S., Maccaferri, F., Mucciarelli, M., Roessler, D., Corbi, F., Dahm, T., Rivalta, E., 2015. Aseismic transient forcing driving the swarm-like seismic sequence in the Pollino range, Southern Italy. *Geophys. J. Int.* 201. <https://doi.org/10.1093/gji/ggv111>.
- Passarelli, L., Rivalta, E., Shuler, A., 2014. Dike intrusions during rifting episodes obey scaling relationships similar to earthquakes. *Sci. Rep.* 4, 3886. <https://doi.org/10.1038/srep03886>.
- Peng, Z., Gombert, J., 2010. An integrated perspective of the continuum between earthquakes and slow-slip phenomena. *Nat. Geosci.* 3, 599–607. <https://doi.org/10.1038/ngeo940>.
- Reasenber, P., 1985. Second-order moment of central California seismicity, 1969–1982. *J. Geophys. Res.* 90 (B7), 5479–5495.
- Riedel, C., Tryggvason, A., Brandsdóttir, B., Dahm, T., Stefansson, R., Hensch, M., Böðvarsson, R., Vogfjörð, K.S., Jakobsdóttir, S., Eken, T., Herber, R., Holmjarn, J., Schnese, M., Thölen, M., Hofmann, B., Sigurdsson, B., Winter, S., 2006. First results from the North Iceland experiment. *Mar. Geophys. Res.* 27 (4), 267–281. <https://doi.org/10.1007/s11001-006-9007-0>.
- Riedel, C., Tryggvason, A., Dahm, T., Stefansson, R., Böðvarsson, R., Guðmundsson, G.B., 2005. The seismic velocity structure north of Iceland from joint inversion of local earthquake data. *J. Seismol.* 9 (4), 383–404. <https://doi.org/10.1007/s10950-005-8721-4>.
- Rögnvaldsson, S., Slunga, R., 1993. Routine fault plane solutions for local networks: a test with synthetic data. *Bull. Seismol. Soc. Am.* 83, 1232–1247.
- Rögnvaldsson, S.T., Guðmundsson, A., Slunga, R., 1998. Seismotectonic analysis of the Tjörnes Fracture Zone, an active transform fault in north Iceland. *J. Geophys. Res.* 103, 30117–30129.
- Roland, E., McGuire, J.J., 2009. Earthquake swarms on transform faults. *Geophys. J. Int.* 178, 1677–1690. <https://doi.org/10.1111/j.1365-246X.2009.04214.x>.
- Schurr, B., Asch, G., Hainzl, S., Bedford, J., Hoechner, A., Palo, M., Wang, R., Moreno, M., Bartsch, M., Zhang, Y., Oncken, O., Tilmann, F., Dahm, T., Victor, P., Barrientos, S., Vilotte, J.P., 2014. Gradual unlocking of plate boundary controlled initiation of the 2014 Iquique earthquake. *Nature* 512 (7514), 299–302. <https://doi.org/10.1038/nature13681>.
- Segall, P., Rice, J.R., 1995. Dilatancy, compaction, and slip instability of a fluid-infiltrated fault. *J. Geophys. Res.* 100, 22155–22171.
- Segall, P., Rubin, A.M., Bradley, A.M., Rice, J.R., 2010. Dilatant strengthening as a mechanism for slow slip events. *J. Geophys. Res.* 115, B12305. <https://doi.org/10.1029/2010JB007449>.
- Slunga, R., Rögnvaldsson, S., Böðvarsson, R., 1995. Absolute and relative locations of similar events with application to microearthquakes in southern Iceland. *Geophys. J. Int.* 123, 409–419.
- Vallée, M., Nocquet, J.M., Battaglia, J., Font, Y., Segovia, M., Regnier, M., Mothes, P., Jarrin, P., Cisneros, D., Vaco, S., Yepes, H., Martin, X., Bethoux, N., Chlieh, M., 2013. Intense interface seismicity triggered by a shallow slow slip event in the Central Ecuador subduction zone. *J. Geophys. Res.* 118 (6), 2965–2981. <https://doi.org/10.1002/jgrb.50216>.
- Vidale, J.E., Shearer, P.M., 2006. A survey of 71 earthquake bursts across southern California: exploring the role of pore fluid pressure fluctuations and aseismic slip as drivers. *J. Geophys. Res.* 111. <https://doi.org/10.1029/2005JB004034>.
- Villegas-Lanza, J.C., Nocquet, J.M., Rolandone, F., Vallée, M., Tavera, H., Bondoux, F., Tran, T., Martin, X., Chlieh, M., 2016. A mixed seismic-aseismic stress release episode in the Andean subduction zone. *Nat. Geosci.* 9 (2), 150–154. <https://doi.org/10.1038/ngeo2620>.
- Wei, S., Helmlinger, D., Owen, S., Graves, R.W., Hudnut, K.W., Fielding, E.J., 2013. Complementary slip distributions of the largest earthquakes in the 2012 Brawley swarm, Imperial Valley, California. *Geophys. Res. Lett.* 40 (5), 847–852. <https://doi.org/10.1002/grl.50259>.
- Wells, D.L., Coppersmith, K.J., 1994. New empirical relationships among magnitude, rupture length, rupture width, rupture area, and surface displacement. *Bull. Seismol. Soc. Am.* 84 (4), 974–1002.
- Wessel, P., Smith, W.H., 1998. New, improved version of Generic Mapping Tools released. *Eos Trans. AGU* 79 (47), 579.
- Zencher, F., Bonafede, M., Stefansson, R., 2006. Near-lithostatic pore pressure at seismogenic depths: a thermoporoelastic model. *Geophys. J. Int.* 166 (3), 1318–1334. <https://doi.org/10.1111/j.1365-246X.2006.03069.x>.

3.3.2 Size distribution of Parkfield's microearthquakes reflects changes in surface creep rate

Published as: T. Tormann, S. Wiemer, S. Metzger, A. Michael, J. L. Hardebeck (2013). Size distribution of Parkfield's microearthquakes reflects changes in surface creep rate. *Geophysical Journal International*, **193**, 1474–1478. doi:10.1093/gji/ggt093

Supporting information: –

Scientific application: This paper studies the temporal variations of the seismic scaling law (b-value) and fault creep rates based on observations along a creeping section of the San Andreas fault. We found that, when creep slows down and loading increases, more large earthquakes occur. This suggests that b-values can act as temporal and spatial stress meters.

Methodological advances: Temporal resolution of b-values in comparison to temporarily resolved creep rates.

Individual Contributions: The study was designed and conducted by TT and SW. I contributed with the deformation analysis and synthetic modeling of creep. TT, SW and me contributed to the writing, AM and JH to the pre-review.



EXPRESS LETTER

Size distribution of Parkfield's microearthquakes reflects changes in surface creep rate

T. Tormann,¹ S. Wiemer,¹ S. Metzger,^{1,2} A. Michael³ and J. L. Hardebeck³

¹Swiss Seismological Service, ETH Zurich, Switzerland. E-mail: thessa@sed.ethz.ch

²Helmholtz Centre Potsdam, GFZ Potsdam, Germany

³U.S. Geological Survey, Menlo Park, USA

Accepted 2013 March 5. Received 2013 February 27; in original form 2012 December 14

SUMMARY

The nucleation area of the series of M_6 events in Parkfield has been shown to be characterized by low b -values throughout the seismic cycle. Since low b -values represent high differential stresses, the asperity structure seems to be always stably stressed and even unaffected by the latest main shock in 2004. However, because fault loading rates and applied shear stress vary with time, some degree of temporal variability of the b -value within stable blocks is to be expected. We discuss in this study adequate techniques and uncertainty treatment for a detailed analysis of the temporal evolution of b -values. We show that the derived signal for the Parkfield asperity correlates with changes in surface creep, suggesting a sensitive time resolution of the b -value stress meter, and confirming near-critical loading conditions within the Parkfield asperity.

Key words: Time-series analysis; Earthquake interaction, forecasting, and prediction; Seismicity and tectonics; Statistical seismology.

1 INTRODUCTION

The size distribution of earthquakes—described by the b -value from the Gutenberg & Richter (1944) law: $\log(\text{Number of events with magnitude} \geq M) = a - bM$ —has been shown to be inversely proportional to differential stresses: from acoustic emissions during fracture experiments in the laboratory (e.g. Amitrano 2003) to natural earthquakes in the crust (Schorlemmer & Wiemer 2005; Spada *et al.* 2013); the higher the differential stresses, the lower the b -values. b -Values have therefore been suggested to act as a crude stress meter for the crust, allowing us to image relative stress distributions, highlighting, for example, along faults areas of anomalous low b -values, that is, high stresses, so-called asperities, which are likely to emanate future larger ruptures (e.g. Wiemer & Wyss 1997). One well-studied example is the spatial distribution of b -values in Parkfield: a segment of the San Andreas Fault in central California, which is known for its series of six $M \sim 6$ events occurring relatively regularly over the last 150 yr (Bakun & Lindh 1985), and which is widely regarded among seismologists to be an ideal natural laboratory for improving our understanding of the earthquake cycle, the identification of main shock precursors and the development and testing of prediction models (e.g. Bakun *et al.* 2005). For this reason, back in the 1980s, dense and high-quality networks of monitoring instruments from various fields of Earth sciences were installed at the site of the 'Parkfield Experiment' (Bakun & Lindh 1985) to capture a wide range of geophysical signals of the approaching event and reveal possible precursors. Thus, the most recent Parkfield main shock was extremely well recorded, when it

occurred in 2004, much later than expected. Despite the wealth of data, no unambiguous precursors were observed (Bakun *et al.* 2005). However, a low b -value anomaly in the nucleation area of the moderate main shocks had been documented before the latest event (Wiemer & Wyss 1997; Schorlemmer *et al.* 2004); and this structure reflects the approximate extent of the slip and aftershock distribution of the 2004 event, that is, it successfully 'post-casted' the location of the M_6 event (Schorlemmer & Wiemer 2005). Tormann *et al.* (2012) re-evaluated the data for the pre- and post-main shock phases and found the asperity to be a stably stressed volume through the seismic cycle: shape and amplitude of the low b -value volume remains the same after the 2004 main shock. Fig. 1(a) shows the spatial b -value distribution derived from the last three decades of seismicity. A first-order time-series analysis of the asperity b -values showed that the 2004 event has not imprinted on the b -values beyond the first few months of aftershocks. The overall levels before and after the main shock are unchanged and, if converted into expected recurrence times of the M_6 events, they are consistent with the observed interevent times.

In this study, we discuss techniques and uncertainties in detailed temporal b -value analysis and focus on second-order effects of the Parkfield time-series, namely the variation that is seen over the two decades before the main shock. This could be regarded as random fluctuation around a mean value, was it not for a data set of surface creep measurements from atop the asperity volume: the changes in creep rate correlate strongly with the signal seen in the b -value time-series and suggest that the state of stress at the fault at seismogenic depths is related to aseismic creep seen on the surface.

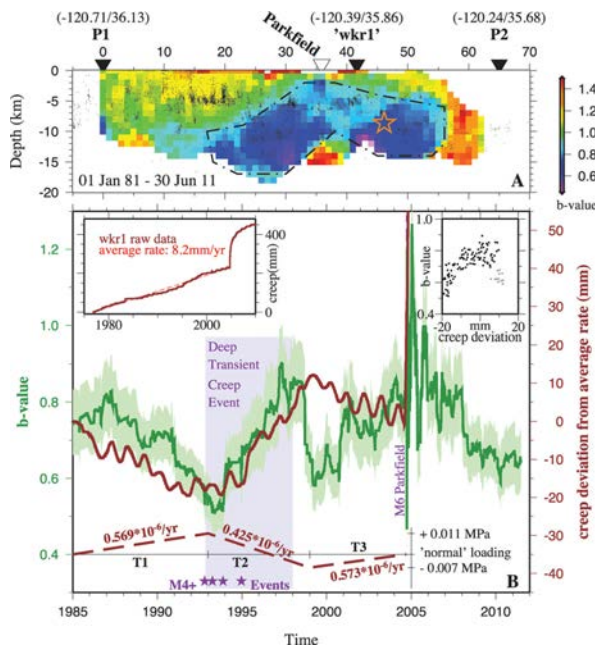


Figure 1. (a) b -Value cross-section for Parkfield’s microseismicity $M \geq 1.3$ since 1981; star: 2004 M_6 hypocentre; line: follows the $b = 0.87$ contour surrounding the asperity volume as defined in Tormann *et al.* (2012). (b) b -value time-series of asperity volume; Inset left: raw creep data collected from ‘wkr1’; Mainframe: green: b -value evolution with standard error estimate (Shi & Bolt 1982), brown: deviation of creep from the average rate, that is, in 1993 the observed displacement on the instrument is ~ 20 mm ‘behind’ the expected displacement, in 2000 it is ~ 10 mm ‘ahead’, dashed brown line: from creep and therewith strain rate derived changes in loading relative to the expected normal loading based on the average creep rate of 8.2 mm yr^{-1} , purple shading: time period of a deep transient creep event in the asperity (Gao *et al.* 2000), accompanied by four M_4 – 5 earthquakes (purple stars); Inset right: correlation plot of b -value time-series versus creep rate changes, sampled on a monthly basis, grey: data sampled during period of influence of the 5-d cluster.

2 THE B -CREEP CORRELATION OBSERVATION

Among the Parkfield monitoring instruments is the Work Ranch creepmeter (‘wkr1’), which is located atop the centre of the asperity that produces the regular moderate earthquakes (Fig. 1a). Creep data on that instrument has been collected since 1976 (Fig. 1b, left-side inset), and as most creepmeters, ‘wkr1’ observes small-scale seasonal changes, but is regarded largely unaltered by rainfall events, and is mostly driven by tectonic signals (Roeloffs 2001). We remove the average creep rate of 8.2 mm yr^{-1} (1980 to before the 2004 event), and find a pattern of alternating decelerated and accelerated creep velocity phases over the two decades prior to the latest main shock (Fig. 1b). The average annual creep rate between 1985 and 1993 is with 6.1 mm yr^{-1} only ~ 75 per cent of long-term average, during the following 6 yr it accelerates to 12.9 mm yr^{-1} , more than twice the previous velocity, and nearly 160 per cent of the long-term average, and after 1999 it slows down again to 5.9 mm yr^{-1} .

We calculate the time-series of b -values from within the low- b -value asperity volume (see Section 3 for the discussion of the method) and observe two separate properties of the temporal evolution (Fig. 1b): (1) As documented in Tormann *et al.* (2012), the first-order observation is a constant level of b for the pre- and

post-main shock phases, with only a brief increase from the after-shock sequence. (2) Beyond that, we resolve second-order changes around the mean b -value, exceeding ± 30 per cent over the last three decades: we observe three alternating ~ 6 yr phases of decreasing, increasing and again decreasing b -values, before we measure very briefly, but sharply increased values (reaching $b > 1$) in the direct aftermath of the M_6 event and decreasing b -values since then (Fig. 1b). The period of increasing b -values starting in 1993, coincides with the onset of a documented transient slip event in the asperity volume (Gao *et al.* 2000; Murray & Segall 2005), which was possibly initiated, but at least accompanied by a series of four M_4 – 5 earthquakes and an increased seismicity rate of about 30 per cent above the average 1981–2004 rate. We observe a sudden deviation from the overall trends for a ~ 2 -yr period around 2000, when the b -values drop sharply. Much of this signal is produced by a 5-d cluster in mid-September 1998, rupturing within a 3×1.6 km fault patch located at 8 km depth. The eight $M \geq 1.3$ events have a mean magnitude of 2.4, while the asperity events following that cluster and through to the end of the ‘anomaly’ have a mean magnitude of 1.9, that is, all b -value estimates from time frames including this cluster (1998.75–2000.8) are decreased.

Comparing the two data sets we find that, with the exception of that short cluster-dominated period, the trends in the creep rate until 2004 are robustly correlated with the evolution of the b -value measured by the microseismicity right beneath the creepmeter (Fig. 1b and right-side inset). Decreasing b -values correlate with less surface creep, and vice versa. The observed changes in surface creep are therewith related to the (unknown) state of stress and strain at the fault at seismogenic depth. However, for the years after the 2004 main shock, the creep signal is strongly dominated by shallow afterslip (Barbot *et al.* 2009) that likely masks the deeper processes, which our b -values represent; we therefore do not compare the post-main shock data directly, but note that, overall, the annual creep rates since the main shock are decelerating non-linearly and contemporaneously the b -values are decreasing. Sudden changes in b -values, such as the drop in 1998 or the peak in 2004 are due to active clusters, which are to be expected in most studies given that seismicity clusters, and need to be treated individually and interpreted separately from long-term trends.

To develop an idea of the order of stress changes that Parkfield’s b -values reflect, we use the different creep rates of 6.1 , 12.9 and 5.9 mm yr^{-1} , as observed during time periods T1, T2 and T3 (Fig. 1b) to model the shear strain across that slowly creeping section of the fault and calculate the accumulated shear stress, that is, faster creeping reduces the strain/stress accumulation rate, and vice versa. We assume a relative plate motion of 33 mm yr^{-1} across the San Andreas Fault (Murray & Langbein 2006) and, for the sake of simplicity, we describe each fault creep variation with a uniform, rectangular dislocation in an elastic half-space (Savage & Burford 1973). The model segment extends from the surface down to 15 km depth (Murray & Langbein 2006) and is 20 times longer than the real Parkfield section to eliminate edge effects. The modelled maximum shear strain rates $\dot{\epsilon}_s$ across the central part of the model segment are then transformed into shear stress rates $\dot{\sigma}_s$ using the relationship $\dot{\sigma}_s = \mu \dot{\epsilon}_s$ that connects stress and strain with the shear modulus $\mu = 30 \text{ GPa}$ (Murray & Segall 2005). Integrated over the different time periods T1–T3, the shear stress reveals the overall stress accumulation. These numbers are then compared to the ‘expected’ stress accumulation of the average creep rate, as measured until the 2004 Parkfield earthquake (8.2 mm yr^{-1}). Due to the lower than average creep rates in T1, we find an additional stress build up at the end of T1 of 0.011 MPa above the ‘normal loading’ from long-term creep

velocities, while at the end of T2, the stress build up is 0.007 MPa below the expected value (Fig. 1b). This variation is about an order of magnitude above the level of tide induced stresses (10^3 Pa, Tanaka *et al.* 2006), and tiny compared to the estimated absolute stress levels along the fault, which range from about 20 MPa in the weak fault hypothesis up to 160 MPa in the strong fault hypothesis (e.g. Scholz 2000).

We note that the above observation represents the data of only one creepmeter; but the two closest instruments next to 'wkr1' ('xta1' and 'crr1') have been reported for similarly accelerated velocities between 1993 and 1999 compared to their long-term trends (Roeloffs 2001). While our calculated amplitudes of stress variation probably reflect the specifics of the 'wkr1' instrument, the overall finding of correlating b -value and creep rate changes seems to be a more general pattern for the Parkfield asperity.

3 b -VALUE TIME-SERIES ANALYSIS: HOW TO RESOLVE DETAILS RELIABLY

Detailed temporal variation in b -values, such as shown in Fig. 1(b) can only be meaningfully documented and interpreted if the data and analysis techniques have been carefully chosen. In general, temporal variations of b -values are more difficult to identify than spatial variations (Wiemer *et al.* 1998); they are often of lower amplitude than their spatial counterparts and easily mimicked or masked by inhomogeneities in the catalogue or by the combination of spatial variability and changes in activity rate. To reliably analyse maximum likelihood b -values (Aki 1965) through time and establish the significance of potential changes the following issues need to be addressed:

(1) Data quality: homogeneity of reporting

Inhomogeneities of earthquake reporting are common in all earthquake catalogues and are an obstacle for a number of statistical analyses. Especially for interpreting b -values, it is important to use high quality and consistent earthquake catalogues, because changes in the monitoring network and processing inhomogeneity with time can introduce shifts and stretches in the magnitude scales which can mimic or mask changes in b -values (e.g. Zuniga & Wiemer 1999; Tormann *et al.* 2010).

The Parkfield segment of the San Andreas Fault is one of the best monitored fault segments in the world, and different high-quality data sets are available online. Schorlemmer *et al.* (2004) have shown that the spatial b -value distribution is consistent between the different data sets, that is, the ANSS and HRSN catalogues. We use the ANSS catalogue between 1981 January 1 and 2011 June 30 and verify that the introduction of the new M_L scaling in 2009 May, other than in southern California, did not alter the statistics of the local microseismicity magnitude range (Tormann *et al.* 2010).

(2) M_c variability

The correct assessment of the completeness magnitude, M_c , of an earthquake sample is critical for the correct estimate of the b -value: if M_c is underestimated, b -values will be systematically biased towards too low values. Especially, important for temporal b -value analysis is the verification of the completeness level through time, for example, M_c usually decreases when the network is improved and new instruments are added, and it often increases temporarily after large earthquakes (e.g. Woessner & Wiemer 2005).

For the Parkfield asperity, we assess M_c using the maximum curvature estimate and adding 0.2 for safety. We confirm a reasonable estimate of $M_c = 1.3$, as published by Schorlemmer *et al.* (2004).

We verify that the overall shape of the time-series does not change for at least $1.1 \leq M_c \leq 1.8$.

(3) Spatially homogeneous volume

In the presence of spatially heterogeneous b -values, local changes in activity rate can cause apparent changes in b through time (e.g. Wiemer *et al.* 1998). It is important, before interpreting changes in temporal b -value evolution, to verify that they are not unintended artefacts from emphasizing different spatially distinct volumes that are seismically active during different periods, instead of true temporal changes in the behaviour within the same volume. The temporal analysis, therefore, needs to be restricted to a volume that is spatially homogeneous. To identify potential regions, Wiemer *et al.* (1998) have proposed the technique of differential b -value mapping, in which they calculate b -value grids for two subsequent time periods and map the percentual difference for all nodes that have a b -value estimate in both periods, and show a difference in these estimates beyond a certain statistical significance level. This technique highlights areas of significantly increased or decreased b -values, but is in its resolution and spatial coverage highly dependent on and limited to the choice of time periods. It is an effective approach if the approximate time of a potential change is known or suspected beforehand, for example, an independent geodetic observation or a large close or distant main shock; it is less suitable for an 'uninformed' analysis of temporal b -value evolution.

We introduce a Spatial Homogeneity Detecting technique (SHOD), which evaluates for a given volume the spatial homogeneity through time by combining spatial and temporal analysis of b -values: we first map the spatial distribution of b -values to select the volume for the temporal analysis and assign each earthquake in the sample volume the closest b -value from the spatial mapping. At each time step, we calculate the b -value from the current time window of the sample and, in addition, the mean of the associated spatial b -values from the events of that time frame. If that spatial curve follows the curve of the time-series, the temporal signal is artificial and produced by sampling different subvolumes at different times, that is, the underlying earthquake sample was spatially inhomogeneous. For a homogeneous volume, the spatial curve will be more or less flat. Figs 2(a) and (b) show this effect for a synthetic catalogue, and (c) verifies that the spatial curve for the Parkfield asperity volume (Fig. 1a, all earthquakes inside the $b = 0.87$ contour) is well behaved.

(4) Constant-time-windows or fixed-number-of-events approach?

Temporal b -value studies often use fixed length time windows to estimate b -values through time. We argue that this approach has severe disadvantages in a time-series of significantly varying activity rates: one can either use small time windows and be able to track immediate changes, for example, due to a main shock and its early aftershocks, but then create many empty time bins in less active parts of the series; or else one keeps the windows long enough to fill every bin, but then lose the detailed information on any abrupt changes and create an apparent shift due to considering 'too old' data/processes in each estimate (Fig. 3). The alternative is to instead use moving windows of a fixed number of N events. The choice of N is subjective and determines the level of uncertainty in each b -value estimate (higher for smaller N), and the degree of smoothing/damping of signals (stronger for larger N). This fixed N technique provides an estimate at each point in time, which represent data from different lengths of time windows, though: from a few days or weeks during an active aftershock sequence to several years in seismically quiet periods.

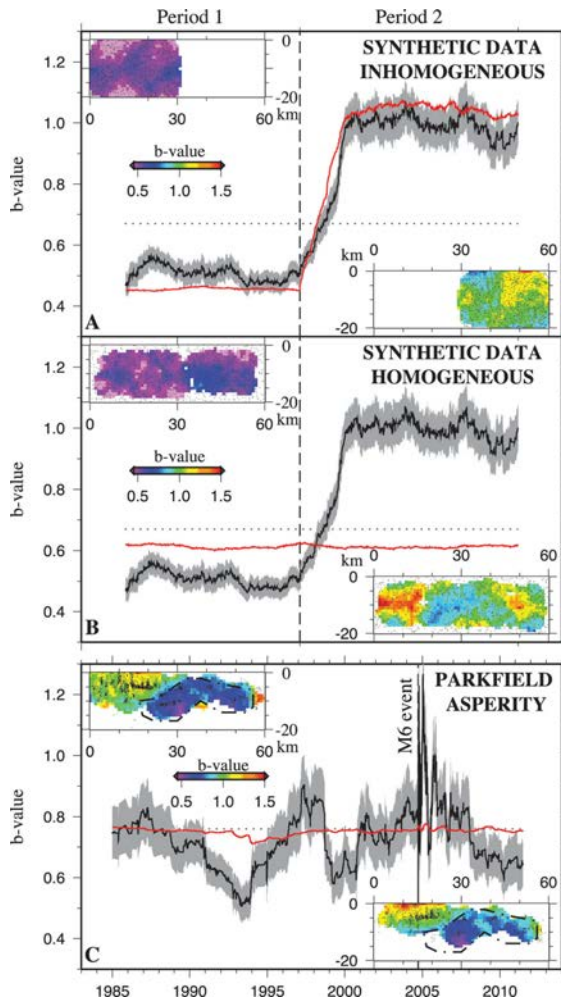


Figure 2. SHOD: spatial homogeneity detector for temporal b -value analysis. (a and b) Synthetic example of a spatially (a) inhomogeneous volume (two distinct regions of different b -values and activation periods, 0–30 km during period 1 and 30–60 km during period 2), and a (b) homogeneous volume (evenly distributed events throughout the full volume), both with $b = 0.5$ in period 1 and $b = 1$ in period 2. Black/grey: b -value time-series and formal uncertainty, red: mean of closest spatial b -values, dotted line: overall mean b -value of the volume. Cross-sections: spatial b -value distributions for time periods 1 and 2. (c) Analysis applied to Parkfield data, cross-sections cover before and after the 2004 main shock, flat red curve confirms spatial homogeneity, so temporal variations in the black data are not artefacts.

We use the average annual number of events within the Parkfield asperity between 1981 and 2011, $\bar{N}_{\text{ann}} = 68$, which results in individual window lengths averaging around 3 yr. We demonstrate the differences between the alternative approaches for window sizes of 3 months–3 yr compared to \bar{N}_{ann} -event sampling (Fig. 3). Apart from the explained limits of the constant time window sampling, the choice of either that or the constant number approach does not matter for the shape of the curve. We verified that changing the value of N within reasonable limits (e.g. $50 \leq N \leq 150$) also preserves the general shape of the time-series.

(5) Step sizes

A further free parameter is the overlap between successive b -value estimates in the time-series, which is a trade-off between smoothing and number of data points together with the independence of the

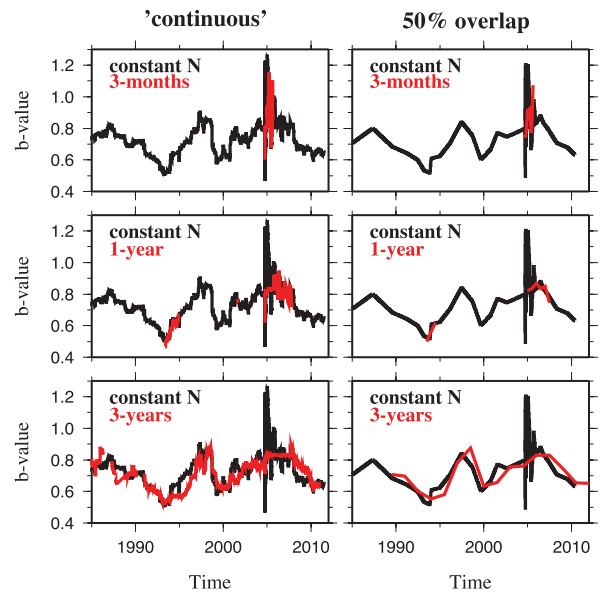


Figure 3. Comparison of b -value time-series for different sampling techniques: constant number, N , of events (black) versus constant time, T , windows (red): always $N = 68$, T increases from 3 months to 3 yr (top to bottom); left-hand panels show continuous sampling for either of the combinations, that is, windows are moved by one-event or 1-d steps, respectively; right-hand panels show the same combinations for 50 per cent overlap sampling: windows are moved by half their length, that is 34 events or 1.5 months, 0.5 and 1.5 yr, respectively. The gaps in the T curves represent times of too little activity to calculate b -values, the 3-yr sampling does not capture the abrupt change due to the 2004 main shock.

starting point. The smaller the overlap, that is, the larger the step size relative to the window length, the larger the sensitivity to the ‘gridding’, that is, the starting time or event.

We prefer the continuous approach of moving the window by one event at a time, and note that the overall shape is retrieved with any step size, from continuous to no overlap (Fig. 3).

(6) Data display

b -Values from temporal analysis are either plotted at the beginning, middle or end of the time window that they represent. We argue that the latter choice is the most sensible to physically understand the resolved signals of the time evolution, since it represents the b -values as result of previous seismicity, that is, changes that are caused by a large event with its immediate aftershocks will plot at/after their actual occurrence, not before, as would happen for either of the alternative display modes and be confusing for interpretation. We note that with this choice, the Parkfield time-series starts in 1985 although it uses all events since 1981 (Fig. 1b).

(7) Significance check

Each of the above factors influences the shape of the b -value time-series and adds uncertainty to the formal standard deviation (Shi & Bolt 1982) of the estimated b -value, which is mostly driven by the number of events in the earthquake sample. Any temporal b -value study interested in details of the time-series needs to carefully address the above points and establish that the interpreted signals are meaningful beyond uncertain fluctuation. We evaluate the sensitivity of our results to the choice of all these free parameters within sensible ranges, and find the major structures to be common for all choices, confirming the robustness of the signal.

4 DISCUSSION AND CONCLUSION

The observation of a correlation between seismic and geodetic transients, shown here, is at least the second of its kind: from Japanese data, Wiemer *et al.* (2005) documented a correlation between an increase in b -values in the Tokai region and a contemporaneously accelerated subsidence rate.

The temporal correlation between b -value transients and creep data is fully consistent with a model where the size distribution of the microseismicity responds to changes in the stressing regime. When creep slows down and loading stresses on the fault increase, little rough patches on the fault tend to break not one by one, but in groups, creating more often larger microearthquakes, decreasing the b -value, implying higher probabilities for larger magnitude earthquakes. In times of accelerating creep, stresses are released to a higher degree aseismically, tiny rough patches on the fault can break on their own, without jumping to neighbouring patches, the magnitudes of the microseismicity are preferably small, the b -values high. The suggestion is that b -values thus can act as a stress meter not only in a spatial sense but also have the temporal resolution to track loading levels through time.

Stress perturbations caused by tides are relatively small; this led Tanaka *et al.* (2006) to argue that local stress conditions must be close to a critical state for tidal stresses to trigger earthquakes. In a systematic study of tidal triggered earthquakes they could identify strong correlations of small magnitude earthquake occurrence rates and tidal stress changes in focal regions prior to major earthquakes, but lost the signal after the main ruptures (i.e. significant stress releases). Based on their conclusions, the Parkfield b -creep correlation observation is plausible, if the stress state is near critical such that there is always the possibility of moderate events (Tormann *et al.* 2012). Then, the distribution of event sizes can be modulated by small changes in the stress state. This differs from previous results in which b -values were thought to only react to drastic changes in the environment (Wiemer *et al.* 1998).

The small-scale fluctuations are apparently also not the driving factor in the timing of a major event, since the 2004 main shock did not occur at a b -value minimum. The triggering mechanism for the $M6$ type events remains unknown for the time being.

Our results suggest that monitoring b -values through time can resolve major changes in local stress fields as previously documented in a volcanic environment for a magma intrusion (Wiemer *et al.* 1998) and along-fault for the Loma Prieta $M7$ earthquake (Tormann *et al.* 2012), and has the potential to indicate near-critically stressed structures. This is particularly valuable, since the mere comparison of absolute b -values does not allow a direct translation into stress levels, they only represent relative stress distributions. By estimating the strain-sensitivity of b -value time-series using geodetic data, an improved assessment of the current loading stage of hazardous asperities may become possible.

ACKNOWLEDGEMENTS

We thank J. Rubinstein, A. Llenos and an anonymous reviewer for helpful comments. Earthquake data were obtained from <http://www.ncedc.org/anss/catalog-search.html> (last accessed 19 March 2013) and creepmeter data from John Langbein's database at <ftp://ehzftp.wr.usgs.gov/langbein/CREEP/> (last accessed 19 March 2013). Figures were produced with the generic mapping tools [<http://gmt.soest.hawaii.edu/>] (last accessed 19 March 2013). Part of this study was funded through SNF grant PMPDP2 134174.

REFERENCES

- Aki, K., 1965. Maximum likelihood estimate of b in the formula $\log N = a - bM$ and its confidence limits, *Bull. Earthq. Res. Inst.*, **43**, 237–239.
- Amitrano, D., 2003. Brittle-ductile Ttransition and associated seismicity: experimental and numerical studies and relationship with the b value, *J. geophys. Res.*, **108**(B1), doi:10.1029/2001JB000680.
- Bakun, W.H. & Lindh, A.G., 1985. The Parkfield, California, earthquake prediction experiment, *Science*, **229**, 619–624.
- Bakun, W.H. *et al.*, 2005. Implications for prediction and hazard assessment from the 2004 Parkfield earthquake, *Nature*, **437**, 969–974.
- Barbot, S., Fialko, Y. & Bock, Y., 2009. Postseismic deformation due to the Mw 6.0 2004 Parkfield earthquake: stress-driven creep on a fault with spatially variable rate-and-state friction parameters, *J. geophys. Res.*, **114**(B7), doi:10.1029/2008JB005748.
- Gao, S., Silver, P.G. & Linde, A.T., 2000. Analysis of deformation data at Parkfield, California: detection of a long-term strain transient, *J. geophys. Res.*, **105**, 2955–2967.
- Gutenberg, B. & Richter, C.F., 1944. Frequency of earthquakes in California, *Bull. seism. Soc. Am.*, **34**, 185–188.
- Murray, J.R. & Langbein, J., 2006. Slip on the San Andreas Fault at Parkfield, California, over two earthquake cycles, and the implications for seismic hazard, *Bull. seism. Soc. Am.*, **96**(4B), S283–S303.
- Murray, J.R. & Segall, P., 2005. Spatiotemporal evolution of a transient slip event on the San Andreas Fault near Parkfield, California, *J. geophys. Res.*, **110**(B9), doi: 10.1029/2005JB003651.
- Roeloffs, E., 2001. Creep rate changes at Parkfield, California 1966–1999: seasonal, precipitation induced, and tectonic, *J. geophys. Res.*, **106**, 16525–16547.
- Savage, J.C. & Burford, R.O., 1973. Geodetic determination of relative plate motion in central California, *J. geophys. Res.*, **78**, 832–845.
- Scholz, C.H., 2000. Evidence for a strong San Andreas Fault, *Geology*, **28**(2), 163–166.
- Schorlemmer, D. & Wiemer, S., 2005. Earth science: microseismicity data forecasts rupture area, *Nature*, **434**, doi:10.1038/4341086a.
- Schorlemmer, D., Wiemer, S. & Wyss, M., 2004. Earthquake statistics at Parkfield: 1. Stationarity of b Values, *J. geophys. Res.*, **109**(B12), doi:10.1029/2004JB003234.
- Shi, Y. & Bolt, B.A., 1982. The standard error of the magnitude-frequency b value, *Bull. seism. Soc. Am.*, **72**, 1677–1687.
- Spada, M., Tormann, T., Wiemer, S. & Enescu, B., 2013. Generic dependence of the frequency-size distribution of earthquakes on depth and its relation to the strength profile of the crust, *Geophys. Res. Lett.*, **40**, in press.
- Tanaka, S., Sato, H., Matsumura, S. & Ohtake, M., 2006. Tidal triggering of earthquakes in the subducting Philippine Sea Plate beneath the locked zone of the plate interface in the Tokai Region, Japan, *Tectonophysics*, **417**, 69–80.
- Tormann, T., Wiemer, S. & Hauksson, E., 2010. Changes of reporting rates in the Southern Californian Earthquake Catalog, introduced by a new definition of ML, *Bull. seism. Soc. Am.*, **100**(4), 1733–1742.
- Tormann, T., Wiemer, S. & Hardebeck, J., 2012. Earthquake recurrence models fail when earthquakes fail to reset the stress field, *Geophys. Res. Lett.*, **39**, doi:10.1029/2012GL052913.
- Wiemer, S. & Wyss, M., 1997. Mapping the frequency-magnitude distribution in asperities: an improved technique to calculate recurrence times? *J. geophys. Res.*, **102**, 15115–15128.
- Wiemer, S., McNutt, S.R. & Wyss, M., 1998. Temporal and three-dimensional spatial analyses of the frequency-magnitude distribution near Long Valley Caldera, California, *Geophys. J. Int.*, **134**, 409–421.
- Wiemer, S., Yoshida, A., Hosono, K., Noguchi, S. & Takayama, H., 2005. Correlating seismicity parameters and subsidence in the Tokai Region, Central Japan, *J. geophys. Res.*, **110**(B10), doi:10.1029/2003JB002732.
- Woessner, J. & Wiemer, S., 2005. Assessing the quality of earthquake catalogues: estimating the magnitude of completeness and its uncertainty, *Bull. seism. Soc. Am.*, **95**, 684–698.
- Zuniga, F.R. & Wiemer, S., 1999. Seismicity patterns: are they always related to natural causes? *Pure appl. Geophys.*, **155**, 713–726.

4 Synthesis

This cumulative habilitation thesis presented eleven self-contained, peer-reviewed research articles and that explain space-geodetic observations of recent crustal processes using analytical, numerical and/or geological models. Among those are three first-authored by me (*Metzger et al.*, 2017, 2020, 2021a), one counts as equal first-authorship (*Zubovich et al.*, 2022), one was compiled by a PhD student under my supervision (*Hoffmann et al.*, 2018), two include major contributions of me (*Peña et al.*, 2022; *Zubovich et al.*, 2016), and four minor contributions (*Kufner et al.*, 2021; *Moreno et al.*, 2018; *Passarelli et al.*, 2018; *Tormann et al.*, 2013). Three data publications provide access to GNSS survey data in a receiver-independent exchange format (RINEX, *Metzger et al.*, 2019, 2021c), respectively, full-resolution InSAR time-series of the Greater Pamir (*Metzger et al.*, 2021b).

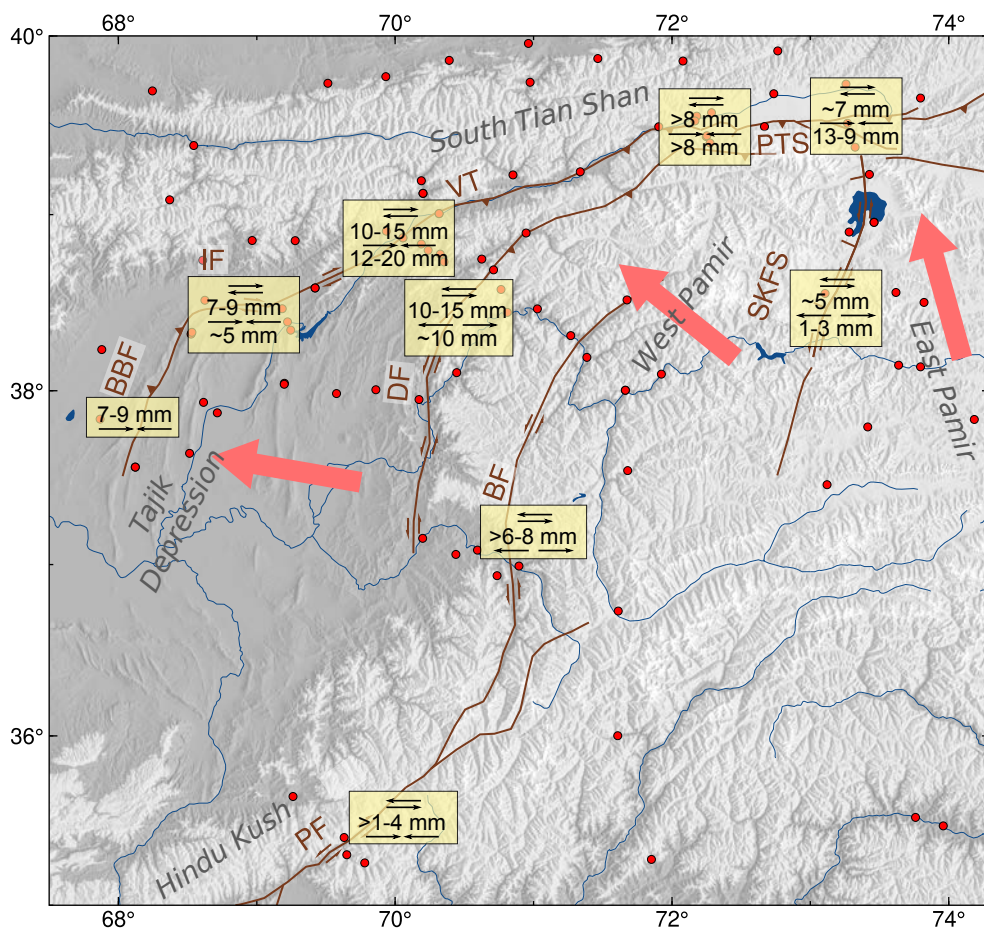


Figure 4.1: Synthesis of first-order kinematics (reddish arrows) and yearly slip constraints in the Greater Pamir as constrained in the work presented here (*Metzger et al.*, 2017, 2020, 2021a; *Kufner et al.*, 2021; *Zubovich et al.*, 2016, 2022) and unpublished analysis. The arrows in the yellow frames symbolize slip sense (dextral/sinistral slip and compression/extension). The red dots mark sGNSS markers. BBF – Babatag back-thrust fault, BF – Badakhshan fault, DF – Darvaz fault, IF – Ilyak fault, PTS – Pamir thrust system, SKFS – Sarez-Karakul fault system, VT – Vakhsh thrust fault.

The publications focusing on the Pamir provide insight into its recent kinematics in unprecedented resolution (Figure 4.1). I have quantified the long-term slip-rates of the three most important faults bounding the Pamir to the north and northwest, that is, the Main Pamir thrust system, bifurcating WSW-ward into the sinistral-transpressive Darvaz and the dextral-transpressive Vakhsh fault (*Metzger et al.*, 2020, 2021a; *Zubovich et al.*, 2016, 2022). The slip rates confirm westward collapse of the highly-fractured West Pamir into the low-altitude Tajik Depression. The depression itself exhibits E-W shortening, which is mostly accommodated by the westernmost backthrust of the ~N-aligned fold-thrust-belt and at its northern boundary, the Ilyak fault that links to the Vakhsh fault further east, together separating the depression and the Pamir from the (South) Tian Shan further north. All of

these faults accommodate between 10-20 mm/yr of slip, which is surprisingly high for a continental setting. The Vakhsh and the Ilyak fault have a rather shallow locking depth of ~ 1 km or less, probably due to the presence of low-friction, Jurassic evaporites deposited after the closure of the Thetys ocean. In the depression, seismicity occurs only below the sedimentary layers (Kufner *et al.*, 2018), hence, internal deformation is mostly aseismic and the layers are conveyed westwards.

Further south, the Hindu Kush does not show localized, but rather distributed, strain accumulation, which might be connected to the ongoing slab-break off (Kufner *et al.*, 2021). This hypothesis is supported by seismicity distributed along the submontane regions south and north of the orogen. A most prominent fault of the Hindu Kush, the Panjsheer fault, accommodates at least a few mm/yr of slip, but – given the slow deformation gradient – appears to be locked with a much higher locking depth than, e.g., the Darvaz and Vakhsh fault further north. Elongating the Panjsheer fault towards north and bending parallelly to the Darvaz fault towards NE, the Badakhshan fault seems to be locked, too, but accommodates a bit higher slip than the former one (Kufner *et al.*, 2021).

The 2015 $M_w 7.2$ Sarez earthquake ruptured the sub-vertical Sarez-Karakul fault system that separates the collapsing West Pamir from the (internally stable) East Pamir in a sinistral fashion (Metzger *et al.*, 2017; Simran *et al.*, 2017). The rupture occurred at an ~ 80 km-long fault segment that forms the superficial NE-continuation of the Indian indenter at depth. Recently, Elliott *et al.* (2020) published evidence for active faulting further towards SW of the fault. These traces suggest that the (poorly-located) 1911 $M 7$ Sarez earthquake (Kulikova *et al.*, 2016) – that had a similar faulting mechanism – actually ruptured the Pamir just above the Indian margin of the indenter. Most interestingly, the 2015 earthquake also had a significant impact on the Darvaz fault (Metzger *et al.*, 2020) and the Main Pamir thrust system (Zubovich *et al.*, 2022), which are located at 150-200 km distance, are unconnected to the Sarez-Karakul fault system and follow a different strike. Space-geodetic data showed a – most probably dynamic – slip activation of these two faults of a few mm. This shows that conventional Coulomb failure stress change models and the classic concept of a fault damage zone do not hold here (Bloch *et al.*, 2022). Our very recent, combined analysis of aftershock catalogs and InSAR time-series shows that two subsequent earthquakes rupturing the Pamir’s northern ($M 6.4$ Sary-Tash earthquake) and northeastern margin ($M 6.6$ Muji earthquake) in 2016 were likely triggered by fluid migration (Bloch *et al.*, 2022), while visco-elastic relaxation processes can be neglected (Jin *et al.*, 2022).

From a more methodological perspective, the Sarez earthquake served as a case study to test the impact of slip-patch subsampling on the model robustness and quality (Metzger *et al.*, 2017): By comparing an iterative, multi-stage, data-driven approach with slip patch sizes governed by the spatial density of input data, and a conventional model with uniform slip patch sizes, I could show that a data-driven model stabilizes the slip parameter uncertainties even at increasing patch depth, and that the overall data misfit improves. I have also constantly updated my GNSS trajectory modeling strategy (originally developed in my PhD work in Iceland) such that it accounts for post-seismic decay of any earthquake of relevance (Moreno *et al.*, 2018), and corrects sGNSS time-series trajectories by making use of knowledge gained from nearby-collected cGNSS data, such as seasonal signals (Hoffmann *et al.*, 2018) or co-seismic offsets (Zubovich *et al.*, 2022). I have also improved my InSAR data-processing skills in several aspects: I have designed a work flow to tie individual InSAR deformation rate maps to a supra-regional, three-dimensional reference frame spanned by GNSS rates (Metzger *et al.*, 2021a), and learned how to process heritage data from the Japanese ALOS radar satellite (Peña *et al.*, 2022).

Using the GNSS trajectory modeling mentioned just before we produced an interseismic locking map of the Northern Chile-Southern Peru seismic gap, and constrained the afterslip following the 2014 $M_w 8.1$ Iquique-Pisagua earthquake (Hoffmann *et al.*, 2018). The data also highlight a seismotectonic barrier just south of the rupture segment with increased coupling, bringing this segment closer to failure. I applied the same models to GNSS time-series collected in southern Chile to constrain co-seismic offsets caused by the 2016 $M_w 7.6$ southern Chile earthquake (Moreno *et al.*, 2018). This earthquake was the first large earthquake after the great 1960 $M_w 9.5$ Chile earthquake, suggesting that the occurrence of moderate-sized deeper, and great shallow earthquakes is in fact controlled by variations in pore fluid pressure. At any case, the significance of fluid dynamics to the seismic cycle becomes more and more acknowledged (Peña *et al.*, 2022): Afterslip estimates of the 2010 $M_w 8.8$

Maule earthquake derived from InSAR and GNSS time-series strongly depend on the assumption, whether or not poro-elasticity is accounted for. Plus, there exists a spatial correlation (and thus mechanical coupling) between aftershocks and increased, post-seismic pore pressure changes.

The two studies in California and Iceland exemplify the benefit of geodetic data when aseismic processes are to be studied. In the California shear zone we found a correlation between changes of geodetic strain and variations of b-values (Gutenberg-Richter law) along a creeping segment of the San Andreas Fault, making the b-values a useful proxy for stress meters, confirming near-critical loading (*Tormann et al., 2013*). In North Iceland rift zone, geodetic time-series provided constraints to study the strain release during tectonic earthquake swarms, whose contributions to release tectonic strain at plate-boundaries was so far underestimated (*Passarelli et al., 2018*).

5 Outlook

5.1 Tackling societal problems with space-based observations

The launch of the Sentinel-1 satellites in 2014/16 and the analysis of 20+ yr-long GNSS time-series have pushed tectonic geodesy on a next level in terms of data accuracy (sub-millimeters) and spatiotemporal density (meters and seconds). Also in terms of processing capabilities, data access, product interchangeability, and analysis routines the community of tectonic geodesy slowly catches up with the seismotectonic community. The seismologists already operate rather efficiently along these lines, but mind, they also had a head start of a few decades. These methodological advances open doors to a variety of new research opportunities linked to rapid disaster assessment (e.g. *Barnhart et al., 2019; Pilger et al., 2021; Yun et al., 2015*), multi-method signal detection and source model approaches (e.g. *Bedford and Bevis, 2018; Bevis and Brown, 2014; Heimann et al., 2019; Metzger et al., 2013a; Vasyura-Bathke et al., 2020*), as well as a more complex analysis of coupled solid earth processes driven by mantle, plate, and climate dynamics. One rather pressing and also elegant application of InSAR are coastal uplift estimates (*Nicholls et al., 2021; Tay et al., 2022*). Driven partially by the seismic cycle, partially by the anthropogenic reservoir extraction, an accurate knowledge of recent uplift is fundamental to mitigate the effect of the ongoing sea level rise (*IPCC, 2019; Nicholls and Cazenave, 2010*).

Sentinel-1 InSAR time-series are capable to reflect seasonal signals and transient mass movement, similar to GNSS time-series that are more accurate and dense-in-time but spatially sparse. InSAR rate maps help to better understand how local and regional processes affect individual GNSS stations, e.g. by localized, regional mass changes. On a much larger scale, we can now create continental-scale deformation rate maps and time-series (e.g. *Metzger et al., 2021a; Ou et al., 2022; Weiss et al., 2020*) revealing subtle but temporally stable long-wavelength processes rooted in the upper mantle (e.g. *Pollitz et al., 2001*) but highly relevant for the topography as we know it today (e.g. *Cao et al., 2022; Grandin et al., 2012; Liu et al., 2022*).

The new wealth of space-geodetic data must be analyzed in an efficient fashion that includes statistical and machine-learning methods (e.g. *Rouet-Leduc et al., 2021*) and the awareness of the complexity of the earth system, where cause and effect are not obviously/directly linked in space or time but sometimes lag behind in time, or are offset in space. Space-geodetic observations are capable to detect atmospheric, near-surface, crustal and upper mantle processes in four dimensions (space and/or time) and the manifold applications discussed here show that it is impossible to assign tectonic geodesy to one of the core disciplines of Earth sciences as they are classically taught at German universities. Tectonic geodesy is an Earth *system* science and students must be trained in the use of multi-faceted Big Data, while simultaneously obtaining insight in the systemic complexity of our Earth. The University of Potsdam (UP) has already recognized the demand in academia and on the job market for such experts by striving to offer modern master degrees that include both, training in data analysis and a look across the (own disciplinary) pond.

The public and industrial sector is getting access to automatically-generated high-resolution InSAR time-series provided by national ground motion agencies, as for example, of Norway¹, Germany², even of whole Europe, as recently published by the ESA Copernicus initiative³. The products successfully retrieve localized deformation caused by near-surface processes such as landslides or infrastructure instabilities. Nevertheless, it is crucial

¹insar.ngu.no

²bodenbewegungsdienst.bgr.de

³egms.land.copernicus.eu

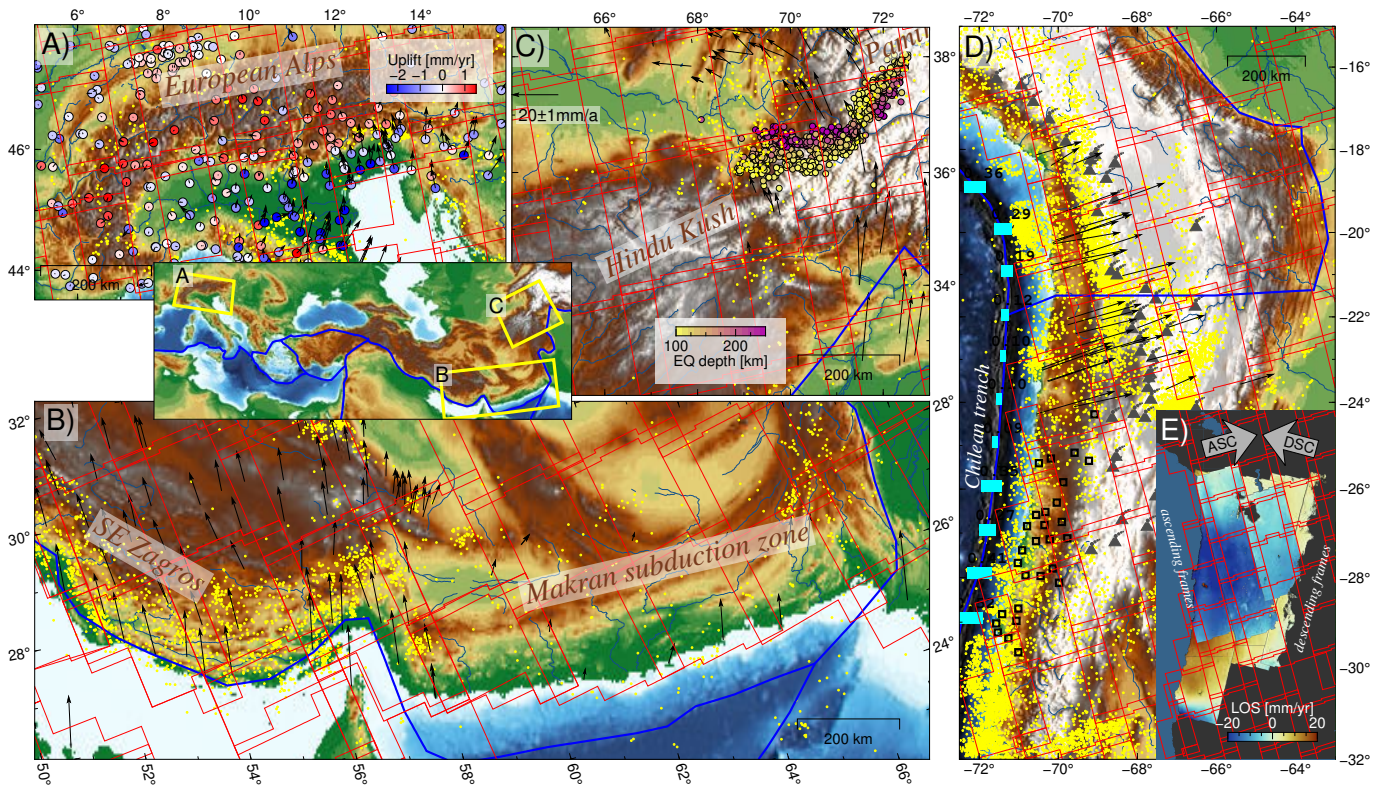


Figure 5.1: Orogens at different evolutionary stages, each exhibiting signal of a different dominant process. Recent deformation rates are indicated by black vectors, SAR units outlined in red, crustal seismicity plotted as yellow dots. a) Deformation in the Alps is dominated by glacial isostatic adjustment. b) Deformation style and seismicity in the SE Zagros and Makran subduction zone strongly differ by the abundance of salt (Zagros), respectively, sedimentary trench in fill (Makran). c) The Hindu Kush undergoes slab-break off marked by intermediate depth seismicity. d) The Andes exhibit fore-arc and back-arc deformation and variations in trench infill (blue bars indicate km-thickness). e) Example of preliminary InSAR time-series data covering the Central Andes.

that they should be interpreted by people with an educational background in remote sensing and earth system science. Also, it is yet to be validated if these products created mostly by engineers also provide robust tectonic deformation data. Thus, the need of specialists in remote sensing (better: tectonic geodesy) outside the academic sector increases. Since 2015, I offer in-depth training in the MSc curricula of Geoscience and Remote Sensing at the University of Potsdam on how to create and interpret open-access radar-interferometric products to constrain not only tectonic (crustal) sources but also near-surface, anthropogenic processes. As a positive side effect, the students gain hands-on practice in 2D-signal analysis and fundamental modeling concepts such as linear and non-linear inversion, uncertainty analysis, model assumptions and more. My course is very popular among the students: They are fascinated by the powerfulness and versatility of radar interferometry and often strive to include InSAR data analysis in their future work.

5.2 Examples of systemic research questions

One example of a systemic research question to better understand the complexity of mountain building and subduction/collision would be the creation of orogen-wide surface deformation rate maps. These could be used to unravel multiple processes responsible for vertical deformation, all leaving a distinct, depth-dependent spatio-temporal imprint at the surface. The shape of the Earth's surface is defined by the balance of tectonics and climate. Contributing sources are located near the surface (mass flux), in the lithosphere (plate compression/extension), and in the asthenosphere (isostatic compensation). Asthenospheric processes are probably the key driver of uplift, but we lack observations to understand the overall coupling. I thus envision to extract those long-wavelength signals of asthenospheric processes. Despite the instrumental, spatio-temporal limitations – our data base offers a geologic snapshot after all – I can extract those signals by 1) swapping time for space and study orogens at different stages of formation (Figure 5.1), 2) apply and update a fast and automated signal detection algorithm

originally being developed for GNSS positioning time-series (*Bedford and Bevis, 2018*) and, 3) extract also the—usually discarded—rates from the radar burst-overlap area (*Li et al., 2021*). The burst-overlap analysis allows me to extract N-S shortening rates, to which conventional InSAR is insensitive, and, thus, correctly align multiple radar tiles even in remote places, where GNSS observations are sparse or inexistent. Using analytical and thermo-mechanical modeling I want to better understand the impact of erosion/sedimentation to tectonic strain and the dynamics between elastic strain and plastic deformation and the today’s net uplift of orogens. Four orogens at different stages of maturity could be used to tackle different research questions related to strain accumulation, mountain growth and asthenospheric processes (Figure 5.1): Ongoing oceanic subduction at the Central Andes, the SE Zagros/Makran subduction zones that nearly reached collision stage, plate collision in the Hindu Kush, and the Alps representing the terminal stage of collision. Each study area has the potential to answer stage-specific research questions: What causes the residual tectonics in the Alps, when the post-glacial, isostatic signal has been removed, what is the net uplift signal, and how many Alpine slopes are instable (Figure 5.1a)? What is the influence on salt (SE-Zagros, seismically very active), respectively fluvial sediments (Makran, nearly aseismic) on the deformation style (Figure 5.1b)? Can we observe uplift due to slab break-off in the Hindu Kush (5.1c, *Kufner et al., 2021*)? And finally, what is the influence on erosion and subduction channel infill on the Central Andes to the strain pattern, and, more specifically, to the forearc and backarc deformation style? Can we observe and quantify relaxation pulses spatially emerging from megathrust earthquakes (Figure 5.1d)? Such a project would provide big, new observation data to study shallow and deep processes at multiple scales. Preliminary data bases exist for each region (ALPSHAPE⁴, *De Zan et al., 2021*; *Metzger et al., 2021a*; *Plattner et al., 2021*) and would only need to be updated in space and/or time.

Apart from that, a fifth natural lab I want to investigate on is the Dinarides-Albanides-Hellenides to better understand plate-locking, tsunami-generic potential of, and upper-crustal faulting along Europe’s most active plate-boundary. Given the data wealth and methodologic advances to extract N–S shortening at mm-scale (*Li et al., 2021*), this understudied region can now be exploited in great detail.

In summary, the individual applications presented in Chapter 3 and the two projects described above show that the research field of tectonic geodesy overlaps with, respectively helps to tackle fundamental questions posed in geology, geophysics, georisks, geomorphology, neotectonics, seismology, geodesy, remote sensing, even hydrogeology and petrology (reservoir and pore-pressure changes). Thus, the applications are manifold, there is still so much to do and the data are far from being over-exploited. Therefore I want to encourage the geoscience community across all disciplines to consider complementing its methods with the analysis of the fascinating and multi-purpose space-geodetic data!

⁴ongoing, part of the DFG priority project “Mountain building in 4D”

Bibliography

- Amos, N., and M. Gerald (1974), Postseismic viscoelastic rebound, *Science*, 183(4121), 204–206, doi:10.1126/science.183.4121.204.
- Angermann, D., J. Klotz, and C. Reigber (1999), Space-geodetic estimation of the Nazca-South America Euler vector, *Earth and Planetary Science Letters*, 171(3), 329–334, doi:10.1016/S0012-821X(99)00173-9.
- Bakun, W. H., and A. G. Lindh (1985), The Parkfield, California, earthquake prediction experiment, *Science*, 229, 619–624, doi:10.1126/science.229.4714.619.
- Barnhart, W. D., G. P. Hayes, and D. J. Wald (2019), Global Earthquake Response with Imaging Geodesy: Recent Examples from the USGS NEIC, *Remote Sensing*, 11(11), doi:10.3390/rs11111357.
- Bedford, J., and M. Bevis (2018), Greedy Automatic Signal Decomposition and Its Application to Daily GPS Time Series, *Journal of Geophysical Research: Solid Earth*, 123(8), 6992–7003, doi:10.1029/2017JB014765.
- Bedford, J., M. Moreno, B. Schurr, M. Bartsch, and O. Oncken (2015), Investigating the final seismic swarm before the Iquique-Pisagua 2014 Mw8.1 by comparison of continuous GPS and seismic foreshock data, *Geophysical Research Letters*, 42(10), 3820–3828, doi:10.1002/2015GL063953.
- Bedford, J., M. Moreno, O. Oncken, B. Schurr, T. John, J. C. Baez, and M. Bevis (2020), Months-long thousand-kilometre-scale wobbling before great subduction earthquakes, *Nature*, 580, 628–635, doi:10.1038/s41586-020-2212-1.
- Benioff, H. (1951), Global strain accumulation and release as revealed by great earthquakes, *GSA Bulletin*, 62(4), 331–338, doi:10.1130/0016-7606(1951)62[331:GSAARA]2.0.CO;2.
- Berardino, P., G. Fornaro, R. Lanari, and E. Sansosti (2002), A new algorithm for surface deformation monitoring based on small baseline differential SAR interferograms, *IEEE Transactions on Geoscience and Remote Sensing*, 40(11), 2375–2383, doi:10.1109/TGRS.2002.803792.
- Bevis, M., and A. Brown (2014), Trajectory models and reference frames for crustal motion geodesy, *Journal of Geodesy*, 88, 283–311, doi:10.1007/s00190-013-0685-5.
- Bloch, W., S. Metzger, B. Schurr, X. Yuan, L. Ratschbacher, S. Reuter, Q. Xu, J. Zhao, S. Murodkulov, and I. Oimuhammadzoda (2022), The 2015–2017 Pamir Earthquake Sequence: Fore-, Main-, and Aftershocks, Seismotectonics, Fault Interaction, and Fluid Processes, *Earth and Space Science Open Archive (subm. to Geophysical, Journal International)*, doi:10.1002/essoar.10508392.3.
- Bock, Y., D. C. Agnew, P. Fang, J. F. Genrich, B. H. Hager, T. A. Herring, K. W. Hudnut, R. W. King, S. Larsen, J.-B. Minster, K. Stark, S. Wdowinski, and F. K. Wyatt (1993), Detection of crustal deformation from the Landers earthquake sequence using continuous geodetic measurements, *Nature*, 361, 337–340, doi:10.1038/361337a0.
- Bunge, H.-P., M. A. Richards, C. Lithgow-Bertelloni, J. R. Baumgardner, S. P. Grand, and B. A. Romanowicz (1998), Time Scales and Heterogeneous Structure in Geodynamic Earth Models, *Science*, 280(5360), 91–95, doi:10.1126/science.280.5360.91.

- Bürgmann, R., S. Ergintav, P. Segall, E. H. Hearn, S. McClusky, R. E. Reilinger, H. Woith, and J. Zschau (2002), Time-Dependent Distributed Afterslip on and Deep below the İzmit Earthquake Rupture, *Bulletin of the Seismological Society of America*, 92(1), 126–137, doi:10.1785/0120000833.
- Burtman, V. S., and P. Molnar (1993), Geological and Geophysical Evidence for Deep Subduction of Continental Crust Beneath the Pamir, in *Geological and Geophysical Evidence for Deep Subduction of Continental Crust Beneath the Pamir*, vol. 281, Geological Society of America, doi:10.1130/SPE281.
- Cannell, D. M., and N. J. Lord (1993), George Green, Mathematician and Physicist 1793–1841, *The Mathematical Gazette*, 77(478), 26–51.
- Cao, Y., S. Jónsson, and S. Hreinsdóttir (2022), Iceland kinematics from insar, *Earth and Space Science Open Archive*, p. 26, doi:10.1002/essoar.10512371.1.
- Cavalié, O., E. Pathier, M. Radiguet, M. Vergnolle, N. Cotte, A. Walpersdorf, V. Kostoglodov, and F. Cotton (2013), Slow slip event in the Mexican subduction zone: Evidence of shallower slip in the Guerrero seismic gap for the 2006 event revealed by the joint inversion of InSAR and GPS data, *Earth and Planetary Science Letters*, 367, 52–60, doi:10.1016/j.epsl.2013.02.020.
- Cervelli, P., M. H. Murray, P. Segall, Y. Aoki, and T. Kato (2001), Estimating source parameters from deformation data, with an application to the March 1997 earthquake swarm off the Izu Peninsula, Japan, *Journal of Geophysical Research: Solid Earth*, 106(B6), 11,217–11,237, doi:10.1029/2000JB900399.
- Christensen, N. I. (1996), Poisson’s ratio and crustal seismology, *Journal of Geophysical Research: Solid Earth*, 101(B2), 3139–3156, doi:10.1029/95JB03446.
- De Zan, F., H. Ansari, A. Parizzi, R. Shau, M. Eineder, S. Montazeri, V. Navarro Sanchez, and T. Walter (2021), Large-scale interferometric processing of Sentinel-1 data over the Atacama desert – a contribution to the TecVolSA Project, *Fringe 2021, the 11th International Workshop on “Advances in the Science and Applications of SAR Interferometry and Sentinel-1 InSAR”*, doi:www.youtube.com/watch?v=pow_dPDUydA.
- Dragert, H., K. Wang, and T. S. James (2001), A Silent Slip Event on the Deeper Cascadia Subduction Interface, *Science*, 292(5521), 1525–1528, doi:10.1126/science.1060152.
- Elliott, A., J. Elliott, J. Hollingsworth, G. Kulikova, B. Parsons, and R. Walker (2020), Satellite imaging of the 2015 M7.2 earthquake in the Central Pamir, Tajikistan, elucidates a sequence of shallow strike-slip ruptures of the Sarez-Karakul fault, *Geophysical Journal International*, 221(3), 1696–1718, doi:10.1093/gji/ggaa090.
- Elliott, J. R., R. J. Walters, and T. J. Wright (2016), The role of space-based observation in understanding and responding to active tectonics and earthquakes, *Nature Communications*, 7, 1–16, doi:10.1038/ncomms13844.
- Ergintav, S., R. Bürgmann, S. McClusky, R. Çakmak, R. E. Reilinger, O. Lenk, A. Barka, and H. Özener (2002), Postseismic Deformation near the İzmit Earthquake (17 August 1999, M7.5) Rupture Zone, *Bulletin of the Seismological Society of America*, 92(1), 194–207, doi:10.1785/0120000836.
- Farr, T. G., and M. Kobrick (2000), Shuttle radar topography mission produces a wealth of data, *EOS, Transactions American Geophysical Union*, 81(48), 583–585, doi:https://doi.org/10.1029/EO081i048p00583.
- Graham, L. (1974), Synthetic interferometer radar for topographic mapping, *Proceedings of the IEEE*, 62(6), 763–768, doi:10.5194/10.1109/PROC.1974.9516.
- Grandin, R., M.-P. Doin, L. Bollinger, B. Pinel-Puysségur, G. Ducret, R. Jolivet, and S. N. Sapkota (2012), Long-term growth of the Himalaya inferred from interseismic InSAR measurement, *Geology*, 40(12), 1059–1062, doi:10.1130/G33154.1.
- Hayes, G. P., G. L. Moore, D. E. Portner, M. Hearne, H. Flamme, M. Furtney, and G. M. Smoczyk (2018), Slab2 – a comprehensive subduction zone geometry model, *Science*, 362(6410), 58–61, doi:10.1126/science.aat4723.

- Hearn, E. H. (2003), What can GPS data tell us about the dynamics of post-seismic deformation?, *Geophysical Journal International*, 155(3), 753–777, doi:10.1111/j.1365-246X.2003.02030.x.
- Hearn, E. H., R. Bürgmann, and R. E. Reilinger (2002), Dynamics of İzmit Earthquake Postseismic Deformation and Loading of the Düzce Earthquake Hypocenter, *Bulletin of the Seismological Society of America*, 92(1), 172–193, doi:10.1785/0120000832.
- Heimann, S., H. Vasyura-Bathke, H. Sudhaus, M. P. Isken, M. Kriegerowski, A. Steinberg, and T. Dahm (2019), A Python framework for efficient use of pre-computed Green's functions in seismological and other physical forward and inverse source problems, *Solid Earth*, 10(6), 1921–1935, doi:10.5194/se-10-1921-2019.
- Hoffmann, F., S. Metzger, M. Moreno, Z. Deng, C. Sippl, F. Ortega-Culaciati, and O. Oncken (2018), Characterizing Afterslip and Ground Displacement Rate Increase Following the 2014 Iquique-Pisagua Mw8.1 Earthquake, Northern Chile, *Journal of Geophysical Research: Solid Earth*, 123(5), 4171–4192, doi:10.1002/2017JB014970.
- Huang, Z., and D. Zhao (2013), Mechanism of the 2011 Tohoku-oki earthquake (Mw9.0) and tsunami: Insight from seismic tomography, *Journal of Asian Earth Sciences*, 70-71, 160–168, doi:10.1016/j.jseas.2013.03.010.
- IPCC (2019), United Nation Intergovernmental Panel on Climate Change: Special Report on the Ocean and Cryosphere in a Changing Climate, *Cambridge University Press, Summary for Policymakers*, 3–35, doi:10.1017/9781009157964.001.
- Ischuk, A., R. Bendick, A. Rybin, P. Molnar, S. F. Khan, S. Kuzikov, S. Mohadjer, U. Saydullaev, Z. Ilyasova, G. Schelochkov, and A. V. Zubovich (2013), Kinematics of the Pamir and Hindu Kush regions from GPS geodesy, *Journal of Geophysical Research: Solid Earth*, 118(5), 2408–2416, doi:10.1002/jgrb.50185.
- Jara, J., A. Ozdemir, U. Dogan, R. Jolivet, Z. Cakir, and S. Ergintav (2022), Slow slip events captured by GNSS along the central section of the North Anatolian Fault, *EGU General Assembly 2022*, 75, EGU22–9541, doi:10.5194/egusphere-egu22-9541.
- Jin, Z., Y. Fialko, A. Zubovich, and T. Schöne (2022), Lithospheric Deformation Due To the 2015 M7.2 Sarez (Pamir) Earthquake Constrained by 5 years of Space Geodetic Observations, *Journal of Geophysical Research: Solid Earth*, 127(4), doi:10.1029/2021JB022461.
- Kääb, A., and M. Vollmer (2000), Surface Geometry, Thickness Changes and Flow Fields on Creeping Mountain Permafrost: Automatic Extraction by Digital Image Analysis, *Permafrost and Periglacial Processes*, 11(4), 315–326, doi:10.1002/1099-1530(200012)11:4<315::AID-PPP365>3.0.CO;2-J.
- Kagan, Y. Y., and D. D. Jackson (2013), Tohoku Earthquake: A Surprise?, *Bulletin of the Seismological Society of America*, 103(2B), 1181–1194, doi:10.1785/0120120110.
- Klotz, J., D. Angermann, M. G. W., R. Porth, C. Reigber, J. Reinking, J. Viramonte, R. Perdomo, V. H. Rios, S. Barrientos, R. Barriga, and O. Cifuentes (1999), GPS-derived Deformation of the Central Andes Including the 1995 Antofagasta Mw=8.0 Earthquake, *Pure and Applied Geophysics*, 3–4(154), 709–730, doi:10.1007/s000240050249.
- Klotz, J., Z. Deng, M. Moreno, G. Asch, M. Bartsch, and M. Ramatschi (2017), IPOC cGPS - continuous-mode GPS data in the IPOC Region, Northern Chile, *GFZ Data Services*, doi:10.5880/GFZ.1.1.2017.001.
- Kosari, E., M. Rosenau, and O. Oncken (2022), Strain Signals Governed by Frictional-Elastoplastic Interaction of the Upper Plate and Shallow Subduction Megathrust Interface Over Seismic Cycles, *Tectonics*, 41(5), e2021TC007,099, doi:10.1029/2021TC007099.
- Kreemer, C., G. Blewitt, and E. C. Klein (2014), A geodetic plate motion and Global Strain Rate Model, *Geochemistry, Geophysics, Geosystems*, 15(10), 3849–3889, doi:10.1002/2014GC005407.

- Kufner, S., B. Schurr, L. Ratschbacher, S. Murodkulov, S. Abdulhameed, A. Ischuk, S. Metzger, and N. Kakar (2018), Seismotectonics of the Tajik Basin and surrounding mountain ranges, *Tectonics*, 37(8), 2404–2424, doi:10.1029/2017TC004812.
- Kufner, S., N. Kakar, M. Bezada, W. Bloch, S. Metzger, X. Yuan, J. Mechie, L. Ratschbacher, S. S. Murodkulov, Z. Deng, and B. Schurr (2021), The Hindu Kush slab break-off as revealed by deep structure and crustal deformation, *Nature Communications*, 12(1), 1685, doi:10.1038/s41467-021-21760-w.
- Kulikova, G., B. Schurr, F. Krüger, E. Brzoska, and S. Heimann (2016), Source parameters of the Sarez-Pamir earthquake of 1911 February 18, *Geophysical Journal International*, 205(2), 1086–1098, doi:10.1093/gji/ggw069.
- Lamb, S., R. Arnold, and J. D. Moore (2018), Locking on a megathrust as a cause of distributed faulting and fault-jumping earthquakes, *Nature Geoscience*, 11(11), 871–875, doi:10.1038/s41561-018-0230-5.
- Lazecký, M., K. Spaans, P. J. González, Y. Maghsoudi, Y. Morishita, F. Albino, J. Elliott, N. Greenall, E. Hatton, A. Hooper, D. Juncu, A. McDougall, R. J. Walters, C. S. Watson, J. R. Weiss, and T. J. Wright (2020), LiCSAR: An Automatic InSAR Tool for Measuring and Monitoring Tectonic and Volcanic Activity, *Remote Sensing*, 12(15), 2430, doi:10.3390/rs12152430.
- Li, X., S. Jónsson, and Y. Cao (2021), Interseismic Deformation From Sentinel-1 Burst-Overlap Interferometry: Application to the Southern Dead Sea Fault, *Geophysical Research Letters*, 48(16), e2021GL093481, doi:10.1029/2021GL093481.
- Liu, L., M. D. Zoback, and P. Segall (1992), Rapid Intraplate Strain Accumulation in the New Madrid Seismic Zone, *Science*, 257(5077), 1666–1669, doi:10.1126/science.257.5077.1666.
- Liu, S., J.-M. Nocquet, X. Xu, S. Jónsson, G. Chen, X. Tan, and Y. Klinger (2022), recent-day uplift of the East Kunlun Shan, Northern Tibetan Plateau, *EGU General Assembly 2022, Vienna, Austria*, (EGU22-10281), doi:10.5194/egusphere-egu22-10281.
- Mai, P. M., and G. C. Beroza (2000), Source Scaling Properties from Finite-Fault-Rupture Models, *Bulletin of the Seismological Society of America*, 90(3), 604–615, doi:10.1785/0119990126.
- Massonnet, D., and K. L. Feigl (1998), Radar interferometry and its application to changes in the Earth's surface, *Reviews of Geophysics*, 36(4), 441–500, doi:10.1029/97RG03139.
- Massonnet, D., M. Rossi, C. Carmona, F. Adragana, G. Peltzer, K. Feigl, and T. Rabaute (1993), The displacement field of the Landers earthquake mapped by radar interferometry, *Nature*, (364), 138–142, doi:10.1038/364138a0.
- Massonnet, D., K. Feigl, M. Rossi, and F. Adragana (1994), Radar interferometric mapping of deformation in the year after the Landers earthquake, *Nature*, 369, 227–230, doi:10.1038/369227a0.
- Menke, W. (1989), *Geophysical Data Analysis: Discrete Inverse Theory*, Elsevier, New York, p. 289pp.
- Metzger, S., S. Jónsson, and H. Geirsson (2011), Locking depth and slip-rate of the Húsavík Flatey fault, North Iceland, derived from continuous GPS data 2006–2010, *Geophysical Journal International*, 187(2), 564–576, doi:10.1111/j.1365-246X.2011.05176.x.
- Metzger, S., S. Jónsson, G. J. K. Danielsen, S. Hreinsdóttir, F. Jouanne, D. Giardini, and T. Villemin (2013a), Present kinematics of the Tjörnes Fracture Zone, North Iceland, from campaign and continuous GPS measurements, *Geophysical Journal International*, 192(2), 441–455, doi:10.1093/gji/ggs032.
- Metzger, S., S. Jónsson, G. J. K. Danielsen, S. Hreinsdóttir, F. Jouanne, D. Giardini, and T. Villemin (2013b), Present kinematics of the Tjörnes fracture zone, North Iceland, from campaign and continuous GPS measurements, *Geophysical Journal International*, 192(2), 441–455, doi:10.1093/gji/ggs032.

- Metzger, S., B. Schurr, L. Ratschbacher, H. Sudhaus, S. Kufner, T. Schöne, Y. Zhang, M. Perry, and R. Bendick (2017), The 2015 Mw7.2 Sarez strike-slip earthquake in the Pamir interior: Response to the underthrusting of India's western promontory, *Tectonics*, 36(11), 2407–2421, doi:10.1002/2017TC004581R.
- Metzger, S., A. Ischuk, A. Akhmedov, Z. Ilyasova, M. Moreno, S. Murodkulov, and Z. Deng (2019), Survey mode GPS data in the West Pamir, Tajikistan, Central Asia, 2013–2016, *GFZ Data Services*, doi:10.5880/GFZ.4.1.2019.007.
- Metzger, S., A. Ischuk, Z. Deng, L. Ratschbacher, M. Perry, S. Kufner, R. Bendick, and M. Moreno (2020), Dense GNSS profiles across the northwestern tip of the India-Asia collision zone: triggered slip and westward flow of the Peter the First range, Pamir, into the Tajik depression, *Tectonics*, 39(2), 1–20, doi:10.1029/2019TC005797.
- Metzger, S., L. Gagala, L. Ratschbacher, M. Lazecký, Y. Maghsoudi, and B. Schurr (2021a), Tajik Depression and Greater Pamir Neotectonics from InSAR Rate Maps, *Journal of Geophysical Research: Solid Earth*, 126, e2021JB022,775, doi:10.1029/2021JB022775.
- Metzger, S., M. Lazecký, and Y. Maghsoudi (2021b), High-resolution rate maps from the Tajik basin and the Pamir, *GFZ Data Services*, doi:10.5880/GFZ.4.1.2021.005.
- Metzger, S., N. Kakar, A. Zubovich, M. Borisov, S. Saif, A. H. Panjsheri, J. R. Rahmani, M. Y. Zaryab, M. T. Rezai, Z. Deng, R. Bendick, S.-K. Kufner, and J. Okoev (2021c), Survey mode GNSS data, acquired 2014–2019 in the Afghan Hindu Kush and across northern Pamir margin, Central Asia, *GFZ Data Services*, doi:10.5880/GFZ.4.1.2021.003.
- Mohadjer, S., R. Bendick, A. Ischuk, S. Kuzikov, A. Kostuk, U. Saydullaev, S. Lodi, D. M. Kakar, A. Wasy, M. A. Khan, P. Molnar, R. Bilham, and A. V. Zubovich (2010), Partitioning of India-Eurasia convergence in the Pamir-Hindu Kush from GPS measurements, *Geophysical Research Letters*, 37(4), doi:10.1029/2009GL041737.
- Moreno, M., J. Bedford, J.-C. Baez, J. Klotz, F. Hoffmann, Z. Deng, I. Urrutia, C. Rojas, M. Shrivastava, F. Ortega-Culaciati, and E. Contreras-Reyes (2017), Survey Mode GPS data in the IPOC Region, Central Andes, Chile, *GFZ Data Services*, doi:10.5880/GFZ.4.1.2017.003.
- Moreno, M., S. Li, D. Melnick, J. R. Bedford, J. C. Baez, M. Motagh, S. Metzger, S. Vajedian, C. Sippl, B. D. Gutknecht, E. Contreras-Reyes, Z. Deng, A. Tassara, and O. Oncken (2018), Chilean megathrust earthquake recurrence linked to frictional contrast at depth, *Nature Geoscience*, 11(4), 285–290, doi:10.1038/s41561-018-0089-5.
- Morishita, Y., M. Lazecký, T. J. Wright, J. R. Weiss, A. Hooper, and J. R. Elliott (2020), LiCSBAS: An open-source InSAR time series analysis package integrated with the LiCSAR automated Sentinel-1 InSAR processor, *Remote Sensing*, 12(3), 5–8, doi:10.3390/rs12030424.
- Mosegaard, K., and A. Tarantola (1995), Monte-carlo sampling of solutions to inverse problems, *Journal of Geophysical Research: Solid Earth*, 100(B7), 12,431–12,447, doi:10.1029/94JB03097.
- Nicholls, R. J., and A. Cazenave (2010), Sea-Level Rise and Its Impact on Coastal Zones, *Science*, 328(5985), 1517–1520, doi:10.1126/science.1185782.
- Nicholls, R. J., D. Lincke, J. Hinkel, S. Brown, A. T. Vafeidis, B. Meyssignac, S. E. Hanson, J.-L. Merkens, and J. Fang (2021), A global analysis of subsidence, relative sea-level change and coastal flood exposure, *Nature Climate Change*, 11(4), 338–342, doi:10.1038/s41558-021-00993-z.
- Norabuena, E. O., T. H. Dixon, S. Stein, and C. G. Harrison (1999), Decelerating Nazca-South America and Nazca-Pacific plate motions, *Geophysical Research Letters*, 26(22), 3405–3408, doi:10.1029/1999GL005394.
- Okada, Y. (1985), Surface deformation due to shear and tensile faults in a half-space, *Bulletin of the Seismological Society of America*, 75(4), 1135–1154, doi:10.1785/BSSA0750041135.

- Ou, Q., S. Daout, J. R. Weiss, L. Shen, M. Lazecký, T. J. Wright, and B. E. Parsons (2022), Large-Scale Interseismic Strain Mapping of the NE Tibetan Plateau From Sentinel-1 Interferometry, *Journal of Geophysical Research: Solid Earth*, 127(6), e2022JB024176, doi:10.1029/2022JB024176.
- Passarelli, L., E. Rivalta, S. Jónsson, M. Hensch, S. Metzger, S. S. Jakobsdóttir, F. Maccaferri, F. Corbi, and T. Dahm (2018), Scaling and spatial complementarity of tectonic earthquake swarms, *Earth and Planetary Science Letters*, 482, 62–70, doi:10.1016/j.epsl.2017.10.052.
- Peltzer, G., P. Rosen, F. Rogez, and K. Hudnut (1998), Poroelastic rebound along the Landers 1992 earthquake surface rupture, *Journal of Geophysical Research: Solid Earth*, 103(B12), 30,131–30,145, doi:10.1029/98JB02302.
- Peña, C., S. Metzger, O. Heidbach, J. Bedford, B. Bookhagen, M. Moreno, O. Oncken, and F. Cotton (2022), Role of Poroelasticity During the Early Postseismic Deformation of the 2010 Maule Megathrust Earthquake, *Geophysical Research Letters*, 49(9), e2022GL098144, doi:10.1029/2022GL098144.
- Peng, Z., and J. Gomberg (2010), An integrated perspective of the continuum between earthquakes and slow-slip phenomena, *Nature Geoscience*, 3(9), 599–607, doi:10.1038/ngeo940.
- Perry, M., N. Kakar, A. Ischuk, S. Metzger, R. Bendick, P. Molnar, and S. Mohadjer (2018), Little Geodetic Evidence for Localized Indian Subduction in the Pamir-Hindu Kush of Central Asia, *Geophysical Research Letters*, 46(1), 109–118, doi:10.1029/2018GL080065.
- Pilger, C., P. Gaebler, P. Hupe, A. C. Kalia, F. M. Schneider, A. Steinberg, H. Sudhaus, and L. Ceranna (2021), Yield estimation of the 2020 Beirut explosion using open access waveform and remote sensing data, *Scientific Reports*, 11, 14,144, doi:10.1038/s41598-021-93690-y.
- Plattner, C., A. Parizzi, S. Carena, S. Rieger, A. M. Friedrich, A. Abolghasem, and F. DeZan (2021), Long-lived afterslip of the 2013 Mw6.1 Minab earthquake detected by Persistent Scatterer interferometry along the Irer fault (western Makran-Zagros transition zone, Iran), *Geophysical Journal International*, 229(1), 171–185, doi:10.1093/gji/ggab456.
- Pollitz, F. F., G. Peltzer, and R. Bürgmann (2000), Mobility of continental mantle: Evidence from postseismic geodetic observations following the 1992 Landers earthquake, *Journal of Geophysical Research: Solid Earth*, 105(B4), 8035–8054, doi:10.1029/1999JB900380.
- Pollitz, F. F., C. Wicks, and W. Thatcher (2001), Mantle Flow Beneath a Continental Strike-Slip Fault: Postseismic Deformation After the 1999 Hector Mine Earthquake, *Science*, 293(5536), 1814–1818, doi:10.1126/science.1061361.
- Rouet-Leduc, B., R. Jolivet, M. Dalaison, P. A. Johnson, and C. Hulbert (2021), Autonomous extraction of millimeter-scale deformation in InSAR time series using deep learning, *Nature Communications*, 12, 6480, doi:10.1038/s41467-021-26254-3.
- Savage, J. C. (1983), A dislocation model of strain accumulation and release at a subduction zone, *Journal of Geophysical Research*, 88, 4984–4996, doi:10.1029/JB088iB06p04984.
- Savage, J. C. (1990), Equivalent strike-slip earthquake cycles in half-space and lithosphere-asthenosphere earth models, *Journal of Geophysical Research: Solid Earth*, 95(B4), 4873–4879, doi:10.1029/JB095iB04p04873.
- Schmidt, D. A., and R. Bürgmann (2003), Time-dependent land uplift and subsidence in the Santa Clara valley, California, from a large interferometric synthetic aperture radar data set, *Journal of Geophysical Research: Solid Earth*, 108(B9), 2416, doi:10.1029/2002JB002267.

- Schöne, T., C. Zech, K. Unger-Shayesteh, V. Rudenko, H. Thoss, H.-U. Wetzel, A. Gafurov, J. Illigner, and A. Zubovich (2013), A new permanent multi-parameter monitoring network in Central Asian high mountains: from measurements to data bases, *Geoscientific Instrumentation, Methods and Data Systems*, 2(1), 97–111, doi:10.5194/gi-2-97-2013.
- Sieh, K., D. H. Natawidjaja, A. J. Meltzner, C.-C. Shen, H. Cheng, K.-S. Li, B. W. Suwargadi, J. Galetzka, B. Philibosian, and R. L. Edwards (2008), Earthquake Supercycles Inferred from Sea-Level Changes Recorded in the Corals of West Sumatra, *Science*, 322(5908), 1674–1678, doi:10.1126/science.1163589.
- Simran, S., P. Gilles, Z. Ailin, M. Lingsen, L. Cunren, L. Paul, and F. Eric (2017), Fault geometry of 2015, Mw7.2 Murghab, Tajikistan earthquake controls rupture propagation: Insights from InSAR and seismological data, *Earth and Planetary Science Letters*, 462, 132–141, doi:j.epsl.2017.01.018.
- Socquet, A., J. P. Valdes, J. Jara, F. Cotton, A. Walpersdorf, N. Cotte, S. Specht, F. Ortega-Culaciati, D. Carrizo, and E. Norabuena (2017), An 8 month slow slip event triggers progressive nucleation of the 2014 Chile megathrust, *Geophysical Research Letters*, 44(9), 4046–4053, doi:10.1002/2017GL073023.
- Stein, S., R. J. Geller, and M. Liu (2012), Why earthquake hazard maps often fail and what to do about it, *Tectonophysics*, 562-563, 1–25, doi:10.1016/j.tecto.2012.06.047.
- Takai, N., M. Shigefuji, S. Rajaure, S. Bijukchhen, M. Ichiyangi, M. R. Dhital, and T. Sasatani (2016), Strong ground motion in the Kathmandu Valley during the 2015 Gorkha, Nepal, earthquake, *Earth, Planets and Space*, 68(1), 10, doi:10.1186/s40623-016-0383-7.
- Tarantola, A. (2005), *Inverse problem theory and methods for model parameter estimation*, SIAM.
- Tay, C., E. O. Lindsey, S. T. Chin, J. W. McCaughey, D. Bekaert, M. Nguyen, H. Hua, G. Manipon, M. Karim, B. P. Horton, T. Li, and E. M. Hill (2022), Sea-level rise from land subsidence in major coastal cities, *Nature Sustainability*, 193(3), doi:10.1038/s41893-022-00947-z.
- Tormann, T., S. Wiemer, S. Metzger, A. Michael, and J. L. Hardebeck (2013), Size distribution of Parkfield's microearthquakes reflects changes in surface creep rate, *Geophysical Journal International*, 193(3), 1474–1478, doi:10.1093/gji/ggt093.
- Torres, R., P. Snoeij, D. Geudtner, D. Bibby, M. Davidson, E. Attema, P. Potin, B. Rommen, N. Floury, M. Brown, I. N. Traver, P. Deghaye, B. Duesmann, B. Rosich, N. Miranda, C. Bruno, M. L'Abbate, R. Croci, A. Pietropaolo, M. Huchler, and F. Rostan (2012), GMES Sentinel-1 mission, *Remote Sensing of Environment*, 120, 9–24, doi:10.1016/j.rse.2011.05.028.
- United Nation Resolution (2015), Transforming our world: the 2030 Agenda for Sustainable Development, *A/RES/70/1, Adopted by General Assembly on 25 Sept. 2015*.
- van Hinsbergen, D. J. J., P. C. Lippert, G. Dupont-Nivet, N. McQuarrie, P. V. Doubrovine, W. Spakman, and T. H. Torsvik (2012), Greater India Basin hypothesis and a two-stage Cenozoic collision between India and Asia, *Proceedings of the National Academy of Sciences of the United States of America*, 109(20), 7659–7664, doi:10.1073/pnas.1117262109.
- Vasyura-Bathke, H., J. Dettmer, A. Steinberg, S. Heimann, M. P. Isken, O. Zielke, P. M. Mai, H. Sudhaus, and S. Jónsson (2020), The Bayesian Earthquake Analysis Tool, *Seismological Research Letters*, 91(2A), 1003–1018, doi:10.1785/0220190075.
- Wang, K., Y. Hu, and J. He (2012), Deformation cycles of subduction earthquakes in a viscoelastic Earth, *Nature*, 484(7394), 327–332, doi:10.1038/nature11032.

- Weiss, J. R., R. J. Walters, Y. Morishita, T. J. Wright, M. Lazecky, H. Wang, E. Hussain, A. J. Hooper, J. R. Elliott, C. Rollins, C. Yu, P. J. González, K. Spaans, Z. Li, and B. Parsons (2020), High-Resolution Surface Velocities and Strain for Anatolia From Sentinel-1 InSAR and GNSS Data, *Geophysical Research Letters*, 47(17), e2020GL087376, doi:10.1029/2020GL087376.
- Werner, C., U. Wegmüller, T. Strozzi, and A. Wiesmann (2000), GAMMA SAR and interferometric processing software, *Proceedings of the ERS-ENVISAT symposium, Gothenburg, Sweden*, p. 1620.
- Wright, T. J., B. Parsons, P. C. England, and E. J. Fielding (2004), InSAR Observations of Low Slip Rates on the Major Faults of Western Tibet, *Science*, 305(5681), 236–239, doi:10.1126/science.1096388.
- Xu, X., D. T. Sandwell, and B. R. Smith-Konter (2020), Coseismic Displacements and Surface Fractures from Sentinel-1 InSAR : 2019 Ridgecrest Earthquakes, *Seismological Research Letters*, 91(4), 1997–1985, doi:10.1785/0220190275.
- Yu, C., Z. Li, N. T. Penna, and P. Crippa (2018), Generic Atmospheric Correction Model for Interferometric Synthetic Aperture Radar Observations, *Journal of Geophysical Research: Solid Earth*, 123(10), 9202–9222, doi:10.1029/2017JB015305.
- Yun, S.-H., K. Hudnut, S. Owen, F. Webb, M. Simons, P. Sacco, E. Gurrola, G. Manipon, C. Liang, E. Fielding, P. Milillo, H. Hua, and A. Coletta (2015), Rapid Damage Mapping for the 2015 Mw7.8 Gorkha Earthquake Using Synthetic Aperture Radar Data from COSMO-SkyMed and ALOS-2 Satellites, *Seismological Research Letters*, 86(6), 1549–1556, doi:10.1785/0220150152.
- Zandt, G., and C. J. Ammon (1995), Continental crust composition constrained by measurements of crustal Poisson's ratio, *Nature*, 374, 152–154, doi:10.1038/374152a0.
- Zubovich, A. V., X.-Q. Wang, Y. G. Scherba, G. G. Schelochkov, R. Reilinger, C. Reigber, O. I. Mosienko, P. Molnar, W. Michajljow, V. I. Makarov, J. Li, S. I. Kuzikov, T. A. Herring, M. W. Hamburger, B. H. Hager, Y.-M. Dang, V. D. Bragin, and R. T. Beisenbaev (2010), GPS velocity field for the Tien Shan and surrounding regions, *Tectonics*, 29(6), doi:10.1029/2010TC002772.
- Zubovich, A. V., T. Schöne, S. Metzger, O. I. Mosienko, S. Mukhamediev, A. Sharshebaev, and C. Zech (2016), Tectonic interaction between the Pamir and Tien Shan observed by GPS, *Tectonics*, 35(2), 283–292, doi:10.1002/2015TC004055.
- Zubovich, A. V., S. Metzger, T. Schöne, J. Kley, O. Mosienko, C. Zech, B. Moldobekov, and A. Sharshebaev (2022), Cyclic fault slip under the magnifier: Co- and postseismic response of the Pamir front to the 2015 Mw7.2 Central Pamir earthquake, *Tectonics*, 41, e2022TC007213.

Acknowledgements

My post-doctoral journey to achieve scientific independence was a tough mental struggle: More than once I longed for somebody insinuating what to study with which methods and in what part of the world! Now, in retrospection, I realize that my initial post-doctoral helplessness was partially a natural consequence of entering a completely new research environment, and I had to catch up with a lot of basic knowledge I was never properly trained in. So, without this six-year household position and the luxurious legal and financial state support for young parents, academia would have lost me. So thanks, GFZ and thanks, Germany! Beyond the economics, I was mentally and scientifically carried along during that time by so many clever, motivating, likeable, compassionate, interesting, fun and supporting people:

Bodo, Freysteinn, Roland and Peter for supporting my – rather spontaneous – idea to write a habilitation.

Most substantial are the GNSS-survey teams in Tajikistan, Kyrgyzstan, and Afghanistan under the lead of Anatoly Ischuk, Alexander Zubovich/Mikhael Borisov, and Najib Kakar. I am particularly thankful to the Afghan team (S. S., A. P., J. R. and Y. Z.) and in humble admiration how it spat in the devils face to collect high-quality GNSS data for the international scientific community *right* under the eyes of the Taliban. Without the tireless commitment and extremely useful knowledge of the local conditions of all these people, none of the GNSS data presented here would have been acquired.

Tilo Schöne invited me to the analysis of the high-rate GNSS data collected at the Pamir's northern margin, which opened whole new research opportunities. As important was the support of the first-class geodesists Mitja Bartsch and Zhiguo Deng that reliably provided me with daily positioning time-series.

I am proud of the European Union and her pioneering work in handling radar data in an open-access, democratic fashion across borders since long. For technical InSAR questions I could always consult with my clever fellow sufferers Henriette Sudhaus, Hannes Vasyura-Bathke and Julia Neelmeijer, and – once LiCSAR/LiCSBAS came to life – Jonathan Weiss, Milan Lazecký, Yasser Maghsoudi and Yu Morishita from the famous COMET crew. Jonathan Bedford and Marcos Moreno were the people to discuss time-series issues, and my room mates Sofia Kufner and Wasja Bloch were always keen to explain the reliability of seismic observations and the beauty (and madness) of *awk* and GMT.

Bernd Schurr, Lothar Ratschbacher and Łukasz Gała were my teachers on the regional tectonics. Without them my data interpretations would be useless. Onno Oncken helped to put everything in a greater scientific context. Rebecca Bendick, on the other hand, reminds me that one should keep the eyes constantly open for another possible solution and that it is the *people* that count, not the *digits*.

Felix Hoffmann, Thorben Schöfisch, Marcus Liefeld and Najib were my guinea pigs of supervision techniques and I want to thank them for this (and to apologize).

I enjoy being part of the Lithosphere Dynamics section at GFZ under the lead of Onno Oncken (now Claudio Faccenna) and Franziska Alberg. It feels good to be part of such a multi-disciplinary, multi-national group that challenges you everyday in how to communicate and transfer science among geoscientific peers.

Last, but not least, the ever-present doubts of my role in science and the frequent motivation lows are so much easier to conquer when being aware of esteemed colleagues like Eleonora Rivalta, Henriette, Julia, Rebecca, Hoby Razafindrakoto, Eline Le Breton, and Silvia Crosetto. You rock, girls, you are seen, and you are damn important!